

Structural and biochemical characterization of enzymes used by  
anaerobic energy extremophiles for sulfur and carbon  
transformation

Dissertation

zur Erlangung des Doktorgrades

der Naturwissenschaften

- Dr. rer. Nat.-

dem Fachbereich 2 Biologie/Chemie

der Universität Bremen

vorgelegt von

**Marion Jespersen**



Die vorliegende Arbeit wurde in der Zeit vom Juni 2019 bis August 2023 am Max-Planck-Institut für Marine Mikrobiologie in Bremen im Rahmen des Programms „International Max Planck Research School for Marine Microbiology: MarMic“, in der Gruppe „Mikrobielle Metabolismen“ angefertigt.

Gutachter: Dr. Tristan Wagner

Gutachterin: PD. Dr. Christiane Dahl

Gutachterin: Prof. Dr. Inês Cardoso Pereira

Prüfer: Prof. Dr. Rudolf Amann

Prüfer: Dr. Tristan Wagner

Prüferin: PD. Dr. Christiane Dahl

Prüferin: Prof. Dr. Inês Cardoso Pereira

Tag des Promotionskolloquiums: 24.08.2023

© 2023

Marion Jespersen

ORCID: 0000-0002-8859-3335

*The river knows everything; one can learn everything from it.  
You have already learned from the river that its good to strive downwards, to sink,  
to seek the depths.*

- Hermann Hesse, Siddhartha



# Contents

Summary .....	9
Zusammenfassung.....	11
Abbreviations.....	13
Chapter I Introduction.....	15
1.1 Hydrogenotrophic methanogenic archaea .....	17
1.4 Sulfate-reducing bacteria and alkanotrophic archaea .....	26
1.5 <i>Methanotherix</i> - an acetoclastic methanogen with the ability to reduce CO <sub>2</sub> .....	31
1.6 Autotrophic acetogens and their CO <sub>2</sub> and H <sub>2</sub> transformation capabilities.....	33
1.8 Research questions of the thesis .....	41
1.9 Contributions to the Manuscripts.....	43
Chapter II Assimilatory sulfate reduction in the marine methanogen <i>Methanothermococcus thermolithotrophicus</i> .....	47
Chapter III Structural and spectroscopic insights into the redox cycles of the active site of the [NiFeSe] and [NiFe] hydrogenases of group 3.....	115
Chapter IV Structures of the sulfite detoxifying F <sub>420</sub> -dependent enzyme from <i>Methanococcales</i> .....	149
Chapter V Structural elucidation of the dissimilatory sulfate-reduction pathway of an ethane-degrading microbial consortium .....	215
Chapter VI Structure of a methane-generating enzyme isolated from wastewater treatment plant sludge .....	263
Chapter VII CO <sub>2</sub> -Fixation Strategies in Energy Extremophiles: What Can We Learn From Acetogens? .....	285
Chapter XIII Discussion and perspectives .....	307
8.1 A unique pathway to assimilate sulfate in <i>Methanothermococcus thermolithotrophicus</i> .....	307
8.2 A snapshot of the SO <sub>4</sub> <sup>2-</sup> reduction pathway from an ethanotrophic consortium.....	318
8.3 Crystallization as a selective process to ultimately separate individual proteins from microbial dark matter .....	319

8.4 CO <sub>2</sub> fixation machinery of autotrophic acetogens as a promising avenue for carbon sequestration - Hyt/FdhA, a case study.....	320
8.5 Concluding remarks.....	326
References for Introduction and Discussion .....	329
Appendix.....	345
Acknowledgements.....	347



# Summary

Anaerobic microorganisms shape the global element cycle and offer the potential for the discovery of new enzymes with powerful bioconversion abilities. Yet, little is known about them because many microbes are difficult to isolate and cultivate. This thesis studies the metabolic pathways of methanogens, sulfate-reducing bacteria, and autotrophic acetogens, using pure cultures and microbial communities. As their metabolisms provide near-zero ATP yield under physiological conditions, they rely on energy-saving mechanisms to enable survival and growth. The **goal of my PhD thesis** is to explore the sophisticated machinery and efficient pathways of these energy extremophiles and to unravel, at the molecular level, the key players involved in assimilatory and energetic processes, particularly for the elements sulfur and carbon.

**Chapter II** reports how the marine methanogen *Methanothermococcus thermolithotrophicus* assimilates sulfate through a unique combination of assimilatory and dissimilatory-like sulfate reduction enzymes and provides a snapshot of the first sulfate assimilation pathway from a methanogen. **Chapter III** describes the F<sub>420</sub>-dependent [NiFe] hydrogenase (Frh), which provides reduced F<sub>420</sub> to fuel several metabolic pathways in methanogens. The [NiFeSe] and [NiFe] isoforms have been structurally characterized, and spectroscopic studies of the [NiFe] active site capture different redox states. **Chapter IV** describes the structural organization and the electron transfer path of the F<sub>420</sub>-dependent sulfite reductase, the final enzyme in the sulfate reduction pathway of *M. thermolithotrophicus*, demonstrating unidirectional sulfite reduction and proposing it as the template for the primordial sulfite reductase. **Chapter V** explores the sulfate reduction machinery from an ethane-degrading sulfate-reducing consortium. The main cytosolic enzymes of the dissimilatory sulfate-reducing bacterium were purified and structurally characterized, leading to surprises regarding their organization. In **Chapter VI**, I purify the methyl-coenzyme M reductase (MCR) from *Methanotherrix*, a methanogen considered to be the prime methane producer. The originality lies in the methodology, as the enzyme was isolated from a wastewater sediment sludge and ultimately purified by crystallization. **Chapter VII** reviews the CO<sub>2</sub> fixation strategies of autotrophic acetogenic bacteria by using the structural information obtained from enzymes belonging to hydrogenotrophic methanogens. **In summary**, this work has revealed a unique metabolic pathway and enzymes, providing valuable insights to their reaction mechanisms and potential applications.



# Zusammenfassung

Anaerobe Mikroorganismen prägen den globalen Elementkreislauf und bieten das Potenzial zur Entdeckung neuer Enzyme mit leistungsfähigen biochemischen Umwandelungs-kapazitäten. Dennoch ist wenig über sie bekannt, da viele Mikroben schwierig zu isolieren und zu kultivieren sind. In dieser Arbeit werden die Stoffwechselwege von Methanogenen, Sulfat reduzierenden Bakterien und autotrophen Acetogenen unter Verwendung von Reinkulturen und Mesokosmenproben untersucht. Da ihre Stoffwechselprozesse unter physiologischen Bedingungen kaum ATP-Ausbeute liefern, sind sie auf energiesparende Mechanismen angewiesen, um das Überleben und Wachstum zu gewährleisten. **Ziel meiner Doktorarbeit** ist es, die ausgeklügelte Maschinerie und effizienten Stoffwechselwege dieser Energie-Extremophilen zu erforschen und auf molekularer Ebene die Hauptakteure bei assimilatorischen und energetischen Prozessen, insbesondere für die Elemente Schwefel und Kohlenstoff, zu entschlüsseln.

**Kapitel II** berichtet, wie die marine Methanogene *Methanothermococcus thermolithotrophicus* Sulfat durch eine einzigartige Kombination von assimilatorischen und dissimilatorisch-ähnlichen Sulfatreduktionsenzymen assimiliert, und liefert einen Schnapschuss des ersten Sulfatassimilationsweges einer methanogenen Mikrobe. In **Kapitel III** wird die F<sub>420</sub>-abhängige [NiFe]-Hydrogenase (Frh) beschrieben, die reduziertes F<sub>420</sub> für verschiedene Stoffwechselprozesse in Methanogenen bereitstellt. Die [NiFeSe]- und [NiFe]-Isoformen wurden strukturell charakterisiert, und spektroskopische Untersuchungen des [NiFe]-aktiven Zentrums zeigen den gesamten Redoxzyklus. **Kapitel IV** beschreibt die strukturelle Organisation und den Elektronentransferweg der F<sub>420</sub>-abhängigen Sulfitreduktase, dem letzten Enzym im Sulfatreduktionsweg von *M. thermolithotrophicus*. Das Enzym führt eine unidirektionale Sulfitreduktion durch und wird als Modell für die ursprüngliche Sulfitreduktase vorgeschlagen. **Kapitel V** erforscht die Maschinerie der Sulfat Reduktion eines Ethan-abbauenden, Sulfat-reduzierenden Konsortiums. Die Hauptenzymkomplexe des dissimilatorischen Sulfat reduzierenden Bakteriums wurden aufgereinigt und strukturell charakterisiert, was zu überraschenden Erkenntnissen über ihre Organisation führte. In **Kapitel VI** reinige ich die Methyl-Coenzym-M-Reduktase (MCR) aus einem Methanotrix auf, einem Methanogen, das als wichtigster Methanproduzent gilt. Die Originalität liegt in der Methodik, da das Enzym aus

Abwassersedimentschlamm isoliert und schließlich durch Kristallisation aufgereinigt wurde. In **Kapitel VII** werden die CO<sub>2</sub>-Fixierungsstrategien autotropher acetogener Bakterien anhand der Strukturinformationen von Enzymen hydrogenotropher Methanogenen untersucht.

Zusammenfassend lässt sich sagen, dass diese Arbeit einen einzigartigen Stoffwechselweg und Enzyme aufgedeckt hat, die wertvolle Einblicke in ihre Reaktionsmechanismen und potentiellen Anwendungen liefern.

# Abbreviations

APSR	APS reductase
APSK	APS kinase
ANME	Anaerobic methanotrophic archaea
AOA	Anaerobic oxidation of alkanes
AOE	Anaerobic oxidation of ethane
AOM	Anaerobic oxidation of methane
ATPS	ATP sulfurylase
APS	Adenosine 5'-phosphosulfate
CODH/ACS	CO dehydrogenase/Acetyl-CoA synthase
DIET	Direct interspecies electron transfer
Dsr	Dissimilatory sulfite reductase
ECR	Ethyl-CoM reductase
FNir	F <sub>420</sub> -dependent nitrite reductase
Frh	F <sub>420</sub> reducing hydrogenase
Fsr	F <sub>420</sub> -dependent sulfite reductase
Ftr	Formylmethanofuran:H <sub>4</sub> MPT formyltransferase
HDCR	Hydrogen dependent CO <sub>2</sub> reductase
HytA-E <sub>1,2</sub> /FdhA	NADP-specific [FeFe]-hydrogenase with a Formate dehydrogenase
Mcr	Methyl-coenzyme M reductase
Methenyl-H <sub>4</sub> MPT <sup>+</sup>	Methenyltetrahydromethanopterin
PAP	3'-Phosphoadenosine-5'-phosphate
PAPP	PAP phosphatase
PAPS	3'-Phosphoadenosine-5'-phosphosulfate
PAPSR	PAPS reductase
aSir	Assimilatory sulfite reductase
SMTZ	Sulfate methane transition zone
SRB	Sulfate reducing bacteria
SRM	Sulfate reducing microorganisms



# Chapter I

## Introduction

Our modern society faces two major challenges: to prevent further global warming caused by the accumulation of greenhouse gases in the atmosphere and to maintain a supply of green energy to meet our growing needs. Renewable energy in the form of dihydrogen ( $\text{H}_2$ , the simplest and most abundant molecule in the universe), produced chemically from wind and solar sources (e.g. by electrolysis of water), has great potential for transient energy storage. Its oxidation generates electricity on demand, and its combustion releases a large amount of energy without generating greenhouse gases, making it an attractive means to replace fossil fuels and reduce  $\text{CO}_2$  emissions<sup>1,2</sup>. However, its instability makes it difficult to store and transport over long periods of time<sup>2,3</sup>. Scientists are therefore exploring ways to combine carbon capture with the conversion of  $\text{H}_2$  into safer and more stable energy sources such as formate ( $\text{HCOO}^-$ ), methane ( $\text{CH}_4$ ), and other renewable biofuels<sup>4-6</sup>. Despite progress in this area, activating the highly stable  $\text{CO}_2$  molecule remains a challenging task for chemists<sup>4</sup>. One promising approach involves the use of microorganisms, such as methanogenic archaea, or acetogenic bacteria, which are efficient gas converters (**Figure 1**)<sup>7-9</sup>.

What these microbes have in common is that they use ancient metabolic pathways that likely evolved in the earliest stages of Life on Earth, possibly more than 3.5 billion years ago<sup>10-12</sup>. Inorganic gases, such as  $\text{H}_2$ ,  $\text{H}_2\text{S}$ ,  $\text{CO}$ , and  $\text{CO}_2$ , were abundant on early Earth, and microbes evolved highly efficient catalysts to convert these simple molecules into biomass and energy. However, the Gibbs free energy of the metabolic reactions is close to the equilibrium, meaning that the metabolisms have a very low chemical energy yield and the microbes have adapted their physiology and metabolism to subsist at the thermodynamic limit of Life<sup>13</sup>. One of the greatest mysteries is how these organisms can survive in conditions that provide only marginal energy for cell growth and division and seem to barely sustain basic cellular functions<sup>14</sup>. Having evolved before the Great Oxygenation Event (about 2.3 billion years ago), they are anaerobes that contain a variety of oxygen-sensitive metallo-containing enzymes that have specialized over billions of years to catalyze challenging reactions. Despite their ancient origins, restriction to anoxic niches,

and energy constraints, organisms such as methanogenic archaea, sulfate-reducing bacteria, and acetogenic bacteria have shaped, are shaping, and will continue to shape our planet, as they are key drivers of the carbon cycle<sup>15-18</sup>. In addition, they have proven to be essential pillars of anaerobic biotechnological processes, by converting pollutants, such as waste gases, into valuable resources that can be used for carbon sequestration or as renewable energy sources<sup>19,20</sup>. By harnessing the power of anaerobic energy extremophiles, we can move closer to combating climate change while meeting our energy needs in a sustainable way. However, to fully exploit the potential of promising microbial candidates, we need to expand our knowledge about their physiology, evolutionary trajectories, and enzymatic machinery. In this thesis, we are conducting fundamental research on metabolic pathways and specific enzymes from energy extremophiles that might provide new avenues for applied research. As Max Planck himself said: “Insight must precede application”.

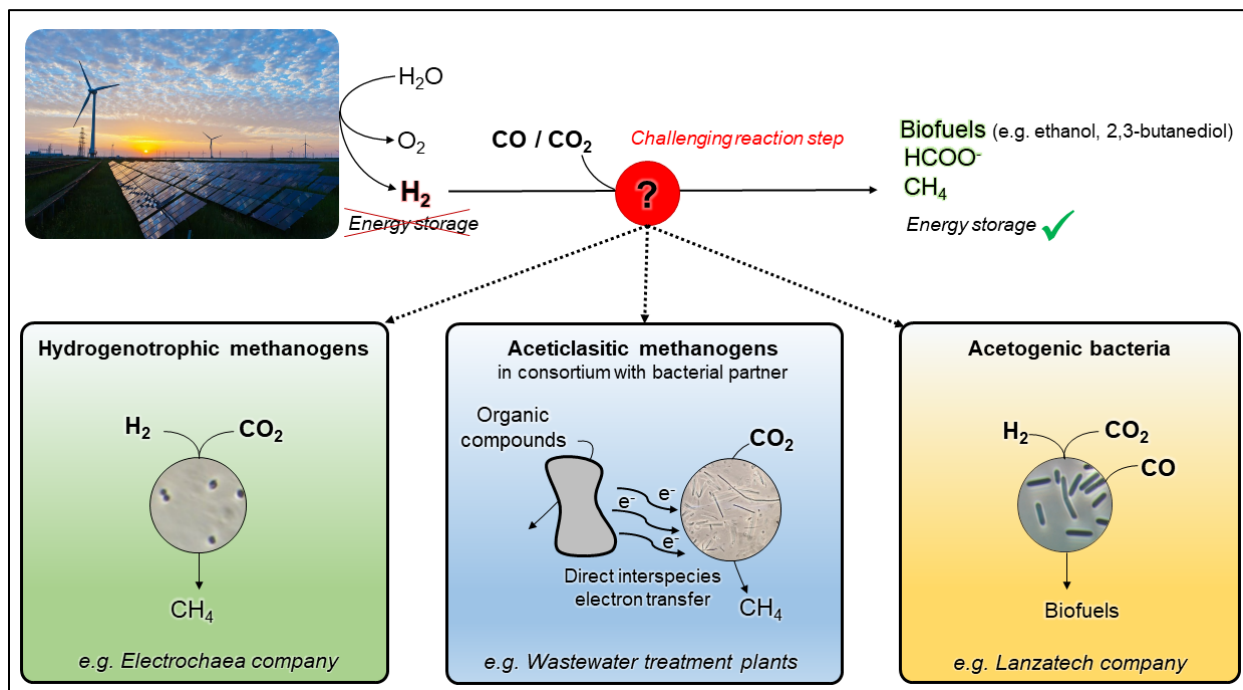


**Figure 1. Examples of microorganisms used to process CO<sub>2</sub>/CO capture while facilitating safe energy storage.** The companies Electrochaeta (<https://www.electrochaeta.com/>) and LanzaTech (<https://lanzatech.com/>) are already successfully using a hydrogenotrophic methanogen and an acetogenic bacterium respectively as gas converters.



## 1.1 Hydrogenotrophic methanogenic archaea

The simplest hydrocarbon CH<sub>4</sub> has become a valuable energy carrier in our society and is used in various applications, ranging from heating to being an ingredient in common fabrics, fertilizers, or rocket engines<sup>21-23</sup>. However, it is also the second most potent anthropogenic greenhouse gas after CO<sub>2</sub> (ref. 24). CH<sub>4</sub> can absorb significantly more energy and has a global warming potential 28-36 times higher than CO<sub>2</sub> (ref. 25). Regulating the atmospheric input of this hydrocarbon is therefore a critical step in global climate management.

The largest biogenic source of CH<sub>4</sub> on Earth are methanogenic microorganisms, which are responsible for half of the CH<sub>4</sub> produced annually (about 1 billion tons of CH<sub>4</sub> per year)<sup>15</sup>, and thus regulate the climate on a global scale<sup>26</sup>. All known methanogens are strictly anaerobic archaea, predominantly belonging to the phylum *Euryarchaeota*, but have also been discovered in the phyla *Verstraetearchaeota*, and microbes carrying genes that encode for the complete or partial methanogenesis pathway have recently been found in *Korarchaeota* and putatively *Bathyarchaeota*<sup>27-30</sup>. To date, they have been classified into eight orders: *Methanococcales*, *Methanopyrales*, *Methanobacteriales*, *Methanomicrobiales*, *Methanosarcinales*, *Methanocellales*, *Methanonatronarchaeales* and *Methanomassiliicoccales*<sup>15,31,32</sup>. Based on the substrates used for CH<sub>4</sub> production, three main methanogenesis pathways have been described: hydrogenotrophic (H<sub>2</sub>/CO<sub>2</sub>, HCOO<sup>-</sup>), methylotrophic (methylated compounds) and acetoclastic (acetate). However, it should be noted that some methanogens can use alternative substrates such as carbon monoxide (CO), alcohols, or iron in the presence of H<sub>2</sub> (ref. 33).

Methanogens can also be classified into two groups based on the presence or absence of b-type cytochromes<sup>15</sup>. Methanogens with b-type cytochromes (all members of the order *Methanosarcinales*) were reported to have a wider substrate range and higher growth yields than the methanogens that lack cytochromes<sup>15,34</sup>.

Hydrogenotrophic methanogenesis is the most widespread methanogenic pathway and has been proposed as the ancestral form of CH<sub>4</sub> production<sup>27</sup>. Hydrogenotrophic methanogens occur in environments characterized by the absence of electron acceptors other than CO<sub>2</sub> (refs. 15,35). They grow chemoautotrophically on H<sub>2</sub>, CO<sub>2</sub> (Reaction 1) or HCOO<sup>-</sup> and conserve energy by producing CH<sub>4</sub>. Under physiological conditions, only half of an ATP is generated per CH<sub>4</sub> formed, which is about 60 times less ATP than when a molecule of glucose is completely oxidized by aerobes.



Biogenic CH<sub>4</sub>, produced by methanogens, is already being used as an alternative to fossil natural gas. For example, the company Electrochaea uses a selectively evolved hydrogenotrophic methanogen to synthesize renewable CH<sub>4</sub> from CO<sub>2</sub> and H<sub>2</sub> (**Figure 1**, <https://www.electrochaea.com/>). The power-to-gas process allows the recycling of CO<sub>2</sub> (e.g. from industrial processes) and the use of renewable H<sub>2</sub> generated from renewable electricity to produce CH<sub>4</sub> that can be injected into the gas grid.

This technology, which harnesses the metabolic capabilities of hydrogenotrophic methanogens, is already leading the way towards a carbon-neutral society. However, to fully exploit the potential of these microorganisms, they need to be better understood and the cultivation conditions need to be optimized.

### **Alternative sulfur substrates to H<sub>2</sub>S for hydrogenotrophic methanogens**

One bottleneck in the cultivation of methanogens is the requirement for hydrogen sulfide (H<sub>2</sub>S). It serves as a sulfur source and creates the reducing conditions necessary for the growth (-200 to -300 mV)<sup>37</sup>. Like most organisms that originated before the Great Oxygenation Event (~2.4 billion years ago), methanogens show a remarkable tolerance to sulfide<sup>38</sup>. By growing on H<sub>2</sub>S/HS<sup>-</sup>, methanogens can incorporate sulfide via interprotein persulfide or directly into proteins and cofactors<sup>39-41</sup>. In fact, most of the biological sulfur compounds are sulfides, present in the form of organic thiols, such as the proteinogenic amino acids methionine and cysteine, prosthetic groups and coenzymes (e.g. FeS centers or thiazole), and many secondary metabolites<sup>41</sup>.

However, H<sub>2</sub>S is expensive, corrosive, explosive, and highly toxic to humans. It can diffuse across cell membranes, bind to and precipitate metal cations, ultimately damaging respiratory and metabolic processes<sup>42,43</sup>. Methanogens that could use alternative sources of sulfur with higher oxidation states would greatly simplify their cultivation. The best solution would be sulfate (SO<sub>4</sub><sup>2-</sup>) as it is cheap, safe, and easy to handle. While few methanogens have been shown to grow on H<sub>2</sub>S/HS<sup>-</sup>, metal sulfides, elemental sulfur, and sulfite (SO<sub>3</sub><sup>2-</sup>)<sup>44-46</sup>, only one methanogen has been reported so far to grow on SO<sub>4</sub><sup>2-</sup> as its sole sulfur source: *Methanothermococcus thermolithotrophicus*<sup>45</sup>.

Although  $\text{SO}_4^{2-}$  is widely assimilated in the microbial world, this ability of a methanogen is surprising for many reasons. First,  $\text{CH}_4$  production usually occurs in anoxic environments where  $\text{HS}^-/\text{S}^{2-}$  cannot be oxidized to  $\text{SO}_4^{2-}$ , meaning that  $\text{CH}_4$  production and  $\text{SO}_4^{2-}$  reduction are often spatially separated<sup>15,47</sup>. However, the coexistence of methanogenesis and  $\text{SO}_4^{2-}$  reduction has been observed in the sulfate-methane transition zone (SMTZ)<sup>48</sup>, where  $\text{SO}_4^{2-}$  reducing microorganisms (SRM) compete with hydrogenotrophic methanogens for the substrate  $\text{H}_2$ . Due to lower thresholds for  $\text{H}_2$ , and a thermodynamically more favorable metabolism,  $\text{H}_2$ -utilizing SRMs outcompete hydrogenotrophic methanogens<sup>49</sup>. In addition,  $\text{SO}_4^{2-}$  reduction produces toxic intermediates such as  $\text{SO}_3^{2-}$ , which can inhibit methanogenesis by directly interfering with the methyl-coenzyme M reductase (MCR), the central enzyme of the methanogenic pathway<sup>50</sup>. However, in 1986 it was shown that certain methanogens can grow on  $\text{SO}_3^{2-}$  as a sole source of sulfur despite its toxicity<sup>45</sup> and in 2005 the enzyme that confers  $\text{SO}_3^{2-}$  tolerance to these methanogens was discovered: the  $\text{F}_{420}$ -dependent sulfite reductase (Fsr)<sup>46</sup>. Another argument against  $\text{SO}_4^{2-}$  reduction in methanogens is the energy cost of the process. The inert  $\text{SO}_4^{2-}$  ion cannot be directly reduced to the  $\text{HS}^-/\text{S}^{2-}$ , but must first be activated by the investment of at least two ATPs (referred to the high-energy phosphoanhydride bonds in ATP) - a considerable energy requirement for an energy-limited organism.

Despite all listed arguments, *M. thermolithotrophicus* was successfully grown on 4.4 mM  $\text{SO}_4^{2-}$  in 1986 (ref. 46). Understanding the molecular mechanisms by which this methanogen assimilates  $\text{SO}_4^{2-}$  is of great interest, as this knowledge could be used to transfer the system to genetically tractable methanogenic models already used in biotechnology<sup>51</sup>. Interestingly, based on genomic and environmental metaproteomic analyses of anaerobic methanotrophic archaea (ANME) and other methanogens, it appears that the potential for  $\text{SO}_4^{2-}$  reduction is spread across *Euryarchaeota*<sup>52,53</sup>. Two  $\text{SO}_4^{2-}$  assimilation-associated enzymes have been biochemically characterized as a thioredoxin-dependent APS reductase and PAPS reductase from the hydrogenotrophic methanogen *Methanocaldococcus jannaschii*, but the  $\text{SO}_4^{2-}$  activating enzymes are absent from the genome, making the physiological roles of these two enzymes elusive<sup>54,55</sup>.

It is puzzling that so far only *M. thermolithotrophicus* has been successfully cultivated exclusively on  $\text{SO}_4^{2-}$ . No functional or structural data are currently available to explain how *M. thermolithotrophicus* acquires  $\text{SO}_4^{2-}$ . As an energy-limited organism, it is likely that *M.*

*thermolithotrophicus* has evolved alternative strategies to reduce  $\text{SO}_4^{2-}$  in an energy-efficient manner (such as electron bifurcation or coupled reactions<sup>56</sup>). One strategy would be to couple  $\text{SO}_4^{2-}$  reduction with  $\text{H}_2$  oxidation, for example by stimulating the conversion rates with appropriate electron shuttles.

A very important electron carrier in methanogens is the cofactor  $\text{F}_{420}$  (**Figure 2**).  $\text{F}_{420}$  is a flavin derivative, but due to some substitutions, it performs a two-electron hydride transfer like NAD(P)H and has a much lower standard redox potential (-340 mV and up to -380 mV under physiological conditions) than riboflavin, FAD or FMN (-210 mV, -220 mV, -190 mV, respectively)<sup>57</sup>. Due to its redox potential and high intracellular concentrations, this cofactor stimulates metabolic fluxes to catalyze a wide range of challenging enzymatic redox reactions. The spectral properties of reduced and oxidized  $\text{F}_{420}$  also make it a valuable tool in enzymology for monitoring  $\text{F}_{420}$ -dependent enzymes. The coenzyme is found in six orders of the archaeal phylum *Euryarchaeota*: *Methanobacteriales*, *Methanopyrales*, *Methanomicrobiales*, *Methanocellales*, *Methanosarcinales*, and *Methanococcales*, to which *M. thermolithotrophicus* belongs, but has not yet been identified in *Methanomassiliicoccales*<sup>58,59</sup>.

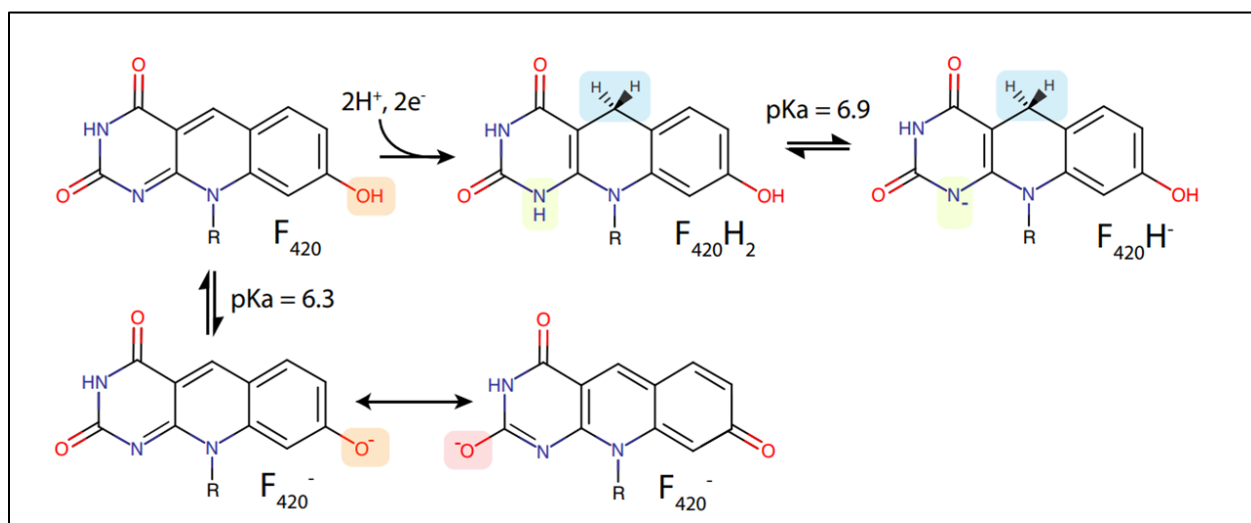


**Figure 2.**  $\text{F}_{420}$  protonation states, redox transitions, and associated spectral shifts. Changes in the protonation state of  $\text{F}_{420}$  and  $\text{F}_{420}\text{H}_2$  as a result of the change in external pH,  $\text{R}=\text{F}_{420}$  tail group (reprinted with permission granted under Creative Commons license from Grinter and Greening (2021)<sup>57</sup>).

## F<sub>420</sub>-reducing [NiFe] hydrogenases provide the fuel for assimilatory and energy-conserving pathways in methanogens

The preferred route for reducing F<sub>420</sub> during hydrogenotrophic methanogenesis is by coupling it to H<sub>2</sub> oxidation, a reaction performed by the F<sub>420</sub>-reducing hydrogenase (Frh). Like all hydrogenases, Frh catalyzes the reversible oxidation of H<sub>2</sub> to two protons and two electrons.



This simplest chemical reaction (Reaction 2) is highly valuable for clean energy conversion. The majority of the H<sub>2</sub> produced today is derived from steam-reformed methane and produces a substantial amount of CO<sub>2</sub> (ref. 61). In contrast, hydrogenases catalyze the reaction without producing greenhouse gas emissions and at rates comparable to platinum electrodes by using earth-abundant transient metals in their active site, making them an attractive target for mimicry chemistry<sup>62</sup>.

Based on their active site metallocluster, hydrogenases are classified into the mononuclear [Fe], [FeFe] and [NiFe] hydrogenases, to which Frh belongs (**Figure 3**)<sup>63</sup>.

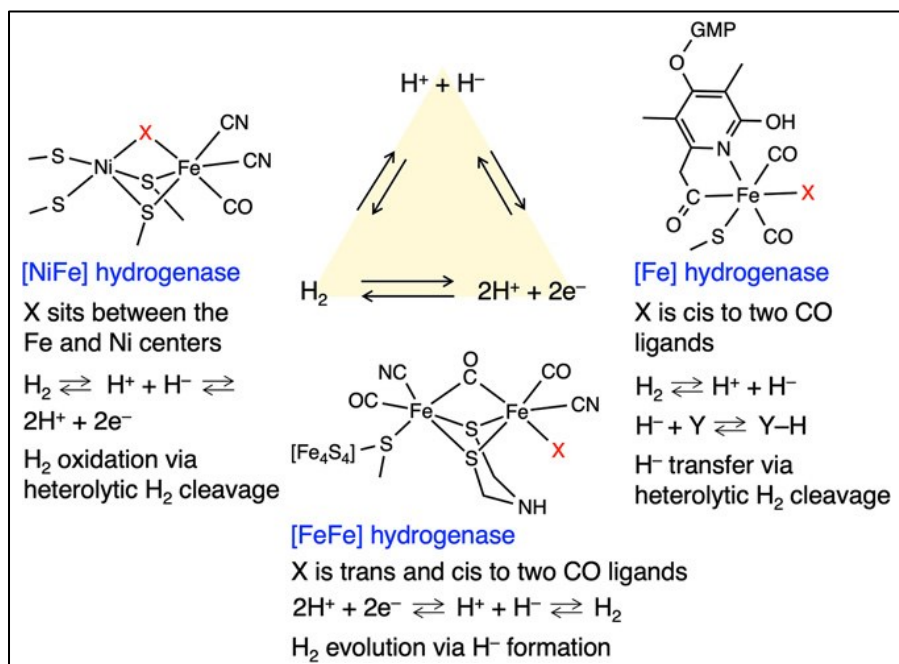


**Figure 3. Structure of the active sites in [NiFe] hydrogenase, [FeFe] hydrogenase, and [Fe] hydrogenase.** This figure was reprinted with permission granted under Creative Commons license from Ogo et al. (2020)<sup>64</sup>.

The mononuclear [Fe] hydrogenase, has been found in methanogenic archaea and only one bacterial genus<sup>60,65</sup>. This enzyme carries out the reversible reduction of methenyltetrahydromethanopterin (methenyl-H<sub>4</sub>MPT<sup>+</sup>)<sup>60</sup>, an intermediate in the methanogenesis pathway, with H<sub>2</sub> using a unique iron-guanylylpyridinol cofactor<sup>60</sup>. [FeFe] hydrogenases, considered to be the most active hydrogenases, have only been described in bacteria and lower eukaryotes and have not yet been discovered in archaea, whereas [NiFe] hydrogenases have been found in bacteria and archaea<sup>60</sup>. [NiFe] and [FeFe] hydrogenases are the two most common hydrogenases in nature<sup>66</sup>. [FeFe] hydrogenases are more active towards H<sub>2</sub> production and are irreversibly damaged when exposed to O<sub>2</sub>. [NiFe] hydrogenases, on the other hand, are less sensitive to O<sub>2</sub> but have been reported to be more active towards H<sub>2</sub> oxidation<sup>67</sup>. On the basis of molecular phylogeny, [NiFe] hydrogenases are classified into four groups. Group I contains generally membrane-bound H<sub>2</sub> uptake hydrogenases; group II contains uptake hydrogenases and sensory hydrogenases. Frh belongs to group III, which also includes NAD(P)<sup>+</sup>-reducing, methylviologen-reducing, and bidirectional NAD(P)<sup>+</sup>-reducing hydrogenases and group IV contains energy-converting hydrogenases<sup>63</sup>.

To date, four different subtypes of [NiFe] hydrogenases and one [Fe] hydrogenase have been identified in methanogens<sup>60,68</sup>. The four [NiFe] hydrogenases are: (1) Frh (FrhABG), (2) the membrane-associated energy-converting hydrogenases (EchA-F, EhaA-T, EhbA-Q, and MbhA-N), (3) the cytoplasmic heterodisulfide reductase (HdrABC) associated hydrogenase (MvhADG) and (4) the membrane-associated methanophenazine-reducing hydrogenase (VhtACG, only in cytochrome-containing methanogens)<sup>63</sup>. At low concentrations of nickel, methanogens have been shown to up-regulate the [Fe] hydrogenases to replace the F<sub>420</sub>-reducing [NiFe] hydrogenase<sup>60</sup>. It is worth noting that not all of the five hydrogenases are found in all methanogens. For example, the [Fe] hydrogenase is absent from cytochrome-containing methanogens, which include all members of the *Methanosarcinales*<sup>60</sup>.

In [NiFe] hydrogenases, the catalysis of H<sub>2</sub> oxidation or production takes place at the [NiFe] center, and the electrons for the reaction are transferred from or to the catalytic center via Fe-S clusters, which differ in composition and number. In the case of the F<sub>420</sub>-reducing hydrogenase, the electrons obtained by the heterolytic cleavage of H<sub>2</sub> are passed via a four [4Fe-4S] cluster relay to a FAD, where the F<sub>420</sub> is bound and can be reduced. Frh consists of three subunits: FrhA, which

contains the [NiFe] active site, FrhB that contains one [4Fe-4S] cluster and the FAD, and FrhG, which harbors three [4Fe-4S] clusters (**Figure 4**)<sup>63</sup>.

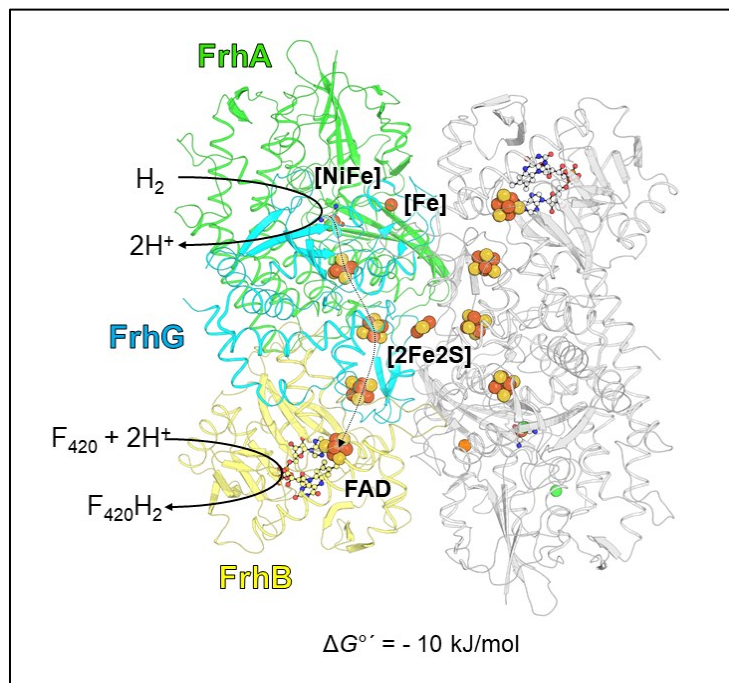


**Figure 4.** The  $F_{420}$ -reducing hydrogenase (Frh) from *Methanosarcina barkeri* (PDB: 6QGR). The dimer is shown in cartoon representation with one protomer colored according to its subunits. The adjacent protomer, which establishes the dimer is shown in white cartoon. The cofactors are shown in spheres, with the atoms oxygen, nitrogen, sulfur, phosphorus, nickel, and iron colored in red, blue, light yellow, brown, green, and orange. The carbon is colored green for the [NiFe] center in FrhA, light yellow for the FAD of FrhB, and white for the adjacent protomer.

All [NiFe] hydrogenases share a similar active site structure, which includes a nickel atom that is anchored to the protein by four conserved cysteines, two of which bridge the nickel and iron metals (**Figure 3**)<sup>63</sup>. In the case of the [NiFeSe] hydrogenases, a subclass of [NiFe] hydrogenases, a selenocysteine replaces one cysteine to coordinate the nickel atom. The low-spin  $Fe^{2+}$  is ligated by CO and  $CN^-$  ligands and remains redox inactive throughout the catalysis, while the Ni atom changes its oxidation state between  $Ni^{3+}$ ,  $Ni^{2+}$  or  $Ni^{1+}$  depending on the reaction stage. In its inactive, oxidized form, a third bridging ligand ( $OH^-$ ) is coordinated between the Ni and the Fe (Ni-B, **Figure 5**). However, this ligand changes identity during the reaction cycle, depending on the redox state of the enzyme (**Figure 5**). Once activated by  $H_2$ , the bridging position is shown to be either vacant or carry a hydride. Throughout the catalytic cycle, the enzyme undergoes various

intermediate states, and many structural determinants of efficient H<sub>2</sub> binding at the active site are not properly understood. By studying Frh from the methanogenic model organism *Methanosarcina barkeri*, it was possible to trap a new state of the H<sub>2</sub>-binding [NiFe] intermediate<sup>62</sup>. So far, there are only two structures of Frh available<sup>62,69</sup>. Investigating Frh from a phylogenetically different methanogen, such as *Methanothermococcus thermolithotrophicus*, may provide new insights into the catalytic cycle, which would help to build more efficient bio-inspired [NiFe] catalysts for H<sub>2</sub> production.

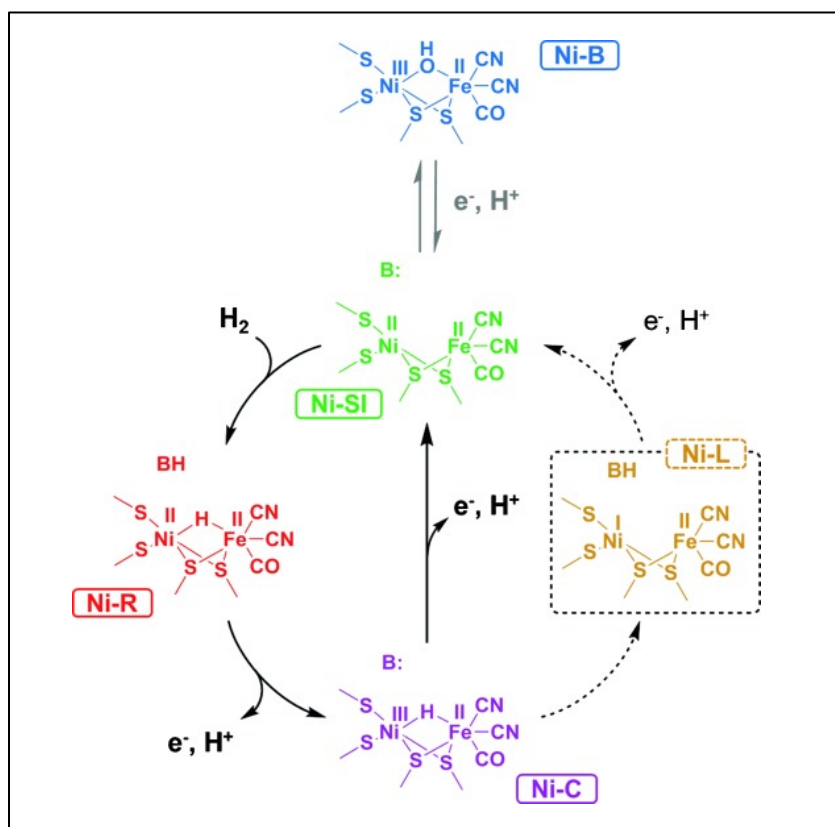


**Figure 5.** H<sub>2</sub> oxidation (black) and anaerobic inactivation (gray) of [NiFe] hydrogenase. This figure is reprinted with permission granted under the license ID 5570940775642 from Hidalgo et al. (2015)<sup>70</sup>.



## The F<sub>420</sub>-dependent sulfite reductase detoxifies SO<sub>3</sub><sup>2-</sup> and allows its assimilation

The F<sub>420</sub> reduced by Frh is used to fuel several assimilation pathways, such as for carbon (e.g. via methanogenesis), nitrogen (via the glutamate synthase, Wagner et al. in preparation), and also sulfur assimilation by the Group I F<sub>420</sub>-dependent sulfite reductase (Fsr)<sup>46</sup>. Fsr was first identified in the hyperthermophilic archaeon *M. jannaschii*, a strictly hydrogenotrophic methanogen isolated from a deep-sea hydrothermal vent. In such an environment, polymetal sulfides are emitted which oxidize sulfur to SO<sub>3</sub><sup>2-</sup>, which the methanogen must detoxify<sup>71</sup>. When exposed to SO<sub>3</sub><sup>2-</sup>, *M. jannaschii* expresses Fsr in large quantities, making it the second most abundant enzyme in the cytoplasm<sup>46</sup>. Fsr performs the efficient reduction of SO<sub>3</sub><sup>2-</sup> through a unique fusion of two catalytic units: an F<sub>420</sub>H<sub>2</sub>-oxidase as the N-terminal half, which is electronically coupled to a C-terminal dissimilatory-like siroheme sulfite reductase (**Figure 6**)<sup>46</sup>.

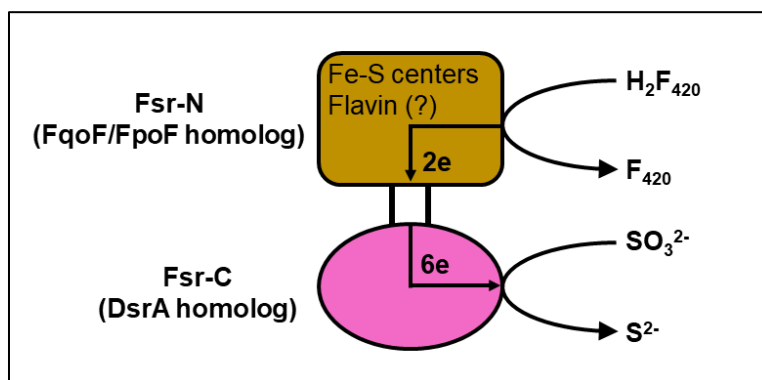


**Figure 6. The coenzyme F<sub>420</sub>-dependent sulfite reductase.** Fsr-N, residues 1–311 of Fsr; Fsr-C, residues 325–620 of Fsr. The N-terminal half showed sequence similarities to FqoF and FpoF, which are the F<sub>420</sub>H<sub>2</sub> dehydrogenase subunits of F<sub>420</sub>H<sub>2</sub>:quinone oxidoreductase (Fqo) complex of *Archaeoglobus fulgidus* and F<sub>420</sub>H<sub>2</sub>:phenazine oxidoreductase (Fpo) complex of *Methanosarcina mazei*<sup>46</sup>. The indication for the presence of [Fe-S] clusters in Fsr came from a primary sequence analysis. The scheme has been modified with permission granted under the Creative Commons CC-BY license from Johnson and Mukhopadhyay, 2005, J Biol Chem<sup>46</sup>.

Based on phylogenetic and comparative structural analyses, there are two distinct groups of Fsr: Group I and Group II<sup>53,72</sup>. Group II Fsr has been found in the genome of anaerobic methanotrophic archaea (except for *Candidatus Methanoperedens nitroreducens*) and *Methanosarcinales*, but its physiological role remains unclear, as it does not show sulfite reductase activity<sup>53,72</sup>. The heterologously expressed enzyme has been reported to be active as an F<sub>420</sub>-dependent nitrite

reductase (FNir), albeit at very low enzymatic rates<sup>53,72</sup>. In contrast, Group I Fsr has been identified in methanogens belonging to the *Methanococcales*, *Methanopyrales*, and *Methanobacteriales*, except *Methanohalobium evestigatum* (*Methanosarcinales*), which contains both groups of Fsr<sup>53</sup>.

In addition to its activity as a sulfite reductase, it has recently been reported that the role of Group I Fsr is further extended to an FNir in *M. jannaschii*<sup>73</sup>. The FNir activity might be of physiological importance when considering that deep-sea hydrothermal vents provide a constant supply of nitrite ( $\text{NO}_2^-$ ) at very low concentrations<sup>73-75</sup>. Like  $\text{SO}_3^{2-}$ ,  $\text{NO}_2^-$  oxidizes the Ni(I) center of the coenzyme F<sub>430</sub>, the prosthetic group of MCR, thereby inhibiting methanogenesis. FNir would prevent  $\text{NO}_2^-$  damage by converting it to ammonia, which can be further assimilated<sup>73</sup>.

Interestingly, Fsr shares low sequence similarity with both assimilatory and dissimilatory sulfite reductases<sup>46,76</sup>. Hydrogenotrophic methanogenesis and dissimilatory sulfate reduction are two of the oldest known biological energy-conserving systems<sup>38,77</sup>. Considering the early origin of methanogens, it has been proposed that Fsr may be the progenitor of assimilatory and dissimilatory sulfite reductases<sup>76</sup>. Structural data on Fsr would therefore be invaluable in explaining how the enzyme works at the molecular level, in particular the electron relay, and may provide new insights into the evolution of sulfite.

## 1.4 Sulfate-reducing bacteria and alkanotrophic archaea

### Sulfate-reducing bacteria

While *Methanothermococcus thermolithotrophicus* reduces  $\text{SO}_4^{2-}$  to assimilate sulfur, many microorganisms use it as a terminal electron acceptor to conserve energy<sup>78</sup>. Dissimilatory  $\text{SO}_4^{2-}$  reduction (DSR) is mediated by a wide variety of phylogenetically and physiologically distinct bacteria and archaea that can use  $\text{H}_2$  or a large diversity of organic compounds as electron donors to synthesize ATP, thereby producing  $\text{H}_2\text{S}$  and play an important role in the mineralization of organic carbon<sup>17,79-81</sup>. They are key organisms in many low-energy environments and metabolize at low rates, which requires physiological adaptations such as a highly efficient substrate uptake<sup>14,82</sup>. However, despite the importance of DSR, the energy metabolism of SRMs remains poorly understood<sup>82</sup>.

While the process of assimilatory and dissimilatory  $\text{SO}_4^{2-}$  reduction can be very similar, the enzyme that catalyze the reactions differ (**Figure 7**). In both cases, cells must transport  $\text{SO}_4^{2-}$  across the hydrophobic membrane into the cytoplasm, which is a critical first step that regulates the rate of  $\text{SO}_4^{2-}$  reduction<sup>83</sup>. It has been proposed that thermophilic SRMs have the genomic potential to express members of the CysP (sulfate: $\text{H}^+$  symporter), as well as putative CysZ-type (high-affinity proton-dependent transporter) and SUIP (anion:anion exchange or anion uptake carrier)  $\text{SO}_4^{2-}$  transporters, depending on their environment<sup>83,84</sup>.

Since the  $\text{SO}_4^{2-}/\text{SO}_3^{2-}$  reduction potential of  $E^{0'} = -516$  mV, is too negative to be overcome by biological systems<sup>78</sup>, the inert  $\text{SO}_4^{2-}$  ion must be activated inside the cell. An ATP sulfurylase - the first enzyme in the dissimilatory and the assimilatory  $\text{SO}_4^{2-}$  reduction pathways - catalyzes the transfer of the adenylyl group from one ATP to  $\text{SO}_4^{2-}$ , producing adenosine 5'-phosphosulfate (APS) and pyrophosphate ( $\text{PP}_i$ ). This increases the reduction potential to  $E^{0'} = -60$  mV, a potential that allows reduction by intracellular electron donors<sup>18,78</sup>. Two non-homologous ATP sulfurylases (ATPS) have been described so far: CysDN and Sat. The heterodimeric CysDN requires one GTP and one ATP per activated  $\text{SO}_4^{2-}$  and is probably only used in the assimilatory pathway due to the energetic requirement of three ATP equivalents<sup>85</sup>. The homo-oligomeric Sat requires only one ATP to catalyze the reaction and is involved in both dissimilatory and assimilatory  $\text{SO}_4^{2-}$  reduction<sup>53</sup>. The products pyrophosphate ( $\text{PP}_i$ ) and APS inhibit the ATPS and must be effectively transformed. The  $\text{PP}_i$  is hydrolyzed into inorganic phosphate ( $\text{P}_i$ ) by a pyrophosphatase. In the assimilatory pathway, APS can be further phosphorylated by an APS kinase (APSK) to 3'-phosphoadenosine 5'-phosphosulfate (PAPS), which can then either serve as a substrate for sulfotransferases or be reduced to  $\text{SO}_3^{2-}$  and 3'-phosphoadenosine 5'-phosphate (PAP) by a PAPS reductase (**Figure 7**). Alternatively, APS can be reduced directly by an APS reductase, as in the dissimilatory  $\text{SO}_4^{2-}$  reduction pathway. Although the assimilatory and dissimilatory APS reductases catalyze the reduction of APS to  $\text{SO}_3^{2-}$  and AMP, they are different enzymes with different reaction mechanisms and electron donors. The dissimilatory pathway contains a non-heme heterodimeric iron-sulfur protein and requires a FAD to perform the reduction reaction<sup>86</sup>. Assimilatory APS reductases are homo-multimeric enzymes that contain one [4Fe-4S] cluster and are thioredoxin dependent<sup>87</sup>. The reduction of  $\text{SO}_3^{2-}$  to  $\text{HS}^-/\text{H}_2\text{S}$  is catalyzed in both pathways by a siroheme- and [4Fe-4S] cluster-containing sulfite reductase, as previously described for Fsr. While assimilatory  $\text{SO}_3^{2-}$  reductases are monomeric enzymes that directly reduce  $\text{SO}_3^{2-}$  to sulfide,

dissimilatory enzymes are heterodimers and require additional partners for the complete reduction of  $\text{SO}_3^{2-}$  (ref. 88).

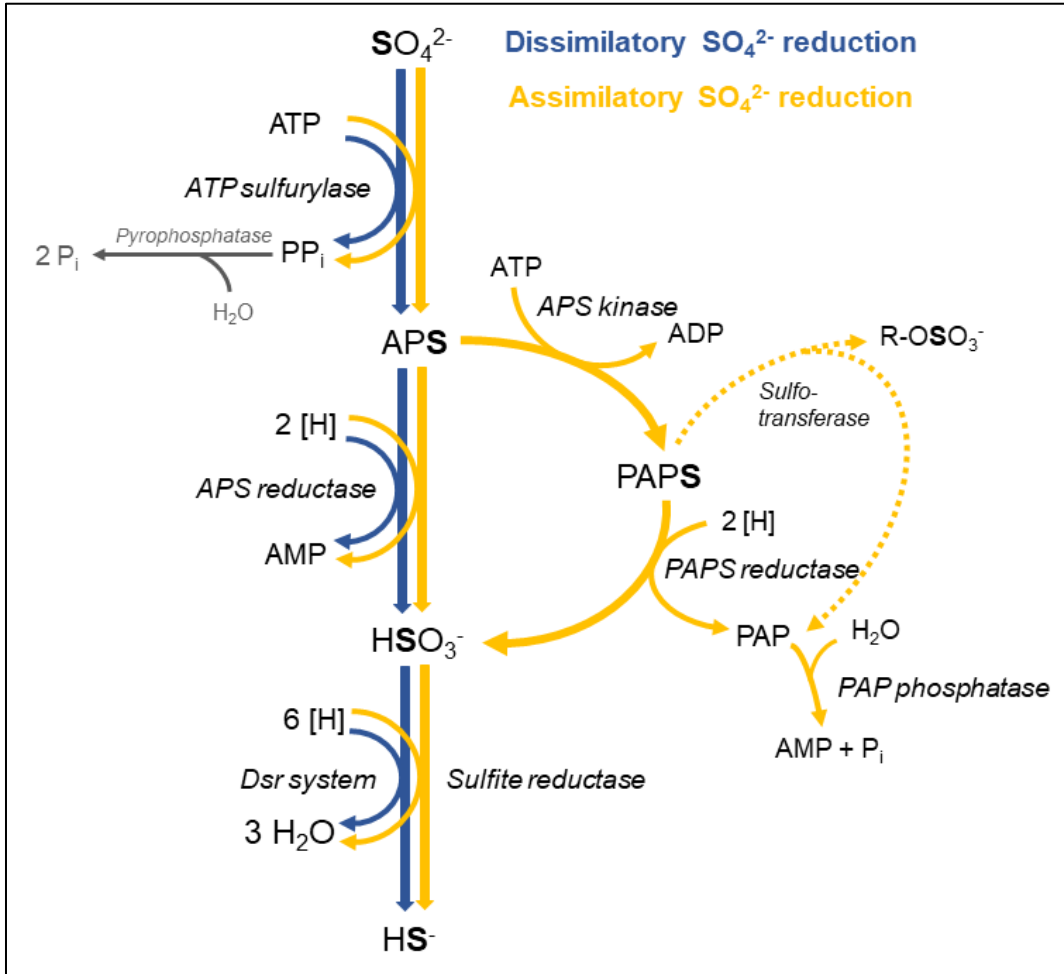


**Figure 7. Scheme of the dissimilatory and assimilatory  $\text{SO}_4^{2-}$  reduction pathways.** The path of dissimilatory  $\text{SO}_4^{2-}$  reduction is shown by blue arrows and the one for assimilation is in yellow. While  $\text{SO}_4^{2-}$  can be assimilated by reducing APS directly to sulfite, it can also be further phosphorylated to PAPS from which the sulfo-group can be transferred by a sulfotransferase to an alcohol or amine acceptor (dashed lines). Alternatively, the PAPS can be reduced to PAP and sulfite.

## Anaerobic oxidation of alkanes (AOA)

Dissimilatory  $\text{SO}_4^{2-}$  reduction is estimated to account for more than half of the global anaerobic degradation of biological matter and is therefore a key process in the global carbon cycle<sup>17,82</sup>. For example, SRB regulate the flux of  $\text{CH}_4$  into our atmosphere by forming syntrophic partnerships with ANME<sup>89</sup>. By catalyzing the anaerobic oxidation of  $\text{CH}_4$ , ANME are a major biological sink for this potent hydrocarbon, converting around 80% of the  $\text{CH}_4$  emanated from the ocean floor<sup>90</sup>. Closely related to methanogens, ANME belong to the phylum of *Euryarchaeota* and form three distinct groups: ANME-1, ANME-2, and ANME-3, all of which catalyze the complete oxidation of  $\text{CH}_4$  to  $\text{CO}_2$  via the reverse methanogenic pathway<sup>90,91</sup>. While ANME usually form syntrophic consortia with SRB<sup>92</sup>, the anaerobic oxidation of  $\text{CH}_4$  (AOM) can also be coupled to the reduction of  $\text{NO}_3^-$ ,  $\text{Fe}^{3+}$ , or  $\text{Mn}^{4+}$  in partner-independent manner<sup>93-95</sup>. This process occurs in many environments such as terrestrial mud volcanoes<sup>96</sup>, landfills<sup>97</sup>, or in freshwater<sup>98,99</sup>, but was first discovered in marine sediments<sup>100,101</sup>.

Recently, it has been shown that anaerobic archaeal alkanotrophy is not restricted to  $\text{CH}_4$ , but can be extended to short (from C1 to C4), mid and long-chain alkanes<sup>102-105</sup>. The current hypothesis (for alkanes other than  $\text{CH}_4$ ) is that the alkane is first activated by an MCR-like enzyme following the thiyl radical mechanism, forcing the formation of an alkyl-coenzyme M (alkyl-S-CoM) and free coenzyme B (CoB-SH). The alkyl-CoM is oxidized and converted to acetyl-CoA, which will be turned into  $\text{CO}_2$  and  $\text{CH}_3\text{-H}_4\text{MPT}$ , and the latter is oxidized via the reverse methanogenesis pathway. The many oxidation reactions result in the formation of reducing equivalents that must be evacuated. With the exception of some ANME that use alternative electron acceptors (e.g.  $\text{NO}_3^-$ ), most alkane oxidizers transfer the reducing equivalents to a  $\text{SO}_4^{2-}$  reducing bacterial partner. However, how reducing equivalents are exchanged within the consortium is not yet fully understood. Most of the work to elucidate this question has been carried out on ANME, and it has been proposed that the organisms exchange intermediate substrates, such as CO, acetate, formate, or methyl sulfide to neutralize excess reducing equivalents. However, this seems an unlikely process for most compounds, as maintaining the gradient of transferred intermediates would significantly reduce the energy gain, and none of the proposed intermediates have been measured in AOM enrichment cultures or yielded a response in the bacterial partner organism<sup>106-108</sup>. An alternative suggestion was that ANME perform a partial reduction of  $\text{SO}_4^{2-}$  and the bacterial

partner disproportionates zero-valent sulfur<sup>109</sup>. Indeed, enzymes associated with  $\text{SO}_4^{2-}$  reduction have been found in the three ANME groups, but based on characterized homologs and the lack of associated energy conserving complexes, they are likely to be involved in sulfur assimilation<sup>53</sup>. Furthermore, the only SRB isolated from a consortium is *Ca. D. auxilii*, which is incapable of sulfur disproportionation but performs obligate  $\text{SO}_4^{2-}$  reduction<sup>110</sup>. To date, there is no proliferating culture that performs  $\text{SO}_4^{2-}$  dependent AOM in which alkane-oxidizing archaea thrive without their bacterial partners, suggesting an obligate syntrophy. The most agreed-on theory is that the consortium performs a direct interspecies electron transfer (DIET). The  $\text{SO}_4^{2-}$  reducing bacterial partner expresses genes for conductive pili production, and both the bacterium and ANME express extracellular cytochromes that are proposed to facilitate the interspecies electron transfer<sup>108,111</sup>. In many habitats,  $\text{SO}_4^{2-}$  dependent AOM operates at an energy yield close to the thermodynamic equilibrium - the bare minimum to support microbial Life<sup>15</sup>. Accordingly, ANME show a slow growth rate with doubling times of 7 months, which complicates the study of this very important consortium<sup>112</sup>.

### **A microbial consortium to pioneer the biochemical studies of anaerobic alkanotrophy**

So far, the fastest metabolic turnover of a culture consisting of an alkane-degrading archaeon and *Ca. D. auxilii* is a thermophilic ethane ( $\text{C}_2\text{H}_6$ ) oxidizing consortium (doubling of sulfide produced within a week)<sup>113</sup>. *Candidatus* *Ethanoperedens* thermophilum and its partner bacterium *Ca. D. auxilii* were isolated from hydrothermal sediments of the Guaymas Basin (Gulf of California) and enriched on  $\text{C}_2\text{H}_6$  (ref. 113). The lower energy yield required to activate  $\text{C}_2\text{H}_6$  compared to  $\text{CH}_4$  may be one of the reasons for the faster growth of this consortium. The other reason is probably the overall higher energy yield of the  $\text{SO}_4^{2-}$  dependent  $\text{C}_2\text{H}_6$  oxidation (Reaction 3)<sup>102</sup>. The reducing equivalents liberated by the anaerobic oxidation of ethane (AOE) by *Ca. E. thermophilum* are consumed by *Ca. D. auxilii* in the reduction of  $\text{SO}_4^{2-}$  to  $\text{S}^{2-}$ .

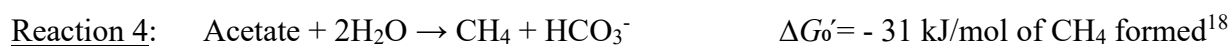
**Reaction 3:**  $4\text{C}_2\text{H}_6 + 7\text{SO}_4^{2-} + 14\text{H}^+ \rightarrow 8\text{CO}_2 + 7\text{H}_2\text{S} + 12\text{H}_2\text{O}$   $\Delta G^\circ = -73.2$  kJ/mol of  $\text{C}_2\text{H}_6$  (ref. 105)

The ethane-activating enzyme from *Ca. E. thermophilum* was directly purified from the heterogeneous consortium and its crystal structure revealed<sup>102</sup>. After this proof of concept, it would

be worthwhile to use the same approach to study the catabolic enzymes of the dissimilatory  $\text{SO}_4^{2-}$  reduction pathway of *Ca. D. auxilii*, as no structural data are currently available for the ATP sulfurylase from a dissimilatory SRB. In-depth characterization of the biochemistry of the consortium using a native approach could provide new insights into how  $\text{SO}_4^{2-}$  reduction fuels  $\text{C}_2\text{H}_6$  oxidation, or how DIET works<sup>114</sup>.

### **1.5 *Methanotherix* - an acetoclastic methanogen with the ability to reduce $\text{CO}_2$**

The process of DIET has mainly been studied between acetoclastic methanogens and bacterial partners, as they are critical in the final step of the trophic chain. Acetoclastic methanogens use acetate to assimilate carbon and conserve energy, producing  $\text{CH}_4$  and  $\text{CO}_2$  (Reaction 4), although the overall reaction is close to thermodynamic equilibrium.



Although an estimated two-thirds of the biologically produced  $\text{CH}_4$  is derived from acetate ( $\text{CH}_3\text{COO}^-$ ), only two archaeal genera are known to use it as a substrate for methanogenesis: *Methanosarcina* and *Methanotherix* (formerly known as *Methanosaeta*)<sup>115</sup>. While *Methanosarcina* is metabolically diverse (hydrogenotrophic, methylotrophic, and acetoclastic) and more specialized in the use of methylated compounds compared to acetate, *Methanotherix* was long thought to be an obligate acetoclastic methanogen<sup>115,116</sup>.

Because of its high affinity for acetate and its wide abundance in nature, *Methanotherix* has been proposed to be the main producer of  $\text{CH}_4$  on planet Earth<sup>115</sup>. For example, *Methanotherix* species play an important role in wastewater treatment plants, where they carry out the final step in the degradation of organic matter. In anaerobic sludge of wastewater, microbial communities break down macromolecules (such as polysaccharides, lipids, and proteins) into simple components ( $\text{H}_2$ ,  $\text{CO}_2$ , formate, and acetate) from which methanogens produce  $\text{CH}_4$  (ref. 117). Anaerobic sludge communities are highly diverse and heterogeneous, but *Methanotherix* and *Methanosarcina* appear to be a relatively permanent and active part of these communities and are key players in biogas production<sup>117</sup>.

## **DIET-mediated CO<sub>2</sub> fixation in *Methanotherix***

Interestingly, certain *Methanotherix* species exhibit faster growth in a syntrophic community compared to when acetate is their sole energy source<sup>118</sup>. *Methanotherix* was long thought to rely solely on acetate as a substrate for CH<sub>4</sub> production, but surprisingly its genome encodes all the enzymes required to reduce CO<sub>2</sub> to CH<sub>4</sub> via the hydrogenotrophic pathway<sup>119</sup>. Unlike some *Methanosarcina* species, *Methanotherix* lacks the genes encoding enzyme complexes known to be required for cellular hydrogen uptake (e.g. [NiFe] hydrogenases)<sup>15,115,116</sup>. However, *Methanotherix* species can directly accept electrons from their bacterial partner (e.g. *Geobacter* species) via DIET to reduce CO<sub>2</sub> to CH<sub>4</sub> (ref. 118). The DIET provides an energy source to support the growth of *Methanotherix* under these conditions, but the molecular details (e.g. electron shuttles) are unknown<sup>119</sup>. Understanding the mechanism has great biotechnological potential, as it is possible to use the syntrophic community to increase the amount of CH<sub>4</sub> and reduce CO<sub>2</sub> during biogas production. Despite its global importance, *Methanotherix* is less studied than *Methanosarcina*, due to its long incubation times and low cell yields under laboratory conditions. In addition, a stable co-culture of *Methanotherix* with its natural partners is difficult to maintain, limiting the study of its CO<sub>2</sub>-fixing ability.

## **A method to characterize metabolic enzymes from complex microbial communities**

*Methanotherix* species are relatively abundant and highly metabolically active in anaerobic wastewater sludge<sup>117</sup>. Therefore, a direct purification of an active sludge sample could allow the isolation and study of the main catabolic enzymes of the methanogen, including the one which could be used in the CO<sub>2</sub> fixation process occurring during DIET. As the sample would be obtained from a mesocosm, which is a controlled experimental system that replicates specific environmental conditions on a smaller scale, it would represent a complex heterogeneous microbial community, likely harboring several multispecies of *Methanotherix*. This makes the conventional approach of isolating a specific protein by classical chromatographic purification very difficult. In 2012, Shima and colleagues succeeded in isolating the MCR of ANME from bacterial mats using the selective process of crystallization<sup>120</sup>. As the crystalline state of a protein represents its ultimate pure form, separation, washing, and dissolution of the crystal would be a way to isolate a protein for its biochemical characterization. Based on the success with the enrichment culture of *Ca. E.*



thermophilum, it would be interesting to develop a similar approach to gain new insights into *Methanotherix* such as its MCR. This enzyme is ubiquitous in methanogens and anaerobic alkanotrophic archaea and has been studied intensively, not only because of its impact on our planet, but also to understand the chemistry behind the biological alkane activation<sup>15</sup>. However, all X-ray structures of MCR show the F<sub>430</sub> cofactor in an inactive Ni(II) state. The study of the MCR of an acetoclastic methanogen, the most abundant methanogen on Earth, which is thought to have a higher O<sub>2</sub> tolerance than other methanogens and can even fix CO<sub>2</sub> under certain conditions, possibly allows the trapping of the active Ni(I) state<sup>121,122</sup>.

The isolation and the study of the MCR from a *Methanotherix* obtained from a mesocosm would be the starting point for characterizing the other enzymes involved in DIET-dependent CO<sub>2</sub> fixation and acetoclastic methanogenesis.

## 1.6 Autotrophic acetogens and their CO<sub>2</sub> and H<sub>2</sub> transformation capabilities

Important providers of acetate in anaerobic environments, such as wastewater sludge or marine sediments, are acetogenic bacteria. These facultative autotrophs can grow on a variety of substrates such as sugars, alcohols, or fatty acids, as well as by the oxidation of inorganic gases like H<sub>2</sub> or carbon monoxide (CO), which makes them an important players in anaerobic food webs<sup>13</sup>. Acetogens, which produce acetate from two molecules of CO<sub>2</sub> (Reaction 5), are intensively used in biotechnology, where their metabolic capabilities are harnessed for carbon remediation<sup>123</sup>.

Reaction 5:  $4\text{H}_2 + 2\text{HCO}_3^- + \text{H}^+ \rightarrow \text{Acetate} + 4\text{H}_2\text{O}$   $\Delta G^\circ = -104.6 \text{ kJ/mol of Acetate formed}$ <sup>18</sup>

### The reductive acetyl-CoA pathway of autotrophic acetogens

The two molecules of CO<sub>2</sub> required for acetate production by acetogenic bacteria are metabolized via the reductive acetyl-CoA pathway. Like hydrogenotrophic methanogens, autotrophic acetogens use the reductive acetyl-CoA pathway to assimilate carbon from H<sub>2</sub> and CO<sub>2</sub>, but they also rely on it for energy conservation<sup>124</sup>.

Of the six ways of autotrophic carbon fixation, the reductive acetyl-CoA pathway is likely the most ancient and consumes the least ATP equivalents<sup>125</sup>. It is often postulated as the metabolic

origin of Life because it is linear, thermodynamically favorable, occurs in archaea and bacteria, and was presumably present in the last universal common ancestor (LUCA)<sup>12,125-127</sup>. However, this pathway constrains the acetogens to thrive at the “thermodynamic limit of Life”, as they receive less than 0.5 moles of ATP per mole of acetate under physiological conditions<sup>13,56</sup>. Despite their energy limitation, autotrophic acetogens have adapted to survive in a wide range of conditions and have shown surprisingly fast growth rates under laboratory conditions (doubling times of a few hours when grown on H<sub>2</sub> and CO<sub>2</sub>)<sup>15,128</sup>.

The reductive acetyl-CoA pathway consists of two branches, each requiring one molecule of CO<sub>2</sub>: The methyl and carbonyl branch. While hydrogenotrophic methanogens and acetogens share a conserved mechanism for activating the carbonyl branch, they use different strategies for CO<sub>2</sub> reduction in the methyl branch<sup>126</sup>. The overall reductive acetyl-CoA pathway and its differences between methanogens and acetogens will be discussed in detail in **Chapter VII**. Therefore, the following section will focus on the CO<sub>2</sub> fixation strategies used by acetogens to fuel the carbon entry point of the methyl branch. Acetogens have evolved a variety of CO<sub>2</sub>-reducing enzymes that use a similar set of modules<sup>126</sup>. Understanding the mechanistic basis of the CO<sub>2</sub> fixation machinery of autotrophic acetogens may be the key to designing efficient catalysts that perform the reversible hydrogenation of CO<sub>2</sub> to formate at high rates and under ambient temperature and pressure conditions. Acetogens have evolved machinery that can be over 1,000 times more efficient than chemical catalysts operating under comparatively moderate conditions<sup>129</sup>.

### ***Clostridium autoethanogenum* as a gas converter**

A successful industrial acetogen is *Clostridium autoethanogenum*, known for its ability to perform syngas fermentation. It can convert CO, CO<sub>2</sub>, and H<sub>2</sub> from steel mill off-gases into valuable products such as acetate, ethanol, or 2,3-butanediol<sup>130-132</sup>. The company LanzaTech has recently commercialized the gas-to-ethanol process by using *C. autoethanogenum*<sup>13</sup>. Because of its interesting transformation abilities, many transcriptomics, metabolomics, genome-scale metabolic modelling, genetic and structural studies have been and are being performed on *C. autoethanogenum* to understand and to optimize the model organism<sup>133-136</sup>. Although CO is toxic to most organisms, *C. autoethanogenum* can use it as its sole carbon and energy source<sup>131</sup>. This is made possible by the CO dehydrogenase/acetyl-CoA synthase (CODH/ACS) complex, which is

part of the carbonyl branch and has recently been structurally characterized<sup>133</sup>. The organization of the CODH/ACS complex of *C. autoethanogenum* refuted the common assumption that acetogens share the same type of machinery. The enzyme ensures rapid conversion of CO by increasing gas accessibility and allows for simultaneous CO oxidation and acetyl-CoA production, providing reducing equivalents (such as reduced ferredoxin) and acetyl-CoA to the cell<sup>133</sup>. CO oxidation is coupled to ferredoxin reduction, and under physiological conditions, the saturation of reduced ferredoxin would lead to cellular accumulation of CO, which would damage metallo-containing proteins and could therefore be lethal to the microbe. Here, the HytA-E<sub>1,2</sub>/FdhA (referred to as Hyt/Fdh) complex is thought to come into play to dissipate the reducing power and at the same time orchestrate the first step of the methyl branch by reducing CO<sub>2</sub>.

### **Hyt/Fdh: A NADP-specific [FeFe] hydrogenase in a functional complex with a formate dehydrogenase**

The main cellular function of the seven-subunit complex (HytABCDE<sub>1</sub>E<sub>2</sub>FdhA encoded by a single operon, **Figure 8**) is the conversion of CO<sub>2</sub> to formate, which can be assimilated by the formyl-tetrahydrofolate synthetase<sup>131</sup>. The reversible CO<sub>2</sub> reduction reaction, catalyzed by the formate dehydrogenase, can use two alternative electron sources: the first possible electron source for CO<sub>2</sub> reduction comes from the H<sub>2</sub>-oxidation. Direct electron coupling of the [FeFe] hydrogenase (HytA) and the formate dehydrogenase (FdhA, W-dependent) facilitate the reversible hydrogenation of CO<sub>2</sub> to formate, a process identical to that of the H<sub>2</sub>-dependent CO<sub>2</sub> reductase (HDCR, see below). Alternatively, electrons can be derived from the simultaneous oxidation of NADPH (oxidized at the NADPH-oxidation site HytB) and reduced ferredoxin through an electron confurcation event<sup>13,131</sup>. Electron confurcation is an energy-coupling process, in which electrons of different redox potential (obtained from different donors) are converged to a single electron acceptor<sup>56</sup>. During electron bifurcation, the reverse scenario occurs: electrons from one donor molecule are split and transferred to acceptors with different redox potentials, allowing for the generation of low and high-energy electron pairs to drive simultaneous endergonic and exergonic reactions<sup>56</sup>. At the start of my PhD all electron bifurcation/confurcation mechanisms known relied on quinones (Q cycle) or flavins<sup>137,138</sup>. In Hyt/Fdh complex, the electrons derived from the confurcation event can be used to generate H<sub>2</sub> by the [FeFe] hydrogenase, thereby preventing

saturation of reduced ferredoxin in the cell<sup>131</sup>. The [FeFe] hydrogenase would exhaust the surplus of electrons generated during CO oxidation, maintaining high rates of the CO dehydrogenase and avoiding cellular damage from CO<sup>131</sup>. The site where the electron confurcation/bifurcation occurs is not identified yet. HytB, the site where NADPH gets oxidized, contains a flavin and could in theory perform flavin-based electron bifurcation<sup>138,139</sup>. However, HytB exhibits a high similarity (62 %) with the NADH-oxidase subunit Nqo1 of complex I from *Thermus thermophilus*<sup>138</sup>, and the residues surrounding and interacting with the flavin are almost identical between HytB and Nqo1, which is not known to bifurcate electrons. The bifurcation/confurcation properties of flavins are strongly influenced by the protein environment, in which a positively charged residue (Lys or Arg) is required to stabilize the fully reduced flavin, as shown by previous work<sup>140-142</sup>. If HytB is not the bifurcating subunit then a new mechanism involving different cofactor(s) might act and will certainly occur in the same way in all acetogenic electron-bifurcating [FeFe] hydrogenases<sup>143</sup>. Since the formate production using ferredoxin and NADPH is dependent on the hydrogenase, it was suggested that electron bifurcation is mediated by the active site of HytA.

Even though *C. autoethanogenum* is used in many applications, the molecular mechanism behind its efficient formate-generating machinery is still elusive. To expand the potential of *C. autoethanogenum* as a gas-converter, it is of high interest to unveil how the complex is structurally organized, how the electrons are flowing through the different modules, and to confirm if the hydrogenase can be used as an electron exhauster. As Hyt/Fdh resembles a fusion of the two characterized complexes HDCR and the electron bifurcating [FeFe] hydrogenase, which were both structurally elucidated within the last year<sup>129,144</sup>, insights about Hyt/Fdh can possibly be derived by learning from these two complexes.

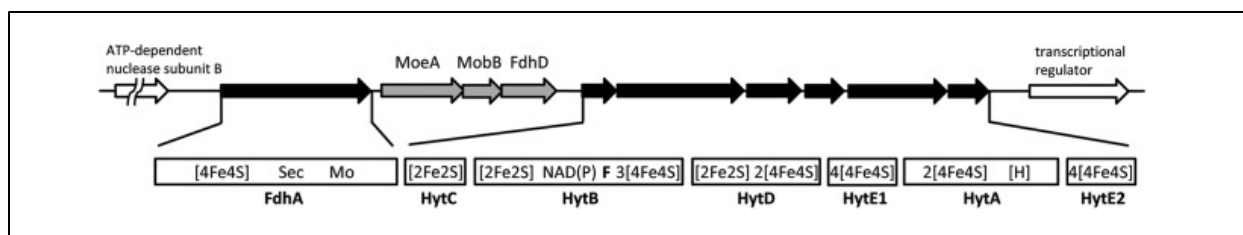


**Figure 8. Operon of Hyt/Fdh from *C. autoethanogenum*.** The *C. autoethanogenum* genomic region around the *hyt-fdh* gene cluster encoding electron-bifurcating NADP- and ferredoxin-dependent [FeFe]-hydrogenase in complex with formate dehydrogenase. The gene products MoeA, MobB, and FdhD that are not found in the purified enzyme complex are involved in molybdopterin cofactor synthesis and formate dehydrogenase maturation. Cofactor binding sites were deduced from the amino acid sequences of the proteins. Sec, selenocysteine; Mo, molybdopterin, to which either molybdate or tungstate can be bound; F, flavin; [H], H-cluster of [6Fe4S], the active site of [FeFe]-hydrogenase. The figure was reprinted with permission granted under Creative Commons license from Wang et al., 2013, J Bacteriol.<sup>131</sup>

### The electron-bifurcating [FeFe] hydrogenase HydABC

[FeFe] hydrogenases are the most efficient enzymes for catalytic H<sub>2</sub> production and are often found to be a part of multimeric enzyme complexes that catalyze a variety of reactions like in Hyt/Fdh or HDCR<sup>131,145,146</sup>. The oxidation or production of H<sub>2</sub> by [FeFe] hydrogenases is operated by the H-cluster, the active site of the [FeFe] hydrogenase that consists of a [4Fe-4S] cluster bound by a cysteine to one of the two iron metals (called "proximal" or "distal" depending on their position relative to the [4Fe-4S] cluster) that are ligated by CO and CN<sup>-</sup> ligands like the nickel and iron atom of [NiFe] hydrogenases (**Figure 3**)<sup>147</sup>. The first electron bifurcating [FeFe] hydrogenase was discovered in the hyperthermophilic and anaerobic bacterium *Thermotoga maritima* that uses NADH and reduced ferredoxin to produce H<sub>2</sub> through a confurcation event<sup>145</sup>. The electron-bifurcating [FeFe] hydrogenase HydABC of acetogenic bacteria, like *Acetobacterium woodii* and *Thermoanaerobacter kivui*, performs the reverse reaction and reduce low-potential ferredoxins by oxidizing H<sub>2</sub> (refs. 144,145,148). HydABC does not contain a classical bifurcating flavin and should rely on a different electron bifurcation mechanism<sup>145</sup>. Katsyv et al. recently showed that the [FeFe] hydrogenases from *A. woodii* and *T. kivui* harbor a single flavin mononucleotide (FMN) cofactor that establishes electron transfer pathways to the NAD<sup>+</sup> or NADP<sup>+</sup> (respectively for *A. woodii* or *T. kivui*) and ferredoxin reduction sites by a mechanism that is different from conventional flavin-based electron bifurcation enzymes<sup>144</sup>. The FMN site of the complex can switch between two modes: one where NAD(P)<sup>+</sup> is reduced (exergonic process), and another mode

for Fd reduction (endergonic process). This switch is achieved by adjusting the binding affinity of  $\text{NAD(P)}^+$  through the reduction of the conserved B2 cluster (**Figure 9**). The conformational changes in the HydBC unit are proposed to create a barrier that prevents electrons from flowing back from the Fd reduction pathway to the FMN site. The presence of a unique iron-sulfur cluster environment around the FMN cofactor, which is shared by all members of the HydABC clade, is essential for the bifurcation process (**Figure 9**)<sup>144</sup>.

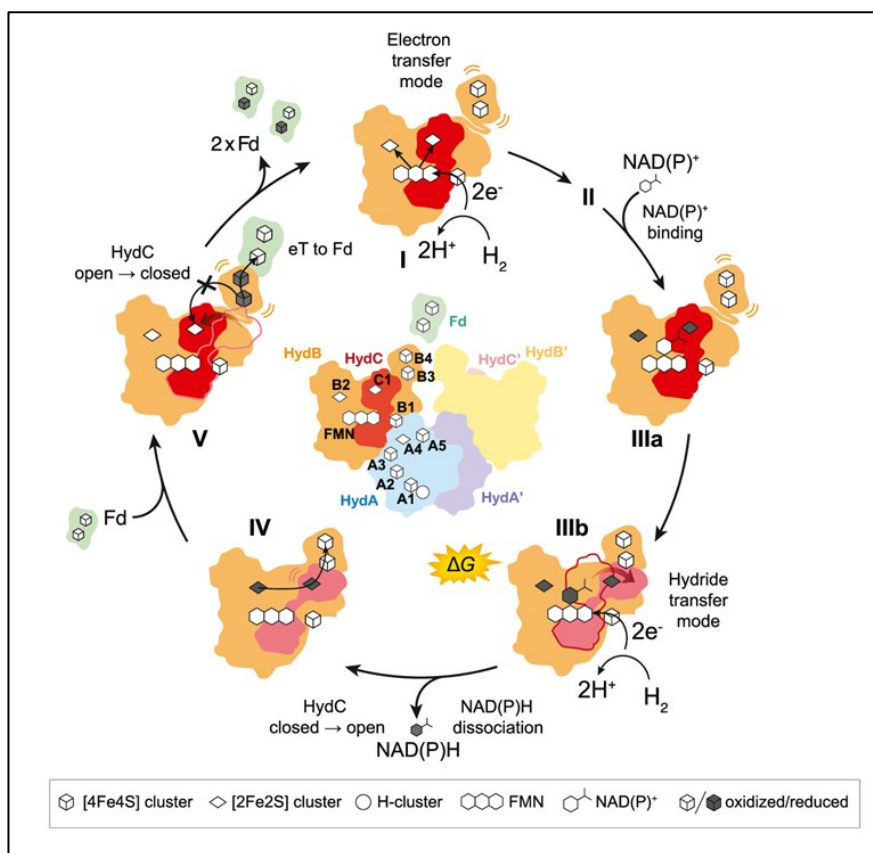


**Figure 9. Proposed catalytic cycle of HydABC according to Katsyv et al., 2023.** Putative electron bifurcation mechanism of HydABC (only the HydBC subunits are shown for simplicity).  $\text{H}_2$ -oxidation by the H-cluster in the HydA subunit leads to the reduction of FMN and subsequent electron transfer to B2 and C1. Reduction of B2 increases the binding affinity of  $\text{NAD(P)}^+$ . Reduction of C1 triggers conformational changes in HydC that open toward the HydB C-ter domain. Another  $\text{H}_2$ -oxidation step leads to electron transfer to the nucleotide binding site and  $\text{NAD(P)H}$  formation. Reduction and dissociation of the nucleotide decrease the C1–B3 distance, which allows for electron transfer to the HydB C-terminal (C-ter) domain.  $\text{NAD(P)H}$  dissociates and HydC transitions into a closed state that prevents electron backflow to the FMN site. Ferredoxin (Fd) binding allows for electron transfer from the HydB C-ter domain, leading to oxidized HydABC, and reinitiation of a new catalytic cycle. The image was reprinted with permission from Katsyv et al. 2023 *J. Am. Chem. Soc.* 2023, 145, 10, 5696-5709 (ref. 144).

## The hydrogen-dependent CO<sub>2</sub> reductase (HDCR)

HDCR, the enzyme that performs the reversible reduction of CO<sub>2</sub> into formate with H<sub>2</sub> as an electron donor, has been studied in a few model acetogens, such as the mesophilic acetogen *Acetobacterium woodii*<sup>149</sup>. Like Hyt/Fdh, the physiological function of HDCR is to catalyze the first reaction of the Wood-Ljungdahl pathway<sup>146</sup>. The HDCR from *A. woodii* consists of two catalytically active subunits, the formate dehydrogenase (FdhF2, Mo-dependent) and a [FeFe] hydrogenase (HydA2), connected by two 4 x [4Fe-4S] cluster containing modules (HycB2 and HycB3)<sup>149</sup>. While many hydrogenases are CO sensitive, the [FeFe] hydrogenase from *A. woodii* is completely CO tolerant<sup>149</sup>. Its CO-tolerance and its high activity (almost 2,000 times more effective than the fastest known chemical catalysts)<sup>146</sup> make the HDCR from *A. woodii* an interesting target for the conversion of syngas (containing H<sub>2</sub>, CO<sub>2</sub>, and CO). However, to use HDCR as a blueprint for designing efficient catalysts, it is necessary to understand the organization and the molecular mechanism of the complex. In 2016, it was shown that HDCR from *A. woodii* forms filaments and that the polymerization state of the enzyme is coupled to the enzymatic activity<sup>146</sup>. A major step towards a better understanding was recently achieved by the cryo-EM structure of HDCR from thermophilic acetogen *Thermoanaerobacter kivui*<sup>129</sup>. Here, HDCR forms cellular filaments, with a minimum repeating unit of a hexamer consisting of a formate dehydrogenase module (FdhF) linked in an arrangement by three electron-transfer modules (one HycB3 and two HycB4) to two hydrogenases (HydA2)<sup>129</sup>. HycB3 and HycB4 form the backbone of the filament (**Figure 10**). Tomography showed that *T. kivui* HDCR filaments bundle into ring-shaped superstructures that attach to the plasma membrane and are thought to provide stability and enhance HDCR activity<sup>129</sup>.

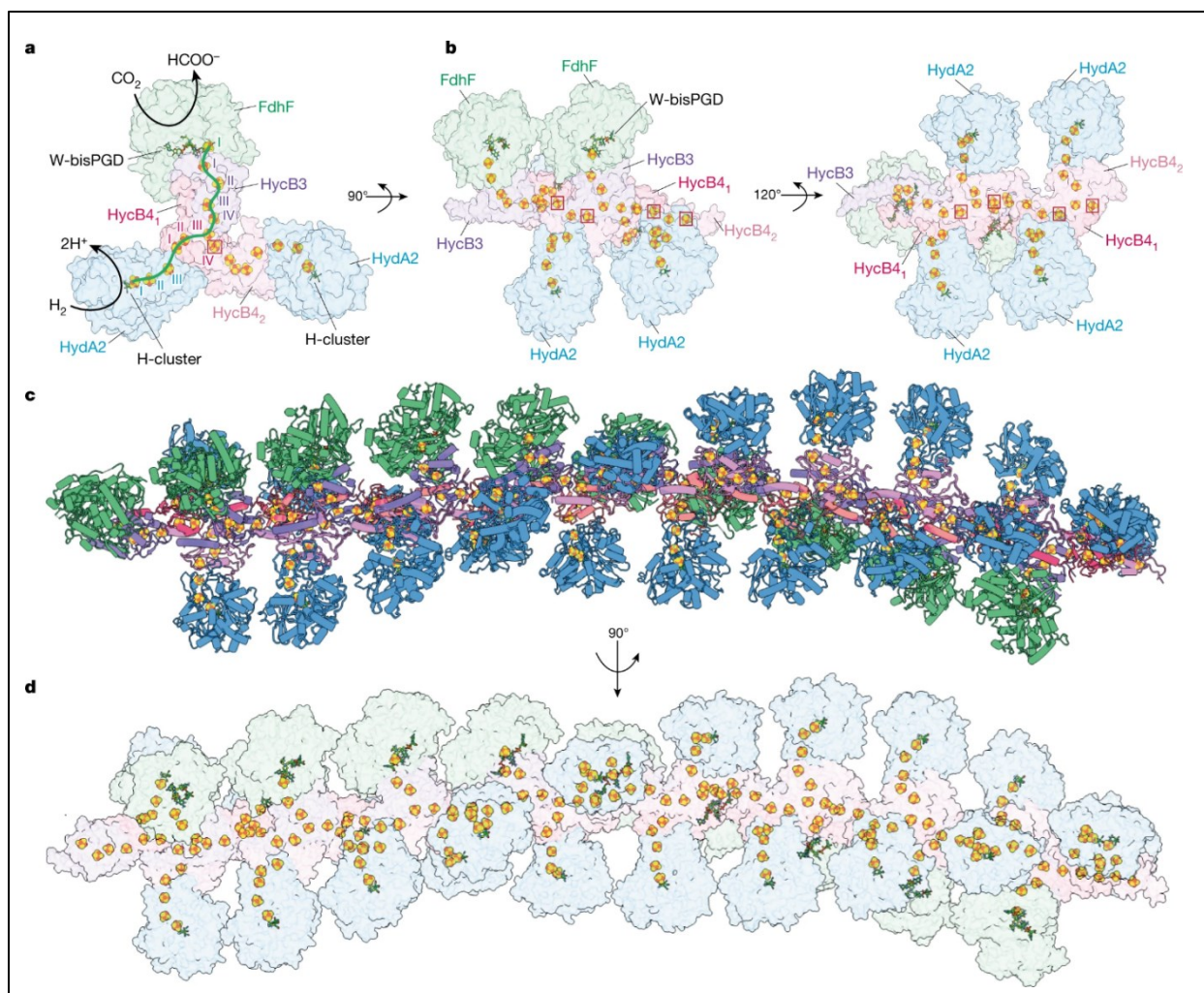


**Figure 10. The hydrogen-dependent CO<sub>2</sub> reductase (HDCR) from *Thermoanaerobacter kivui*.** Front view showing electron connectivity within the repeating unit of the HDCR filament. Subunits are shown in transparent surface representation. The shortest electron transfer pathway between H<sub>2</sub> oxidation and CO<sub>2</sub> reduction is highlighted. **b**, Side views showing electron connectivity within the HDCR filament. The [4Fe4S]-cluster HycB4 IV that is likely to be relevant for electron transfer between the repeating HDCR units is marked with red boxes. **c**, Model of a dodecameric HDCR filament shown in ribbon representation; subunits are colored as in (a). **d**, Central electron wire of the modelled HDCR filament, shown as a transparent surface overlaid with positions of the [4Fe4S]-clusters (orange and yellow spheres). This figure is reprinted with permission granted under the license ID 5572390319199 from Dietrich et al. (2022)<sup>129</sup>.



## 1.8 Research questions of the thesis

Microorganisms that rely on ancient metabolic pathways have evolved highly specialized and optimized enzymatic machinery to conserve energy or assimilate carbon from simple inorganic gases and play important roles in modern ecosystems and in biotechnology. My thesis aims to better understand the underlying enzymatic mechanisms involved in sulfate and carbon assimilation in methanogens, sulfate-reducing bacteria, and autotrophic acetogens. These results would lead to the optimization of cultivation conditions and expand the biotechnological potential of these extremophiles. Based on this aim, my thesis tested these hypotheses:

H1: *Methanothermococcus thermolithotrophicus* assimilates  $SO_4^{2-}$  by using a unique strategy.

**Chapter II** investigates how the hydrogenotrophic methanogen *Methanothermococcus thermolithotrophicus* can grow on  $SO_4^{2-}$  despite toxic intermediates and the required energy investment. Physiological studies, and biochemical and structural analyses of the  $SO_4^{2-}$  assimilating enzymes will reveal the organization of the complexes, the electron transfer path, and the catalytic site organization of the enzymes.

H2: The  $F_{420}$ -reducing hydrogenase (Frh) from *Methanothermococcus thermolithotrophicus* allows to characterize the [NiFe] redox states. *M. thermolithotrophicus* has been proven to be a valuable model organism for structural biology. In **Chapter III**, we will use it to purify and characterize the Frh and provide new insights into its overall organization and active site.

H3: The structure of the  $F_{420}$ -dependent sulfite reductase can reveal its mechanism and provides new insights about the common ancestor of the assimilatory and dissimilatory sulfite reductases.

Fsr has been proposed as a primordial sulfite reductase, potentially present before the divergence of assimilatory and dissimilatory sulfite reductases. In **Chapter IV** structural studies and EPR spectroscopy of Fsr from two *Methanococcales* provide new insights into the reaction mechanism and the evolutionary trajectory of sulfite reductases.

H4: Purification of enzymes from a sulfate-reducing ethane-oxidizing enrichment culture can reveal new features of the dissimilatory sulfate reduction pathway. In **Chapter V**, the native purification of the main cytosolic enzymes of the dissimilatory sulfate reduction pathway from an ethane oxidizing enrichment culture allows the structural elucidation of the complete dissimilatory sulfate reduction pathway.

H5: The selective power of crystallization can be used to isolate and characterize a single enzyme from a microbial mesocosm. **Chapter VI** attempts the purification of a highly expressed catabolic enzyme from a wastewater sludge sample. Despite the inhomogeneity of the sample, crystallization will allow to purify the targeted enzyme.

H6: Structural information from hydrogenotrophic methanogens will reveal common features and differences with acetogenic CO<sub>2</sub> fixation systems. **Chapter VII** reviews the CO<sub>2</sub> fixation strategies of hydrogenotrophic methanogens and autotrophic acetogens. The study of the structurally elucidated CO<sub>2</sub> fixation machinery of methanogens will allow the description of similarities and differences with acetogenic systems.

## 1.9 Contributions to the Manuscripts

### **Chapter II: “Assimilatory sulfate-reduction in the marine methanogen *Methanothermococcus thermolithotrophicus*”**

Marion Jespersen, Tristan Wagner

*Published in: Nature Microbiology • 05 June 2023. DOI: 10.1038/s41564-023-01398-8*

Author contributions: MJ cultivated the methanogens, and purified and crystallized all proteins described in this study. MJ performed all biochemical characterization. MJ and TW collected X-ray data and solved the structures. MJ and TW refined all models and validated the models. TW and MJ designed the research and contributed to the writing of the article.

### **Chapter III: “Structural and spectroscopic insights into the redox cycles of the active site of the [NiFeSe] and [NiFe] hydrogenases of group 3”**

Provisional author list: Marion Jespersen, Christian Lorent, Olivier Nicolas Lemaire, Ingo Zebger, Tristan Wagner

*Manuscript in preparation.*

Author contributions: MJ and TW cultivated the methanogens. MJ, ONL, and TW, purified and crystallized the [NiFe] hydrogenase, and TW purified and crystallized the [NiFeSe] hydrogenase. MJ performed all biochemical characterization. MJ, ONL, and TW collected X-ray data and solved the structures. MJ and TW refined all models and validated the models. CL and IZ performed all spectroscopic studies and analyses. TW, CL, and IZ designed the research. MJ wrote the initial version of the manuscript and all authors contribute to the writing of the article.

### **Chapter IV: “Structures of the sulfite detoxifying F<sub>420</sub>-dependent enzyme from *Methanococcales*”**

Marion Jespersen, Antonio J. Pierik, Tristan Wagner

*Published in: Nature Chemical Biology • 19 January 2023. DOI: 10.1038/s41589-022-01232-y*

Author contributions: MJ cultivated both methanogens and purified and crystallized both Fsr. MJ performed all biochemical characterizations. MJ and TW collected X-ray data and solved the structures. MJ refined both Fsr models and MJ with TW validated the models. MJ and AJP performed the redox titration experiments and AJP the spectroscopic analyses. TW and MJ designed the research. All co-authors contributed to the writing of the article.

### **Chapter V: “Structural elucidation of the dissimilatory sulfate-reduction pathway of an ethane-degrading microbial consortium”**

Marion Jespersen, Olivier Nicolas Lemaire, Cedric Jasper Hahn, Gunter Wegener, Tristan Wagner

*Manuscript in preparation*

Author contributions: MJ, ONL, and TW designed the research. CJH and GW maintained and cultivated the microbial enrichment. ONL purified the enzymes. MJ performed all biochemical characterization. ONL and TW collected X-ray data. MJ, ONL and TW solved the structures. MJ and TW built, refined and validated the models. MJ wrote the initial version of the manuscript and MJ, ONL, and TW are working on the manuscript with contributions from the co-authors.

### **Chapter VI: “Structure of a methane-generating enzyme isolated from wastewater treatment plant sludge”**

Provisional author list: Marion Jespersen, Grace d’Angelo, Almud Lonsing, Sonja Dunemann, Marie-Caroline Müller, Nevena Maslač, Bruno Hüttel, Manuel Liebeke, Jens Harder, and Tristan Wagner

*Manuscript in preparation*

Author contributions: TW, JH, MJ, MCM, and NM designed the research. JH collected the wastewater treatment samples. MJ purified and crystallized the MCR directly from the sludge, MJ and TWA solved the structures, refined and validated the models. GA and ML performed mass spectrometry, AL performed FISH, SD and BH sequenced and analyzed the metagenome. TW wrote the initial version of the article and all co-authors are contributing to the manuscript writing.

## **Chapter VII: “CO<sub>2</sub>-Fixation Strategies in Energy Extremophiles: What Can We Learn From Acetogens?”**

Olivier Nicolas Lemaire, Marion Jespersen, Tristan Wagner

*Published in: Frontiers in Microbiology Volume 11 • 03 April 2020. DOI: 10.3389/fmicb.2020.00486*

Author contributions: All authors participated to the manuscript writing.

This thesis was founded by the Deutsche Forschungsgemeinschaft (DFG) Schwerpunktprogramm 1927 “Iron-sulfur for Life” (WA 4053/1-1, M.J.) and the Max Planck Society.



## Chapter II

### Assimilatory sulfate reduction in the marine methanogen *Methanothermococcus thermolithotrophicus*

**Marion Jespersen<sup>1</sup> and Tristan Wagner<sup>1\*</sup>**

<sup>1</sup> Microbial Metabolism research group, Max Planck Institute for Marine Microbiology, Bremen, Germany.

\*Correspondence: [twagner@mpi-bremen.de](mailto:twagner@mpi-bremen.de)

*Nature Microbiology*

Received 28 February 2023; accepted 26 April 2023

Published online 5 June 2023

The pdf-document of this publication is not displayed due to copyright reasons. This chapter displays the accepted manuscript. The publication can be accessed at:

<https://www.nature.com/articles/s41564-023-01398-8#Sec32>

DOI: 10.1038/s41564-023-01398-8

## Abstract

*Methanothermococcus thermolithotrophicus* is the only known methanogen that grows on sulfate as its sole sulfur source, uniquely uniting methanogenesis and sulfate reduction. Here we use physiological, biochemical, and structural analyses to provide a snapshot of the complete sulfate reduction pathway of this methanogenic archaeon. We find that later steps in this pathway are catalysed by atypical enzymes. PAPS (3'-phosphoadenosine-5'-phosphosulfate) released by the APS kinase is converted into sulfite and 3'-phosphoadenosine-5'-phosphate (PAP) by a PAPS reductase that is similar to the APS reductases of dissimilatory sulfate reduction. A non-canonical PAP phosphatase then hydrolyses PAP. Finally, the F<sub>420</sub>-dependent sulfite reductase converts sulfite to sulfide for cellular assimilation. While metagenomic and metatranscriptomic studies suggest that the sulfate reduction pathway is present in several methanogens, the sulfate assimilation pathway in *M. thermolithotrophicus* is distinct. We propose that this pathway was 'mix-and-matched' through the acquisition of assimilatory and dissimilatory enzymes from other microorganisms and then repurposed to fill a unique metabolic role.



## Main Text

The most common methane-producing microorganisms have a high demand for sulfur due to their specific enzymes and metabolism. While most of those methanogens use sulfides ( $\text{HS}^-$ ), some have been shown to metabolize higher oxidation states of sulfur or even metal sulfides (for example,  $\text{FeS}_2$ ) for sulfur acquisition<sup>1-5</sup>. However, *Methanothermococcus thermolithotrophicus* is the only known methanogen capable of growing on sulfate ( $\text{SO}_4^{2-}$ ) as its sole sulfur source<sup>4,6</sup>. The metabolism of this marine hydrogenotroph, isolated from geothermally heated sea sediments near Naples (Italy), is paradoxical, as  $\text{SO}_4^{2-}$  reduction should lead to several physiological obstacles for a methane-producing microbe. First, methanogens commonly thrive in reduced sulfidic environments where all electron acceptors other than  $\text{CO}_2$  are depleted, including  $\text{SO}_4^{2-}$  (refs. 7,8). Second, at the interface where methanogens and  $\text{SO}_4^{2-}$  ions coexist, hydrogenotrophic methanogens must compete with dissimilatory  $\text{SO}_4^{2-}$ -reducing microorganisms for the common substrate dihydrogen ( $\text{H}_2$ )<sup>9</sup>. Third, methanogens live at the thermodynamic limits of Life and the adenosine triphosphate (ATP) hydrolysis coupled to  $\text{SO}_4^{2-}$ -reduction would be a substantial investment for such energy-limited microorganisms<sup>4,8,10</sup>. Finally, the  $\text{SO}_4^{2-}$  reduction pathway generates toxic intermediates that would interfere with cellular processes.

To assimilate  $\text{SO}_4^{2-}$ , the organism would have to capture the anion and transport it into the cell using a transporter. Inside the cell,  $\text{SO}_4^{2-}$  is activated by an ATP sulfurylase (ATPS) to generate adenosine 5'-phosphosulfate (APS)<sup>11-13</sup>. From there, organisms can use different strategies (Extended Data Fig. 1, routes a-c): (1a) APS is directly reduced by an APS reductase (APSR) to generate AMP and  $\text{SO}_3^{2-}$ . (1b) Alternatively, APS can be further phosphorylated to 3'-phosphoadenosine-5'-phosphosulfate (PAPS) by the APS kinase (APSK). A PAPS reductase (PAPSR) will reduce PAPS to  $\text{SO}_3^{2-}$  and the toxic nucleotide 3'-phosphoadenosine 5'-phosphate (PAP). PAP must be quickly hydrolysed to AMP and inorganic phosphate by a PAP phosphatase (PAPP). In both scenarios, the final step is carried out by a siroheme-containing sulfite reductase, which reduces the  $\text{SO}_3^{2-}$  into  $\text{HS}^-$ . The latter can then be incorporated into biomass. (1c) In a different pathway, the sulfite group of PAPS is transferred to another acceptor to build up sulfated metabolites. Route 1a is very similar to the dissimilatory pathway (Extended Data Fig. 1, route 2). However, dissimilatory APSRs and dissimilatory sulfite reductases are structurally and

phylogenetically distinct from their assimilatory counterparts and indirectly couple their reactions to membrane pumps, allowing for energy conservation<sup>14-16</sup>.

Genes encoding putative enzymes associated with  $\text{SO}_4^{2-}$ -reduction have been found in the genomes of multiple methanogens<sup>13</sup>, including *M. thermolithotrophicus*. For this methanogen, a theoretical, albeit incomplete,  $\text{SO}_4^{2-}$ -assimilation pathway can be hypothesized. Here we elucidated the complete  $\text{SO}_4^{2-}$ -reduction machinery of this archaeon and describe how this one methanogen can convert  $\text{SO}_4^{2-}$  into an elementary block of Life.

## Results

### A marine methanogen consuming $\text{SO}_4^{2-}$

Cultures grown on  $\text{Na}_2\text{S}$  were successively transferred to a sulfur-free medium until no growth was observed. *M. thermolithotrophicus* showed robust growth when at least 100  $\mu\text{M}$  of  $\text{Na}_2\text{SO}_4$  was supplemented in the medium and reached similar cell yields as the  $\text{Na}_2\text{S}$  grown culture. Under these cultivation conditions,  $\text{SO}_4^{2-}$  is consumed over time as cell density increases (Fig. 1a). When cells are grown only on  $\text{Na}_2\text{S}$ , no  $\text{SO}_4^{2-}$  could be detected (Fig. 1a), indicating that *M. thermolithotrophicus* is not performing sulfide oxidation.

We then challenged the  $\text{SO}_4^{2-}$ -grown culture by switching from batch to fermenter conditions, where  $\text{H}_2\text{S}$  can escape to the gas phase and does not accumulate compared to flask conditions. In this open system with temperature and pH controlled, *M. thermolithotrophicus* grew to a maximum  $\text{OD}_{600\text{nm}}$  of 6.45 within 19 hours (Fig. 1b).

One way to determine whether *M. thermolithotrophicus* relies on canonical enzymes of the  $\text{SO}_4^{2-}$  reduction pathway is to use molybdate ( $\text{MoO}_4^{2-}$ ). The structural analogue of  $\text{SO}_4^{2-}$  binds to the ATPS and triggers molybdolysis, which hydrolyses ATP to AMP and pyrophosphate ( $\text{PP}_i$ ), resulting in cellular energy depletion<sup>17,18</sup>. A  $\text{MoO}_4^{2-}:\text{SO}_4^{2-}$  molar ratio of 0.004:1 is sufficient to inhibit the activity of dissimilatory  $\text{SO}_4^{2-}$ -reducing bacteria for 168 hours, an effect mainly due to molybdolysis by ATPS<sup>19-21</sup>.  $\text{SO}_4^{2-}$  assimilation is also affected by  $\text{MoO}_4^{2-}$ , as demonstrated by studies on plants<sup>22</sup>. In the latter, growth inhibition occurred when  $\text{MoO}_4^{2-}$  was in excess compared to  $\text{SO}_4^{2-}$  and the ATPS activity was notably affected at a 1:1 ratio<sup>18</sup>. When applied on *M.*

*thermolithotrophicus*, a high  $\text{MoO}_4^{2-}:\text{Na}_2\text{S}$  ratio of 12.5:1 did not disturb growth of the  $\text{Na}_2\text{S}$ -culture, indicating that  $\text{MoO}_4^{2-}$  is not interfering with their basal metabolism. In contrast, a  $\text{MoO}_4^{2-}:\text{SO}_4^{2-}$  ratio of 6.25:1 was inhibitory to the  $\text{SO}_4^{2-}$ -grown culture, while a 1:1 ratio was not (Fig. 1c, Extended Data Fig. 2a).  $\text{SO}_4^{2-}$  addition to the  $\text{MoO}_4^{2-}$ -inhibited culture restored growth (Extended Data Fig. 2b), indicating the reversibility of inhibition and its strict control by the  $\text{MoO}_4^{2-}:\text{SO}_4^{2-}$  ratio rather than the  $\text{MoO}_4^{2-}$  concentration. In comparison, in *Archaeoglobus fulgidus*, an archaeon that performs dissimilatory  $\text{SO}_4^{2-}$ -reduction to conserve energy, we observed growth inhibition at a  $\text{MoO}_4^{2-}:\text{SO}_4^{2-}$  ratio of 0.001:1 (Fig. 1c, Extended Data Fig. 2c). These results suggest that *M. thermolithotrophicus* reduces  $\text{SO}_4^{2-}$  via an assimilatory pathway containing a functional ATPS. Genes coding for putative standalone ATPS and APSK were indeed on the same locus in the genome of the strain DSM2095 that we had re-sequenced (Fig. 1d)<sup>13,23</sup>. To confirm their functions, the ATPS and APSK from *M. thermolithotrophicus* (*MtATPS* and *MtAPSK*, respectively) were further characterized.

### **A classic ATPS/APSK to activate $\text{SO}_4^{2-}$**

The activity of the recombinantly expressed *MtATPS* and *MtAPSK* was tested via a coupled assay (Fig. 2a, Supplementary Fig. 1) and a specific activity of  $0.070 \pm 0.004$   $\mu\text{mol}$  of oxidized NADH  $\text{min}^{-1} \text{mg}^{-1}$  of *MtATPS* was measured. Under these conditions, the rate-limiting step was the pyrophosphatase activity. This highlights the need for rapid pyrophosphate degradation (Fig. 2a) to avoid a retro-inhibition as previously shown for other ATPS<sup>24</sup>. A  $\text{MoO}_4^{2-}:\text{SO}_4^{2-}$  ratio of 1:1.25 decreased the activity by half (see Methods), corroborating that ATPS is also reacting with  $\text{MoO}_4^{2-}$  as shown in other homologues<sup>18,21</sup>.

The structure of *MtATPS* was refined to 1.97-Å resolution and obtained in an apo state despite co-crystallization with APS and  $\text{SO}_4^{2-}$  (Extended Data Table 1). While the crystal packing suggests a homotetrameric assembly in two crystalline forms, size exclusion chromatography and surface analysis using PISA ([www.ebi.ac.uk/pdbe/pisa/](http://www.ebi.ac.uk/pdbe/pisa/)) confirmed a homodimeric state similar to bacterial homologues (Extended Data Fig. 3a and Supplementary Fig. 2). The structure exhibits the typical ATPS fold comprised of three domains (domain I, 1-156; domain II, 164-314 and domain III, 320-382, Fig. 2b). The dimeric interface is mainly organized by the domain III as observed in *T. thermophilus*, a notable difference compared with other structural homologues

(Extended Data Fig. 3a, b) (ref. 25-27). Similar to many thermophilic bacteria and archaea, the domain III contains a zinc-binding domain (320-343; Extended Data Fig. 3c, d) that might contribute to the thermal stability<sup>27</sup>. *MtATPS* superposition with structural homologues shows a slight domain rearrangement probably due to the absence of substrate (Extended Data Fig. 3b). All residues critical for the reaction are conserved in *MtATPS*, arguing for a conserved reaction mechanism (Fig. 2c,d, Extended Data Figs. 3e, f and 4a, and Supplementary Fig. 3).

The APS kinase model from *M. thermolithotrophicus*, *MtAPSK*, was refined to 1.77 Å. *MtAPSK* forms a homodimer with an organisation very similar to bacterial enzymes, which was expected due to its high sequence conservation (Extended Data Figs. 4b and 5a). Despite co-crystallization and soaking the crystals with APS and MgCl<sub>2</sub>, the *MtAPSK* structure was obtained in its apo state with a bound phosphate at the expected position of the ATP β-phosphate (Fig. 2e and Extended Data Fig. 5b, c). The N terminus and region 125-152 (the latter is involved in substrate binding<sup>28,29</sup>) could not be modelled due to the lack of electron density. However, the residues binding the substrates and Mg<sup>2+</sup> are conserved (Fig. 2f, Extended Data Fig. 5b, c and Supplementary Fig. 4), suggesting that *MtAPSK* should be functional, as confirmed by the coupled enzyme assay.

### **An exonuclease-derived PAP phosphatase**

If the ATPS and APSK are active, they will produce PAPS, an intermediate that could follow the metabolic routes 1b or 1c (Extended Data Fig. 1). Both routes will lead to the production of the toxic product PAP, which inhibits sulfotransferases and exoribonucleases, and disrupts RNA catabolism<sup>30,31</sup>. Therefore, it needs to be efficiently hydrolysed by a PAP phosphatase. While the genome did not contain any related PAP phosphatase, a gene coding for a putative phosphoesterase (Fig. 1d) was found in the genomic environment harbouring the ATPS and APSK genes. This PAP phosphatase candidate, belonging to the DHH family, was recombinantly expressed and produced inorganic phosphate (P<sub>i</sub>) from PAP at fast rates (50.2 ± 5.9 μmol of P<sub>i</sub> released min<sup>-1</sup> mg<sup>-1</sup> of purified enzyme with manganese). The activity was stimulated by manganese addition and showed a high specificity towards PAP (Fig. 3a).

To decipher the mechanism of this uncanonical PAP phosphatase (named *MtPAPP*), the enzyme was co-crystallized with manganese and PAP. The structure, solved by molecular replacement

with a template generated by AlphaFold2 (refs. 32,33), was refined to 3.1 Å resolution and contained the product AMP and an ion in its active site, modelled as a partially occupied  $Mn^{2+}$  (Extended Data Table 1). While the *MtPAPP* sequence does not align with homologues belonging to the DHH family (except for the DHH motif), it shares an overall fold similar to the exonuclease RecJ or the oligoribonuclease NrnA from *Bacillus subtilis* (*BsNrnA* which also exhibits PAP phosphatase activity; Extended Data Fig. 6a)<sup>34-36</sup>. The monomer is composed of an N-terminal (DHH, residues 1-180) and a C-terminal domain (DHHA1, residues 211-315) interconnected by a linker region (residues 181-210), forming a central groove (Fig. 3b). The DHH domain contains the catalytic site and the DHHA1 domain serves as a scaffold to bind the substrate with high specificity (Fig. 3b,c and Extended Data Fig. 6b). The motif coordinating the  $Mn^{2+}$  ion in RecJ and *BsNrnA* is perfectly conserved in *MtPAPP*<sup>34,36</sup>, therefore we expect that in its active state, *MtPAPP* would be loaded with two  $Mn^{2+}$ . The first one, partially observed in the structure, is coordinated by four aspartates (Asp8, Asp10, Asp57, Asp127) and a long-range interaction with His6. The absent second  $Mn^{2+}$  would be coordinated by the Asp10, Asp57, Asp127, the DHH motif (His76, His77) as well as by water molecules (Extended Data Fig. 6c). While the AMP shares a similar localization with structural homologues ( $\beta 9\beta 10\beta 11$ ), it is bound by a different interaction with the protein (Extended Data Fig. 6b and Supplementary Fig. 5). The nucleotide binding site would ideally place the 3'-phosphate of the PAP in front of the manganese when the enzyme is in its closed state (Extended Data Fig. 6c). The inter-domain movement, allowed by the linker, would facilitate a rapid exchange of the substrate/product, increasing the turnover of *MtPAPP*. The complete sequence of this PAP phosphatase was found in the genome of 168 archaea in which the nucleotide binding site is conserved (Fig. 3d,e and Supplementary Fig. 6). This suggests a common enzyme in archaea to detoxify PAP (Extended Data Fig. 7a).

### **A dissimilatory APSR-like enzyme reduces PAPS**

No genes encoding for a canonical PAPS-reductase (route 1b) or sulfo-transferase (route 1c) were found in the *M. thermolithotrophicus* genome. However, genes annotated as a dissimilatory APS reductase ( $\alpha$  and  $\beta$  subunit, APSR; Extended Data Fig. 7b and Supplementary Fig. 7) are present and co-occur with the previously described genes (Fig. 1d).

To experimentally confirm the activity and substrate specificity of this APS-reductase like enzyme, both subunits were co-expressed in *Escherichia coli*, purified and tested for enzyme activity assays (Fig. 4a). In contrast to dissimilatory APSRs which catalyse the reversible reduction of APS to AMP and  $\text{SO}_3^{2-}$  (refs. 37,38), we could not measure the reverse reaction (that is, AMP and  $\text{SO}_3^{2-}$ , or PAP and  $\text{SO}_3^{2-}$  as substrates) for *M. thermolithotrophicus* enzyme by using  $\text{K}_3\text{Fe}(\text{CN})_6$  as an electron acceptor. Instead, we used a coupled enzyme assay to reconstitute the pathway *in vitro* (Extended Data Fig. 8). *MtATPS*, a pyrophosphatase and the *MtAPSK* were used to generate PAPS and *MtPAPP* was added to remove PAP, a potential retro-inhibitor of the reaction<sup>39</sup>. The activity was monitored via the oxidation of reduced methyl viologen ( $\text{MV}_{\text{red}}$ ). When all components were present, a specific enzymatic activity of  $0.114 \pm 0.007 \mu\text{mol}$  of oxidized MV  $\text{min}^{-1} \text{mg}^{-1}$  of the APS-reductase-like enzyme was measured. A fivefold excess of the APS-reductase-like enzyme resulted in a 220% increase of the specific enzyme activity, indicating that the enzyme was the rate-limiting step of the reaction (Extended Data Fig. 8c). However, the accumulation of PAP (induced by the removal of *MtPAPP* or  $\text{Mn}^{2+}$ ) strongly inhibited the activity. The specific enzymatic activity with APS as a substrate (that is, removal of *MtAPSK*) was  $0.007 \pm 0.001 \mu\text{mol}$  of oxidized MV  $\text{min}^{-1} \text{mg}^{-1}$  of the APS-reductase-like enzyme (Fig. 4a). Considering the complexity of this coupled enzyme assay, kinetic parameters could not be determined. However, the assay did provide insights about the substrate specificity and confirmed that the APS-reductase-like enzyme from *M. thermolithotrophicus* exhibits traits of a PAPS reductase.

To gain further molecular insights into the unconventional APS-reductase-like enzyme from *M. thermolithotrophicus*, the enzyme was crystallized under anaerobic conditions. The structure was solved by a single-wavelength anomalous dispersion experiment measured at the Fe K-edge and refined to 1.45 Å resolution (Extended Table 1). The complex organizes as a  $\alpha_2\beta_2$  heterotetramer, with the same assembly as dissimilatory APS reductases (Fig. 4b and Extended Data Fig. 9). It is, however, drastically different from characterized single-domain assimilatory APS/PAPS reductases, which are thioredoxin/glutathione-dependent. Assimilatory APS/PAPS reductases share no sequence or structural homology with the *M. thermolithotrophicus* enzyme, and several motifs that are proposed to mediate substrate binding and catalytic activity in assimilatory APS/PAPS-reductases are absent (Extended Data Fig. 9) (ref. 40).

In *M. thermolithotrophicus* the  $\alpha$ -subunit, containing the flavin adenine dinucleotide (FAD), is a member of the fumarate reductase family<sup>37,41,42</sup> and the  $\beta$  subunit is mainly composed of a ferredoxin-like domain in which two [4Fe–4S] clusters are coordinated by eight cysteine residues (Fig. 4c). While there are no assimilatory P/APS reductase homologues to *M. thermolithotrophicus* enzyme, it shares 38% sequence identity with the  $\alpha$  subunit of the dissimilatory APS reductase from *A. fulgidus* (*AfAPSR* PDB: 2FJA, rmsd of 1.02 Å for 437 C $\alpha$  aligned on the  $\alpha$  subunit). The residues coordinating APS, invariable in the dissimilatory family, differ in *M. thermolithotrophicus* and might provoke a switch of specificity from APS to PAPS. Despite a short soak with PAP, the putative substrate pocket contains only solvent, and we used the *AfAPSR* to artificially model PAPS in the active site of the enzyme (Fig. 4d,e). The different substitutions mainly carried by the loop 104-123 would accommodate the additional 3'-phosphate group by salt-bridge interactions and hydrogen bonds (Fig. 4d-f). In APS reductases, however, a conserved glutamine ( $\alpha$ 145 in *A. fulgidus*) would clash with this phosphate group. The catalytic residues proposed in dissimilatory APS reductases are retained in the enzyme of *M. thermolithotrophicus* (Extended Data Fig. 9, Supplementary Fig. 7). We therefore propose an identical reaction mechanism on the basis of a nucleophilic attack of the atom N5 of FAD on the sulfur PAPS, which creates a FAD-PAPS intermediate that decays to PAP and FAD-SO<sub>3</sub><sup>2-</sup> (refs. 37,42). Taking together the enzyme rates and the structural analysis, we propose that *M. thermolithotrophicus* harbours a unique class of PAPS reductase (*MtPAPSR*) used to convert PAPS into SO<sub>3</sub><sup>2-</sup> and PAP.

### **The F<sub>420</sub>-dependent sulfite reductase catalyses the last step of the pathway**

The SO<sub>3</sub><sup>2-</sup> generated by *MtPAPSR* must be further reduced to HS<sup>-</sup>. In hydrogenotrophic methanogens, SO<sub>3</sub><sup>2-</sup> damages the methane-generating machinery and must be detoxified by the F<sub>420</sub>-dependent sulfite reductase (Fsr)<sup>23,43</sup>. We previously identified and characterized Group I Fsr in *M. thermolithotrophicus* (*MtFsr*) and determined a robust enzymatic activity towards SO<sub>3</sub><sup>2-</sup> (ref. 23). Besides a second Fsr isoform, *M. thermolithotrophicus* does not contain other potential sulfite reductases. While mass spectrometry confirmed that the Fsr isolated from SO<sub>4</sub><sup>2-</sup>-grown cells is the characterized Group I *MtFsr*, the physiological role of the second Fsr isoform remains unknown<sup>23</sup>. Therefore, *MtFsr* is the best candidate to catalyse the final reduction of SO<sub>3</sub><sup>2-</sup> to HS<sup>-</sup>. Native polyacrylamide gel electrophoresis (native PAGE) with cell extracts of cultures grown on different

sulfur substrates confirmed the absence of *MtFsr* from cells grown on  $\text{Na}_2\text{S}$  and its high abundance in cells grown on  $\text{SO}_3^{2-}$  (refs. 23,43).

We determined a specific sulfite reductase activity of  $18.42 \pm 0.13 \mu\text{mol}$  of oxidized MV  $\text{min}^{-1} \text{mg}^{-1}$  of cell extract from  $\text{Na}_2\text{SO}_3$ -grown cells, in comparison to  $7.31 \pm 0.63 \mu\text{mol}$  of oxidized MV  $\text{min}^{-1} \text{mg}^{-1}$  of cell extract from  $\text{Na}_2\text{SO}_4$ -grown cells, whereas cell extract from an  $\text{Na}_2\text{S}$ -grown culture had a specific sulfite reductase activity of  $3.04 \pm 0.25 \mu\text{mol}$  of oxidized MV  $\text{min}^{-1} \text{mg}^{-1}$  (Fig. 5a). In agreement, we observed a band compatible with *Fsr* on the native PAGE for the  $\text{SO}_4^{2-}$ -grown culture but in lower amounts compared to  $\text{SO}_3^{2-}$  conditions (Fig. 5b). The *MtFsr* structure recently published by our group was obtained from  $\text{SO}_4^{2-}$ -grown cells, which confirmed that it is the same enzyme expressed as under  $\text{SO}_3^{2-}$  conditions<sup>23</sup>. Taking together, these results argue that *MtFsr* is used as the last enzyme of the  $\text{SO}_4^{2-}$ -reduction pathway (Fig. 5c).

### **Genetic potential is not enough to sustain $\text{SO}_4^{2-}$ growth**

Methanogens commonly use  $\text{HS}^-$  as a sulfur source, and the ones who express Group I *Fsr* can also grow on  $\text{SO}_3^{2-}$  (refs. 13,23,43). Interestingly, some methanogens have genes that encode for proteins of the complete or partial  $\text{SO}_4^{2-}$  reduction pathway (Supplementary Fig. 8) (ref.13). So why is *M. thermolithotrophicus* the only methanogen so far that has been proven to grow on  $\text{SO}_4^{2-}$ ? We used *Methanocaldococcus infernus* as a model organism to investigate this further. *M. infernus* is a marine hyperthermophile that shares a very similar physiology with *M. thermolithotrophicus* and can grow in the same medium. It contains all genes coding for the enzymes characterized in this study except for the described PAPS<sub>R</sub>. However, the *M. infernus* genome encodes for a putative thioredoxin-dependent PAPS<sub>R</sub> and APS<sub>R</sub>, which share high sequence identities with the biochemically characterized assimilatory APS<sub>R</sub> and PAPS<sub>R</sub> from *M. jannaschii* (Fig. 6a and Extended Data Fig. 7b) (refs. 44,45). Therefore, based on genomic information, *M. infernus* should be able to assimilate  $\text{SO}_4^{2-}$ .

*M. thermolithotrophicus* and *M. infernus* were grown in the same medium and under the same cultivation conditions except that *M. infernus* was kept at 75 °C and *M. thermolithotrophicus* at 65 °C. *M. infernus* grew on 2 mM  $\text{Na}_2\text{S}$  and  $\text{Na}_2\text{SO}_3$  but was unable to use  $\text{SO}_4^{2-}$  as a sole source of sulfur in contrast to *M. thermolithotrophicus* (Fig. 6b).



This raises the question about the physiological function of the genes related to  $\text{SO}_4^{2-}$  assimilation in methanogenic archaea. Based on our data, it could be that other methanogens still require these enzymes to acquire sulfur via the route 1c (Extended Data Fig. 1). The sulfur group would be transferred to an acceptor by a non-canonical sulfo-transferase, which might be important for uncharted biosynthetic pathway(s). This could explain why the gene coding for the PAPP is still present in methanogens also harbouring the genes encoding an ATPS as well as an APSK. A counterargument to this hypothesis is the presence of the thioredoxin-dependent PAPSR or APSR, characterized in *M. jannaschii*, which rather argues for route 1b (refs.13,44,45). It is worth noticing that the gene coding for this putative assimilatory APSR also exists in *M. thermolithotrophicus* (WP\_018154242.1). Therefore, further biochemical investigations will be needed to elucidate the physiological roles of these enzymes in methanogens.

## Discussion

This work unveiled the unique  $\text{SO}_4^{2-}$ -assimilation metabolism of a methanogenic archaeon, offering a molecular snapshot of the complete set of enzymes involved in the pathway. *M. thermolithotrophicus* activates  $\text{SO}_4^{2-}$  by a conventional ATPS and APSK, but transforms it further by uncanonical enzymes (Fig. 5c).

PAPS produced by the APSK is usually metabolized by thioredoxin- or glutathione-dependent assimilatory PAPS reductases, which are organized as homo-oligomers. In contrast, *MtPAPSR* inherited the heterotetrameric organization and FAD-based catalytic mechanism from dissimilatory APS reductases (Fig. 4 and Extended Data Figs. 1 and 9). We propose that the substitution of only a few amino acids switched the specificity towards PAPS (Fig. 4d-f), which might have been the result of a fine-tuned evolutionary adaptation to promote assimilatory  $\text{SO}_4^{2-}$  reduction. It would be worthwhile to exchange the residues that confer PAPSR traits at the active site (Ser122, Lys120, Arg121) with those of APSR and observe the effects on substrate affinity.

The generated PAP is efficiently hydrolysed by *MtPAPP*. This PAP phosphatase belongs to the DHH family of phosphoesterases and shares structural homology with exonucleases but has no sequence homology with them. In comparison, conventional PAP phosphatases (part of the FIG superfamily) have a different fold (that is, CysQ) and use three magnesium ions to hydrolyse the

3'-phosphate of PAP<sup>30</sup>. *MtPAPP* appears to be a remarkable example of convergent evolution, illustrating how archaea developed their own apparatus to detoxify PAP efficiently.

Group I Fsr catalyses the final step of the SO<sub>4</sub><sup>2-</sup> reduction pathway. This enzyme shows distinct traits of dissimilatory sulfite reductases, with the active site composition of an assimilatory one<sup>23</sup>. By encoding the *fsr* gene on a different locus and most probably under a different regulator for its expression (for example, sulfite sensor), the methanogen is able to uncouple rapid SO<sub>3</sub><sup>2-</sup> detoxification from expressing the whole SO<sub>4</sub><sup>2-</sup> assimilation machinery. While the *MtATPS*, *MtAPSK*, and *MtPAPSR* show rather slow catalytic rates (see Supplementary Discussion), *MtFsr* and the *MtPAPP* have high specific activities compared with the first steps, triggering the equilibrium towards HS<sup>-</sup> production and efficiently eliminating toxic intermediates. Although our proposed pathway (Fig. 5c) would allow favourable thermodynamics, the first reactions should be regulated to avoid unnecessary ATP hydrolysis. We suspect that *MtATPS*, *MtAPSK*, and *MtPAPSR* are cross-regulated by the accumulation of their own products, as already shown for homologues<sup>39,46,47</sup>, which would allow direct retro-control to harmonize the intracellular sulfur flux.

*M. thermolithotrophicus* lives at the thermodynamic limit of Life but the described SO<sub>4</sub><sup>2-</sup> assimilation requires the hydrolysis of three ATP to ADP for one processed SO<sub>4</sub><sup>2-</sup>. Nevertheless, it is expected that under natural conditions, the benefit of fixing SO<sub>4</sub><sup>2-</sup> counterbalances the energy expenditure. The SO<sub>4</sub><sup>2-</sup>-grown cultures are not hampered by the additional energy requirement, which can be explained by our cultivation conditions that provide a high and constant H<sub>2</sub> partial pressure. Under environmental conditions, with a lower and fluctuating H<sub>2</sub> partial pressure, growth on SO<sub>4</sub><sup>2-</sup> is likely to be more challenging for *M. thermolithotrophicus*. While the methanogen cannot avoid the ATP investment, it may have found an energy-saving strategy for the 8-electron reduction reaction from PAPS to HS<sup>-</sup>. Fsr oxidizes F<sub>420</sub>H<sub>2</sub>, which is reduced back by the F<sub>420</sub>-reducing hydrogenase<sup>23,48</sup>. F<sub>420</sub>H<sub>2</sub> or NAD(P)H would be advantageous electron donors for *MtPAPSR*, but it would require the assistance of an oxidase partner that has not yet been identified. Alternatively, the stand-alone *MtPAPSR* may depend on reduced ferredoxin, which could be obtained from the H<sub>2</sub>-dependent ferredoxin reduction via the Eha/Ehb complex, another advantageous strategy of hydrogenotrophs to provide reducing power to fuel anabolic reactions (proposed in Fig. 5c) (ref. 49).

So far, it appears that the concomitant process of methanogenesis and complete  $\text{SO}_4^{2-}$  reduction to  $\text{HS}^-$  is restricted to *M. thermolithotrophicus*. Strikingly, the only apparent difference between *M. thermolithotrophicus* and other methanogens with the genomic potential to perform  $\text{SO}_4^{2-}$ -reduction is the acquisition of a PAPS reductase, which appears to belong to the dissimilatory family (Supplementary Fig. 8, Extended Data Fig. 7b and Supplementary Discussion). The physiological function of these  $\text{SO}_4^{2-}$ -reduction-associated genes in other methanogens remains to be uncovered, as well as the advantages of assimilating  $\text{SO}_4^{2-}$  for *M. thermolithotrophicus*. From an ecological point of view, it might be beneficial, if not essential, for *M. thermolithotrophicus* survival to be able to switch from  $\text{H}_2\text{S}$  uptake to  $\text{SO}_4^{2-}$  reduction under environmental conditions (see Supplementary Discussion).

The transplantation of the *M. thermolithotrophicus*  $\text{SO}_4^{2-}$  reduction system into methanogenic hosts, which are already used as gas-converters (for example, *Methanothermobacter*), would circumvent the need for highly toxic and explosive  $\text{H}_2\text{S}$  by using inexpensive and abundant  $\text{SO}_4^{2-}$ . Beyond opening fantastic possibilities for safer biotechnological applications, a  $\text{SO}_4^{2-}$ -reducing hydrogenotrophic methanogen also reinforces the question about the extent of an intertwined methanogenesis and sulfate reduction pathway during the evolution of early archaea. *M. thermolithotrophicus* has most probably assembled the entire  $\text{SO}_4^{2-}$  reduction pathway progressively via a “mix-and-match” scenario, providing a competitive advantage under fluctuating sulfur-source conditions and expanding its ecological niches.

## Materials & Methods

**Archaea strains and cultivation media.** *M. thermolithotrophicus* (DSM 2095), *M. infernus* (DSM 11812,) and *A. fulgidus* (DSM 4304) cells were obtained from the Leibniz Institute DSMZ-German Collection of Microorganisms and Cell Cultures (Braunschweig, Germany). *M. thermolithotrophicus* and *M. infernus* were cultivated in the same previously described minimal medium with some modifications<sup>23</sup> (see Extended Data for the complete composition of the media).

**Anaerobic growth of Archaea.** Cell growth was followed spectrophotometrically by measuring the  $\text{OD}_{600}$ . The purity of the culture was checked by light microscopy. The methanogens were

cultivated with  $1 \times 10^5$  Pa of  $\text{H}_2:\text{CO}_2$  with an 80:20 ratio in the gas phase. *M. infernus* was cultivated at 75 °C in 250 ml glass serum flasks and *M. thermolithotrophicus* was grown at 65 °C in flasks or fermenters. The serum flasks were not shaken but standing. *A. fulgidus* was cultivated in anaerobic and sealed 22 ml Hungate tubes, with  $0.8 \times 10^5$  Pa  $\text{N}_2:\text{CO}_2$ . DSM 4304 culture (0.5 ml) was grown in 10 ml of classic media (see Extended Data for the complete media composition) containing a final concentration of 20 mM D/L-lactate. The culture was incubated at 80 °C, standing. All cultures were stored at room temperature in the dark under anaerobic conditions. For the *A. fulgidus* medium, we found that high molybdate concentrations made it unstable. One of the bottles with a high  $\text{MoO}_4^{2-}$  concentration turned yellow (unrelated to  $\text{O}_2$  contamination) and was omitted, resulting in triplicate instead of quadruplicate cultures (Fig. 1c, right panel).

**Adaptation of *M. thermolithotrophicus* to  $\text{SO}_4^{2-}$  and minimal  $\text{SO}_4^{2-}$  requirement.** *M. thermolithotrophicus* cells grown on 2 mM  $\text{Na}_2\text{S}$  were successively transferred to 10 ml sulfur-free cultivation medium. After two transfers, the carry-over sulfur concentration of the inoculum did not support the growth of *M. thermolithotrophicus*. By supplementing 2 mM  $\text{Na}_2\text{SO}_4$ , *M. thermolithotrophicus* growth resumed. No reducing agent was added to cope with the absence of  $\text{HS}^-$ , which normally establishes a suitable reducing environment. Incubation without shaking is particularly important for reproducibility. Therefore, after inoculation, the cultures were incubated at 65 °C, standing for one night followed by shaking at 180 revolutions per minute (r.p.m.) until they reached their maximum  $\text{OD}_{600}$ . The gas phase was refreshed after the overnight incubation to maintain the pressure at  $1 \times 10^5$  Pa of  $\text{H}_2:\text{CO}_2$ . To measure the minimal  $\text{SO}_4^{2-}$  concentration required to sustain growth, sulfur-limited *M. thermolithotrophicus* cells (using an inoculum to media ratio of 1:20) were provided with 2 mM, 1 mM, 0.5 mM, 0.25 mM, 0.1 mM and 0.04 mM  $\text{Na}_2\text{SO}_4$ . Growth was still observable for cells grown on 0.1 mM but not at 0.04 mM  $\text{Na}_2\text{SO}_4$ .

**$\text{SO}_4^{2-}$  measurements via ion chromatography.** Ion chromatography (Methrom ion chromatograph) was used to measure the  $\text{SO}_4^{2-}$  concentrations, analysed via the software IC MagIC Net 3.2. A volume of 8 ml per sample was required, with a maximum concentration of 0.5 mM  $\text{SO}_4^{2-}$ .  $\text{SO}_4^{2-}$ -reducing *M. thermolithotrophicus* cells were therefore grown in 1 L Duran bottles with 100 ml sulfur-free media, which was supplemented with 0.5 mM  $\text{SO}_4^{2-}$  prior to inoculation. As a negative control, 0.5 mM  $\text{Na}_2\text{S}$ -grown *M. thermolithotrophicus* cells were used, inoculated and collected similarly as the  $\text{SO}_4^{2-}$ -reducing cultures. All samples were taken aerobically and were

passed through a 0.45  $\mu\text{M}$  filter (Sartorius). If the cell densities were too high to be filtered, the samples were centrifuged at 13,000  $\times g$  for 7 minutes at 4 °C and the supernatant was taken for ion chromatography measurements. The samples were stored at 4 °C if the measurements were not immediately performed.

**Growth of *M. thermolithotrophicus* in a fermenter.** *M. thermolithotrophicus* was grown in three independent fermenters at 60 °C with 10 mM  $\text{Na}_2\text{SO}_4$  as the sole sulfur source. For each fermenter, 7 l of anaerobic cultivation medium (see Sulfur-free cultivation medium for *Methanococcales*) supplemented with 10 mM  $\text{Na}_2\text{SO}_4$  was continuously bubbled with  $\text{H}_2:\text{CO}_2$  (80:20, 3 l  $\text{min}^{-1}$ ). Under stirring (220 r.p.m.), the medium was inoculated with 360 ml preculture (with an  $\text{OD}_{600}$  higher than 3). One hour after inoculation, the culture was stirred at 800 r.p.m. NaOH (1 M) was used as a base to readjust the pH upon acidification, which was controlled using a pH probe. The cells were grown until late exponential phase ( $\text{OD}_{600}$  of 6.25-6.8) and then immediately transferred in an anaerobic tent ( $\text{N}_2:\text{CO}_2$  atmosphere at a ratio of 90:10). Cells were collected by anaerobic centrifugation for 30 min at 6,000  $\times g$  at 4 °C. The highest  $\text{OD}_{600}$  recorded for *M. thermolithotrophicus* in a  $\text{SO}_4^{2-}$ -grown fermenter was 6.8 after 20 h.  $\text{SO}_4^{2-}$  culture (7 l) with an  $\text{OD}_{600}$  of 6.8 yielded 54 g of cells (wet weight). The cell pellet was transferred in a sealed bottle, gassed with  $0.3 \times 10^5$  Pa  $\text{N}_2$ , flash frozen in liquid  $\text{N}_2$  and stored at -80 °C.

**Synthetic gene constructs.** The DNA sequences of the ATP sulfurylase, the APS kinase, the PAP phosphatase and the PAPS reductase  $\alpha$  and  $\beta$  subunits from *M. thermolithotrophicus* were codon optimized for *E. coli*, synthesized and cloned into pET-28a(+) vectors. For *MtATP,S*, *MtAPSK* and the *MtPAPP* the restriction sites NdeI and BamHI were used, with a stop codon (TGA) incorporated before BamHI. For *MtPAPSR*, a His-tag was placed at the C terminus of the  $\alpha$  subunit and a ribosome binding site was inserted between the coding sequences of the  $\alpha$  and  $\beta$  subunits. The *MtPAPSR* construct had the restriction sites NcoI and BamHI, with one stop codon incorporated after the His-tag for the  $\alpha$  subunit and one stop codon before BamHI for the  $\beta$  subunit. These steps were performed by GenScript (GenScript Corp., Piscataway, NJ, USA). All sequences used are detailed in Supplementary Information under Constructs and gene codon optimisation.

**Enzyme overexpression and purification.** All constructs were overexpressed and purified under aerobic conditions following a similar protocol, except for *MtPAPSR* which was overexpressed and purified under an anaerobic atmosphere. All enzymes were passed on a HisTrap high

performance column (GE Healthcare), followed, if necessary, by tag cleavage and gel filtration (see Extended Data for the complete protocol).

**Protein crystallization.** Purified *MtATPS*, *MtAPSK* and *MtPAPP* were kept in 25 mM Tris/HCl pH 7.6, 10% v/v glycerol, 2 mM D-threitol and 150 mM NaCl. *MtPAPSR* was kept in the same buffer without NaCl. Freshly prepared unfrozen samples were immediately used for crystallization. *MtATPS*, *MtAPSK* and *MtPAPP* crystals were obtained under aerobic conditions at 18 °C. *MtPAPSR* crystals were obtained anaerobically (N<sub>2</sub>:H<sub>2</sub>, gas ratio of 97:3) by initial screening at 20 °C. The sitting drop method was performed on 96-well MRC 2-drop crystallization plates in polystyrene (SWISSCI) containing 90 µl of crystallization solution in the reservoir.

**Crystallization of *MtATPS*.** *MtATPS* (0.7 µl) at a concentration of 14 mg ml<sup>-1</sup> (*MtATPS* form 1, Extended Data Table 1) or at a concentration of 27 mg ml<sup>-1</sup> (*MtATPS* form 2) was mixed with 0.7 µl reservoir solution. *MtATPS* at 27 mg ml<sup>-1</sup> was co-crystallized with 2 mM AMPcPP as well as 2 mM Na<sub>2</sub>SO<sub>4</sub>. For *MtATPS* form 1, transparent star-shaped crystals appeared after a few weeks in the following crystallization condition: 35% w/v pentaerythritol ethoxylate (15/4 EO/OH) and 100 mM 2-(*N*-morpholino)ethanesulfonic acid (MES) pH 6.5. For *MtATPS* form 2, transparent, long but thin plate-shaped crystals appeared after a few weeks in the following crystallization condition: 20% w/v polyethylene glycol 8000, 100 mM MES pH 6.0 and 200 mM calcium acetate.

**Crystallization of *MtAPSK*.** *MtAPSK* (0.7 µl) at a concentration of 17.6 mg ml<sup>-1</sup> was mixed with 0.7 µl reservoir solution and co-crystallized with 2 mM MgCl<sub>2</sub>. Transparent, plate-shaped crystals appeared after a few weeks in the following crystallization condition: 20% w/v polyethylene glycol 3350, and 100 mM tri-sodium citrate pH 5.5. *MtAPSK* was also crystallized with 2 mM MgCl<sub>2</sub> and 2 mM APS but the obtained structures of those crystals were of lower resolution and without any substrate or product present in the active site.

**Crystallization of *MtPAPSR*.** *MtPAPSR* (0.7 µl) at a concentration of 20 mg ml<sup>-1</sup> was mixed with 0.7 µl reservoir solution and co-crystallized with FAD (0.5 mM final concentration). The crystal used for phasing was a brown flat square and appeared after a few days in the following crystallization condition: 40% v/v 2-methyl-2,4-pentanediol and 100 mM Tris/HCl pH 8.0.

The crystal used to refine at high resolution was brown with an elongated plate shape. It appeared after a few days in the following crystallization condition: 35% v/v 2-methyl-2,4-pentanediol, 100

,mM Tris pH 7.0 and 200 mM NaCl. Before transfer to liquid N<sub>2</sub>, the crystal was soaked in 10 mM disodium 3'-phosphoadenosine 5'-phosphate for 7 min.

**Crystallization of *MtPAPP*.** *MtPAPP* (0.7  $\mu$ l) at a concentration of 20 mg ml<sup>-1</sup> was mixed with 0.7  $\mu$ l reservoir solution and co-crystallized with Tb-Xo4 (10 mM final concentration), MnCl<sub>2</sub> (2 mM final concentration) and 2 mM PAP. The Tb-Xo4 is a nucleating/phasing agent<sup>50</sup>, which should increase the crystallization performance; however, in this case the same crystalline form was obtained in absence of the compound and diffracted to similar resolution. Transparent, bipyramid crystals appeared after a few weeks in the following crystallization condition: 1.6 M tri-sodium citrate.

**X-ray crystallography and structural analysis.** *MtPAPSR* crystal handling was done inside the Coy tent under anaerobic atmosphere (N<sub>2</sub>:H<sub>2</sub>, 97:3); the other crystals were handled under aerobic conditions. The crystals were directly plunged in liquid nitrogen or were soaked for 5-30 s in their crystallization solution supplemented with a cryoprotectant before being frozen in liquid nitrogen. For *MtATPS* form 2, 30% glycerol was used as cryoprotectant. For *MtAPSK*, 25% ethylene glycol was used as cryoprotectant.

Crystals were tested and collected at 100 K at different synchrotrons (Extended Data Table 1). Data were processed with autoPROC<sup>51</sup> except for *MtPAPP*, which gave better statistics with indexation by the X-ray Detector Software (XDS) and the scaling step performed with SCALA<sup>52</sup>. All data collection statistics are provided in Extended Data Table 1. *MtATPS* forms 1 and 2, *MtAPSK* and *MtPAPP* were solved by using PHENIX with the following templates: 1V47 (ATPS from *T. thermophilus*) for *MtATPS* form 1, *MtATPS* form 1 for *MtATPS* form 2 and 5CB6 (APS kinase from *Synechocystis* sp.) for *MtAPSK*. For *MtPAPP*, the template was created de novo by AlphaFold 2 (ref. 32).

For *MtPAPSR*, an X-ray fluorescence spectrum on the Fe K-edge was measured to optimize the data collection at the appropriate wavelength. Datasets were collected at 1.73646 Å for the single-wavelength anomalous dispersion experiment. Native datasets were collected at a wavelength of 0.97625 Å on another crystal. Data were processed and scaled with autoPROC<sup>51</sup>. Phasing, density modification and automatic building was performed with CRANK-2 (ref. 53).

All models were manually rebuilt with COOT and further refined with PHENIX<sup>54,55</sup>. During the refinement, non-crystallographic symmetry and translational-liberation screw were applied. For all structures, except for ATPS form 1, hydrogens were added in riding position in the last refinement cycles. Hydrogens were removed in the final deposited models.

All models were validated using MolProbity<sup>56</sup>. Data collection and refinement statistics, as well as PDB identification codes for the deposited models and structure factors are listed in Extended Data Table 1. Figures were generated with PyMOL (Schrödinger). The metal in ATPS was modelled as a zinc using CheckMyMetal<sup>57</sup>.

**High-resolution Clear Native PAGE (hrCN PAGE).** To visualize the expression levels of *MtFsr* when cells were grown on different sulfur sources, hrCN PAGE was performed. *M. thermolithotrophicus* cultures ( $2 \times 10$  ml) were supplemented with either 2 mM Na<sub>2</sub>S, 2 mM Na<sub>2</sub>SO<sub>3</sub>, 2 mM Na<sub>2</sub>S and 2 mM Na<sub>2</sub>SO<sub>4</sub>, or 2 mM Na<sub>2</sub>SO<sub>4</sub> as sulfur substrates and grown for one night at 65 °C, standing. Cells were collected by anaerobic centrifugation at 6,000 x g for 20 min at room temperature and the cell pellets were resuspended in 2 ml lysis buffer (50 mM tricine pH 8.0 and 2 mM sodium dithionite). The cells were sonicated 4 x at 70% intensity for 10 s, followed by a 30 s break (MS 73 probe, SONOPULS Bandelin). The hrCN PAGE was run anaerobically and the protocol is detailed in Extended Data under hrCN PAGE preparation. One gel with an 8–15% acrylamide gradient was run (shown in Fig. 5b) and another one with a 5–15% acrylamide gradient (see Source Data Fig. 5).

**Coupled enzyme activity of the *MtATPS/MtAPSK*.** The activity of both enzymes was determined by the production of ADP which was coupled to NADH oxidation via pyruvate kinase (PK) and the lactate dehydrogenase (LDH)<sup>58</sup>. The assays were performed in a final volume of 100 µl 96-well deep-well plates and spectrophotometrically monitored (Omega multi-mode microplate reader) at 360 nm at 35 °C. KH<sub>2</sub>PO<sub>4</sub> (100 mM) at pH 7.0, supplemented with 1.5 mM MgCl<sub>2</sub> and 100 mM KCl, was used as a buffer. For NADH, a molar extinction coefficient of 4,546.7 cm<sup>-1</sup> M<sup>-1</sup> was experimentally determined for the above-named conditions. To the buffer, 1 mM NADH, 2.5 mM Na<sub>2</sub>SO<sub>4</sub>, 1 mM phosphoenolpyruvate (PEP), 2 mM ATP, 2 U inorganic pyrophosphatase (*Saccharomyces cerevisiae*, 10108987001, Sigma-Aldrich®), 1.1 U ml<sup>-1</sup> lactate dehydrogenase, 0.8 U ml<sup>-1</sup> pyruvate kinase (rabbit muscle, P0294, Sigma-Aldrich) and 0.5 mg ml<sup>-1</sup> *MtAPSK* (all final concentrations) were added. The reaction was started by the addition of 0.5 mg ml<sup>-1</sup> *MtATPS*.



Addition of 0.02 mM Na<sub>2</sub>MoO<sub>4</sub> did not affect activity ( $0.116 \pm 0.027$   $\mu\text{mol}$  of oxidized NADH  $\text{min}^{-1} \text{mg}^{-1}$ ), but the addition of 2 mM Na<sub>2</sub>MoO<sub>4</sub> resulted in a decrease ( $0.068 \pm 0.019$   $\mu\text{mol}$  of oxidized NADH  $\text{min}^{-1} \text{mg}^{-1}$ ). All assays were performed in triplicates.

***MtPAPP* enzyme assay.** The activity of the *MtPAPP* was determined by the production of orthophosphate, which was quantified using the malachite green phosphate assay kit (Sigma-Aldrich) by the formation of a green complex. The assays were performed in 96-well deep-well plates and the absorbance at 620 nm was spectrophotometrically followed (Omega multi-mode microplate reader). Tris/HCl (25 mM) at pH 7.64 was used as a buffer. Buffer, 40  $\mu\text{M}$  PAP or 90  $\mu\text{M}$  of AMP/ADP/ATP/APS or PP<sub>i</sub>, 1 mg  $\text{ml}^{-1}$  bovine serum albumin, 50  $\mu\text{M}$  MnCl<sub>2</sub> and/or 50  $\mu\text{M}$  MgCl<sub>2</sub> (final concentration) were mixed in a 1.5 ml Eppendorf tube on ice. Previously frozen *MtPAPP* (0.5  $\mu\text{g ml}^{-1}$  final concentration) was added and the mixture (final volume of 40  $\mu\text{l}$ ) was immediately incubated for 5 min at 40 °C. Next, 14  $\mu\text{l}$  of the reaction mix was diluted in 66  $\mu\text{l}$  of filtered Milli-Q H<sub>2</sub>O and immediately flash frozen in liquid N<sub>2</sub> to quench the reaction. Then, 20  $\mu\text{l}$  of malachite green reagent was added to the samples, the mixture was incubated at room temperature for 30 min and the formation of the green complex was measured at 620 nm. All assays were performed in triplicates. The measurements presented in Fig. 3a come from two different experiments (left and right subpanels). Both experiments were performed at two different days with the same enzyme preparation.

**Coupled *MtPAPSR* assay.** Since PAPS is unstable at high temperatures, we first tried to determine the activity of *MtPAPSR* in the direction of PAPS production, as previously described for dissimilatory APS reductases for APS production<sup>38</sup>. PAPS oxidation was determined in 50 mM Tris/HCl buffer (pH 7.5) containing 5 mM Na<sub>2</sub>SO<sub>3</sub>, 2 mM PAP or 2 mM AMP (final concentrations) and 3.27  $\mu\text{g ml}^{-1}$  *MtPAPSR*. The reaction was started with a final concentration of 0.5 mM K<sub>3</sub>Fe(CN)<sub>6</sub>. The decrease in absorbance at 420 nm was measured and corrected for the background reaction without enzyme. No activity was detected. Therefore, we used the physiological reaction to monitor *MtPAPSR* activity. To perform the coupled *MtPAPSR* assay, the enzymes needed to be purified at the same time and immediately used for the assay (see Extended Data for the detailed purification protocol for the enzymes used in this assay).

*MtPAPSR* activity assays were carried out in an anaerobic atmosphere (100% N<sub>2</sub>) at 45 °C. The assays were performed in 200  $\mu\text{l}$  final volume in 96-well deep well-plates and

spectrophotometrically monitored on a SPECTROstar Nano microplate reader. HEPES (50 mM, pH 7.0) supplemented with 50 mM KCl, 1.5 mM MnCl<sub>2</sub> and 1.5 mM MgCl<sub>2</sub> was used as a buffer. Reduced methyl viologen (MV<sub>red</sub>, 0.5 mM) served as an electron donor for MtPAPSR. The molar extinction coefficient ( $\epsilon_{600\text{nm}} = 8,133.3 \text{ cm}^{-1} \text{ M}^{-1}$ ) was experimentally determined using the above-named conditions and by reducing methyl viologen with 2 mM sodium dithionite. For the assay, methyl viologen was reduced with carbon monoxide by the CO-dehydrogenase from *Clostridium autoethanogenum* according to a previously published protocol<sup>59</sup>. CO was exchanged for N<sub>2</sub> and the MV<sub>red</sub> was immediately used for the assay. To the buffer and MV<sub>red</sub>, 5 mM ATP, 1 mM sodium dithionite, 0.2 U pyrophosphatase (*E. coli*, MFCD00131379, Sigma-Aldrich), 0.127 mg ml<sup>-1</sup> MtATPS, 0.12 mg ml<sup>-1</sup> MtAPSK, 0.1 mg ml<sup>-1</sup> MtPAPP and 0.0645 mg ml<sup>-1</sup> MtPAPSR were added. The reaction was started by the addition of 5 mM Na<sub>2</sub>SO<sub>4</sub> and followed by oxidation of MV<sub>red</sub> at 600 nm. All assays were performed in triplicates.

**Sulfite reductase activity in cell extracts.** To determine the sulfite reductase activity from *M. thermolithotrophicus*, cultures were grown on either 2 mM Na<sub>2</sub>S, 2 mM Na<sub>2</sub>SO<sub>3</sub> or Na<sub>2</sub>SO<sub>4</sub> in 10 ml of the above-mentioned medium in serum flasks. Cells (9 ml) were collected in late exponential phase (OD<sub>600</sub>: 3.45 for 2 mM Na<sub>2</sub>S, 3.91 for 2 mM Na<sub>2</sub>SO<sub>3</sub>, 3.37 for Na<sub>2</sub>SO<sub>4</sub>) by centrifugation at 6,000 x g for 10 min at 4 °C. The supernatant was discarded and the cell pellets were frozen in liquid N<sub>2</sub>. The pellets were then resuspended in 1 ml 0.5 M KH<sub>2</sub>PO<sub>4</sub> pH 7.0. The cells were lysed by sonication (2 x 10 s at 50% intensity, probe MS73, SONOPULS Bandelin), followed by centrifugation at 4 °C at 15,600 x g. The supernatant was passed through a 0.2 µm filter and the protein concentration was determined by the Bradford method (6.63 mg ml<sup>-1</sup> for 2 mM Na<sub>2</sub>S, 6.14 mg ml<sup>-1</sup> for 2 mM Na<sub>2</sub>SO<sub>3</sub>, and 6.31 mg ml<sup>-1</sup> for Na<sub>2</sub>SO<sub>4</sub>). The activity assays were performed under an anaerobic atmosphere (100% N<sub>2</sub>) at 50 °C, in 96-well deep-well plates and were spectrophotometrically monitored (SPECTROstar Nano microplate reader). The assay mixture contained 0.5 M KH<sub>2</sub>PO<sub>4</sub> pH 7.0, 118 µM MV<sub>red</sub> (final concentration, previously reduced with the equimolar amount of sodium dithionite) and 30 µM Na<sub>2</sub>SO<sub>3</sub> (final concentration). Under these conditions, a molar extinction coefficient of  $\epsilon_{600\text{nm}} = 9,840 \text{ cm}^{-1} \text{ M}^{-1}$  was experimentally determined. The reaction was started by the addition of 0.05 µg of cell extract, followed by oxidation of MV<sub>red</sub> at 600 nm. All assays were performed in triplicates.

**Phylogenetic trees.** For a detailed description of the phylogenetic analysis, see Extended Data<sup>60</sup>.

**Data Availability Statement.** All structures used for structural comparison are accessible from the Protein Data Bank and accordingly cited in the text. The structures were deposited in the Protein Data Bank under the ID: 8A8G for *MtATPS* form 1, 8A8D for *MtATPS* form 2, 8A8H for *MtAPSK*, 8A8K for *MtPAPP* and 8A8O for *MtPAPSR*. The data for this study are available in the paper and its Supplementary Information. Source data are provided with this paper.

**Acknowledgements.** We thank the Max Planck Institute for Marine Microbiology and the Max Planck Society for continuous support. We acknowledge the SOLEIL synchrotron for beam time allocation and the beamline staff of Proxima-1 for assistance with data collection. Furthermore, we thank the staff of beamline X06DA from SLS and P11 at PETRA III. We thank Prof. Dr. Dennis R. Dean for providing us the RE plasmid pDB1281. We are thankful to Christina Probian and Ramona Appel for their continuous support in the Microbial Metabolism laboratory and cultivating *Archaeoglobus fulgidus*. We are grateful to Dr. Gunter Wegener and Martina Alisch from the HGF MPG Joint Research Group for Deep-Sea Ecology and Technology, for their assistance with the ion chromatography measurements. We deeply thank Dr. Ulrich Ermler, Prof. Dr. Julia Fritz-Steuber and Prof. Dr. Guenter Fritz for great discussions and critical comments regarding manuscript. This research was funded by the Max-Planck Gesellschaft and the Novo Nordisk foundation (NNF21OC0070790, TW). MJ was supported by the Deutsche Forschungsgemeinschaft Schwerpunktprogramm 1927 „Iron-sulfur for Life“ (WA 4053/1-1, MJ).

**Author contributions.** MJ cultivated the methanogens, purified and crystallized all proteins described in this study. MJ performed all biochemical characterization. MJ and TW collected X-ray data and solved the structures. MJ and TW refined all models and validated the models. TW and MJ designed the research and contributed to the writing of the article.

**Conflicts of Interest.** The authors declare no conflict of interest.

**Reviewer Information.** *Nature Microbiology* thanks M. Elizabeth Stroupe and the other, anonymous, reviewer(s) for their contribution to the peer review of this work.



## List of Figures

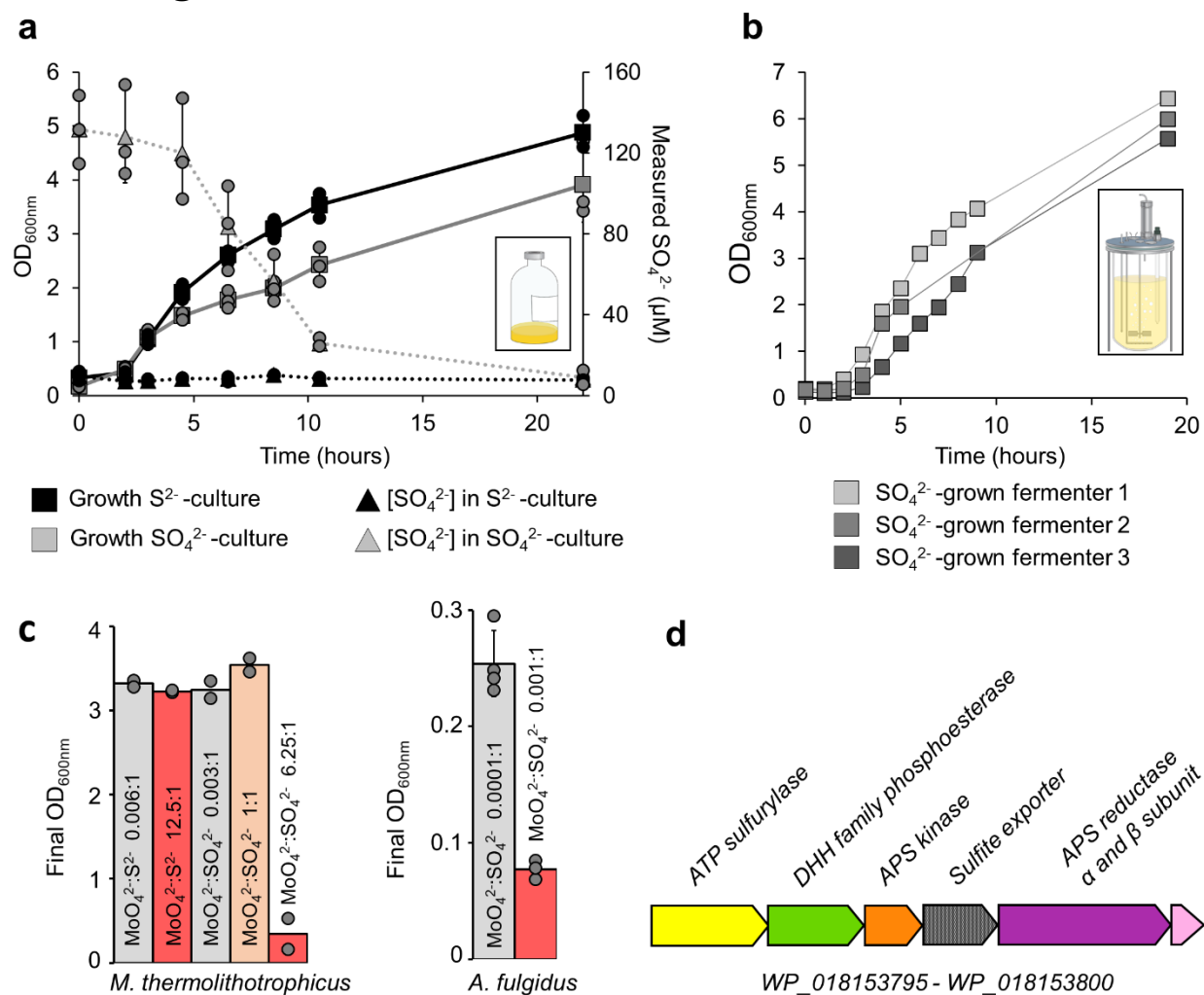


**Fig. 1.** SO<sub>4</sub><sup>2-</sup> growth dependency of *M. thermolithotrophicus*. **a**, *M. thermolithotrophicus* cultures grown on Na<sub>2</sub>S (black squares, 0.5 mM) and Na<sub>2</sub>SO<sub>4</sub> (grey squares, 0.5 mM). The consumption or release of SO<sub>4</sub><sup>2-</sup> in Na<sub>2</sub>S or Na<sub>2</sub>SO<sub>4</sub> cultures are shown by black and grey triangles, respectively. Data are presented as mean ± s.d. and individual values are shown as spheres (*n* = 3 replicates). Differences between expected (0.5 mM) and measured (0.13 mM) SO<sub>4</sub><sup>2-</sup> concentration for the initial point are considered to be due to an artefact from the medium (see Methods). **b**, *M. thermolithotrophicus* grown on 10 mM Na<sub>2</sub>SO<sub>4</sub> in three independent fermenters. The sampling points are visualized by grey squares. **c**, Molybdate (Na<sub>2</sub>MoO<sub>4</sub>) inhibition of Na<sub>2</sub>SO<sub>4</sub> assimilatory and dissimilatory archaea. Growth experiments for *M. thermolithotrophicus* were performed in duplicates and for *A. fulgidus* in quadruplicates (left) or triplicates (right). Data are represented as mean and for the triplicates and quadruplicates ± s.d. **d**, Predicted operon for SO<sub>4</sub><sup>2-</sup> reduction from the whole-genome shotgun sequence of *M. thermolithotrophicus*.

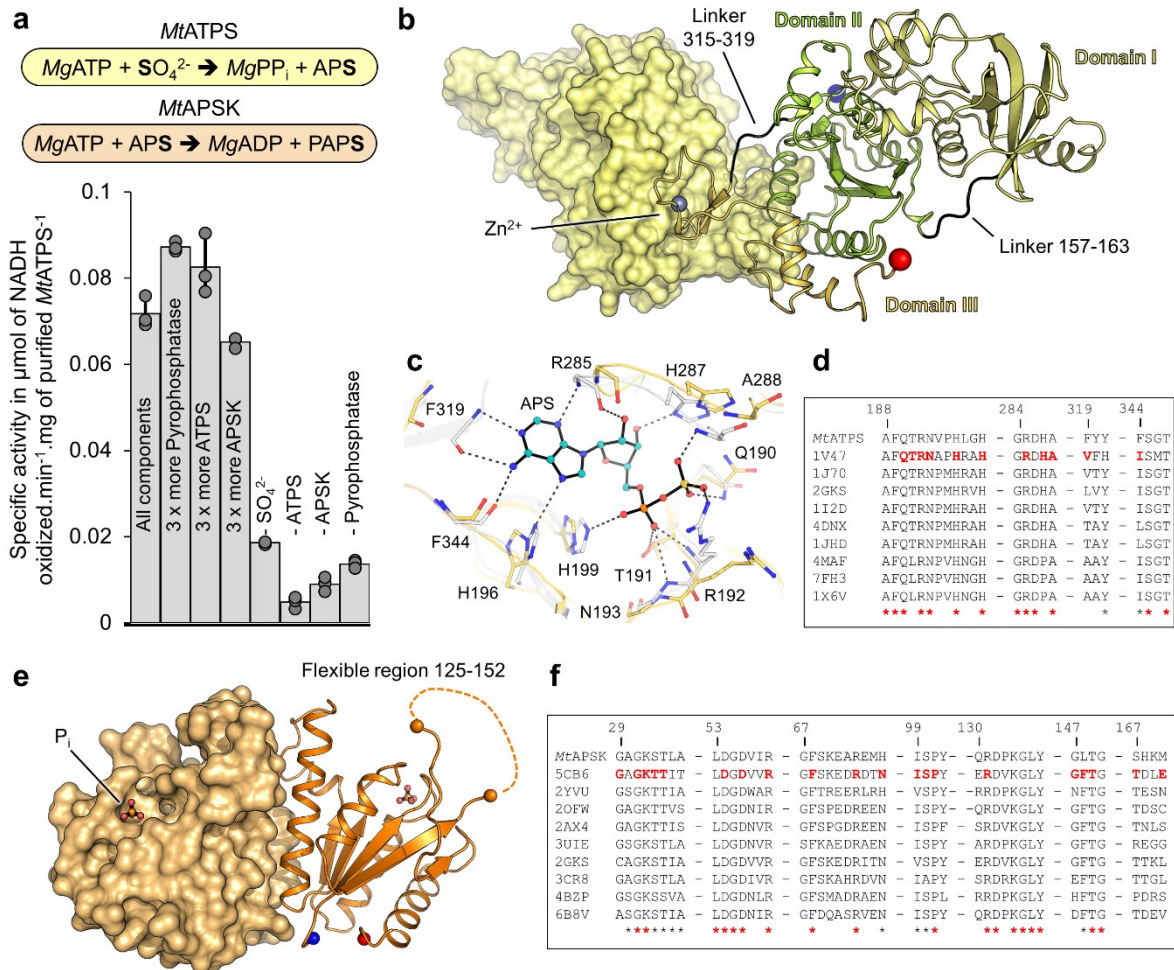


**Fig. 2. *MtATPS* and *MtAPSK* catalyse the first steps of the  $SO_4^{2-}$  reduction pathway.** **a**, Top panel, reactions catalysed by *MtATPS* and *MtAPSK*; Bottom panel, the specific activity of *MtATPS* and *MtAPSK*, determined via a coupled enzyme assay. “-” indicates the absence of the respective reactant. Data are presented as mean  $\pm$  s.d. and individual values are shown as grey spheres ( $n = 3$  replicates). **b**, *MtATPS* homodimeric structure in which one monomer is shown as light yellow surface and the other one in cartoon. **c**, Active site of *MtATPS* (yellow) superposed to the ATPS from *Thermus thermophilus* HB8 (PDB: 1V47, grey) containing the APS shown as balls and sticks with carbon coloured in cyan. Residues involved in the substrate binding are highlighted in sticks and only the ones from *MtATPS* are labelled. Hydrogen bonds between the ATPS from *T. thermophilus* and APS are represented as dashed lines. Nitrogen, oxygen, phosphorus and sulfur are coloured in blue, red, orange and yellow, respectively. **d**, Sequence conservation across ATPS homologues. **e**, *MtAPSK* homodimeric structure in which one monomer is shown in light orange surface and the other one in cartoon. The flexible loop illustrated by the dashed line could not be modelled. In all structures, the N- and C-termini are shown by a blue and red sphere, respectively. **f**, Sequence conservation across APSK homologues. For **d** and **f**, red bold residues are involved in substrate binding, while red and black stars are perfectly and well conserved residues, respectively.

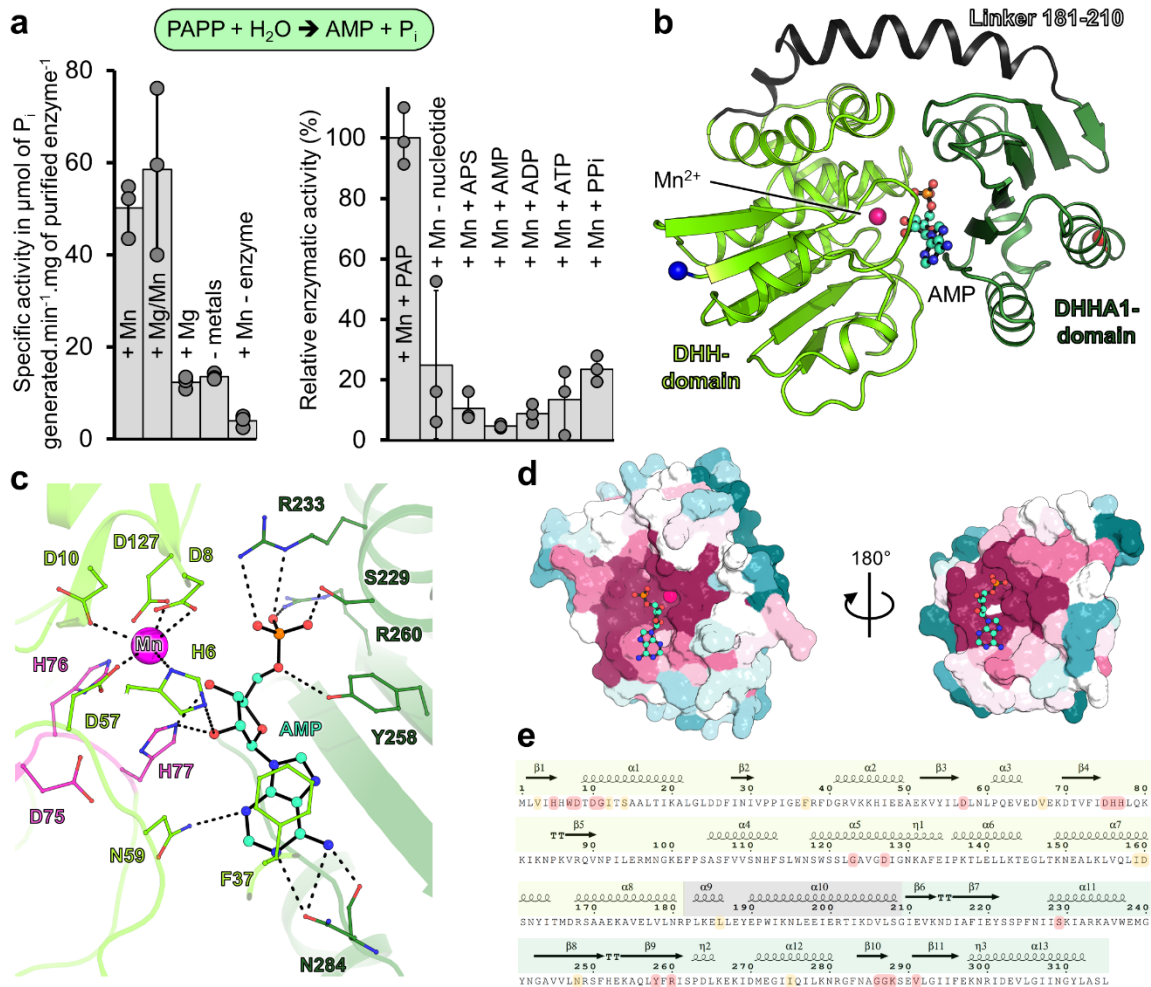


**Fig. 3. A unique type of PAP phosphatase.** **a**, Top panel, reaction catalysed by *MtPAPP*; Bottom panel, specific activity of the *MtPAPP* determined via the production of  $\text{P}_i$  (left) and relative enzymatic activity towards different nucleotides (right). Data are presented as mean  $\pm$  s.d. and individual values are shown as grey spheres ( $n = 3$  replicates). **b**, Organization of *MtPAPP* shown in cartoon representation. The N and C termini are highlighted as blue and red balls, respectively. Carbon, nitrogen, oxygen and phosphorus of AMP is coloured as cyan, blue, red and orange, respectively. **c**, Close-up view of the active site of *MtPAPP*. The residues coordinating the AMP and  $\text{Mn}^{2+}$  ion are highlighted by sticks and coloured as in **b**, with the residues from the DHH motif coloured in pink. **d**, Cut-through view of *MtPAPP* structure shown in surface representation and coloured by its sequence conservation across 168 archaeal homologues. The colour gradient ranges from variable (teal) to conserved (magenta). **e**, Secondary structure representation was done with ESPrpt 3.0 (ref. 61). The coloured frame corresponds to the different domains: DHH domain in light green, linker in grey and DHHA1 domain in darker green. Perfectly and well-conserved residues across 168 archaeal homologues are highlighted in red and yellow, respectively. The secondary structures composing *MtPAPP* are labelled, in which  $\beta$ -sheets,  $\alpha$ -helices, and  $\beta$ -turns are highlighted as arrows, springs and bold TT, respectively.

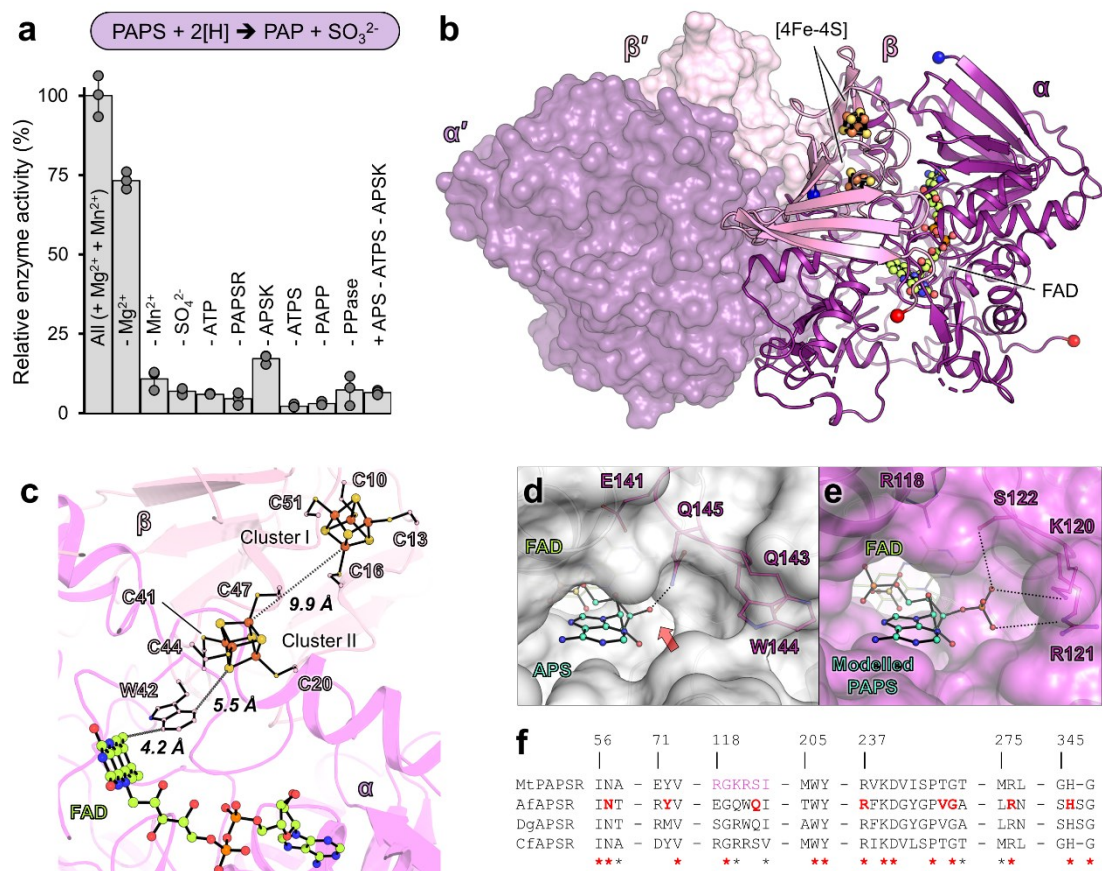


**Fig. 4. *MtPAPSR* has a dissimilatory APS-reductase architecture but is specific to PAPS.** **a**, Top panel, reaction catalysed by *MtPAPSR*; Bottom panel, relative enzyme activity of *MtPAPSR*, determined via a coupled enzyme assay (Extended Data Fig. 8). Data are presented as mean  $\pm$  s.d. and individual values are shown as grey spheres ( $n = 3$  replicates). **b**, *MtPAPSR* organization with one heterodimer in surface representation and the other in cartoon. N and C termini of both subunits are shown as balls and coloured in blue and red, respectively. Heterodimeric partners are labelled with a prime. Carbon, nitrogen, oxygen, phosphorus, iron and sulfur are coloured in lemon, blue, red, orange, brown and yellow, respectively. **c**, Close-up of cofactors and the electron flow. [4Fe–4S] clusters and cysteines coordinating them, FAD and the Trp42 proposed to participate in the electron transfer are shown in sticks and balls and coloured as in panel **b**. **d,e**, Active sites of APSR (**d**) from *A. fulgidus* containing APS (*AfAPSR*, PDB: 2FJA) and *MtPAPSR* with an artificially modelled PAPS (**e**) shown with a transparent surface. Residues involved in substrate recognition (based on modelled PAPS) are in balls and sticks and coloured as in panel **b**. A red arrow points to where PAPS would clash. **f**, Sequence conservation across the alpha subunit of *MtPAPSR*, *AfAPSR*, *Megalodesulfobivrio gigas* (*DgAPSR*, PDB: 3GYX) and the putative APSR from *Caldanaerobius fijiensis* (*CfAPSR*, WP\_073344903), which shares 68% sequence identity with *MtPAPSR*. Residues involved in APS binding for APSR are in bold and red; perfectly and well-conserved residues are highlighted with red and black stars, respectively. Trp206 and Tyr207 are involved in FAD binding. The sequence alignment was done with MUSCLE<sup>61</sup>.



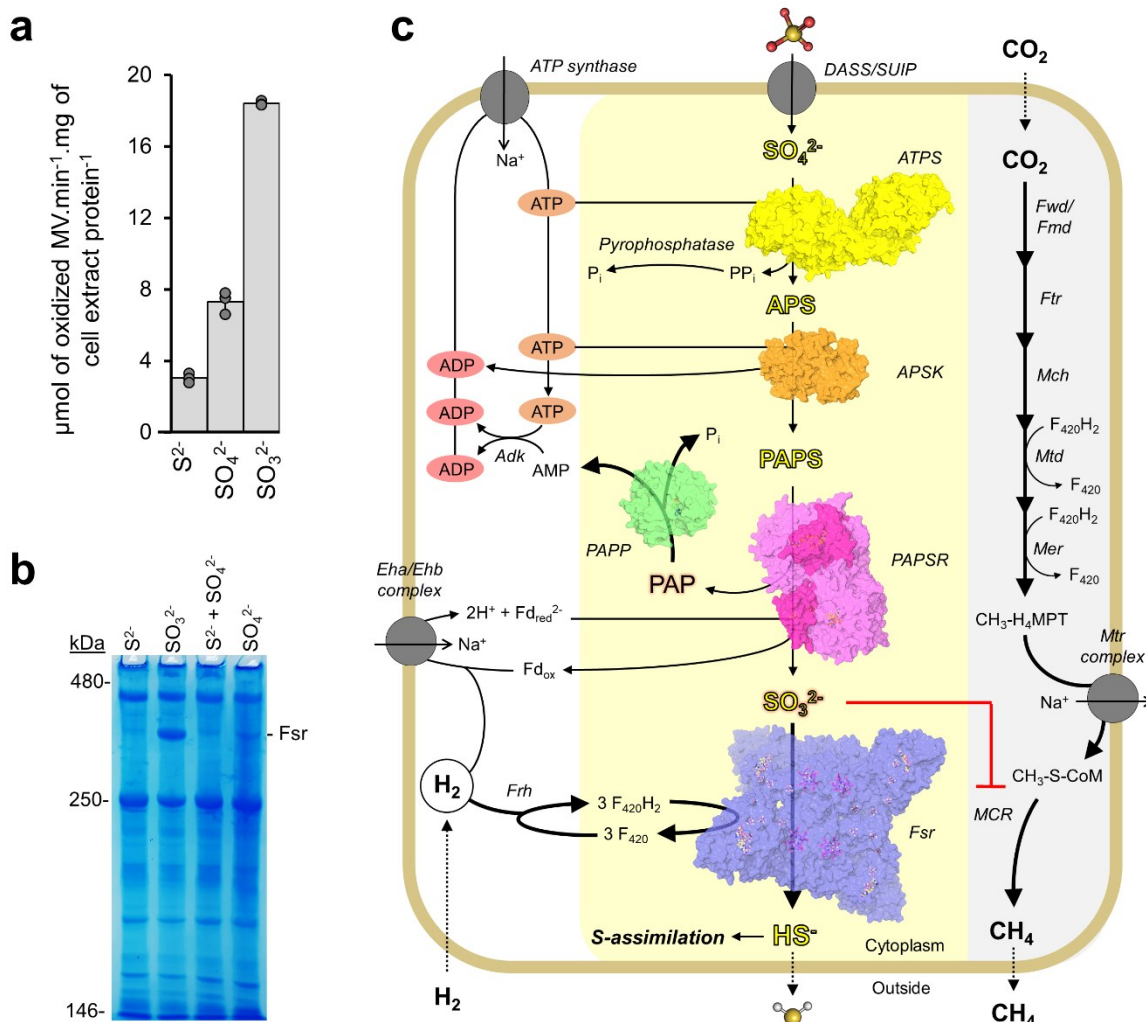


**Fig. 5. Proposed SO<sub>4</sub><sup>2-</sup> assimilation pathway in a methanogen.** **a**, Sulfite-reductase activity in cell extract from *M. thermolithotrophicus* grown on different sulfur sources. Data are presented as mean ± s.d. and individual values are shown as grey spheres ( $n=3$  biologically independent replicates). **b**, hrCN gel with *M. thermolithotrophicus* cell extract grown on different sulfur sources (15 μg protein loaded per sample,  $n=2$  biologically independent duplicates). **c**, Proposed SO<sub>4</sub><sup>2-</sup> assimilation pathway in *M. thermolithotrophicus*. Yellow and grey backgrounds highlight the SO<sub>4</sub><sup>2-</sup> reduction and methanogenesis pathways, respectively. Thick arrows indicate high metabolic fluxes. The structures of the enzymes operating the SO<sub>4</sub><sup>2-</sup>-assimilation pathway are shown in surface representation, with ligands as balls and sticks. Enzymes are abbreviated as follows: Fwd/Fmd, formylmethanofuran dehydrogenases; Ftr, tetrahydromethanopterin (H<sub>4</sub>MPT) formyltransferase; Mch, methenyl-H<sub>4</sub>MPT cyclohydrolase; Mtd, methylene-H<sub>4</sub>MPT dehydrogenase; Mer, 5,10-methylene-H<sub>4</sub>MPT reductase; Mtr, N<sup>5</sup>-CH<sub>3</sub>-H<sub>4</sub>MPT: coenzyme M methyl-transferase; Mcr, methyl-coenzyme M reductase; Adk, adenylate kinase; Frh, F<sub>420</sub>-reducing [NiFe]-hydrogenase; Eha/Ehb, energy-converting hydrogenase. The putative SO<sub>4</sub><sup>2-</sup> transporters belonging to the class DASS/SUIP are proposed to be WP\_018154444/WP\_018154062 and the pyrophosphatase WP\_018154121.

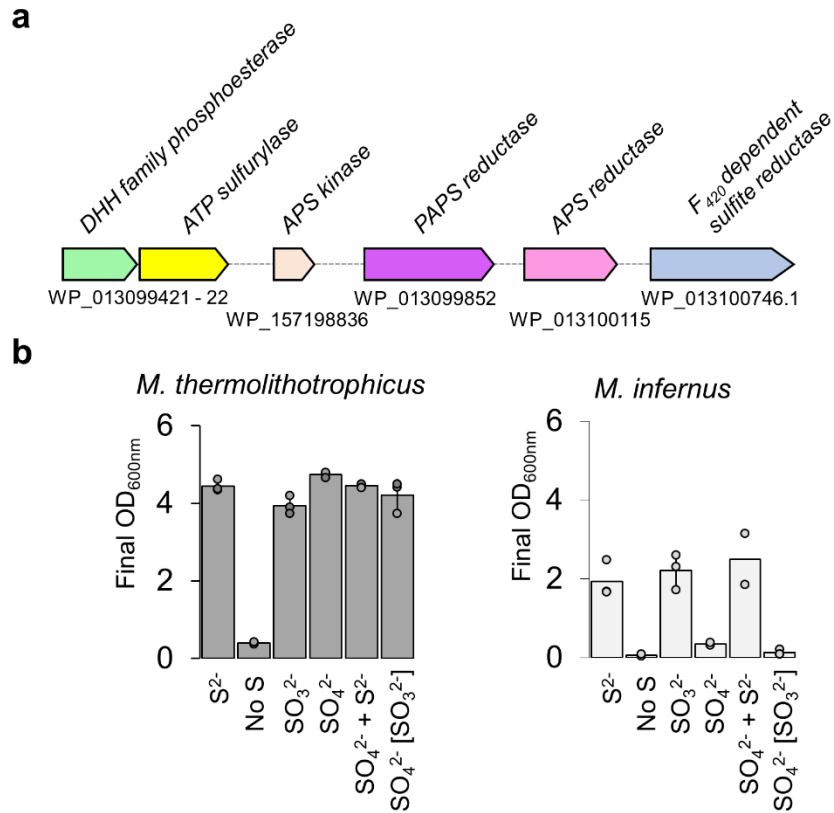


**Fig. 6. SO<sub>4</sub><sup>2-</sup> reduction potential in *Methanococcales*.** **a**, *Methanocaldococcus infernus* has the genomic potential to perform the whole SO<sub>4</sub><sup>2-</sup> assimilation pathway. WP\_013099421 has 59.68% amino acid sequence identity with the *MtPAPP*, WP\_013099422 has 70.60% sequence identity with *MtATPS* and WP\_157198836 has 75.44% sequence identity with *MtAPSK*. The APSR (WP\_013100115) and PAPS<sub>R</sub> (WP\_013099852) are similar to the biochemically characterized APSR and PAPS<sub>R</sub> from *M. jannaschii* (68.64% and 58.35% amino acid sequence identity, respectively), which have been shown to reduce APS/PAPS<sup>44,45</sup>. WP\_013099852 is not homologous to *MtPAPS<sub>R</sub>* but homologous to WP\_018154242, a putative PAPS reductase in *M. thermolithotrophicus*. WP\_013100746 has 65.30% sequence identity to Group I *MtFsr*. **b**, Growth of *M. thermolithotrophicus* and *M. infernus* on 2 mM Na<sub>2</sub>S, without an additional sulfur source, 2 mM Na<sub>2</sub>SO<sub>3</sub>, 2 mM Na<sub>2</sub>SO<sub>4</sub> or 2 mM Na<sub>2</sub>SO<sub>4</sub> with 2 mM Na<sub>2</sub>S. The SO<sub>3</sub><sup>2-</sup> in brackets indicates that it was used as the sulfur substrate for the inoculum. Represented are the maximum OD<sub>600nm</sub> of the cultures, in triplicates, shown as mean ± s.d. *M. infernus* cultures grown without sulfur, Na<sub>2</sub>SO<sub>4</sub> and on Na<sub>2</sub>S with Na<sub>2</sub>SO<sub>4</sub> are in duplicates. The individual data point of each replicate is shown as a sphere.

## References

- 1 Perona, J. J., Rauch, B. J. & Driggers, C. M. in *Molecular mechanisms of microbial evolution Grand Challenges in Biology and Biotechnology* Ch. Chapter 14, 371-408 (2018).
- 2 Eser, B. E., Zhang, X., Chanani, P. K., Begley, T. P. & Ealick, S. E. From suicide enzyme to catalyst: The iron-dependent sulfide transfer in *Methanococcus jannaschii* thiamin thiazole biosynthesis. *J Am Chem Soc* **138**, 3639-3642, doi:10.1021/jacs.6b00445 (2016).
- 3 Liu, Y., Beer, L. L. & Whitman, W. B. Methanogens: a window into ancient sulfur metabolism. *Trends Microbiol* **20**, 251-258, doi:10.1016/j.tim.2012.02.002 (2012).
- 4 Daniels, L., Belay, N. & Rajagopal, B. S. Assimilatory reduction of sulfate and sulfite by methanogenic bacteria. *Appl Environ Microbiol* **51**, 703-709, doi:10.1128/AEM.51.4.703-709.1986 (1986).
- 5 Payne, D., Spietz, R. L. & Boyd, E. S. Reductive dissolution of pyrite by methanogenic archaea. *ISME J* **15**, 3498-3507, doi:10.1038/s41396-021-01028-3 (2021).
- 6 Huber, H., Thomm, M., König, H., Thies, G. & Stetter, K. O. *Methanococcus thermolithotrophicus*, a novel thermophilic lithotrophic methanogen. *Archives of Microbiology* **132**, 47-50, doi:10.1007/BF00690816 (1982).
- 7 Kuivila, K. M., Murray, J. W., Devol, A. H. & Novelli, P. C. Methane production, sulfate reduction and competition for substrates in the sediments of Lake Washington. *Geochimica et Cosmochimica Acta* **53**, 409-416, doi:10.1016/0016-7037(89)90392-X (1989).
- 8 Thauer, R. K., Kaster, A.-K., Seedorf, H., Buckel, W. & Hedderich, R. Methanogenic archaea: ecologically relevant differences in energy conservation. *Nature Reviews Microbiology* **6**, 579-591, doi:10.1038/nrmicro1931 (2008).
- 9 Kristjansson JK, S. P. Why do sulfate-reducing bacteria outcompete methanogenic bacteria for substrates? *Oecologia* **60(2):264-266**, doi:10.1007/BF00379530 (1983).
- 10 Deppenmeier, U. & Müller, V. in *Bioenergetics: Energy Conservation and Conversion* (eds Günter Schäfer & Harvey S. Penefsky) 123-152 (Springer Berlin Heidelberg, 2008).
- 11 Hocking, W. P., Stokke, R., Roalkvam, I. & Steen, I. H. Identification of key components in the energy metabolism of the hyperthermophilic sulfate-reducing archaeon *Archaeoglobus fulgidus* by transcriptome analyses. *Front Microbiol* **5**, 95, doi:10.3389/fmicb.2014.00095 (2014).

- 12 Marietou, A., Roy, H., Jorgensen, B. B. & Kjeldsen, K. U. Sulfate transporters in dissimilatory sulfate reducing microorganisms: A comparative genomics analysis. *Front Microbiol* **9**, 309, doi:10.3389/fmicb.2018.00309 (2018).
- 13 Yu, H. *et al.* Comparative genomics and proteomic analysis of assimilatory sulfate reduction pathways in anaerobic methanotrophic archaea. *Front Microbiol* **9**, 2917, doi:10.3389/fmicb.2018.02917 (2018).
- 14 Ramos, A. R., Keller, K. L., Wall, J. D. & Pereira, I. A. The membrane QmoABC complex interacts directly with the dissimilatory adenosine 5'-phosphosulfate reductase in sulfate reducing bacteria. *Front Microbiol* **3**, 137, doi:10.3389/fmicb.2012.00137 (2012).
- 15 Oliveira, T. F. *et al.* The crystal structure of *Desulfovibrio vulgaris* dissimilatory sulfite reductase bound to DsrC provides novel insights into the mechanism of sulfate respiration. *J Biol Chem* **283**, 34141-34149, doi:10.1074/jbc.M805643200 (2008).
- 16 Santos, A. A. *et al.* A protein trisulfide couples dissimilatory sulfate reduction to energy conservation. *Science (New York, N.Y.)* **350**, 1541-1545, doi:10.1126/science.aad3558 (2015).
- 17 Ellis, R. J. Sulphate activation in higher plants. *Planta* **88**, 34-42, doi:10.1007/BF00396112 (1969).
- 18 Reuveny, Z. Derepression of ATP sulfurylase by the sulfate analogs molybdate and selenate in cultured tobacco cells. *Proceedings of the National Academy of Sciences of the United States of America* **74**, 619-622, doi:10.1073/pnas.74.2.619 (1977).
- 19 Biswas, K. C., Woodards, N. A., Xu, H. & Barton, L. L. Reduction of molybdate by sulfate-reducing bacteria. *Biometals* **22**, 131-139, doi:10.1007/s10534-008-9198-8 (2009).
- 20 Jesus, E., Lima, L., Bernardez, L. A. & Almeida, P. Inhibition of microbial sulfate reduction by molybdate. *Brazilian Journal of Petroleum & Gas* **9**, 95, doi:10.5419/bjpg2015-0010 (2015).
- 21 Zane, G. M., Wall, J. D. & De León, K. B. Novel mode of molybdate inhibition of *Desulfovibrio vulgaris* Hildenborough. *Front Microbiol* **11**, doi:10.3389/fmicb.2020.610455 (2020).
- 22 Zhang, Q., Lee, B.-R., Park, S.-H., Jeong, G.-O. & Kim, T.-H. Molybdate alters sulfate assimilation and induces oxidative stress in white clover (*Trifolium repens* L.). *Journal of The Korean Society of Grassland and Forage Science* **33**, 153-158, doi:10.5333/kgfs.2013.33.3.153 (2013).

- 23 Jespersen, M., Pierik, A. J. & Wagner, T. Structures of the sulfite detoxifying F<sub>420</sub>-dependent enzyme from *Methanococcales*. *Nature Chemical Biology*, doi:10.1038/s41589-022-01232-y (2023).
- 24 Lampreia, J., Pereira, A. S. & Moura, J. G. in *Methods in Enzymology* Vol. 243 241-260 (Academic Press, 1994).
- 25 Parey, K. *et al.* Structural, biochemical and genetic characterization of dissimilatory ATP Sulfurylase from *Allochromatium vinosum*. *PLOS ONE* **8**, e74707, doi:10.1371/journal.pone.0074707 (2013).
- 26 Beynon, J. D. *et al.* Crystal structure of ATP sulfurylase from the bacterial symbiont of the hydrothermal vent tubeworm *Riftia pachyptila*. *Biochemistry* **40**, 14509-14517, doi:10.1021/bi015643l (2001).
- 27 Taguchi, Y., Sugishima, M. & Fukuyama, K. Crystal structure of a novel zinc-binding ATP sulfurylase from *Thermus thermophilus* HB8. *Biochemistry* **43**, 4111-4118, doi:10.1021/bi036052t (2004).
- 28 Herrmann, J., Nathin, D., Lee, S. G., Sun, T. & Jez, J. M. Recapitulating the structural evolution of redox regulation in adenosine 5'-phosphosulfate kinase from Cyanobacteria to Plants. *J Biol Chem* **290**, 24705-24714, doi:10.1074/jbc.M115.679514 (2015).
- 29 Ravilious, G. E., Nguyen, A., Francois, J. A. & Jez, J. M. Structural basis and evolution of redox regulation in plant adenosine-5'-phosphosulfate kinase. *Proceedings of the National Academy of Sciences of the United States of America* **109**, 309-314, doi:10.1073/pnas.1115772108 (2012).
- 30 Erickson, A. I., Sarsam, R. D. & Fisher, A. J. Crystal structures of *Mycobacterium tuberculosis* CysQ, with substrate and products bound. *Biochemistry* **54**, 6830-6841, doi:10.1021/acs.biochem.5b01000 (2015).
- 31 Dichtl, B., Stevens, A. & Tollervey, D. Lithium toxicity in yeast is due to the inhibition of RNA processing enzymes. *The EMBO journal* **16**, 7184-7195, doi:10.1093/emboj/16.23.7184 (1997).
- 32 Jumper, J. *et al.* Highly accurate protein structure prediction with AlphaFold. *Nature* **596**, 583-589, doi:10.1038/s41586-021-03819-2 (2021).
- 33 Senior, A. W. *et al.* Improved protein structure prediction using potentials from deep learning. *Nature* **577**, 706-710, doi:10.1038/s41586-019-1923-7 (2020).

- 34 Mechold, U., Fang, G., Ngo, S., Ogryzko, V. & Danchin, A. YtqI from *Bacillus subtilis* has both oligoribonuclease and pAp-phosphatase activity. *Nucleic Acids Res* **35**, 4552-4561, doi:10.1093/nar/gkm462 (2007).
- 35 Schmier, B. J., Nellersa, C. M. & Malhotra, A. Structural basis for the bidirectional activity of *Bacillus* nanoRNase NrnA. *Scientific Reports* **7**, 11085, doi:10.1038/s41598-017-09403-x (2017).
- 36 Yamagata, A., Kakuta, Y., Masui, R. & Fukuyama, K. The crystal structure of exonuclease RecJ bound to Mn<sup>2+</sup> ion suggests how its characteristic motifs are involved in exonuclease activity. *Proceedings of the National Academy of Sciences of the United States of America* **99**, 5908-5912, doi:10.1073/pnas.092547099 % (2002).
- 37 Chiang, Y. L. *et al.* Crystal structure of Adenylylsulfate reductase from *Desulfovibrio gigas* suggests a potential self-regulation mechanism involving the C terminus of the beta-subunit. *Journal of bacteriology* **191**, 7597-7608, doi:10.1128/jb.00583-09 (2009).
- 38 Fritz, G., Buchert, T. & Kroneck, P. M. The function of the [4Fe-4S] clusters and FAD in bacterial and archaeal adenylylsulfate reductases. Evidence for flavin-catalyzed reduction of adenosine 5'-phosphosulfate. *J Biol Chem* **277**, 26066-26073, doi:10.1074/jbc.M203397200 (2002).
- 39 Schwenn, J. D. & Schriek, U. PAPS-reductase from *Escherichia coli*: characterization of the enzyme as probe for thioredoxins. *Zeitschrift fur Naturforschung. C, Journal of biosciences* **42**, 93-102, doi:10.1515/znc-1987-1-216 (1987).
- 40 Yu, Z., Lemongello, D., Segel, I. H. & Fisher, A. J. Crystal structure of *Saccharomyces cerevisiae* 3'-phosphoadenosine-5'-phosphosulfate reductase complexed with adenosine 3',5'-bisphosphate. *Biochemistry* **47**, 12777-12786, doi:10.1021/bi801118f (2008).
- 41 Schiffer, A., Fritz, G., Kroneck, P. M. H. & Ermler, U. Reaction mechanism of the iron-sulfur flavoenzyme adenosine-5'-phosphosulfate reductase based on the structural characterization of different enzymatic states. *Biochemistry* **45**, 2960-2967, doi:10.1021/bi0521689 (2006).
- 42 Fritz, G. *et al.* Structure of adenylylsulfate reductase from the hyperthermophilic *Archaeoglobus fulgidus* at 1.6-Å resolution. *Proceedings of the National Academy of Sciences of the United States of America* **99**, 1836-1841, doi:10.1073/pnas.042664399 % (2002).
- 43 Johnson, E. F. & Mukhopadhyay, B. A new type of sulfite reductase, a novel coenzyme F<sub>420</sub>-dependent enzyme, from the methanarchaeon *Methanocaldococcus jannaschii*. *J Biol Chem* **280**, 38776-38786, doi:10.1074/jbc.M503492200 (2005).

- 44 Cho, M. K. Discovery of novel 3'-phosphoadenosine-5'-phosphosulfate (PAPS) reductase from methanarcheon *Methanocaldococcus jannaschii*. Available at: <http://hdl.handle.net/2104/8817> (2013).
- 45 Lee, J. S. *et al.* Discovery of a novel adenosine 5'-phosphosulfate (APS) reductase from the methanarcheon *Methanocaldococcus jannaschii*. *Process Biochemistry* **46**, 154-161, doi:10.1016/j.procbio.2010.08.004 (2011).
- 46 Renosto, F., Martin, R. L., Wailes, L. M., Daley, L. A. & Segel, I. H. Regulation of inorganic sulfate activation in filamentous fungi. Allosteric inhibition of ATP sulfurylase by 3'-phosphoadenosine-5'-phosphosulfate. *Journal of Biological Chemistry* **265**, 10300-10308, doi:10.1016/s0021-9258(18)86946-0 (1990).
- 47 Timothy, O., Carol, C. & Segel, I. H. ATP sulfurylase from higher plants: purification and preliminary kinetics studies on the cabbage leaf enzyme. *Plant Physiology* **70**, 39-45 (1982).
- 48 Greening, C. *et al.* Physiology, biochemistry, and applications of F<sub>420</sub>- and F<sub>o</sub>-dependent redox reactions. *Microbiol Mol Biol Rev* **80**, 451-493, doi:10.1128/MMBR.00070-15 (2016).
- 49 Lie, T. J. *et al.* Essential anaplerotic role for the energy-converting hydrogenase Eha in hydrogenotrophic methanogenesis. *Proceedings of the National Academy of Sciences of the United States of America* **109**, 15473-15478, doi:10.1073/pnas.1208779109 (2012).
- 50 Engilberge, S. *et al.* Crystallophore: a versatile lanthanide complex for protein crystallography combining nucleating effects, phasing properties, and luminescence. *Chemical Science* **8**, 5909-5917, doi:10.1039/C7SC00758B (2017).
- 51 Vonrhein, C. *et al.* Data processing and analysis with the *autoPROC* toolbox. *Acta Crystallographica Section D* **67**, 293-302, doi:10.1107/S0907444911007773 (2011).
- 52 Winn, M. D. *et al.* Overview of the *CCP4* suite and current developments. *Acta Crystallogr D Biol Crystallogr* **67**, 235-242, doi:10.1107/S0907444910045749 (2011).
- 53 Pannu, N. S. *et al.* Recent advances in the *CRANK* software suite for experimental phasing. *Acta Crystallogr D* **67**, 331-337, doi:10.1107/S0907444910052224 (2011).
- 54 Emsley, P., Lohkamp, B., Scott, W. G. & Cowtan, K. Features and development of *Coot*. *Acta Crystallographica Section D-Biological Crystallography* **66**, 486-501, doi:10.1107/S0907444910007493 (2010).

- 55 Liebschner, D. *et al.* Macromolecular structure determination using X-rays, neutrons and electrons: recent developments in *Phenix*. *Acta Crystallogr D* **75**, 861-877, doi:10.1107/S2059798319011471 (2019).
- 56 Chen, V. B. *et al.* *MolProbity*: all-atom structure validation for macromolecular crystallography. *Acta Crystallogr D* **66**, 12-21, doi:10.1107/S0907444909042073 (2010).
- 57 Zheng, H. *et al.* CheckMyMetal: a macromolecular metal-binding validation tool. *Acta Crystallogr D Struct Biol* **73**, 223-233, doi:10.1107/s2059798317001061 (2017).
- 58 Wayllace, N. Z. *et al.* An enzyme-coupled continuous spectrophotometric assay for glycogen synthases. *Molecular Biology Reports* **39**, 585-591, doi:10.1007/s11033-011-0774-6 (2012).
- 59 Lemaire, O. N. & Wagner, T. Gas channel rerouting in a primordial enzyme: Structural insights of the carbon-monoxide dehydrogenase/acetyl-CoA synthase complex from the acetogen *Clostridium autoethanogenum*. *Biochimica et Biophysica Acta (BBA) - Bioenergetics* **1862**, 148330, doi:10.1016/j.bbabi.2020.148330 (2021).
- 60 Tamura, K., Stecher, G. & Kumar, S. MEGA11: Molecular evolutionary genetics analysis version 11. *Molecular Biology and Evolution* **38**, 3022-3027, doi:10.1093/molbev/msab120 % (2021).
- 61 Edgar, R. C. MUSCLE: a multiple sequence alignment method with reduced time and space complexity. *BMC Bioinformatics* **5**, 113, doi:10.1186/1471-2105-5-113 (2004).



## Extended Data

### Extended materials and methods.

All plots presented in the study were generated with Microsoft Excel 16 (16.05356.1000).

All microbial cultures were spectrophotometrically monitored on a Spectrophotometer UV/VIS UVmini-1240 SHIMADZU.

**Sulfur-free cultivation medium for *Methanococcales*.** Per liter of medium: 558 mg of  $\text{KH}_2\text{PO}_4$  (final concentration 4.1 mM), 1 g of  $\text{KCl}$  (13.4 mM), 25.13 g of  $\text{NaCl}$  (430 mM), 840 mg of  $\text{NaHCO}_3$  (10 mM), 367.5 mg of  $\text{CaCl}_2 \cdot 2 \text{H}_2\text{O}$  (2.5 mM), 7.725 g of  $\text{MgCl}_2 \cdot 6 \text{H}_2\text{O}$  (38 mM), 1.18 g of  $\text{NH}_4\text{Cl}$  (22.06 mM), 61.16 mg of nitrilotriacetic acid (0.32 mM), 6.16 mg of  $\text{FeCl}_2 \cdot 4 \text{H}_2\text{O}$  (0.031 mM), 10  $\mu\text{l}$  of 2 mM  $\text{Na}_2\text{SeO}_3 \cdot 5 \text{H}_2\text{O}$  stock (0.02  $\mu\text{M}$ ), 3.3 mg of  $\text{Na}_2\text{WO}_4 \cdot 2 \text{H}_2\text{O}$  (0.01 mM) and 2.42 mg of  $\text{Na}_2\text{MoO}_4 \cdot 2 \text{H}_2\text{O}$  (0.01 mM) were dissolved under constant stirring with 750 ml of deionized  $\text{H}_2\text{O}$  ( $\text{dH}_2\text{O}$ ). 1 ml of 1.5 mM resazurin and 10 ml of sulfur-free trace elements (see below) were subsequently added. In flasks the pH was set to either 7.6 with 50 mM Tris/HCl as buffer or to 6.2 with 50 mM 2-(*N*-morpholino)ethanesulfonic acid (MES). For the fermenter, 10 mM MES pH 6.2 was used as a buffer. The medium was filled up to a final volume of 1 l by the addition of  $\text{dH}_2\text{O}$ .

The cultivation media were transferred in a 1 l pressure protected DURAN laboratory bottle with a magnetic stirring bar. The Duran flask was closed with a butyl rubber stopper and degassed by applying 3 min of vacuum, followed by 30 seconds addition of  $1 \times 10^5 \text{ Pa}$   $\text{N}_2:\text{CO}_2$  atmosphere (90:10), under constant magnetic stirring. This was repeated for a minimum of 15 cycles and at the final gas addition step, an overpressure of  $0.3 \times 10^5 \text{ Pa}$   $\text{N}_2:\text{CO}_2$  was applied.

**Trace element composition for *Methanococcales*.** A 100-fold-concentrated trace element solution was prepared by first dissolving 1.36 g of nitrilotriacetic acid (7.1 mM) in 800 ml  $\text{dH}_2\text{O}$  under magnetic stirring. The pH was shifted to 6.2 by adding NaOH pellets. 89.06 mg of  $\text{MnCl}_2 \cdot 4 \text{H}_2\text{O}$  (0.45 mM), 183.3 mg of  $\text{FeCl}_3 \cdot 6 \text{H}_2\text{O}$  (0.68 mM), 60.27 mg of  $\text{CaCl}_2 \cdot 2 \text{H}_2\text{O}$  (0.41 mM), 180.8 mg of  $\text{CoCl}_2 \cdot 6 \text{H}_2\text{O}$  (0.76 mM), 90 mg of  $\text{ZnCl}_2$  (0.66 mM), 37.64 mg of  $\text{CuCl}_2$  (0.28 mM), 46 mg of  $\text{Na}_2\text{MoO}_4 \cdot 2 \text{H}_2\text{O}$  (0.19 mM), 90 mg of  $\text{NiCl}_2 \cdot 6 \text{H}_2\text{O}$  (0.38 mM) and 30 mg of  $\text{VCl}_3$

(0.19 mM) was added separately. The trace element mixture was filled up to a final volume of 1 l with dH<sub>2</sub>O.

**Media for *Archaeoglobus fulgidus*.** The media were modified from DSMZ media 399. It was prepared in a Widdel flask and contains per liter of dH<sub>2</sub>O: 0.14 g of KH<sub>2</sub>PO<sub>4</sub>, 0.25 g of NH<sub>4</sub>Cl, 18 g of NaCl, 3.45 g of MgSO<sub>4</sub> · 7 H<sub>2</sub>O, 4 g of MgCl<sub>2</sub> · 6 H<sub>2</sub>O, 0.34 g of KCl, 0.14 g of CaCl<sub>2</sub> · 2 H<sub>2</sub>O and 1 ml of Fe(NH<sub>4</sub>)<sub>2</sub>(SO<sub>4</sub>)<sub>2</sub> · 6 H<sub>2</sub>O (1.91 mg ml<sup>-1</sup>). The media was autoclaved for 25 minutes at 121 °C. Afterwards, the solution was transferred in a 1 l Duran bottle. 1 X 10<sup>3</sup> Pa N<sub>2</sub>:CO<sub>2</sub> (90:10) overpressure was applied during the addition of 1 ml of the trace elements M141 (see below), 0.05 mg of vitamin B<sub>12</sub> (sterile filtered), 1 ml of a Se/Wo-solution (400 mg NaOH, 8 mg of Na<sub>2</sub>WO<sub>4</sub> · 2 H<sub>2</sub>O, 6 mg of Na<sub>2</sub>SeO<sub>3</sub> · 5 H<sub>2</sub>O were solved in 1 l dH<sub>2</sub>O and autoclaved at 121 °C for 25 minutes), 1 ml of riboflavin (17.5 mM of acetic acid, 2.5 mg of riboflavin 5'-monophosphate sodium salt dihydrate were dissolved in 100 ml dH<sub>2</sub>O, sterile filtered and stored in the dark at 4 °C), 0.1 ml of a thiamine solution (for a 100 ml solution 10 mg thiamine chloride hydrochloride were dissolved in 50 mM Na<sub>2</sub>HPO<sub>4</sub>/H<sub>3</sub>PO<sub>4</sub> pH 3.7, sterile filtered and stored in autoclaved brown flasks at 4 °C until usage), 1 ml of 1 mg ml<sup>-1</sup> resazurin, 30 ml of 1 M NaHCO<sub>3</sub>, and 1 ml of 5-vitamin mix (see below). For the Na<sub>2</sub>S grown cultures, 2 ml of 1 M Na<sub>2</sub>S and some crystals of sodium dithionite (until colour loss) were added but omitted for the Na<sub>2</sub>SO<sub>4</sub>-grown culture. The pH was adjusted to 6.9 using 2 M HCl.

**Trace element composition for *Archaeoglobus fulgidus*.** The 10 x trace element solution was modified from DSMZ media 141. 1.5 g nitrilotriacetic acid were dissolved in 80 ml Milli-Q H<sub>2</sub>O, and the pH was set to 6.5 using 1 M KOH. Subsequently 3 g of MgSO<sub>4</sub> · 7 H<sub>2</sub>O, 0.5 g of MnSO<sub>4</sub> · H<sub>2</sub>O, 1 g of NaCl, 100 mg of FeSO<sub>4</sub> · 7 H<sub>2</sub>O, 152 mg of CoCl<sub>2</sub> · 6 H<sub>2</sub>O, 100 mg of CaCl<sub>2</sub> · 2 H<sub>2</sub>O, 180 mg of ZnSO<sub>4</sub> · 7 H<sub>2</sub>O, 10 mg of CuSO<sub>4</sub> · 5 H<sub>2</sub>O, 20 mg of KAl(SO<sub>4</sub>)<sub>2</sub> · 12 H<sub>2</sub>O, 10 mg of H<sub>3</sub>BO<sub>3</sub>, 10 mg of Na<sub>2</sub>MoO<sub>4</sub> · 2 H<sub>2</sub>O and 30 mg of NiCl<sub>2</sub> · 6 H<sub>2</sub>O were added and a pH 7.0 was set with 1 M KOH and the solution was filled up to 100 ml with Milli-Q H<sub>2</sub>O. The trace elements were autoclaved at 121 °C for 25 minutes and then stored at room temperature in the dark.

***Archaeoglobus fulgidus* 5 - vitamin mix.** 15 mg pyridoxine hydrochloride, 10 mg nicotinic acid, 5 mg calcium-D(+)-pantothenate, 4 mg 4-aminobenzoic acid, and 1 mg D(+)-biotin were dissolved in 100 ml 10 mM Na<sub>2</sub>HPO<sub>4</sub> at pH 7.1, sterile filtered and stored at 4 °C until usage.

**Protein overexpression.** The *MtATPS*, *MtAPSK* and *MtPAPP* constructs expressed in *Escherichia coli* strain BL21(DE3) were cultivated in 1 to 3 l of Lysogeny Broth (per liter of medium: 10 g tryptone, 5 g yeast extract, 10 g NaCl) supplemented with a final concentration of 50  $\mu\text{g ml}^{-1}$  kanamycin. Cultures were incubated by shaking at 220 rotation per minute (r.p.m.) at 37 °C until an OD<sub>600nm</sub> of 0.6–0.8 was reached. Induction was performed by adding a final concentration of 0.75 mM isopropyl  $\beta$ -D-1-thiogalactopyranoside (IPTG), and the cells were incubated for another hour by shaking at 37 °C. Cells were harvested by centrifugation at 5,000  $\times$  g for 20 min at 21 °C. Cell pellets were frozen in liquid N<sub>2</sub> and stored at -80 °C until further use.

For overexpression of the *MtPAPSR* construct, *E. coli* BL21(DE3) was previously transformed with the plasmid pDB1282. The transformed cells were grown in a fermenter at 34 °C containing 8 L of modified Terrific Broth medium. For 8 l medium 96 g tryptone, 112 g yeast extract, 40 g glycerol, 4 g ferric ammonium citrate, 21 g MOPS pH 7.4 were dissolved in 7.2 l dH<sub>2</sub>O and autoclaved. Then 800 ml TB salts (10 x; 18.5 g KH<sub>2</sub>PO<sub>4</sub>, 100.32 g K<sub>2</sub>PO<sub>4</sub>, autoclaved) supplemented with glucose (28 mM final, sterile filtered), kanamycin (50  $\mu\text{g/ml}$  final, sterile filtered), ampicillin (100  $\mu\text{g/ml}$  final, sterile filtered) and riboflavin (20  $\mu\text{g/ml}$  final), were added. The preculture was grown in classic Terrific Broth medium. The cells were gassed with a constant flow of 15 x 10<sup>4</sup> Pa compressed air until they reached an OD<sub>600</sub> of 1.74, then the gas was switched to a constant flow of 15 x 10<sup>4</sup> Pa N<sub>2</sub>, to establish anaerobic conditions. Next, the cells were induced with a final concentration of 0.2% L-arabinose, 25 mM sodium fumarate dibasic, 2 mM cysteine hydrochloride and 50  $\mu\text{M}$  IPTG followed by incubation for one hour at 28 °C. The cells were harvested under anaerobic conditions by centrifugation at 5,000  $\times$  g for 20 min at 4 °C. Cell pellets were frozen in liquid N<sub>2</sub> and stored at -80 °C until further use.

***MtATPS*, *MtAPSK* and *MtPAPP* tag-cleavage and purification.** 6 g, 9 g and 7 g (wet weight) of respectively *MtATPS*, *MtAPSK*, *MtPAPP*-overexpressed *E.coli* cells were thawed under warm water and were resuspended in 22-50 ml lysis buffer (50 mM Na<sub>2</sub>HPO<sub>4</sub> pH 8.0, 500 mM NaCl, 20 mM imidazole, 5% glycerol) on ice. The cell lysate was homogenized by sonication: 10 cycles with 1 min at 80% intensity followed by 1.5 min break (probe KE76, SONOPULS Bandelin) and cell debris were removed via centrifugation (45,000  $\times$  g, 50 min at 4 °C). The filtered sample was applied to a 5 ml HisTrap high performance column (GE healthcare), which was previously equilibrated with lysis buffer. The column was then washed with 2 column volumes of lysis buffer.

A gradient of 0.02 to 0.3 M imidazole was applied for 40 min at a flow rate of 1.5 ml min<sup>-1</sup> and fractions of 1 ml were collected. *MtATPS* eluted between 0.1 and 0.15 M imidazole, *MtAPSK* between 0.12 and 0.2 M and *MtPAPP* eluted between 0.13 and 0.22 M imidazole. The protein fractions were pooled and the buffer was exchanged for phosphate buffer saline (137 mM NaCl, 2.7 mM KCl, 10 mM Na<sub>2</sub>HPO<sub>4</sub>, 1.8 mM KH<sub>2</sub>PO<sub>4</sub> pH 7.4) by using 30-kDa-cutoff filter (6 ml, Merck Millipore, Darmstadt, Germany) for *MtATPS* and *MtAPSK* and a 10-kDa-cutoff filter for *MtPAPP*. The proteins were concentrated to 3 ml for the *MtPAPP* and 5 ml for the *MtATPS* and *MtAPSK*. The *MtPAPP* with the His-Tag was immediately passed onto a Superdex 200 Increase 10/300 GL (GE Healthcare), equilibrated in storage buffer (25 mM Tris/HCl pH 7.6, containing 5% v/v glycerol and 2 mM dithiothreitol), as the protein aggregated with time. *MtPAPP* eluted at a flow rate of 0.8 ml min<sup>-1</sup> in a sharp Gaussian peak at an elution volume of 75 ml. The fractions of interest containing *MtPAPP* were concentrated with a 10 kDa cut-off centrifugal concentrator to 150 µl and the protein was directly used for crystallization. The concentration of purified *MtPAPP*, estimated by the Bradford method, was 20 mg ml<sup>-1</sup>.

For the *MtATPS* and *MtAPSK*, 50 µl of 0.1 U mg<sup>-1</sup> Thrombin (from bovine plasma, Sigma-Aldrich) was added to the 5 ml of protein and incubated overnight at 22 °C to remove the His-Tag of the enzymes. The samples were then passed onto a HiLoad® 16/600 Superdex® 200 pg (GE Healthcare), equilibrated in storage buffer (25 mM Tris/HCl pH 7.6, containing 150 mM NaCl, 10% v/v glycerol and 2 mM dithiothreitol). *MtATPS* and *MtAPSK* eluted at a flow rate of 0.8 ml min<sup>-1</sup> in a sharp Gaussian peak at an elution volume of 68 ml and 81 ml, respectively. The fractions of interest containing the proteins were concentrated with a 30-kDa cut-off centrifugal concentrator (6 ml, Merck Millipore, Darmstadt, Germany) to 150 µl and the proteins were immediately used for crystallization. The concentration of purified *MtATPS*, estimated by the Bradford method, was 27 mg ml<sup>-1</sup> and 17.6 mg ml<sup>-1</sup> for *MtAPSK*.

***MtPAPS reductase purification.*** 26 g (wet weight) of *MtPAPSR*-overexpressed *E.coli* cells from the fermenter were thawed under warm water and transferred to an anaerobic tent containing an atmosphere of N<sub>2</sub>:CO<sub>2</sub> (with a 90:10 ratio). 120 ml lysis buffer (50 mM Na<sub>2</sub>HPO<sub>4</sub>, 500 mM NaCl, 20 mM imidazole, 2 mM dithiothreitol, 5% glycerol) was added and cells were lysed by sonication: 5 cycles with 1 min at 75% intensity followed by 3 min break (probe KE76, SONOPULS Bandelin). Cell debris were removed anaerobically via centrifugation (45,000 x g, 45 min at 4 °C).

The supernatant was transferred to a Coy tent (N<sub>2</sub>:H<sub>2</sub> atmosphere with a 97:3 ratio) under yellow light at 20 °C and filtered through a 0.2 µm filter (Sartorius). The filtered sample was applied to a 5 ml HisTrap high performance column (GE healthcare), which was previously equilibrated with lysis buffer. The column was then washed with 2 column volumes of lysis buffer. A gradient of 0.02 to 0.3 M Imidazole was applied for 40 min at a flow rate of 1.5 ml min<sup>-1</sup> and fractions of 1 ml were collected. *MtPAPSR* eluted between 0.04 and 0.15 M imidazole. The fractions of interest were merged and diluted with 4 volumes of 50 mM Tricine/NaOH pH 8.0 and 2 mM dithiothreitol. The sample was filtered through 0.2 µm and was loaded on a 5 ml Q sepharose high performance column (GE healthcare). A gradient of 0 to 0.55 M NaCl was applied for 90 min with a flow rate of 1 ml min<sup>-1</sup>. Fractions of 1.5 ml were collected. *MtPAPSR* eluted between 0.11 and 0.52 M NaCl. The purest *MtPAPSR* fractions were pooled and the buffer was exchanged for storage buffer (25 mM Tris/HCl pH 7.6, containing 10% v/v glycerol and 2 mM dithiothreitol) by using 30 kDa cut-off filter (6 ml, Merck Millipore, Darmstadt, Germany) and *MtPAPSR* was concentrated to 400 µl. The concentrated sample was passed onto a Superdex 200 Increase 10/300 GL (GE Healthcare), equilibrated in storage buffer. *MtPAPSR* eluted at a flow rate 0.4 ml min<sup>-1</sup> in a sharp Gaussian peak at an elution volume of 12.5 ml. The fractions of interest containing *MtPAPSR* were concentrated with a 30 kDa cut-off centrifugal concentrator to 300 µl and the protein was directly used for crystallization. For the activity assays *MtPAPSR* was incubated with 0.5 mM FAD for 15 min to promote cofactor integrity, followed by buffer exchange to remove excess FAD using a 30 kDa cut-off concentrator. The concentration of purified *MtPAPSR*, estimated by the Bradford method, was 20 mg ml<sup>-1</sup>.

**Enzyme purification for coupled *MtPAPSR* assay.** For each step, the *MtATPS*, *MtAPSK* and *MtPAPP* were handled under aerobic conditions and on ice, while the *MtPAPSR* was always kept in an anaerobic atmosphere and at 25 °C. To save time, the His-tags were not cleaved off. We previously saw that the tag did not interfere with the activity of these enzymes.

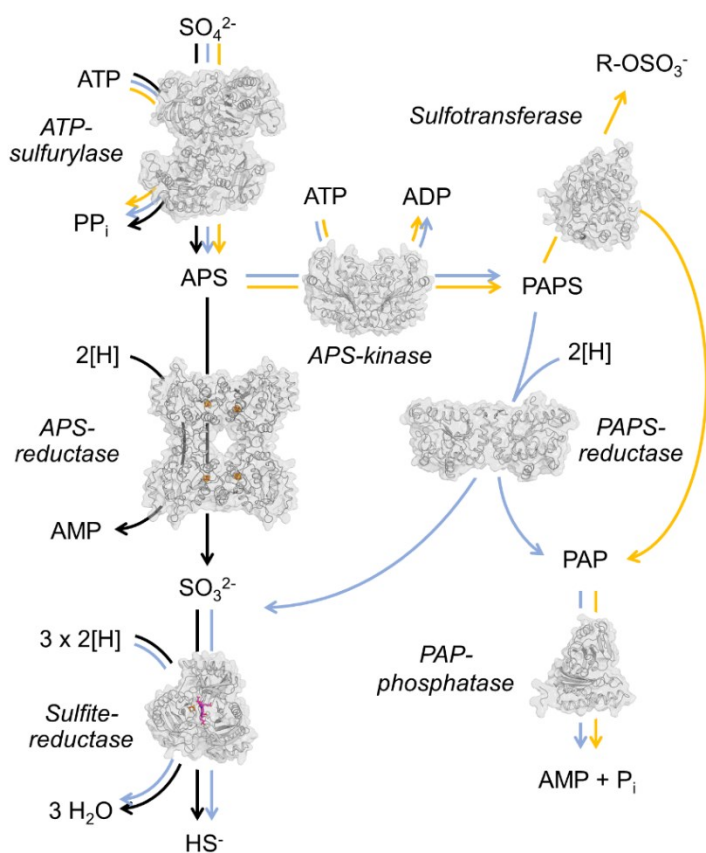
5.4 g, 7.6 g, 6.3 g and 11.0 g (wet weight) of recombinantly expressed *MtATPS*, *MtAPSK*, *MtPAPSR* and *MtPAPP* cells (as described above), respectively, were resuspended in 30 ml lysis buffer (50 mM Na<sub>2</sub>HPO<sub>4</sub>, pH 8.0, 500 mM NaCl, 20 mM imidazole, 5% glycerol), separately. The cells were broken by the following sonication protocol: 5 cycles with 30 seconds at 75% intensity followed by 1.5 min break (probe KE76, SONOPULS Bandelin) and cell debris were removed

anaerobically via centrifugation (45,000 x g, 45 min at 4 °C). The filtered supernatant was applied on a Ni-NTA gravity column (1 ml Ni-NTA resin equilibrated with lysis buffer). The column was washed with 8 ml lysis buffer, then the proteins were eluted by applying 3 ml elution buffer (50 mM Na<sub>2</sub>HPO<sub>4</sub>, pH 8.0, 500 mM NaCl, 300 mM imidazole, 5% glycerol). The flow trough was collected, filtered and injected onto a Superdex 200 Increase 10/300 GL (GE Healthcare), equilibrated in storage buffer (25 mM Tris/HCl pH 7.6, containing 10% v/v glycerol and 2 mM DTT). The fractions containing the sample of interest were pooled and concentrated using 10 kDa (*MtPAPP*) and 30 kDa cut-off centrifugal concentrator (Sartorius). The yield of this purification was: 2 ml of *MtATPS* at 11 mg ml<sup>-1</sup>, 1.5 ml of *MtAPSK* at 8 mg ml<sup>-1</sup>, 2 ml of the *MtPAPP* at 3 mg ml<sup>-1</sup> and 2 ml of the *MtPAPSR* at 4.5 mg ml<sup>-1</sup>.

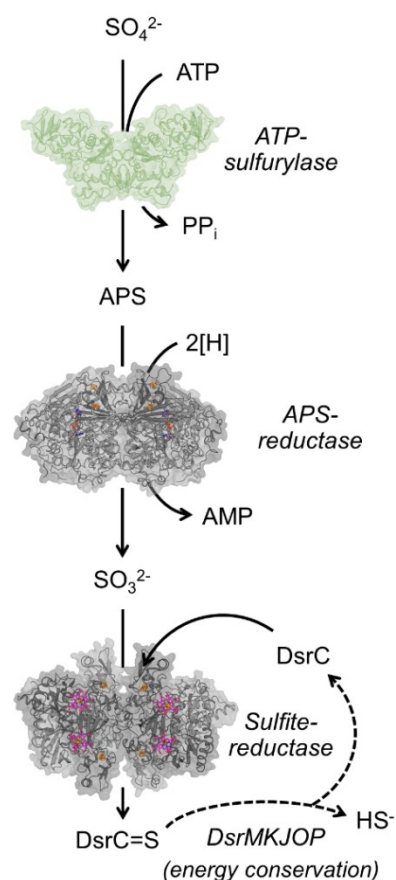
**High resolution clear native PAGE preparation.** The whole process was performed anaerobically in an anoxic chamber. Anaerobic fresh or frozen samples were used. Glycerol (20% v/v final) was added to each sample and 0.001% w/v ponceau S serves as a marker for protein migration. The electrophoresis cathode buffer contained 50 mM tricine; 15 mM Bis-Tris, pH 7; 0.05% w/v sodium deoxycholate; 0.01% w/v dodecyl maltoside and 2 mM of DTT. The anode buffer contained 50 mM Bis-Tris buffer pH 7 and 2 mM DTT. High resolution clear native PAGE were carried out using a 5 to 15% linear polyacrylamide gradient and gels were run with a constant 40 mA current (PowerPac™ Basic Power Supply, Bio-Rad).

**Phylogenetic trees.** Phylogenetic analyses were performed using MEGA11.0 by applying default parameters<sup>60</sup>. Homolog proteins were first identified and obtained from NCBI using BLASTP (E-value cut-off of 1e1). The protein sequences were then aligned using MUSCLE and all homologs were identified through an iterative alignment evaluation based on characterized proteins and manual filtering. The evolutionary history was inferred using the Neighbor-Joining method. The bootstrap consensus tree inferred from 2000 replicates is taken to represent the evolutionary history of the taxa analysed. Branches corresponding to partitions reproduced in less than 50% bootstrap replicates are collapsed. The percentage of replicate trees in which the associated taxa clustered together in the bootstrap test (2000 replicates) are shown next to the branches. The evolutionary distances were computed using the JTT matrix-based method and are in the units of the number of amino acid substitutions per site.

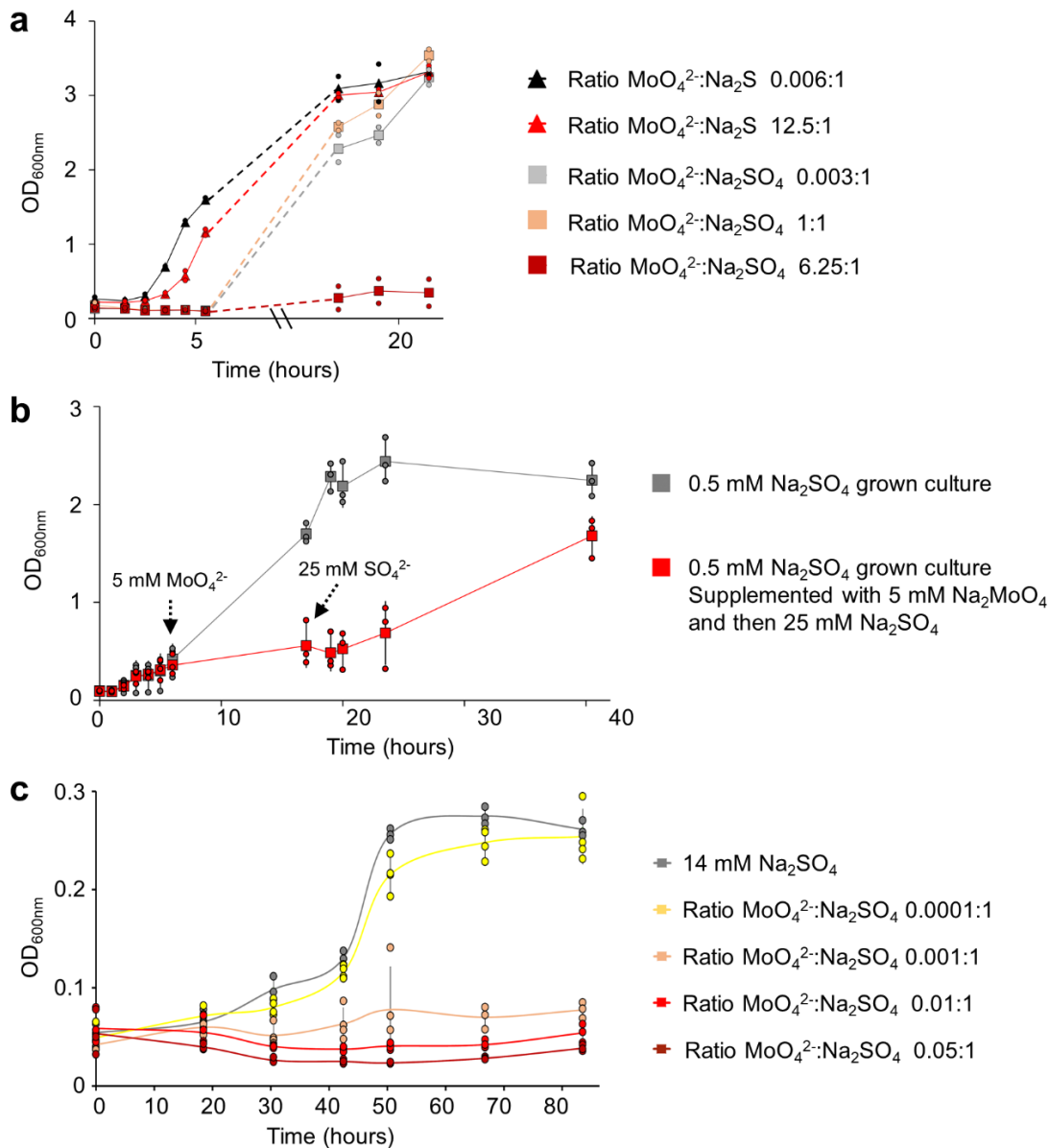
### Assimilatory $\text{SO}_4^{2-}$ -reduction (1) Routes: a) b) c)



### Dissimilatory $\text{SO}_4^{2-}$ -reduction (2)

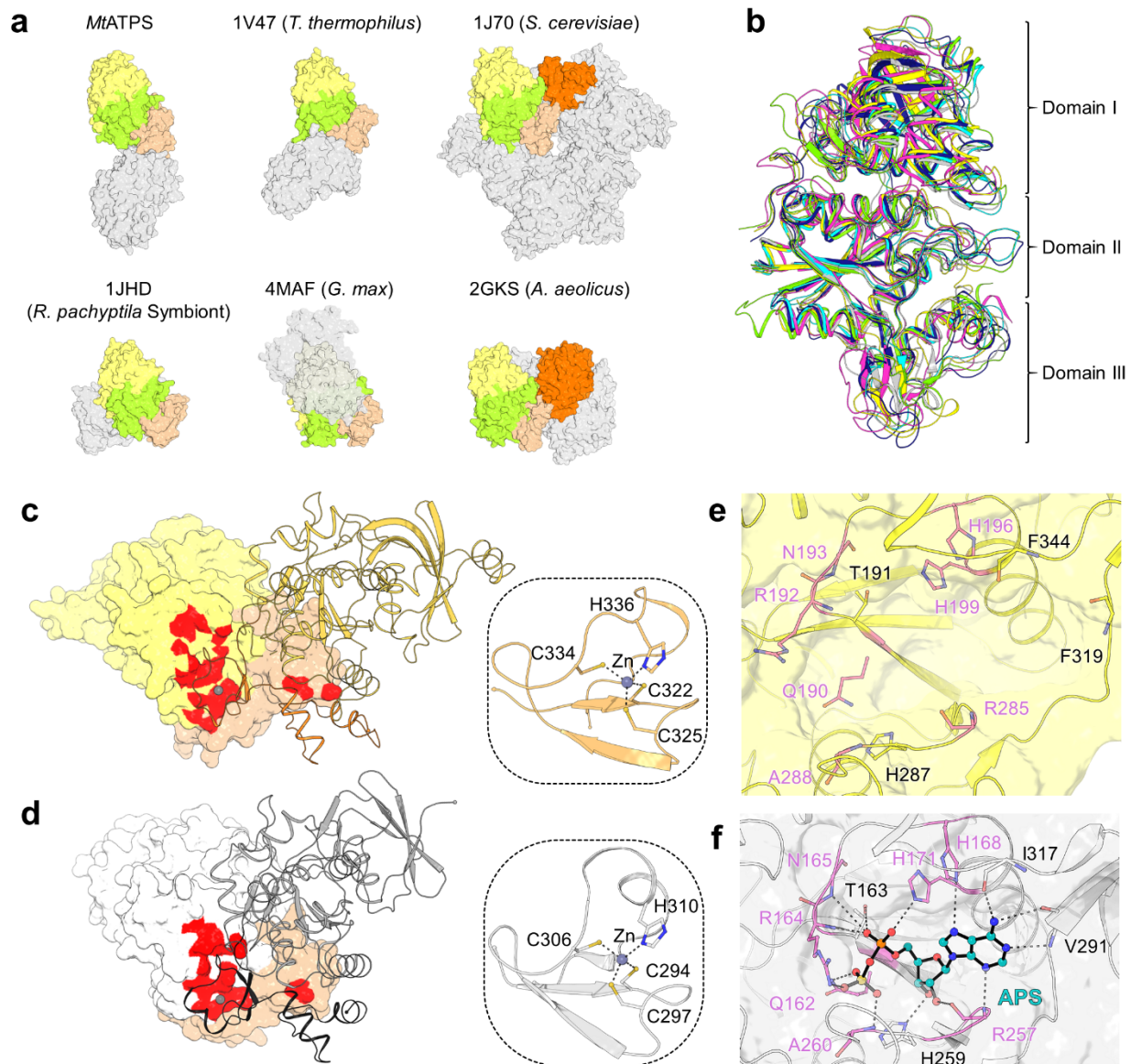


**Extended Data Figure 1. Sulfate ( $\text{SO}_4^{2-}$ )-reduction pathways. Assimilatory  $\text{SO}_4^{2-}$ -reduction.** (Route 1a, 1b, 1c)  $\text{SO}_4^{2-}$  is activated by the ATP-sulfurylase (for example *Glycine max*, PDB: 4MAF) to APS. (1a) APS gets directly reduced to sulfite ( $\text{SO}_3^{2-}$ ) and AMP by a one [4Fe-4S]-cluster containing APS reductase (e.g. *Pseudomonas aeruginosa*, PDB: 2GOY, thioredoxin dependent). (1b, c) Alternatively, the APS gets further phosphorylated by an APS kinase (for example *Arabidopsis thaliana*, PDB: 3UIE) to produce PAPS. (1b) A PAPS-reductase (*Saccharomyces cerevisiae*, PDB: 2OQ2, thioredoxin dependent) converts PAPS into  $\text{SO}_3^{2-}$  and PAP. The PAP will be hydrolysed to inorganic phosphate ( $\text{P}_i$ ) and AMP by a PAP phosphatase (for example *Mycobacterium tuberculosis*, PDB: 5DJJ). (1a, b) A sulfite reductase (*Escherichia coli*, PDB: 1AOP) reduces the  $\text{SO}_3^{2-}$  into  $\text{S}^{2-}$ , which can then be incorporated into biomass. In the route 1c, a sulfotransferase (for example *A. thaliana*, PDB: 5MEK) catalyses the transfer of the sulfo-group ( $\text{R-OSO}_3^-$ ) from PAPS to an alcohol or amine acceptor. **Dissimilatory  $\text{SO}_4^{2-}$ -reduction.**  $\text{SO}_4^{2-}$  is activated by the ATPS to APS and further reduced to  $\text{SO}_3^{2-}$  by an APS reductase (for example *Archaeoglobus fulgidus*, PDB: 2FJA), which contains two [4Fe-4S]-cluster and a FAD. A sulfite reductase (for example *A. fulgidus*, PDB: 3MM5) reduces the  $\text{SO}_3^{2-}$  and branches it on the carrier DsrC. The membrane complex DsrMKJOP (for example *Allochrochromatium vinosum*) reduces the sulfur into  $\text{HS}^-$  concomitantly with ion translocation for energy conservation. Sirohemes and [4Fe-4S]-clusters are represented in sticks and spheres, with carbon, oxygen, nitrogen, sulfur and iron coloured in pink, red, blue, yellow and orange. The ATPS of *A. fulgidus* was modelled using Alphafold2<sup>32</sup> and coloured in green. The bifunctional ATP sulfurylase CysDN using an additional GTP, was not presented here to simplify the scheme.

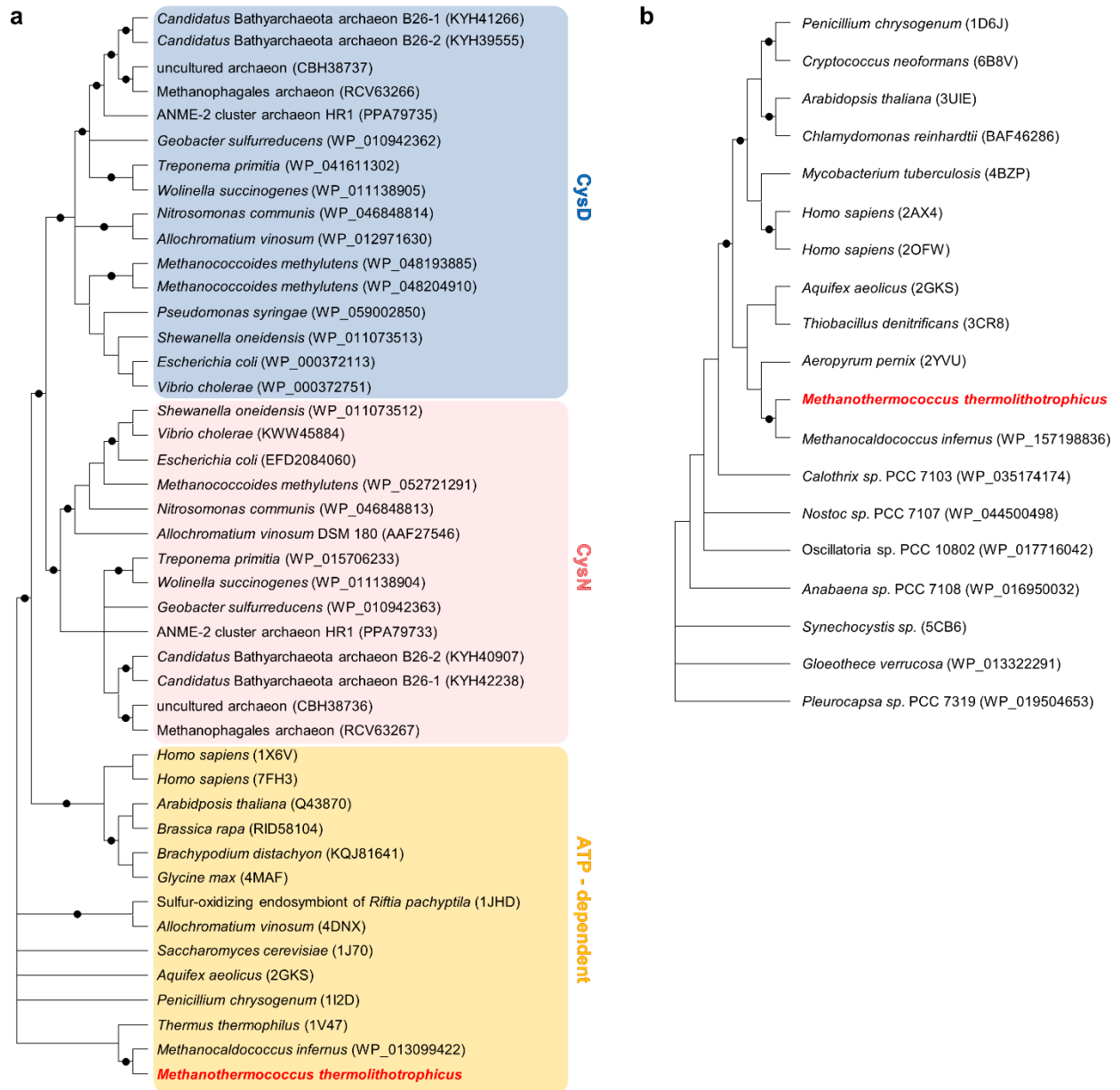


**Extended Data Figure 2. Impact of Molybdate (MoO<sub>4</sub><sup>2-</sup>) on SO<sub>4</sub><sup>2-</sup>-reducing archaea.** **a**, MoO<sub>4</sub><sup>2-</sup> tolerance of *M. thermolithotrophicus*. The archaeon was grown on SO<sub>4</sub><sup>2-</sup> (grey square), SO<sub>4</sub><sup>2-</sup> supplemented with an equimolar amount of MoO<sub>4</sub><sup>2-</sup> (wheat square) and SO<sub>4</sub><sup>2-</sup> supplemented with an excess of MoO<sub>4</sub><sup>2-</sup> (dark red square). As a control, Na<sub>2</sub>S grown cultures (S<sup>2-</sup>, black triangle) and Na<sub>2</sub>S grown cultures with an excess of MoO<sub>4</sub><sup>2-</sup> (red triangle) were used. This growth experiment was performed in duplicates. **b**, Effect of MoO<sub>4</sub><sup>2-</sup>:SO<sub>4</sub><sup>2-</sup> ratios in *M. thermolithotrophicus* cultures grown on 0.5 mM Na<sub>2</sub>SO<sub>4</sub>. Grey squares indicate the growth curve of SO<sub>4</sub><sup>2-</sup>-reducers without addition of MoO<sub>4</sub><sup>2-</sup>. The red squares indicate the growth curve of SO<sub>4</sub><sup>2-</sup> reducers exposed to 5 mM of MoO<sub>4</sub><sup>2-</sup>, followed by the addition of 25 mM Na<sub>2</sub>SO<sub>4</sub>. Black, dashed arrows indicate time of MoO<sub>4</sub><sup>2-</sup> and SO<sub>4</sub><sup>2-</sup> addition. This growth experiment was performed in triplicates. **c**, *Archaeoglobus fulgidus* sensitivity towards MoO<sub>4</sub><sup>2-</sup>. Here, a MoO<sub>4</sub><sup>2-</sup>:SO<sub>4</sub><sup>2-</sup> ratio of 0.001:1 is sufficient to inhibit growth of *A. fulgidus*. The data shown are quadruplicates except for the lowest and the highest MoO<sub>4</sub><sup>2-</sup>:SO<sub>4</sub><sup>2-</sup> ratio, which were performed in triplicates. All experiments are represented as data mean and for b, c ± standard deviation (s.d.).

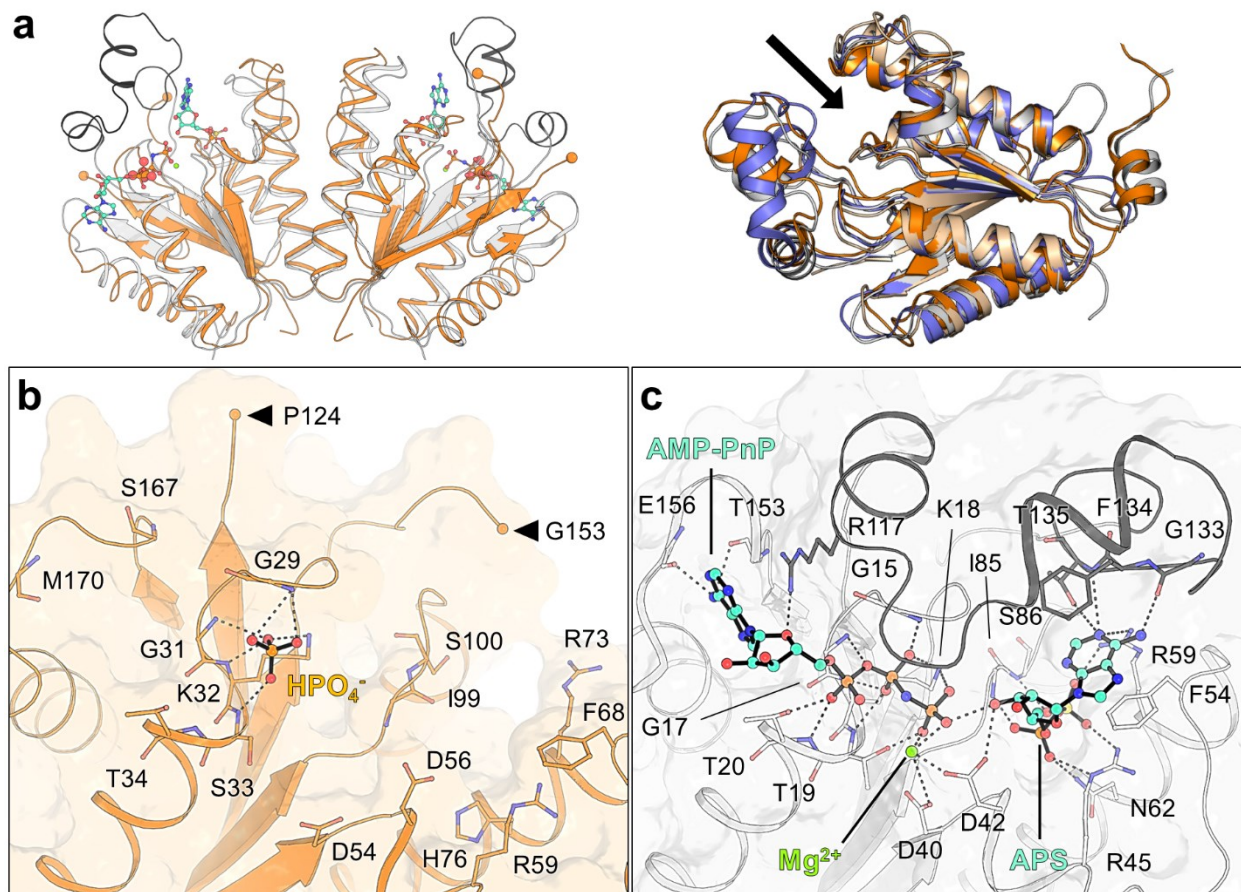




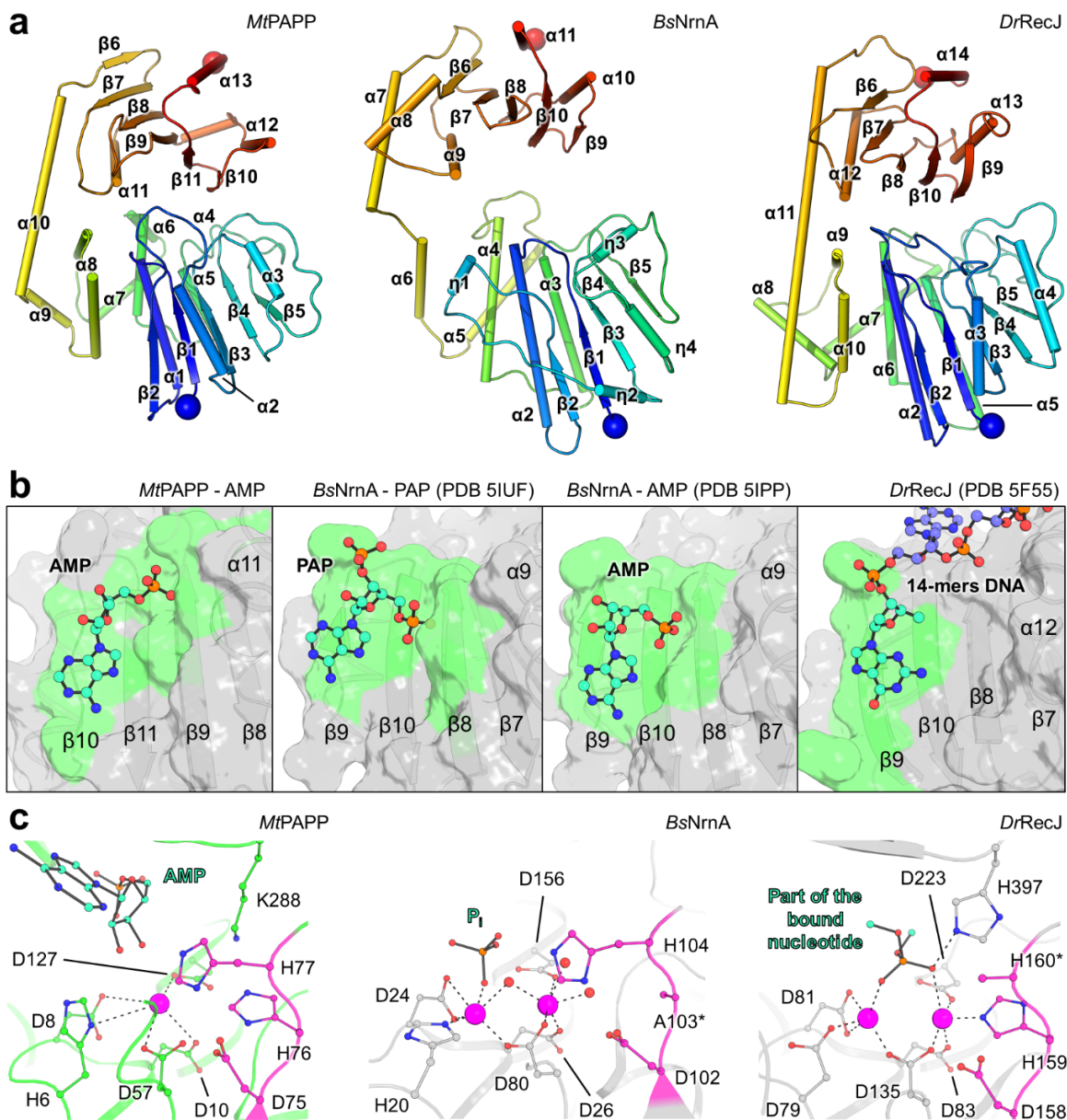
**Extended Data Figure 3. ATP sulfurylase of *M. thermolithotrophicus* (*MtATPS*).** **a**, Comparison of ATPS in surface representation, coloured by the domain composition I (yellow), II (light green), III (wheat) and APS kinase (dark orange). The grey surfaces corresponds to the opposing monomer. *ScATPS* organizes as homo-hexamers. **b**, Monomers of *MtATPS* (yellow), *TtATPS* (grey), *ScATPS* (navy blue), *RrsATPS* (magenta), *GmATPS* (green) and *AaATPS* (cyan) are superposed on domain II and shown as cartoons. Abbreviations and rmsd can be found in Supplementary Table 1. **c,d**, Surface area involved in the oligomerization of *MtATPS* (c) and *TtATPS* (d). One monomer is shown in surface representation and one monomer is displayed in cartoon. The monomer-monomer contacts, established by the domain III of one chain (in orange for *MtATPS* and black for *TtATPS*), are shown as a red surface. The wheat coloured surface highlights domain III. The framed inlet is a close up of the Zn binding motif and residues coordinating the Zn are drawn as sticks. Carbon, nitrogen and sulfur are coloured as orange/white, blue and yellow, respectively. **e, f**, Catalytic site of *MtATPS* (apo, e) and *TtATPS* with bound APS (f). Elements are coloured as in inlets (c, d) with oxygen and phosphorus in red and orange, respectively. Residues belonging to the canonical motifs of the ATPS are highlighted by pink coloured carbon atoms.



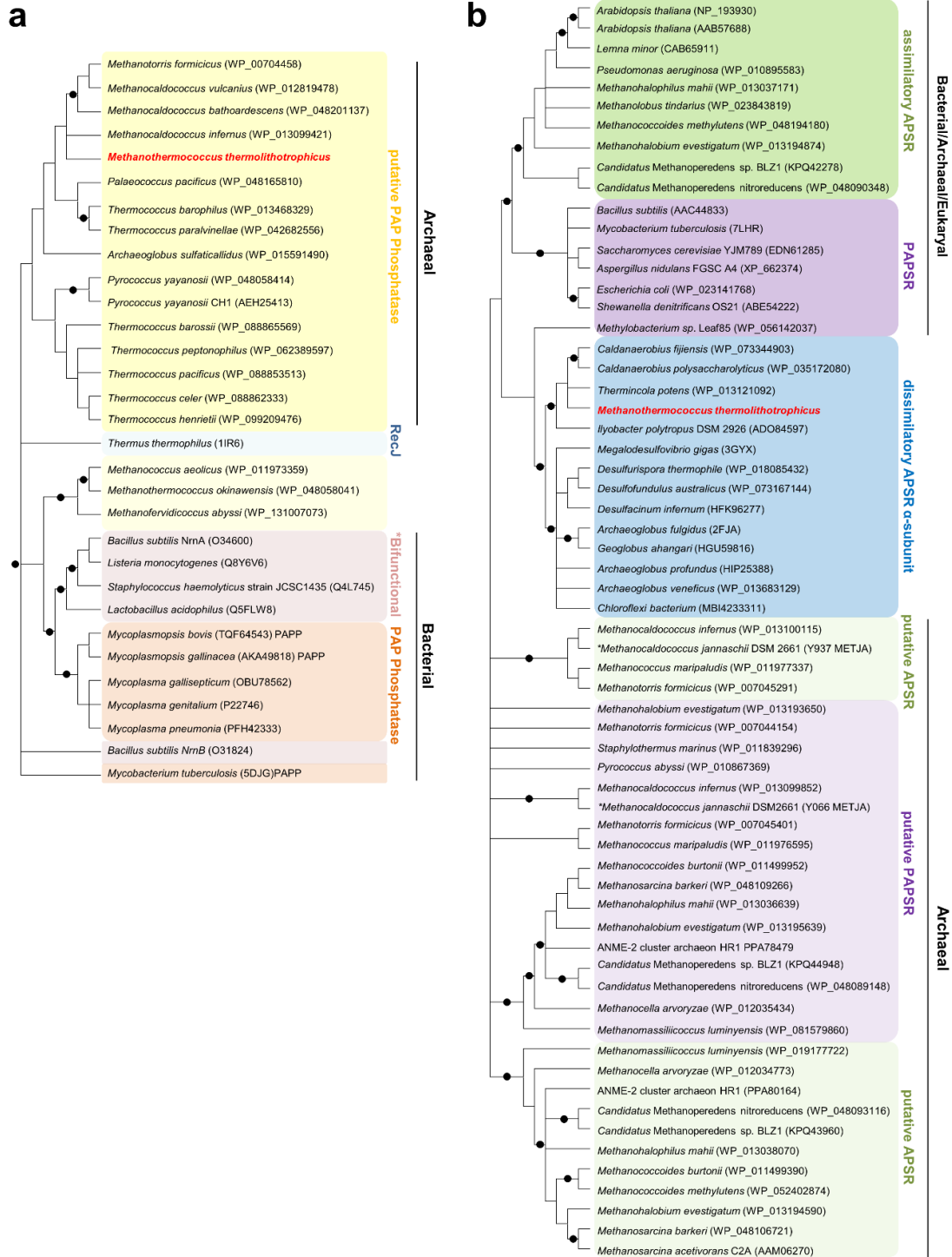
**Extended Data Figure 4. Phylogenetic analysis of *MtATPS* and *MtAPSK*.** **a**, The heterodimeric sulfate adenylyltransferase (CysDN) with the homo-oligomeric ATP-dependent sulfurylase (sat) and **b**, APS kinases. For panel a: the heterodimeric assimilatory ATP sulfurylase is composed of a regulatory GTPase subunit CysN (light red) and a catalytic subunit CysD (blue). Sat is involved in both assimilatory and dissimilatory  $\text{SO}_4^{2-}$  reduction (light orange). *MtATPS* and *MtAPSK* are highlighted in bold red. Bootstrap support values  $\geq 90\%$  are shown as dots on interior nodes.



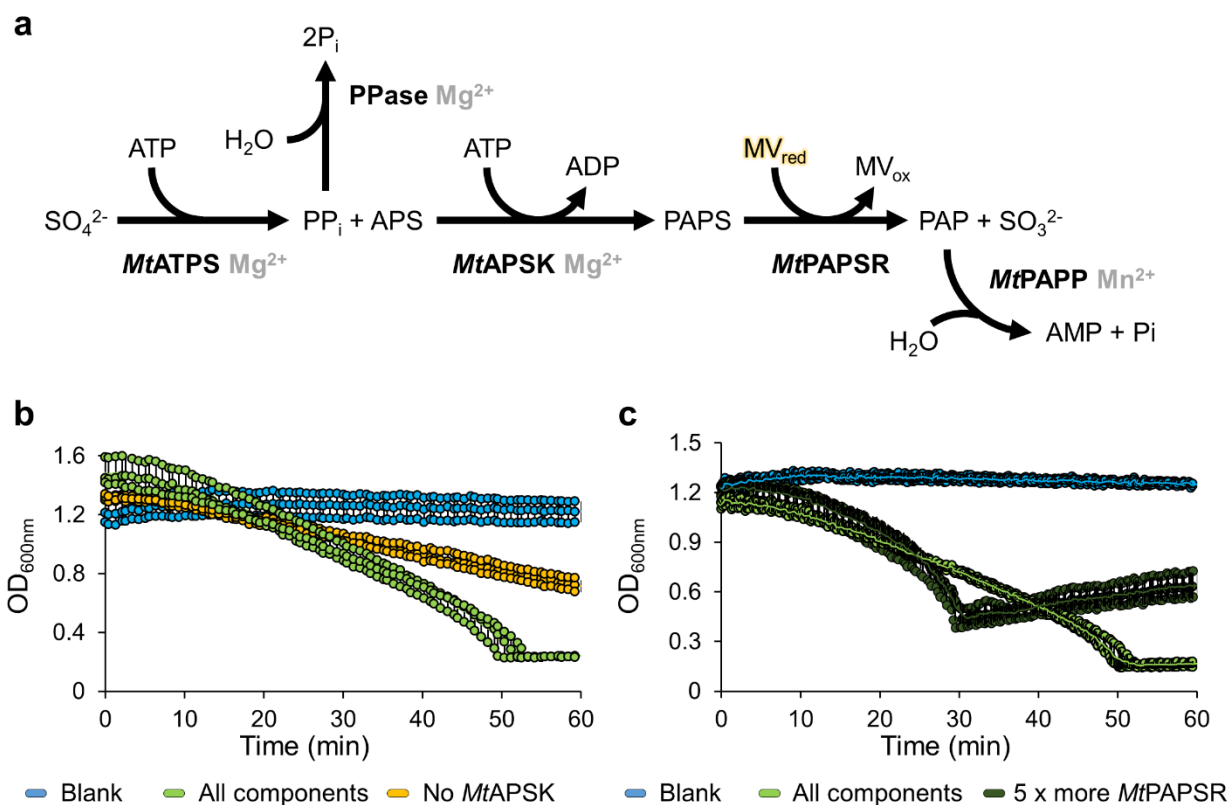
**Extended Data Figure 5. *MtAPSK* belongs to the APSK family.** **a**, Left panel, homodimeric *MtAPSK* apo (orange) superposed to its closest homologue *Synechocystis* sp. PCC 6803 (*SsAPSK*, white, PDB: 5CB6) in complex with APS and AMP-PnP. The ligands are shown in sticks and spheres and the missing part 125-152 in *MtAPSK* (indicated by balls) is highlighted in black in *SsAPSK*. Carbon, nitrogen, oxygen, sulfur and phosphorus are coloured in light orange/white/cyan, blue, red, yellow and orange, respectively. Right panel: superposition of *MtAPSK* (wheat), *AtAPSK* (orange, PDB: 3UIE), *ApAPSK* (slate, PDB: 2YVU) and *PcAPSK* (white, PDB: 1M7H) on one monomer and shown in cartoon. The active site position is indicated by a black arrow. Abbreviations and rmsd can be found in Supplementary Table 2. **b**, **c**, Catalytic site of apo *MtAPSK* (**b**) and *SsAPSK* bound to APS and AMP-PnP (**c**). Elements are coloured as in (a), left panel. In (b), arrows indicate the missing part 125-152.



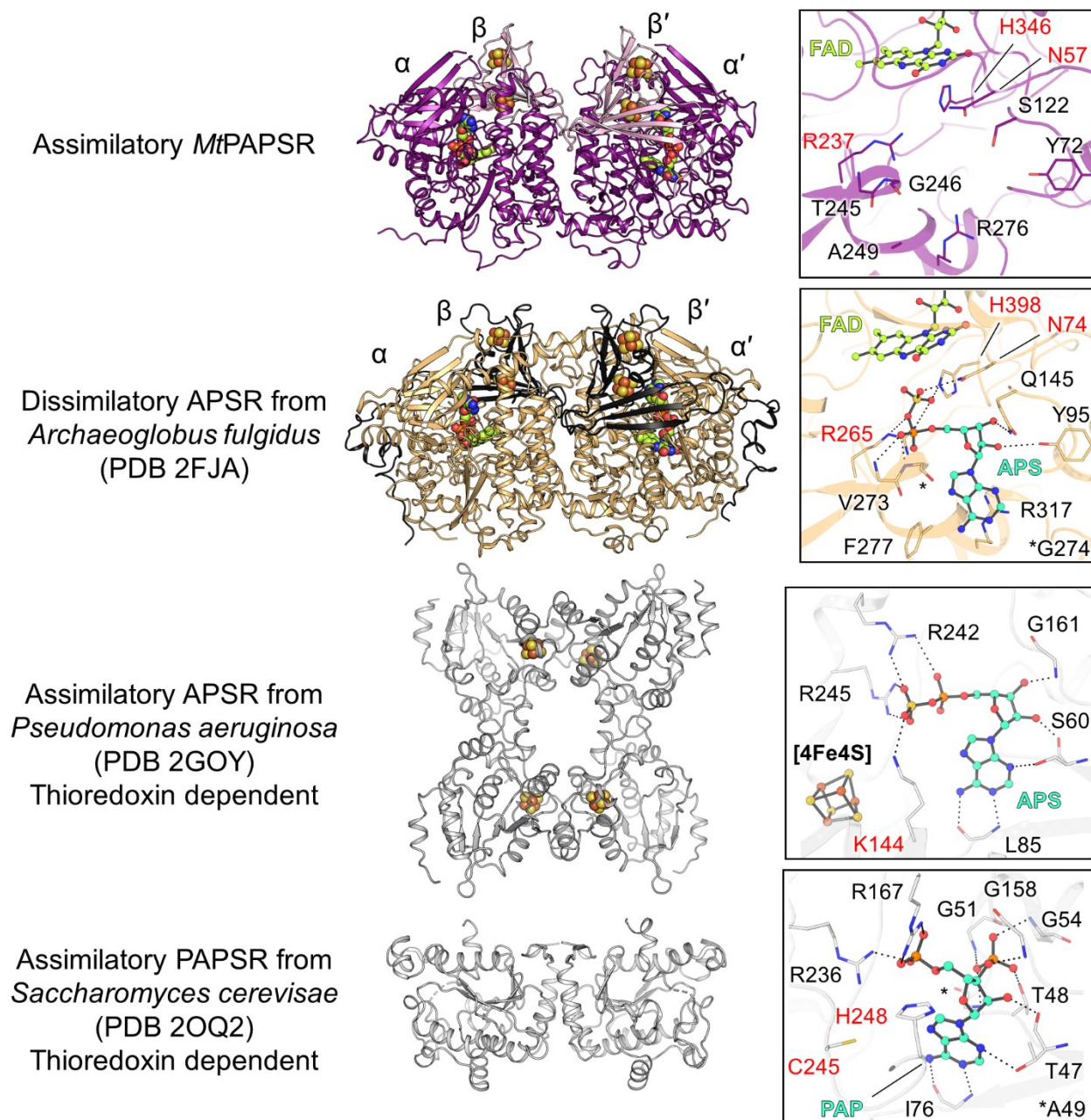
**Extended Data Figure 6. *MtPAPP* shares similar structural features with exonucleases.** **a**, Folding conservation across the *MtPAPP*, the NanoRNase A from *Bacillus subtilis* (*BsNrnA*, PDB: 5IUF) and the recombinase RecJ from *Deinococcus radiodurans* (*DrRecJ*, PDB: 5F55). For *BsNrnA* and *DrRecJ*, the structures only represent the DHH and DHHA1 domains and the secondary structure motifs are renumbered to simplify the comparison with *MtPAPP*. **b**, Differences in the nucleotide binding between *MtPAPP*, NanoRNase A and the recombinase RecJ with the surface residues interacting with the ligand coloured in green. **c**, Close-up of the  $Mn^{2+}$  coordination between *MtPAPP*, *BsNrnA* (PDB: 5IZO) and *DrRecJ* (PDB: 5F55).  $Mn^{2+}$  are shown as purple spheres and the residues coordinating them are highlighted as stick and balls. Carbon, nitrogen, oxygen and phosphorus atoms are coloured respectively in green/grey, blue, red and orange. Residues belonging to the canonical DHH-motif have pink coloured carbon atoms. The structure used for *BsNrnA* is the His103Ala variant, and the side chain of the His160 has not been modelled in the *DrRecJ* structure.



**Extended Data Figure 7. Phylogenetic analysis of *MtPAPP* and *MtPAPSR*.** **a**, PAP phosphatases with bifunctional oligoribonucleases and PAP phosphatases, as well as exonucleases (RecJ), and **b**, dissimilatory APS reductases ( $\alpha$ -subunit) and (putative) assimilatory APS/PAPS reductases. *MtPAPSR* and *MtPAPP* are highlighted in bold red. Bootstrap support values  $\geq 90\%$  are shown as dots on interior nodes. Asterisks (\*) in front of *Methanocaldococcus jannaschii* sequences highlight the two enzymes previously biochemically characterized.



**Extended Data Figure 8. *In vitro* reconstitution of the  $\text{SO}_4^{2-}$  reduction pathway to measure *MtPAPSR* activity.** **a**, Scheme of the coupled enzyme assay used to measure *MtPAPSR* activity via the oxidation of reduced methyl viologen ( $\text{MV}_{\text{red}}$ ) at 600 nm under an  $\text{N}_2$ -atmosphere and at 45 °C. The enzymes were recombinantly expressed in *E.coli*, except for the pyrophosphatase, which was commercially obtained. The reaction mix contained all enzymes, metals ( $\text{Mn}^{2+}$ ,  $\text{Mg}^{2+}$ ), HEPES buffer at pH 7.0 and the substrates  $\text{SO}_4^{2-}$  and ATP. The reaction was started by the addition of  $\text{SO}_4^{2-}$ . **b**, **c**, “Blank” corresponds to a solution containing the buffer, the substrates,  $\text{MV}_{\text{red}}$  and dithionite but no enzymes. “All components” contained every compound shown in scheme (a). **b**, Substrate specificity of *MtPAPSR*. “No *MtAPSK*” corresponds to all components except *MtAPSK*, which prevented the generation of PAPS from APS. With APS as the substrate, a specific enzymatic activity of  $0.007 \pm 0.001 \mu\text{mol}$  of oxidized MV  $\text{min}^{-1} \text{mg}^{-1}$  of PAPS was measured, which is only 6.54% of the activity with the APSK (corresponds to Fig. 4a, +APS -ATPS -APSK). The difference can be attributed to an instability of the added APS. **c**, Impact of different concentrations of *MtPAPSR* on the activity: A fivefold addition of *MtPAPSR* resulted in a stimulation of the MV oxidation rate by 220 % (shown in dark green squares, “5 × more *MtPAPSR*”). After 30 minutes the fivefold addition of the *MtPAPSR* reductase led to aggregation, which is why the  $\text{OD}_{600}$  started to increase after this time point. All experiments were performed in triplicates and represented as data mean  $\pm$  s.d.



**Extended Data Figure 9. Comparison of a dissimilatory APS reductase and assimilatory P/APS reductases with the *MtPAPSR*.** All structures are shown in cartoon with their (metallo)-cofactors in balls and sticks. Close-ups of the active sites (on the right) with residues important for substrate binding are highlighted as balls and sticks. The dissimilatory APS reductase from *Archaeoglobus fulgidus* is a heterotetramer, composed of two ( $\alpha\beta$ )-subunits. Each  $\beta$ -subunit contains two [4Fe-4S]-cluster and each  $\alpha$ -subunit one FAD. The presented assimilatory APSR from *Pseudomonas aeruginosa* is a homotetramer. It contains one [4Fe-4S]-cluster per monomer. The assimilatory PAPS from *Saccharomyces cerevisiae* is homodimeric. The elements oxygen, nitrogen, phosphorus, sulfur and iron are coloured red, blue, orange, yellow and brown. The carbon of the substrate/product is coloured in cyan, and in yellow for the FAD. Catalytic residues are highlighted with red labels.

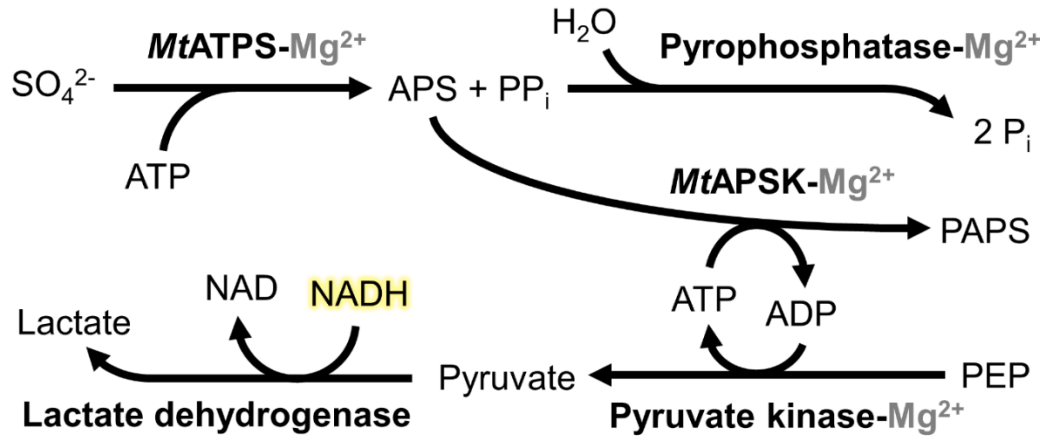
**Extended Data Table 1.** X-ray analysis statistics for the presented structures.

	<i>MtATPS</i> form 1	<i>MtATPS</i> form 2	<i>MtAPSK</i>	<i>MtPAPP</i>	<i>MtPAPSR</i> Fe K edge	<i>MtPAPSR</i>
<b>Data collection</b>						
Synchrotron source	SOLEIL, Proxima-I	SOLEIL Proxima-I	SLS, X06DA	SLS, X06DA	PETRAIII, P11	SLS, X06DA
Wavelength (Å)	1.00000	1.03320	1.00003	1.64566	1.73646	0.97625
Space group	<i>I</i> 222	<i>C</i> 2	<i>P</i> 2 <sub>1</sub>	<i>I</i> 4	<i>P</i> 2 <sub>1</sub>	<i>P</i> 2 <sub>1</sub>
Resolution (Å)	78.79 – 1.97 (2.22– 1.97)	65.94–2.10 (2.16–2.10)	47.74– 1.77 (1.81– 1.77)	126.38 – 3.10 (3.27 – 3.10)	85.51 – 1.89 (2.17 – 1.89)	86.04 – 1.45 (1.64 – 1.45)
Cell dimensions						
a, b, c (Å)	55.70, 154.46, 157.57	185.28, 54.52, 85.43	51.54, 176.18, 51.61	174.05, 174.05, 183.80	63.53, 122.82, 88.53	63.71, 123.65, 88.84
$\alpha, \beta, \gamma$ (°)	90, 90, 90	90, 95.91, 90	90, 105.78, 90	90, 90, 90	90, 105.01, 90	90, 104.44, 90
$R_{\text{merge}}$ (%) <sup>a</sup>	15.1 ( 174.0)	13.5 (114.9)	4.4 (92.8)	19.7 (248.3)	20.0 (169.8)	7.9 (105.6)
$R_{\text{pim}}$ (%) <sup>a</sup>	4.2 (48.3)	5.5 (47.5)	1.8 (39.8)	5.6 (68.0)	6.9 (62.5)	3.3 (42.5)
$CC_{1/2}$ <sup>a</sup>	0.998 (0.641)	0.997 (0.57)	1.0 (0.685)	0.998 (0.477)	0.998 (0.6)	0.997 ( 0.567)
$I/\sigma_I$ <sup>a</sup>	12.7 (1.6)	10.2 (1.6)	22.7 (1.7)	12.3 (1.1)	12.0 (1.8)	11.9 (1.7)
Spherical completeness <sup>a</sup>	58.2 (9.9)	82.3 (51.2)	80.0 (64.5)	92.1 (100.0)	55.7 (8.3)	62.3 (10.2)
Ellipsoidal completeness <sup>a</sup>	93.2 (62.3)	95.6 (98.3)	83.1 (96.3)	/	91.8 (59.4)	95.0 (73.8)
Redundancy <sup>a</sup>	13.7 (13.9)	6.9 (6.6)	6.8 (6.2)	13.3 (14.3)	18.2 (14.4)	6.8 (7.1)
Nr. unique reflections <sup>a</sup>	28,197 (1,410)	41,069 (2,053)	68,557 (3,427)	45,681 (7,240)	58,277 (2,915)	146,296 (7,316)
<b>Refinement</b>						
Resolution (Å)	49.73 – 1.97	52.28 – 2.10	44.04 – 1.77	57.79 – 3.10		1.45
Number of reflections	28,185	41,057	68,551	45,643		14,6283
$R_{\text{work}}/R_{\text{free}}$ (%) <sup>b</sup>	18.85/21.79	19.86/23.94	15.40/18.09	18.57/21.96		15.14/17.80
Number of atoms						
Protein	3,155	6,205	4,753	15,234		10368
Ligands/ions	49	71	88	183		223
Solvent	208	354	606	0		879
Mean B-value (Å <sup>2</sup> )	42.81	39.09	37.12	94.96		32.18
Molprobity clash score, all atoms	2.99	2.09	3.38	4.67		3.34
Ramachandran plot						
Favoured regions (%)	97.11	97.45	99.30	96.92		97.75
Outlier regions (%)	0	0	0	0		0
rmsd <sup>c</sup> bond lengths (Å)	0.011	0.005	0.007	0.004		0.007
rmsd <sup>c</sup> bond angles (°)	1.138	0.823	0.935	0.613		0.917
<b>PDB ID code</b>	8A8G	8A8D	8A8H	8A8K		8A8O

<sup>a</sup> Values relative to the highest resolution shell are within parentheses. <sup>b</sup>  $R_{\text{free}}$  was calculated as the  $R_{\text{work}}$  for 5% of the reflections that were not included in the refinement. <sup>c</sup> rmsd, root mean square deviation.



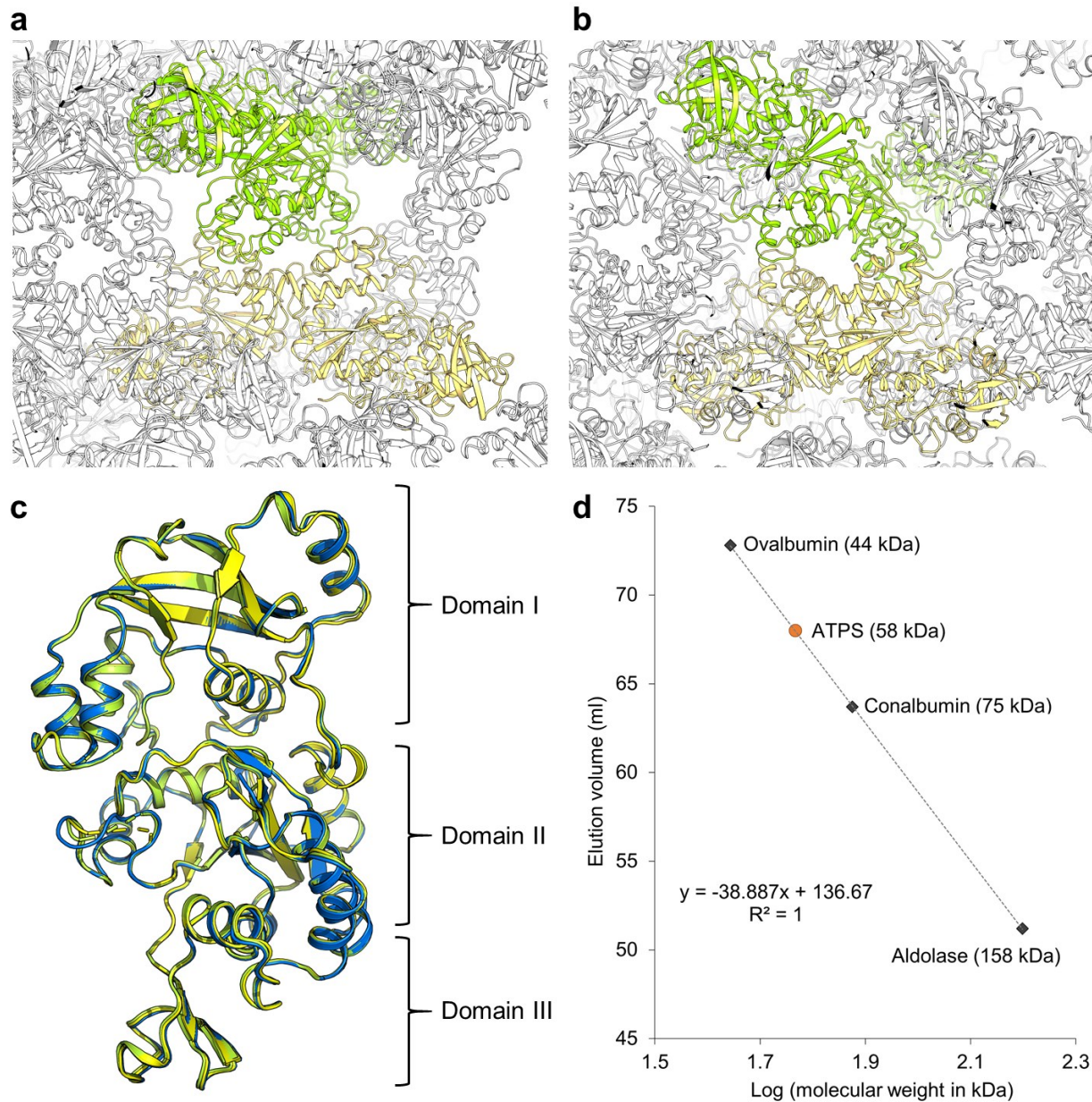
## Supplementary Information



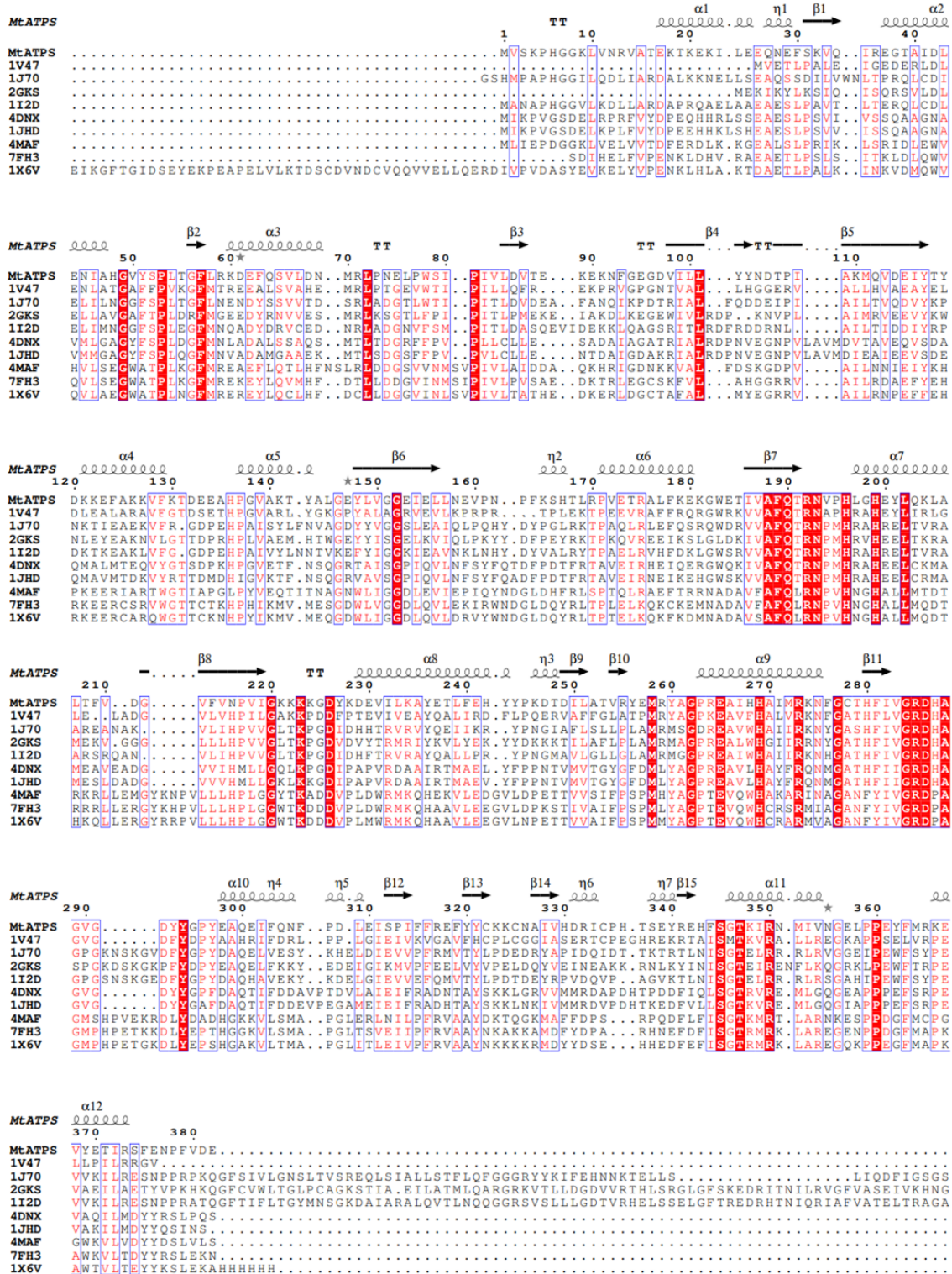
**In presence  
of  $\text{MoO}_4^{2-}$**



**Supplementary Figure 1. Coupled enzyme assay and  $\text{MoO}_4^{2-}$  inhibition.** Scheme of the coupled enzyme assay used in this study and impact of  $\text{MoO}_4^{2-}$  addition. When  $\text{MoO}_4^{2-}$  binds to the active site of the ATP-sulfurylase, ATP is hydrolysed into AMP and  $\text{PP}_i$  (molybdolysis).



**Supplementary Figure 2. Crystalline packing of *MtATPS* suggests a homotetramer. a, b,** Packing of the crystalline form 1 (a) and 2 (b) containing a monomer and a dimer in the asymmetric unit, respectively. All *MtATPS* are shown as cartoons with the main dimeric unit coloured in light yellow. The opposite dimer, related by a 2-fold axis symmetry, is coloured in light green and suggest a tetrameric unit, contradicted by the PISA server and gel filtration (see panel d). **c,** The two monomers from *MtATPS* form 2 superpose well (rmsd 0.253 Å for 348 C $\alpha$ , coloured in yellow and green) as well as the monomer from *MtATPS* form 1 (rmsd 0.238 Å for 331 C $\alpha$ , coloured as blue). **d,** Gel filtration profile of *MtATPS* and a high molecular weight calibration kit (GE Healthcare). The obtained experimental molecular weight of 58 kDa is smaller than the expected dimeric form (89 kDa calculated from the sequence) but refutes a homotetrameric arrangement.



**Supplementary Figure 3. Sequence conservation across *MtATPS* with homologues.** Perfectly conserved residues are highlighted with a red background. Sequence alignment was done using MUSCLE<sup>1</sup>, secondary structure prediction was performed with ESPrift 3.0<sup>2</sup>. For more information regarding the PDB accession numbers, see Supplementary Table 1.

*Mt*APSK

```

MtAPSK ..... 1
5CB8 ..... MGSS
2YVU ..... M
2AX4 ..... QA
3UIE ..... NST
2GKS EEIKSLGLDKIVAFQTRNPMHRVHEELTKRAMEKVGGLLLHPVVGLTKPGDVDVYTRMRYKVLVEKYDYDKKTTILAFPLAMRMAGPR
3CR8 ALFVRRGWRIIAWQARQPMHRAQYEFCLKSAIENEANLLHPQVGGDI TEAPAYFGLVRSFLAIRDR.FPAATTQLSLLPAPPEASGR
4BZP .....
6B8V ..... MA

```

*Mt*APSK

```

MtAPSK EELNNG .....
5CB8 HHHHHH .....
2YVU QALTTY .....
2AX4 HHVSRN .....
3UIE NIKWHE .....
2GKS EALWHGI IRRNYGATHFIVGRDHASPGKDSKPKPFYDPEAQELFKKYEDEIGIKMVPFEELVYVPELDQYVEINEAKRNLKYINISGT
3CR8 ALLLRAIVARNFGCSLLIAGGEHQPDGGDCRRGEDLTQNRVDP SVAERA EKIGVRLIAYPRMVYVEDRAEHLPEAEAPQG . ARLLTL S G
4BZP .....
6B8V HHHHHH ..... MATNITFH

```

*Mt*APSK

```

MtAPSK ..... ENSLLKNLE ..... DGF T I W L T G P S G A G K S T L A Y A L E K K L L E K G F R V E I L D G D V I R N T L Y P N I G F S K E
5CB8 ..... S S G L V P R G S H M Q Q ..... R G V I W L T G L S G A G K T T I T H A L E K K L R D S G Y R L E V L D G D V V R T N L T K G L G F S K E
2YVU ..... ..... K C I E ..... K G I V V W L T G L P G S G K T T I A T R L A D L L Q K E G Y R V E V L D G D W A R T T V S E G A G F T R E
2AX4 ..... K R G Q V V G T R G G F ..... R G C T V W L T G L S G A G K T T I S F A L E E Y L V S H A I P C Y S L D G D N V R H L N R N L G F S P G
3UIE ..... C S V E K V D R Q R L L D Q ..... K G C V I W V T G L S G S G K S T L A C A L N Q M L Y Q K G K L C Y I L D G D N V R H G L N R D L S F K A E
2GKS E I R E N F L K G R K L P E W F T R P E V A E I L A E T Y V P K H Q G F C V W L T G L P C A G K S T I A E I L A T M L Q A R G R K V T L D G D V V R T H L S R G L G F S K E
3CR8 E E F Q R R M R A G L K I P E W S P P E V L A E L H R Q T P P R E R Q G F T V F F T G L S G A G K S T L A R A L A A R L M E M G G R C V T L D G D V I R H R L S E L G F S K A
4BZP ..... S P P ..... R K T V W F T G L S G S G K S S V A M L V E R K L L E K G I S A Y V L D G D N R H G L N A D L G F S M A
6B8V P G A V T Q D E R D T L L G Q ..... K G C T V W L T G L S A S G K S T I A T A L E Q H L L H K K L H A Y R L D G D N R F G L N R D L G F S Q A

```

*Mt*APSK

```

MtAPSK ..... 80 ..... 90 ..... 100 ..... 110 ..... 120 ..... 130 ..... 140 ..... 150
MtAPSK A R E M H N R V V I H L A K T L S K N G V I T T V S L I S P Y R A V R E Y A R K E I Q N ..... F M E V Y I H S F L E V R T Q R D P K G L Y A K A L K G E T K G T T G Y D G V Y
5CB8 D R D T N I R R I G F V S H L L T R N G V I V L S A I S P Y A A I R Q E V K H T I G D ..... F L E V F V N A P L A V C E E R D P K G L Y A K A R S G E I K G F T G I D D P Y
2YVU E R L R H L K R I A W I A R L L A R N G V I V I C S F V S P Y K Q A R N M V R I I V E E G . I P F L E Y V K A S L E E V I R R D P K G L Y K K A L K G E L E N F T G I T D P Y
2AX4 D R E E N I R R I A E V A K L F A D A G L V C I T S F I S P F A K D R E N A R K I H E S A G . L P F F E I F V D A P L N I C E S R D P K G L Y K R A R A G E I K G F T G I D S D Y
3UIE D R A E N I R R V G E V A K L F A D A G I I C I A S L I S P Y R T D R D A C R S L L P E G D . . . F V E V F M D V P L S V C E A R D P K G L Y K L A R A G K I K G F T G I D D P Y
2GKS D R I T N I L R V G F V A S E I V K H N G V V I C A L V S P Y R S A R N Q V R N M M E E G K . . . F I E V F V D A P V E V C E E R D P K G L Y K K A K E G L I K G F T G V D D P Y
3CR8 H R D V N V R R I G F V A S E I T K N R G I A I C A P I A P Y R Q T R R D V R A M I E A V G . . . G F V E I H V A T P I E T C E S R D P K G L Y A K A R A G L I P E F T G V S D P Y
4BZP D R A E N L R L S H V A T L L A D C G H L V L V P A I S P L A E H R A L A R K V H A D A G . I D F F E V F C D T P L Q D C E R R D P K G L Y A K A R A G E I T H E F T G I D S P Y
6B8V S R V E N I R R I G E V S L L F A L S S T I S V T A F I S P Y I S D R Q L A R E L H E K H S S A I P F I E V F I D A P L S V V E Q R D P K G L Y K K A R A G E I K D E F T G I S A P Y

```

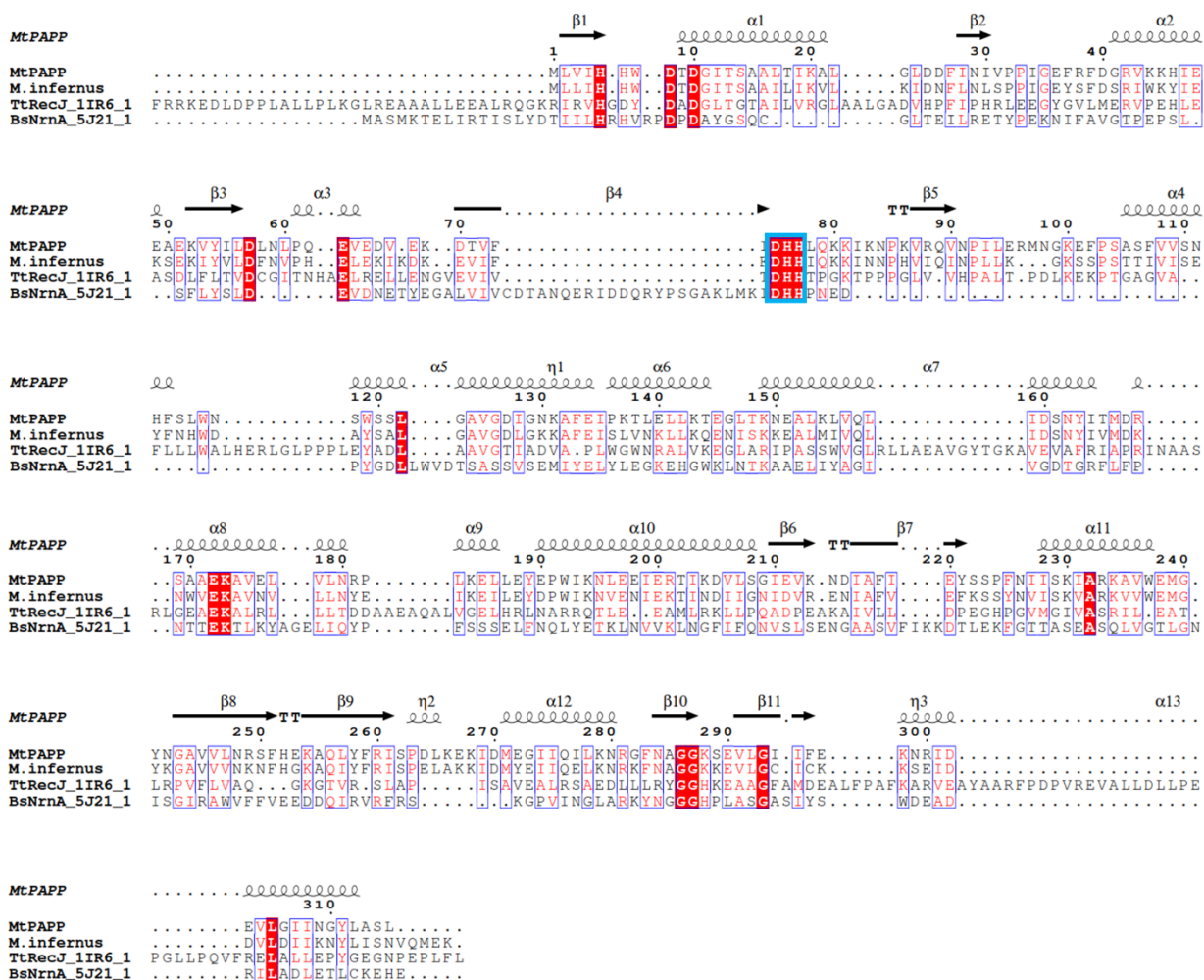
*Mt*APSK

```

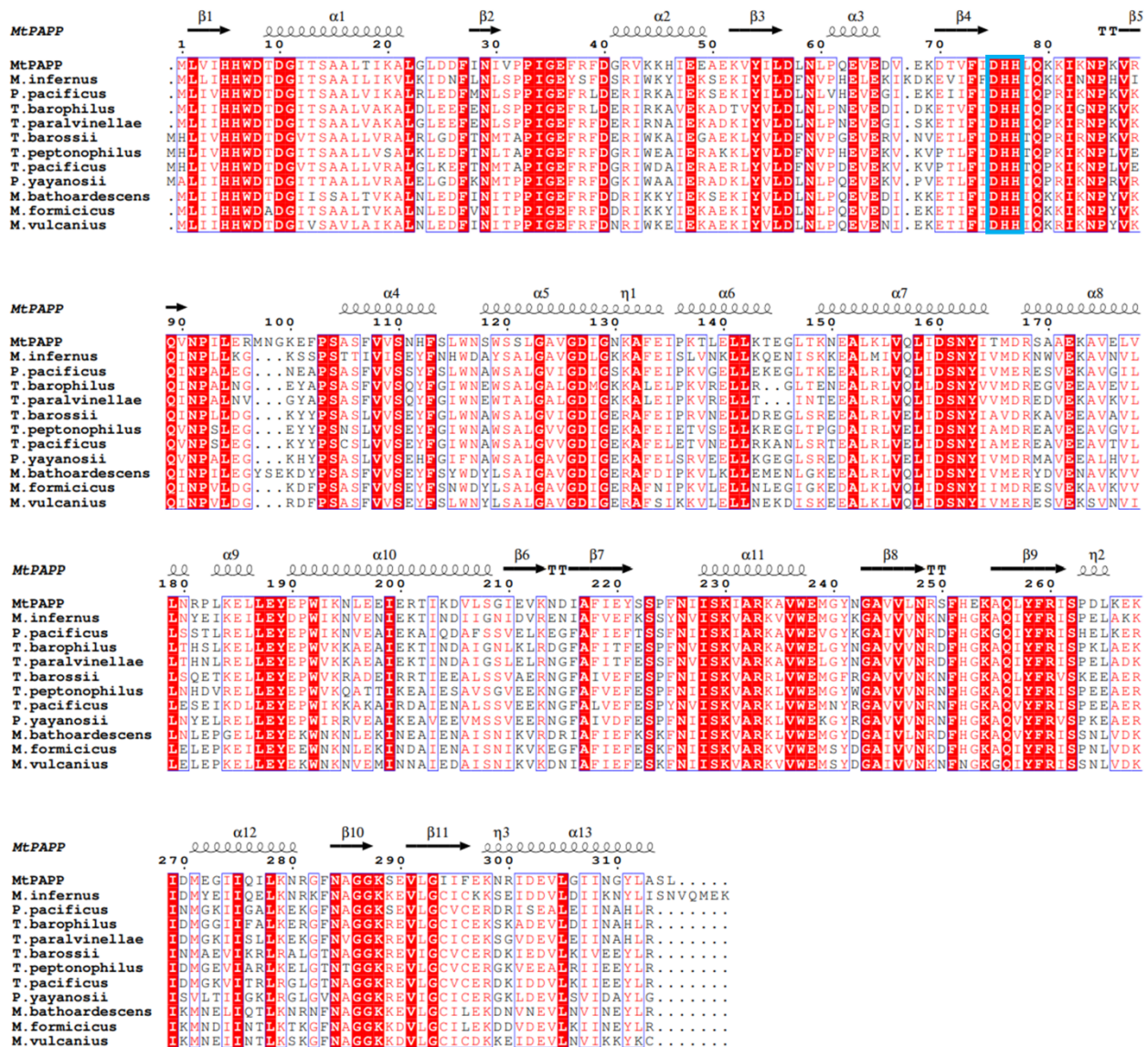
MtAPSK ..... 160 ..... 170 ..... 180
MtAPSK E P P E N P E L K I T E S H K M S I E E E V D T V I R T A Q K L G Y L .....
5CB8 E P P T N P D V E C . R T D L E E L D E S V G K I W Q K L V D L K Y I E G . . . . .
2YVU E P P E N P Q L V L D T E S N T I E H N V S Y L Y S L V K A . . V I E . . . . .
2AX4 E K P E T P E R V L . K T N L S T V S D C V H Q V V E L L Q E Q N I V P Y . . . . .
3UIE E P P L N C E I S L G R E G G T S P I E M A E K V V G Y L D N K G Y L Q A . . . . .
2GKS E P P V A P E V R V . D T T K L T P E E S A L K I L E F L K K E G F I K D . . . . .
3CR8 E V P E T P E L A I . D T T G L A I D E A V Q Q I L L K L E H E G Y L R L E H H H H H
4BZP Q R P K N P D L R L . . T P D R S I D E Q A Q E V I D L L E S . . . . .
6B8V E A P A N P E I H I . R T D E V D V A G A V E I I T K Y L A D N G L I P A . . . . .

```

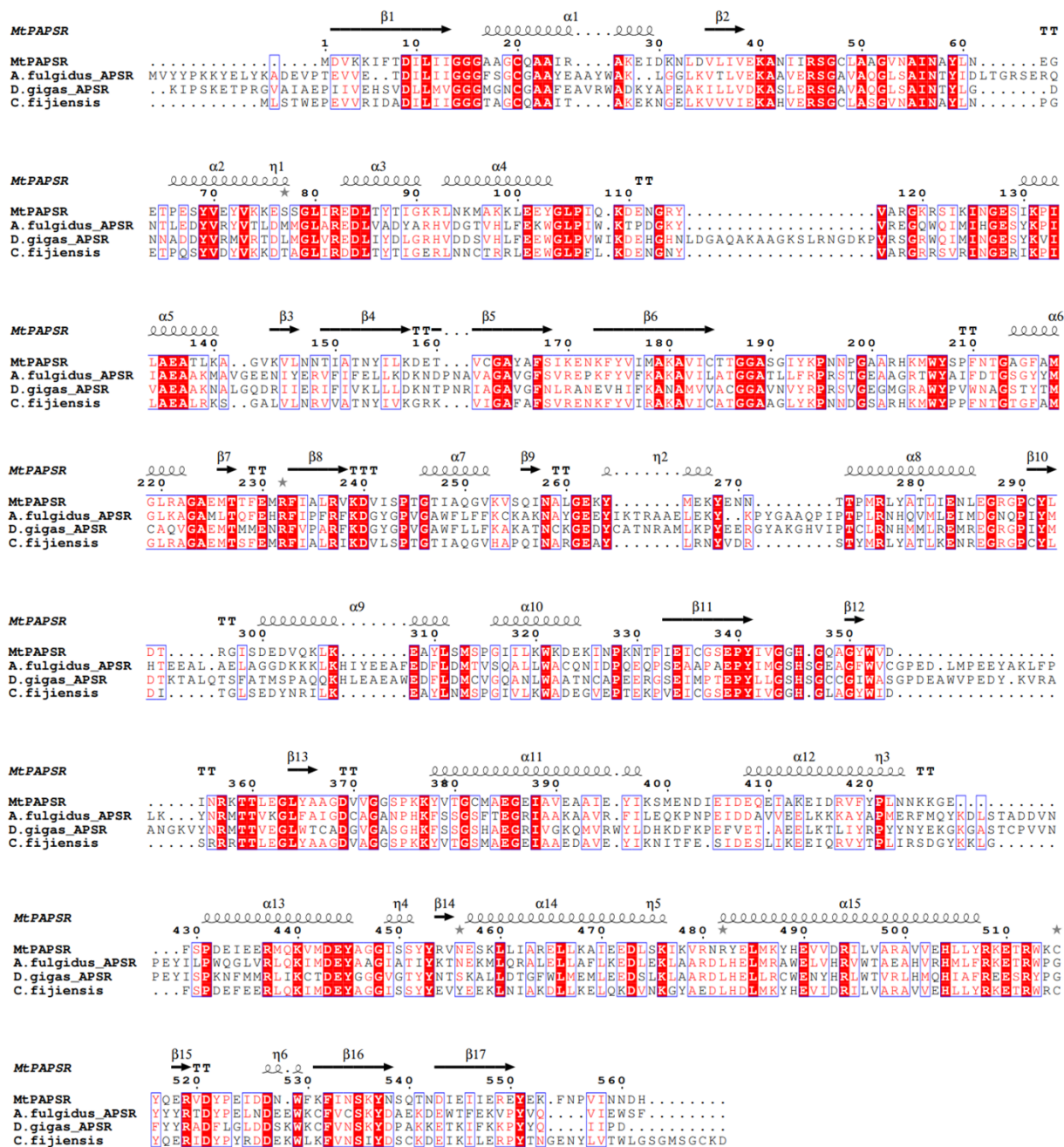
**Supplementary Figure 4. Sequence conservation across *Mt*APSK with other APS-kinases.** Perfectly conserved residues are highlighted with a red background. Sequence alignment was done using MUSCLE<sup>1</sup>, secondary structure prediction was performed with ESPrnt 3.0<sup>2</sup>. For more information regarding the PDB accession numbers, see Supplementary Table 2.



**Supplementary Figure 5. Sequence conservation across MtPAPP with the putative PAPP from *Methanocaldococcus infernus* and structural homologues.** Perfectly conserved residues are highlighted with a red background and a blue box highlights the DHH motif. MtPAPP: *Methanothermococcus thermolithotrophicus* PAP-phosphatase; M.infernus: *Methanocaldococcus infernus* (WP\_013099421, putative PAPP); TtRecJ: *Thermus thermophilus* exonuclease RecJ (PDB: 1IR6); BsNrna\_5J21: *Bacillus subtilis* bifunctional oligoribonuclease and PAP-phosphatase NrnA (PDB: 5J21). To allow a correct alignment, the “MGSSHHHHHHENLYFQS”-tag from BsNrna\_5J21 was removed. Sequence alignment was done using MUSCLE<sup>1</sup>, secondary structure prediction was performed with ESPrnt 3.0<sup>2</sup>.



**Supplementary Figure 6. Sequence alignment of *MtPAPP* with archaeal homologues.** Perfectly conserved residues are highlighted with a red background and a blue box highlights the DHH motif. *MtPAPP*: *Methanothermococcus thermolithotrophicus* PAP-phosphatase; *M.infernus*: *Methanocaldococcus infernus* (WP\_013099421); *P.pacificus*: *Palaeococcus pacificus* (WP\_048165810); *T.barophilus*: *Thermococcus barophilus* (WP\_013468329); *T.paralvinellae*: *Thermococcus paralvinellae* (WP\_042682556); *T.barossii*: *Thermococcus barossii* (WP\_088865569); *T.peptonophilus*: *Thermococcus peptonophilus* (WP\_062389597); *T.pacificus*: *Thermococcus pacificus* (WP\_088853513); *P.yyanosii*: *Pyrococcus yyanosii* (WP\_048058414); *M.bathoardescens*: *Methanocaldococcus bathoardescens* (WP\_048201137); *M.formicicus*: *Methanotorris formicicus* (WP\_007044583); *M.vulcanius*: *Methanocaldococcus vulcanius* (WP\_012819478). Sequence alignment was done using MUSCLE<sup>1</sup>, secondary structure prediction was performed with ESPrnt 3.0<sup>2</sup>.



**Supplementary Figure 7. Sequence alignment of dissimilatory APS-reductases with *MtPAPSR*.** Perfectly conserved residues are highlighted with a red background. *MtPAPSR*: PAPS-reductase from *Methanothermococcus thermolithotrophicus*, *A.fulgidus\_APSR*: alpha subunit of the APSR from *Archaeoglobus fulgidus* (PDB: 2FJA), *D.gigas\_APSR*: alpha subunit of the APSR from *Megalodesulfovibrio gigas* (PDB: 3GYX), and *C.fijiensis*: the putative APSR from *Caldanaerobius fijiensis* (*CfAPSR*, WP\_073344903, closest homologue of *MtPAPSR* alpha). Sequence alignment was done using MUSCLE<sup>1</sup>, secondary structure prediction was performed with ESPrnt 3.0<sup>2</sup>.

	ATP-sulfurylase (reference WP_018153795)	PAP-phosphatase (reference WP_018153796)	APS-kinase (reference WP_018153797)	PAPS-reductase alpha subunit (reference WP_018153799)
<b>Methanopyrales</b>	/	/	/	/
<b>Methanococcales</b>				/
	<i>Methanoterris formicicus</i> (WP_048115642.1; 78 %)	<i>Methanoterris formicicus</i> (WP_007044583.1; 68 %)	<i>Methanoterris formicicus</i> (WP_007044585.1; 76 %)	
	<i>Methanocaldococcus bathoardescens</i> (WP_048201136.1; 79 %)	<i>Methanocaldococcus bathoardescens</i> (WP_048201137.1; 67 %)	<i>Methanocaldococcus bathoardescens</i> (WP_048201139.1; 75 %)	
	<i>Methanocaldococcus</i> sp. SG7 (WP_214399893.1; 73 %)	<i>Methanocaldococcus</i> sp. SG7 (WP_214399894.1; 62 %)	<i>Methanocaldococcus</i> sp. SG7 (WP_214399895.1; 76 %)	
	<i>Methanocaldococcus infernus</i> (WP_013099422.1; 71 %)	<i>Methanocaldococcus infernus</i> (WP_013099421.1; 60 %)	<i>Methanocaldococcus infernus</i> (WP_157198836.1; 75 %)	
	<i>Methanocaldococcus vulcanius</i> (WP_012819477.1; 77 %)	<i>Methanocaldococcus vulcanius</i> (WP_012819478.1; 64 %)	<i>Methanocaldococcus vulcanius</i> (WP_012819479.1; 76 %)	
	<i>Methanoterris formicicus</i> Mc-S-70 (EHP86153.1; 78 %)			
<b>Methanobacteriales</b>	/	/	/	/
	<i>Methanoregulaceae</i> archaeon (NTV00908.1; 33 %)		<i>Methanoregulaceae</i> archaeon (RPI39683.1; 47 %)	
<b>Methanomicrobiales</b>	<i>Methanomicrobiales</i> archaeon HGW-Methanomicrobiales-1 (PKL70343.1; 39 %)	/	<i>Methanomicrobiaceae</i> archaeon (MBN2735040.1; 49 %)	/
			<i>Methanoregula formicica</i> (WP_015284456.1; 44 %)	
<b>Methanomassiliicoccales</b>	/	/	/	/
	<i>Methanosarcinales</i> archaeon (RLG37318.1; 57 %)	<i>Methanosarcinales</i> archaeon (RLG38197.1; 28 %)	<i>Methanosarcinales</i> archaeon (RLG37639.1; 53 %)	<i>Methanosarcinales</i> archaeon (RLG30695.1; 34 %)
	<i>Methanosarcinales</i> archaeon (TRZ88670.1; 57 %)	<i>Methanosarcinales</i> archaeon (MCD4846224.1; 32 %)	<i>Methanosarcinales</i> archaeon (MCD4846223.1; 50 %)	<i>Methermiccoccus shengliensis</i> (WP_052353262.1; 40 %)
<b>Methanosarcinales</b>	<i>Candidatus</i> Methanoperedens sp. (NJD52436.1; 57 %)	<i>Methanohalobium evestigatum</i> (WP_013194595.1; 33 %)	<i>Methanohalobium evestigatum</i> (WP_013194596.1; 51 %)	<i>Candidatus</i> Methanoperedenaceae archaeon GB37 (CAD7771153.1; 36 %)
	<i>Methanohalophilus mahii</i> (WP_013037172.1; 55 %)		<i>Methanococcolides orientis</i> (WP_233084240.1; 49 %)	<i>Candidatus</i> Methanoperedenaceae archaeon GB50 (CAD7770084.1; 36 %)
	<i>Methanohalophilus</i> sp. RSK (WP_123135802.1; 54 %)		<i>Methanohalophilus profundus</i> (WP_129597714.1; 48 %)	
	+ 23 more		<i>Methanohalophilus portucalensis</i> (WP_072358461.1; 50 %)	
			+ 25 more	
<b>Methanofastidiosia</b>	/	/	/	/

**Supplementary Figure 8. SO<sub>4</sub><sup>2-</sup>-reduction associated genes across the seven orders of methanogens.** The protein sequences from the biochemically and structurally characterized enzymes from *M. thermolithotrophicus* were used as reference. The NCBI accession numbers of the proteins (left) as well as the amino acid sequence identity (in %) in comparison to *M. thermolithotrophicus* enzymes are shown in brackets. Homologues below 28 % sequence identity or with a coverage below 85 % are not shown.



**Supplementary Table 1. Sequence and structural alignment of *MtATPS*.** Sequence alignment was performed using PyMOL version 2.2.0 (Schrödinger, LLC).

Name of the organisms	Abbreviation	PDB code	Alignment on Domain II Rmsd in Å (aligned C $\alpha$ )	Overall alignment Rmsd in Å (aligned C $\alpha$ )
<i>Methanothermococcus thermolithotrophicus</i>	<i>MtATPS</i>			
<i>Thermus thermophilus</i>	<i>TtATPS</i>	1V47	1.07 (121)	1.78 (296)
<i>Saccharomyces cerevisiae</i>	<i>ScATPS</i>	1J70	1.06 (112)	1.61 (266)
<i>Aquifex aeolicus</i>	<i>AaATPS</i>	2GKS	1.25 (125)	1.55 (272)
<i>Penicillium chrysogenum</i>	<i>PcATPS</i>	1I2D	1.12 (112)	1.54 (279)
<i>Allochromatium vinosum</i>	<i>AvATPS</i>	4DNX	0.83 (116)	1.44 (257)
<i>Riftia pachyptila symbiont</i>	<i>RrsATPS</i>	1JHD	0.92 (124)	1.42 (260)
<i>Glycine max</i>	<i>GmATPS</i>	4MAF	1.27 (110)	2.33 (315)
<i>Homo sapiens</i>	<i>HsATPS1</i>	1X6V	1.25 (105)	1.98 (252)
<i>Homo sapiens</i>	<i>HsATPS2</i>	7FH3	1.10 (105)	1.83 (261)

**Supplementary Table 2. Sequence and structural alignment of *Mt*APSK.** Sequence alignment was performed using PyMOL version 2.2.0 (Schrödinger, LLC).

Name of the organisms	Abbreviation	PDB code	Overall alignment Rmsd in Å (aligned C $\alpha$ )
<i>Methanothermococcus thermolithotrophicus</i>	<i>Mt</i> APSK		
<i>Synechocystis sp.</i> PCC 6803	<i>Ss</i> APSK	5CB6	1.33 (129)
<i>Arabidopsis thaliana</i>	<i>At</i> APSK	3UIE	1.59 (104)
<i>Aeropyrum pernix</i>	<i>Ap</i> APSK	2YVU	1.18 (117)
<i>Penicillium chrysogenum</i>	<i>Pc</i> APSK	1M7H	1.00 (120)
<i>Homo sapiens</i>	<i>Hs</i> APSK1	2OFW	1.13 (111)
<i>Homo sapiens</i>	<i>Hs</i> APSK2	2AX4	1.25 (123)
<i>Aquifex aeolicus</i>	<i>Aa</i> APSK	2GKS	1.77 (124)
<i>Thiobacillus denitrificans</i>	<i>Td</i> APSK	3CR8	1.14 (116)
<i>Mycobacterium tuberculosis</i>	<i>Mt</i> APSK	4BZP	1.13 (111)
<i>Cryptococcus neoformans</i>	<i>Cn</i> APSK	6B8V	0.81 (111)

## Constructs and gene codon optimisation.

### ATP-sulfurylase sequence from *M. thermolithotrophicus*

(NCBI Accession number: WP\_018153795.1)

MVSKPHGGKLVNRVATEKTKEKILEEQNEFSKVQIREGTAIDLLENIAHGVSPLTGFLRKDEFQSVLDNMR  
LPNELPWSIPIVLDVTEKEKNFGEVDVILLYYNDTPIAKMQVDEIYTYDKKEFAKKVFKTDEEAHPGVAKT  
YALGEYLVGGEIELLNEVPNPFKSHLTRPVETRALFKEKKGWETIVAFQTRNVPHLGHEYLQKLALTFVDGV  
FVNPVIGKKKKGDYKDEVILKAYETLFEHYYPKDTDILATVRYEMRYAGPREAIHHAIMRKNFGCTHFIVG  
RDHAGVGDYYGPYEAQEIQNFPDLEISPIFFREFYCKKCNNAIVHDIRICPHTSEYREHFSGTKIRNMIVNGE  
LPPEYFMRKEVYETIRSFENPFVDE

### Codon optimized *Mt*ATP-sulfurylase sequence cloned into pET-28a(+):

CATATGGTTAGCAAGCCGCACGGTGGCAAACCTGGTGAATCGTGTGGCGACCGAGAAGACCAAGGAGA  
AGATCCTGGAAGAACAGAACGAATTCAGCAAGGTGCAGATCCGTGAGGGTACCGCGATCGACCTGGA  
AAACATTGCGCATGGTGTGTACAGCCCGCTGACCGGCTTCTGCGTAAAGACGAGTTTCAAAGCGTTC  
TGGATAACATGCGTCTGCCGAACGAACCTGCCGTGGAGCATCCCGATTGTGCTGGATGTTACCGAGAAG  
GAGAAGAACTTTGGCGAGGGCGACGTGATTCTGCTGTACTATAACGATACCCCGATCGCGAAGATGCA  
GGTTGACGAGATTTACACCTATGATAAGAAAGAATTCGCGAAGAAAGTGTTTAAGACCGACGAGGAA  
GCGCACCCGGGTGTTGCGAAAACCTACGCGCTGGGCGAGTATCTGGTGGGTGGCGAGATCGAACTGCT  
GAACGAAGTCCGAACCCGTTCAAGAGCCACACCCTGCGTCCGGTTGAAACCCGTGCGCTGTTCAAGG  
AGAAAGGTTGGGAAACCATTGTGGCGTTTCAGACCCGTAACGTTCCGCACCTGGGTCACGAATACCTG  
CAAAAACCTGGCGCTGACCTTCGTGGATGGCGTGTGTTGTTAACCCGGTTATCGGTAAGAAAAAGAAAG  
CGACTACAAGGATGAAGTGATTCTGAAAGCGTACGAAACCCTGTTTCGAACACTACTATCCGAAGGACA  
CCGATATCCTGGCGACCGTTCGTTACGAGATGCGTTATGCGGGTCCGCGTGAAGCGATCCACCATGCG  
ATTATGCGTAAAAACTTCGGTTGCACCCACTTTATTGTGGGTGCGTACCACGCGGGTGTGGTGATTAC  
TATGGCCCGTATGAGGCGCAGGAAATTTCCAAAACCTTCCGGACCTGGAGATCAGCCCGATTTTCTTT  
CGTGAATTCTACTATTGCAAGAAATGCAACGCGATCGTGCACGATCGTATTTGCCCGCACACCAGCGA  
GTACCGTGAACACTTTAGCGGTACCAAAAATCCGTAACATGATTGTTAACGGCGAGCTGCCGCCGGAAT  
ATTTTATGCGTAAGGAAGTTTATGAGACCATCCGTAGCTTTGAGAACCCGTTTGTGATGAGTGAGGA  
TCC

### Restriction sites (NdeI and BamHI)

### APS-kinase sequence from *M. thermolithotrophicus*

(NCBI Accession number: WP\_018153797.1)

MSEELNNGENSLKLNLEDGFTIWLTGSPGAGKSTLAYALEKKLLEKGFVVEILDGDVIRNTLYPNIGFSKEA  
REMHNRRVVIHLAKLLSKNGVITIVSLISPYRAVREYARKEIQNFMEVYIHSPLVRIQRDPKGLYAKALKGEI  
KGLTGYDGVYEEPENPELKIESHKMSIEEEVDTVIRTAQKLGYL

**Codon optimized *Mt*APS-kinase sequence cloned into pET-28a(+):**

CATATGAGCGAGGAACTGAACAACGGCGAAAACAGCCTGCTGAAGAACCTGGAGGACGGCTTCACCA  
TTTGGCTGACCGGTCCGAGCGGTGCGGGCAAGAGCACCTGGCGTACGCGCTGGAAAAGAACTGCT  
GGAGAAAGGCTTCCGTGTGGAAATCCTGGACGGTGATGTTATTCGTAACACCCTGTATCCGAACATTG  
GCTTTAGCAAGGAAGCGCGTGAGATGCACAACCGTGTGGTTATCCACCTGGCGAAGCTGCTGAGCAA  
AACGGTGTGATCACCATTGTTAGCCTGATCAGCCCGTACCGTGCGGTGCGTGAATATGCGCGTAAAGA  
GATCCAGAACTTTATGGAAGTGTACATTCACAGCCCGCTGGAAGTGCATCAACGTGACCCGAAGG  
GCCTGTATGCGAAGGCGCTGAAAGGTGAAATTAAGGTCTGACCGGCTACGATGGTGTATGAGGAA  
CCGAAAACCCGGAGCTGAAGATCGAGAGCCACAAAATGAGCATTGAGGAAGAGGTGGATACCGTTA  
TCCGTACCGCGCAGAACTGGGTTACCTGTGAGGATCC

**Restriction sites (NdeI and BamHI)**

**PAP-phosphatase sequence from *M. thermolithotrophicus***

(NCBI Accession number: WP\_018153796.1)

MLVIHHWDTDGITSAALTIKALGLDDFINIVPPIGEFRDGRVKKHIEEAEKVYILDNLNPQEVEDVEKDTV  
IDHHLQKKIKNPKVRQVNPILERMNGKEFPSASFVSNHFSLWNSWSSLGAVGDIGNKA FEIPKTLELLKTE  
GLTKNEALKLVQLIDSNYITMDRSAAEKAVELVLNRPLKELLEYPWIKNLEEIERTIKDVLSGIEVKNDIAF  
IEYSSPFNIISKIARKAVWEMGYNGAVVLNRSFHEKAQLYFRISPDLKEKIDMEGIIQILKNRGNAGGKSEV  
LGIIFEKNR IDEVLGIINGYLASL

**Codon optimized *Mt*PAPP sequence cloned into pET-28a(+):**

CATATGCTGGTGATTCACTGACCGATGGTATCACCAGCGCGGCGCTGACCATTAAGCGCT  
GGGTCTGGACGATTTATCAACATTGTTCCGCCGATCGGCGAGTCCGTTTTGACGGTTCGTGTGAAGAA  
ACACATCGAGGAAGCGGAAAAAGTTTACATTCTGGATCTGAACCTGCCGCAGGAAGTGGAAGACGTT  
GAGAAGGATACCGTGTATCGACCACCACCTGCAGAAGAAAATTAAGAACCCGAAAGTGCCTCAAG  
TTAACCCGATCCTGGAGCGTATGAACGGCAAAGAGTTCCCGAGCGCGAGCTTTGTGGTTAGCAACCAC  
TTCAGCCTGTGGAACAGCTGGAGCAGCCTGGGTGCGGTGGGTGATATCGGTAACAAGGCGTTTGAGAT  
TCCGAAAACCCCTGGAGCTGCTGAAGACCGAAGGTCTGACCAAGAACGAAGCGCTGAAACTGGTTCAA  
CTGATCGACAGCAACTACATTACGATGGACCGTAGCGCGGCGGAGAAGGCGGTGGAAGTGGTTCTGA  
ACCGTCCGCTGAAAGAGCTGCTGGAGTATGAACCGTGGATTAAGAACCTGGAGGAAATCGAACGTAC  
CATTAAAGACGTGCTGAGCGGCATCGAGGTTAAGAACGATATCGCGTTCATTGAATACAGCAGCCCGT  
TTAACATCATTAGCAAGATTGCGCGTAAAGCGGTTTGGGAGATGGGCTACAACGGTGCCTGGTTCTG  
AACCGTAGCTTCCACGAAAAAGCGCAGCTGTATTTTCGTATCAGCCCGACCTGAAGGAGAAAATTGA  
TATGGAAGGCATCATTCAAATCCTGAAAAACCGTGGTTTCAACGCGGGTGGCAAGAGCGAAGTGCTG  
GGTATCATTTTTGAGAAGAACCGTATCGACGAAGTTCTGGGCATCATTAACGGTTATCTGGCGAGCCT  
GTGAGGATCC

**Restriction sites (NdeI and BamHI)**

## PAPS-reductase subunit sequences from *M. thermolithotrophicus*

### PAPS-reductase subunit alpha sequence from *M. thermolithotrophicus*

(NCBI Accession number: WP\_018153799.1)

MDVKKIFTDILIIGGGAAGCQAAIRAKEIDKNLDVLIVEKANIIRSGCLAAGVNAINAYLNEGETPESYVEYV  
KKESGLIREDLTYTIGKRLNKMAKKLEEYGLPIQKDENGRYVARGKRSIKINGESIKPILAEATLKAGVKV  
LNNTIATNYILKDETVCGAYAFSIKENKFYVIMAKAVICTTGGASGIYKPNPGAARHKMWYSPFNTGAGF  
AMGLRAGAEMTTFEMRFIALRVKDVISPTGTIAQGVKVSQINALGEKYMKEYENNTTPMRLYATLIENLEG  
RGPCYLDTRGISDEDVQKLKEAYLSMSPGIILKWKDEKINPKNTPIEICGSEPYIVGGHGQAGYWVDINRKT  
TLEGLYAAGDVVGGSPKKYVTGCMAGEIEAVEAAIEYIKSMENDIEIDEQEIAKEIDRVFYPLNNKKGEFSP  
DEIEERMQKVMDEYAGGISSYYRVNESKLLIARELLKAIEEDLSKIKVRNRYELMKYHEVVDRILVARAVV  
EHLLYRKETRWCYQERVDYPEIDDNWFKFINSKYNSQTNDIEIIEIEYEFKFNPVINNDH

### PAPS-reductase subunit beta sequence from *M. thermolithotrophicus*

(NCBI Accession number: WP\_018153800.1)

MTIRIIEEICIGCGLCTKVCPGNLLYQREDGKSEIMDKRDCWDCAACVKECPVNAIEMYLQPEIGGRGSTLK  
AKKTDSDSIVWIITDNNGEEVIEVKNKKTFDM

**Codon optimized PAPS-reductase sequences cloned into pET-28a(+):**

CCATGG47GGATGTTAAGAAGATATTCACAGATATACTCATAATAGGTGGTGGTGCAGCAGGTTGCCA  
GGCAGCAATAAGGGCAAAGGAGATAGATAAGAACCTCGATGTTCTCATAGTTGAGAAGGCCAAACATA  
ATAAGGTCAGGTTGCCTCGCAGCAGGTGTTAACGCAATAAACGCATACCTCAACGAGGGTGAGACAC  
CCGAGTCATACGTTGAGTACGTTAAGAAGGAGTCATCAGGTCTCATAAGGGAGGATCTCACATACACA  
ATAGGTAAGAGGCTCAACAAGATGGCAAAGAAGCTCGAGGAGTACGGTCTCCCCATACAGAAGGATG  
AGAACGGTAGGTACGTTGCAAGGGGTAAGAGGTCAATAAAGATAAACGGTGAGTCAATAAAGCCCAT  
ACTCGCAGAGGCAACACTCAAGGCAGGTGTTAAGGTTCTCAACAACACAATAGCAACAACTACATA  
CTCAAGGATGAGACAGTTTGCGGTGCATACGCATTCTCAATAAAGGAGAACAAGTTCTACGTTATAAT  
GGCAAAGGCAGTTATATGCACAACAGGTGGTGCATCAGGTATATAACAAGCCCAACAACCCCGGTGCA  
GCAAGGCACAAGATGTGGTACTCACCTTCAACACAGGTGCAGGTTTCGCAATGGGTCTCAGGGCAGG  
TGCAGAGATGACAACATTCGAGATGAGGTTTCATAGCACTCAGGGTTAAGGATGTTATATCACCCACAG  
GTACAATAGCACAGGGTGTTAAGGTTTACAGATAAACGCACTCGGTGAGAAGTACATGGAGAAGTA  
CGAGAACAACAACACCCATGAGGCTCTACGCAACACTCATAGAGAACCCTCGAGGGTAGGGGTCCC  
TGCTACCTCGATACAAGGGGTATATCAGATGAGGATGTTTCAGAAGCTCAAGGAGGCATACCTCTCAAT  
GTCACCCGGTATAATACTCAAGTGGAAGGATGAGAAGATAAACCCCAAGAACACACCCATAGAGATA  
TGCGGTTACAGAGCCCTACATAGTTGGTGGTACGGTACAGGCAGGTTACTGGGTTGATATAAACAGGAA  
GACAACACTCGAGGGTCTCTACGCAGCAGGTGATGTTGTTGGTGGTTCACCCAAGAAGTACGTTACAG  
GTTGCATGGCAGAGGGTGAGATAGCAGTTGAGGCAGCAATAGAGTACATAAAGTCAATGGAGAACGA  
TATAGAGATAGATGAGCAGGAGATAGCAAAGGAGATAGATAGGGTTTTCTACCCCTCAACAACAAG  
AAGGGTGAGTTCTACCCGATGAGATAGAGGAGAGGATGCAGAAGGTTATGGATGAGTACGCAGGTTG  
GTATATCATCATACTACAGGGTTAACGAGTCAAAGCTCCTCATAGCAAGGGAGCTCCTCAAGGCAATA  
GAGGAGGATCTCTCAAAGATAAAGGTTAGGAACAGGTACGAGCTCATGAAGTACCACGAGGTTGTTG  
ATAGGATACTCGTTGCAAGGGCAGTTGTTGAGCACCTCCTCTACAGGAAGGAGACAAGGTGGAAGTG

CTACCAGGAGAGGGTTGATTACCCCGAGATAGATGATAACTGGTTCAAGTTCATAAACTCAAAGTACA  
ACTCACAGACAAACGATATAGAGATAATAGAGAGGGAGTACGAGAAGTTCAACCCCGTTATAAACAA  
CGATCACAGCAGCGGCCACCACCACCACCACCTGAGCTAGCATGACTGGTGGACAGCAAATGGG  
TCGCGAAGGAGATATACCATGACAATAAGGATAATAGAGGAGATATGCATAGGTTGCGGTCTCTGCAC  
AAAGGTTTGCCCCGGTAACCTCCTCTACCAGAGGGAGGATGGTAAGTCAGAGATAATGGATAAGAGG  
GATTGCTGGGATTGCGCAGCATGCGTTAAGGAGTGCCCCGTTAACGCAATAGAGATGTACCTCCAGCC  
CGAGATAGGTGGTAGGGGTTCAACACTCAAGGCAAAGAAGACAGATGATTCAATAGTTTGGATAATA  
ACAGATAACAACGGTGAGGAGGAGGTTATAGAGGTTAAGAACAAGAAGACATTTCGATATGAGGA  
TCC

Red = Insertion of an internal RBS, Blue=linker, Restriction sites (NcoI and BamHI)

## Supplementary Discussion

### Enzymatic rates

The specific activities for the coupled enzymes ATPS-APSK are low but within the range described for other organisms (*i.e.* *Zea mays* ATPS has a specific enzyme activity of 0.000246  $\mu\text{mol}/\text{min}/\text{mg}$ ; *Arabidopsis thaliana* ATPS has a specific enzyme activity of  $\sim 0.145$   $\mu\text{mol}/\text{min}/\text{mg}$ ; *Saccharomyces cerevisiae* ATPS has a specific enzyme activity of 0.69-140  $\mu\text{mol}/\text{min}/\text{mg}$  according to the Brenda database).

*Mt*ATPS, *Mt*APSK and *Mt*PAPSR are assimilating enzymes. Therefore, their turnover may not be as high as dissimilatory ones. They may even be tightly regulated (*i.e.* competitive inhibition by end products, as shown by the retro-inhibition of PAP in the absence of PAPP) to avoid excessive cellular energy consumption.

We cannot exclude that our experimental set-up had a negative effect on the enzymatic rates, as we could not use high salt concentrations (high  $\text{KPO}_4^{2-}$  concentrations have been shown to increase enzymatic activity for certain hydrogenotrophic methanogens<sup>3</sup>, but cannot be used here as  $\text{PO}_4^{2-}$  is a reaction product that would disturb the assay equilibrium), nor could we work at physiological temperature (65 °C) because we used enzymes from mesophiles (*i.e.* pyrophosphatase from *E. coli*) in the coupled assays. In addition, the artificial electron donor methyl viologen is a surrogate, and the physiological electron donor could significantly favour the reaction towards sulfite production, thus triggering the equilibrium.

### **Origin of the enzymes constituting the $\text{SO}_4^{2-}$ -assimilatory pathway**

Our structural and phylogenetic analyses suggest that *MtATPS* and *MtAPSK* are closely related to the thermophilic gram-negative bacterium *Thermus thermophilus* and marine archaeon *Aeropyrum pernix*, respectively. Since ATPS and APSK coding genes have only been found in less than 40 methanogens (Supplementary Fig. 8), it would argue for a lateral gene transfer rather than an ancestral origin common to all methanogens followed by the loss of these genes<sup>4</sup>. Retrieving the original donors to the different methanogen species would require deeper analyses and a larger set of sequences.

The tree suggests that *MtPAPSR* is of bacterial origin and was probably acquired by horizontal gene transfer from a bacterium (possibly from *Thermincola potens* or within its clade).

The archaeal PAP phosphatases form their own clade. Once more, only a limited number of methanogen genomes harbour a PAPP coding gene (Supplementary Fig. 8). Therefore, the genes might have been horizontally transferred from an archaeon (e.g. belonging to the *Thermococcales*). Since archaeal PAP-phosphatases belong to the DHH family, we propose that this new class probably evolved from an ancestor containing the DHH motif.

It has been proposed that methanogenesis and sulfate reduction may have been intertwined pathways for more than 3.4 Gyr.<sup>5</sup> Sulfate assimilation might have been more prevalent in ancient methanogens, and while most of them lost the ability to assimilate  $\text{SO}_4^{2-}$ , some may have retained the required enzymes and adapted them to serve a hitherto unknown sulfur trafficking function. The pathway presented in our work would require a set of genes that only a few methanogenic genomes encode. If sulfate reduction was used in ancient methanogens, then it is unlikely that it was the one described in *M. thermolithotrophicus*.

### **Why would *M. thermolithotrophicus* assimilate $\text{SO}_4^{2-}$ ?**

The archaeon was collected in geothermally heated sediments in an active volcanic area close to the shore of Naples. If the environment mimics a volcanic area, there could be soluble iron ( $\text{Fe}^{2+}$ ) that will react with the sulfide and, with that, deplete it as bioavailable sulfur. While other methanogens have been shown to use metal sulfides as a source of iron and sulfur, this still needs to be clarified for *M. thermolithotrophicus*. Volcanic sulfate aerosols or marine sulfate ions are an alternative sulfur source. As shown in our results, a sulfate concentration in the range of 100  $\mu\text{M}$

would be enough to sustain robust sulfur assimilation that should be available in this niche. Future *in situ* work and meta-transcriptomics on samples from this site would provide additional clues if *M. thermolithotrophicus* is indeed fixing sulfate in its native environment.



## References

- 1 Edgar, R. C. MUSCLE: a multiple sequence alignment method with reduced time and space complexity. *BMC Bioinformatics* **5**, 113, doi:10.1186/1471-2105-5-113 (2004).
- 2 Robert, X. & Gouet, P. Deciphering key features in protein structures with the new ENDscript server. *Nucleic Acids Res* **42**, W320-W324, doi:10.1093/nar/gku316 (2014).
- 3 Setzke, E., Hedderich, R., Heiden, S. & Thauer, R. K. H<sub>2</sub>: heterodisulfide oxidoreductase complex from *Methanobacterium thermoautotrophicum*. **220**, 139-148, doi.org/10.1111/j.1432-1033.1994.tb18608.x (1994).
- 4 Fuchsman, C. A., Collins, R. E., Rocap, G. & Brazelton, W. J. J. P. Effect of the environment on horizontal gene transfer between bacteria and archaea. **5** (2017).
- 5 Susanti, D. & Mukhopadhyay, B. An intertwined evolutionary history of methanogenic archaea and sulfate reduction. *PLoS One* **7**, doi:10.1371/journal.pone.0045313 (2012).



## Chapter III

Structural and spectroscopic insights into the redox cycles of the active site of the [NiFeSe] and [NiFe] hydrogenases of group 3

**Marion Jespersen<sup>+1</sup>, Christian Lorent<sup>+2</sup>, Olivier N. Lemaire<sup>1</sup>, Ingo Zebger<sup>\*2</sup>, and Tristan Wagner<sup>\*1</sup>**

<sup>1</sup> Max Planck Institute for Marine Microbiology, Celsiusstraße 1, 28359 Bremen, Germany.

<sup>2</sup>Institut für Chemie, Technische Universität Berlin, Straße des 17. Juni 135, 10623 Berlin, Germany

*Manuscript in preparation*

## Abstract

Hydrogenases catalyze the production of H<sub>2</sub>, a promising renewable and green energy carrier, and group 3 [NiFe]-hydrogenases are attractive models for the improvement of bioinspired industrial catalysts. Here, we explored the natural diversity concealed in the marine world by isolating a [NiFe] and a [NiFeSe] containing F<sub>420</sub>-reducing hydrogenase from a methanogen phylogenetically distant from previously studied models. While the [NiFeSe] containing isoform is highly similar to the homologs, the [NiFe] hydrogenase showed interesting features in its oligomerisation, and structural aspects, which stimulated further investigation. Compared to homologs, the active [NiFe] enzyme showed a dynamic equilibrium switching from a dodecameric to a dimeric state, with the latter yielding high quality crystals diffracting to 1.65 Å, allowing a precise description of the [NiFe] center. Modifications at the second coordination sphere did not impair the formation of the hydrogen-binding Ni<sub>a</sub>-S state of the [NiFe] center, which exhibits the typical seesaw coordination geometry, as confirmed by *in crystallo* spectroscopy. Resonance Raman, infrared and electron paramagnetic resonance spectroscopies performed in solution elucidated for the first time the complete redox state repertoire of the active site for the F<sub>420</sub>-reducing hydrogenases, promoting the hydrogenase from the marine thermophilic archaeon as an excellent template to study catalytic states in this biotechnologically relevant enzyme.

## Main text, Results and Discussion

Molecular dihydrogen ( $H_2$ ) has great potential as a clean, renewable, and high-energy-density fuel. However, industrial applications require expensive and noble metals, such as platinum, for  $H_2$  production.<sup>[1-2]</sup> The biological  $H_2$  production catalysed by [NiFe] hydrogenases offers a natural and sustainable solution for  $H_2$  cycling using abundant base metals, with conversion rates comparable to platinum electrodes.<sup>[3]</sup> Therefore, their use in biotechnological applications requires a comprehensive knowledge of the structural and mechanistic factors that determine their reactivity. It has been recently shown that group 3 [NiFe] hydrogenases can be used to dissect the most oxidized catalytic redox state ( $Ni_a-S$ ) and would be a suitable blueprint for the further development of sustainable synthetic  $H_2$ -conversion catalysts.<sup>[4]</sup> The structural description of group 3 [NiFe] hydrogenases has so far been restricted to the terrestrial model organisms, *Methanothermobacter marburgensis* and *Methanosarcina barkeri*.<sup>[2, 4-5]</sup> Here, we characterise two native hydrogenases from a methanogen belonging to the exclusively marine *Methanococcales* by a synergistic approach of biochemistry, crystallography and spectroscopy, providing an unprecedented functional understanding of these  $F_{420}$ -reducing hydrogenases (Frh).

The Frh catalyses the reversible oxidation of  $H_2$  coupled to the reduction of the coenzyme  $F_{420}$  reduction (8-hydroxy-5-dezaflavin,  $\Delta G^{o'} = -10$  kJ/mol).<sup>[5-6]</sup> This cofactor is one of the main electron carriers in these methanogens, distributing reducing power to the central energy metabolism and fuelling anabolic pathways.<sup>[7]</sup> The overall reaction requires three components: the large subunit (FrhA) that harbours the [NiFe] centre and oxidizes  $H_2$ , and the small subunit (FhrG), which contains 3x [4Fe-4S] clusters to transfer electrons to the flavin adenine dinucleotide (FAD) located in the  $F_{420}$ -reducing module (FrhB, which contains an additional [4Fe-4S] cluster). FrhABG dimerises and builds up dodecameric assemblies of about 16 nm in diameter with a spherical shape and a hollow core<sup>[2, 4]</sup> that have been hypothesised to provide stability, protect redox centres or keep the metal clusters at optimal distances.<sup>[2, 5]</sup>

The genome of *M. thermolithotrophicus* encodes two Frh isoforms: a [NiFeSe] and a [NiFe] containing enzyme. Apart from the important exchange of a cysteine for a selenocysteine in the active site of the [NiFeSe] Frh, the FrhA subunits of both enzymes show a highly conserved sequence, also when compared to the structural homologs mentioned above. The FrhB subunits of

the [NiFeSe] and [NiFe] containing enzymes are identical at the nucleotide level (**Figs. S1-3**). In contrast, FrhG of the [NiFe] Frh shows insertions and numerous substitutions compared to the [NiFeSe] one.

For the initial purification of Frh, cells were grown in a medium containing high concentrations of selenium. As a result, the purified Frh sample contained a mixture of two isoforms, corresponding to [NiFeSe] and [NiFe] Frh, which were separated by the crystallisation process. A [NiFeSe] Frh crystal and two crystalline forms of the [NiFe] Frh, cubic (*MtFrh<sup>cube</sup>*) and trigonal (*MtFrh<sup>dimer1</sup>*), were obtained. However, based on initial higher resolution X-ray crystallographic data, we focused on the [NiFe] Frh and cultivated *M. thermolithotrophicus* at low Se concentrations, resulting in a higher expression of the [NiFe] isoform<sup>[8]</sup>. The obtained protein preparation was crystallized and yielded two additional crystalline forms of the [NiFe] hydrogenase: an orthorhombic (*MtFrh<sup>dimer2</sup>*) and a second trigonal form (*MtFrh<sup>dimer3</sup>*), detailed in **Table S1**.

[NiFeSe] Frh and [NiFe] Frh share the basic organization previously observed<sup>[4-5]</sup> and form a dimer of FrhABG heterotrimers. While the [NiFeSe] Frh and *MtFrh<sup>cube</sup>* further oligomerize as a dodecamer (**Fig. 1A**), the three other forms (i.e. *MtFrh<sup>dimer1-3</sup>*) arrange as a dimer. Size exclusion chromatography (**Fig. S4A-B**), native polyacrylamide gel electrophoresis (PAGE, **Fig. S4C**), and bioinformatics analyses (**Fig. S5**) suggest that *MtFrh* exhibits oligomeric dynamics in solution, oscillating between the dimeric and dodecameric states. The different oligomers retain H<sub>2</sub>-oxidase activity on native PAGE, and the purified enzyme has a specific activity of  $185.6 \pm 6.1 \mu\text{mol}$  of reduced F<sub>420</sub> min<sup>-1</sup> mg<sup>-1</sup> of *MtFrh* at 50 °C with H<sub>2</sub> as an electron donor. Considering the molecular crowding in the cytoplasm and the high expression levels of Frh (~1 % of total cytoplasmic protein)<sup>[2]</sup>, we propose that *MtFrh* forms the ~1.2 MDa complex *in vivo*.

The [NiFeSe] Frh and [NiFe] Frh structures are superimposable with the other two structural homologues and do not show any conformational shifts induced by the different active site coordination or by the different oligomeric states. **Figure S6** compares all Frh structures, highlighting similar distances in the electron relay. It also shows variations in the occupancy of the [2Fe-2S] cluster, which is proposed to link the protomers electronically, which is likely to be an artefact of the purification or oxidative damage.

We obtained the first structure of a group 3 [NiFeSe] hydrogenase, refined to 3.11 Å, providing a snapshot of its active site (**Fig. 1B**). The [NiFeSe] active site of *MtFrh* is very similar in terms of geometry and composition to the well-characterized [NiFeSe] hydrogenase from *Desulfovibrio vulgaris*, albeit with substitutions in the second coordination shell (**Figs. S1 and S7**). Based on the high-resolution models from *D. vulgaris*, we have modelled the [NiFeSe] in the reduced state, which is also consistent with the [NiFe] Frh obtained in this work.

In [NiFe] Frh, the FrhG subunit contains an N-terminal extension that forms a  $\beta$ -hairpin, which interacts with a  $\beta$ -sheet of the FrhA subunit. As the [NiFe] *MtFrh* was isolated from a thermophilic organism, this organization might contribute to the thermal stability of the enzyme<sup>[9]</sup>. However, in the mesophilic *M. barkeri*, a similar  $\beta$ -hairpin, but from FrhA, also interacts with the same  $\beta$ -sheet, potentially contributing to the overall stability of the protein (**Fig. S8**).

The three *MtFrh*<sup>dimer</sup> forms have a similar active site configuration, and we have used the *MtFrh*<sup>dimer2</sup> for further description, as it has the highest resolution of 1.65 Å. The deeply buried active site of *MtFrh*<sup>dimer2</sup> superposes well to the structure described by Ilina and colleagues<sup>[3]</sup>, with a distorted seesaw geometry of the [NiFe] centre and an apparent vacant site between the two metals (**Fig. 2A**).<sup>[10]</sup> The ligand-to-metal distances are in the range of the *MbFrh* structure, albeit with some shifts, particularly between the Cys66 and the two metals (**Fig. 2B**). To identify and further characterize the [NiFe] state, we performed spectroscopic studies by infrared (IR), resonance Raman (RR) and electron paramagnetic resonance (EPR). *In crystallo* spectroscopy was applied on the *MtFrh*<sup>dimer</sup> form 3 due to the abundance of crystal material and crystal size (see Materials and Methods).

RR spectroscopy on *MtFrh* crystals confirmed the presence of [4Fe-4S] and [2Fe-2S] clusters in an oxidized state (**Fig. S9**)<sup>[11]</sup>. This is in contrast to an earlier study on the Frh from *Methanosarcina barkeri* (*MbFrh*), which lacked signals from the [2Fe-2S] centre and showed more reduced [4Fe-4S] clusters (**Fig. S9**).<sup>[4]</sup> Moreover, IR and RR spectroscopy on the crystals detected the presence of the Ni<sub>a</sub>-S state, previously observed in *MbFrh*.<sup>[4]</sup> This state was postulated as

mandatory for the thermodynamically favourable binding of H<sub>2</sub> and corroborated the vacant position observed in the crystal structure (**Fig. 2**).<sup>[4, 12]</sup>

To gain further insight into the redox chemistry of the [NiFe] centre, we then performed IR spectroscopy on the protein in solution to probe different redox intermediates on the basis of their characteristic CO and CN<sup>-</sup> vibrations<sup>[13]</sup>. After reduction with sodium dithionite, the active site resides predominantly in the fully reduced Ni<sub>a</sub>-SR state, with a minor population in the Ni<sub>a</sub>-C state (**Fig. 3**). During the slow diffusion of air into the IR cell, the solution is reoxidized, forming the Ni<sub>a</sub>-S state after 4 hours. Further oxidation yields an IR signature that could be from the fully oxidized Ni<sub>r</sub>-B and/or Ni<sub>u</sub>-A state, which starts to form after 5 hours. Notably, as soon as the Ni<sub>a</sub>-S state is formed (4 h), the overall intensity of the CO and CN signals starts to decrease drastically. After 8 hours, only 40 % of the initial intensity is present. This may be due to a particular sensitivity of the unsaturated active site (Ni<sub>a</sub>-S) to reactive oxygen species, which may be formed at the FAD during reoxidation. The soluble NAD<sup>+</sup>-reducing [NiFe] hydrogenase from *Hydrogenophilus thermoluteolus*, also classified as group 3, can most likely resist such oxidative stress by forming an unusual glutamate-coordinated high-valent redox state in the presence of oxygen.<sup>[14]</sup>

To verify the true nature of the most oxidized redox states and to further investigate the electronic structure of the other cofactors, EPR spectroscopy was applied. At 10 K, the as-isolated sample remains EPR silent, indicating a fully oxidized iron-sulfur cluster chain and FAD (**Fig. S10A**), and a diamagnetic active site in agreement with the observations from RR (**Fig. 2C and S9**). After exposure to H<sub>2</sub>, distinct signals related to the [4Fe4S] cluster and a semiquinone radical can be observed. This verifies that the enzymes can be reduced by H<sub>2</sub> alone, without the need for the substrate F<sub>420</sub>. The signals from iron-sulphur clusters and FAD disappear on reoxidation with air. Instead, weak features appear in the spectral range characteristic of paramagnetic redox states of the active site. Further analyses at 20 K revealed the typical rhombic signature of the Ni<sub>u</sub>-A and the Ni<sub>r</sub>-B (**Fig. S10B**), which has not been observed before for group 3 hydrogenases, indicating a rather conventional electronic structure of these active site states as observed in standard hydrogenases.<sup>[1]</sup>



Overall, our study promotes how group 3 [NiFe] hydrogenases could serve as excellent models to further characterise the different catalytic events dictated by the versatile redox chemistry of the [NiFe] centre. Among these intermediates, the hydrogen-binding Ni<sub>a</sub>-S state, first described by protein crystallography and complemented by *in crystallo* vibrational spectroscopy on MbFrh, has now been extended to its marine homologue. Spectroscopic methods have once again demonstrated their power to probe the full redox state repertoire of a [NiFe] active site *in vitro*.

Hydrogenases are sophisticated biocatalysts that combine high substrate selectivity conferred by tunnelling systems (**Fig. S11**), efficient turnover with rapid electron transfer via FeS cluster relays, and stabilization of the catalyst by the protein matrix.<sup>[10b, 15]</sup> These metalloenzymes represent one of our brighter solutions for future green energy and may serve as blueprints for synthetic catalysts that can compete or even surpass these bio machines.



## List of Figures

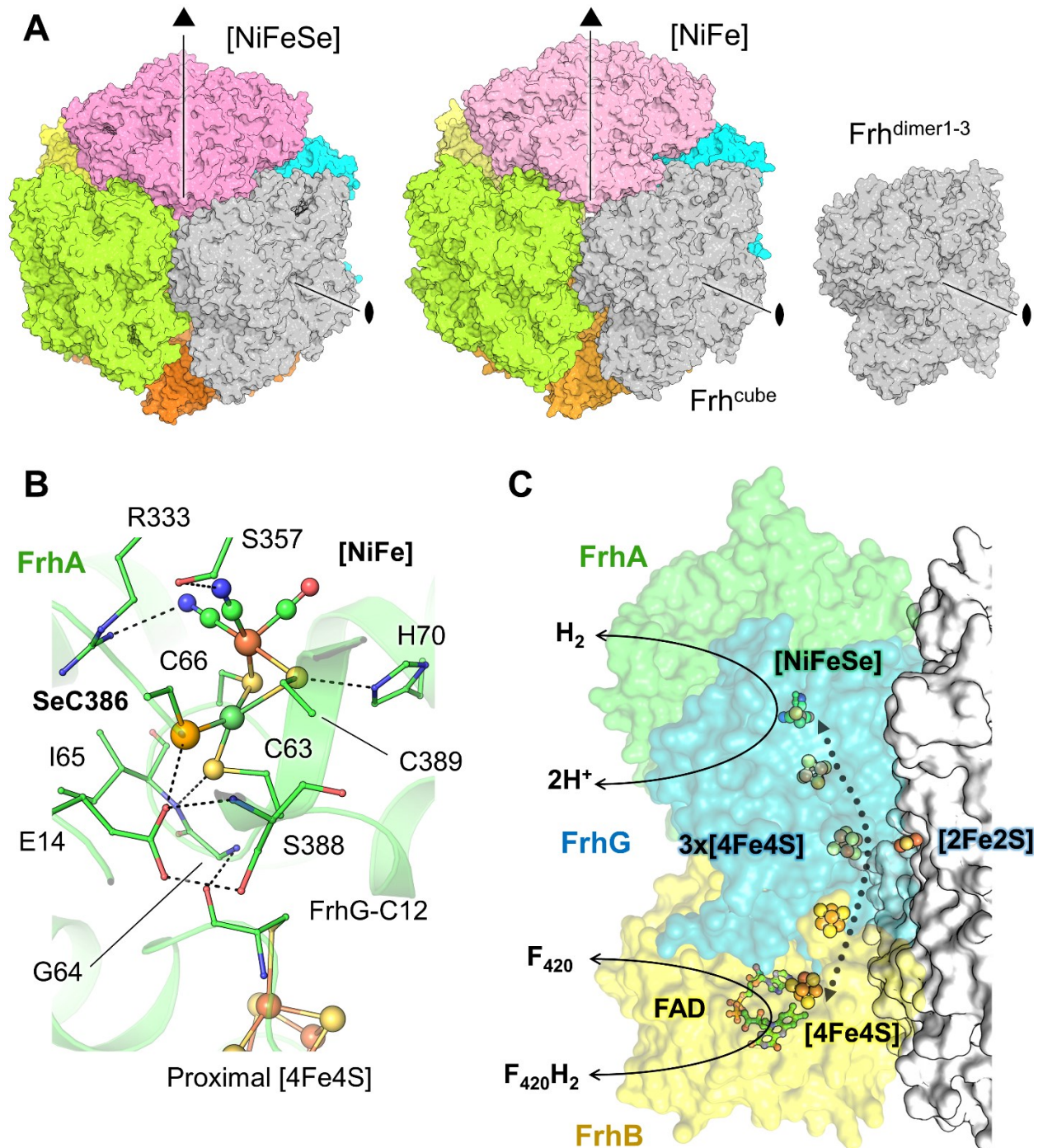


**Figure 1.** A) Overall architecture of the dodecameric and dimeric forms of the Frh from *M. thermolithotrophicus*. Each Frh dimer is shown in a different color. B) Active site of the [NiFeSe]-Frh with its metallo-center highlighted as spheres. Close contacts to the [NiFeSe] and hydrogen bonds are indicated by dashes. C) The atoms carbon, nitrogen, oxygen, sulfur, iron and nickel are colored respectively in green, blue, red, yellow, orange and green.

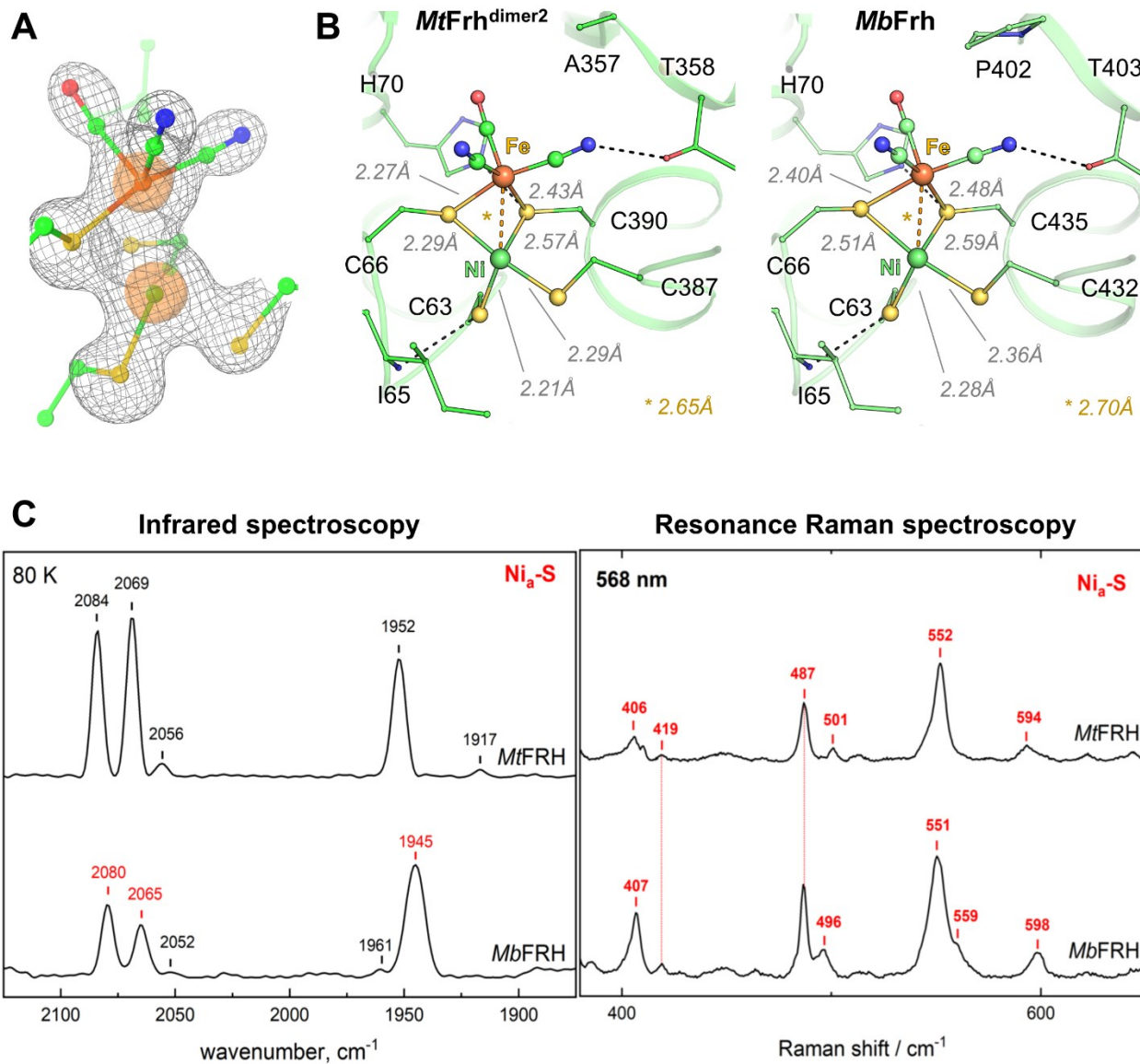


**Figure 2.** A) Close-up of the [NiFe] catalytic site in *MtFrh*<sup>dimer2</sup>. The  $2F_o-F_c$  map of the metal and sulfur atoms is contoured to  $2.5\text{-}\sigma$ , and the  $2F_o-F_c$  map of the nickel and iron is additionally contoured to  $12\text{-}\sigma$  and shown in an orange surface. B) Comparison of the active sites and ligand-metal distances between Frhs. The atoms carbon, nitrogen, oxygen, sulfur, iron and nickel are coloured respectively in light green, blue, red, yellow, orange and green. Dashes indicate close interaction between the [NiFe] centre and the protein. C) Spectroscopy performed on [NiFe] Frh crystals compared with *MbFrh* from Ilina et al.<sup>3</sup>.

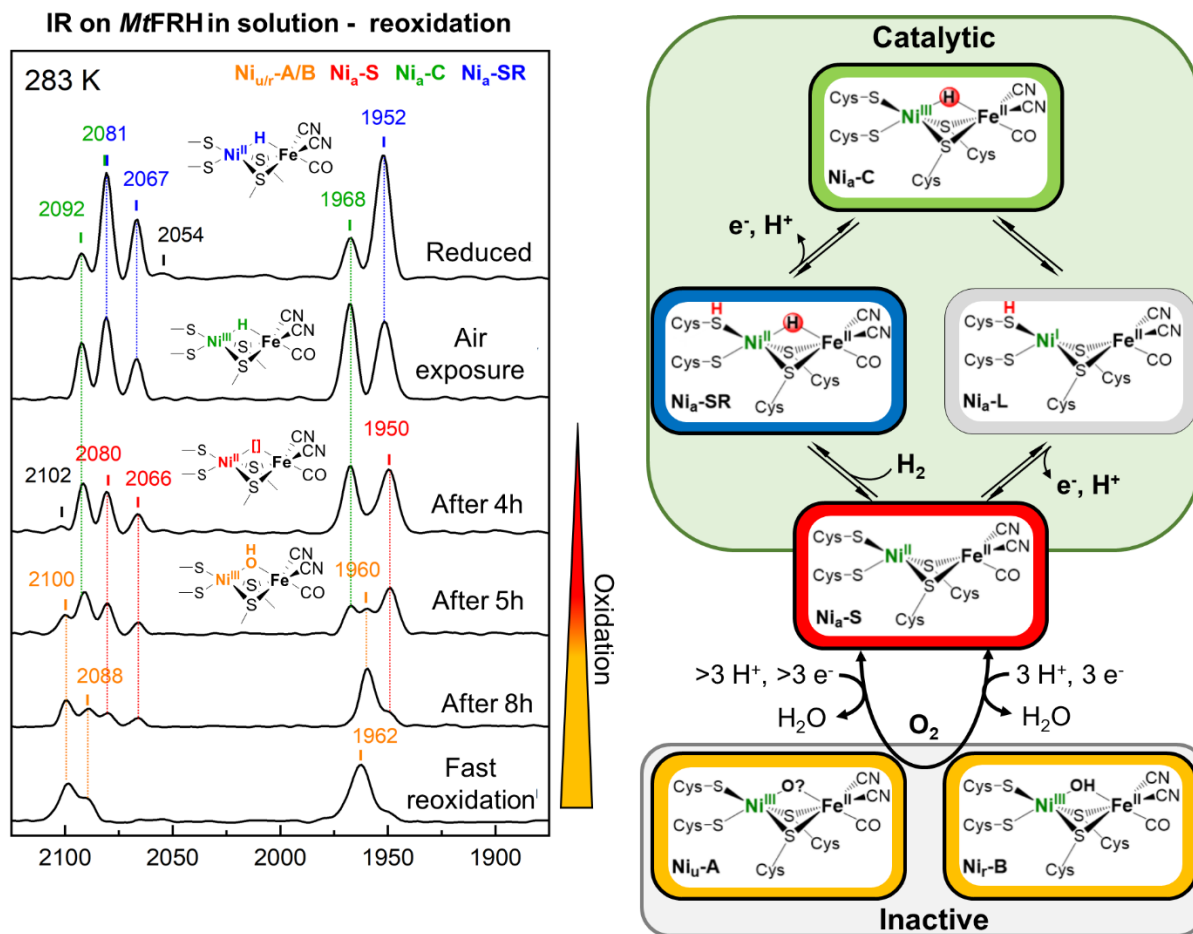


**Figure 3.** Infrared spectroscopy of *Mt*FRh in solution and its reoxidation by air. The proposed catalytic mechanism and oxidative inactivation of the [NiFe] centre is depicted on the right panel.<sup>[1]</sup>



## References

- [1] W. Lubitz, H. Ogata, O. Rüdiger, E. Reijerse, *Chemical reviews* **2014**, *114*, 4081-4148.
- [2] D. J. Mills, S. Vitt, M. Strauss, S. Shima, J. Vonck, *eLife* **2013**, *2*, e00218.
- [3] A. K. Jones, E. Sillery, S. P. J. Albracht, F. A. Armstrong, *Chemical Communications* **2002**, 866-867.
- [4] Y. Ilina, C. Lorent, S. Katz, J.-H. Jeoung, S. Shima, M. Horch, I. Zebger, H. Dobbek, **2019**, *58*, 18710-18714.
- [5] S. Vitt, K. Ma, E. Warkentin, J. Moll, A. J. Pierik, S. Shima, U. Ermler, *J Mol Biol* **2014**, *426*, 2813-2826.
- [6] E. L. Hendrickson, J. A. Leigh, *Journal of bacteriology* **2008**, *190*, 4818-4821.
- [7] R. Grinter, C. Greening, *FEMS Microbiology Reviews* **2021**, *45*.
- [8] F. M. Valente, C. C. Almeida, I. Pacheco, J. Carita, L. M. Saraiva, I. A. Pereira, *Journal of bacteriology* **2006**, *188*, 3228-3235.
- [9] H. Huber, M. Thomm, H. König, G. Thies, K. O. Stetter, *Archives of Microbiology* **1982**, *132*, 47-50.
- [10] aR. P. Happe, W. Roseboom, A. J. Pierik, S. P. J. Albracht, K. A. Bagley, *Nature* **1997**, *385*, 126-126; bA. Volbeda, E. Garcin, C. Piras, A. L. de Lacey, V. M. Fernandez, E. C. Hatchikian, M. Frey, J. C. Fontecilla-Camps, *Journal of the American Chemical Society* **1996**, *118*, 12989-12996.
- [11] S. Todorovic, M. Teixeira, *J Biol Inorg Chem* **2018**, *23*, 647-661.
- [12] aM. Bruschi, M. Tiberti, A. Guerra, L. De Gioia, *Journal of the American Chemical Society* **2014**, *136*, 1803-1814; bM. Horch, J. Schoknecht, M. A. Mroginski, O. Lenz, P. Hildebrandt, I. Zebger, *Journal of the American Chemical Society* **2014**, *136*, 9870-9873.
- [13] K. A. Bagley, E. C. Duin, W. Roseboom, S. P. Albracht, W. H. Woodruff, *Biochemistry* **1995**, *34*, 5527-5535.
- [14] aC. J. Kulka-Peschke, A.-C. Schulz, C. Lorent, Y. Rippers, S. Wahlefeld, J. Preissler, C. Schulz, C. Wiemann, C. C. M. Bernitzky, C. Karafoulidi-Retsou, S. L. D. Wrathall, B. Procacci, H. Matsuura, G. M. Greetham, C. Teutloff, L. Lauterbach, Y. Higuchi, M. Ishii, N. T. Hunt, O. Lenz, I. Zebger, M. Horch, *Journal of the American Chemical Society* **2022**, *144*, 17022-17032; bJ. Preissler, S. Wahlefeld, C. Lorent, C. Teutloff, M. Horch, L. Lauterbach, S. P. Cramer, I. Zebger, O. Lenz, *Biochimica et Biophysica Acta (BBA) - Bioenergetics* **2018**, *1859*, 8-18; cY. Shomura, M. Taketa, H. Nakashima, H. Tai, H.

Nakagawa, Y. Ikeda, M. Ishii, Y. Igarashi, H. Nishihara, K.-S. Yoon, S. Ogo, S. Hirota, Y. Higuchi, *Science (New York, N.Y.)* **2017**, *357*, 928-932.

[15] D. M. A. Smith, S. Raugei, T. C. Squier, *Physical Chemistry Chemical Physics* **2014**, *16*, 24026-24033.

**Author Contributions.** MJ and TW cultivated the methanogens. MJ, ONL, and TW, purified and crystallized the [NiFe] hydrogenase, and TW purified and crystallized the [NiFeSe] hydrogenase. MJ performed all biochemical characterization. MJ, ONL, and TW collected X-ray data and solved the structures. MJ and TW refined all models and validated the models. CL and IZ performed all spectroscopic studies and analyses. TW, CL, and IZ designed the research. MJ wrote the first version of the manuscript, which was supplemented by ONL, TW, CL and IZ and all authors will continue to work on it.

**Conflicts of Interest.** The authors declare no conflict of interest.



## Supporting Information

### Materials and Methods

**Experimental Procedures.** Cell growth, preparation of the cell extract, protein purification, characterization, and crystallization were carried out under anoxic conditions, unless specified otherwise. All buffers were repeatedly degassed by vacuum and flushing with N<sub>2</sub>.

***Methanothermococcus thermolithotrophicus* strain.** *M. thermolithotrophicus* DSM 2095 cells were obtained from the Leibniz Institute DSMZ-German Collection of Microorganisms and Cell Cultures (Braunschweig) and cultivated in a previously described minimal medium with some modifications.<sup>[1]</sup>

**Cultivation medium.** Per liter of medium: 558 mg KH<sub>2</sub>PO<sub>4</sub> (final concentration 4.1 mM), 1 g KCl (13.4 mM), 25.13 g NaCl (430 mM), 840 mg NaHCO<sub>3</sub> (10 mM), 368 mg CaCl<sub>2</sub>·2H<sub>2</sub>O (2.5 mM), 7.725 g MgCl<sub>2</sub>·6H<sub>2</sub>O (38 mM), 6.62 g (NH<sub>4</sub>)<sub>2</sub>SO<sub>4</sub> (50.1 mM), 61.16 mg nitrilotriacetic acid (0.32 mM), 6.16 mg FeCl<sub>2</sub>·4H<sub>2</sub>O (0.031 mM), 0.38 mg Na<sub>2</sub>SeO<sub>4</sub> (2 μM), 3.3 mg Na<sub>2</sub>WO<sub>4</sub>·2H<sub>2</sub>O (0.01 mM) and 2.42 mg Na<sub>2</sub>MoO<sub>4</sub>·2H<sub>2</sub>O (0.01 mM) were dissolved under constant stirring in a measuring cylinder with 750 ml of deionized H<sub>2</sub>O (dH<sub>2</sub>O). Resazurin was added to a final concentration of 0.0015 mM and 10 ml of sulfur-free trace elements (see below) were added subsequently. 50 mM MES was used as a buffer and the pH was set to 6.2 with KOH. The media were filled up to a final volume of 1 liter by the addition of deionized H<sub>2</sub>O.

**Trace element composition.** A 100-fold-concentrated trace element solution was prepared by first dissolving 1.36 g nitrilotriacetic acid (7.1 mM) in 800 ml dH<sub>2</sub>O under magnetic stirring. The pH was shifted to 6.6 by NaOH addition. Then, 89.06 mg MnCl<sub>2</sub>·4H<sub>2</sub>O (0.45 mM), 183.3 mg FeCl<sub>3</sub>·6H<sub>2</sub>O (0.68 mM), 60.27 mg CaCl<sub>2</sub>·2H<sub>2</sub>O (0.41 mM), 180.8 mg CoCl<sub>2</sub>·6H<sub>2</sub>O (0.76 mM), 90 mg ZnCl<sub>2</sub> (0.66 mM), 37.64 mg CuCl<sub>2</sub> (0.28 mM), 46 mg Na<sub>2</sub>MoO<sub>4</sub>·2H<sub>2</sub>O (0.19 mM) and 90 mg NiCl<sub>2</sub>·6H<sub>2</sub>O (0.38 mM) were added separately. The trace element mixture was filled up to a final volume of 1 liter with deionized H<sub>2</sub>O.

**Culture of *M. thermolithotrophicus*.** Cells used for the purification of [NiFeSe]-Frh, [NiFe]-Frh<sup>cube</sup> and [NiFe]-Frh<sup>dimer1</sup> were prepared as in [2]. [NiFe]-Frh<sup>dimer2</sup> and [NiFe]-Frh<sup>dimer3</sup> were prepared as in [3].

**Purification of the F<sub>420</sub>-reducing hydrogenases from *M. thermolithotrophicus*.** All enzymes were purified using a similar protocol, the most optimised of which is detailed here. The frozen cells (55.3 g) were thawed under warm water and transferred to an anaerobic tent filled with an atmosphere of N<sub>2</sub>/CO<sub>2</sub> (90:10). Cells were lysed by osmotic shock through the addition of 220 ml lysis buffer (50 mM Tricine/NaOH pH 8.0, 2 mM dithiothreitol (DTT)). Cell lysate was homogenized by sonication: 11 cycles at 77% intensity with 30 pulses followed by 2 min break (probe MS76, SONOPULS Bandelin). Cell debris were removed anaerobically via centrifugation (21,000g, one hour at 10 °C). The supernatant was transferred to a Coy tent (N<sub>2</sub>/H<sub>2</sub> atmosphere of 97:3) under yellow light 20 °C and was filtered through a 0.2- $\mu$ m filter. The filtered sample was separated in two halves, both applied to a 25-ml DEAE fast-flow column (GE Healthcare), which was previously equilibrated with lysis buffer. After loading the column was washed with 2 column volumes (CV) of lysis buffer. A gradient of 0.1 to 0.6 M NaCl was applied for 120 min at a flow rate of 2.5 ml min<sup>-1</sup> and fractions of 4 ml were collected. *MtFrh* eluted between 0.3 and 0.373 M NaCl. The pooled fractions (~ 100 ml) were diluted with 200 ml lysis buffer and filtered through a 0.2- $\mu$ m filter. The filtered sample was separated in two halves, both loaded on a 15-ml Q Sepharose high-performance column (GE Healthcare), washed with 2 CV of 0.15 M NaCl, and a gradient of 0.15 to 0.55 M NaCl was applied for 120 min with a flow rate of 1 ml min<sup>-1</sup>. Fractions of 1.6 ml were collected. *MtFrh* eluted between 0.43 and 0.46 M NaCl. The pooled fractions were filtered and applied to a 10 ml hydroxyapatite type 1 (Bio-Scale Mini CHT cartridges, BioRad) equilibrated with HAP buffer (20 mM K<sub>2</sub>HPO<sub>4</sub>/HCl pH 7.0 and 2 mM DTT). The column was washed with 2 CV of HAP buffer and the elution was performed with a gradient of 0.02 to 0.5 M K<sub>2</sub>HPO<sub>4</sub> in 60 min at a flow rate of 2 ml min<sup>-1</sup> with 3-ml fractions. *MtFrh* eluted between 0.07 and 0.185 M K<sub>2</sub>HPO<sub>4</sub> and the respective fractions were pooled. The pool was diluted 1:1 with HIC buffer (25 mM Tris/HCl pH 7.6, 2 M (NH<sub>4</sub>)<sub>2</sub>SO<sub>4</sub> and 2 mM DTT), and filtered through a 0.2- $\mu$ m filter. The sample was applied onto a Source15Phe 4.6/100 PE column (GE Healthcare) previously equilibrated with the HIC buffer. The column was washed with 2 CV of 25 mM Tris-HCl pH 7.6, 1.0 M (NH<sub>4</sub>)<sub>2</sub>SO<sub>4</sub> and 2 mM DTT buffer. *MtFrh* was eluted in a gradient of 1 to 0 M (NH<sub>4</sub>)<sub>2</sub>SO<sub>4</sub> in

60 min at a flow rate of 0.7 ml min<sup>-1</sup> and a fractionation volume of 1 ml. *MtFrh* eluted between 0.65 and 0.5 M (NH<sub>4</sub>)<sub>2</sub>SO<sub>4</sub> and the respective fractions were pooled. The pool was diluted with three volumes of lysis buffer, separated in two halves both loaded on a Mono Q 5/50 GL (Cytiva). *MtFrh* was eluted in 10 to 50 mM NaCl in 45 min at a flow rate of 1 ml min<sup>-1</sup> and 0.5 ml fractions were collected. Frh eluted between 44 and 47 mM NaCl and these fractions were pooled and concentrated in 100-kDa-cutoff filter (6 ml, Merck Millipore) to 300 µl. Sample was separated in two halves, both applied onto a Superdex 200 Increase 10/300 GL (GE Healthcare), equilibrated in storage buffer (25 mM Tris-HCl pH 7.6, containing 10 % v/v glycerol and 2 mM DTT) and the elution was performed at a flow rate of 0.4 ml min<sup>-1</sup> and 0.4 ml fractions were collected. *MtFrh* eluted in two Gaussian peaks at an elution volume of 10.4 ml and 11.4 ml, corresponding to pool A and pool B from Fig. S3. The fractions from the two peaks were pooled separately and concentrated by a 100-kDa-cutoff filter. From the 55.3 g of *M. thermolithotrophicus* cells, a total of 1.64 mg Frh were purified. Frh was immediately used for crystallization, the enzyme assays and for the native gels. The remaining sample was aliquoted and anaerobically flash frozen in liquid N<sub>2</sub> and stored at -80 °C. *MtFrh* lost its activity after more than one cycle of thawing-freezing.

**Enzymatic assay.** Prior to the enzymatic assay, *MtFrh* was incubated with 0.5 mM FAD for 30 min under an N<sub>2</sub>/H<sub>2</sub> (97:3) atmosphere. To remove excess of FAD, the samples was concentrated in a 100-kDa-cutoff filter and the buffer was exchanged for fresh storage buffer. Activity measurements were performed with a Agilent Cary 60 UV-Vis spectrophotometer at 60 °C in 100 mM KH<sub>2</sub>PO<sub>4</sub> buffer pH 7.5 in a 1-ml sealed quartz cuvette. The gas phase of the cuvette was exchanged several times with H<sub>2</sub>/CO<sub>2</sub> (80:20, 2 × 10<sup>4</sup> Pa). To monitor the reduction of F<sub>420</sub>, 24.2 µM F<sub>420</sub> was added to the KH<sub>2</sub>PO<sub>4</sub> buffer. The reaction was started by the addition of 0.33 µg *MtFrh*. All experiments were performed in triplicate. For F<sub>420</sub>, a molecular extinction coefficient of 41.50 mM<sup>-1</sup>.cm<sup>-1</sup> at 420 nm was experimentally determined in these conditions. The purification of F<sub>420</sub> has been previously described in [4].

**Protein crystallization.** The purified enzymes were kept in 25 mM Tris/HCl pH 7.6, 10% v/v glycerol and 2 mM DTT. Crystals were obtained anaerobically (N<sub>2</sub>/H<sub>2</sub>, 97:3) by initial screening at 20 °C using the sitting-drop method on 96-well MRC two-drop crystallization plates in polystyrene (SWISSCI) containing 90 µl of crystallization solution in the reservoir or in

CombiClover crystallization plates. All enzymes were co-crystallized with the addition of 2 mM final FAD, except for [NiFe]-*MtFrh*<sup>dimer3</sup> that was crystallized as isolated. [NiFeSe]-*MtFrh*, [NiFe]-*MtFrh*<sup>cube</sup> and [NiFe]-*MtFrh*<sup>dimer1</sup> were crystallized as a mixture at a protein concentration of 16 mg ml<sup>-1</sup>. [NiFe]-*MtFrh*<sup>dimer2</sup> and [NiFe]-*MtFrh*<sup>dimer3</sup> were crystallized at a concentration of 6.1 and 38.8 mg ml<sup>-1</sup>, respectively. The crystallization solution to obtain the different crystals are the following: [NiFeSe]-*MtFrh*, 28% v/v Polyethylene glycol 400, 100 mM HEPES pH 7.5, and 200 mM CaCl<sub>2</sub>; [NiFe]-*MtFrh*<sup>cube</sup>, 1.5 LiSO<sub>4</sub> and 100 mM HEPES pH 7.5; [NiFe]-*MtFrh*<sup>dimer1</sup>, 45% w/v Pentaerythritol ethoxylate (3/4 EO/OH) 270, 100 mM HEPES pH 7.5, and 200 mM (NH<sub>4</sub>)<sub>2</sub>SO<sub>4</sub>; [NiFe]-*MtFrh*<sup>dimer2</sup>, 45.00 % w/v Pentaerythritol propoxylate (17/8 PO/OH) and 100 mM Tris pH 8.5; [NiFe]-*MtFrh*<sup>dimer3</sup>, 30% v/v Polyethylene glycol 400, 100 mM MES pH 6.5, and 200 mM LiSO<sub>4</sub>.

**Data collection, processing and refinement.** All crystals were directly frozen in liquid nitrogen, except for the crystal of [NiFe]-*MtFrh*<sup>cube</sup> that was first soaked in the crystallization solution supplemented with 30% v/v glycerol. Data were collected at 100 K at the different synchrotrons and beamlines states in Table S1. All data were integrated with *autoPROC*<sup>[5]</sup>, except for [NiFe]-*MtFrh*<sup>cube</sup> and [NiFe]-*MtFrh*<sup>dimer1</sup> that were processed with XDS and scale with *scala* from the CCP4 suite. All models were solved by molecular replacement using Phaser from PHENIX. *MmFrh* (PDB code 4OMF) was used as a template to solve [NiFeSe]-*MtFrh* and [NiFe]-*MtFrh*<sup>dimer1</sup>. All other structures were solved by using [NiFe]-*MtFrh*<sup>dimer1</sup> as template for molecular replacement. All models were manually optimized with *COOT*<sup>[6]</sup>. Refinement was performed with PHENIX.refine<sup>[7]</sup> or Buster<sup>[8]</sup> without applying non-crystallography symmetry for the models refined with PHENIX. All models were refined by using a translation-libration screw and by adding hydrogens in riding positions. The different structures were validated by the molprobit tool integrated with PHENIX.

**High resolution clear native PAGE** were prepared and run as in <sup>[9]</sup>.

**Figure construction.** All structural figures were generated with PyMOL version 2.2.0. Figure S1-3 were generated with ESPript<sup>[10]</sup> by using a sequence alignment from MUSCLE<sup>[11]</sup> and the [NiFeSe]-*MtFrh*<sup>dimer1</sup> as structural template for the secondary structure.

**IR spectroscopy.** Transmission cell: *MtFrh* protein solution (0.3 mM) was transferred into a homemade, gastight IR transmission cell containing two CaF<sub>2</sub> windows separated, typically, by a 50- $\mu$ m Teflon spacer. For evaluating the integrity of the protein backbone in solution, the optical path length was reduced to 2  $\mu$ m and the concentration increased to 0.5 mM to monitor amide bands. All IR spectra were recorded with 2 cm<sup>-1</sup> spectral resolution on a Bruker Tensor 27 FT-IR spectrometer using a liquid-N<sub>2</sub> cooled MCT detector. Absorbance spectra were calculated using the buffer solution (100 mM Tris-HCl, pH 8.0, 150 mM NaCl, 5 mM desthiobiotin) as a reference. The Bruker OPUS software 6.5 or higher was used for data evaluation.

**IR microscope.** To perform in situ IR spectroscopy of *MtFrh* solutions, a 3- $\mu$ l drop of protein solution (1 mM) was placed on a 1.5 mm thick MgF<sub>2</sub> window. After adding a 40- $\mu$ m steal spacer, a second 1.5-mm MgF<sub>2</sub> window was carefully placed on top of it in order to form a homogenous protein film. This sandwich cell was then transferred to a precooled liquid-N<sub>2</sub>-cooled cryo-stage (Linkam Scientific instruments) at 277-283 K, and IR spectra were recorded via a Bruker Tensor 27 FT-IR spectrometer connected to a Bruker Hyperion 3000 IR microscope equipped with a 20 $\times$  IR transmission objective and an MCT detector. Protein crystals of ReMBH (Figures 2B and 5A) were handled the same way, but without using a second window and a steal spacer. For illumination experiments, the focused beam of a collimated 455-nm LED was used. To perform cryogenic IR spectroscopy on H<sub>2</sub>-incubated *MtFrh*, protein crystals were mounted on an optical plate in an anaerobic S4 box and frozen in liquid N<sub>2</sub> until further usage. Protein lyophilizate was prepared as described above, and IR spectra were recorded with a Hyperion 3000 IR microscope. The optical pathlength of the lyophilized drops may vary on a sample-to-sample basis since they shrunk due to water removal to a sponge-like form with undefined dimension.

**EPR spectroscopy.** A 9.3-GHz X-Band continuous-wave Bruker EMXplus spectrometer equipped with an ER 4122 SHQE resonator was used for recording EPR spectra. The parameters were set as follows: modulation amplitude: 10 G, modulation frequency: 100 kHz, microwave power: 1 mW. An Oxford EPR 900 He-flow cryostat equipped with an Oxford ITC4 controller was used to control the temperature. All data were processed using the Bruker Xenon software (version 1.1b58).

**RR Spectroscopy.** Resonance Raman spectra were recorded using a LabRam HR-800 Jobin Yvon confocal Raman spectrometer connected to a liquid-N<sub>2</sub>-cooled charge-coupled device (CCD). The spectra were accumulated at 80 K using a liquid-N<sub>2</sub>-cooled cryo-stage (Linkam Scientific instruments). The 458 and 514-nm lines of an Ar<sup>+</sup> ion laser or the 568-nm line of a Kr<sup>+</sup> ion laser with an overall power of 1-2 mW were used for excitation. The laser beam was focused at a 2-4 μm spot on the surface of the compressed lyophilizate, a frozen drop (3 μL, 1 mM protein concentration) or a single crystal. All RR spectra displayed consist of an average of 30-100 individual spectra, each accumulated for 100-180 s. Frequency calibration was performed using toluene as an external standard.

**Table S1.** X-ray analysis statistics for *MtFrh*.

	<b>[NiFeSe]-Frh</b>	<b>Frh<sup>cube</sup></b>	<b>Frh<sup>dimer1</sup></b>	<b>Frh<sup>dimer2</sup></b>	<b>Frh<sup>dimer3</sup></b>
<b>Data collection</b>					
Synchrotron source	SLS PX II	ESRF FIP	ESRF FIP	SLS PX I	SOLEIL PX I
Wavelength (Å)	1.73818	1.38710	1.38710	1.00003	1.73891
Space group	<i>P</i> 6 <sub>3</sub>	<i>P</i> 2 <sub>1</sub> 3	<i>P</i> 3 <sub>2</sub> 21	<i>C</i> 222 <sub>1</sub>	<i>P</i> 3 <sub>1</sub> 21
Resolution (Å)	140.88 – 3.12 (3.31 – 3.12)	49.10 – 2.85 (3.00 – 2.85)	48.86 – 2.30 (2.42 – 2.30)	69.27 – 1.65 (1.79– 1.65)	127.41 – 3.13 (3.35– 3.13)
Cell dimensions					
a, b, c (Å)	162.67, 162.67, 276.46	282.07, 282.07, 282.07	192.71, 192.71, 386.21	95.03, 163.48, 128.83	196.61, 196.61, 192.07
α, β, γ (°)	90, 90, 120	90, 90, 90	90, 90, 120	90, 90, 90	90, 90, 120
R <sub>merge</sub> (%) <sup>a</sup>	31.0 (131.3)	21.7 (149.7)	9.1 (59.7)	11.2 (235.4)	30.4 (244.9)
R <sub>pim</sub> (%) <sup>a</sup>	15.0 (61.4)	8.5 (57.2)	4.2 (30.4)	2.6 (56.0)	6.9 (54.5)
CC <sub>1/2</sub> <sup>a</sup>	0.978 (0.373)	0.988 (0.433)	0.998 (0.565)	0.999 (0.588)	0.997 (0.620)
I/σ <sub>I</sub> <sup>a</sup>	5.9 (1.5)	6.0 (1.2)	13.6 (2.8)	16.1 (1.5)	10.0 (1.6)
Spherical completeness <sup>a</sup>	73.3 (22.6)	100.0 (100.0)	99.8 (99.1)	77.3 (18.2)	69.0 (18.8)
Ellipsoidal completeness <sup>a</sup>	92.7 (74.9)	/	/	94.1 (59.9)	95.1 (67.7)
Redundancy <sup>a</sup>	5.2 (5.5)	7.6 (7.8)	5.7 (4.7)	20.1 (18.4)	20.2 (21.1)
Nr. unique reflections <sup>a</sup>	54,111 (2,706)	173,025 (25,112)	365,266 (52491)	92,187 (4,460)	52,281 (2,616)
<b>Refinement</b>					
Resolution (Å)		48.37 – 2.85	48.18 – 2.30		
Number of reflections		172,884	365,159		
R <sub>work</sub> /R <sub>free</sub> <sup>b</sup> (%)		17.45/19.26	17.29/19.36		
Molecules/asymmetric unit	4 x (FrhABG)	4 x (FrhABG)	4 x (FrhABG)	1 x (FrhABG)	2 x (FrhABG)
Number of atoms					
Protein		28,190	28,200		
Ligands/ions		480	578		
Solvent		55	2103		
Mean B-value (Å <sup>2</sup> )		79.50	54.08		
Molprobrity clash score, all atoms		4.87	1.61		
Ramachandran plot					
Favoured regions (%)		95.81	97.05		
Outlier regions (%)		0.39	0.28		
rmsd <sup>c</sup> bond lengths (Å)		0.010	0.010		
rmsd <sup>c</sup> bond angles (°)		1.24	1.23		

<sup>a</sup>Values relative to the highest resolution shell are within parentheses. <sup>b</sup>R<sub>free</sub> was calculated as the R<sub>work</sub> for 5 % of the reflections that were not included in the refinement. <sup>c</sup>rmsd, root mean square deviation.

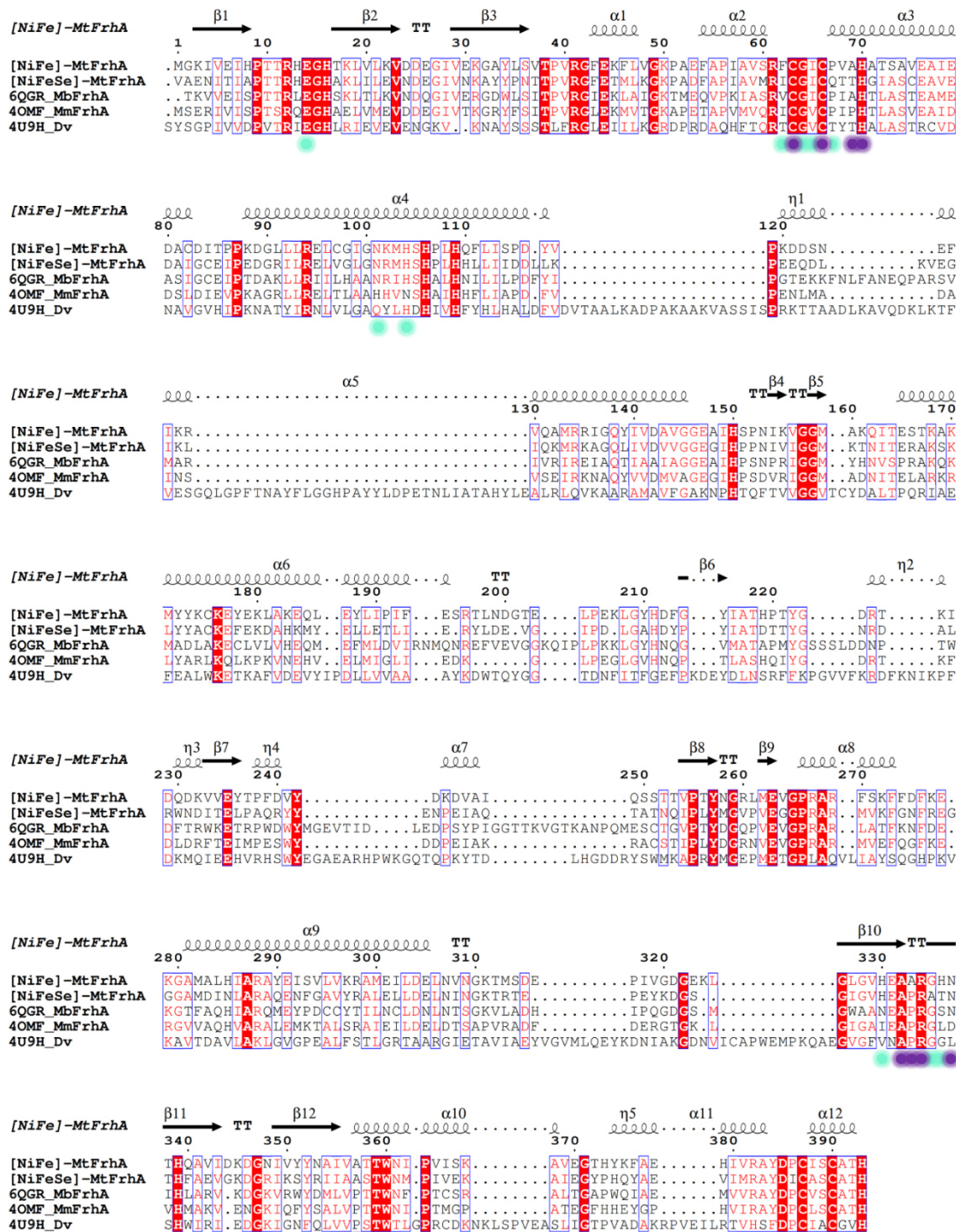


**Fig. S1.** Alignment of FrhA from the [NiFe]-MtFrh (WP\_018154259), [NiFeSe]-MtFrh (WP\_245547917, Cys386 is a SeCys), MbFrh, MmFrh and the [NiFeSe]-hydrogenase from *Desulfovibrio vulgaris* strain Miyazaki. Sequence alignment was done using Muscle, and the picture was created with ESPrnt 3.0.<sup>[10, 12]</sup> Residues part of the first and second [NiFe] shell of interactions are highlighted by purple and cyan dots, respectively.



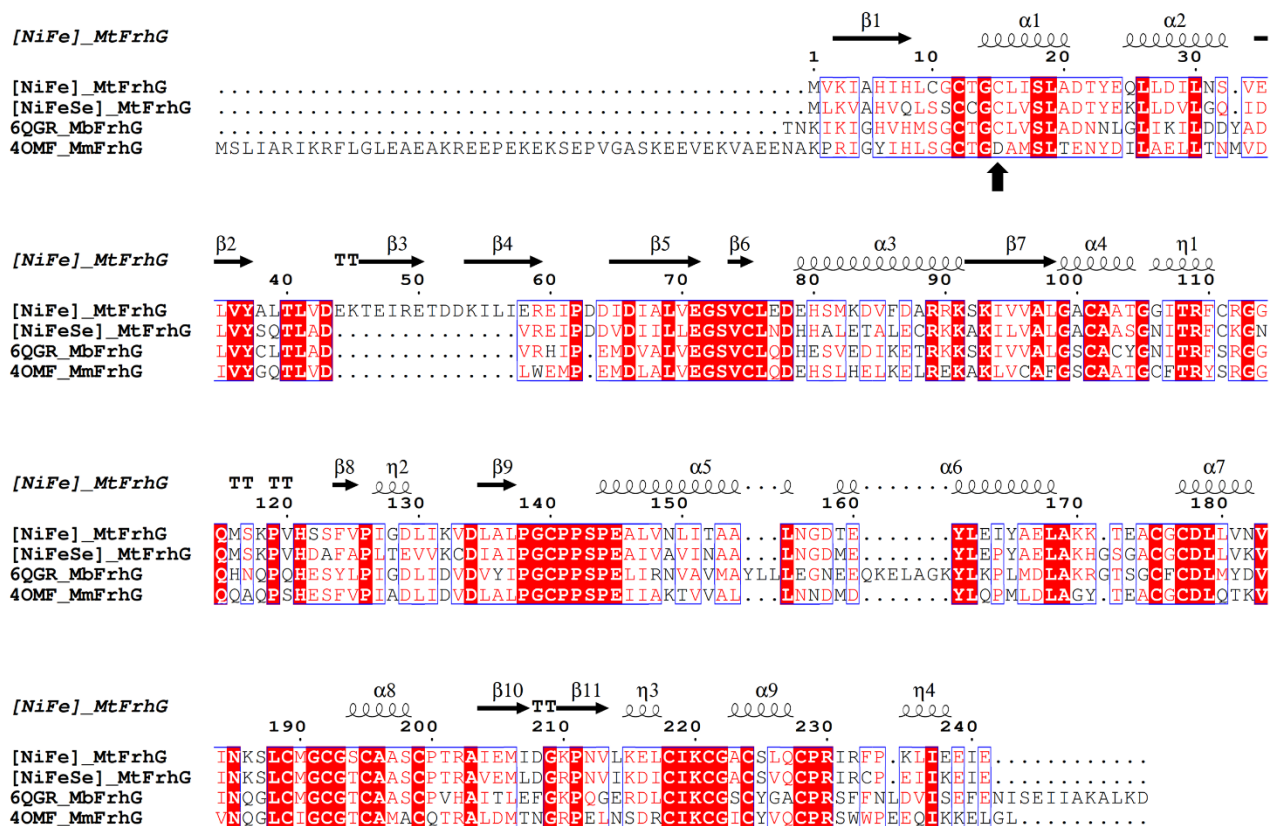


**Fig. S2.** Alignment of FrhG from the [NiFe]-*MtFrh* (WP\_018154257), [NiFeSe]-*MtFrh* (WP\_018154657), *MbFrh* and *MmFrh*. Sequence alignment was done using Muscle, and the picture was created with ESPript 3.0.<sup>[10, 12]</sup> The Asp60 axial ligand of the proximal [4Fe-4S]-cluster in *MmFrhG* is highlighted by a black arrow.

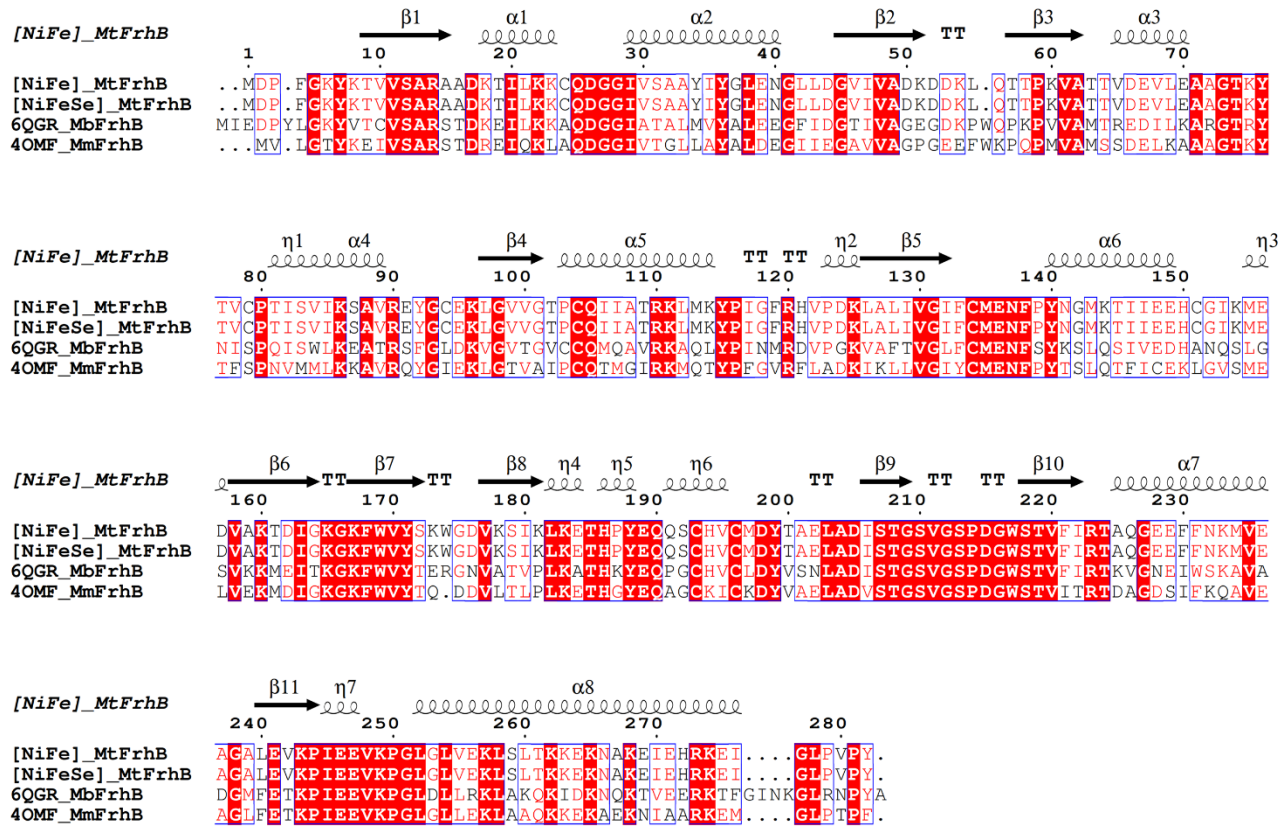


**Fig. S3.** Alignment of FrhB from the [NiFe]-MtFrh (WP\_018154257), [NiFeSe]-MtFrh, MbFrh and MmFrh. Sequence alignment was done using Muscle, and the picture was created with ESPrpt 3.0.<sup>[10, 12]</sup> MtFrhs share the same nucleotide sequence.

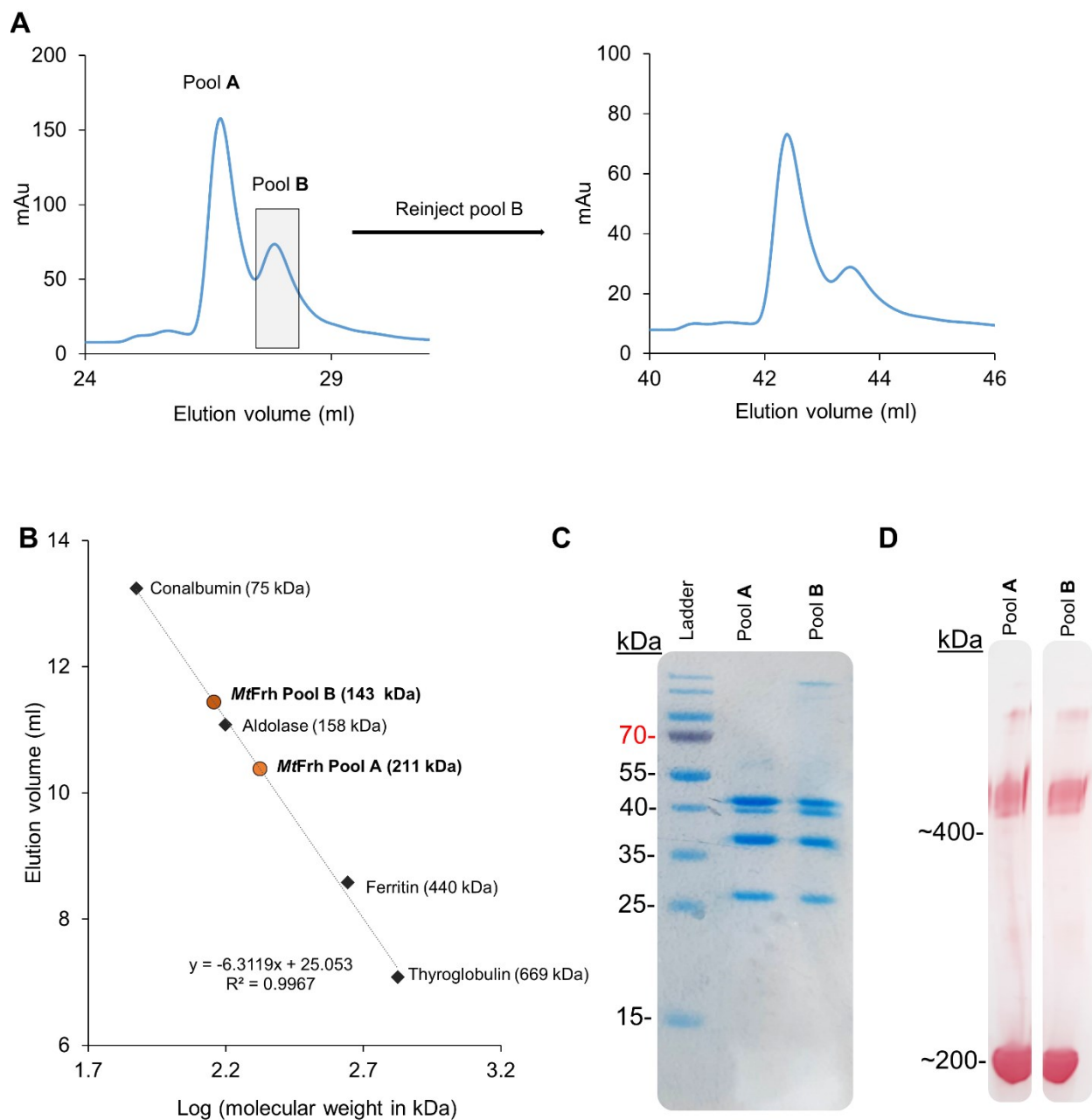


**Fig. S4.** [NiFe]-*MtFrh* shows a dynamic oligomeric behavior. A) Purified *MtFrh* sample elutes in two major populations from a size exclusion column, labelled as Pool A and Pool B. Reinjecting one population, here Pool B, results in the same profile (left chromatogram). (B) The sizes of the two populations correspond to a size of 143 and 211 kDa. (C) SDS-PAGE profile from the two purified *MtFrh* pools (5  $\mu$ g per pool was loaded). (D) hrCN-PAGE of the two *MtFrh* pools (5  $\mu$ g loaded). The blue dye corresponds to the methyl viologen that is reduced upon H<sub>2</sub> oxidation by Frh.

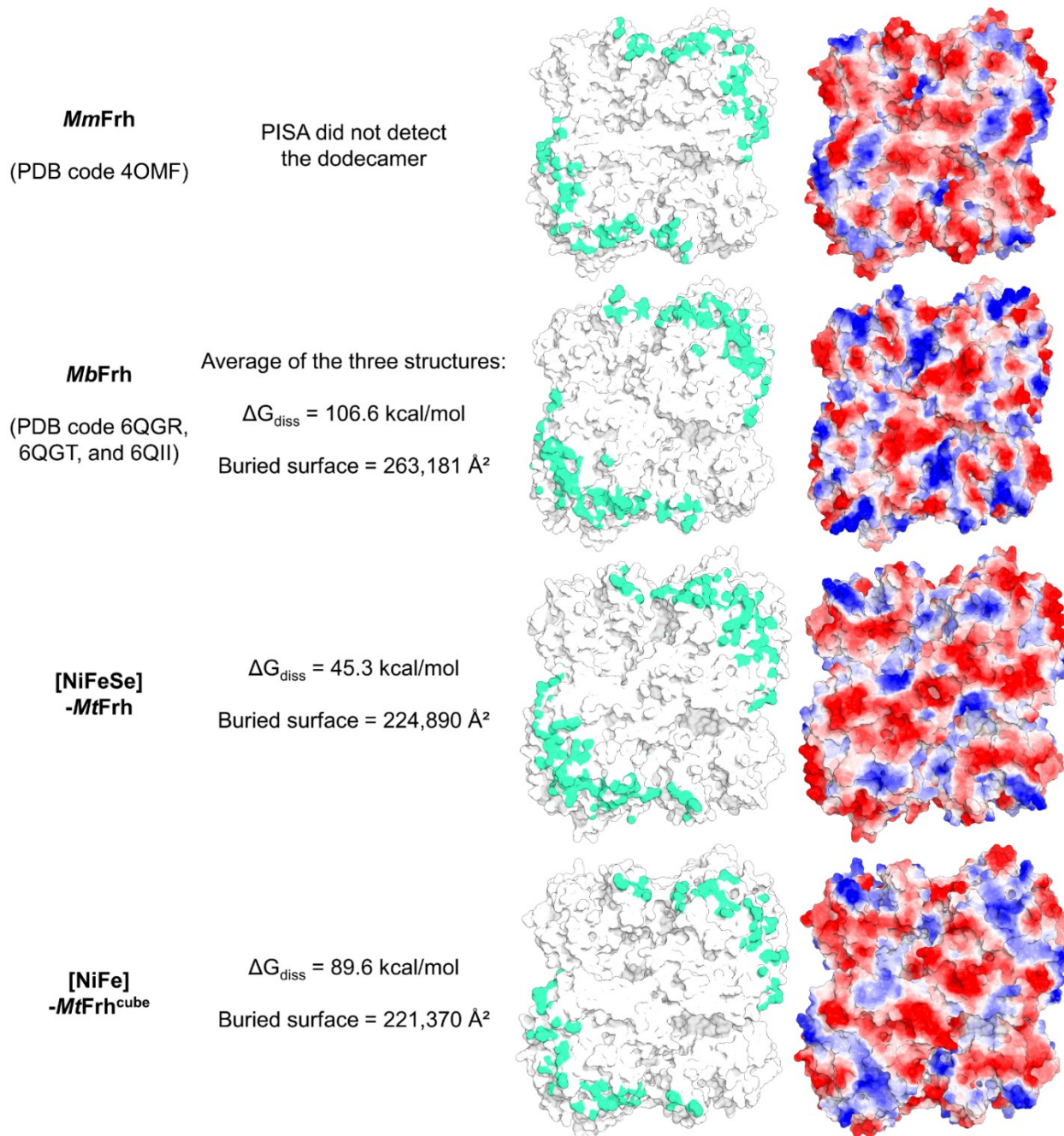


**Fig. S5.** Dimer-Dimer interaction in the dodecameric quaternary assembly. All models are represented as a surface. The cyan colour on the left panels highlights residues interacting with the next Frh dimer in the dodecameric assembly. Blue and red colour reflect the electrostatic charges from negative (red) to positive (blue). The view is taken from inside the cube's hollow core in both panels. Notable, the three-fold axis symmetry in [NiFeSe], generated by the dodecamer assembly, is stabilized by a cation (modelled as Mg<sup>2+</sup> in the structure) coordinated by the Glu279 from FrhA. A similar cation binding site lying at the three-fold axis has been observed in *Mb*Frh and is coordinated by Asn322 from FrhA.

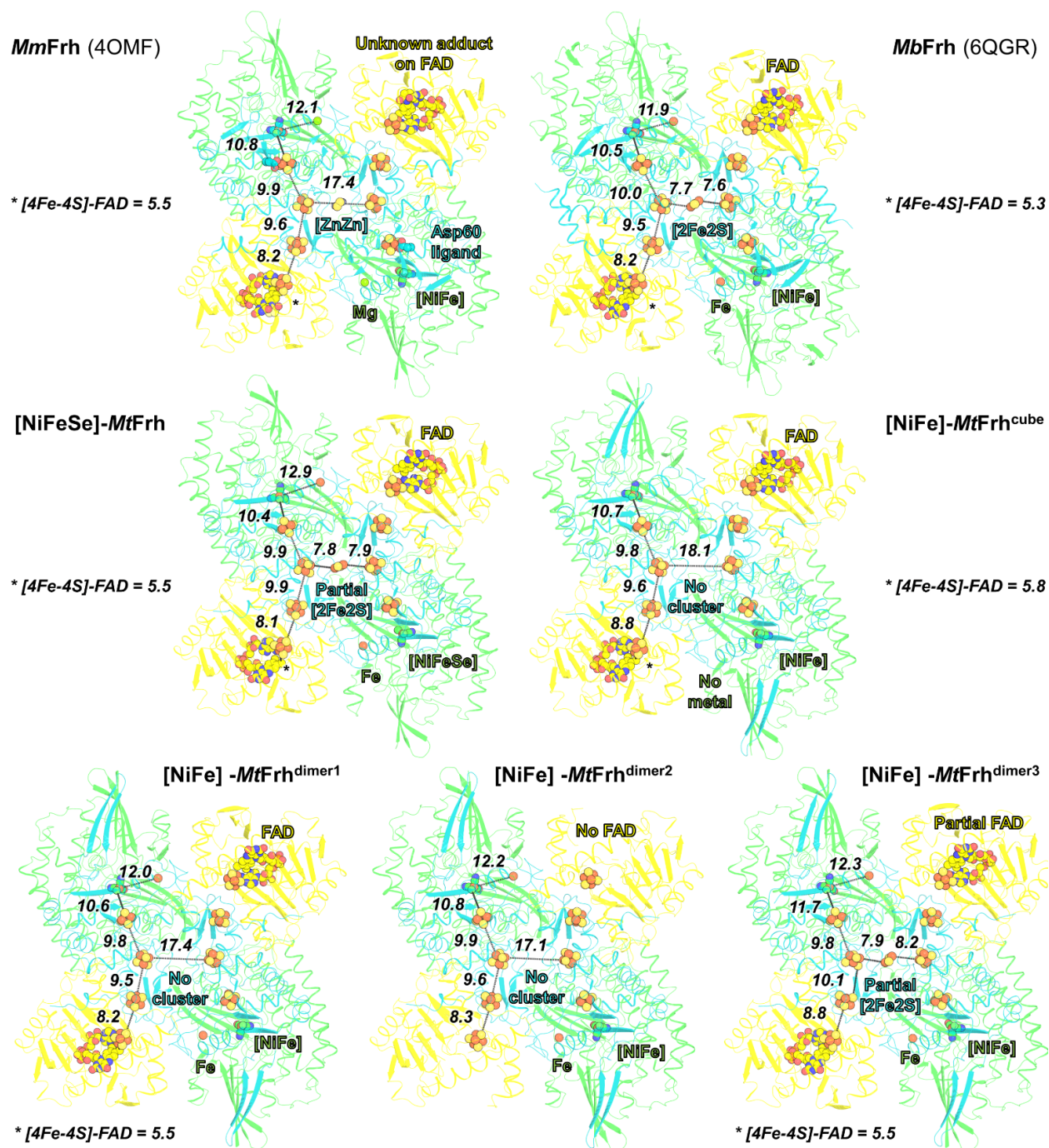


**Fig. S6.** Overall structural comparison between Frhs structures. The electron transfer path, highlighted by dashes with the distances in Å, is shown. The differences in metallocofactors/FAD/[FeS]-cluster ligand composition for each form are summarized directly in the figure. For instance, no electron density was detected for the [2Fe2S] cluster bridging both FrhABG [NiFe]-MtFrh<sup>cube</sup> and MtFrh<sup>dimer1-2</sup> and was therefore not modelled. For all models, FrhA, FrhG and FrhB are coloured in green, cyan and yellow, respectively. The metalloclusters, FAD, and Asp60 from MmFrh are represented in balls and sticks. The colour of the carbon atoms for the ligands is attributed to the subunits it belongs. Nitrogen, oxygen, sulfur, phosphorus and iron atoms are coloured blue, red, yellow, brown and orange, respectively.

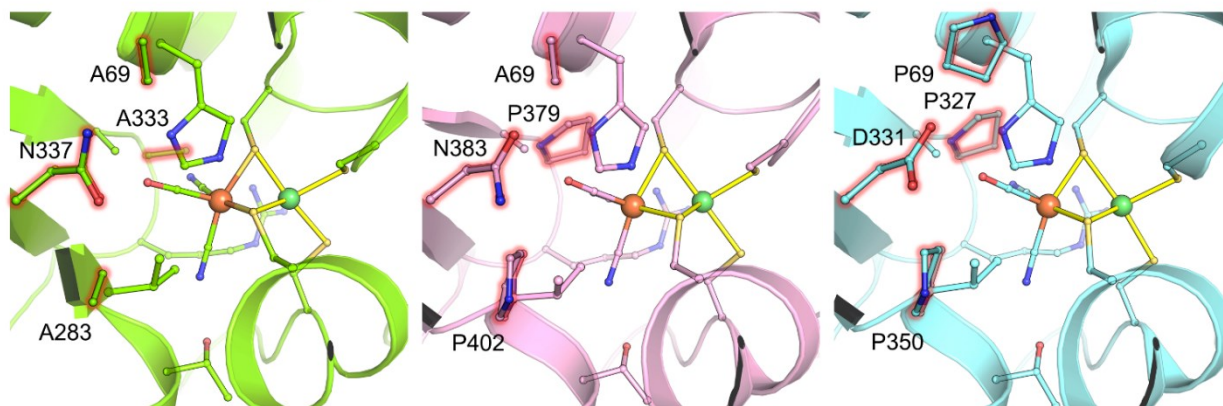


**Fig. S7. A:** Details of the first and second coordination shell in Frhs. The first coordination sphere of the [NiFe]-centre is perfectly conserved among structurally characterized Frhs, but differences can be seen in the second coordination sphere. The positions 283 and 379 (*Mt*Frh numbering) in the vicinity of the iron atom are occupied by prolines in *Mm*Frh and *Mb*Frh, being in *Mt*Frh replaced by alanines, a less rigid but more hydrophobic residue. The positions 69 and 337 are occupied by an alanine and an asparagine, respectively, as in *Mb*Frh but at the difference of *Mm*Frh (Figure S1).

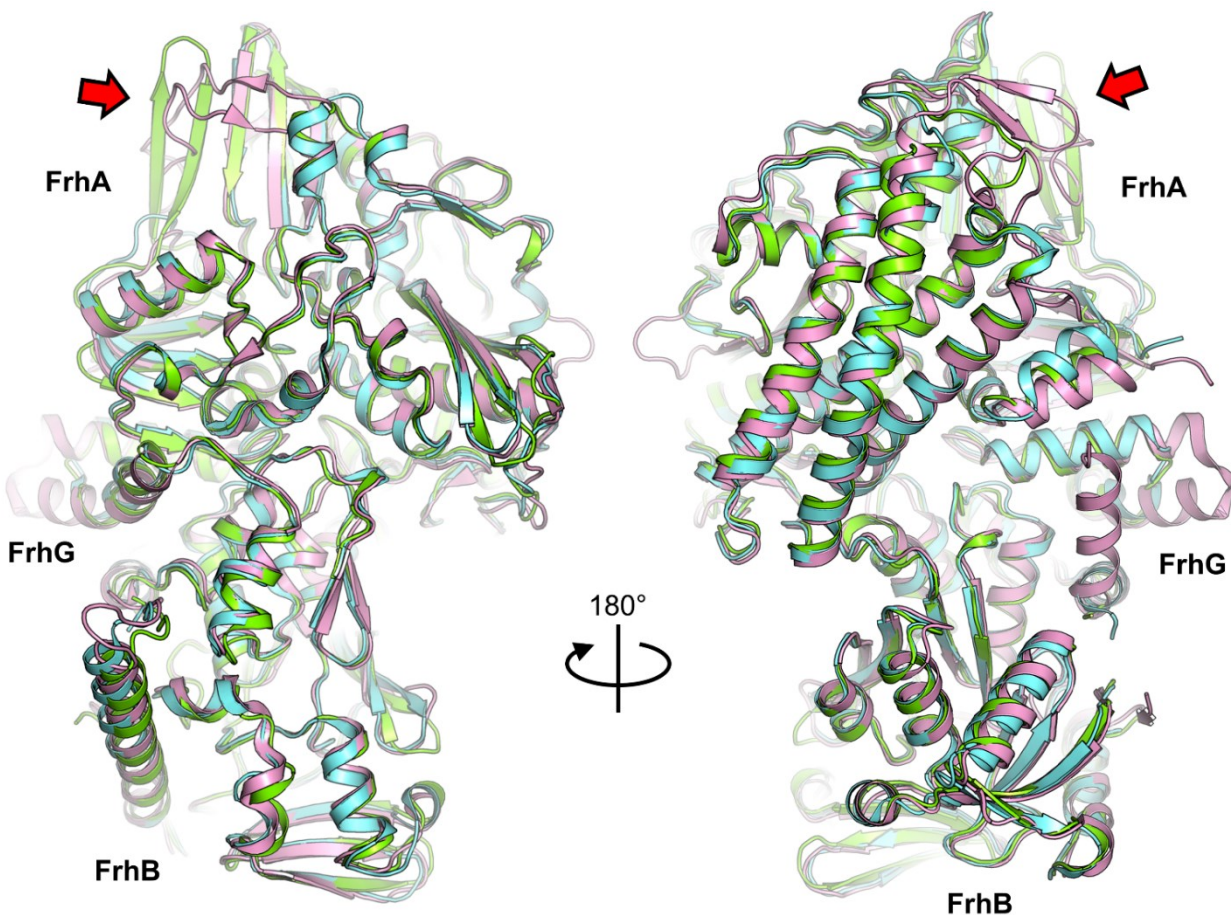


**Fig. S8.** Superposition of all characterized group 3 [NiFe] hydrogenases. The models are displayed in cartoon with [NiFe]-*MtFrh*<sup>dimer1</sup>, *MbFrh* (PDB 6QGR) and *MmFrh* (PDB 4OMF) coloured in green, pink and cyan, respectively. The extensions from [NiFe]-*MtFrhG* and *MbFrhA* gathering at a similar position are highlighted by red arrows. The superposition of [NiFe]-*MtFrh* dimer with one dimeric unit of the dodecamer shows only minor deviations (rmsd of 0.65 Å for 1475-C $\alpha$  aligned).

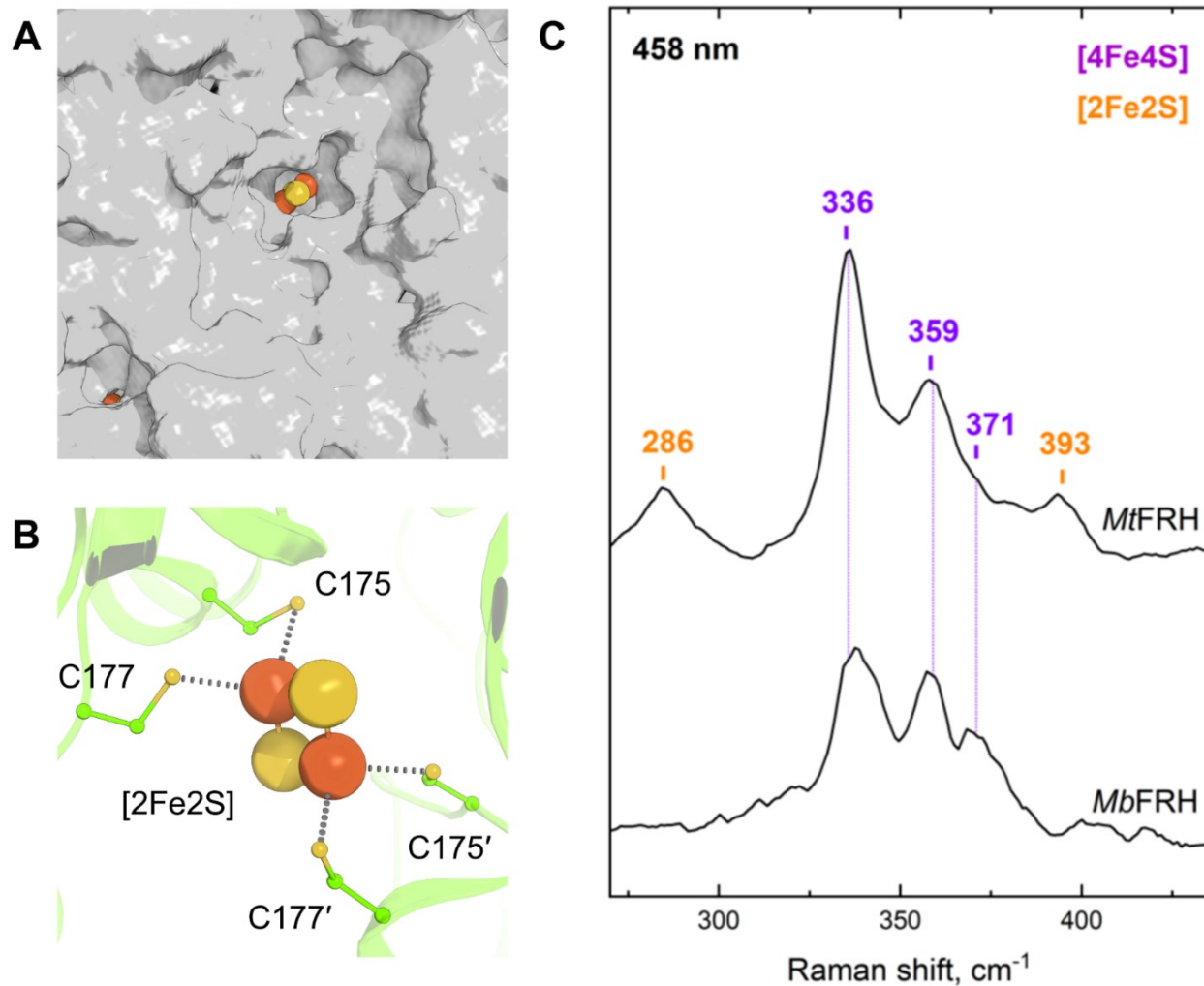


**Fig S9.** Coordination and redox state of the [2Fe2S]-cluster at the dimeric interface of [NiFe]-*MtFrh*<sup>dimer3</sup>. A) The [2Fe2S]-cluster is directly exposed to the solvent, as shown by the protein's surface coloured in grey. B) Two cysteines from each FrhG protomer coordinate the [2Fe-2S]. The two cysteines of the dimeric partner are labelled with a prime ('). C) Resonance Raman spectra from Frh crystals to determine the redox states of the [4Fe4S] and [2Fe2S] cluster in *MtFrh* in comparison to *MbFrh*.<sup>[3]</sup> Spectral contributions from the FeS clusters are more intense/pronounced and exhibit also some other features than in *MtFrh*, suggesting a larger amount of oxidized species. In line with this, the additional bands at 286 and 393 cm<sup>-1</sup> can be assigned to the oxidized form of the [2Fe2S] cluster. The [2Fe2S]-centre has been proposed to enable the distribution of electrons among individual protomers of the dodecameric enzyme, which was corroborated by EPR experiments on *MbFrh*.<sup>[3]</sup> Indeed, the [2Fe2S] cluster connects the two electron transfer chains in a dimer, which would otherwise be separated by at least 17 Å, thereby likely allowing cooperativity in the complexes.



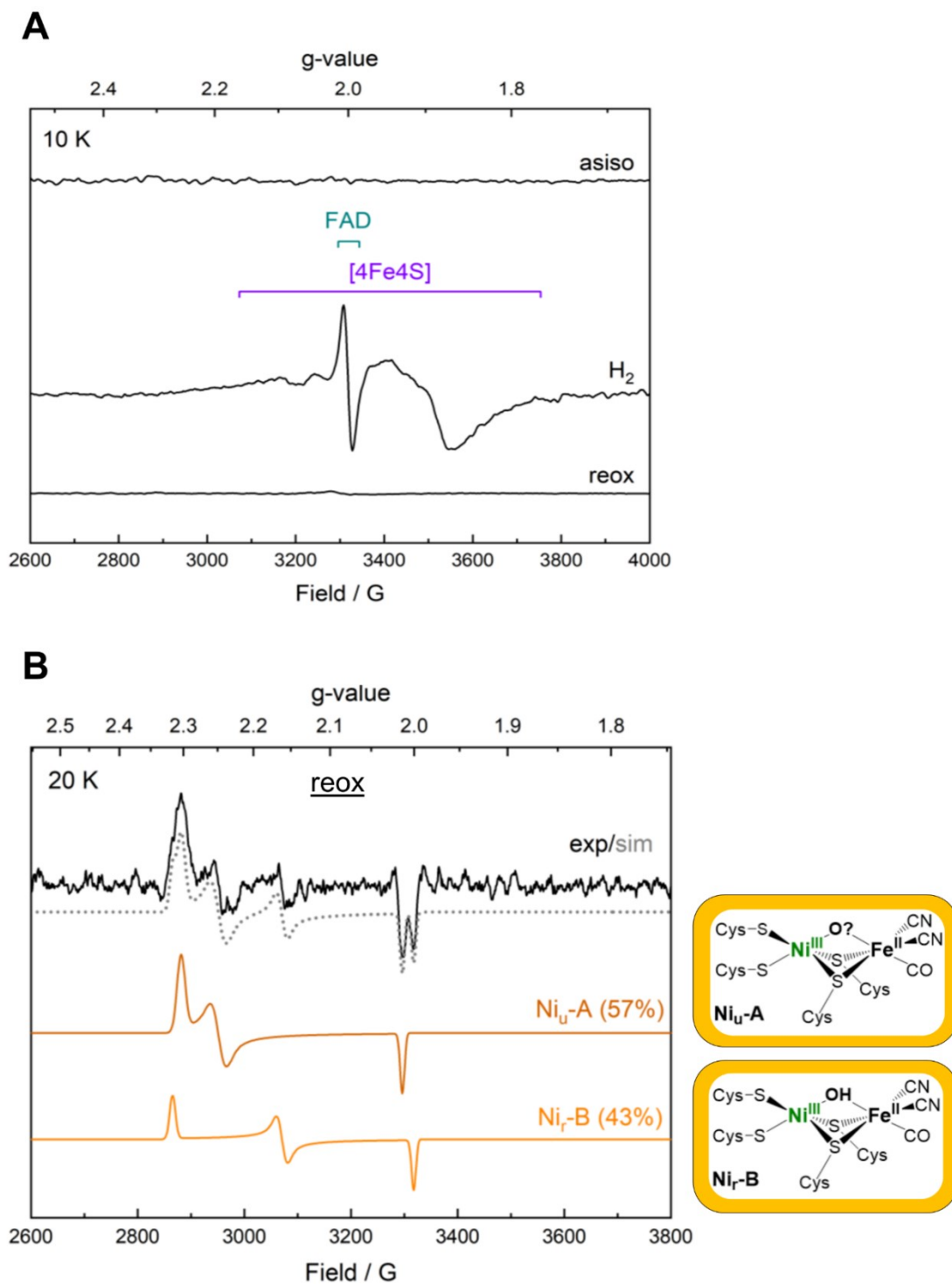


**Fig. S10.** A) At 10 K the as isolated sample remains EPR silent indicating a fully oxidized iron-sulfur cluster chain and FAD. After exposure to H<sub>2</sub> distinct signals related to [4Fe4S] cluster and a semiquinone radical can be observed. This verifies, that the enzymes can be reduced by H<sub>2</sub>, without the need of the other substrate F<sub>420</sub>. B) EPR spectroscopy indicates a partial oxidized state in solution. At 20 K the typical rhombic signature of the Ni<sub>u</sub>-A and the Ni<sub>r</sub>-B state could be deconvoluted in the reoxidized sample by simulations.

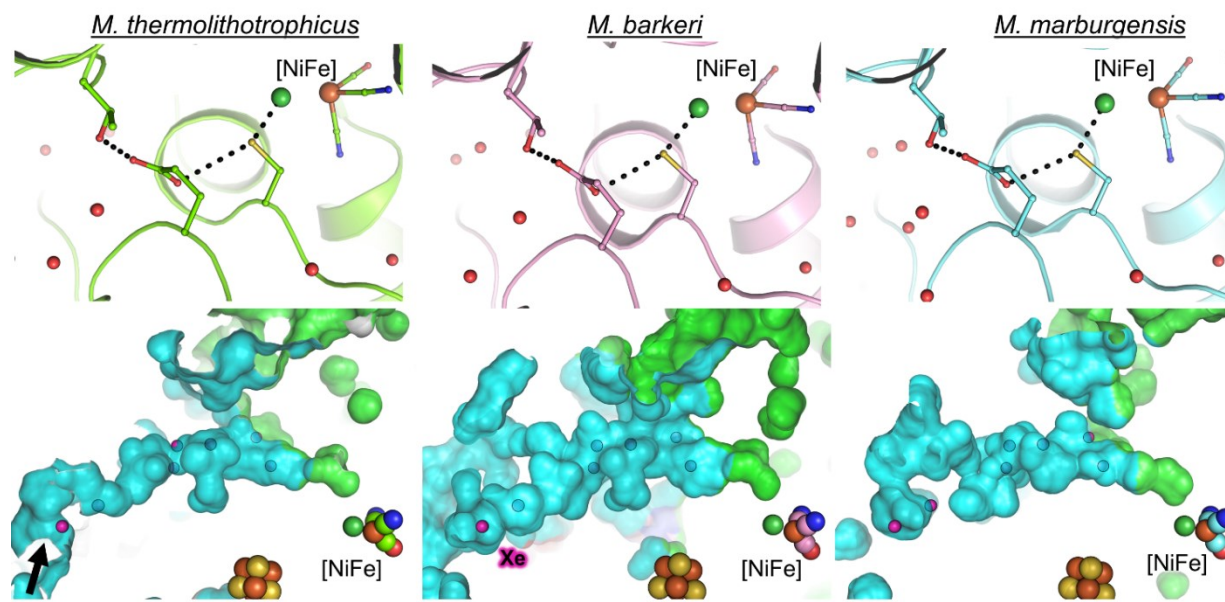


**Fig. S11.** Proposed proton transfer (upper row) and gas channels (lower row) in the structurally characterized group 3 [NiFe]-hydrogenases. Upper row: Shown is the proposed proton transfer according to Tai et al. 2019.<sup>[13]</sup> *MtFrh* is shown in green cartoon, *MbFrh* in violet (PDB 6QGR) and *MmFrh* in cyan (PDB 4OMF). The cysteine and glutamate that are proposed to contribute to the proton transfer to the [NiFe]-centre are shown in sticks, water molecules are represented as red spheres and the metals of [NiFe]-centre are shown in spheres with its ligands shown as sticks. Lower row: Shown are the proposed gas channels based on the channel identified via xenon derivatization experiments in *MbFrh*<sup>[14]</sup>. The pink spheres correspond to xenon atoms, which were superposed to the *MtFrh*<sup>dimer1</sup> and *MmFrh* structures to predict their hydrophobic gas channels. Cofactors are shown in spheres and the atoms carbon, nitrogen, oxygen, sulfur, phosphorus and iron atoms are colored as green/violet/cyan, blue, red, yellow, brown and orange, respectively.

## References for Supplementary Information

- [1] B. Mukhopadhyay, E. F. Johnson, R. S. Wolfe, *Appl Environ Microbiol* **1999**, *65*, 5059-5065.
- [2] T. Wagner, J. Koch, U. Ermler, S. Shima, **2017**, *357*, 699-703.
- [3] M. Jespersen, T. Wagner, *Nature Microbiology* **2023**.
- [4] M. Jespersen, A. J. Pierik, T. Wagner, *Nature Chemical Biology* **2023**.
- [5] C. Vonnrhein, C. Flensburg, P. Keller, A. Sharff, O. Smart, W. Paciorek, T. Womack, G. Bricogne, *Acta Crystallographica Section D* **2011**, *67*, 293-302.
- [6] P. Emsley, B. Lohkamp, W. G. Scott, K. Cowtan, *Acta Crystallogr D Biol Crystallogr* **2010**, *66*, 486-501.
- [7] D. Liebschner, P. V. Afonine, M. L. Baker, G. Bunkoczi, V. B. Chen, T. I. Croll, B. Hintze, L. W. Hung, S. Jain, A. J. McCoy, N. W. Moriarty, R. D. Oeffner, B. K. Poon, M. G. Prisant, R. J. Read, J. S. Richardson, D. C. Richardson, M. D. Sammito, O. V. Sobolev, D. H. Stockwell, T. C. Terwilliger, A. G. Urzhumtsev, L. L. Videau, C. J. Williams, P. D. Adams, *Acta Crystallogr D Struct Biol* **2019**, *75*, 861-877.
- [8] G. Bricogne, E. Blanc, M. Brandl, C. Flensburg, P. Keller, W. Paciorek, P. Roversi, A. Sharff, O. Smart, C. Vonnrhein, *Global Phasing Ltd, Cambridge, UK* **2017**.
- [9] O. N. Lemaire, T. Wagner, *Biochimica et Biophysica Acta (BBA) - Bioenergetics* **2021**, *1862*, 148330.
- [10] X. Robert, P. Gouet, *Nucleic Acids Res* **2014**, *42*, W320-W324.
- [11] R. C. Edgar, *BMC Bioinformatics* **2004**, *5*, 113.
- [12] F. Sievers, A. Wilm, D. Dineen, T. J. Gibson, K. Karplus, W. Li, R. Lopez, H. McWilliam, M. Remmert, J. Söding, J. D. Thompson, D. G. Higgins, **2011**, *7*, 539.
- [13] H. Tai, K. Nishikawa, Y. Higuchi, Z. W. Mao, S. Hirota, *Angewandte Chemie (International ed. in English)* **2019**, *58*, 13285-13290.

- [14] Y. Ilina, C. Lorent, S. Katz, J.-H. Jeoung, S. Shima, M. Horch, I. Zebger, H. Dobbek, **2019**, 58, 18710-18714.

## Chapter IV

### Structures of the sulfite detoxifying F<sub>420</sub>-dependent enzyme from *Methanococcales*

**Marion Jespersen<sup>1</sup>, Antonio J. Pierik<sup>2</sup> and Tristan Wagner<sup>1</sup> \***

<sup>1</sup> Max Planck Institute for Marine Microbiology, Celsiusstraße 1, 28359 Bremen, Germany.

<sup>2</sup> Biochemistry, Faculty of Chemistry, University of Kaiserslautern, Erwin-Schrödinger-Straße 54, 67663, Kaiserslautern, Germany

*Nature Chemical Biology*

Received 08 June 2022; accepted 22 November 2022

Published online 19 January 2023

Correspondence to Tristan Wagner (twagner@mpi-bremen.de)

The pdf-document of this publication is not displayed due to copyright reasons. This chapter displays the accepted manuscript. The publication can be accessed at:

<https://www.nature.com/articles/s41589-022-01232-y>

DOI: 10.1038/s41589-022-01232-y

## Abstract

Methanogenic archaea are main actors in the carbon cycle but are sensitive to reactive sulfite. Some methanogens use a sulfite detoxification system that combines an  $F_{420}H_2$ -oxidase with a sulfite reductase, both of which are proposed precursors of modern enzymes. Here, we present snapshots of this coupled system, named coenzyme  $F_{420}$ -dependent sulfite reductase (Group I Fsr), obtained from two marine methanogens. Fsr organizes as a homotetramer, harboring an intertwined six-[4Fe-4S] cluster relay characterized by spectroscopy. The wire, spanning 5.4 nm, electronically connects the flavin to the siroheme center. Despite a structural architecture similar to dissimilatory sulfite reductases, Fsr shows a siroheme coordination and a reaction mechanism identical to assimilatory sulfite reductases. Accordingly, the reaction of Fsr is unidirectional, reducing sulfite or nitrite with  $F_{420}H_2$ . Our results provide structural insights into this unique fusion, in which a primitive sulfite reductase turns a poison into an elementary block of Life.

## Main text

When cold seawater permeates through sediments or enters hydrothermal vent walls, a partial oxidation of sulfide ( $\text{HS}^-$ ,  $\text{S}^{2-}$ ) results in the formation of (bi)sulfite ( $\text{HSO}_3^-$ ),  $\text{SO}_3^{2-}$ , a highly reactive intermediate of the sulfur cycle<sup>1</sup>. Methanogenic archaea are extremely sensitive to this strong nucleophile, which results in the collapse of methanogenesis, their central energy metabolism<sup>2</sup>. Despite its toxic effects, many hydrogenotrophic methanogens thrive in environments where they are exposed to fluctuating  $\text{SO}_3^{2-}$  concentrations, especially methanogens living in proximity to hydrothermal vents or in geothermally heated sea sediments<sup>3-6</sup>.

When exposed to  $\text{SO}_3^{2-}$ , the hyperthermophile *Methanocaldococcus jannaschii*<sup>3</sup> expresses high amounts of the Group I coenzyme  $\text{F}_{420}$ -dependent sulfite reductase (referred to as *MjFsr*), which confers not only protection, but also the ability to grow on  $\text{SO}_3^{2-}$  as sole sulfur source (for example, in the absence of  $\text{S}^{2-}$ )<sup>5,7</sup>. Because of this trait, the *fsr* gene has been used as a genetic marker<sup>7,8</sup>.

Fsr is composed of an N-terminal half belonging to the  $\text{F}_{420}$ -reducing hydrogenase  $\beta$ -subunit family (FrhB; Supplementary Fig. 1) and a C-terminal half made of a single sulfite/nitrite reductase repeat<sup>5,9</sup> (S/NiRR, from here on referred to as sulfite reductase domain). All known sulfite reductases reduce  $\text{SO}_3^{2-}$  using a magnetically coupled siroheme–cysteine–[4Fe–4S] center<sup>10</sup>. This metallocofactor is also used by nitrite reductases to reduce nitrite ( $\text{NO}^{2-}$ ), a side reaction observed in many sulfite reductases<sup>11</sup>.

Until now, several groups of sulfite reductases have been identified, which are, depending on their biological function, spectroscopic properties and molecular composition, generally classified into assimilatory or dissimilatory ones, in addition to two biochemically uncharacterized predicted sulfite reductases (Supplementary Fig. 1)<sup>6,11,12</sup>. The only structural data obtained so far are from aSirs (assimilatory) and dSirs (dissimilatory, here, dSirs refer to DsrAB), and therefore this study will use them for comparison. While aSirs are monomeric enzymes that directly reduce  $\text{SO}_3^{2-}$  to  $\text{S}^{2-}$  for assimilation, dissimilatory enzymes are organized by the heterodimers DsrA/DsrB, in which DsrA harbors an inactive catalytic site (referred to as structural; Extended Data Fig. 1)<sup>11-14</sup>. Under physiological conditions, dSirs catalyze the first two-electron reduction step and transfer the sulfur species intermediate to the sulfur-carrier protein DsrC used for energy conservation (Extended Data Fig. 1)<sup>15</sup>. In the absence of DsrC,

DsrAB releases some  $S^{2-}$ , as well as the reaction intermediates trithionate and thiosulfate<sup>15–17</sup>. Structural and evolutionary studies suggest that aSirs and dSirs originated from a common progenitor<sup>12,14</sup>, a primitive Sir that contained a catalytic siroheme–[4Fe–4S] and was operating by itself. The gene encoding this ancestral enzyme was duplicated, and in the dSir case, the duplicated version evolved into DsrB, while DsrA was retained for structural function. In the case of aSir, the original and duplicated genes fused and only one active siroheme–[4Fe–4S] was retained. On the basis of sequence and phylogenetic analyses, it has been suggested that *fsr* evolved before the duplication event and therefore represents a primordial sulfite reductase<sup>5,18,19</sup>. Alternatively, *fsr* could have arisen through lateral gene transfer followed by gene fusion events. Besides its evolutionary importance, the electron-donor module of Fsr, the  $F_{420}H_2$ -oxidase, is directly fused to its sulfite reductase domain. This fusion allows the enzyme to perform the entire six-electron reduction of  $SO_3^{2-}$  on its own via an unknown electronic relay, using electrons from reduced  $F_{420}$ . The coenzyme  $F_{420}$  is a deazaflavin derivative present at high cytoplasmic concentrations in methanogens<sup>5,20–22</sup> and can be reduced by the  $F_{420}$ -reducing hydrogenase (FrhABG; Supplementary Fig. 1). Due to the difference in the redox potentials of the  $F_{420}/F_{420}H_2$  ( $\Delta E^{0'} = -350$  mV) and  $HSO_3^-/HS^-$  ( $\Delta E^{0'} = -116$  mV) couples, the overall reaction is extremely exergonic ( $\Delta G^{0'} = -135$  kJ mol<sup>-1</sup> per converted  $SO_3^{2-}$ ) and promotes  $SO_3^{2-}$  detoxification at very high rates<sup>5</sup>. Because of this efficiency and its temperature stability, Fsr is an attractive catalyst for chemists.

Here, we present the X-ray crystal structures of Fsr isolated from two *Methanococcales* as well as the electron paramagnetic resonance (EPR) spectroscopy characterization of its metallocofactors, providing the first snapshots and molecular insights, to our knowledge, into this prototypical sulfite reductase.

### **Identification of Fsr in *Methanothermococcus thermolithotrophicus***

*MjFsr*, previously characterized<sup>5,7,19</sup>, turned out to be less suitable for our structural studies due to crystallization defects (see below). Therefore, we took an alternative organism belonging to the same order (*Methanococcales*). *Methanothermococcus thermolithotrophicus* is a fast-growing thermophile isolated from geothermally heated marine sediments that has already demonstrated its advantages for structural biology<sup>23</sup>. It was previously shown that this archaeon can grow on 1 mM  $SO_3^{2-}$  as a sole



sulfur source<sup>4</sup>. The participation of Fsr in this process has not yet been investigated and the *fsr* gene appeared to be absent in the 55 contigs of the deposited shotgun genome (assembly number ASM37696v1, Bioproject: PRJNA182394). After adaptation, we confirmed that *M. thermolithotrophicus* could grow on  $\text{SO}_3^{2-}$ , even at concentrations up to 40 mM (Extended Data Fig. 2a). When cell extracts of both organisms were passed on native PAGE, a distinct band at  $\approx 300$  kDa was observed for the cultures grown on  $\text{SO}_3^{2-}$  (Extended Data Fig. 2b,c). Based on the band intensity, which is comparable to that of the methyl coenzyme M reductase (MCR, the main catabolic enzyme and one of the highest expressed in the cell), as in *M. jannaschii*<sup>5</sup>, we concluded that Fsr is present in *M. thermolithotrophicus*.

The closed circular genomic sequence of strain DSM 2095 was obtained and contains two entire *fsr* genes, one of which shares 80.4% sequence identity, and a second isoform that shares 75.6% sequence identity with *MjFsr* (Supplementary Fig. 2). The purified Fsr in this study has the closest sequence identity (80.4%) to *MjFsr*, as confirmed by mass spectrometry.

Fsr from both organisms was purified natively under anaerobic atmosphere and yellow light (Extended Data Fig. 2d,e). SDS–PAGE profiles and sulfite reductase activity assays were used to follow the enzyme during the purification. *MtFsr* exhibits the typical absorbance of [4Fe–4S] clusters and siroheme–[4Fe–4S]-containing proteins, as shown for *MjFsr* (Extended Data Fig. 2f)<sup>5,24</sup>. Based on the native PAGE and gel filtration profiles, *MtFsr* is organized as a homotetramer in solution (Extended Data Fig. 2c,g), similar to *MjFsr*<sup>5</sup>.

### **The F<sub>420</sub>H<sub>2</sub>-oxidase domain flanks a sulfite reductase core**

A single-wavelength anomalous dispersion experiment was performed to solve the *MjFsr* crystal structure. *MtFsr* was solved by molecular replacement, using *MjFsr* as a template. The crystal structures of both Fsr superpose well (Extended Data Fig. 3a) and were refined to 2.30 Å for *MjFsr* and 1.55 Å for *MtFsr* (Fig. 1 and Extended Data Table 1). Since *MjFsr* has pseudo-merohedral twinning and a lower resolution compared to *MtFsr*, the latter was used for the in-depth structural and biochemical analysis.

As shown in Fig. 1, Fsr is organized as follows: the N-terminal ferredoxin domain (*MtFsr* residues 1–57 containing two [4Fe–4S] clusters) is linked to the F<sub>420</sub>H<sub>2</sub>-oxidase domain (*MtFsr* residues 58–

336, harboring the flavin and one [4Fe–4S] cluster), which is connected to the C-terminal sulfite reductase domain (*MtFsr* residues 339–484, 546–618) that binds the siroheme–[4Fe–4S] and has an inserted ferredoxin domain (*MtFsr* residues 485–545, containing two [4Fe–4S] clusters). The tetrameric structure of the protein is established by a dimer of two homodimers over a large contact area through the two additional ferredoxin domains and the C-terminal part of the sulfite reductase domain (562–618 in *MtFsr*, 562–620 in *MjFsr*; Extended Data Fig. 3b). The homotetramer has the overall shape of a butterfly, composed of a sulfite reductase core flanked by the F<sub>420</sub>H<sub>2</sub>-oxidase domain. Notably, the asymmetric unit of *MtFsr* contains four tetramers (including 96 [4Fe–4S] clusters), providing insights on its natural flexibility (Extended Data Fig. 4a–c).

The F<sub>420</sub>H<sub>2</sub>-oxidase domain of Fsr is almost identical between *MjFsr* and *MtFsr* (root mean square deviation (r.m.s.d.) = 0.33 Å for 277-C $\alpha$  aligned) and superposes well with FrhB from *Methanothermobacter marburgensis* (PDB 4OMF (ref. 25), with a r.m.s.d. = 0.92 Å for 179-C $\alpha$  aligned) and *Methanosarcina barkeri* (PDB 6QGR (ref. 26), with a r.m.s.d. = 0.98 Å for 179-C $\alpha$  aligned; Fig. 2a). The overall fold is perfectly conserved between the F<sub>420</sub>H<sub>2</sub>-oxidase domain of Fsr and FrhB, except for the helix  $\alpha$ 1 of FrhB, which became a loop in Fsr. The active site of the F<sub>420</sub>H<sub>2</sub>-oxidase domain of Fsr contains a flavin adenine dinucleotide (FAD; Supplementary Fig. 3), which is similarly bound in Fsr and FrhB (Supplementary Fig. 4). No electron density could be found despite cocrystallization with F<sub>420</sub>H<sub>2</sub> (see Methods). Nevertheless, the reduced F<sub>420</sub>-binding site is presumably located in a positively charged cleft that would complement the charges of the acidic gamma-carboxy groups (Supplementary Fig. 3c)<sup>25,26</sup>.

### **A [4Fe–4S] cluster relay connects both active sites**

The distance between the isoalloxazine ring from the FAD to the closest siroheme–[4Fe–4S] is approximately 40 Å. Electrons delivered by reduced F<sub>420</sub> must therefore travel through an electron-transfer relay of metallocofactors. The first part of this relay, located in the N-terminal ferredoxin and F<sub>420</sub>H<sub>2</sub>-oxidase domains, shares high structural homologies with FrhBG. Indeed, FrhG and the N-terminal ferredoxin domain of Fsr are located at the same position of the F<sub>420</sub>-oxidoreductase domain (Fig. 2b,c), resulting in a similar electron relay. This homology suggests a common origin that may have evolved by fusion (for Fsr) or by duplication and fusion (for FrhG).

As illustrated in Fig. 3, the overall electronic path consists of five [4Fe–4S] clusters connected by short edge-to-edge distances (<11.5 Å). Dimerization is critical because half of the relay is provided by the second protomer. An intraelectron transfer between both Fsr dimers is unlikely due to the long distance between the nearest clusters (that is, 18.9 and 19.5 Å).

The electrons on the isoalloxazine ring can be transferred directly to the [4Fe–4S] cluster 1, which is located in the F<sub>420</sub>H<sub>2</sub>-oxidase domain. From there they are passed on to the clusters 2 and 3 in the N-terminal ferredoxin domain. The extended loop 171–189 in Fsr serves as a platform to specifically bind both ferredoxin domains, and the Glu 180 coordinates the [4Fe–4S] cluster 3 (monodentate, 2.22 Å; Fig. 3, Extended Data Fig. 5 and Supplementary Fig. 5). The electrons continue to flow through the clusters 4' and 5' in the inserted ferredoxin domain and finally reach the siroheme–[4Fe–4S].

Sequence analyses indicated four [4Fe–4S] clusters and the one coupled to the siroheme<sup>5</sup>. But both Fsr structures revealed an additional cluster ([4Fe–4S] cluster 1), which has a noncanonical binding sequence (PCX<sub>40</sub>CX<sub>54</sub>CX<sub>2</sub>C). Strikingly, the four predicted clusters have completely different binding residues compared to primary structural analysis (Extended Data Fig. 5). Each [4Fe–4S] cluster has a divergent protein environment: cluster 1 is surrounded by basic residues; clusters 2 and 5 have a hydrophobic shell; clusters 4 and 6 are in a more polar environment; and cluster 3 has a glutamate ligand. These differences may reflect the need to establish a 'redox potential ladder' to allow a smooth one-way transfer of electrons. To investigate the electron-transfer path, electrochemical experiments followed by EPR spectroscopy were performed.

### **Redox properties of the metal cofactors**

EPR spectroscopy at 10 K (Extended Data Fig. 6a–d) revealed that in as-isolated *MtFsr* high-spin ( $S = 5/2$ ) and low-spin ( $S = 1/2$ ) signals typical for the siroheme in sulfite reductases<sup>27,28</sup> were absent, neglecting the sharp axial  $S = 5/2$  EPR signal around  $g = 6$ , which, quantified by double integration of its simulation spectrum ( $g = 6.22, 5.92$  and  $1.98$ ), is at most 3% of *MtFsr*. Apparently, on purification under strictly anaerobic conditions, the siroheme remains in its ferrous state. After methylene blue oxidation or on dye-mediated redox titration with  $E_{m,7.5} = -104$  mV (all potentials refer to potentials versus the H<sub>2</sub>/H<sup>+</sup> normal hydrogen electrode) an intense rhombic  $S = 5/2$  EPR signal with  $g = 6.7$  and

5.1 appeared (Fig. 4a,b). The spectrum could be simulated with three components: a main species with  $g = 6.70$  and  $5.10$  (78%), a less abundant species (19%) with  $g = 6.80$  and  $5.08$ , but narrower linewidth, and the sharp axial  $g = 6$  species already seen in as-isolated *MtFsr*. For both rhombic components  $g = 1.95$  was taken as the third  $g$  value, as the experimental spectrum contained a weak  $[3\text{Fe-4S}]^{1+}$  signal from limited  $[4\text{Fe-4S}]^{2+}$  breakdown upon oxidation. In sulfite reductase and other hemoproteins multiple high-spin species are common<sup>29</sup>. Addition of  $\text{SO}_3^{2-}$  to methylene blue-oxidized *MtFsr* led to disappearance of the siroheme ferric high-spin signals and formation of a weak low-spin EPR signal, of which only the highest  $g$  value (2.8) was detectable, as in other sulfite reductases<sup>30</sup>.

In an enzyme approaching the complexity of the complex I, it is not feasible to determine all individual redox potentials of its five regular  $[4\text{Fe-4S}]^{1+/2+}$  cubanes and the siroheme-bridged cubane. First, on the basis of distances in *Fsr*, extensive magnetic coupling<sup>31</sup> between neighboring cubanes is anticipated, blurring individual EPR features. Second, the coupling between the ferrous siroheme and its cysteine-bridged reduced cubane leads to complex mixtures of sharp  $g = 1.94$ , broader  $g = 2.29$  and very anisotropic  $S = 3/2$  mimicking signals<sup>32</sup>. Third, we had to avoid sodium dithionite inherently containing  $\text{SO}_3^{2-}$  and therefore used sodium borohydride-reduced  $\text{F}_{420}$ , while following the solution potential with mediators. One  $[4\text{Fe-4S}]^{1+/2+}$  cubane with simulated  $g$  values of 2.064, 1.927 and 1.85 was reduced at a relatively high potential and is also detected in as-isolated *Fsr* (Fig. 4a,c). From the amplitude of the second derivative of the experimental EPR spectrum at  $g = 2.064$ ,  $E_{m,7.5} = -275$  mV was estimated from fitting to the Nernst equation with  $n = 1$  (Fig. 4c). The signal ‘disappeared’ on further reduction with  $E_{m,7.5} = -350$  mV in a manner indicating cooperativity ( $n = 2$ ).

As super-reduction to  $[4\text{Fe-4S}]^0$  is unlikely ( $E_m = -790$  mV (ref. 33)), we interpret this phenomenon as reduction of two neighboring clusters of the  $g = 2.064$  cluster. This cluster thus is number 2, 3 or 4’ (the siroheme cubane typically has a very low potential<sup>27</sup>). In the absence of sufficiently differing EPR features below  $-350$  mV we double integrated the EPR spectra. On the basis of iron content divided by 24 (siroheme does not release Fe ions in acid) we quantified  $4.5 \pm 0.5$  spin/subunit at the lowest attainable potential ( $-526$  mV), which most likely corresponds to the five regular clusters. A fit for the spin integral as a function of the redox potential included the experimental  $E_{m,7.5} = -275$  mV and  $E_{m,7.5} = -350$  mV for both neighboring clusters. Avoiding

overfitting, we could satisfactorily reproduce the data for five redox transitions with three midpoint potentials: one at  $E_{m,7.5} = -275$  mV (experimental), one at a low potential to represent the lowest potential region ( $E_{m,7.5} = -435$  mV) and three times  $E_{m,7.5} = -350$  mV for the other three clusters (which includes the two clusters leading to broadening of the  $g = 2.064$  signal). In the low-field region, a species with unusual  $g$  values was detected (simulated  $g$  values 5.05, 3.05 and 1.96) at very low potential (Fig. 4d). It was accompanied in some samples by an isotropic  $g = 4.3$  signal. But, since the integrated intensity was maximally 5% of the  $g = 5.05$  species and non-Nernstian behavior was seen, it was not considered physiologically relevant. It has previously been shown that such a  $g = 5.05$  species is not from a  $S = 3/2$  system but from transitions of the siroheme- $\text{Fe}^{2+}$  exchange coupled to  $[4\text{Fe}-4\text{S}]^{1+}$  ( $J/D \approx -0.2$  and  $E/D \approx 0.11$ , in which  $J$ ,  $D$  and  $E$  are the effective Heisenberg exchange coupling parameter and the spin Hamiltonian zero-field splitting parameters of the spin quintet, respectively; Extended Data Fig. 6c)<sup>32</sup>. In full agreement with findings on the *Escherichia coli* assimilatory reductase<sup>27</sup> a very low potential ( $E_{m,7.5} = -445$  mV) was estimated.

### A prototypical sulfite reductase

The C-terminal domain of Fsr represents the simplest sulfite reductase crystallized so far. While Fsr shares the common fold of sulfite reductases (Extended Data Fig. 7a and Supplementary Fig. 6)<sup>9,13,14</sup>, it lacks the large N- and C-terminal extensions found in aSirs and dSirs, which presumably serve to strengthen dimerization and to interact with partners<sup>34</sup> (Fig. 5a–c). Without these extensions, Fsr is much more compact - possibly a thermophilic trait. Each Fsr protomer contains one functional siroheme center. In comparison, dSirs harbor one functional and one structural siroheme center in each DsrAB heterodimer, while aSirs have lost one siroheme-[4Fe-4S] site (Extended Data Fig. 7b–d). Although Fsr is phylogenetically more distant from aSirs than from dSirs, it superposes well with the first and second halves of aSirs (Supplementary Figs. 6–10). The position of the C terminus of Fsr coincides with the beginning of the linker connecting the two half domains in aSirs (Extended Data Fig. 7a,b and Supplementary Figs. 7 and 8). This detail corroborates the theory that modern aSirs evolved by duplication and fusion events. The inserted ferredoxin domain in Fsr is at the same position as the ferredoxin domain in DsrA or DsrB (Extended Data Fig. 7a,c,d and Supplementary Figs. 9 and 10). There is a remarkable three-dimensional conservation of the electron connectors between Fsr, DsrA, DsrB and even the aSir

from *Zea mays*, where the external [2Fe–2S] ferredoxin sits on the core of the sulfite reductase<sup>35</sup> (Fig. 5a–c). Such a conserved position suggests a common origin, but could also be due to the restricted access of the [4Fe–4S]–siroheme and the selection pressure towards an optimized distance for electron transfer.

### **Fsr has traits of assimilatory sulfite reductases**

While the sirohemes of DsrAB are partially surface exposed to interact with DsrC (Extended Data Fig. 1)<sup>13</sup>, the Fsr sirohemes are buried but still accessible via a positively charged solvent channel (Extended Data Fig. 8). As in DsrAB, the two sirohemes within one Fsr dimer are in close proximity (9.4 Å; Supplementary Fig. 11)<sup>14</sup>.

The binding of the siroheme in *MjFsr* and *MtFsr* is highly conserved. It is mainly anchored by positively charged residues from one protomer, while the dimeric partner binds the adjacent [4Fe–4S] cluster establishing the siroheme–[4Fe–4S] center, as reported for other sulfite reductases<sup>14</sup>. On the basis of the observed electron density, we tentatively modeled a  $\text{SO}_3^{2-}$  bound to the siroheme iron (2.3 Å; Extended Data Fig. 8b) in *MjFsr*. In *MtFsr*, the axial ligand is a single atomic species at all sites of the asymmetric unit, which is in proximity but not covalently bound to the iron (2.9 Å; Extended Data Fig. 8c). The anion  $\text{HS}^-$  was modeled in the electron density based on the pH 5.5 in the crystallization solution. This species could be the result of cocrystallizing Fsr with reduced  $\text{F}_{420}$ , which might have forced the complete reduction of bound  $\text{SO}_3^{2-}$ .

In *MjFsr*, four positively charged residues (Arg 355, Arg 423, Lys 460 and Lys 462), which are perfectly conserved across sulfite reductases (Fig. 5d,e and Supplementary Figs. 7 and 9), bind the  $\text{SO}_3^{2-}$  and two water molecules. In *MtFsr*, the modeled  $\text{HS}^-$  is bound by Arg 423, Lys 460 and Lys 462, and one water molecule is stabilized by Arg 355 (Fig. 5f). Group II Fsr found in the genome of anaerobic methanotrophic archaea<sup>6</sup> (except for '*Candidatus Methanoperedens nitroreducens*') and *Methanosarcinales*, should have a larger binding pocket and two arginines of Group I Fsr are replaced by a lysine and glycine. This suggests that the functionally uncharacterized Group II Fsr has a different substrate specificity<sup>6,17</sup>. Interestingly, the second isoform found in *M. thermolithotrophicus* harbors one arginine but exchanged the other one for a threonine (Thr 438; Supplementary Fig. 2), indicating an alternative physiological function.

The active site of Fsr shows the same traits as an assimilatory sulfite reductase: an arginine at position 388, and the coordination of the siroheme-coupled [4Fe–4S] cluster by the canonical motif (CX<sub>5</sub>CX<sub>n</sub>CX<sub>3</sub>C; Fig. 5d,f). In comparison, DsrAs contain a conserved threonine where aSirs have arginine ( $\alpha$ Thr 136 in *Desulfovibrio vulgaris* and  $\alpha$ Thr 133 in *Archaeoglobus fulgidus*) and the catalytically active [4Fe–4S] cluster coupled to the siroheme of DsrB is coordinated by the canonical motif CX<sub>n</sub>CCX<sub>3</sub>C (Fig. 5e). Fsr must therefore follow the same catalytic path as aSirs; the six-electron reduction of SO<sub>3</sub><sup>2-</sup> to S<sup>2-</sup> should be unidirectional, without the formation or consumption of intermediates (for example, thiosulfate or trithionate). *MtFsr* did not accept thiosulfate as an electron acceptor, which is in agreement with the findings for *MjFsr*<sup>5</sup>. We also monitored F<sub>420</sub>-reduction by *MtFsr* with S<sup>2-</sup> as substrate (up to 10 mM) and observed no reaction. The addition of 10 mM S<sup>2-</sup> to 1.4 mM of Na<sub>2</sub>SO<sub>3</sub> also had no effect on the F<sub>420</sub>H<sub>2</sub> oxidation rate. Taken together, these results support that Fsr indeed acts like an aSir.

On the basis of its equal  $V_{\max}$  but six-fold lower  $K_m$  value (Table 1), *MtFsr* prefers NO<sub>2</sub><sup>-</sup> over SO<sub>3</sub><sup>2-</sup>, a property that may expand its role from sulfite detoxification to ammonium production, as *M. thermolithotrophicus* has been reported to grow on nitrate as a sole source of nitrogen<sup>36</sup>. If the archaeon uses a nitrate reductase, NO<sub>2</sub><sup>-</sup> would accumulate and Fsr would be a suitable candidate for NO<sub>2</sub><sup>-</sup> conversion. In addition, we have shown that *MtFsr* reduces selenite (SeO<sub>3</sub><sup>2-</sup>) in vitro with a relative activity of 20.7 ± 7.5% compared to SO<sub>3</sub><sup>2-</sup> (see Methods). These promiscuous activities could expand the physiological range of the enzyme, but also its biotechnological applications.

## Discussion

Some methanogens show a remarkable tolerance to SO<sub>3</sub><sup>2-</sup>, one of the sulfur-reactive species that can cause oxidative damage to the methanogenic machinery. Besides the possibility that those methanogens can keep low intracellular SO<sub>3</sub><sup>2-</sup> concentrations through pumping mechanisms, the cytoplasmic Group I Fsr is used as a first line of defense to convert toxic SO<sub>3</sub><sup>2-</sup> into HS<sup>-</sup>, which can then be used for sulfur assimilation. The efficient SO<sub>3</sub><sup>2-</sup> detoxification strategy of *Methanococcales* relies on the enormous amount of expressed Fsr, which constitutes 5–10% of the cellular protein (Extended Data Fig. 2b,c and Methods), but also on the use of abundant F<sub>420</sub>H<sub>2</sub>, which can be rapidly regenerated via H<sub>2</sub> oxidation by Frh<sup>22</sup>.

Fsr discloses a ‘cofactor swapping’ between two subunits forming a homodimer in a head-to-tail configuration, which dimerizes with a second homodimer, creating a butterfly-shaped tetramer. As a result, the centrally located sulfite reductase domains are surrounded by F<sub>420</sub>H<sub>2</sub>-oxidase domains. These shuttle electrons via three [4Fe–4S] cluster from one subunit to the other two [4Fe–4S] cluster and the siroheme–cysteine–[4Fe–4S] cofactor of the other subunit within the functional dimer. In contrast to the bidirectional hydrogenase Frh, which maintains an isopotential of  $E'^0 \approx -400$  mV (ref. 25), the different metalloclusters of Fsr must establish a downhill redox potential from the FAD to the siroheme–[4Fe–4S]. Our electrochemical and spectroscopic studies indicate that the electrons carried by F<sub>420</sub>H<sub>2</sub> are immediately transferred to the siroheme–[4Fe–4S] (Fig. 4a,b and Extended Data Fig. 6a). The metallocofactors should ensure efficient electron transfer rather than serving as a transient storage, and a cascade of redox potential from -380 mV (F<sub>420</sub>/F<sub>420</sub>H<sub>2</sub> redox potential under certain physiological conditions<sup>22</sup>) to -116 mV ( $E'^0$  of HSO<sub>3</sub><sup>-</sup>/HS<sup>-</sup>) is expected.

Once reduced, the siroheme–[4Fe–4S] could transfer the electrons to the sulfur species covalently bound to its Fe. dSirs physiologically perform a two-electron reduction to allow the transfer of the sulfur intermediate to DsrC. In contrast, aSirs and Fsr perform a three times two-electron reduction to release HS<sup>-</sup>. A positively charged environment around the active site attracts SO<sub>3</sub><sup>2-</sup> and an organized water network has been proposed to provide fast proton transfer via the Grothuss mechanism, allowing successive SO<sub>3</sub><sup>2-</sup> reduction (Extended Data Fig. 8a)<sup>16,37</sup>. Despite a strikingly similar position of the residues involved in substrate binding, aSirs/Fsr and dSirs react differently. With the possibility of genetically modifying *M. maripaludis* or *M. jannaschii*, it would be worthwhile to exchange the residues that confer aSir traits at the active site (Arg 388, Cys 428) with dSir ones and observe the effects on the phenotype<sup>7,8</sup>.

Throughout evolution, sulfite reductases have been kept to detoxify SO<sub>3</sub><sup>2-</sup> as well as to conserve energy by dissimilatory SO<sub>3</sub><sup>2-</sup> reduction or oxidation of H<sub>2</sub>S<sup>38</sup>. Based on sequence and structural similarity with enzymes from different superfamilies, it has been proposed that modern sulfite reductases originated from a primordial Sir/Nir that functioned as a self-complementary homodimer<sup>18</sup>. A snapshot of this progenitor can be derived from the Fsr structure, as the organization of its sulfite reductase domain is highly simplified (Extended Data Fig. 9). The evolution of Fsr is still a matter of debate but it needs to be thoroughly studied, as its discovery



has reinforced the question of whether sulfate respiration or methanogenesis was the primeval means of energy conservation during the evolution of early Archaea<sup>39,40</sup>. Both metabolisms, related to each other, possibly coexisted or even coexist still<sup>6,18,41</sup>. Methanogens might have lost the genes required for complete sulfate dissimilation over time, but kept the sulfite reductase to adapt to environments where  $\text{SO}_3^{2-}$  fluctuations do occur. However, *M. thermolithotrophicus* appears to use a complete sulfate-reduction pathway, as it is able to grow on sulfate as its sole sulfur source<sup>4</sup>. This assimilation pathway requires  $\text{SO}_3^{2-}$  as an intermediate, and Fsr is expected to orchestrate its reduction. Although further studies need to investigate whether this methanogen can also express other enzymes of the sulfate-reduction pathway, the structural elucidation of Fsr provides the first snapshot of a sulfate reduction-associated enzyme in a methanogen.

## Methods

### Methanogenic archaea strains and cultivation medium

*M. jannaschii* (DSM 2661) and *M. thermolithotrophicus* (DSM 2095) cells were obtained from the Leibniz Institute DSMZ-German Collection of Microorganisms and Cell Cultures (Braunschweig) and cultivated in a previously described minimal medium with some modifications<sup>42</sup>.

### Reagents used for this study

Lists of reagents and providers are provided in Supplementary Table 1.

### Sulfur-free cultivation medium for *Methanococcales*

Per liter of medium: 558 mg  $\text{KH}_2\text{PO}_4$  (final concentration 4.1 mM), 1 g KCl (13.4 mM), 25.13 g NaCl (430 mM), 840 mg  $\text{NaHCO}_3$  (10 mM), 368 mg  $\text{CaCl}_2 \cdot 2\text{H}_2\text{O}$  (2.5 mM), 7.725 g  $\text{MgCl}_2 \cdot 6\text{H}_2\text{O}$  (38 mM), 1.18 g  $\text{NH}_4\text{Cl}$  (22.06 mM), 61.16 mg nitrilotriacetic acid (0.32 mM), 6.16 mg  $\text{FeCl}_2 \cdot 4\text{H}_2\text{O}$  (0.031 mM), 10  $\mu\text{l}$  2 mM  $\text{Na}_2\text{SeO}_3 \cdot 5\text{H}_2\text{O}$  stock (0.02  $\mu\text{M}$ ), 3.3 mg  $\text{Na}_2\text{WO}_4 \cdot 2\text{H}_2\text{O}$  (0.01 mM) and 2.42 mg  $\text{Na}_2\text{MoO}_4 \cdot 2\text{H}_2\text{O}$  (0.01 mM) were dissolved under constant stirring in a measuring cylinder with 750 ml of deionized  $\text{H}_2\text{O}$  ( $\text{dH}_2\text{O}$ )<sup>42</sup>. Resazurin (1 ml,

1.5 mM) was added (0.0015 mM) and 10 ml of sulfur-free trace elements (see below) were added subsequently. For *M. jannaschii*, 30.24 g PIPES (100 mM final) was used as a buffer and a pH 7.0 was adjusted using sodium hydroxide pellets. For *M. thermolithotrophicus* the pH was set to either 7.6 with 50 mM Tris–HCl as buffer or to 6.2 with 50 mM MES. The media were filled up to a final volume of 1 liter by the addition of dH<sub>2</sub>O.

The cultivation media were transferred in a 1 l pressure-protected Duran laboratory bottle with a magnetic stirring bar. The Duran flask was closed with a butyl rubber stopper and degassed by applying 3 min of evacuation, followed by 30 seconds of ventilation with  $1 \times 10^5$  Pa N<sub>2</sub> atmosphere, under constant magnetic stirring. This was repeated 15 times and at the final ventilation step an overpressure of  $0.3 \times 10^5$  Pa N<sub>2</sub> was applied.

### **Trace element composition**

A 100-fold-concentrated trace element solution was prepared by first dissolving 1.36 g nitrilotriacetic acid (7.1 mM) in 800 ml dH<sub>2</sub>O under magnetic stirring. The pH was shifted to 6.2 by adding NaOH pellets. Then, 89.06 mg MnCl<sub>2</sub>·4H<sub>2</sub>O (0.45 mM), 183.3 mg FeCl<sub>3</sub>·6H<sub>2</sub>O (0.68 mM), 60.27 mg CaCl<sub>2</sub>·2H<sub>2</sub>O (0.41 mM), 180.8 mg CoCl<sub>2</sub>·6H<sub>2</sub>O (0.76 mM), 90 mg ZnCl<sub>2</sub> (0.66 mM), 37.64 mg CuCl<sub>2</sub> (0.28 mM), 46 mg Na<sub>2</sub>MoO<sub>4</sub>·2H<sub>2</sub>O (0.19 mM), 90 mg NiCl<sub>2</sub>·6H<sub>2</sub>O (0.38 mM) and 30 mg VCl<sub>3</sub> (0.19 mM) were added separately. The trace element mixture was filled up to a final volume of 1 liter with dH<sub>2</sub>O.

### **Anaerobic growth of *Methanococcales***

For all studied archaea, cell growth was measured spectrophotometrically by measuring the optical density at 600 nm (OD<sub>600</sub>). To control the purity of the culture, samples were taken and analyzed via light microscopy. Both methanogens were cultivated at 65 °C, unless stated otherwise, with  $1 \times 10^5$  Pa of H<sub>2</sub>/CO<sub>2</sub> in the gas phase. *M. jannaschii* was cultivated in flasks and *M. thermolithotrophicus* was cultivated in flasks or a fermenter.

### **Growth of *M. jannaschii***

Duran bottles (10× 1 liter) were sealed with butyl rubber stoppers and the gas phase was exchanged for H<sub>2</sub>/CO<sub>2</sub> (80:20, 1 × 10<sup>5</sup> Pa). A 100-ml portion of anaerobic cultivation media was transferred into each bottle (ratio 1:10 of medium/gas phase), with 1 mM Na<sub>2</sub>SO<sub>3</sub> as a sole sulfur source. A portion of 5 ml of overnight culture (OD<sub>600</sub> of 0.9) was used as an inoculum for 100 ml media. No additional reductant was added. The cultures were placed at 65 °C, with standing for at least one hour, followed by overnight shaking at 180 rotations per minute without light. The cells were collected in exponential phase with a final OD<sub>600</sub> of 1.83 by immediately transferring them in an anaerobic tent (N<sub>2</sub>/CO<sub>2</sub> atmosphere at a ratio of 90:10), followed by anaerobic centrifugation for 30 min at 6,000g at 4 °C. The cell pellet was transferred in a sealed bottle gassed with 0.3 × 10<sup>5</sup> Pa N<sub>2</sub> and flash frozen in liquid N<sub>2</sub> to be stored at -80 °C.

### **Growth of *M. thermolithotrophicus* for Fsr crystallization**

*M. thermolithotrophicus* was grown in a fermenter at 50 °C with 10 mM sulfate (SO<sub>4</sub><sup>2-</sup>) as sole sulfur substrate. Since SO<sub>3</sub><sup>2-</sup> could be an intermediate in the SO<sub>4</sub><sup>2-</sup> reduction pathway it would require the expression of Fsr. Therefore, 1.5 l of anaerobic cultivation medium with 10 mM SO<sub>4</sub><sup>2-</sup> were continuously bubbled with H<sub>2</sub> and CO<sub>2</sub> (80:20, 2 × 10<sup>4</sup> Pa) and inoculated with 100 ml preculture (OD<sub>600</sub> of 4.2). Since the fermenter is an open system, we set a more alkaline pH (7.6) to prevent evaporation of produced S<sup>2-</sup>. Here, it should predominantly be present in the form of HS<sup>-</sup>, and not H<sub>2</sub>S, and therefore stay for longer time in the medium. The pH was checked every two hours by using a pH indicator. The cells were grown until late exponential phase (OD<sub>600</sub> of 2.97) and then immediately transferred in an anaerobic tent (N<sub>2</sub>/CO<sub>2</sub> atmosphere at a ratio of 90:10). Cells were collected by anaerobic centrifugation for 30 min at 6,000g at 4 °C. A 1.5-l culture with an OD<sub>600</sub> of 2.97 yielded 19.25 g of cells (wet weight). The cell pellet was transferred in a sealed bottle, gassed with 0.3 × 10<sup>5</sup> Pa N<sub>2</sub>, flash frozen in liquid N<sub>2</sub> and stored at -80 °C.

### **Growth of *M. thermolithotrophicus* for Fsr activity assays**

To perform enzymatic activity assays, *M. thermolithotrophicus* was directly grown on 2 mM Na<sub>2</sub>SO<sub>3</sub>. The ten 1-l Duran bottles were sealed with butyl rubber stoppers and the gas phase was

exchanged for H<sub>2</sub> and CO<sub>2</sub> (80:20, 1 × 10<sup>5</sup> Pa). A 100 ml of anaerobic cultivation media containing 50 mM MES at pH 6.2 was transferred in each bottle (ratio of 1:10 of medium/gas phase), with 2 mM Na<sub>2</sub>SO<sub>3</sub> final as a sole sulfur source. A 5-ml portion of overnight-grown culture (OD<sub>600</sub> of 1.7) was used as an inoculum for 100 ml of media. No additional reductant was added. The cultures were placed at 65 °C, with standing overnight. The cells were grown until early exponential phase (OD<sub>600</sub> of 0.8), since we assumed that most SO<sub>3</sub><sup>2-</sup> has not been converted into HS<sup>-</sup> yet and that Fsr should be highly expressed and active. The cells were immediately collected by transferring them in an anaerobic tent (N<sub>2</sub>/CO<sub>2</sub> atmosphere at a ratio of 90:10), followed by anaerobic centrifugation for 30 min at 6,000g at 4 °C. The cell pellet was transferred in a sealed bottle, gassed with 0.3 × 10<sup>5</sup> Pa N<sub>2</sub>, flash frozen in liquid N<sub>2</sub> and stored at -80 °C.

### **Sulfite growth inhibition**

*M. thermolithotrophicus* was grown on different Na<sub>2</sub>SO<sub>3</sub> concentrations to determine the growth-inhibiting threshold. For this, 250-ml serum flasks were sealed with a butyl rubber stopper and the gas phase was exchanged for H<sub>2</sub> and CO<sub>2</sub> (80:20, 1 × 10<sup>5</sup> Pa). A 10-ml portion of anaerobic cultivation media with a pH set at 6.2 with 50 mM MES was transferred into each bottle. Then, different Na<sub>2</sub>SO<sub>3</sub> concentrations (2 mM, 10 mM, 20 mM, 30 mM and 40 mM final) were added in triplicate as a sole sulfur source, and 2 mM Na<sub>2</sub>S was used as a control. The cultures grew at 65 °C for 22 hours, with standing. The three biological replicates for each setup are represented as dots in Extended Data Fig. 2a, with the standard deviation shown as bars.

### **Growth of *M. thermolithotrophicus* for titrations and EPR spectroscopy**

Due to the high demand of MtFsr for titration and EPR spectroscopy experiments, *M. thermolithotrophicus* was grown in one 10-l fermenter with SO<sub>4</sub><sup>2-</sup> as a sole sulfur substrate and in another 10-l fermenter with SO<sub>3</sub><sup>2-</sup> as a sole sulfur source, to boost MtFsr natural expression. The fermenter containing SO<sub>4</sub><sup>2-</sup> was performed as described above with an inoculum of 350 ml (OD<sub>600</sub> of 3.2). A 7.4-l culture with an OD<sub>600</sub> of 4.8 yielded 74 g of cells (wet weight). In the SO<sub>3</sub><sup>2-</sup> fermenter, *M. thermolithotrophicus* was grown at 50 °C in 7 l anaerobic cultivation medium with a pH of 6.2 supplemented with 5 mM SO<sub>3</sub><sup>2-</sup> as a sole sulfur substrate, continuously bubbled with

H<sub>2</sub> and CO<sub>2</sub> (80:20, 2 × 10<sup>4</sup> Pa). A 600-ml preculture (OD<sub>600</sub> of 2.34) was used as inoculum. The cells were grown until an OD<sub>600</sub> of 2.48 and then immediately transferred in an anaerobic tent (N<sub>2</sub>/CO<sub>2</sub> atmosphere at a ratio of 90:10). Cells were collected by anaerobic centrifugation for 30 min at 6,000g at 4 °C and a final yield of 51 g of cells (wet weight) was obtained. The cell pellets were transferred in a sealed bottle, gassed with 0.3 × 10<sup>5</sup> Pa N<sub>2</sub>, flash frozen in liquid N<sub>2</sub> and stored at -80 °C.

### **Genome sequencing of *M. thermolithotrophicus***

*M. thermolithotrophicus* was anaerobically grown in the above-described medium and 2 mM Na<sub>2</sub>S was used as a sulfur source. A total culture volume of 20 ml was used. Cells were aerobically collected by centrifugation (30 min, 6,000g at 4 °C). DNA was extracted and purified based on ref. 43. Quality control, library preparation and sequencing (PacBio Sequel II) were performed in the Max Planck-Genome-Centre (Cologne).

### **Purification of Fsr**

All steps were performed under the strict exclusion of oxygen and daylight. Protein purifications were carried out in a Coy tent with an N<sub>2</sub> and H<sub>2</sub> atmosphere (97:3) at 20 °C under yellow light. For both Fsr, three to five chromatography steps were used with some variations. Fsr purification was further followed via activity assays and on the basis of absorbance peaks at wavelengths of 280, 420 and 595 nm. Each elution profile was systematically controlled by SDS–PAGE to select the purest fractions.

### **Purification of *MjFsr***

*M. jannaschii* cells (13.5 g wet weight) were thawed under warm water and transferred in an anaerobic tent (N<sub>2</sub>/CO<sub>2</sub> atmosphere at a ratio of 90:10). Cells were diluted by three volumes of lysis buffer (50 mM Tricine/NaOH pH 8.0, 2 mM dithiothreitol (DTT)) and disrupted by sonication: 7 cycles at 62% intensity with 30 pulses followed by 1 min break (probe MS76, SONOPULS Bandelin). Cell debris was removed anaerobically via centrifugation (21,000g, one

hour, room temperature). The protein concentration (measured by Bradford) of the supernatant was estimated to 4.68 mg ml<sup>-1</sup>. The supernatant was transferred to a Coy tent (N<sub>2</sub>/H<sub>2</sub> atmosphere of 97:3) under yellow light at 20 °C. The sample was diluted with two volumes of lysis buffer and passed through a 0.2-µm filter (Sartorius). The filtered sample was loaded on a 10-ml Q Sepharose high-performance column (GE Healthcare), which was previously equilibrated with 5 column volumes (CV) of lysis buffer. The column was then washed with 2 CV of lysis buffer. *MjFsr* was eluted by a gradient of NaCl (from 0.1 to 0.6 M) in 27 CV at a flow rate of 1.5 ml min<sup>-1</sup> in fraction sizes of 3.5 ml. *MjFsr* eluted between 0.37 and 0.41 M NaCl. The fractions of interest were pooled and 1:1 diluted with HIC buffer (25 mM Tris– HCl pH 7.6, 2 M (NH<sub>4</sub>)<sub>2</sub>SO<sub>4</sub> and 2 mM DTT). The sample was filtered and applied to a Source15Phe 4.6/100 PE column (GE Healthcare) previously equilibrated with the HIC buffer. The column was then washed with 2 CV of 25 mM Tris–HCl pH 7.6, 1.4 M (NH<sub>4</sub>)<sub>2</sub>SO<sub>4</sub> and 2 mM DTT buffer. The elution was performed at a flow rate of 0.8 ml min<sup>-1</sup> by a decreasing gradient of (NH<sub>4</sub>)<sub>2</sub>SO<sub>4</sub> (1.4 to 0 M) over 90 min, with a fractionation size of 2 ml. *Fsr* eluted in the fractions at 0.9 to 0.78 M (NH<sub>4</sub>)<sub>2</sub>SO<sub>4</sub>. Those fractions were merged and concentrated using a 30-kDa-cutoff filter (Merck Millipore). The concentrated sample was passed through a 0.2-µm filter and injected on a Superdex 200 Increase 10/300 GL (GE Healthcare) equilibrated in storage buffer (25 mM Tris– HCl pH 7.6, containing 10% v/v glycerol and 2 mM DTT). The elution was performed at a flow rate of 0.4 ml min<sup>-1</sup> in the storage buffer. *MjFsr* eluted as a sharp Gaussian peak at 10.4 ml. The pooled samples were concentrated by passing them through a 30-kDa-cutoff filter, and the final concentration was measured by the Bradford method (Bio-Rad). The sample was immediately crystallized at a concentration of 6.1 mg ml<sup>-1</sup>.

### **Purification of *MtFsr* for crystallization**

Cells (19.25 g wet weight) derived from a fermenter were thawed under warm water and transferred to an anaerobic tent containing an atmosphere of N<sub>2</sub>/CO<sub>2</sub> (90:10). Cells were lysed by osmotic shock through the addition of 60 ml lysis buffer (50 mM Tricine/NaOH pH 8.0, 2 mM DTT). Cell lysate was homogenized by sonication: 3 cycles at 70% intensity with 30 pulses followed by 1 min break (probe MS76, SONOPULS Bandelin) and cell debris was removed anaerobically via centrifugation (21,000g, one hour at 4 °C). The supernatant was transferred in

a Coy tent (N<sub>2</sub>/H<sub>2</sub> atmosphere of 97:3), with yellow light at 20 °C. The sample was filtered through a 0.2- $\mu$ m filter (Sartorius) and was passed onto a DEAE fast-flow column (30 ml), equilibrated with lysis buffer. The column was then washed with 2 CV of lysis buffer. *MtFsr* was eluted with a gradient of 0.1 to 0.6 M NaCl in 120 min at a flow rate of 2.5 ml min<sup>-1</sup> and in fractionation sizes of 4 ml. *MtFsr* eluted between 0.3 and 0.39 M NaCl. The fractions of interest were merged, diluted by 3 volumes of lysis buffer and filtered through a 0.2- $\mu$ m filter. The filtered sample was loaded on a 15-ml Q Sepharose high-performance column, equilibrated with lysis buffer. The column was washed with 2 CV of lysis buffer. A gradient of 0.15 to 0.55 M NaCl in 120 min with a flow rate of 1 ml min<sup>-1</sup> was performed and fractions of 1.5 ml were collected. *MtFsr* eluted between 0.49 and 0.53 M NaCl. Fractions of interest were pooled and diluted with 2 volumes of HAP buffer (20 mM K<sub>2</sub>HPO<sub>4</sub>/HCl pH 7.0 and 2 mM DTT) and subsequently filtered through a 0.2- $\mu$ m filter. The filtered sample was applied to a 10-ml hydroxyapatite column type 1 (Bio-Scale Mini CHT cartridges, BioRad) equilibrated with HAP buffer. The column was washed with 2 CV of HAP buffer and a gradient of 0.02 to 0.5 M K<sub>2</sub>HPO<sub>4</sub> for 60 min at a flow rate of 2 ml min<sup>-1</sup> was performed and 3-ml fractions were collected. *MtFsr* eluted between 0.28 and 0.39 M K<sub>2</sub>HPO<sub>4</sub> and the respective fractions were pooled. The pool was diluted 1:3 with 25 mM Tris-HCl pH 7.6, 2 M (NH<sub>4</sub>)<sub>2</sub>SO<sub>4</sub> and 2 mM DTT (HIC buffer). The filtered sample was applied to a Source15Phe 4.6/100 PE column (GE Healthcare) previously equilibrated with the HIC buffer. The column was then washed with 2 CV of HIC buffer. A gradient of (NH<sub>4</sub>)<sub>2</sub>SO<sub>4</sub> ranging from 2 to 1 M was performed for 30 min at a flow rate of 0.8 ml min<sup>-1</sup> with a fractionation size of 1 ml. *MtFsr* eluted between 1.38 and 1.23 M (NH<sub>4</sub>)<sub>2</sub>SO<sub>4</sub> and the respective fractions were pooled. The buffer was exchanged for the storage buffer (25 mM Tris-HCl pH 7.6, containing 10% v/v glycerol and 2 mM DTT) by using a 30-kDa-cutoff filter (6 ml, Merck Millipore) and *MtFsr* was concentrated to 11.06 mg ml<sup>-1</sup> in a volume of 120  $\mu$ l. The protein concentration was estimated by the Bradford method. The sample was immediately crystallized.

### **Purification of *MtFsr* for enzyme activity assays**

SO<sub>3</sub><sup>2-</sup>-grown cells (8 g wet weight) were thawed under warm water and transferred to an anaerobic tent containing an atmosphere of N<sub>2</sub>/CO<sub>2</sub> (90:10). Cells were lysed by osmotic shock through the addition of 60 ml lysis buffer (50 mM Tricine/NaOH pH 8.0, 2 mM DTT). Cell lysate was

homogenized by sonication: 9 cycles at 75% intensity with 30 pulses followed by 1 min break (probe KE76, SONOPULS Bandelin) and cell debris was removed anaerobically via centrifugation (21,000g, one hour at 4 °C). The supernatant was transferred to a Coy tent (N<sub>2</sub>/H<sub>2</sub> atmosphere of 97:3) under yellow light at 20 °C and was diluted with 90 ml lysis buffer, filtered through a 0.2- $\mu$ m filter. The filtered sample was applied to a 10-ml DEAE fast-flow column (GE Healthcare), which was previously equilibrated with lysis buffer. The column was then washed with 2 CV of lysis buffer. A gradient of 0.1 to 0.6 M NaCl was applied for 120 min at a flow rate of 2.5 ml min<sup>-1</sup> and fractions of 4 ml were collected. *MtFsr* eluted between 0.34 and 0.4 M NaCl. The fractions of interest were merged and diluted by 3 volumes of lysis buffer. The filtered sample was loaded on a 10-ml Q Sepharose high-performance column (GE Healthcare) and a gradient of 0.15 to 0.55 M NaCl was applied for 120 min with a flow rate of 1 ml min<sup>-1</sup>. Fractions of 1.5 ml were collected. *MtFsr* eluted between 0.49 and 0.53 M NaCl. The *MtFsr* fractions were pooled, and three times diluted with HAP buffer (20 mM K<sub>2</sub>HPO<sub>4</sub>/HCl pH 7.0 and 2 mM DTT). The filtered sample was applied to a 10-ml hydroxyapatite type 1 (Bio-Scale Mini CHT cartridges, BioRad) equilibrated with HAP buffer. The column was washed with 2 CV of HAP buffer and a gradient of 0.02 to 0.5 M K<sub>2</sub>HPO<sub>4</sub> in 60 min at a flow rate of 2 ml min<sup>-1</sup> was performed. Fraction sizes of 1.5-ml were collected. *MtFsr* eluted between 0.25 and 0.42 M K<sub>2</sub>HPO<sub>4</sub> and the respective fractions were pooled. The pool was diluted with 3 volumes of HIC buffer (25 mM Tris-HCl pH 7.6, 2 M (NH<sub>4</sub>)<sub>2</sub>SO<sub>4</sub> and 2 mM DTT). The filtered sample was applied to a Source15Phe 4.6/100 PE column (GE Healthcare) previously equilibrated with the HIC buffer. The column was then washed with 2 CV of 25 mM Tris-HCl pH 7.6, 1.6 M (NH<sub>4</sub>)<sub>2</sub>SO<sub>4</sub> and 2 mM DTT buffer. *MtFsr* was eluted in a gradient of 1.6 to 0.8 M of (NH<sub>4</sub>)<sub>2</sub>SO<sub>4</sub> in 25 min at a flow rate of 0.8 ml min<sup>-1</sup> and a fractionation size of 1 ml. *MtFsr* eluted between 1.43 and 1.28 M (NH<sub>4</sub>)<sub>2</sub>SO<sub>4</sub> and the respective fractions were pooled. The buffer was exchanged for the storage buffer (25 mM Tris-HCl pH 7.6, containing 10% v/v glycerol and 2 mM DTT) by using a 30-kDa-cutoff filter (6 ml, Merck Millipore) and *MtFsr* was concentrated to 900  $\mu$ l. The concentrated sample was passed onto a Superdex 200 Increase 10/300 GL (GE Healthcare), equilibrated in storage buffer. *MtFsr* eluted at a flow rate 0.4 ml min<sup>-1</sup> in a sharp Gaussian peak at an elution volume of 10.01 ml (Extended Data Fig. 2g). To determine the apparent molecular weight of *MtFsr*, standard proteins (conalbumin, aldolase and ferritin, purchased from GE Healthcare) were passed at the same flow rate and in the same buffer. The fractions of interest



containing *MtFsr* were concentrated with a 30-kDa-cutoff centrifugal concentrator to 1 ml and the protein was directly used for enzymatic activity assays. The concentration of purified *MtFsr*, estimated by the Bradford method, was 3.41 mg ml<sup>-1</sup>.

### **Purification of *MtFsr* for titrations and EPR spectroscopy**

For the titrations and EPR spectroscopic measurements two separate purifications were carried out starting either with 34 g cells (wet weight) derived from a SO<sub>3</sub><sup>2-</sup>-grown fermenter, or with 49.5 g cells (wet weight) derived from a SO<sub>4</sub><sup>2-</sup>-grown fermenter. Cells were thawed under warm water and transferred to an anaerobic tent containing an atmosphere of N<sub>2</sub>/CO<sub>2</sub> (90:10). Cells were lysed by osmotic shock through the addition of 180 ml and 240 ml lysis buffer (50 mM Tricine/NaOH pH 8.0, 2 mM DTT), respectively. The cell lysates were homogenized by sonication: 4 cycles at 72% intensity with 60 pulses followed by 1.30 minute break (probe MS76, SONOPULS Bandelin) and the cell debris was removed anaerobically via centrifugation (21,000g, 1 h at 10 °C). The supernatant was transferred in a Coy tent (N<sub>2</sub>/H<sub>2</sub> atmosphere of 97:3), with yellow light at 20 °C.

The purification steps were carried out as described in ‘Purification of *MtFsr* for crystallization’. In the final purification step the buffer was exchanged by dilution and concentration in storage buffer (25 mM Tris–HCl pH 7.6, containing 10% v/v glycerol and 2 mM DTT) by using 30-kDa-cutoff filter (6 ml, Merck Millipore). *MtFsr* derived from the SO<sub>3</sub><sup>2-</sup>-grown fermenter was concentrated to 18 mg ml<sup>-1</sup> in a volume of 4.54 ml, and for the SO<sub>4</sub><sup>2-</sup>-grown fermenter *MtFsr* was concentrated to 20 mg ml<sup>-1</sup> in a volume of 1.24 ml. The protein concentrations were estimated by the Bradford method.

### **Mass spectrometry identification**

Purified *MtFsr* (1 µg) was digested with trypsin and analyzed by mass spectrometry (ThermoFisher Q Exactive HF coupled to an Easy-nLC 1200) as described in ref. 44.

## **Protein crystallization**

The purified enzymes were kept in 25 mM Tris–HCl pH 7.6, 10% v/v glycerol and 2 mM DTT. Fresh, unfrozen samples were immediately used for crystallization. Crystals were obtained anaerobically (N<sub>2</sub>/H<sub>2</sub>, 97:3) by initial screening at 20 °C using the sitting-drop method on 96-well MRC two-drop crystallization plates in polystyrene (SWISSCI) containing 90 µl of crystallization solution in the reservoir.

### **Crystallization of *MjFsr***

*MjFsr* (0.5 µl) at a concentration of 6.1 mg ml<sup>-1</sup> was mixed with 0.5 µl reservoir solution. Black, long, plate-shaped crystals appeared after a few days in the following crystallization conditions: 45% v/v 2-methyl-2,4-pentanediol, 100 mM Bis–Tris pH 5.5 and 200 mM calcium chloride.

### **Crystallization of *MtFsr***

*MtFsr* at a concentration of 11 mg ml<sup>-1</sup> was cocrystallized with FAD (0.5 mM final concentration) and F<sub>420</sub>H<sub>2</sub> (15.5 µM final concentration). The protein sample (0.6 µl) was mixed with 0.6 µl reservoir solution. Thick, square-shaped, brown crystals appeared after a few days. The reservoir solution contained 200 mM lithium sulfate, 100 mM Bis–Tris, pH 5.5 and 25% w/v polyethylene glycol 3350.

## **X-ray crystallography and structural analysis**

Crystal handling was done inside the Coy tent under anaerobic atmosphere (N<sub>2</sub>/H<sub>2</sub>, 97:3). *MjFsr* crystals were directly plunged in liquid nitrogen, whereas *MtFsr* crystals were soaked in their crystallization solution supplemented with 20% v/v ethylene glycol as a cryo-protectant before being frozen in liquid nitrogen. Crystals were tested and collected at 100 K at the Synchrotron Source Optimisée de Lumière d'Énergie Intermédiaire du LURE (SOLEIL), PROXIMA-1 beamline; the Swiss Light Source, X06DA–PXIII; and at PETRA III, P11.

### ***MjFsr***

After an X-ray fluorescence spectrum on the Fe K-edge, datasets were collected at 1.74013 Å to perform the single-wavelength anomalous dispersion experiment. Native datasets were collected at a wavelength of 0.97857 Å on the same crystal. Data were processed and scaled with autoPROC<sup>45</sup>. The resolution limits in each cell direction were as follows:  $a = 2.43$  Å,  $b = 2.62$  Å and  $c = 2.19$  Å. Phasing (obtained maximum CFOM for the substructure determination was 69), density modification and automatic building were performed with CRANK-2 (ref. 46). The asymmetric unit of *MjFsr* contains two half homotetramers. The model was then manually built with Coot and further refined with PHENIX<sup>47,48</sup>. X-ray crystallographic data were twinned, and the refinement was performed by applying the following twin law -k, -h, -l. During the refinement translational-liberation screw was applied.

### ***MtFsr***

Data were processed and scaled with autoPROC. The resolution limits in each cell direction were as follows:  $a = 1.69$  Å,  $b = 1.55$  Å and  $c = 1.81$  Å. The structure was solved by molecular replacement with phaser from PHENIX, using *MjFsr* as a template<sup>48</sup>. The asymmetric unit of *MtFsr* contains four homotetramers. This crystalline form presents a notable translational noncrystallographic symmetry (14%). The model was then manually rebuilt with Coot and further refined with PHENIX. During the refinement, noncrystallographic symmetry and translational liberation screw were applied. In the last refinement cycles, hydrogens were added in riding positions. Hydrogens were omitted from the final deposited model. In one of the chains (chain N), the lid region 204–253 has two different conformations, and both were tentatively modeled.

All models were validated through the MolProbity server<sup>49</sup>. B-factors, MolProbity scores and rotamer outliers in Extended Data Table 1 were calculated based on the available PDB structures with PHENIX. The other values in Extended Data Table 1 were derived from the original first PDB reports. Data collection and refinement statistics, as well as PDB identification codes for the deposited models and structure factors, are listed in Extended Data Table 1. Figures were generated with PyMOL (Schrödinger, LLC). Structural comparison was performed with the dissimilatory sulfite reductases from *D. vulgaris* (2V4J), *A. fulgidus* (3MM5) and with the assimilatory sulfite reductase from *E. coli* (1AOP) and *Z. mays* (5H92).

### **Purification of the F<sub>420</sub>-reducing hydrogenase from *M. thermolithotrophicus***

*MtFrh* was required to reduce F<sub>420</sub> and was purified from the same batch of cells as *MtFsr* used for crystallization. The activity of *MtFrh* after each purification step was followed by the reduction of methyl viologen in the N<sub>2</sub>/H<sub>2</sub> tent (97:3). The assay was performed in 120 µl of 0.5 M KH<sub>2</sub>PO<sub>4</sub>/NaOH pH 7.6 containing 1.7 mM of oxidized methyl viologen. The addition of 2 µl from the fractions containing Frh led to a blue coloration.

*MtFrh* was in the same pool as *MtFsr* used for crystallization, for the DEAE and the Q Sepharose columns. The Q Sepharose column performed the separation of the two target proteins. *MtFrh* eluted between 0.48 and 0.49 M NaCl from the Q Sepharose column. The filtered sample was applied to a 10-ml hydroxyapatite type 1 (Bio-Scale Mini CHT cartridges, BioRad) equilibrated with HAP buffer (20 mM K<sub>2</sub>HPO<sub>4</sub>/HCl pH 7.0 and 2 mM DTT). The column was then washed with 2 CV of HAP buffer. The elution was performed with a gradient of 0.02 to 0.5 M K<sub>2</sub>HPO<sub>4</sub> in 60 min at a flow rate of 2 ml min<sup>-1</sup> with 3-ml fractions. *MtFrh* eluted between 0.22 and 0.37 M K<sub>2</sub>HPO<sub>4</sub> and the respective fractions were pooled. The pool was diluted 1:1 with the HIC buffer (25 mM Tris-HCl pH 7.6, 2 M (NH<sub>4</sub>)<sub>2</sub>SO<sub>4</sub> and 2 mM DTT). The filtered sample was applied onto a Source15Phe 4.6/100 PE column (GE Healthcare) previously equilibrated with the HIC buffer. The column was then washed with 2 CV of 25 mM Tris-HCl pH 7.6, 1.0 M (NH<sub>4</sub>)<sub>2</sub>SO<sub>4</sub> and 2 mM DTT buffer. *MtFrh* was eluted in a gradient of 1 to 0 M (NH<sub>4</sub>)<sub>2</sub>SO<sub>4</sub> in 30 min at a flow rate of 0.8 ml min<sup>-1</sup> and a fractionation size of 1 ml. *MtFrh* eluted between 0.4 and 0.15 M (NH<sub>4</sub>)<sub>2</sub>SO<sub>4</sub> and the respective fractions were pooled. The buffer was exchanged for the storage buffer (25 mM Tris-HCl pH 7.6, containing 10% v/v glycerol and 2 mM DTT) by using a 30-kDa-cutoff filter (6 ml, Merck Millipore) and *MtFrh* was concentrated to 4.97 mg ml<sup>-1</sup> in 100 µl. The purified sample was aliquoted and anaerobically flash frozen in liquid N<sub>2</sub> and stored at -80 °C. *MtFrh* lost its activity after more than one cycle of thawing-freezing.

### **Purification of oxidized F<sub>420</sub>**

Since F<sub>420</sub> is highly sensitive to light, all steps were carried out under yellow light or by covering the sample with aluminum foil. About 10 g (wet weight) of *M. thermolithotrophicus* cells from a 1.5-l fermenter were anaerobically lysed by osmotic shock and sonication (see above). The sample was centrifuged at 45,000g for 60 min at 4 °C. The supernatant was transferred in a Coy

tent containing an atmosphere of N<sub>2</sub>/H<sub>2</sub> (97:3). The sample was filtered and passed onto a 30-ml DEAE Sepharose column equilibrated with 50 mM Tricine/NaOH pH 8.0 and 2 mM DTT. F<sub>420</sub> was eluted by a gradient of 0 to 0.6 M NaCl. The samples containing F<sub>420</sub> were determined on the basis of the absorbance profile at 420 nm and eluted between 0.48 M and 0.58 M NaCl. Pooled fractions were moved outside the tent and diluted with one volume of HIC-F<sub>420</sub> buffer (25 mM Tris HCl pH 7.6, 2 M (NH<sub>4</sub>)<sub>2</sub>SO<sub>4</sub>). (NH<sub>4</sub>)<sub>2</sub>SO<sub>4</sub> powder was directly added to the diluted sample to reach a final concentration of 3 M (NH<sub>4</sub>)<sub>2</sub>SO<sub>4</sub> and was stirred for one hour at room temperature. The sample was centrifuged at 4,000g for 20 minutes at room temperature. The supernatant was filtered through a 0.2- $\mu$ m filter and loaded on a 30-ml Phenyl-Sepharose high-performance column, equilibrated with HIC-F<sub>420</sub> buffer. F<sub>420</sub> was eluted by washing the column with the HIC-F<sub>420</sub> buffer, at a flow rate of 2 ml min<sup>-1</sup> and 1-ml fractions were collected. The fractions containing F<sub>420</sub> were pooled and filtered through a 0.2- $\mu$ m filter. The sample was diluted by 50 volumes of 5 mM Tris-HCl pH 8.0 and loaded overnight on a 5-ml Q Sepharose high-performance column, equilibrated in 5 mM Tris-HCl pH 8.0. The following steps were performed at 4 °C. The column containing the bound F<sub>420</sub> was washed with 5 CV of 20 mM (NH<sub>4</sub>)HCO<sub>3</sub> precooled at 4 °C. F<sub>420</sub> elution was performed by adding 1 M (NH<sub>4</sub>)HCO<sub>3</sub> and collected in a brown serum flask. (NH<sub>4</sub>)HCO<sub>3</sub> was removed by evacuation at 37 °C for 2 hours under constant stirring. (NH<sub>4</sub>)HCO<sub>3</sub>-free F<sub>420</sub> powder was obtained by freeze drying. The purity of the preparation was checked by measuring the ratio of Abs<sub>247</sub>/Abs<sub>420</sub> in 25 mM Tris buffer pH 8.8. A pure sample would have a ratio value of 0.85 (ref. 50). F<sub>420</sub> concentration was estimated by measuring the absorbance at 420 nm in 25 mM Tris buffer pH 7.5 ( $\epsilon_{420} = 41.4 \text{ mM}^{-1} \text{ cm}^{-1}$ ). The final concentration of oxidized F<sub>420</sub> used for this study was 3.15 mM and 7.53 mM.

### **Reduction of F<sub>420</sub> for enzyme assays**

For enzyme activity assays and cocrystallization of *MtFsr* with F<sub>420</sub>H<sub>2</sub>, the oxidized F<sub>420</sub> needed to be reduced. Dithionite was not used since it contains 10–20% (m/m) sodium sulfite and generates further SO<sub>3</sub><sup>2-</sup> as product. All steps were performed under the strict exclusion of oxygen and under yellow light. First, the aerobic gas phase of the F<sub>420</sub> stock was exchanged several times for N<sub>2</sub>. The sample was then transferred in a Coy tent with an atmosphere containing a N<sub>2</sub>/H<sub>2</sub> mixture (97:3). The reduction took place in 1.4 ml 200 mM KH<sub>2</sub>PO<sub>4</sub>, pH 7.0, 0.5 mM F<sub>420</sub>, and

5  $\mu\text{l}$  of 5  $\text{mg ml}^{-1}$  purified *MtFrh* was added. Outside the tent, in a brown serum flask, the gas phase was exchanged three times for  $\text{H}_2$  and  $\text{CO}_2$  by evacuation and gassing with  $1 \times 10^5$  Pa  $\text{H}_2$  and  $\text{CO}_2$  (80:20) at room temperature. The reduction of  $\text{F}_{420}$  was observed by the color shift from yellow to transparent. Frh was removed by passing the sample through a 10-kDa-cutoff filter. Since reduced  $\text{F}_{420}$  is not stable and oxidizes with time, aliquoted  $\text{F}_{420}\text{H}_2$  without Frh was immediately flash frozen in liquid  $\text{N}_2$  and stored at  $-80^\circ\text{C}$ .

### **Reduction of $\text{F}_{420}$ for redox titrations**

$\text{F}_{420}$  is the physiological electron donor for Fsr and was therefore used as the reductant for the redox titrations. Oxidized  $\text{F}_{420}$  was purified as described before. Since both the reduction of  $\text{F}_{420}$  with Frh is not complete and  $\text{F}_{420}\text{H}_2$  is not stable over time, we reduced  $\text{F}_{420}$  with sodium borohydride, as previously described<sup>51</sup>. The reduction of  $\text{F}_{420}$  was performed in an anaerobic chamber with an  $\text{N}_2/\text{H}_2$  atmosphere of 97:3 at  $25^\circ\text{C}$ .  $\text{F}_{420}\text{H}_2$  was generated by reducing 100  $\mu\text{l}$   $\text{F}_{420}$  at 7.53 mM with a few sodium borohydride crystals in a 10 mM Tris-HCl solution at pH 7.6, followed by destruction of excess borohydride by acidification with 50  $\mu\text{l}$  1 M hydrochloric acid. After the hydrogen evolution ceased, the pH was readjusted by the addition of 50  $\mu\text{l}$  1 M Tris-HCl pH 8.0. The generated  $\text{F}_{420}\text{H}_2$  was prepared freshly for each experiment and used immediately.

### **Enzymatic assays**

Enzymatic Fsr measurements were performed in 200 mM  $\text{KH}_2\text{PO}_4$  buffer pH 7.0 under strict exclusion of hydrogen and oxygen.  $\text{F}_{420}$  was reduced by Frh as previously described. The oxidation of the reduced electron donor  $\text{F}_{420}$  was followed spectrophotometrically at 420 nm. For  $\text{F}_{420}\text{H}_2$ , a molecular extinction coefficient of  $33.82 \text{ mM}^{-1} \text{ cm}^{-1}$  at 420 nm was experimentally determined for the above-mentioned conditions.

The assays for the specific enzyme activity were performed at  $65^\circ\text{C}$  in a 1-ml quartz cuvette closed with a butyl rubber stopper. The gas phase of the cuvette was exchanged several times with  $\text{N}_2$ . To monitor the reduction of  $\text{SO}_3^{2-}$ , 1.4 mM  $\text{Na}_2\text{SO}_3$  and 47.3  $\mu\text{M}$   $\text{F}_{420}\text{H}_2$  were added to the  $\text{KH}_2\text{PO}_4$  buffer. Once the spectrophotometer (Agilent Cary 60 UV-Vis) displayed a stable

signal, the reaction was started by the addition of 0.19  $\mu\text{g}$  *MtFsr*. To investigate whether *MtFsr* can use substrates other than  $\text{SO}_3^{2-}$ , we provided 1.4 mM of disodium thiosulfate ( $\text{S}_2\text{O}_3^{2-}$ ), 1.4 mM sodium nitrite ( $\text{NO}_2^-$ ) or 1.4 mM disodium selenite ( $\text{SeO}_3^{2-}$ ). We further tested whether *MtFsr* can function in the reverse way by providing 1.4 mM  $\text{Na}_2\text{S}$  as an electron donor and 47.3  $\mu\text{M}$  of oxidized  $\text{F}_{420}$ . All experiments were performed in triplicate.

The  $\text{app}K_m$  and  $\text{app}V_{\text{max}}$  of *MtFsr* for  $\text{SO}_3^{2-}$  and  $\text{NO}_2^-$  were determined at 50 °C under an anaerobic atmosphere (100%  $\text{N}_2$ ). The assays were performed in 96-deep-well plates and monitored spectrophotometrically (FLUOstar Omega Multi-Mode Microplate Reader). To determine the  $\text{app}K_m$  and  $\text{app}V_{\text{max}}$  of *MtFsr*, 0–500  $\mu\text{M}$   $\text{Na}_2\text{SO}_3$  or  $\text{NaNO}_2$  and 50  $\mu\text{M}$   $\text{F}_{420}\text{H}_2$  were added to the 200 mM  $\text{KH}_2\text{PO}_4$  buffer pH 7.0 and the reaction was started by the addition of 3.8 ng *MtFsr*. All experiments were performed in triplicate with a standard deviation represented by the  $\pm$  sign. Kinetic parameters were calculated based on the ic50.tk server by applying a Hill coefficient of 1 (<http://www.ic50.tk/kmvmax.html>).

### **EPR spectroscopy**

The midpoint potentials of the [4Fe–4S] centers and the siroheme of *MtFsr* were determined from EPR signal intensities and EPR integrals of the various redox states. All titrations were performed in a Coy tent ( $\text{N}_2/\text{H}_2$ , 97:3), at 25 °C in the dark. A volume of 3.32 or 3 ml for the reductive or oxidative titrations with  $\text{F}_{420}\text{H}_2$  or potassium ferricyanide at an initial *MtFsr* concentration of 4.07 or 2.7  $\text{mg ml}^{-1}$  (in 100 mM Tris–HCl, pH 7.6), respectively, was stirred under anaerobic conditions. The solution potential was measured with an InLab ARGENTHAL (Mettler) microelectrode (Ag/AgCl, +207 mV versus  $\text{H}_2/\text{H}^+$  with in-built platinum counter electrode) in the presence of the respective mediator mix. *MtFsr* was preincubated for 30 minutes before each titration with the mediator mix and assay buffer. The amount of *MtFsr* available and the necessary protein concentration to obtain a satisfying signal-to-noise ratio for the EPR spectra precluded multiple titrations. Thus, values reported were from a single redox titration for the siroheme and from two redox titrations for the Fe/S signals.

The mediator mix for the reductive titration contained methylene blue, resorufin, indigo carmine, 2-hydroxy-1,4-naphthoquinone (50  $\mu\text{M}$ ), sodium anthraquinone-2-sulfonate, phenosafranin,

safranin T, neutral red, benzyl and methyl viologen (all at a final concentration of 25  $\mu\text{M}$ , except 2-hydroxy-1,4-naphthoquinone). For the oxidative titration the mediator mix contained methylene blue, resorufin, indigo carmine, 2-hydroxy-1,4-naphthoquinone (all at a final concentration of 20  $\mu\text{M}$ ). After adjustment of the potential by microliter additions of  $\text{F}_{420}\text{H}_2$  or potassium ferricyanide and 3 minutes equilibration, EPR samples were taken. For this, 300  $\mu\text{l}$  of the mix were withdrawn, removed from the anaerobic glovebox in EPR tubes after attachment of a 5-cm piece of 3 mm  $\times$  7 mm (internal diameter  $\times$  outer diameter) natural rubber tubing sealed with a 5-mm outer diameter acrylic glass stick at the other end. The samples were stored in liquid nitrogen until EPR spectra were recorded.

*MtFsr* as isolated was already in a partially reduced state. To obtain the completely oxidized form, 675  $\mu\text{l}$  *Fsr* at 20  $\text{mg ml}^{-1}$  was incubated for 30 minutes with 2 mM methylene blue. The sample was then passed through a Sephadex G-25M column (previously equilibrated with 100 mM Tris–HCl pH 7.6) to remove the methylene blue. This methylene blue-treated *Fsr* (1.28 ml) was collected at a concentration of 5.65  $\text{mg ml}^{-1}$  and 300  $\mu\text{l}$  was directly taken frozen for EPR spectroscopy of *Fsr* in its oxidized form.

Samples from the same methylene blue-treated *Fsr* (passed through a Sephadex G-25M column) at 5.09  $\text{mg ml}^{-1}$  final concentration were incubated for 5 minutes with 10 mM  $\text{Na}_2\text{SO}_3$ , and then stored in liquid nitrogen. All EPR spectra were recorded on a Bruker Elexsys E580 X band spectrometer (digitally upgraded) with a 4122HQE cavity linked to an ESR 900 Oxford Instruments helium flow cryostat. Cryocooling was performed by a Stinger (Cold Edge Technologies) closed-cycle cryostat driven by an F-70 Sumitomo helium compressor. Our local glassblower produced EPR tubes from Ilmasil PN tubing (outer diameter 4.7 mm and 0.5 mm wall thickness, Qsil). Before use, the tubes were extensively cleaned with pipe cleaners to remove inadvertent contaminants. EPR spectra were simulated with Easyspin<sup>52</sup>. The concentration of *Fsr* for the spin integration (using a 1 mM  $\text{Cu}^{2+}$ –EDTA solution as standard) was obtained by dividing the Fe concentration, as determined with the ferene method<sup>29</sup>, by 24, since siroheme does not release Fe. Fitting to the Nernst equation was performed in Excel.



### High-resolution clear-native PAGE

To visualize the expression levels of Fsr in HS<sup>-</sup>- versus SO<sub>3</sub><sup>2-</sup>-grown cultures, and to estimate the oligomerization of Fsr, high-resolution clear-native-PAGE (hrCN-PAGE) was performed. 10 ml of *M. thermolithotrophicus* and *M. jannaschii* cultures, with either 2 mM Na<sub>2</sub>S or 2 mM Na<sub>2</sub>SO<sub>3</sub> as sulfur source, were grown for one night at 65 °C, with standing. Cells were collected by anaerobic centrifugation at 6,000g for 20 min at room temperature and the cell pellets were resuspended in 2 ml of 50 mM Tricine/NaOH pH 8.0 and 2 mM DTT. The cells were anaerobically sonicated four times at 70% intensity for 10 seconds, followed by a 30-second break (MS 73 probe, SONOPULS Bandelin). The hrCN-PAGE was run anaerobically and the protocol was adapted from ref. 53. Linear polyacrylamide gradient gels (8–15%) were prepared under aerobic conditions but then transferred into an anoxic chamber (atmosphere of N<sub>2</sub>/CO<sub>2</sub>, 90:10), where the gels were equilibrated in anaerobic cathode buffer (50 mM Tricine; 15 mM Bis-Tris, pH 7.0; 0.05% w/v sodium deoxycholate; 0.01% w/v dodecyl maltoside and 2 mM DTT) overnight. Fresh and anaerobic samples were diluted with the lysis buffer to a final concentration of 1 mg ml<sup>-1</sup> and a volume of 12 µl per sample was loaded onto the gel, as well as 2 µl of the Native-Mark Unstained Protein Standard ladder (ThermoFisher). Glycerol (20% v/v final) was added to each sample and 0.001% w/v Ponceau S served as a marker for protein migration. The electrophoresis anode buffer contained 50 mM Bis-Tris buffer pH 7.0 and 2 mM DTT. The hrCN gels were run with a constant 40-mA current (PowerPac Basic Power Supply, BioRad). After electrophoresis, the protein bands were aerobically stained with Instant Blue (Expedeon).

## References

1. Jannasch, H. W. & Mottl, M. J. Geomicrobiology of deep-sea hydrothermal vents. *Science* **229**, 717–725 (1985).
2. Balderston, W. L. & Payne, W. J. Inhibition of methanogenesis in salt marsh sediments and whole-cell suspensions of methanogenic bacteria by nitrogen oxides. *Appl. Environ. Microbiol.* **32**, 264–269 (1976).
3. Jones, W. J., Leigh, J. A., Mayer, F., Woese, C. R. & Wolfe, R. S. *Methanococcus jannaschii* sp. nov., an extremely thermophilic methanogen from a submarine hydrothermal vent. *Arch. Microbiol.* **136**, 254–261 (1983).
4. Daniels, L., Belay, N. & Rajagopal, B. S. Assimilatory reduction of sulfate and sulfite by methanogenic bacteria. *Appl. Environ. Microbiol.* **51**, 703–709 (1986).
5. Johnson, E. F. & Mukhopadhyay, B. A new type of sulfite reductase, a novel coenzyme F<sub>420</sub>-dependent enzyme, from the methanarchaeon *Methanocaldococcus jannaschii*. *J. Biol. Chem.* **280**, 38776–38786 (2005).
6. Yu, H. et al. Comparative genomics and proteomic analysis of assimilatory sulfate reduction pathways in anaerobic methanotrophic archaea. *Front. Microbiol.* **9**, 2917 (2018).
7. Johnson, E. F. & Mukhopadhyay, B. Coenzyme F<sub>420</sub>-dependent sulfite reductase-enabled sulfite detoxification and use of sulfite as a sole sulfur source by *Methanococcus maripaludis*. *Appl. Environ. Microbiol.* **74**, 3591–3595 (2008).
8. Susanti, D., Frazier, M. C. & Mukhopadhyay, B. A genetic system for *Methanocaldococcus jannaschii*: an evolutionary deeply rooted hyperthermophilic Methanarchaeon. *Front. Microbiol.* **10**, 1256 (2019).
9. Crane, B. R., Siegel, L. M. & Getzoff, E. D. Sulfite reductase structure at 1.6 Å: evolution and catalysis for reduction of inorganic anions. *Science* **270**, 59–67 (1995).
10. Brânzanic, A. M. V., Ryde, U. & Silaghi-Dumitrescu, R. Why does sulfite reductase employ siroheme. *Chem. Commun.* **55**, 14047–14049 (2019).
11. Crane, B. R. & Getzoff, E. D. The relationship between structure and function for the sulfite reductases. *Curr. Opin. Struct. Biol.* **6**, 744–756 (1996).
12. Dhillon, A., Goswami, S., Riley, M., Teske, A. & Sogin, M. Domain evolution and functional diversification of sulfite reductases. *Astrobiology* **5**, 18–29 (2005).
13. Oliveira, T. F. et al. The crystal structure of *Desulfovibrio vulgaris* dissimilatory sulfite reductase bound to DsrC provides novel insights into the mechanism of sulfate respiration. *J. Biol. Chem.* **283**, 34141–34149 (2008).

14. Schiffer, A. et al. Structure of the dissimilatory sulfite reductase from the hyperthermophilic archaeon *Archaeoglobus fulgidus*. *J. Mol. Biol.* **379**, 1063–1074 (2008).
15. Santos, A. A. et al. A protein trisulfide couples dissimilatory sulfate reduction to energy conservation. *Science* **350**, 1541–1545 (2015).
16. Parey, K., Warkentin, E., Kroneck, P. M. H. & Ermler, U. Reaction cycle of the dissimilatory sulfite reductase from *Archaeoglobus fulgidus*. *Biochemistry* **49**, 8912–8921 (2010).
17. Heryakusuma, C. et al. A reduced F<sub>420</sub>-dependent nitrite reductase in an anaerobic methanotrophic archaeon. *J. Bacteriol.* **204**, e00078-22 (2022).
18. Susanti, D. & Mukhopadhyay, B. An intertwined evolutionary history of methanogenic archaea and sulfate reduction. *PLoS ONE* **7**, e45313 (2012).
19. Johnson, E. F. & Mukhopadhyay, B. in *Microbial Sulfur Metabolism* (eds. Dahl, C. & Friedrich, C. G.) Ch. 16 (Springer, 2008).
20. Shah, M. V. et al. Cofactor F<sub>420</sub>-dependent enzymes: an under-explored resource for asymmetric redox biocatalysis. *Catalysts* **9**, 868 (2019).
21. DiMarco, A. A., Bobik, T. A. & Wolfe, R. S. Unusual coenzymes of methanogenesis. *Annu. Rev. Biochem.* **59**, 355–394 (1990).
22. Greening, C. et al. Physiology, biochemistry, and applications of F<sub>420</sub>- and F<sub>0</sub>-dependent redox reactions. *Microbiol. Mol. Biol. Rev.* **80**, 451–493 (2016).
23. Wagner, T., Koch, J., Ermler, U. & Shima, S. Methanogenic heterodisulfide reductase (HdrABC-MvhAGD) uses two noncubane [4Fe-4S] clusters for reduction. *Science* **357**, 699–703 (2017).
24. Moura, I. et al. Low-spin sulfite reductases: a new homologous group of non-heme iron-siroheme proteins in anaerobic bacteria. *Biochem. Biophys. Res. Commun.* **141**, 1032–1041 (1986).
25. Vitt, S. et al. The F<sub>420</sub>-reducing [NiFe]-hydrogenase complex from *Methanothermobacter marburgensis*, the first X-ray structure of a group 3 family member. *J. Mol. Biol.* **426**, 2813–2826 (2014).
26. Ilina, Y. et al. X-ray crystallography and vibrational spectroscopy reveal the key determinants of biocatalytic dihydrogen cycling by [NiFe] hydrogenases. *Angew. Chem. Int. Ed. Engl.* **58**, 18710–18714 (2019).
27. Janick, P. A. & Siegel, L. M. Electron paramagnetic resonance and optical spectroscopic evidence for interaction between siroheme and Fe<sub>4</sub>S<sub>4</sub> prosthetic groups in *Escherichia coli* sulfite reductase hemoprotein subunit. *Biochemistry* **21**, 3538–3547 (1982).

28. Huynh, B. H., Kang, L., DerVartanian, D. V., Peck, H. D. & LeGall, J. Characterization of a sulfite reductase from *Desulfovibrio vulgaris*. Evidence for the presence of a low-spin siroheme and an exchange-coupled siroheme-[4Fe-4S] unit. *J. Biol. Chem.* **259**, 15373–15376 (1984).
29. Pierik, A. J. & Hagen, W. R.  $S=9/2$  EPR signals are evidence against coupling between the siroheme and the Fe/S cluster prosthetic groups in *Desulfovibrio vulgaris* (Hildenborough) dissimilatory sulfite reductase. *Eur. J. Biochem.* **195**, 505–516 (1991).
30. Day, E. P. et al. Magnetization of the sulfite and nitrite complexes of oxidized sulfite and nitrite reductases: EPR silent spin  $S=1/2$  states. *Biochemistry* **27**, 2126–2132 (1988).
31. Prince, R. C. & Adams, M. W. W. Oxidation-reduction properties of the two  $Fe_4S_4$  clusters in *Clostridium pasteurianum* ferredoxin. *J. Biol. Chem.* **262**, 5125–5128 (1987).
32. Christner, J. A. et al. Exchange coupling between siroheme and [4Fe-4S] cluster in *E. coli* sulfite reductase. Mössbauer studies and coupling models for a 2-electron reduced enzyme state and complexes with sulfide. *J. Am. Chem. Soc.* **106**, 6786–6794 (1984).
33. Guo, M., Sulc, F., Ribbe, M. W., Farmer, P. J. & Burgess, B. K. Direct assessment of the reduction potential of the [4Fe-4S](1+/0) couple of the Fe protein from *Azotobacter vinelandii*. *J. Am. Chem. Soc.* **124**, 12100–12101 (2002).
34. Askenasy, I. et al. The N-terminal domain of *Escherichia coli* assimilatory NADPH-sulfite reductase hemoprotein is an oligomerization domain that mediates holoenzyme assembly. *J. Biol. Chem.* **290**, 19319–19333 (2015).
35. Kim, J. Y., Nakayama, M., Toyota, H., Kurisu, G. & Hase, T. Structural and mutational studies of an electron transfer complex of maize sulfite reductase and ferredoxin. *J. Biochem.* **160**, 101–109 (2016).
36. Belay, N., Jung, K. Y., Rajagopal, B. S., Kremer, J. D. & Daniels, L. Nitrate as a sole nitrogen source for *Methanococcus thermolithotrophicus* and its effect on growth of several methanogenic bacteria. *Curr. Microbiol.* **21**, 193–198 (1990).
37. Codorniu-Hernández, E. & Kusalik, P. G. Probing the mechanisms of proton transfer in liquid water. *Proc. Natl Acad. Sci. USA* **110**, 13697–13698 (2013).
38. Loy, A. et al. Reverse dissimilatory sulfite reductase as phylogenetic marker for a subgroup of sulfur-oxidizing prokaryotes. *Environ. Microbiol.* **11**, 289–299 (2009).
39. Canfield, D. E., Habicht, K. S. & Thamdrup, B. The Archean sulfur cycle and the early history of atmospheric oxygen. *Science* **288**, 658–661 (2000).
40. Ueno, Y., Yamada, K., Yoshida, N., Maruyama, S. & Isozaki, Y. Evidence from fluid inclusions for microbial methanogenesis in the early Archaean era. *Nature* **440**, 516–519 (2006).

41. Liu, Y. F. et al. Genomic and transcriptomic evidence supports methane metabolism in *Archaeoglobi. mSystems* **5**, e00651-19 (2020).

## References Methods

42. Mukhopadhyay, B., Johnson, E. F. & Wolfe, R. S. Reactor-scale cultivation of the hyperthermophilic methanarchaeon *Methanococcus jannaschii* to high cell densities. *Appl. Environ. Microbiol.* **65**, 5059–5065 (1999).

43. Martín-Platero, A. M., Valdivia, E., Maqueda, M. & Martínez-Bueno, M. Fast, convenient, and economical method for isolating genomic DNA from lactic acid bacteria using a modification of the protein ‘salting-out’ procedure. *Anal. Biochem.* **366**, 102–104 (2007).

44. Kulak, N. A., Pichler, G., Paron, I., Nagaraj, N. & Mann, M. Minimal, encapsulated proteomic-sample processing applied to copy-number estimation in eukaryotic cells. *Nat. Methods* **11**, 319–324 (2014).

45. Vonnrhein, C. et al. Data processing and analysis with the autoPROC toolbox. *Acta Crystallogr. D Biol. Crystallogr.* **67**, 293–302 (2011).

46. Pannu, N. S. et al. Recent advances in the CRANK software suite for experimental phasing. *Acta Crystallogr. D Biol. Crystallogr.* **67**, 331–337 (2011).

47. Emsley, P., Lohkamp, B., Scott, W. G. & Cowtan, K. Features and development of Coot. *Acta Crystallogr. D Biol. Crystallogr.* **66**, 486–501 (2010).

48. Liebschner, D. et al. Macromolecular structure determination using X-rays, neutrons and electrons: recent developments in Phenix. *Acta Crystallogr. D Biol. Crystallogr.* **75**, 861–877 (2019).

49. Chen, V. B. et al. MolProbity: all-atom structure validation for macromolecular crystallography. *Acta Crystallogr. D Biol. Crystallogr.* **66**, 12–21 (2010).

50. Schönheit, P., Keweloh, H. & Thauer, R. K. Factor F<sub>420</sub> degradation in *Methanobacterium thermoautotrophicum* during exposure to oxygen. *FEMS Microbiol. Lett.* **12**, 347–349 (1981).

51. Deppenmeier, U., Blaut, M., Mahlmann, A. & Gottschalk, G. Membrane bound F<sub>420</sub>H<sub>2</sub>-dependent heterodisulfide reductase in methanogenic bacterium strain Göl and *Methanobolus tindarius*. *FEBS Lett.* **261**, 199–203 (1990).

52. Stoll, S. & Schweiger, A. EasySpin, a comprehensive software package for spectral simulation and analysis in EPR. *J. Magn. Reson.* **178**, 42–55 (2006).

53. Lemaire, O. N. et al. Small membranous proteins of the TorE/NapE family, crutches for cognate respiratory systems in Proteobacteria. *Sci. Rep.* **8**, 13576 (2018).

54. Wagner, T., Wegner, C. E., Kahnt, J., Ermler, U. & Shima, S. Phylogenetic and structural comparisons of the three types of methyl coenzyme M reductase from *Methanococcales* and *Methanobacteriales*. *J. Bacteriol.* **199**, e00197-17 (2017).
55. Murphy, M. J., Siegel, L. M., Tove, S. R. & Kamin, H. Siroheme: a new prosthetic group participating in six-electron reduction reactions catalyzed by both sulfite and nitrite reductases. *Proc. Natl Acad. Sci. USA* **71**, 612–616 (1974).
56. Krissinel, E. & Henrick, K. Inference of macromolecular assemblies from crystalline state. *J. Mol. Biol.* **372**, 774–797 (2007).
57. Krissinel, E. & Henrick, K. Secondary-structure matching (SSM), a new tool for fast protein structure alignment in three dimensions. *Acta Crystallogr. D Biol. Crystallogr.* **60**, 2256–2268 (2004).
58. Sievers, F. et al. Fast, scalable generation of high-quality protein multiple sequence alignments using Clustal Omega. *Mol. Syst. Biol.* **7**, 539 (2011).
59. Robert, X. & Gouet, P. Deciphering key features in protein structures with the new ENDscript server. *Nucleic Acids Res.* **42**, W320–W324 (2014).
60. Ebrahim, A. et al. Dose-resolved serial synchrotron and XFEL structures of radiation-sensitive metalloproteins. *IUCrJ* **6**, 543–551 (2019).

## Figures and Tables

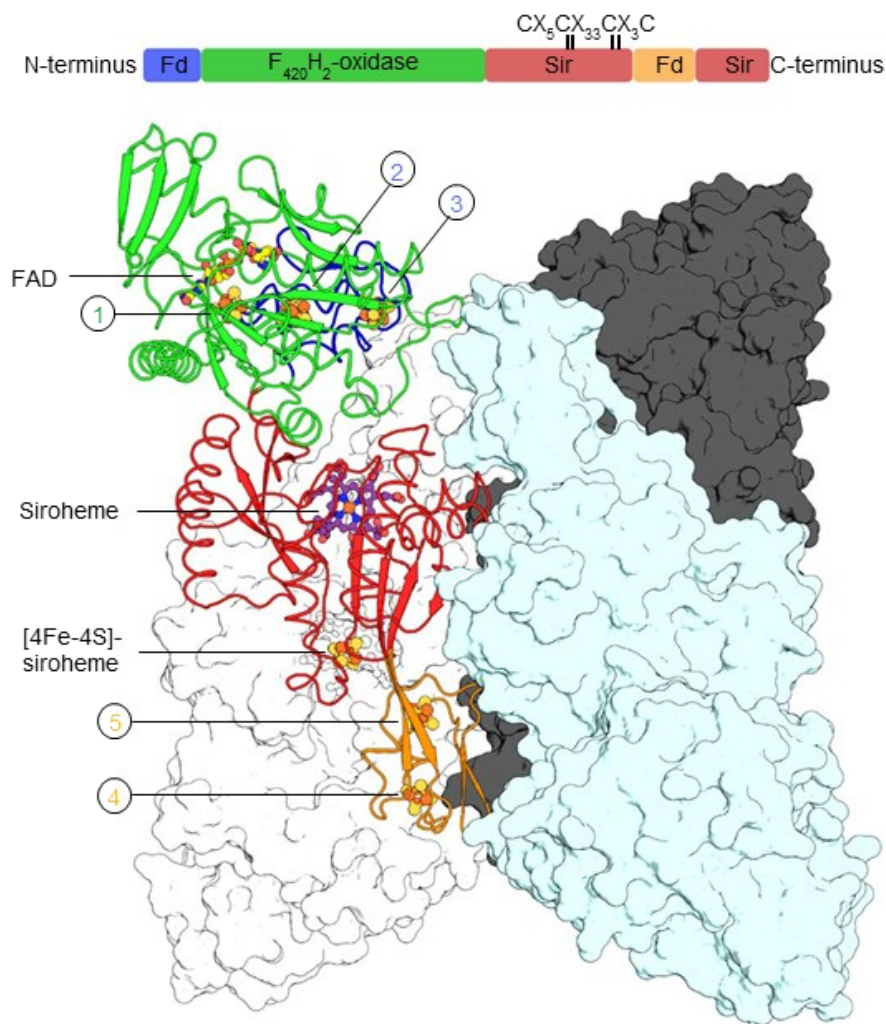


**Figure 1. Domain and structural organization of *MtFsr*.** Visualization of *MtFsr* domains (top panel). The [4Fe–4S] cluster-binding motif in the proximity of the siroheme is highlighted. The main panel shows the tetrameric arrangement of *MtFsr*. Three chains are represented in the surface and colored in white, black and cyan. One monomer of *MtFsr* is represented as a cartoon and colored according to the top panel. [4Fe–4S] clusters are numbered on the basis of their position in the electron relay going from the FAD to the siroheme. The siroheme, FAD and the [4Fe–4S] clusters are represented by balls and sticks. Carbon, nitrogen, oxygen, sulfur and iron atoms are colored as purple (siroheme)/light yellow (FAD), blue, red, yellow and orange, respectively. Fd and Sir stand for ferredoxin domain and sulfite reductase domain, respectively.

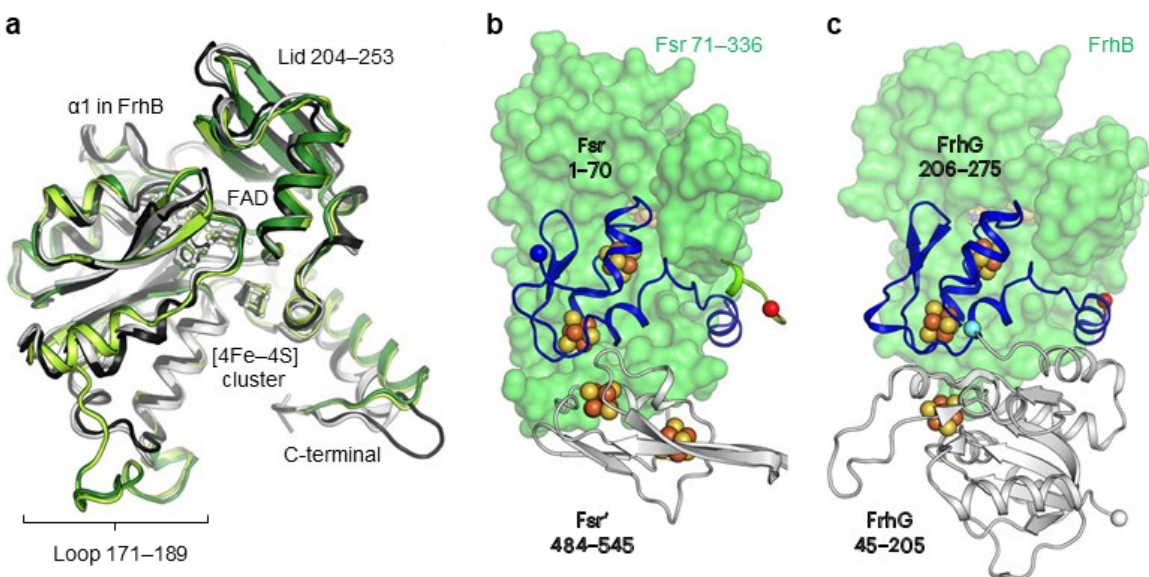


**Figure 2. Comparison of the F<sub>420</sub>H<sub>2</sub>-oxidase domain between Fsr and Frh.** a, Superposition of the F<sub>420</sub>H<sub>2</sub>-oxidase domain in Fsr (*Mj*Fsr in dark green, *Mt*Fsr in light green) with FrhB from *M. barkeri* (black, PDB 6QGR) and FrhB from *M. marburgensis* (white, PDB 4OMF). The extended loops 171–189 in *Mj*Fsr and *Mt*Fsr are highlighted, as well as the lid, which is static in the Frh structures, but more flexible in Fsr (Extended Data Fig. 4b,c). b, Representation of *Mt*Fsr F<sub>420</sub>H<sub>2</sub>-oxidase domain (green surface) and its N-terminal ferredoxin domain (blue cartoon residues 1–70). The N terminus of Fsr and C terminus from the F<sub>420</sub>H<sub>2</sub>-oxidase domain are highlighted by blue and red spheres, respectively. The inserted ferredoxin domain, provided by the opposing monomer (Fsr'), is shown in white cartoon representation. c, Arrangement of FrhB (green surface) with FrhG (cartoon) from *M. marburgensis* (PDB 4OMF). The N-terminal part (45–205) of FrhG is colored in white and its C-terminal part (206–275), structurally equivalent to the N-terminal ferredoxin domain of Fsr, is colored in blue. The cyan ball highlights the connection between both FrhG parts.



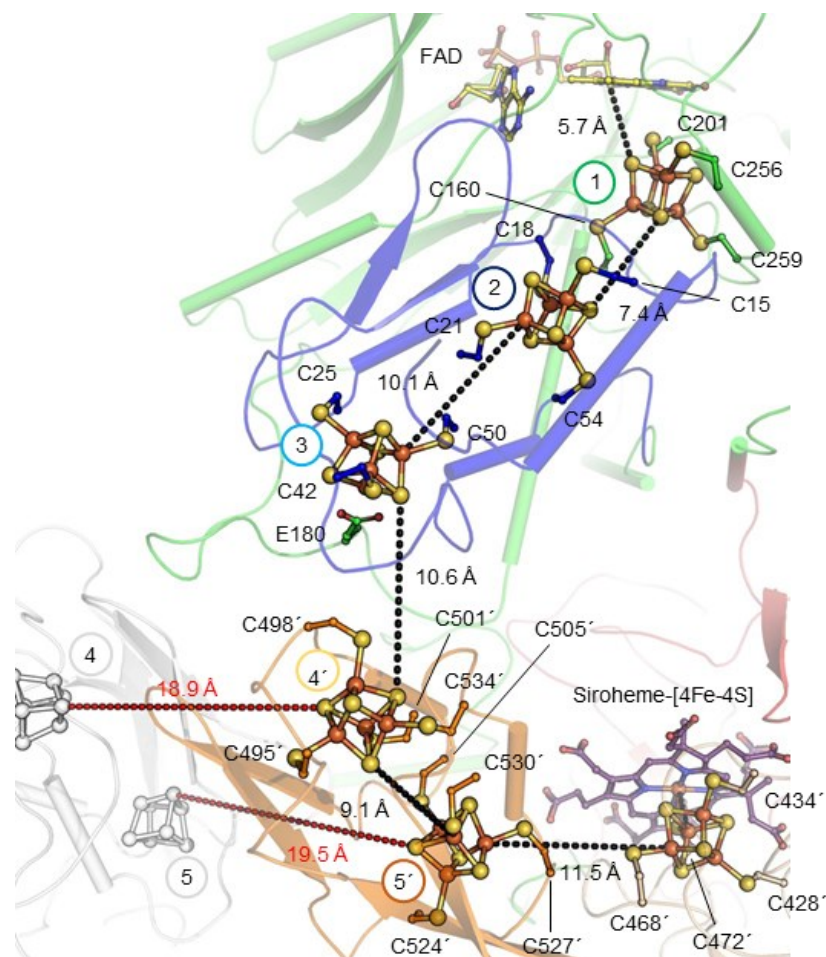


**Figure 3. Electron-transfer relay of *MtFsr*.** *MtFsr*, shown as cartoon, has the same color code and numbering of its [4Fe–4S] clusters (balls and sticks) as in the domain representation in Fig. 1. Edge-to-edge distances connecting the clusters are shown as dashes. The distances to the adjacent [4Fe–4S] clusters of the opposite dimer are shown in red. The primes correspond to the second monomer forming the dimer. The residues binding the clusters are shown as balls and sticks. Carbon atoms are colored by their domain affiliation. Nitrogen, oxygen, sulfur and iron atoms are colored in blue, red, yellow and orange, respectively. Siroheme and FAD are shown as sticks with purple and yellow carbon atoms, respectively.

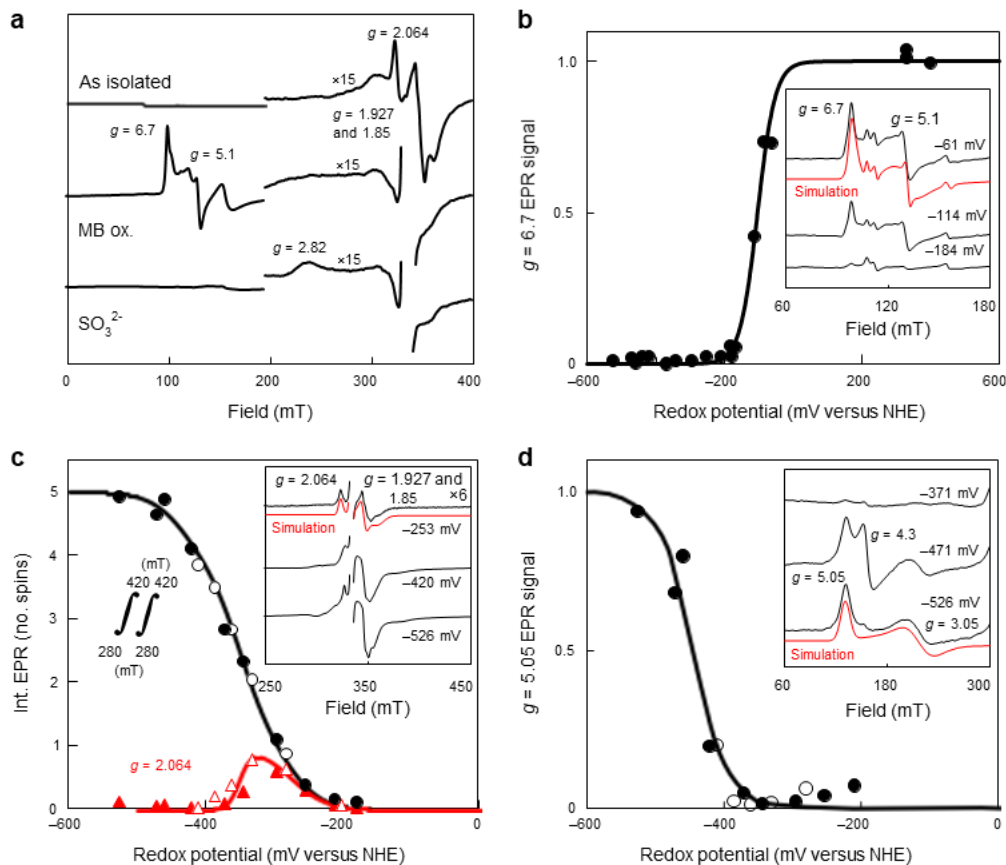


**Figure 4. Determination of the redox potential of the metallocofactors in *MtFsr* via EPR spectroscopy.** a, EPR spectra of as-isolated, methylene blue-oxidized (MB-ox.) and, consecutively,  $\text{Na}_2\text{SO}_3$  (10 mM)-treated *MtFsr*. b–d, Dye-mediated redox titrations of indicated EPR signals (or double integral in c). Representative spectra at three selected potentials are shown in the insets, including g values and simulations (see text). EPR spectra for all samples are in Extended Data Fig. 6a,b,d. Nernst fits for  $n = 1$  with  $E_m = -104$  mV (b),  $-275$ , three times  $-350$  and  $-435$  mV (c) and  $-445$  mV (d) are shown. NHE, normal hydrogen electrode. The fit for  $g = 2.064$  used  $n = 1$  (in red) for  $-275$  mV and  $n = 2$  for  $-350$  mV (in black). EPR conditions: temperature, 10 K; modulation frequency, 100 kHz; modulation amplitude, 1.0 mT; microwave frequency 9.353 GHz; microwave power 20 mW except in c, where 0.2 mW. While one cluster indeed has a measured redox potential of  $-275$  mV and three others are at  $-350$  mV, one of them exhibits a lower potential of  $-435$  mV. The presence of such a low redox potential cluster has already been seen in complex I and does not contradict our hypothesis regarding the electron flow.

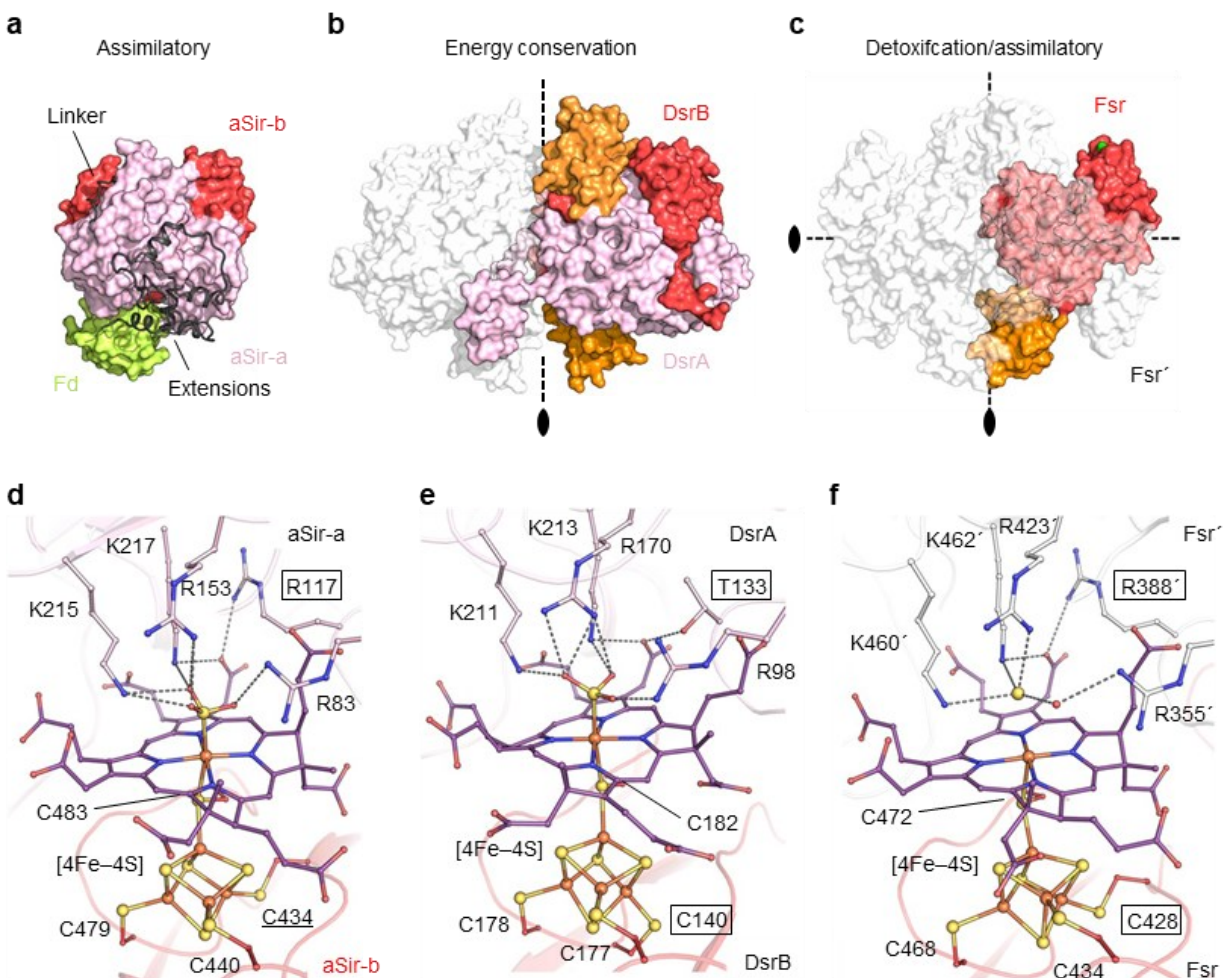
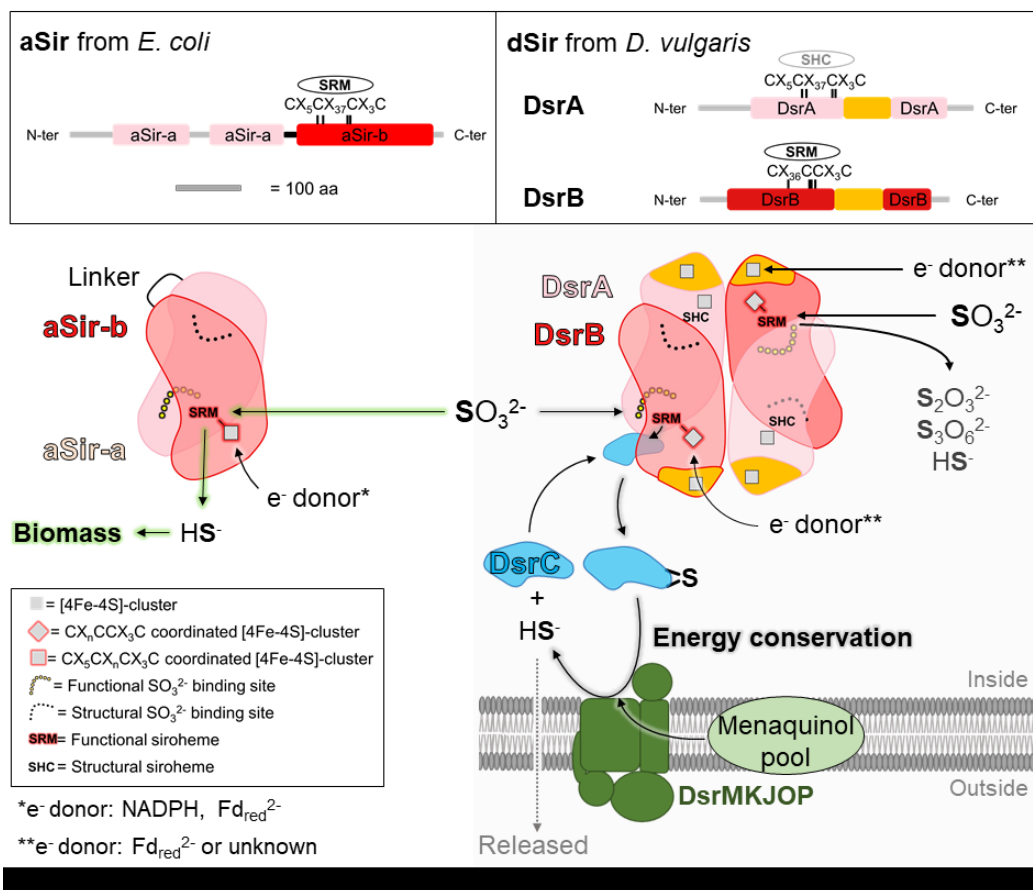


**Figure 5. Overall structural comparison between aSir, dSir and Fsr.** a–c, All structures are represented in surface, dimeric partners shown in white transparent and residues from the opposing monomer are labeled with a prime symbol. The black ovals and black dashed lines indicate the twofold symmetry axes. The inserted ferredoxin domains of DsrAB and *MtFsr* are colored in orange. a, aSir from *Zea mays* with its [2Fe–2S] ferredoxin colored in light green (PDB 5H92). b, DsrAB from *A. fulgidus* (PDB 3MM5). c, *MtFsr* tetramer. For *MtFsr*, the green surface indicates the F<sub>420</sub>H<sub>2</sub>-oxidase position. d–f, Active site of sulfite reductases. Close-up of the active site and the functional siroheme surroundings in *E. coli* aSir (PDB 1AOP) (d), dSir of *A. fulgidus* (PDB 3MM5) (e) and *MtFsr* (f) in which HS<sup>-</sup> was tentatively modeled. Residues coordinating the [4Fe–4S] cluster, the siroheme and the sulfur species are shown as balls and sticks, while sulfur and iron are depicted as spheres. Framed residues highlight the differences between the siroheme–[4Fe–4S] binding in aSirs and dSirs.

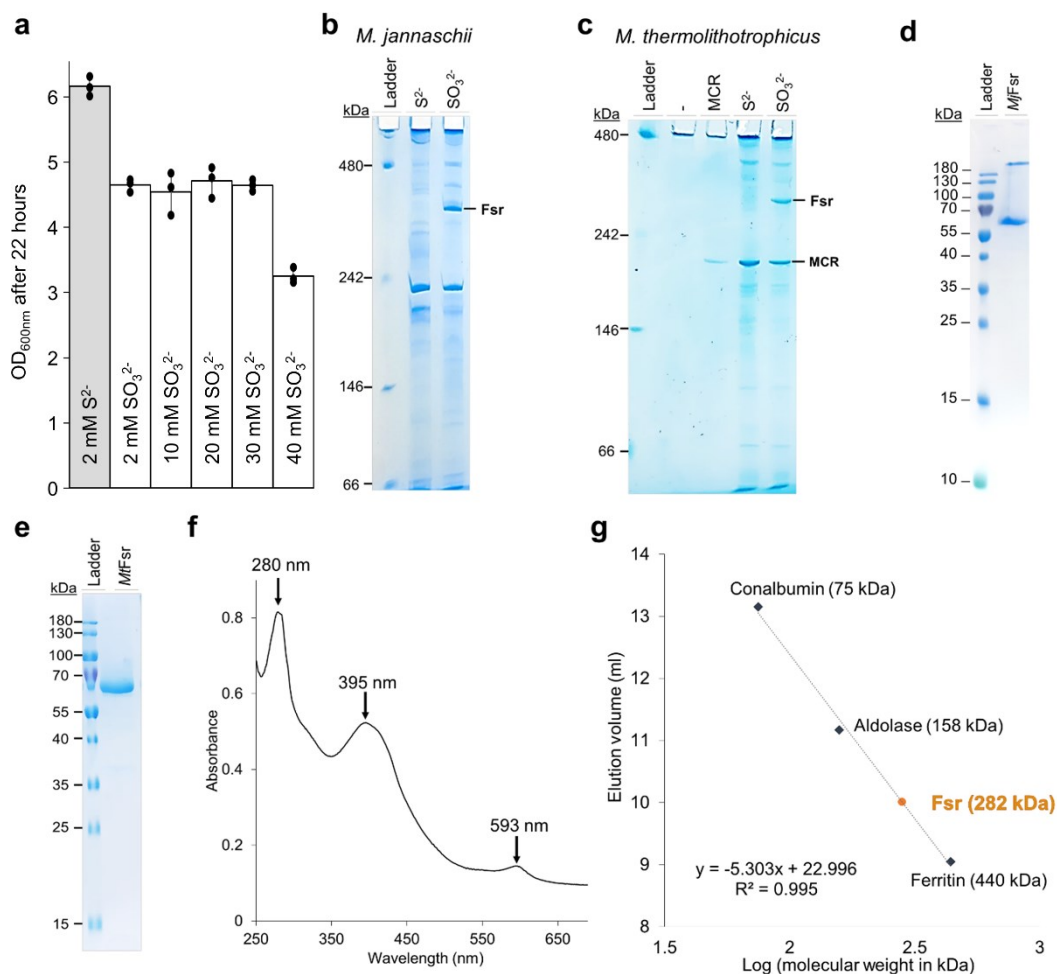
Enzyme	Substrate	Apparent $K_m$ ( $\mu\text{M}$ )	Apparent $V_{\text{max}}$ ( $\mu\text{mol}$ of $\text{F}_{420}\text{H}_2$ oxidized $\text{min}^{-1} \text{mg}^{-1}$ of Fsr)
<i>Mj</i> Fsr, from ref. 5	$\text{SO}_3^{2-}$	$12.2 \pm 1$	16
<i>Mt</i> Fsr	$\text{SO}_3^{2-}$	$15.6 \pm 2.0$	$27.6 \pm 0.9$
<i>Mt</i> Fsr	$\text{NO}_2^-$	$2.5 \pm 0.2$	$27.2 \pm 0.5$

**Table 1. Kinetic parameters of *Mt*Fsr and *Mj*Fsr (mean  $\pm$  s.d.,  $n = 3$  independent experiments)**

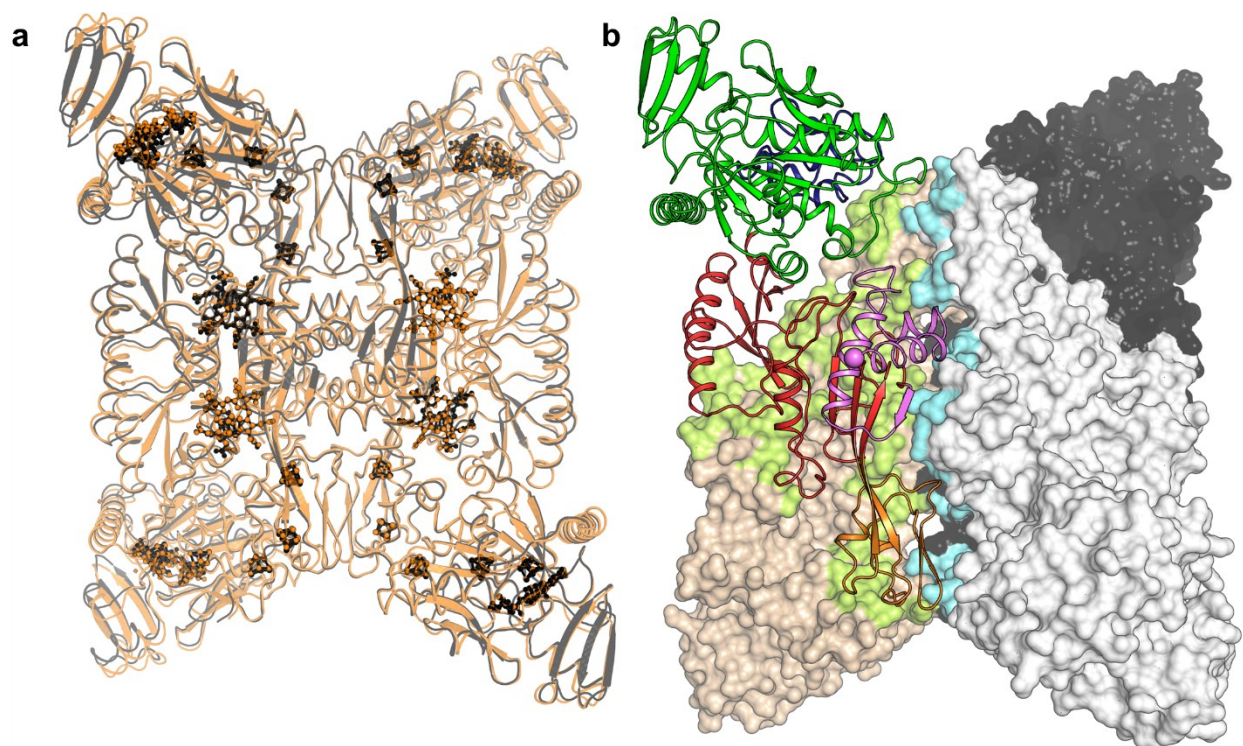
## Extended Data



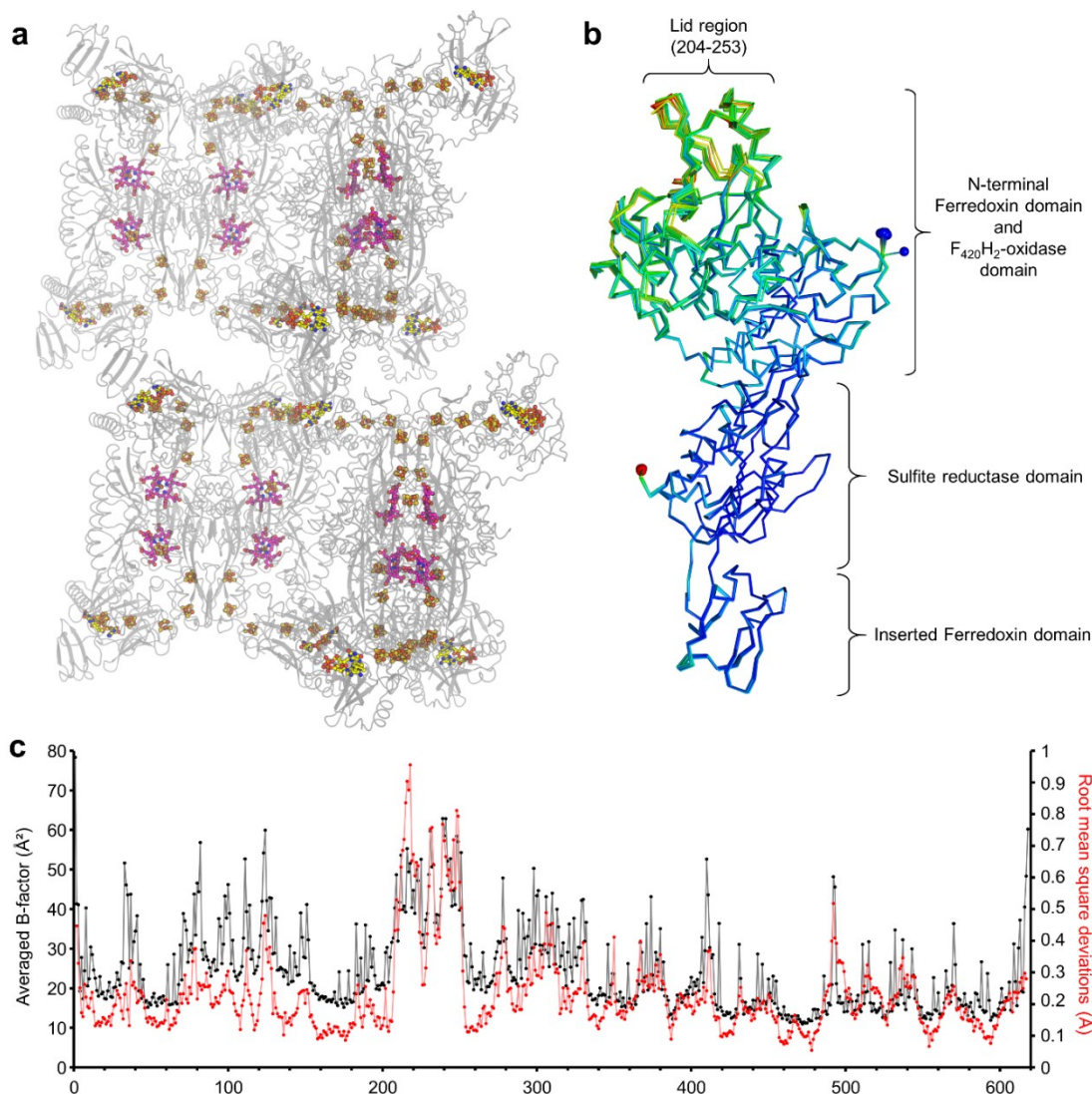
**Extended Data Figure 1. Structural and functional organization of assimilatory (aSir) and dissimilatory (DsrAB) sulfite reductases.** Distinct and conserved domains in aSir as well as dSir are shown in the top panel. The [4Fe-4S]-cluster binding motifs in the proximity of the siroheme or sirohydrochlorin are highlighted. Bottom panel: aSirs (left) are functional monomers that probably evolved through a gene duplication event, where one gene lost its cluster binding motif. The N-terminal half abbreviated as aSir-a (light pink) has a structural function and the C-terminal half abbreviated as aSir-b (red) harbours the active [4Fe-4S]-siroheme. aSirs indirectly use electrons from NADPH (bacteria) or directly via a [2Fe-2S]-cluster containing ferredoxin (plants) to reduce SO<sub>3</sub><sup>2-</sup> to HS<sup>-</sup> in a six-electron reduction reaction<sup>11,35</sup>. The produced sulfide will be used for sulfur assimilation. dSirs (right) are composed of two DsrA (light pink) and two DsrB (red) subunits and receive electrons from reduced ferredoxins (Fd<sub>red</sub><sup>2-</sup>) or so far unknown donors<sup>15</sup>. In absence of DsrC (cyan), DsrAB turns SO<sub>3</sub><sup>2-</sup> to thionates (that is S<sub>2</sub>O<sub>3</sub><sup>2-</sup>, S<sub>3</sub>O<sub>6</sub><sup>2-</sup>) and HS<sup>-</sup>. In presence of DsrC, the intermediate sulfur species bound on the siroheme is transferred to DsrC. In the case of *Desulfovibrio* species, the membrane DsrMKJOP complex (green) fully reduces the DsrC-trisulfide (4 electrons transfer) probably by using the menaquinol pool and generates DsrC and HS<sup>-</sup> via the trisulfide pathway, a key process for energy conservation<sup>15</sup>.



**Extended Data Figure 2. Physiological and biochemical profiles of Fsr from *Methanococcales*.** a, Final OD<sub>600 nm</sub> of *M. thermolithotrophicus* grown on sulfide (S<sup>2-</sup>) and different sulfite (SO<sub>3</sub><sup>2-</sup>) concentrations as a sole sulfur source after 22 hours (mean ± s.d.,  $n = 3$  biologically independent replicates). b, c, hrCNPAGE of cell extracts (12 µg loaded) from *M. jannaschii* (b,  $n = 1$  independent experiment) and *M. thermolithotrophicus* (c,  $n = 3$  independent experiments), grown on 2 mM Na<sub>2</sub>S or 2 mM Na<sub>2</sub>SO<sub>3</sub> as a sole sulfur source. Purified MCR from *M. thermolithotrophicus* (1.7 µg loaded) was used as a control for the hrCNPAGE<sup>54</sup>. d, e, SDS-PAGE profile of purified *MjFsr* (d,  $n = 1$  independent experiment) and *MtFsr* (e,  $n = 3$  independent experiments). f, UV-visible spectrum of 0.33 mg *MtFsr* measured anaerobically (100 % N<sub>2</sub>) in 25 mM Tris-HCl, pH 7.6, 150 mM NaCl, 10 % v/v glycerol and 2 mM DTT. *MtFsr* displays the typical spectra of [Fe-S]-cluster and siroheme containing enzymes<sup>55</sup>, similar to the UV spectrum of *MjFsr* previously determined exhibiting three peaks at 280 nm, 395 nm and 593 nm<sup>5</sup>. g, Molecular weight estimation of *MtFsr* via size exclusion chromatography (Superdex 200 Increase 10/300 GL from GE Healthcare). Apparent molecular weight of purified *MtFsr* (monomeric molecular weight = 69.145 kDa) was estimated to 282 kDa. *MtFsr* is therefore apparently organized as a homotetramer (theoretical molecular weight of the protein in the homotetramer: 276.58 kDa).

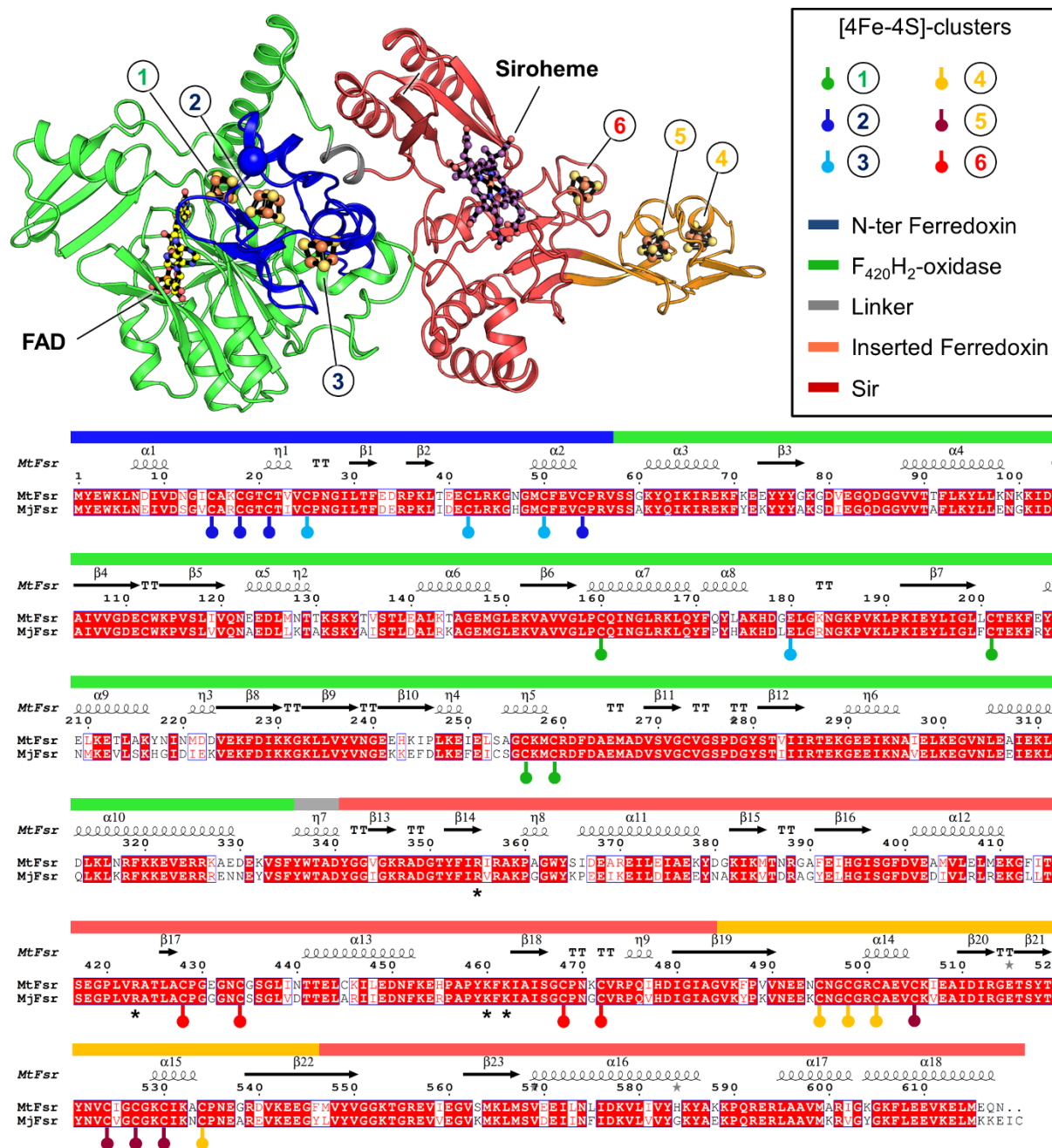


**Extended Data Figure 3. Homotetrameric arrangement of Fsr.** a, Superposition of *MtFsr* (black) with *MjFsr* (orange, rmsd of 0.456 Å for 544-C $\alpha$  aligned). Ligands are shown in balls and sticks and coloured in black and orange for *MtFsr* and *MjFsr*, respectively. b, Surface area involved in the oligomerization in Fsr. Monomers of *MtFsr* are shown in surface representation, with one monomer being displayed in cartoon and coloured by its domain composition: the N-terminal ferredoxin domain in dark blue, F<sub>420</sub>H<sub>2</sub>-oxidase in green, the sulfite reductase domain in red and its inserted ferredoxin domain in orange. The C-terminal segment involved in the oligomerization is coloured in light pink with the C-terminus highlighted as a ball. The monomer-monomer contacts are shown as a green surface and contacts to the adjacent dimer are visualized by a cyan surface. The basic monomer-monomer interface of 2,902-Å<sup>2</sup> for *MtFsr* and 2,971-Å<sup>2</sup> for *MjFsr* is established by the sulfite reductase domain and the two additional ferredoxin domains. The C-terminal part of the sulfite reductase domain (562–618 in *MtFsr*, 562–620 in *MjFsr*), the second ferredoxin domain and the loop 171–189 of the F<sub>420</sub>H<sub>2</sub>-oxidase domain generate the dimer-dimer interface, totalling an area of 3,055-Å<sup>2</sup> for *MtFsr* and 3,037-Å<sup>2</sup> for *MjFsr*. Most of these contacts involve salt bridges. In *MjFsr*, the tetrameric structure is supported by two divalent cations, modelled as calcium ions that are each coordinated by a conserved aspartate from the opposite monomers (Asp511 and water molecules)<sup>56</sup>.

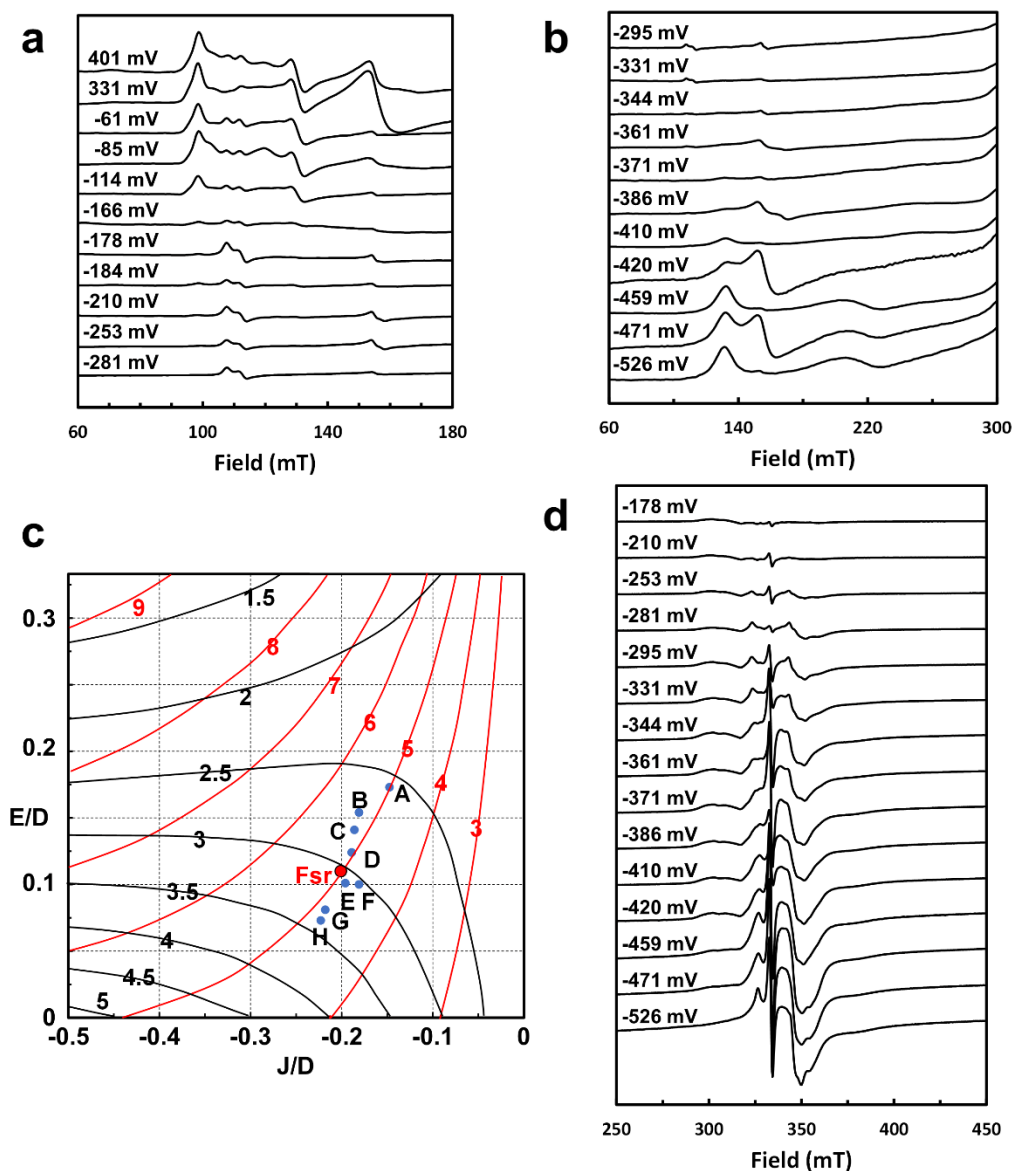


**Extended Data Figure 4. Asymmetric unit content and B-factor profile of *MtFsr*.** a, The four homotetramers contained in the asymmetric unit of *MtFsr* are shown in cartoon and the 96 [4Fe-4S]-clusters, the 16 FADs (in yellow) and 16 sirohemes (in pink) are shown in balls and sticks. To our knowledge, *MtFsr* contains the highest number of clusters seen in an asymmetric unit so far. b, Superposition of all sixteen chains from the asymmetric unit in *MtFsr*, with an average rmsd of 0.14 Å for 514-C $\alpha$  aligned. The N- and C-terminus of each chain are shown by a blue and red sphere, respectively. The models are coloured according to their B-factor values; blue to red indicate low to high B-factors, respectively. c, Averaged B-factor values (in black) for each residue from the 16 chains composing the asymmetric unit of *MtFsr*. The averaged root mean square deviations (rmsd, in red) of the corresponding C $\alpha$  is overlaid on the same graph. Averaged rmsd were calculated by the software superpose<sup>57</sup>.

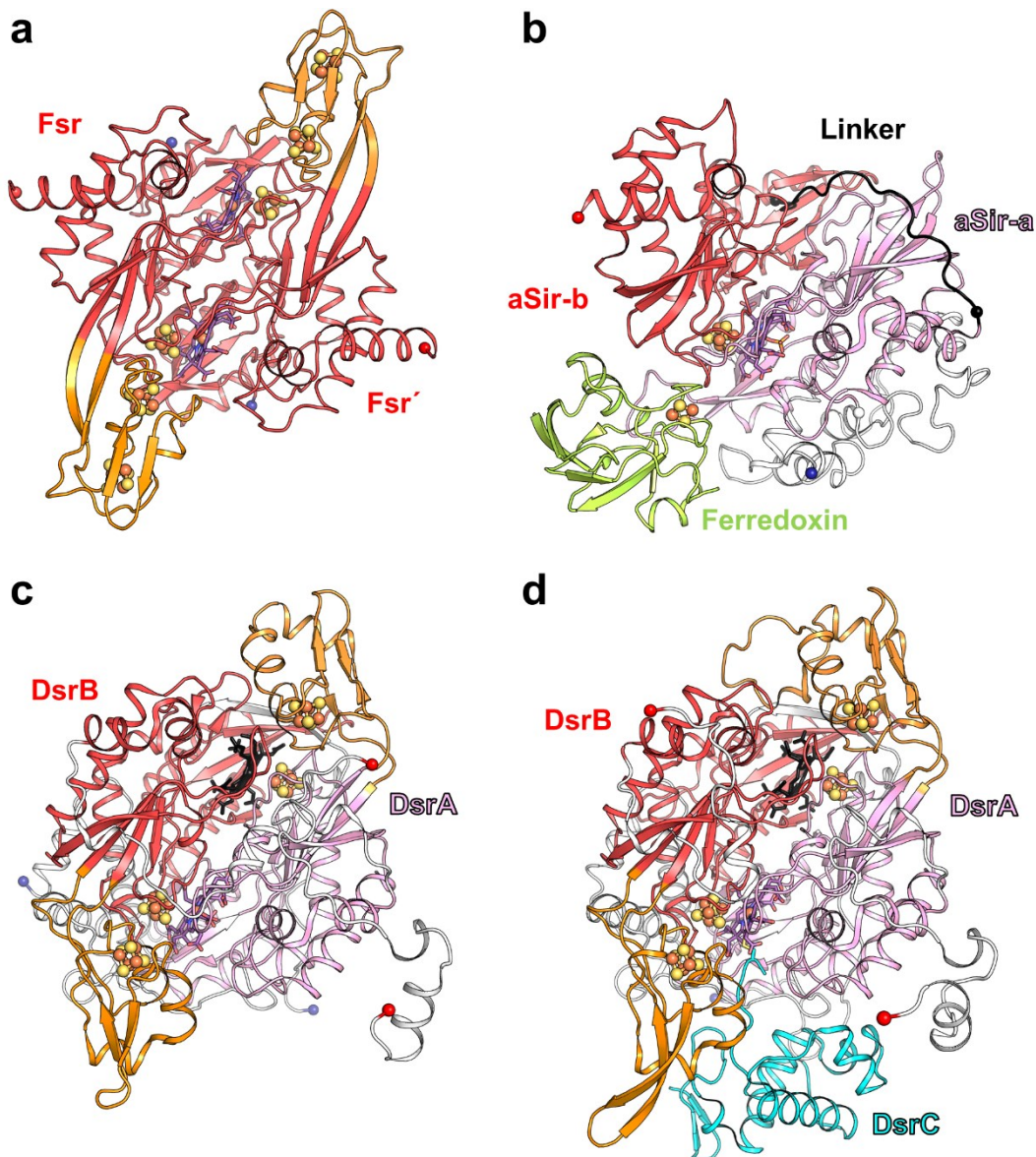




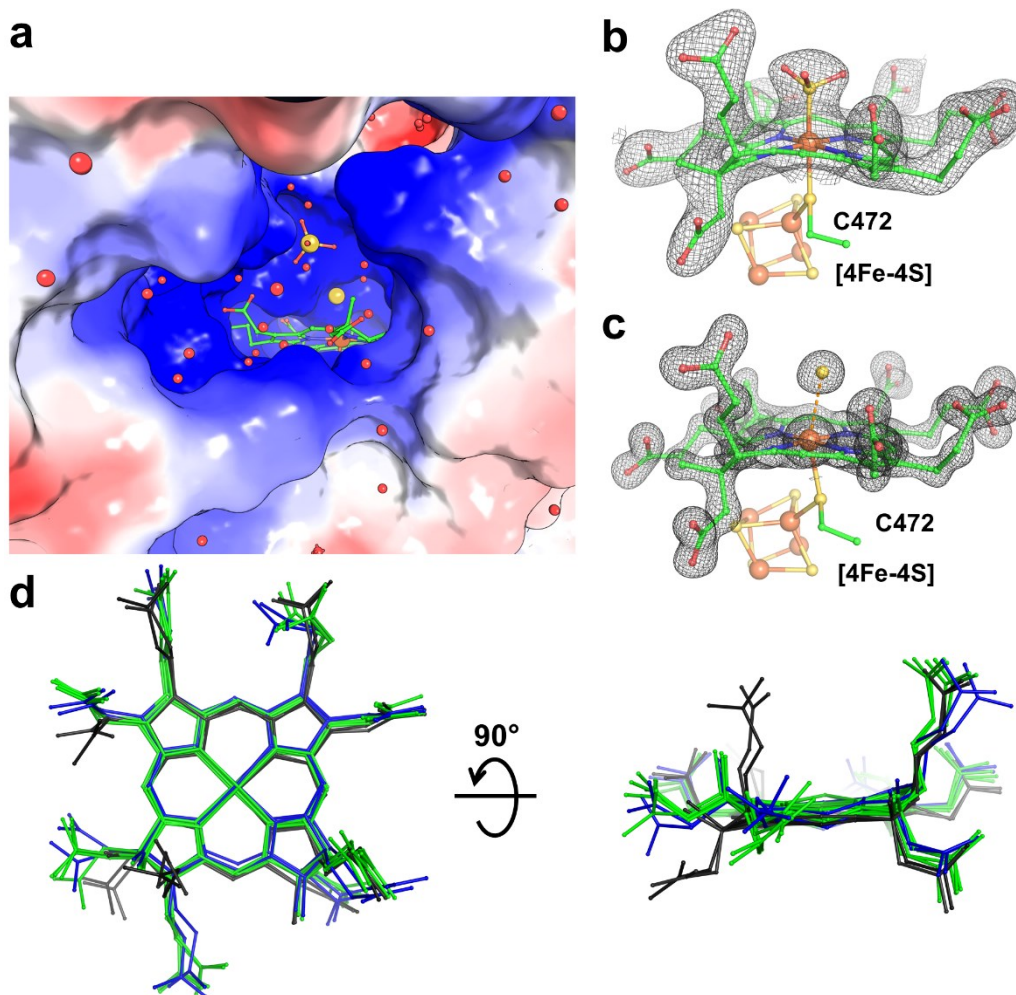
**Extended Data Figure 5. Cluster coordination in Fsr.** The top panel shows the monomeric arrangement of *MtFsr* (in cartoon) coloured by domains. The siroheme (purple), FAD (yellow) and the [4Fe-4S]-clusters are represented in balls and sticks. Nitrogen, oxygen, sulfur, and iron atoms are coloured respectively, in blue, red, yellow and orange. In the bottom panel, cysteines and the glutamate involved in direct [4Fe-4S]-cluster binding are highlighted, as well as the different domains of Fsr. Sequence alignment was done by Clustal Omega<sup>58</sup>, secondary structure prediction was performed with ESPrpt 3.0<sup>59</sup>. Cluster 6 is electronically connected to the siroheme. The black stars (\*) indicate residues near the siroheme, proposed to bind SO<sub>3</sub><sup>2-</sup>.



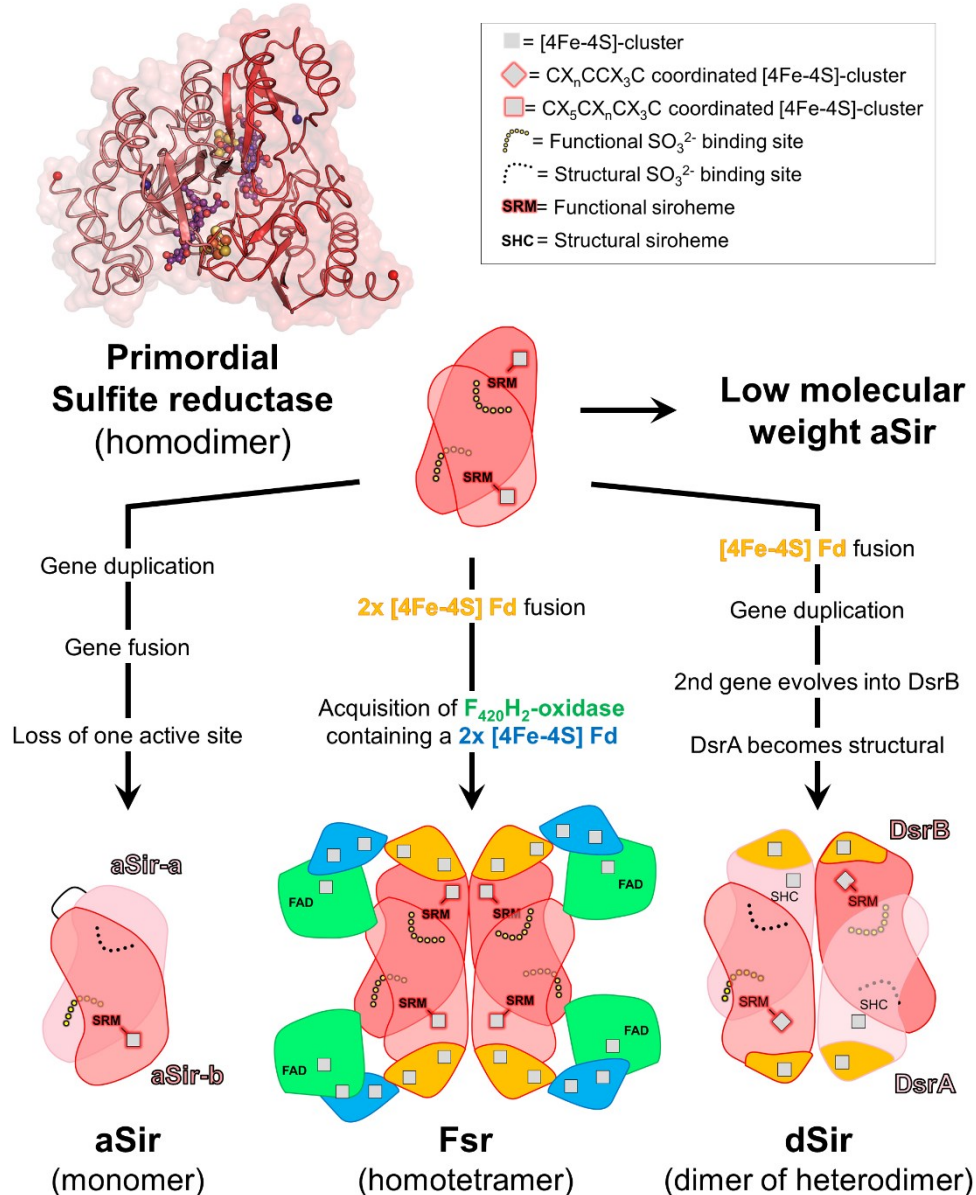
**Extended Data Figure 6. EPR spectra of the dye-mediated redox titrations of *MtFsr* and *g*-values as function of *J/D* and *E/D* as described by J. A. Christner et al. 1984.** a, b and d The redox potentials at which samples were frozen are indicated. EPR intensities were scaled to correct for differences in concentration. EPR conditions: temperature, 10 K; modulation frequency, 100 kHz; modulation amplitude, 1.0 mT; microwave frequency, 9.353 GHz; microwave power, 20 mW (panel d 0.2 mW). c, Contours of the two highest *g*-values of the coupled ferrous siroheme-[4Fe-4S]<sup>1+</sup> system as function of *J/D* and *E/D* according to Fig. 4 from<sup>32</sup>. The blue points are from *E. coli* sulfite reductase: A and B, KCl (two species); C, KF or KBr; E, urea; F, sodium formate; G, (Gdm)<sub>2</sub>SO<sub>4</sub>; H, KBr; D, spinach nitrite reductase; *MtFsr* is shown as red point.



**Extended Data Figure 7. Overall structural comparison between Fsr, aSir and dSir.** Cut-through view shown in cartoon of one dimer for Fsr and DsrAB. Ligands are shown as balls and sticks. a, The sulfite reductase domain with the inserted ferredoxin domain of *MtFsr*. Fsr' corresponds to the opposite monomer. b, aSir from *Zea mays* and its [2Fe-2S]-ferredoxin coloured in light green (PDB 5H92). c, DsrAB from *A. fulgidus* (PDB 3MM5) and d, DsrABC from *D. vulgaris* (PDB 2V4J). The inserted ferredoxin domains of Fsr, DsrA and DsrB are coloured in orange. The catalytic siroheme in DsrAB is coloured in purple and the structural siroheme is coloured in black. DsrAB from *D. vulgaris* contains sirohydrochlorin instead of siroheme.



**Extended Data Figure 8. Siroheme conformation within Fsr.** a, Electrostatic charge profile of *MtFsr* shown in surface is coloured in red and blue to represent acidic and basic patches, respectively. The siroheme is accessible via a positively charged solvent channel. Carbon, oxygen, nitrogen, sulfur and iron are coloured in green, red, blue, yellow and orange, respectively. b and c, Close up of the axial ligands bound on the siroheme of *MjFsr* (b) and *MtFsr* (c). The  $2F_o - F_c$  map of the siroheme and  $\text{SO}_3^{2-}$  are contoured to  $1.5\text{-}\sigma$  in *MjFsr*, while the siroheme and  $\text{HS}^-$  is contoured to  $3\text{-}\sigma$  in *MtFsr*. In *MjFsr* the Fe-siroheme is equidistant ( $2.3 \text{ \AA}$ ) to the sulfur from the modelled  $\text{SO}_3^{2-}$  and the bridging-sulfur of the cysteine 472, suggesting a tight covalent binding. In *MtFsr*, the bridging-sulfur of the cysteine 472 is at a distance of  $2.6 \text{ \AA}$  to the Fe-siroheme and the sulfur from the modelled  $\text{HS}^-$  is  $2.9 \text{ \AA}$  distant to the Fe-siroheme, indicating a loose binding of the  $\text{HS}^-$ , which might result from a reduction event by X-ray radiation<sup>60</sup>. d, Siroheme superposition between aSirs (1AOP, 5H92), dSirs (3MM5, 2V4J) and Fsr. Siroheme from aSirs and Fsr are coloured in green, structural siroheme/sirohydrochlorin from dSirs in black and dSirs functional sirohemes in blue. Superposition analysis shows that the functional sirohemes are arranged in a highly similar manner, whereas the conformation of the structural siroheme or sirohydrochlorin differ, which highlights the strong influence of the protein environment on the siroheme geometry.




**Extended Data Figure 9. Theoretical evolutionary scenario of sulfite reductases.** The proposed route is based on the assumption that aSir, dSir and Fsr could have evolved from a common ancestor. The primordial sulfite reductase model corresponds to the elementary sulfite reductase core of the *MtFsr* structure. The different steps that led to the evolution of this progenitor to modern Fsr can be hypothesized based on its modular organization. In a straightforward and simple model, a ferredoxin with 2 × [4Fe-4 S]-cluster could have been inserted into the elementary sulfite reductase module. Then an F<sub>420</sub>H<sub>2</sub>-oxidase with a ferredoxin domain (Fqo/FpoF-like) would have been fused to the N-terminus of the sulfite reductase domain containing the inserted ferredoxin. Some members of the Sir superfamily might have arisen from one of these steps<sup>18</sup>. Such a hypothesis is exemplified by the similarities between the quaternary organization of Fsr and DsrAB and the active site of Fsr and aSir.

	<i>MjFsr</i> SAD (Fe K edge)	<i>MjFsr</i>	<i>MtFsr</i>
<b>Data collection</b>			
Synchrotron source	SOLEIL, PX1	SOLEIL, PX1	SLS, PXIII
Wavelength (Å)	1.74013	0.97857	1.00004
Space group	<i>C</i> 222 <sub>1</sub>	<i>C</i> 222 <sub>1</sub>	<i>P</i> 1
Resolution (Å)	120.05 – 2.32 (2.54 – 2.32)	78.82 – 2.30 (2.41 – 2.30)	121.28 – 1.55 (1.69 – 1.55)
Cell dimensions			
a, b, c (Å)	167.34 172.34 196.01	167.26 172.20 195.89	113.15, 124.16, 241.06
α, β, γ (°)	90, 90, 90	90, 90, 90	102.28, 95.71, 90.25
R <sub>merge</sub> (%) <sup>a</sup>	37.4 (260.1)	25.1 (162.3)	18.3 (162.3)
R <sub>pim</sub> (%) <sup>a</sup>	10.3 (77.4)	7.0 (45.9)	7.5 (66.4)
CC <sub>1/2</sub> <sup>a</sup>	0.996 (0.596)	0.995 (0.629)	0.996 (0.439)
I/σ <sub>I</sub> <sup>a</sup>	10.4 (1.5)	8.3 (1.6)	8.7 (1.5)
Spherical completeness <sup>a</sup>	74.8 (15.9)	83.2 (32.3)	75.5 (16.6)
Ellipsoidal completeness <sup>a</sup>	95.0 (66.7)	96.0 (94.8)	94.5 (70.9)
Redundancy <sup>a</sup>	26.9 (22.7)	13.9 (13.2)	7.0 (6.9)
Nr. unique reflections <sup>a</sup>	91,281 (4,565)	104,064 (5,203)	1,396,397 (69,018)
<b>Refinement</b>			
Resolution (Å)		64.67 – 2.30	77.29 – 1.55
Number of reflections		104,036	1,396,186
R <sub>work</sub> /R <sub>free</sub> <sup>b</sup> (%)		18.15/20.43	15.88/17.11
Number of atoms			
Protein		19,554	79,363
Ligands/ions		920	3,554
Solvent		772	10,772
Mean B-value overall (Å <sup>2</sup> )		42.44	26.62
Mean B-value ligands (Å <sup>2</sup> )		46.27	23.47
Mean B-value solvent (Å <sup>2</sup> )		39.70	35.94
Molprobit clash score		1.64	3.22
Molprobit score		1.20	1.19
Rotamer outliers (%)		2.37	0.64
Ramachandran plot			
Favoured regions (%)		98.42	97.65
Outlier regions (%)		0	0
rmsd <sup>c</sup> bond lengths (Å)		0.010	0.011
rmsd <sup>c</sup> bond angles (°)		1.38	1.37
<b>PDB ID code</b>		7NP8	7NPA

<sup>a</sup>Values relative to the highest resolution shell are within parentheses. <sup>b</sup>R<sub>free</sub> was calculated as the R<sub>work</sub> for 5% of the reflections that were not included in the refinement. <sup>c</sup>rmsd, root mean square deviation.

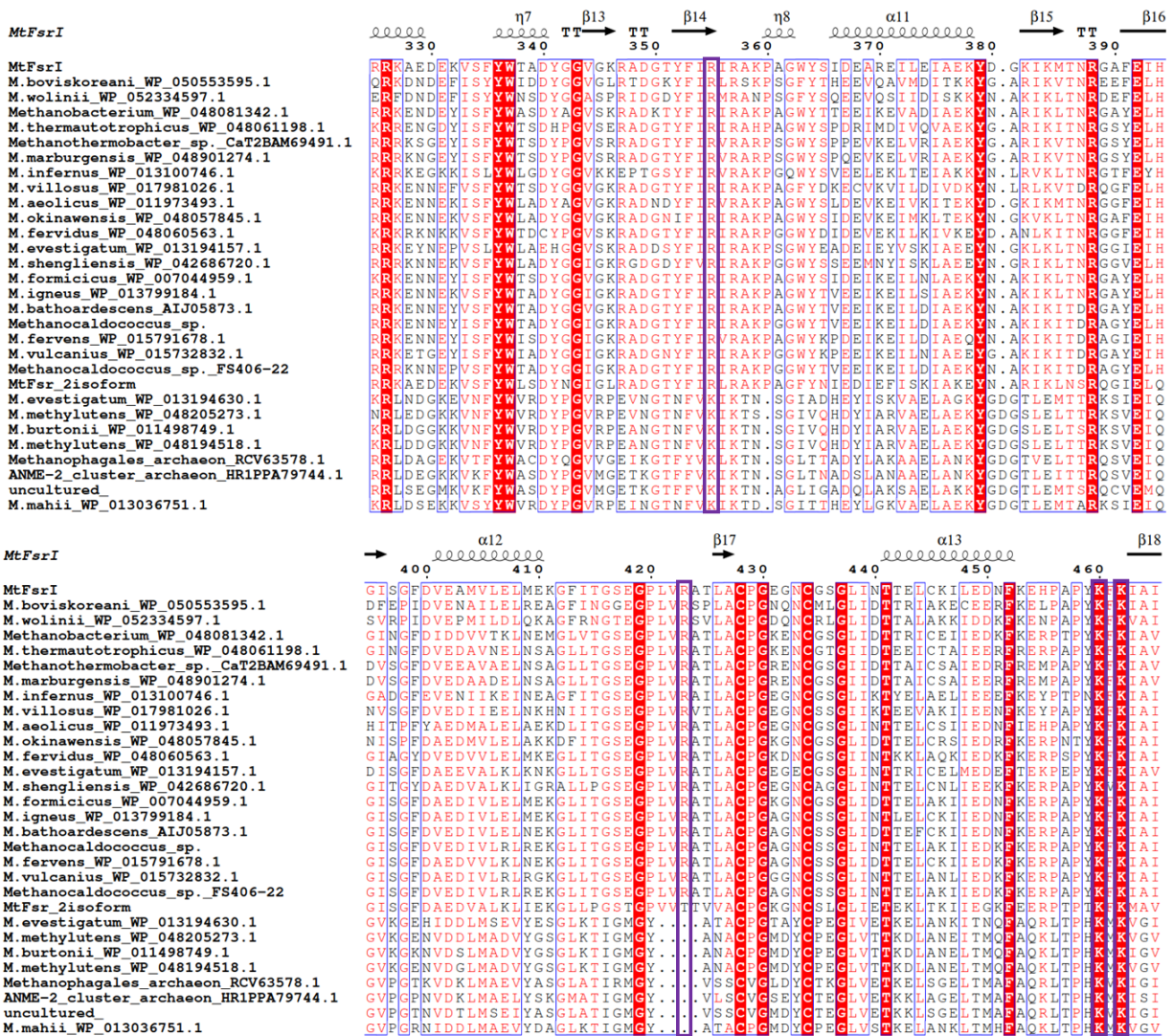
## Supplementary Information



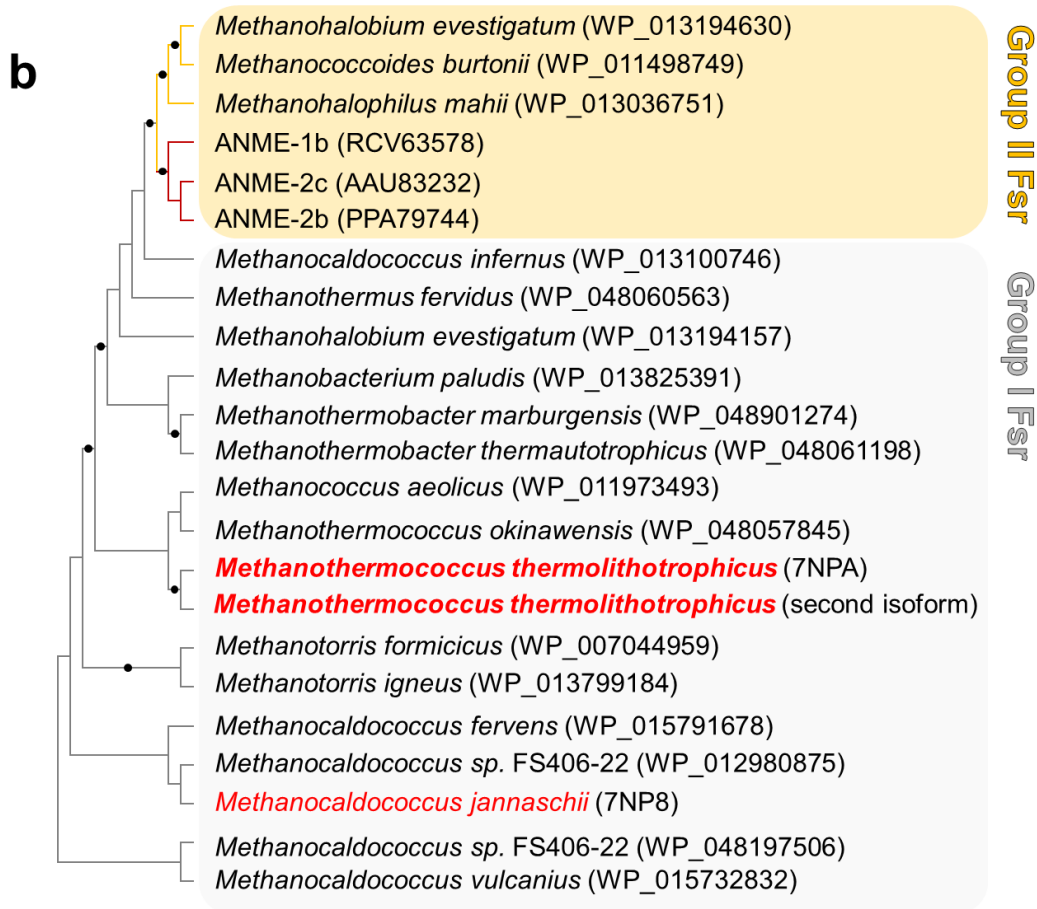
<b>F<sub>420</sub>-oxidoreductases</b>	<b>Sulfite reductases</b>	<b>Biological function</b>
F <sub>420</sub> -oxidase domain of Fsr Group I and II <sup>1</sup>	Group I Fsr <sup>1</sup>	detoxification/assimilatory
F <sub>420</sub> -reducing [NiFe(Se)]-hydrogenases (FrhB) <sup>2</sup>	Group II Fsr <sup>7</sup>	unknown
F <sub>420</sub> H <sub>2</sub> :quinone oxidoreductase (FqoF) <sup>3</sup>	DsrA <sup>8,9</sup>	dissimilatory (inactive)
F <sub>420</sub> H <sub>2</sub> :phenazine oxidoreductase (FpoF) <sup>4</sup>	DsrB <sup>8,9</sup>	dissimilatory
F <sub>420</sub> -dependent glutamate synthase (GOGAT) <sup>5</sup>	ArsC <sup>1</sup>	dissimilatory
Formate dehydrogenase (FdhB) <sup>6</sup>	aSir/Group I Dsr-LP <sup>5</sup>	assimilatory
	Group III Dsr-LP <sup>5</sup>	unknown
	aSir <sup>10,11</sup>	assimilatory

**Supplementary Figure 1.** Domain affiliations of the F<sub>420</sub>-dependent sulfite reductase (Fsr). Top panel, Fsr domain organization. Its N-terminal half belongs to the F<sub>420</sub>-oxidoreductases (left table) as the F<sub>420</sub>-reducing hydrogenase  $\beta$ -subunit (FrhB), together with the F<sub>420</sub>H<sub>2</sub>:quinone oxidoreductase (FqoF), the F<sub>420</sub>H<sub>2</sub>:phenazine oxidoreductase (FpoF), the putative F<sub>420</sub>-dependent glutamate synthase and formate dehydrogenase (GOGAT and FdhB). Its C-terminal half corresponds to the sulfite reductases (right table). Sulfite reductases are generally classified into assimilatory or dissimilatory. Group I Fsr: Group I F<sub>420</sub>-dependent sulfite reductase, Group II Fsr: Group II F<sub>420</sub>-dependent sulfite reductase, DsrA: dissimilatory sulfite reductase  $\alpha$ -Subunit, DsrB: dissimilatory sulfite reductase  $\beta$ -Subunit, ArsC: anaerobic sulfite reductase subunit C, aSir/Group I Dsr-LP: assimilatory-type low-molecular-weight sulfite reductase/Group I dissimilatory sulfite reductase-like proteins, Group III Dsr-LP: Group III dissimilatory sulfite reductase-like proteins, aSir: assimilatory sulfite reductase. References<sup>5-15</sup> are cited accordingly.

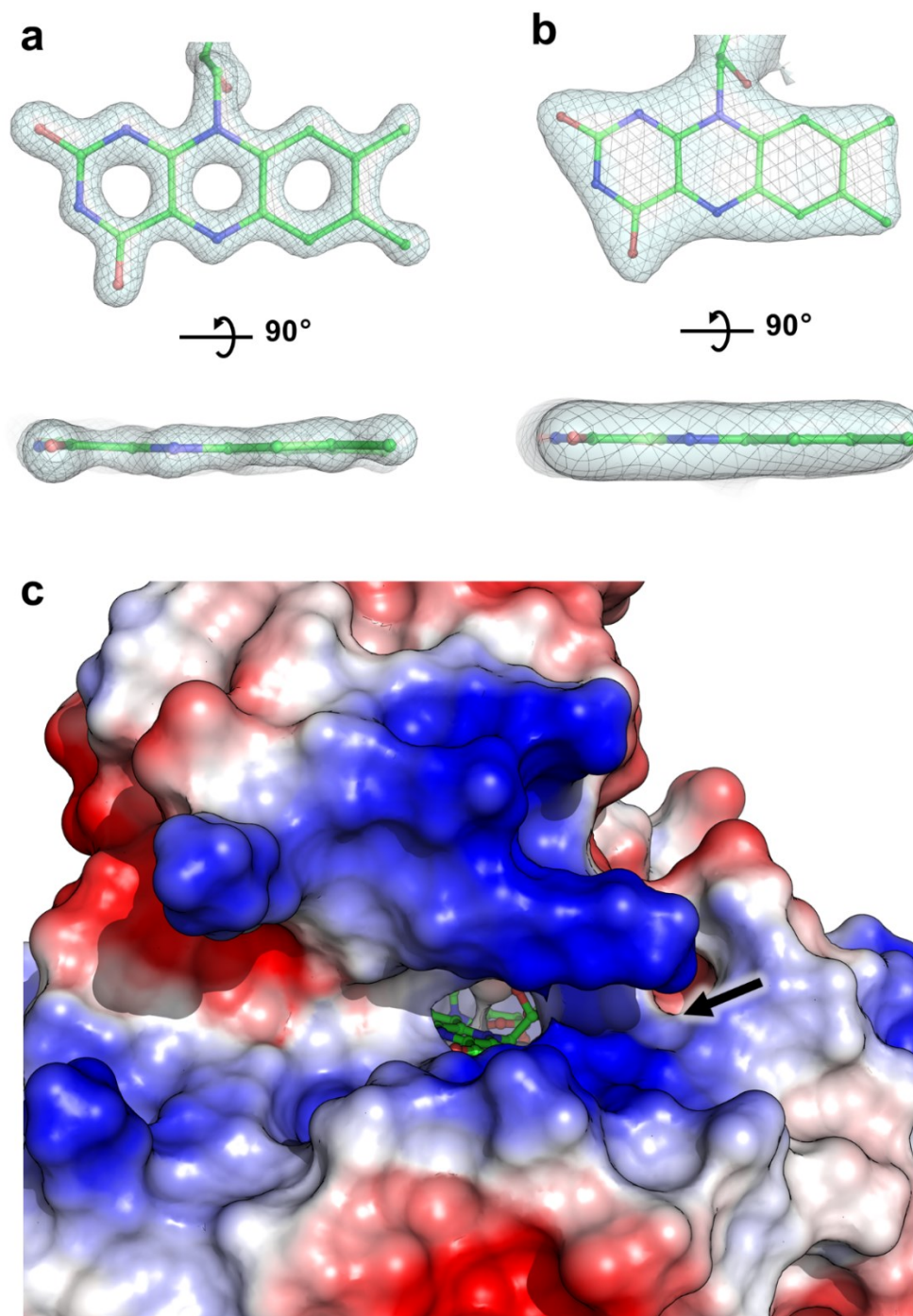
a



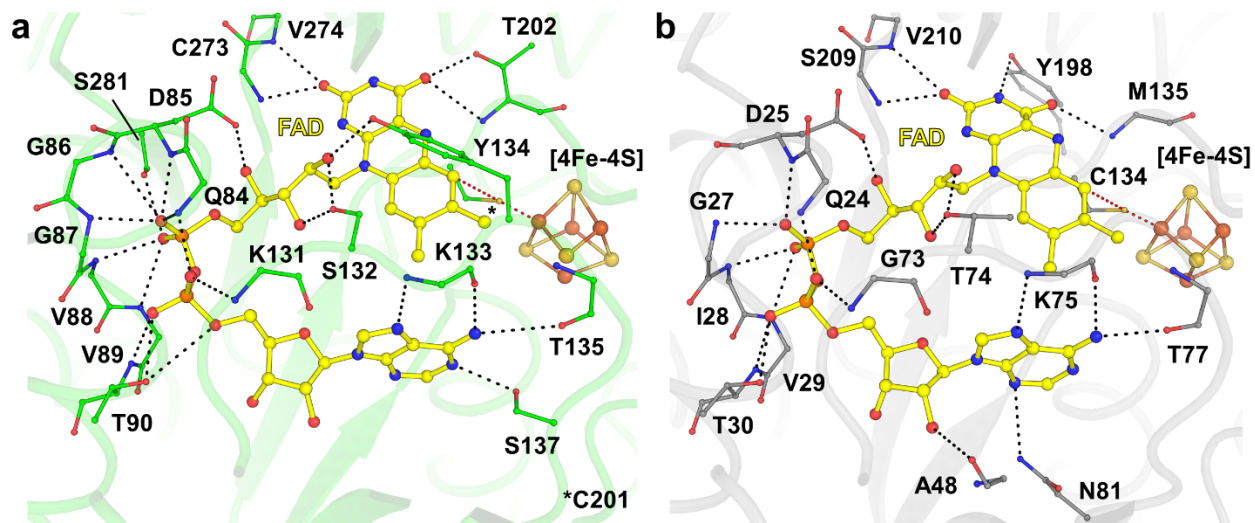




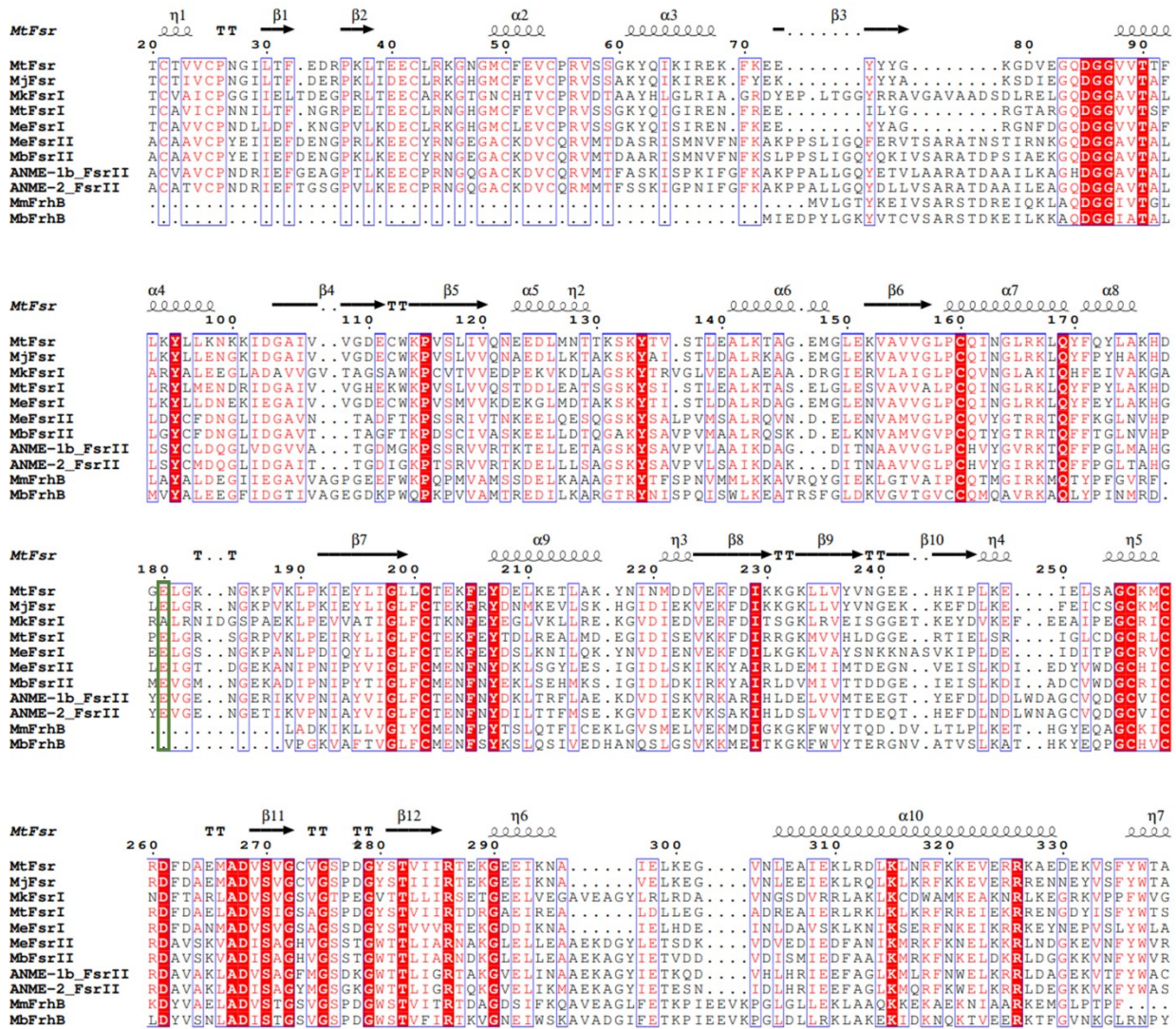
**Supplementary Figure 2.** Differences between Group I and II Fsr. **a**, Sequence conservation across Group I and II Fsr on a selected stretch from the sulfite reductase domain. Perfectly conserved residues are highlighted with a red background. The purple squares highlight the four perfectly conserved residues across functional sulfite reductases (in *M. thermolithotrophicus*: Arg355, Arg423, Lys460 and Lys462). Sequence alignment was done using Clustal Omega<sup>16</sup>, secondary structure prediction was performed with ESPript 3.0<sup>17</sup>. **b**, A neighbor-joining tree was constructed based on the phylogenetic analysis from Yu et al<sup>11</sup>, including the two Fsr sequences from *M. thermolithotrophicus* (in bold red). Protein sequences were obtained from NCBI using BLASTP (E-value cut-off of 1e1), the sequences were then aligned using MUSCLE<sup>18</sup>. Phylogenetic analysis were performed using MEGA11<sup>19</sup>. Protein accession numbers from the NCBI database are shown in parentheses and black dots on the branches represent bootstrap values  $\geq 90\%$ .



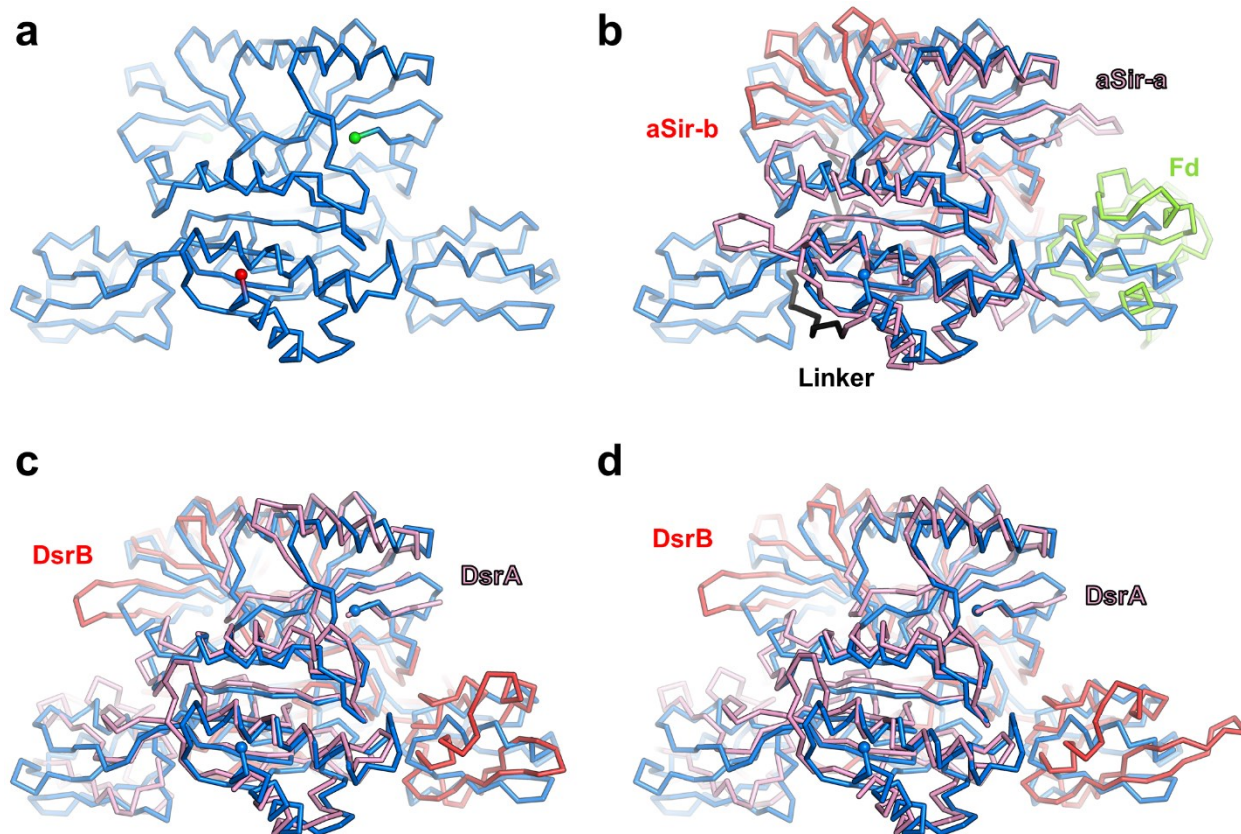
**Supplementary Figure 3.** The Flavin conformation and F<sub>420</sub> docking site. **a** and **b**,  $2F_o-F_c$  map for the FAD in *MtFsr* and *MjFsr* contoured to 3- and 1.5- $\sigma$ , respectively. The isoalloxazine heterocycle is only slightly bent. **c**, Electrostatic charge profile around the F<sub>420</sub>H<sub>2</sub>-oxidase active site in *MtFsr*. Acidic to basic patches on the surface are coloured in red and blue, respectively. The F<sub>420</sub>H<sub>2</sub> is suspected to bind to the positively charged area (indicated by a black arrow) surrounding the FAD.



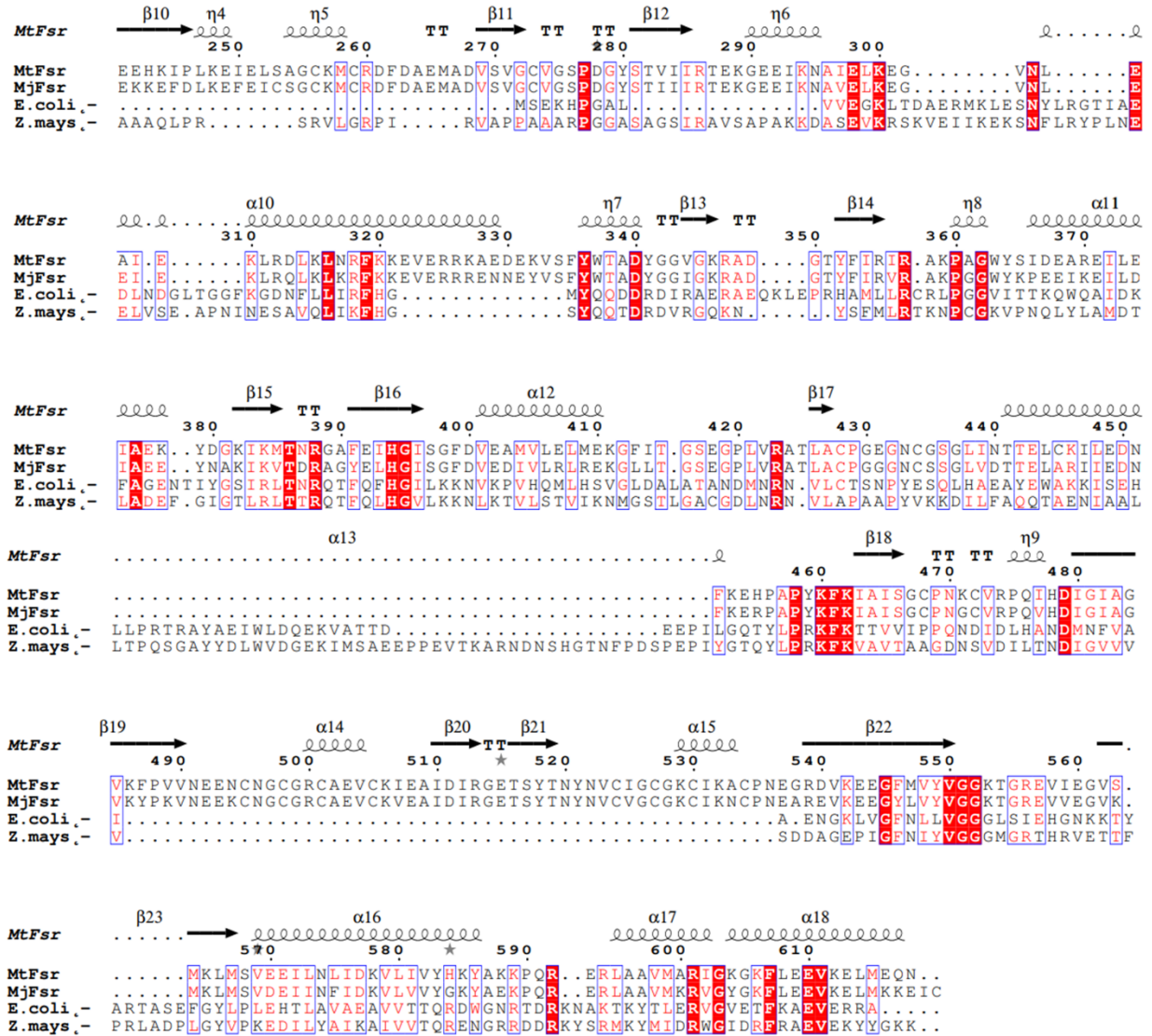
**Supplementary Figure 4.** Comparison of the FAD binding site of the F<sub>420</sub>H<sub>2</sub>-oxidase domain from *MtFsr* and FrhB from *M. marburgensis*. **a**, Close-up of the FAD binding site in the F<sub>420</sub>H<sub>2</sub>-oxidase domain from *MtFsr*. **b**, FAD binding in FrhB from *M. marburgensis* (PDB 4OMF). The residues binding the FAD are represented in balls and sticks and hydrogen bonds involved in FAD binding are shown by black dashes. The connection between the [4Fe-4S]-cluster I and the isoalloxazine ring from the FAD, established by a cysteine, are shown by red dashes.



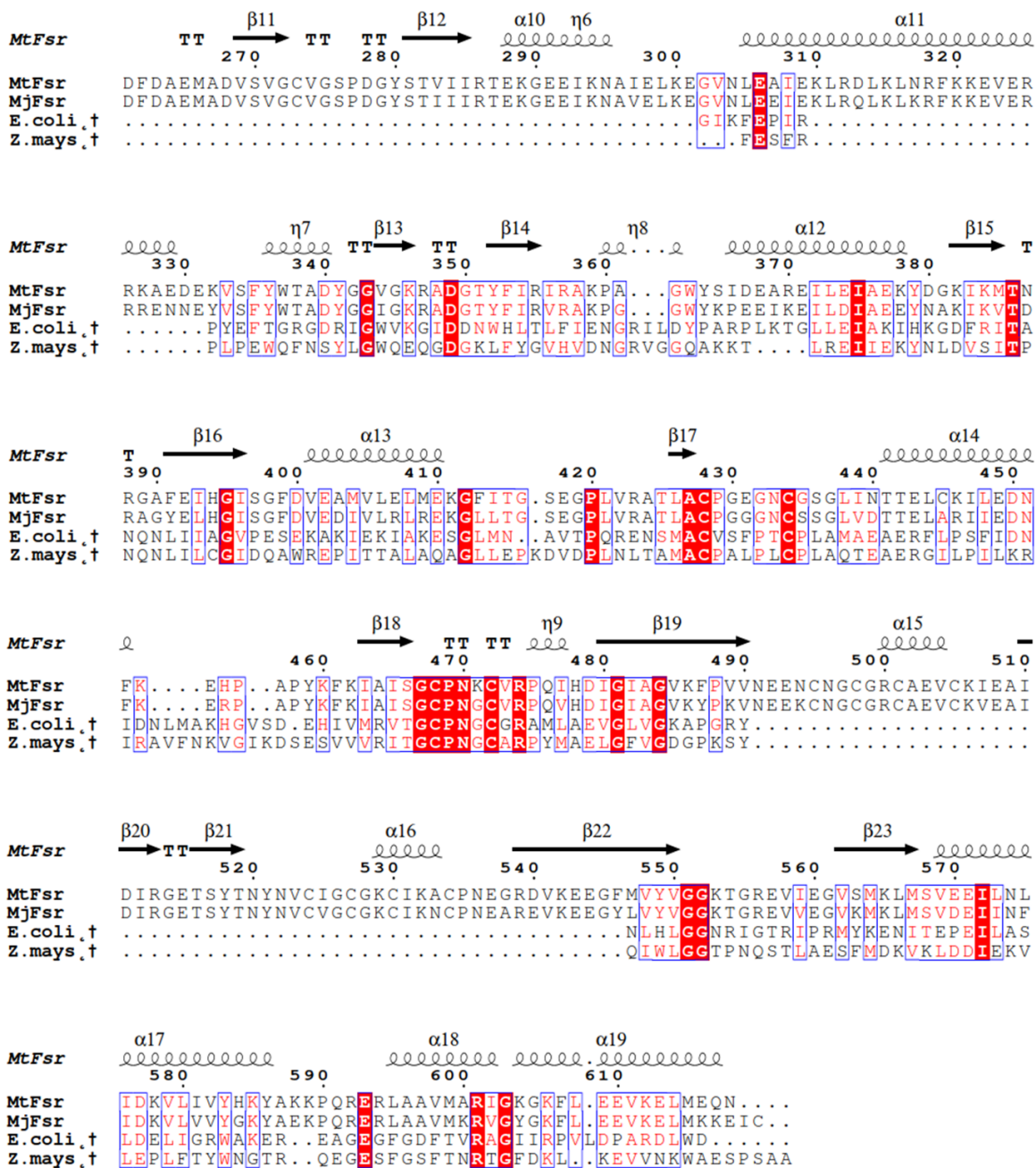
**Supplementary Figure 5.** Sequence conservation across Group I and II Fsr as well as FrhB. Perfectly conserved residues are highlighted with a red background. The glutamate involved in the [4Fe-4S]-cluster 3 binding is shown by a green square. MtFsr: *M. thermolithotrophicus*, MjFsr: *M. jannaschii* (Q58280.1); MkFsrI: *Methanopyrus kandleri* (WP\_011019168.1); MtFsrI: *Methanothermobacter marburgensis* (ADL58324.1); MeFsrI: *Methanohalobium evestigatum* (WP\_013194157.1); MeFsrII: *Methanohalobium evestigatum* (WP\_013194630.1); MbFsrII: *Methanococcoides burtonii* (WP\_011498749.1); ANME-1b\_FsrII: Fsr from Methanophagales archaeon belonging to ANME-1 cluster (RCV63578.1); ANME-2\_FsrII, Fsr from ANME-2 cluster archaeon HR1 (PPA79744.1); MmFrhB: *Methanothermobacter marburgensis* (ADL59254.1); MbFrhB *Methanosarcina barkeri* (WP\_048177139.1). Sequence alignment was done using Clustal Omega<sup>20</sup>, secondary structure prediction was performed with ESPrnt 3.0<sup>17</sup>.



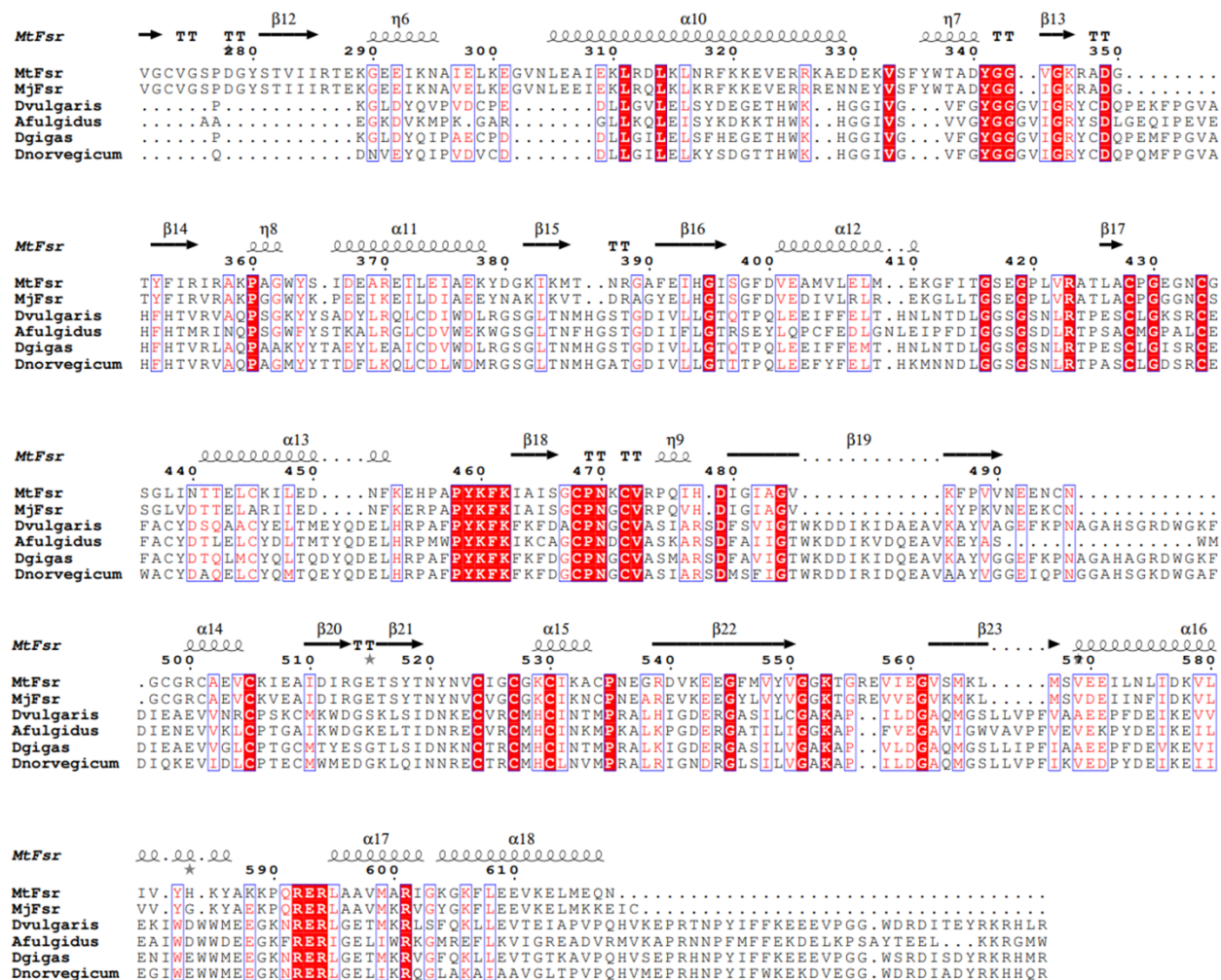
**Supplementary Figure 6.** Fsr shares the common fold of sulfite reductases. **a**, The dimeric sulfite reductase domains of *MtFsr* with its inserted ferredoxin domains are represented in blue ribbon. N- and C-terminus of the Sir domain are shown in green and red spheres, respectively. **b**, Overall superposition of dimeric *MtFsr* (blue) with the aSir from *Zea mays* (PDB 5H92, whole chain rmsd=2.434 Å for 142-C $\alpha$  aligned and a rmsd=0.964 Å for the most conserved region with 47-C $\alpha$  aligned). The aSir-a part from *Zea mays* is coloured in light pink, and the aSir-b part is coloured in red. **c**, Overall superposition of dimeric *MtFsr* with DsrAB (DsrA in pink, DsrB in red) from *Archaeoglobus fulgidus* (PDB 3MM5, whole chain rmsd=4.152 Å for 225-C $\alpha$  aligned and an rmsd=0.921 Å with 53-C $\alpha$  aligned for the most conserved region on one *MtFsr* monomer). **d**, Overall superposition of dimeric *MtFsr* with DsrAB (DsrA in pink, DsrB in red) from *Desulfovibrio vulgaris* (PDB 2V4J, whole chain rmsd=2.819 Å for 157-C $\alpha$  aligned and a rmsd=0.961 Å with 51-C $\alpha$  aligned for the most conserved region on one *MtFsr* monomer). b-d, The extensions contained in aSir and DsrAB which are not common to Fsr have been removed for clarity.



**Supplementary Figure 7.** Sequence conservation across the C-terminal half of Fsr (*MtFsr*: 241-618) and aSir-a. Perfectly conserved residues are highlighted with a red background. *MtFsr*: *M. thermolithotrophicus*; *MjFsr*: *M. jannaschii*; *Z.mays*: *Zea mays* (PDB 5H92, for residues: 1-392); *E.coli*: *Escherichia coli* (PDB 2GEP, for residues: 1-327). Sequence alignment was done using Clustal Omega<sup>20</sup>, secondary structure representation was performed with ESPript 3.0<sup>17</sup>. Arg355 seems not conserved in *E. coli* and *Z. mays* due to a shift of 2 residues in the alignment.

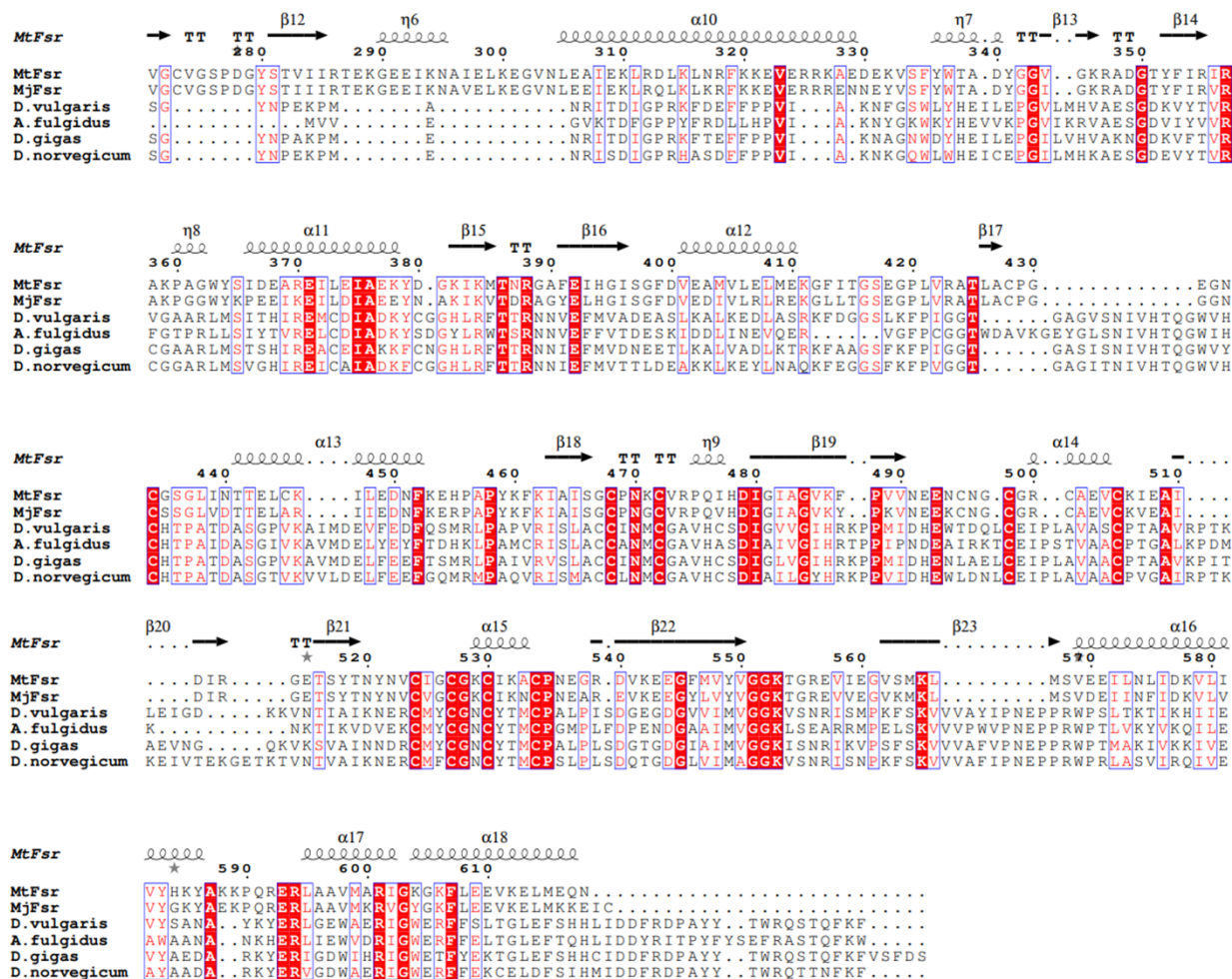


**Supplementary Figure 8.** Sequence conservation across the C-terminal half of Fsr (*MtFsr*: 261-618) and aSir-b. Perfectly conserved residues are highlighted with a red background. *MtFsr*: *M. thermolithotrophicus*; *MjFsr*: *M. jannaschii*; *Z. mays*: *Zea mays* (PDB 5H92, used residues: 393-653); *E.coli*: *Escherichia coli* (PDB 2GEP, shown residues: 328-570). Sequence alignment was done using Clustal Omega<sup>20</sup>, secondary structure representation was performed with ESPrict 3.0<sup>17</sup>.

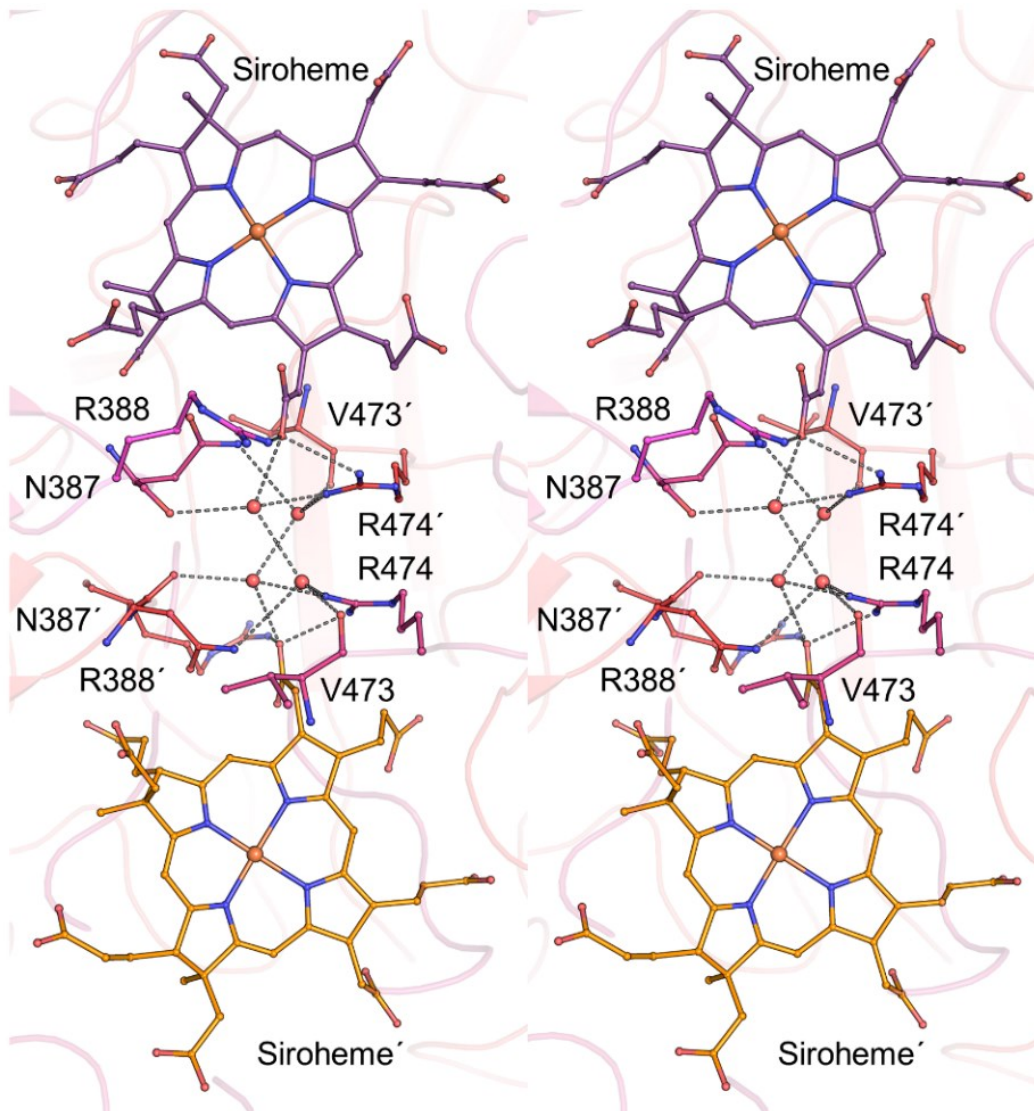


**Supplementary Figure 9.** Sequence conservation across the C-terminal half of Fsr (*MtFsr*: 271-618) and DsrA. Perfectly conserved residues are highlighted with a red background. *MtFsr*: *M. thermolithotrophicus*; *MjFsr*: *M. jannaschii*. *Dvulgaris*: *D. vulgaris* (PDB 2V4J); *Afulgidus*: *Archaeoglobus fulgidus* (PDB 3MM5); *Dgigas*: *Desulfovibrio gigas* (PDB 3OR1); *Dnorvegicum*: *Desulfomicrobium norvegicum* (PDB 2XSJ). Sequence alignment was done using Clustal Omega<sup>20</sup>, secondary structure representation was performed with ESPrift 3.0<sup>17</sup>. Arg355 seems not conserved due to a shift of one residue.





**Supplementary Figure 10.** Sequence conservation across the C-terminal half of Fsr (*MtFsr*: 271-618) and DsrB. Perfectly conserved residues are highlighted with a red background. *MtFsr*: *M. thermolithotrophicus*; *MjFsr*: *M. jannaschii*. *D.vulgaris*: *Desulfovibrio vulgaris* (PDB 2V4J); *A.fulgidus*: *Archaeoglobus fulgidus* (PDB 3MM5); *D.gigas*: *Desulfovibrio gigas* (PDB 3OR1); *D.norvegicum*: *Desulfomicrobium norvegicum* (PDB 2XSJ). Sequence alignment was done using Clustal Omega<sup>20</sup>, secondary structure representation was performed with ESPript 3.0<sup>17</sup>. Arg355 seems not conserved in *A. fulgidus*, *D. vulgaris* and *D. norvegicum* due to a shift of two residues.



**Supplementary Figure 11.** Stereo view of the intra-dimeric sirohemes in *MtFsr*, in which each chain is differently coloured. Primed labels indicate residues belonging to the dimeric partner. Sirohemes, water and residues involved in the channel are represented as balls and sticks. The distance between the two closest siroheme carboxylate groups is 9.4 Å. This close contact would theoretically allow an internal electron transfer between both sirohemes.

**Supplementary Table 1.** Chemical list of reagents used in this article.

<b>Compound</b>	<b>Company</b>	<b>Catalog number</b>
Gas mixture N <sub>2</sub> /H <sub>2</sub> , 95:5	Air Liquide	ARCAL F5
Potassium ferricyanide	Sigma Aldrich	244023
Tris ultrapure	AppliChem	A1086
Methylene blue hydrate	Sigma Aldrich	66720
Resorufin	Sigma Aldrich	73144
Indigo carmine	Sigma Aldrich	131164
2-Hydroxy-1,4-naphthochinon	Sigma Aldrich	H46805
Sodium anthraquinone-2-sulfonate	Sigma Aldrich	123242
Phenosafranin	Sigma Aldrich	199648
Safranin T	Sigma Aldrich	S8884
Neutral red	Sigma Aldrich	N4638
Benzylviologen	Sigma Aldrich	271845
Methylviologen dichloride hydrate	Sigma Aldrich	856177
PD10 desalting (Sephadex GH-25)	Cytiva	17085101
Sodium sulfite	Sigma Aldrich	S4672
Copper (II) sulfate pentahydrate	Sigma Aldrich	209198
Disodium EDTA	AppliChem	131669
KCl	Roth	6781.1
NaCl	Roth	3957.1
NaHCO <sub>3</sub>	Roth	6885.1
CaCl <sub>2</sub> · 2 H <sub>2</sub> O	Roth/Merck	5239.1/1.02382.
MgCl <sub>2</sub> · 6 H <sub>2</sub> O	Roth	2189.1
NH <sub>4</sub> Cl	Merck	1,011,451,000
Nitrilotriacetic acid	Sigma Aldrich	72560
FeCl <sub>2</sub> · 4 H <sub>2</sub> O	Sigma Aldrich	380024
Na <sub>2</sub> SeO <sub>3</sub> · 5 H <sub>2</sub> O	Merck	1.06607
Na <sub>2</sub> WO <sub>4</sub> · 2 H <sub>2</sub> O	Merck	1,066,730,250
Na <sub>2</sub> MoO <sub>4</sub> · 2 H <sub>2</sub> O	Merck	1.06580.1000
Resazurin Sodium Salt	Sigma	R7017
PIPES	Roth	9156.4
Sodium hydroxide pellets	Applichem	131687-1211
Tris Hydrochlorid	Roth	90903
MES	Roth	4259.4
MnCl <sub>2</sub> · 4 H <sub>2</sub> O	Roth	T881.3
FeCl <sub>3</sub> · 6 H <sub>2</sub> O	Fluka	44944
CaCl <sub>2</sub> · 2 H <sub>2</sub> O	Roth/Merck	5239.1/1.02382.
CoCl <sub>2</sub> · 6 H <sub>2</sub> O	Roth	T889.2

ZnCl <sub>2</sub>	Merck	1,088,160,250
NiCl <sub>2</sub> · 6 H <sub>2</sub> O	Sigma Aldrich	654507
VCl <sub>3</sub>	Sigma Aldrich	208272
Sodium sulfite	Sigma Aldrich	71988
Sodium sulfate	Sigma Aldrich	1.06649
Sodium sulfide	Sigma Aldrich	407410
1.4-dithiothreitol	Neolab/BioFroxx	1111GR100
Bradford (Bio-Rad-Protein Assay)	Thermo Fisher	23246
Tris Hydrochlorid	Roth	90903
Ammoniumsulfate	Merck Applichem	1.01211
Glycerol	Applichem	141339.1211
di-Potassium hydrogen phosphate	Roth	P 749.2
Potassium dihydrogen phosphate	Roth	3904.01
Ammoniumhydrogencarbonat	Roth	T871.1
Tris	Serva	37181.02
Sodium borohydride	Sigma Aldrich	452882
HCl, 25%	Sigma Aldrich	100316
Tricine	Roth	6977.3
Bis-Tris	Roth	9140
Sodium deoxycholate	Fluka	30970
Dodecyl maltoside	Roth	CN26.2
Trypsin from bovine pancreas	Sigma Aldrich	T8003
Sodiumnitrite	Sigma Aldrich	31443

## References

- 1 Edgar, R. C. MUSCLE: a multiple sequence alignment method with reduced time and space complexity. *BMC Bioinformatics* **5**, 113, doi:10.1186/1471-2105-5-113 (2004).
- 2 Robert, X. & Gouet, P. Deciphering key features in protein structures with the new ENDscript server. *Nucleic Acids Res* **42**, W320-W324, doi:10.1093/nar/gku316 (2014).
- 3 Setzke, E., Hedderich, R., Heiden, S. & Thauer, R. K. H<sub>2</sub>: heterodisulfide oxidoreductase complex from *Methanobacterium thermoautotrophicum*. *Eur J Biochem.* **220**, 139-148, doi:10.1111/j.1432-1033.1994.tb18608.x (1994).
- 4 Fuchsman, C. A., Collins, R. E., Rocap, G. & Brazelton, W. J. J. P. Effect of the environment on horizontal gene transfer between bacteria and archaea. *PeerJ* **5** (2017).
- 5 Susanti, D. & Mukhopadhyay, B. An intertwined evolutionary history of methanogenic archaea and sulfate reduction. *PLoS One* **7**, doi:10.1371/journal.pone.0045313 (2012).
- 6 Johnson, E. F. & Mukhopadhyay, B. A new type of sulfite reductase, a novel coenzyme F<sub>420</sub>-dependent enzyme, from the methanarchaeon *Methanocaldococcus jannaschii*. *J Biol Chem* **280**, 38776-38786, doi:10.1074/jbc.M503492200 (2005).
- 7 Vitt, S. *et al.* The F<sub>420</sub>-reducing [NiFe]-hydrogenase complex from *Methanothermobacter marburgensis*, the first X-ray structure of a Group 3 family member. *Journal of Molecular Biology* **426**, 2813-2826, doi:10.1016/j.jmb.2014.05.024 (2014).
- 8 Brüggemann, H., Falinski, F. & Deppenmeier, U. Structure of the F<sub>420</sub>H<sub>2</sub>:quinone oxidoreductase of *Archaeoglobus fulgidus* identification and overproduction of the F<sub>420</sub>H<sub>2</sub>-oxidizing subunit. *Eur J Biochem* **267**, 5810-5814, doi:10.1046/j.1432-1327.2000.01657.x (2000).
- 9 Bäumer, S. *et al.* The F<sub>420</sub>H<sub>2</sub>:heterodisulfide oxidoreductase system from *Methanosarcina* species. 2-Hydroxyphenazine mediates electron transfer from F<sub>420</sub>H<sub>2</sub> dehydrogenase to heterodisulfide reductase. *Febs Lett* **428**, 295-298, doi:10.1016/s0014-5793(98)00555-9 (1998).
- 10 Raaijmakers, H. *et al.* Gene Sequence and the 1.8 Å Crystal Structure of the Tungsten-Containing Formate Dehydrogenase from *Desulfovibrio gigas*. *Structure* **10**, 1261-1272, doi:10.1016/S0969-2126(02)00826-2 (2002).
- 11 Yu, H. *et al.* Comparative genomics and proteomic analysis of assimilatory sulfate reduction pathways in anaerobic methanotrophic archaea. *Front Microbiol* **9**, 2917, doi:10.3389/fmicb.2018.02917 (2018).
- 12 Crane, B. R. & Getzoff, E. D. The relationship between structure and function for the sulfite reductases. *Curr Opin Struc Biol* **6**, 744-756, doi:10.1016/S0959-440x(96)80003-0 (1996).

- 13 Dhillon, A., Goswami, S., Riley, M., Teske, A. & Sogin, M. Domain evolution and functional diversification of sulfite reductases. *Astrobiology* **5**, 18-29, doi:10.1089/ast.2005.5.18 (2005).
- 14 Kim, J. Y., Nakayama, M., Toyota, H., Kurisu, G. & Hase, T. Structural and mutational studies of an electron transfer complex of maize sulfite reductase and ferredoxin. *J Biochem* **160**, 101-109, doi:10.1093/jb/mvw016 (2016).
- 15 Yoshimoto, A. & Sato, R. Studies on yeast sulfite reductase. I. Purification and characterization. *Biochim Biophys Acta* **153**, 555-575, doi:10.1016/0005-2728(68)90185-0 (1968).
- 16 Sievers, F. *et al.* Fast, scalable generation of high-quality protein multiple sequence alignments using Clustal Omega. *Mol Syst Biol* **7**, 539, doi:10.1038/msb.2011.75 (2011).
- 17 Robert, X. & Gouet, P. Deciphering key features in protein structures with the new ENDscript server. *Nucleic Acids Res* **42**, W320-324, doi:10.1093/nar/gku316 (2014).
- 18 Edgar, R. C. MUSCLE: a multiple sequence alignment method with reduced time and space complexity. *BMC Bioinformatics* **5**, 113, doi:10.1186/1471-2105-5-113 (2004).
- 19 Tamura, K., Stecher, G. & Kumar, S. MEGA11: Molecular Evolutionary Genetics Analysis Version 11. *Mol Biol Evol* **38**, 3022-3027, doi:10.1093/molbev/msab120 (2021).
- 20 Sievers, F. *et al.* Fast, scalable generation of high-quality protein multiple sequence alignments using Clustal Omega. *Molecular Systems Biology* **7**, doi:ARTN 53910.1038/msb.2011.75 (2011).

# Chapter V

## Structural elucidation of the dissimilatory sulfate-reduction pathway of an ethane-degrading microbial consortium

**Marion Jespersen<sup>1</sup>, Olivier N. Lemaire<sup>1</sup>, Cedric J. Hahn<sup>1</sup>, Gunter Wegener<sup>1,2,3</sup> and Tristan Wagner<sup>1\*</sup>**

<sup>1</sup> Max Planck Institute for Marine Microbiology, Bremen, Germany.

<sup>2</sup> MARUM, Center for Marine Environmental Sciences, University of Bremen, Bremen, Germany.

<sup>3</sup> Alfred Wegener Institute Helmholtz Center for Polar and Marine Research, Bremerhaven, Germany.

*Manuscript in preparation*

## Abstract

Sulfate-reducing bacteria act as electron sinks during the anaerobic oxidation of alkanes catalysed by archaeal symbionts, and thus play an important role in the sulfur and carbon cycles in marine sediments. Here, we report the structural elucidation of the cytosolic dissimilatory sulfate reduction machinery from an ethane-oxidizing microbial enrichment. An ATP-sulfurylase activates sulfate to adenosine 5'-phosphosulfate (APS), which is reduced to AMP and sulfite by an APS-reductase. A dissimilatory sulfite-reductase reduces sulfite to an activated sulfur species, thereby conserving energy. Although the reactions are conserved, the native enzymes show structural differences from their homologues. The most striking is an additional subunit of the ATP-sulfurylase that forms an  $\alpha_4\beta_4$ -complex, while the other two others show closer structural homology to archaeal counterparts. This work demonstrates that a complete cytosolic pathway can be structurally elucidated despite limited and heterogeneous biomass, highlighting future opportunities for biochemical characterisation of microbial transformations from non-isolated microorganisms.



## Introduction

Dissimilatory sulfate reduction is a well-established key process in the global sulfur cycle, and its role in controlling the flux of hydrocarbons from anaerobic sediments to the water column has been highlighted in reports over the last decade<sup>1,2</sup>. Consortia composed of *Halobacteriota* archaea and partner bacteria of the phylum *Desulfobacterota* carry out anaerobic oxidation of alkanes (AOA), such as methane (CH<sub>4</sub>) and ethane (C<sub>2</sub>H<sub>6</sub>), using SO<sub>4</sub><sup>2-</sup> as the final electron acceptor<sup>3,4</sup>. The archaea activate their substrate with the alkyl-Coenzyme M (CoM) reductase<sup>5</sup>. Due to the complexity of the reaction and the fate of the alkyl-CoM, these archaea are specialized for one or more types of hydrocarbons<sup>5</sup>. The oxidation of Alkyl-CoM to CO<sub>2</sub> generates reducing equivalents that need to be removed to avoid the collapse of the central catabolism. As the archaea are unable to directly couple alkane oxidation to SO<sub>4</sub><sup>2-</sup> reduction, they require a syntrophic interaction with sulfate-reducing bacteria (SRB) that act as electron sinks<sup>1,6,7</sup>.

The bacterium *Candidatus Desulfofervidus auxilii* is one of the few SRB that forms syntrophic partnerships with thermophilic alkanotrophs, and has been enriched with archaea that oxidize methane, ethane, propane or butane<sup>3,8,9</sup>. In these microbial consortia, AOA-derived electrons are proposed to be exchanged by direct interspecies electron transfer (DIET), as the consortia partners produce cytochromes and pilus-based nanowires observable by electron microscopy<sup>3,8-11</sup>. The transferred electrons are used in the sulfate dissimilatory pathway, which provides cellular energy to the bacteria (Fig. 1a).

According to the current metabolic model, the dissimilatory SO<sub>4</sub><sup>2-</sup> reduction pathway is organised by a chain of reactions requiring a total of 8 reducing equivalents. First, SO<sub>4</sub><sup>2-</sup> needs to enter the cell via a symport and is then activated by the ATP sulfurylase (ATPS) with adenosine triphosphate (ATP) to form adenosine 5'-phosphosulfate (APS) and pyrophosphate (PP<sub>i</sub>)<sup>12,13</sup>. The two-electron reduction of APS to AMP and sulfite (SO<sub>3</sub><sup>2-</sup>) is catalysed by the dissimilatory APS reductase (APSR). The SO<sub>3</sub><sup>2-</sup> is then further reduced by the dissimilatory sulfite reduction system. Unlike the assimilatory sulfite reductases, the dissimilatory enzymes (DsrAB or dSir) do not perform the unidirectional reduction of SO<sub>3</sub><sup>2-</sup> to S<sup>2-</sup> under physiological conditions<sup>14,15</sup>. It has been shown that DsrAB catalyses the first two-electron reduction step and transfers the intermediate sulfur species to the redox-active sulfur carrier protein DsrC, generating a trisulfide (Fig. 1b)<sup>16</sup>. The final

reduction to  $S^{2-}$  and the recycling of DsrC is likely to be mediated by the DsrMKJOP transmembrane complex<sup>17-19</sup>.

Studying the microbial consortium, rather than isolating both microbes (which is currently not possible for the archaeal partner), would provide valuable insights into metabolic interactions and electron transfer under environmentally relevant conditions. Anaerobic oxidation of ethane (AOE) performed by the thermophilic ethane-degrading consortium of the archaeon *Candidatus* *Ethanoperedens thermophilum* and *Ca. D. auxilii* represents an ideal model to study the whole metabolism and enzymes of the pathways, as recently shown by the characterization of the ethane-activating enzyme<sup>20</sup>. This enrichment has the fastest metabolic turnover reported so far, a complete genome and an established protocol for protein extraction.

Here we present the characterization of the main enzymes of the  $SO_4^{2-}$  dissimilatory pathway purified directly from the ethane-oxidizing enrichment culture and highlight differences with known structural homologues.

## Results

### Identification of $SO_4$ -dissimilatory enzymes from a microbial enrichment culture

This study targets the cytosolic enzymes responsible for  $SO_4^{2-}$  reduction in the ethane-degrading consortium. However, the structural and biochemical characterisation of the enzymes appears to be challenging given the diversity of organisms and the mixture of proteins present in the biological sample. As *Ca.* represents about 30-40 % of the population, and based on transcriptomic data indicating the expected high production of enzymes from catabolic pathways encoded in the bacterial genome (Fig. 1c), the  $SO_4$ -dissimilatory metabolism was investigated using the soluble proteome of the consortium. The slow growth of the cells made it challenging to obtain enough of the ethane-oxidizing biomass. Therefore, two anaerobic purification campaigns were performed to crystallise and biochemically characterize the most abundant proteins of the dissimilatory  $SO_4^{2-}$  reduction pathway. The APSR and the dissimilatory sulfite reductase from *Ca. D. auxilii* (respectively *Da*APSR and *Da*Dsr) were followed during native purification by their intrinsic properties. Specifically, for Dsr purification, we utilized heme staining since it was the only band

visible in the soluble extract (Extended Data Fig 1a). As for APSR, it was detected by typical sodium dodecyl sulfate-polyacrylamide gel electrophoresis (SDS-PAGE) profiling, noting its brown colour and significant abundance. In contrast, the less abundant ATPS could not be completely isolated as it co-eluted with another low molecular weight protein (< 15 kDa). This enzyme was identified using the X-ray crystallography data collected from several crystals and by using an Alphafold2 model<sup>21</sup> as a template to solve the structure of the ATPS of *Ca. D. auxilii* (*DaATPS*). The sequences modelled in the electron density of the structures *DaATPS*, *DaAPSR* and *DaDsr* gave a 100% fit with the proteins encoded in the genome of *Ca. D. auxilii*. The quaternary structures of the three enzymes were examined by size exclusion chromatography. While  $\alpha_2\beta_2$ -APSR (theoretical 176 kDa versus experimental 180 kDa) and  $\alpha_2\beta_2$ -Dsr (theoretical 199 kDa versus experimental 216 kDa) have an excellent fit with respect to their expected molecular weight, the ATPS eluted as a tetramer instead of the expected dimer (theoretical dimer 105 kDa versus experimental 197 kDa), a behaviour confirmed by native PAGE and our structural insights.

### **A new type of ATP sulfurylase**

The activity of the purified ATPS from *Ca. D. auxilii* was monitored by a coupled assay, as the enzyme is retro-inhibited by APS<sup>22</sup>. The addition of an excess of native APSR in the assay prevented the accumulation of APS (Fig. 2a). Because the formation of APS is thermodynamically unfavourable and driven by the immediate hydrolysis of PP<sub>i</sub><sup>23</sup>, a commercial pyrophosphatase was added to avoid PP<sub>i</sub> accumulation. ATPS activity was determined indirectly by measuring the oxidation of reduced methyl viologen upon reduction of the produced APS by the APSR. The specific activity of  $0.039 \pm 0.011$   $\mu\text{mol}$  of oxidized methyl viologen (MV)  $\text{min}^{-1}$   $\text{mg}$  of *DaATPS*<sup>-1</sup> was measured in the presence of Mg<sup>2+</sup> and Mn<sup>2+</sup> ions. Removal of a divalent cation (either Mg<sup>2+</sup> or Mn<sup>2+</sup>) resulted in a decrease in activity, suggesting that *DaATPS* would be stimulated by both metals.

MoO<sub>4</sub><sup>2-</sup> is an inhibitor of the ATPS and therefore SO<sub>4</sub><sup>2-</sup> reduction, as it generates AMP and PP<sub>i</sub> through molybdolysis, which leads to cellular ATP depletion and inhibits the growth of SRB and other SO<sub>4</sub><sup>2-</sup> dependent organisms<sup>24-26</sup>. No *DaATPS* activity was detected when an equimolar ratio

of  $\text{SO}_4^{2-}$  and  $\text{MoO}_4^{2-}$  was used in the enzyme assay. Thus, the active purified enzyme shows traits of previously characterized ATP sulfurylases.

The structure of the first ATP sulfurylase from an SRB, namely *Ca. D. auxilii*, was obtained without substrate bound to the active site and refined to a resolution of 2.34 Å (Extended Data Table 1). The electron density unambiguously revealed an additional protein bound to the enzyme, which is encoded by the gene next to the ATPS characterized here (BLFGPEAP\_02683, Fig. 1c). This small protein, which co-elutes with the ATPS, will now be referred to as the  $\beta$ -subunit. Consistent with the molecular weight estimated by native PAGE and size exclusion chromatography, the surface analysis by PISA<sup>27</sup> suggests that *Da*ATPS forms a ~270 kDa complex corresponding to a dimer of heterotetramers ( $(\alpha_2\beta_2)_2$ , Fig. 2b, Extended Data Fig. 2a and Extended Data Fig. 3a-b)<sup>28-30</sup>. In contrast, all characterised microbial ATP sulfurylases (from the Sat family) consist of a single protein that organises as a homodimer and is homologous to the  $\alpha$ -subunit of *Da*ATPS (Extended Data Fig. 2a)<sup>31</sup>. The closest structural homologue of the  $\alpha$ -subunit is the ATPS from the thermophilic methanogen *Methanothermococcus thermolithotrophicus*, which has been proposed to be of bacterial origin (Supplementary Fig. 1 and Extended Data Table 2)<sup>31</sup>.

The  $\alpha$ -subunit has the typical three-domain fold of ATP sulfurylases (Fig. 2c), but with subtle differences due to their role in dimer-dimer binding and  $\beta$ -subunit interaction, the latter being mainly established by the domains II and III (Extended Data Fig. 2a and Extended Data Fig. 3a,b)<sup>30,31</sup>. Overall, the *Da*ATPS has extensions that are absent in other ATP sulfurylases. In particular, the C-terminus has a 20 amino acid extension that interacts with the domains I and II. As previously described in other thermophilic microorganisms, domain III contains a zinc-binding motif that has been proposed to contribute to the thermophilic stability of the enzyme (Extended Data Fig. 3c)<sup>28,30</sup>. As in the characterised homologs, the active site is established by the domains II and III.

The  $\beta$ -subunit has a C-terminal extension that spans domain II, reinforcing the inter-subunit contacts, totalling an interface of  $\approx 1,700 \text{ \AA}^2$ . The  $\beta$ -subunit appears to be flexible, as indicated by higher b-factor values (Supplementary Fig. 2), and some regions could not be modelled due to a lack of electron density (residues 34-35, 39-63). Interestingly, the protein corresponding to the  $\beta$ -subunit is predominantly present in thermophilic  $\text{SO}_4^{2-}$  reducing or sulfur-disproportionating

bacteria and archaea (Extended Data Fig. 4), suggesting that its physiological role may be temperature related.

Despite the additional subunit and its different organisation, the *Da*ATPS structure has a solvent exposed active site and residues critical for the reaction are conserved, arguing for a conserved reaction mechanism (Fig. 2d and Supplementary Fig. 1), supported by the sensitivity to molybdate.

### **A conventional APS reductase**

The APSR reduces the APS produced by the ATPS via a two-electron transfer reaction (Fig. 1b). The activity of *Da*APSR was monitored by following the oxidation of reduced MV upon APS reduction under anaerobic conditions. The enzyme has a specific activity of  $0.2 \pm 0.005 \mu\text{mol}$  of oxidized MV  $\text{min}^{-1}$  mg of purified *Da*APSR, which is well within the range of the activities of other described APSRs<sup>32</sup>. A single-wavelength anomalous dispersion experiment (SAD) at the Fe K-edge was performed to solve the *Da*APSR crystal structure. The best diffracting crystal, co-crystallized with AMP and  $\text{SO}_3^{2-}$ , was refined to 1.65 Å and was mainly used for analyses (Extended Data Table 1). It should be noted that despite its co-crystallization, no electron density was detected for AMP, and only one  $\text{SO}_3^{2-}$  ion occupies the binding site in front of the FAD. The *Da*APSR complex organizes as an  $\alpha_2\beta_2$  heterotetramer, consistent with our previous experiments (Fig. 1c and 3a, and Extended Data Fig. 1d). As in other structural homologues, the  $\alpha$ -subunit contains a flavin adenine dinucleotide (FAD) and the  $\beta$ -subunit harbours the two [4Fe-4S] clusters clearly identified in the anomalous map (Fig. 3b). The electrons required for APS reduction are transferred from an unknown electron donor to the [4Fe-4S] distal and proximal clusters, a conserved tryptophan (Trp48), and finally reach the FAD where the substrate is bound (Fig. 3c).

Based on the protein sequence, the closest homologue to *Da*APSR is the APSR from *Archaeoglobus fulgidus* (*Af*APSR, PDB: 2FJA) with 59.6% and 63.5% sequence identity and a coverage of 99% and 100% for the  $\alpha$ - and  $\beta$ -subunits, respectively (Supplementary Fig. 3)<sup>31,33,34</sup>. *Af*APSR is also the closest structural homologue compared to the other models, including the PAPSR from *Methanothermococcus thermolithotrophicus* (Extended Data Fig. 5a-c and Table 2). Interestingly, the C-terminal tail of the  $\beta$ -subunit, placed on the surface of the  $\alpha$ -subunit, shows a perfect three-dimensional alignment with *Af*APSR. The tail is further stabilized by a divalent

cation binding site, modelled as zinc due to its presence in the crystallization solution (Fig. 3a and Extended Data Fig. 5c). A comparison of the active sites of *Da*APSR and *Af*APSR shows a perfect conservation of the residues critical for the substrate binding and the catalytic activity (Fig. 3c-d and Supplementary Fig. 3), which corroborates the activity detected *in vitro*.

### **DsrAB from *Ca. D. auxilii* shows similar features to an archaeal homologue**

The dissimilatory sulfite reduction system catalyzes the reduction of  $\text{SO}_3^{2-}$  to  $\text{HS}^-/\text{S}^{2-}$ . The genome of *Ca. D. auxilii* encodes an operon consisting of DsrA and DsrB, which together form the cytosolic DsrAB, and the putative partner DsrD (Fig. 1b-c). DsrD has been characterised as an allosteric activator of DsrAB under respiratory conditions, but is not essential for its activity<sup>35</sup>. The sulfur carrier protein DsrC is located elsewhere in the genome (BLFGPEAP\_00112).

Despite attempting multiple enzymatic assays to assess the sulfite reductase activity in the soluble cell extract as well as the purified enzyme, no rates could be detected (see Materials and Methods). Our attempt to use thiosulfate as a substrate surrogate, as shown for DsrAB from *A. fulgidus*, also resulted in the absence of activity<sup>36</sup>. Therefore, the enzyme may have been inactivated by lysis, loss of a membrane partner, or by inhibitory elements from the enrichment. This enzyme may require an activation process or simply may be strictly dependent on the presence of the membrane complexes for activity. Nevertheless, heme staining on native PAGE (Extended Data Fig. 1a) confirmed the presence of the enzyme.

The structure of *Da*DsrAB was solved by a SAD experiment at the Fe K-edge and refined to a resolution of 2.48 Å (Extended Data Table 1). As suggested by size exclusion chromatography as well as denaturing and native PAGE, *Da*DsrAB is organised as a dimer of heterodimers, as previously observed in all described dissimilatory sulfite reductases (Fig. 4a and Extended Data Fig. 6a-c). The  $\alpha_2\beta_2$  assembly contains a total of two buried and two solvent exposed sirohemes and eight [4Fe-4S] clusters (Fig. 4b, Extended Data Fig. 7a). A striking difference compared to structurally studied bacterial homologues is the absence of DsrC, which was already observed on SDS-PAGE (Fig. 1c and Extended Data Fig. 6a).

As the *dsrA* and *dsrB* genes are paralogous<sup>37,38</sup>, the structures of DsrA and DsrB from *Ca. D. auxilii* are similar (rmsd of 1.831 Å for 230 C $\alpha$  aligned) and share an overall fold that can be

divided into three domains, as previously described<sup>38</sup>. Domain II binds the proximal [4Fe-4S] cluster bound to the siroheme (Fig. 4b, Extended Data Fig. 7b-c)<sup>39</sup>. In DsrA, the cluster is coordinated by the conserved CX<sub>5</sub>CX<sub>37</sub>CX<sub>3</sub>C motif<sup>37,38,40</sup>, which differs in DsrB (CX<sub>36</sub>CCX<sub>3</sub>C, Supplementary Fig. 4 and 5). Domain III binds the distal [4Fe-4S] cluster with a similar motif in DsrA (CX<sub>18</sub>CX<sub>2</sub>CX<sub>2</sub>C) and DsrB (CX<sub>27</sub>CX<sub>2</sub>CX<sub>2</sub>C). DsrA contains a large N-terminus of 44 amino acids that wraps around its own subunit. DsrB harbours an additional C-terminal helix of 10 amino acids that interacts with DsrA. Both extensions, which are absent in other homologues, are located away from the active site entrance and the proposed DsrC binding site (Extended Data Fig. 8). They may therefore have a stabilising role or be important for partner interaction (e.g. electron transfer, Extended Data Fig. 7b-c).

The closest structural homologue for *DaDsrAB* is the DsrABC complex from *Desulfovibrio vulgaris* (PDB: 2V4J, rmsd of 0.438 Å for 380 Ca aligned for DsrA). In this structure and in other characterised bacterial enzymes, DsrA harbours a catalytically inactive sirohydrochlorin, which is proposed to serve a structural purpose<sup>41</sup>. In contrast, *DaDsrAB* contains iron-loaded sirohemes in both DsrA and DsrB, suggesting that both sites are potentially catalytically active and electronically connected (Fig. 4b). However, the site containing a sirohydrochlorin in other homologues is not solvent-accessible, mainly because of a loop (DsrA, residues 298-316) that blocks the access to the siroheme and buries it deep within the protein. This structural organization would allow neither sulfite reduction nor sulfur transfer on DsrC. Nevertheless, this site has a coordination sphere that is relatively different from that of the homologues. Notably, a lysine (DsrB, K182) is present in the vicinity of the Fe atom, where other enzymes harbour hydrophobic and bulky amino acids such as proline in *D. vulgaris* (PDB: 2V4J, P181), tryptophan and methionine in *A. fulgidus* (3MM5, W119 and M170), isoleucine in *M. gigas* (PDB: 3OR2, I181). The exception is the enzyme from *D. norvegicum*, which has a threonine at this position (PDB: 2XSJ, T135). The AlphaFold2-generated<sup>21</sup> model of *DaDsrAB* in complex with *DaDsrC* indicates an absence of any major conformational changes imposed by DsrC docking (Extended Data Fig. 8), corroborating the well-conserved three-dimensional structure of *DaDsrAB* and its homologues (Extended Data Fig. 6 and Extended Data Table 2).

Based on the conservation of all residues required for the reaction (Fig. 4b and Supplementary Fig. 4-5), the similarity of the crystal structures of *DaDsrAB* and homologues, and the conformational

access for DsrC, we propose that the enzyme should follow the catalytic reduction reaction previously described for dissimilatory sulfite reductases, although the purified enzyme remained inactive for  $\text{SO}_3^{2-}$  reduction.

## Discussion

The metabolism of SRB is of concern to modern society due to safety risks to personnel involved in offshore activities, biocorrosion of metals and endospore-producing thermophiles causing food spoilage<sup>23,42</sup>. However, they play a central role in the sulfur cycle by converting  $\text{SO}_4^{2-}$  to  $\text{S}^{2-}$  and in the mineralisation of organic carbon in marine sediments<sup>1,43,44</sup>. Their key role in anaerobic alkane oxidation reinforces their importance in the carbon cycle. Here, we investigated how *Ca. D. auxilii* performs dissimilatory reduction of  $\text{SO}_4^{2-}$  when the reaction is coupled to the ethane oxidation performed by *Ca. E. thermophilum*. Due to the microbial heterogeneity and the limited availability of sufficient biological material, the biomass posed the greatest challenge. By carrying out a large-scale exploration on just two samples, we identified the three main cytosolic enzymes and isolated them by the selective power of crystallisation, allowing their structural characterisation.

The first structurally solved ATP sulfurylase from a SRB has an  $\alpha_4\beta_4$ -oligomerization, in which the flexible  $\beta$ -subunit docks on the periphery of the tetrameric core. The  $\beta$ -subunit is suspected to enhance the thermal stability of the enzyme because it is predominantly present in thermophilic  $\text{SO}_4^{2-}$  reducing or sulfur-disproportionating organisms (Extended Data Fig. 4). Alternatively, its physiological role could be related to regulation of the ATPS, which would explain the low specific activity observed in our assay. The small protein might impact conformational shifts occurring in the  $\alpha$ -subunit under turnover conditions. Snapshots of the ATPS in complex with mimics of catalytic intermediates could provide additional information. Further studies, possibly in genetically tractable organisms or expression systems, have to be undergone in order to solve the function of this new subunit observed in *DaATPS*.

The position of the trapped  $\text{SO}_3^{2-}$  in front of the catalytic FAD and the perfect conservation of the active site residues led to the conclusion that *DaAPSR* is conventional and should reduce APS in the same way as previously described dissimilatory models. In contrast, *DaDsrAB* shows



interesting particularities compared to its bacterial homologues. The most notable differences are the absence of bound DsrC and the presence of sirohemes instead of sirohydrochlorins. However, the enzyme architecture indicates that the substrate cannot access the DsrA sirohemes, suggesting a structural role for the siroheme as proposed for other characterised enzymes<sup>41</sup>. The heme-stained native electrophoresis profile does not suggest any stable DsrABC complex in the soluble extract or at any purification step (Extended Data Fig. 1). In contrast, the AlphaFold2 model argues for a conserved DsrC binding site. Compared to structures that were obtained from axenic cultures, this study differs because of the symbiotic interaction with the archaeon, which could balance the central metabolism in unexpected ways, such as a high abundance of DsrC loaded with the sulfur unit, which would explain the absence of DsrC in the DsrAB complex.

The electrical symbiosis between *Ca. D. auxilii* and *Ca. E. thermophilum* is interesting from a bioenergetic point of view, in particular for the understanding of how electrons are transferred from the membrane to the core metabolism in the bacterium (Fig. 5). According to our proposed model, the reducing equivalents derived from ethane oxidation would converge to the reduced cofactor F<sub>420</sub>. *Ca. E. thermophilum* does not contain hydrogenases or an Rnf system at the membrane. Instead, a F<sub>420</sub>H<sub>2</sub>-dependent methanophenazine reductase would transfer the electrons from the membrane to the cytochrome-containing nanowire of *Ca. D. auxilii*. As previously proposed<sup>8</sup>, the quinone reductase complex could potentially transfer the electrons received from the archaeal partner to the pool of menaquinones, used to fuel the dissimilatory SO<sub>4</sub><sup>2-</sup> reduction pathway. Complete reduction of SO<sub>4</sub><sup>2-</sup> requires eight electrons, which would be transferred in successive events. Based on the literature, we propose that the menaquinone-interacting oxidoreductase complex (QmoABC) provides electrons to the APSR<sup>45-48</sup>. While the donor for the 2-electron reduction step of DsrAB remains to be identified, the DsrC trisulfide could be reduced via a 4-electron reduction reaction catalysed by three possible membrane complexes: DsrMKJOP, Tmc or a heterodisulfide reductase-like complex.

A version of the DsrMKJOP is present in *Ca. D. auxilii*, albeit with some variation. The operon BLFGPEAP\_02664-57, which is highly transcribed under ethane- and SO<sub>4</sub><sup>2-</sup>-dependent growth conditions<sup>3</sup>, contains a homologue of DsrM (02264), DsrK (02663), DsrJ (02662), DsrO (02661-0220), but the DsrP subunit seems to be replaced by a protein of a different family (02658), still annotated as a polysulfide reductase. These differences found in the same genus could be due to

the adaptation of living in a symbiosis, which would provide more plasticity to switch from one archaeon to another. Indeed, when considering the different strategies used by alkane oxidisers, the electron flow might fluctuate and it would be advantageous for the SRB to have several variants of menaquinone with different redox potentials in the membrane to tune the electron flow and optimise the  $\text{SO}_4^{2-}$  reduction pathway. For example, considering the standard redox potentials of menaquinone/menaquinol (-75 mV), the APSR reaction (-60 mV) and  $\text{SO}_3^{2-}$  reduction to  $\text{S}^{2-}$  (-116 mV), thermodynamics would constrain central metabolism under standard conditions. However, due to the “electronic pressure” imposed by alkanotrophic catabolism, the redox potential of menaquinone is expected to be sufficiently low to make the pathway exergonic. The oxidation and reduction of menaquinone will allow energy conservation by proton transfer. This hypothesis is based on the knowledge gained from SRB models, which may be different in the case of alkanotrophic consortia. However, here, we have shown that it is possible to study the biochemistry and structural biology of enzymes isolated from a growing microbial enrichment, and future work in this direction will shed light on the bioenergetics of these consortium-degrading alkanes before they reach our atmosphere.

## Materials & Methods

**Cultivation conditions.** The biomass used for enzyme purification was obtained from a thermophilic AOE enrichment cultured from sediments collected at the Guaymas Basin hydrothermal vents<sup>3</sup>. The culture doubled the amount of produced sulfide in a period of only 7 days and *Ca. E. thermophilum* and *Ca. D. auxilii* make up the majority of the active population<sup>3</sup>. The cultivation conditions for the consortium have been previously described by Hahn et al. 2020.

**Protein extraction and purification.** Exponentially growing Ethane50 culture was used for the protein extraction. The medium was removed with a stainless steel needle by applying overpressure of  $\text{N}_2:\text{CO}_2$  (90:10%). After a 3 min-long flushing with  $\text{N}_2:\text{CO}_2$  (90:10%), the cells were pelleted by centrifugation for 15 min at  $16,250 \times g$  in an anaerobic chamber filled with an  $\text{N}_2/\text{CO}_2$  atmosphere (90:10%) at room temperature and the supernatant was removed. Cells were resuspended in SR medium and stored at  $-80^\circ\text{C}$  under an  $\text{N}_2:\text{CO}_2$  (90:10%) atmosphere until purification.

The proteins were purified twice using similar and reproducible purification protocols. Only one is described. Cell lysis and preparation of extracts were performed in an anaerobic chamber filled with an N<sub>2</sub>/CO<sub>2</sub> atmosphere (90:10%) at room temperature. A volume of 15 ml of sedimented cells was suspended in 16 ml of 50 mM Tricine/NaOH buffer pH 8, 2 mM dithiothreitol (DTT; buffer A). The lysis protocol included a sonication step (BANDELIN Sonopuls HD 2200) followed by five rounds of French Press at around 1,000 PSI (6.9 MPa), yielding a homogenous deep-black extract. The French press cell was flushed with N<sub>2</sub> and washed twice with anoxic buffer A. Soluble extract (60 mg of total proteins) was obtained by ultracentrifugation at 140,000 x g for one hour at 4 °C. Enzyme purification was carried out under anaerobic conditions in a Coy tent, filled with an N<sub>2</sub>/H<sub>2</sub> atmosphere (95:5%), at 20 °C and under yellow light. For each step, chromatography columns were washed with at least three column volumes (CV) with the corresponding loading buffer, and samples were filtered through 0.2 µm filters before loading on the column. During purification, the enzyme was followed by high-resolution Clear Native PolyAcrylamide Gel Electrophoresis (hrCN PAGE, see below), sodium dodecyl sulfate PAGE (SDS PAGE) and absorbance monitoring at 280, 415 and 550 nm.

Extracts were diluted with buffer A to obtain a final 15-fold dilution before being loaded on 4 × 5 ml anion exchanger HiTrap™ Q HP columns (GE Healthcare) equilibrated with the same buffer. After a 2 CV washing, proteins were eluted with a 0 to 0.4 M NaCl linear gradient for 6 CV at a flow rate of 1 ml min<sup>-1</sup>.

**ATP sulfurylase.** The fractions of interest containing *DaATPS* eluted between 0.32 M and 0.35 M NaCl. The pooled fractions were diluted with 3 volumes of an anoxic 50 mM Tris/HCl buffer pH 7.6, 2 mM DTT (buffer B) containing 2 M ammonium sulfate, before being loaded on a Source™ 15PHE 4.6/100 PE (GE Healthcare) equilibrated with the same buffer. After washing, proteins were eluted with a 1.6 to 0 M ammonium sulfate linear gradient for 35 CV at a flow rate of 1 ml min<sup>-1</sup>. The enzyme eluted between 1.25 M and 1.13 M ammonium sulfate. Fractions of interest were pooled, and the buffer was exchanged for 50 mM Tris/HCl buffer pH 7.6, 2 mM DTT, 10% (v/v) glycerol. The purification of the *DaATPS* yielded 0.13 mg of pure enzyme, corresponding to 0.21% of the initial protein content of the soluble extract (total 60 mg).

**APS reductase.** The fractions of interest containing *DaAPSR* eluted between 0.35 M and 0.42 M NaCl. The pooled fractions were diluted with 2.5 volumes of an anoxic 50 mM Tris/HCl buffer,

pH 7.6, 2 mM DTT (buffer B) containing 2 M ammonium sulfate, before being loaded on a Source™ 15PHE 4.6/100 PE (GE Healthcare) equilibrated with the same buffer. After washing, proteins were eluted with a 1.6 to 0 M ammonium sulfate linear gradient for 53 CV at a flow rate of 1 ml min<sup>-1</sup>. The enzyme eluted between 1.25 M and 1.12 M ammonium sulfate. Fractions of interest were pooled and the buffer was exchanged for 50 mM Tris/HCl Buffer pH 7.6, 2 mM DTT, 10% (v/v) glycerol. *DaAPSR* was anaerobically purified to an apparent homogeneity (Fig. 1c). The purification from the enrichment yielded 1.13 mg of pure enzyme, corresponding to 1.88% of the initial protein content.

**Dissimilatory sulfite reductase.** The fractions of interest containing *DaDsrAB* eluted between 0.45 M and 0.52 M NaCl. The pooled fractions were diluted with 2 volumes of an anoxic 50 mM Tris/HCl buffer pH 7.6, 2 mM DTT (buffer B) containing 2 M ammonium sulfate, before loading onto a Source™ 15PHE 4.6/100 PE (GE Healthcare) column equilibrated with the same buffer. After washing, proteins were eluted with a 1.6 to 0 M ammonium sulfate linear gradient for 53 CV at a 1 ml min<sup>-1</sup> flow rate. The enzyme eluted between 0.52 M and 0.28 M ammonium sulfate. Fractions of interest were pooled, and the buffer was exchanged for 50 mM Tris/HCl buffer pH 7.6, 2 mM DTT, 10% (v/v) glycerol. The purification yielded 0.87 mg of pure enzyme, representing 1.46% of the initial protein content.

All proteins were used directly for anaerobic crystallization or were flash-frozen in liquid nitrogen and stored at -80 °C under anaerobic conditions.

**Enzyme assays.** All enzyme assays were performed in an anaerobic atmosphere (100% N<sub>2</sub>) at 45 °C, unless otherwise stated. Assays were performed in 96-deep well plates and monitored spectrophotometrically on a SPECTROstar Nano Microplate Reader at a wavelength of 600 nm. A stock of freshly reduced methyl viologen was prepared by adding 5 mM titanium citrate to 5 mM oxidized methyl viologen under an anaerobic atmosphere.

The activity of *DaATPS* was assessed in 50 mM Tris/HCl pH 7.5, and 0.5 mM reduced methyl viologen (MV<sub>red</sub>) served as the electron donor for *DaAPSR*. A molar extinction coefficient of  $\epsilon_{600\text{nm}} = 8,133.3 \text{ cm}^{-1} \text{ M}^{-1}$  was used. To the buffer and MV<sub>red</sub>, 0.3 mM ATP, 0.3 mM Na<sub>2</sub>SO<sub>4</sub>, 0.05 U pyrophosphatase (*E. coli*, from Sigma-Aldrich), 0.5 mM MgCl<sub>2</sub>, 0.5 mM MnCl<sub>2</sub>, 0.5 mg ml<sup>-1</sup> bovine serum albumin (BSA) and 0.1 mg ml<sup>-1</sup> *DaAPSR* were added in a final reaction volume of 50  $\mu$ l. To observe the effect of molybdate on the ATPS, 0.3 mM Na<sub>2</sub>MoO<sub>4</sub> was supplied in one

condition. The reaction was started by the addition of a final concentration of 0.05 mg ml<sup>-1</sup> *DaATPS* and followed by oxidation of MV<sub>red</sub> at 600 nm. All assays were performed in triplicate.

The activity of *DaAPSR* was assessed by monitoring the oxidation of MV<sub>red</sub> in the presence of APS. 50 mM Tris/HCl pH 7.5 was used as a buffer, to which 0.25 mM MV<sub>red</sub> and 1.5 mM APS were added in a final reaction volume of 100 µl. The reaction was started by the addition of a final concentration of 0.005 mg ml<sup>-1</sup> *DaATPS*.

The activity of DsrAB was assessed by using different protocols.

It was initially measured by monitoring the oxidation of MV<sub>red</sub> during sulfite reduction. The reaction mixture contained 0.25, 0.5 or 5 mM MV<sub>red</sub>; 0.75, 1.5 or 10 mM Na<sub>2</sub>SO<sub>3</sub> in 50 mM Tris/HCl pH 7.5. The reaction was initiated by the addition of a final concentration of 0.05 mg ml<sup>-1</sup> DsrAB, and the decrease in absorbance at 600 nm was monitored. The methyl viologen reacted with sulfite without the addition of enzyme, and no activity was detectable after background correction.

Sulfide production from sulfite in electron-saturated conditions was also assessed. In glass-sealed vials, 10 ml of 50 mM Tris/HCl pH 7.5 and 0.5 mM MV containing a final concentration of 0.19 mg ml<sup>-1</sup> of the hydrogenase-containing Hdr/Mvh complex purified from *Methanothermococcus thermolithotrophicus*<sup>49</sup>, were enzymatically reduced by the addition of 1 x 10<sup>5</sup> Pa of H<sub>2</sub>:CO<sub>2</sub> (80:20%) followed by incubation for 10 minutes at 50 °C. After the reaction, the glass vials were transferred back into the Coy tent, and 1 mM Na<sub>2</sub>SO<sub>3</sub> and 0.5 mg. ml<sup>-1</sup> *DaDsrAB* were added. The gas phase was again exchanged for 1 x 10<sup>5</sup> Pa of H<sub>2</sub>:CO<sub>2</sub> (80:20%), and the reaction mix was incubated in a water bath at 50 °C for 19 hours. The sulfide quantification was performed after the diamine method as previously described<sup>50</sup>. No sulfide could be detected.

Under physiological conditions, DsrAB requires DsrC and DsrMKJOP for the complete reduction of sulfite to sulfide. For DsrAB, sulfide is only a side product. It has been previously shown for DsrAB from *A. fulgidus* that it can use thiosulfate (Na<sub>2</sub>S<sub>2</sub>O<sub>3</sub>) as a substrate with higher enzymatic rates than for sulfite<sup>36</sup>. Therefore, thiosulfate was used as a substrate instead of sulfite. The assays were performed at 50 °C in a 0.8-ml quartz cuvette closed with a butyl rubber stopper. The gas phase of the cuvette was N<sub>2</sub>. To monitor the reduction of S<sub>2</sub>O<sub>3</sub><sup>2-</sup>, a final concentration of 0.05 mg ml<sup>-1</sup> *DaDsrAB* and 1 mM MV<sub>red</sub> were added to the 50 mM KH<sub>2</sub>PO<sub>4</sub> buffer, pH 6.5. Once the

spectrophotometer (Agilent Cary 60 UV–Vis) displayed a stable signal at 650 nm, the reaction was started by the addition of 3 mM Na<sub>2</sub>S<sub>2</sub>O<sub>3</sub>. No activity was detected.

It cannot be excluded that DsrAB is inactive after purification or that the activity is too low for it to be detected. The activity was assessed in soluble extracts. The assays were performed at 50 °C in a 0.8-ml quartz cuvette in a final reaction volume of 400 µl and closed with a butyl rubber stopper. The gas phase of the cuvette was exchanged for N<sub>2</sub>. To monitor the reduction of sulfite, a final concentration of 0.005 mg ml<sup>-1</sup> cell extract and 0.5 mM MV<sub>red</sub> were added to the 50 mM KH<sub>2</sub>PO<sub>4</sub> buffer, pH 6.5. Once the spectrophotometer (Agilent Cary 60 UV–Vis) displayed a stable signal at 600 nm, the reaction was started by the addition of 3 mM Na<sub>2</sub>SO<sub>3</sub>. After correction for the background activity without the enzyme, no activity was detected.

**Crystallization.** The purified enzymes were kept in 50 mM Tris/HCl buffer pH 7.6, 2 mM DTT and 10% (v/v) glycerol and freshly purified samples were used immediately for crystallization. All crystals were obtained anaerobically (N<sub>2</sub>:H<sub>2</sub>, gas ratio of 97:3) by initial screening at 20 °C. The sitting drop method was performed on 96-well MRC 2-drop crystallization plates in polystyrene (SWISSCI) with 90 µl of crystallization solution in the reservoir. For all three proteins, crystals were obtained by the addition of 0.6 µl of samples with 0.6 µl of crystallization solutions.

**ATP sulfurylase.** Rectangular plate-shaped ATPS crystals appeared in 25% w/v polyethylene glycol 3,350 and 100 mM Bis-Tris, pH 5.5. Prior to transfer in liquid N<sub>2</sub>, the crystal was soaked in 20% glycerol for a few seconds.

**APS reductase.** Thick rod-shaped initial crystals used for phasing were obtained in 10% w/v polyethylene glycol 8,000, 100 mM MES pH 6.0 and 200 mM zinc acetate. Prior to transfer in liquid N<sub>2</sub>, the crystal was soaked in 30% glycerol for a few seconds.

The highest resolution was obtained with thick rod-shaped crystal that appeared in 20% w/v polyethylene glycol 3,000, 100 mM imidazole pH 8.0 as well as 200 mM zinc acetate and was cocrystallized with 2 mM AMP and 2 mM Na<sub>2</sub>SO<sub>3</sub>. Prior to transfer to liquid N<sub>2</sub>, the crystal was soaked in 25% ethylene glycol for a few seconds.

**DsrAB.** Black long rod-shaped crystals appeared after a few days in the following crystallization conditions: 25% w/v polyethylene glycol 3,350, 100 mM Tris pH 8.5 and 200 mM magnesium

chloride hexahydrate. Prior to transfer to liquid N<sub>2</sub>, the crystal was soaked in 20% glycerol for a few seconds.

**X-ray data collection, refinement and validation.** All crystals were collected at 100 K at the beamlines listed in Extended Data Table 1. All data were integrated with autoPROC<sup>51</sup>. ATPS was solved by molecular replacement with PHASER from PHENIX<sup>52</sup> using an Alphafold2 model<sup>21</sup>. APSR and DsrAB were solved *ab initio* by a SAD experiment at the Fe K-edge with autosol from PHENIX<sup>53</sup>. The high-resolution structure of APSR was solved by molecular replacement with PHASER by using the *ab initio* model *DaAPSR* as a template. All models were manually optimized with COOT<sup>54</sup>. Refinement was performed with PHENIX.refine<sup>52</sup> or Buster<sup>55</sup> without applying non-crystallography symmetry for the models refined with PHENIX. All models were refined by using a translation-libration screw and by adding hydrogens in riding positions. DsrAB suffered from a slight twinning (twin fraction of 0.09) and was refined appropriately with PHENIX.refined by imposing the following operator: h,-k,-l. The different structures were validated by the molprobity tool integrated with PHENIX. The data collection and refinement statistics are detailed in Extended Data Table 1.

**High resolution Clear Native PAGE (hrCN PAGE).** The hrCN–PAGE protocol was adapted from ref. 56. The electrophoresis was performed in an anaerobic chamber filled with a N<sub>2</sub>:CO<sub>2</sub> (90 %:10 %) atmosphere. Glycerol (20 % v/v final) was added to the samples and 0.001 % (w/v) Ponceau S was used as a protein migration marker. The anaerobic electrophoresis cathode buffer contained a buffer mixture of 50 mM Tricine/NaOH; 15 mM Bis-Tris at a pH 7 supplemented with 0.05 % (w/v) sodium deoxycholate; 0.01 % (w/v) dodecyl maltoside and 2 mM DTT. The anaerobic anode buffer contained 50 mM BisTris buffer, pH 7; 2 mM DTT. hrCN PAGE were carried out using an 8 to 15 % linear polyacrylamide gradient, incubated overnight in an anaerobic tent, soaking in anaerobic cathode buffer. Gels were run at a constant current of 20 mA using a PowerPac<sup>TM</sup> Basic Power Supply (Bio-Rad). After electrophoresis, protein bands were stained with Instant Blue<sup>TM</sup> (Expedeon) or submitted to heme staining.

Heme staining was performed under aerobic conditions, with a protocol adapted from Thomas, Ryan and Levin (1976)<sup>57</sup>. The native gel was first incubated for 30 minutes in a 100 ml solution of 175 mM sodium acetate pH 5, 30% (v/v) ethanol, before being incubated for one hour in the

same solution with the addition of 40 mg 3,3',5,5'-tetramethylbenzidine (TMBZ). The TMBZ was dissolved in ethanol before mixing with acetate buffer. TMBZ solutions before and during incubation were kept in the dark. The reaction was initiated by the addition of 0.5 ml of 30% (v/v) hydrogen peroxide for a final concentration of 49 mM. Staining was performed at room temperature and in the dark.

**Phylogenetic trees.** Phylogenetic analyses were performed using MEGA11.0 by applying default parameters. Homolog proteins were first identified and obtained from NCBI using BLASTP (E177 value cut-off of 1e1). The protein sequences were then aligned using MUSCLE and all homologs were identified through an iterative alignment evaluation based on characterized proteins and manual filtering. The evolutionary history was inferred using the Neighbor-Joining method<sup>58</sup>. The bootstrap consensus tree inferred from 2000 replicates<sup>59</sup> is taken to represent the evolutionary history of the taxa analyzed<sup>59</sup>. Branches corresponding to partitions reproduced in less than 50% bootstrap replicates are collapsed. The percentage of replicate trees in which the associated taxa clustered together in the bootstrap test (2000 replicates) are shown next to the branches<sup>59</sup>. The evolutionary distances were computed using the JTT matrix-based method<sup>60</sup> and are in the units of the number of amino acid substitutions per site. This analysis involved 100 amino acid sequences. All ambiguous positions were removed for each sequence pair (pairwise deletion option). There were a total of 145 positions in the final dataset. Evolutionary analyses were conducted in MEGA11 (ref. 61).

**Acknowledgements.** We thank the Max Planck Institute for Marine Microbiology and the Max Planck Society for continuous support. We acknowledge the SOLEIL synchrotron for beam time allocation and the beamline staff of Proxima-1 for assistance with data collection. Furthermore, we thank the staff of beamline X06DA from SLS and P11 at PETRA III. This research was funded by the Max-Planck Gesellschaft and the Novo Nordisk foundation (NNF21OC0070790, TW). MJ was supported by the Deutsche Forschungsgemeinschaft Schwerpunktprogram 1927 „Iron-sulfur for Life“ (WA 4053/1-1, MJ).

**Author contributions.** CJH and GW provided the consortium, ONL purified and crystallized all proteins described in this study. MJ performed all biochemical characterization. MJ and TW collected X-ray data and solved the structures. MJ and TW refined all models and validated the



models. MJ wrote the first draft, which was further worked on by ONL, TW and GW, and all authors will continue to work on it.

**Conflicts of Interest.** The authors declare no conflict of interest.



## List of Figures

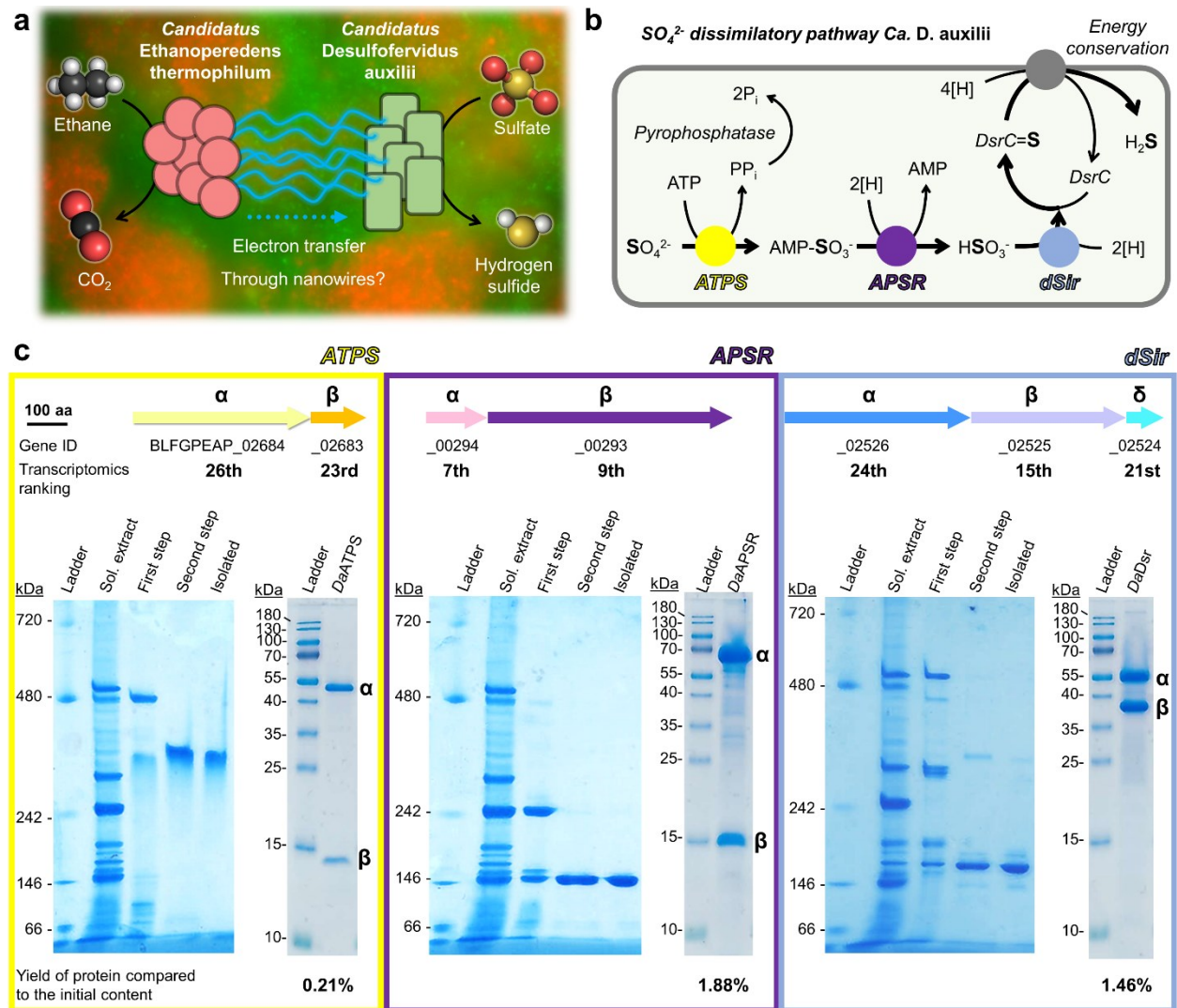


**Fig. 1. The dissimilatory  $\text{SO}_4^{2-}$  reduction pathway of an ethane-oxidizing consortium. a**, Scheme of the AOE process in which *Ca. E. thermophilum* oxidises ethane and transfers electrons to the SRB partner. The scheme is superposed to a fluorescence *in situ* hybridization (FISH) picture of the microbial consortium. **b**, Scheme of the proposed dissimilatory  $\text{SO}_4^{2-}$  reduction pathway of *Ca. D. auxilii*. **c**, Operon organisation (top) and native purification (bottom) of the three complexes involved in the dissimilatory  $\text{SO}_4^{2-}$  reduction pathway of *Ca. D. auxilii*. For native PAGE (left gels): 10  $\mu\text{g}$  was loaded for the soluble extract, 5  $\mu\text{g}$  for the first purification step and 2  $\mu\text{g}$  for the second purification step and the purified complex. For the SDS PAGE (right gels): 1, 4.3 and 4.2  $\mu\text{g}$  were loaded for ATPS, APSR and dSir, respectively. The transcriptomic ranking was taken from reference <sup>3</sup>.

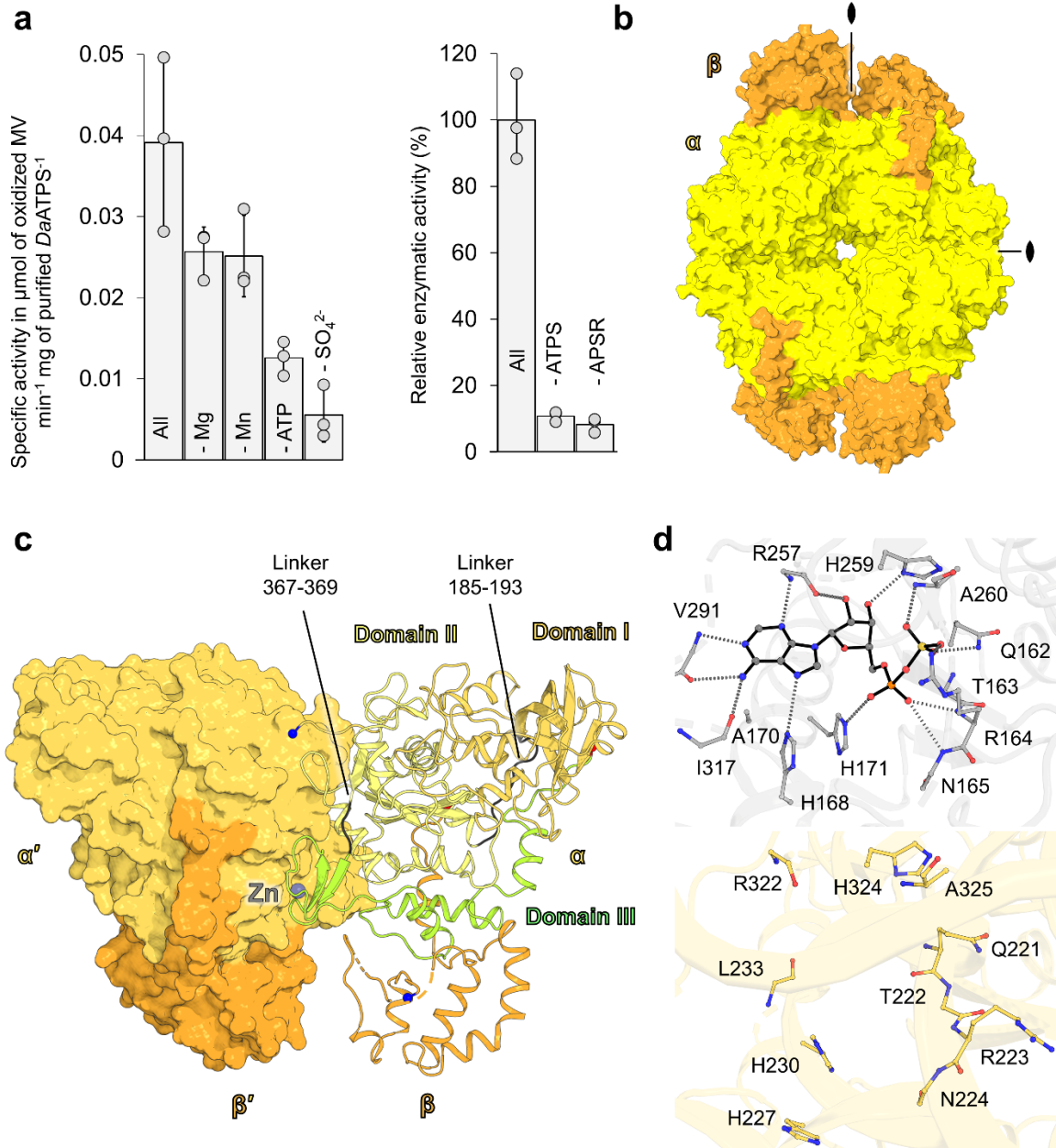


**Fig. 2. *DaATPS* forms octamers.** **a**, Specific activity of the *DaATPS* determined via the oxidation of reduced MV (left) and relative enzymatic activity (right). Data are presented as mean  $\pm$  s.d., and individual values are shown as grey spheres ( $n = 3$  replicates). **b**, *DaATPS* organizes as an  $\alpha_4\beta_4$ -complex with 2-fold symmetry axes indicated. **c**, *DaATPS* heterotetramer organisation. One heterodimer is shown as a surface and the other in a cartoon with the  $\alpha$ -subunit coloured according to the domains (I: 1-184 in light orange; II: 194-366 in yellow, and III: 370-455 in lemon) and linker regions in black. The N- and C-termini of both subunits correspond to blue and red spheres, respectively. **d**, Active sites of *TtATPS* (top, PDB: 1V47, grey) *DaATPS* (bottom, yellow). Residues involved or predicted to be involved in the substrate binding are shown as sticks. Carbon, nitrogen, oxygen, phosphorus and sulfur are coloured in grey/yellow, blue, red, orange and yellow, respectively.

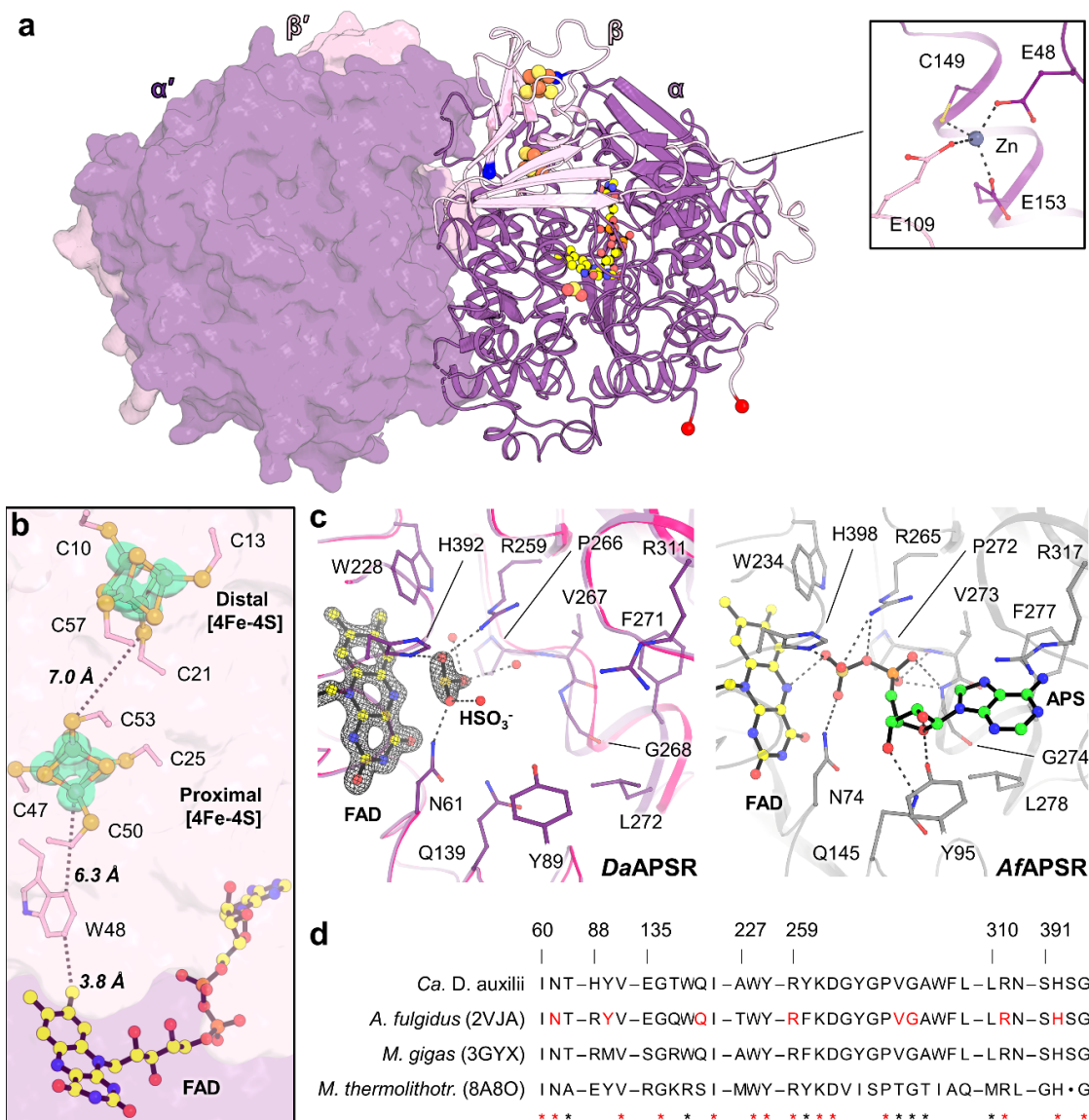


**Fig. 3. APSR of *Ca. D. auxilii*.** **a**, The heterotetramer is represented with one heterodimer shown in surface and the other one as a cartoon. Cofactors, N- (blue) and C-termini (red), are shown as spheres. A close-up of the metal site at the  $\alpha/\beta$  interface is presented. **b**, The electron transfer path from the [4Fe-4S]-clusters to the FAD. The cysteines coordinating the clusters, the conserved Trp48 and the FAD, are shown as balls and sticks with the proposed electron path highlighted by dashes. The anomalous map around the Fe is displayed as a transparent cyan surface and contoured to  $5\text{-}\sigma$ . **c**, Comparison of the sulfite-bound (purple) and APS-bound (grey) active sites of *Da*APSR and *Af*APSR. The  $2F_o-F_c$  map (grey mesh) for the FAD and modelled  $\text{HSO}_3^-$  is contoured to  $2\text{-}\sigma$ . For all panels, atoms are colour coded as follows: yellow/pink/green (C), red (O), blue (N), orange (P), dark yellow (S), and dark orange (Fe). **d**, Sequence conservation (done with MUSCLE<sup>62</sup>) across the alpha subunit with residues involved in APS binding coloured in red. Red and black stars represent perfectly and well-conserved residues, respectively.

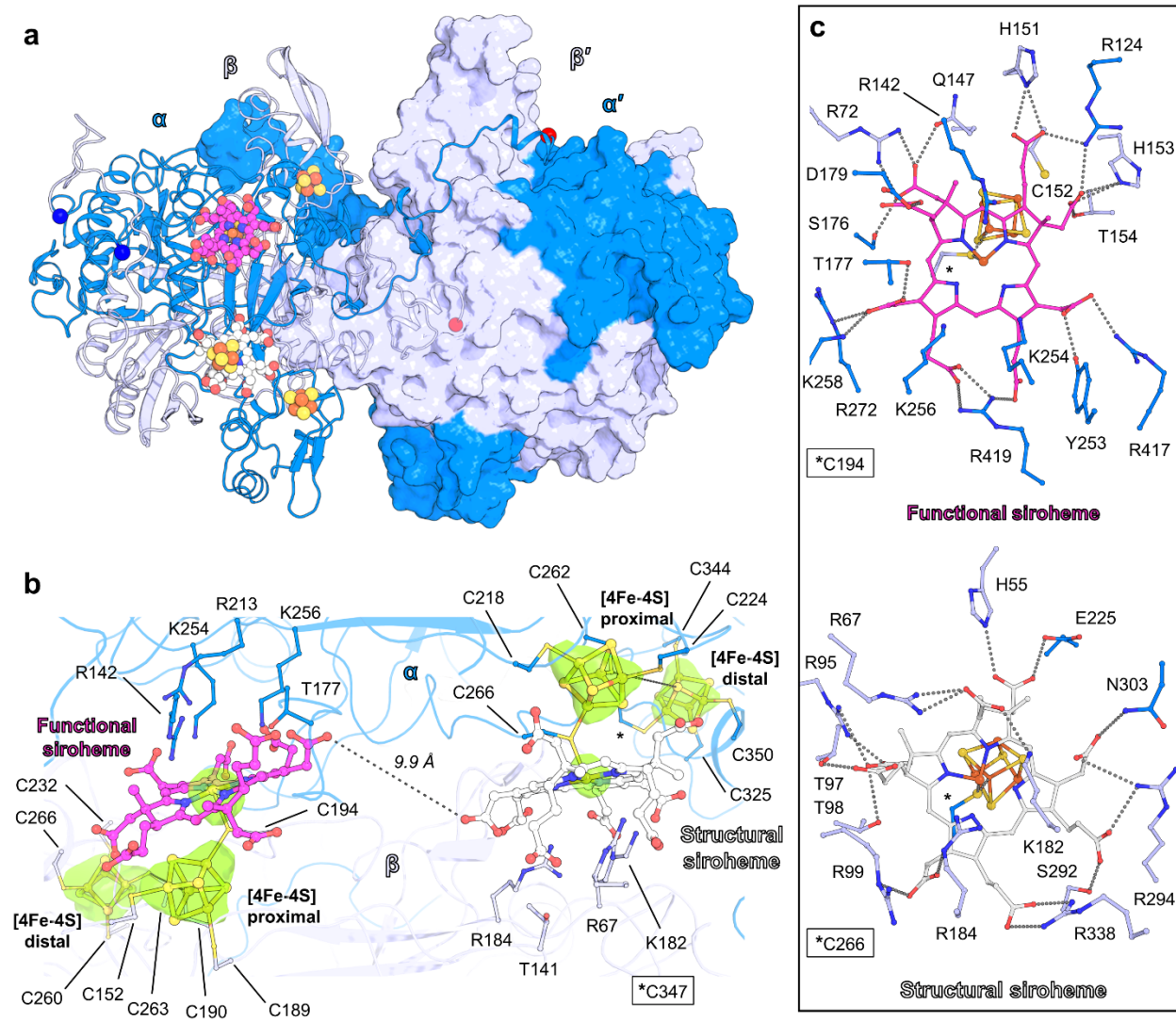


**Fig. 4. The dissimilatory sulfite reductase (DsrAB) from *Ca. D. auxilii*.** **a**, The heterotetramer DsrAB from *Ca. D. auxilii* in which one heterodimer is shown in cartoon and the other dimer in surface representation. The ligands, the N- (blue) and C-termini (red) of both subunits, are shown as spheres. **b**, Electron relay and siroheme sites in a DsrAB heterodimer. The anomalous map obtained after applying non-crystallography symmetry around Fe is displayed as a transparent green surface and contoured to 6- $\sigma$ . The distance between the distal and proximal [4Fe4S]-cluster is 10.2 and 9.6-Å in the  $\alpha$  and  $\beta$ -subunit, respectively (dashed lines). The residues coordinating the [4Fe-4S] clusters and, potentially, the substrate are shown in stick representation. **c**, Residues coordinating the functional (top) and structural (bottom) sirohemes, shown in sticks and balls. For all panels, carbon, oxygen, nitrogen, sulfur and iron are coloured in blue/pink for the functional siroheme/white for the structural siroheme, red, blue, yellow and brown, respectively.

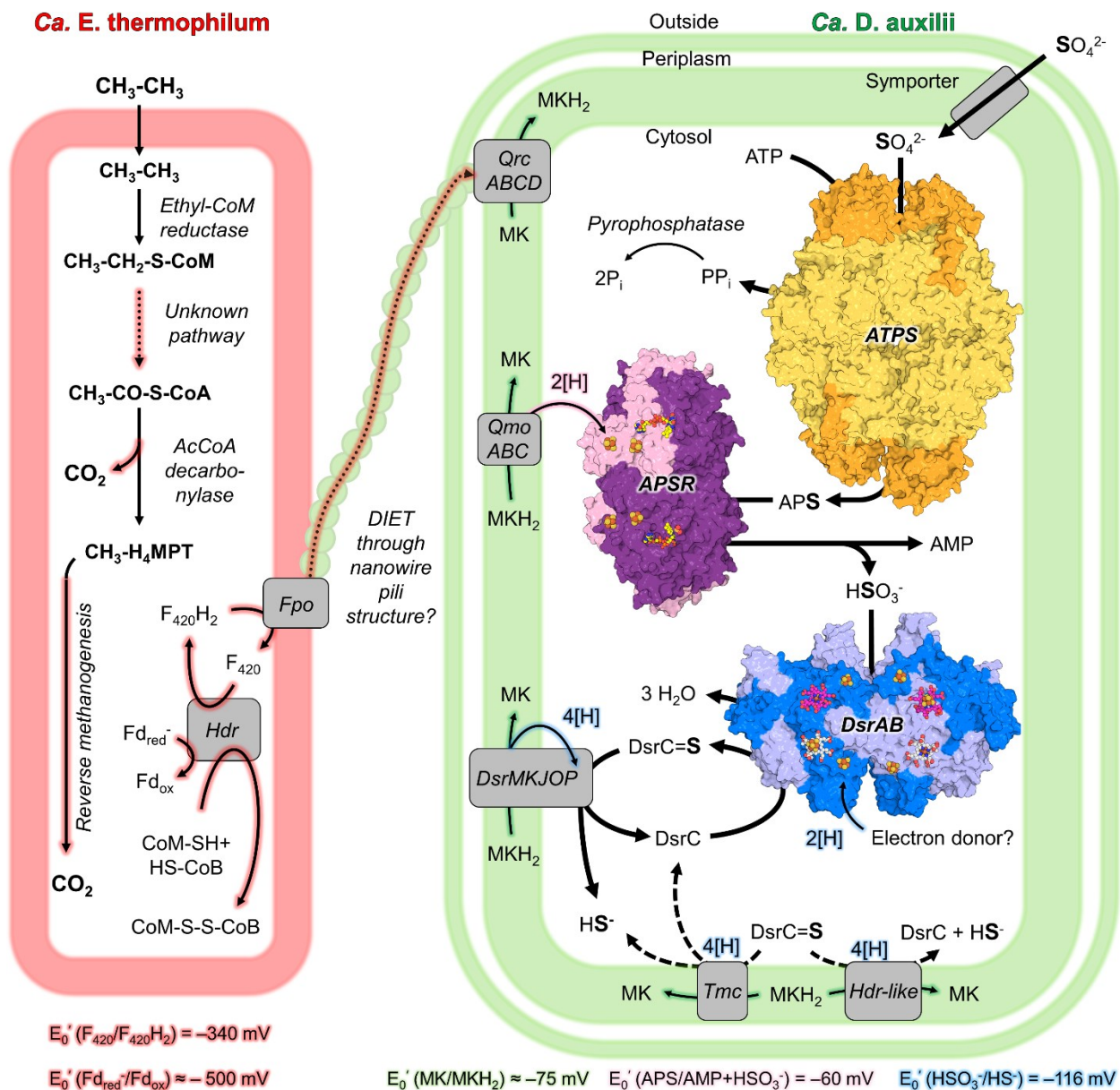


**Fig. 5. Proposed SO<sub>4</sub><sup>2-</sup> reduction pathway of *Ca. D. auxilii* electronically coupled to *Ca. E. thermophilum*.** Redox reactions proposed to be involved in the oxidation of ethane and the reduction of sulfate are highlighted with glow, with the colour corresponding to the redox couple at the bottom of the figure. The heterodisulfide reductase (Hdr) is thought to perform a ferredoxin-dependent (Fd) electron-conformation, providing the pool of reduced F<sub>420</sub> and allowing the heterodisulfide (CoM-S-S-CoB) to be recycled for the ethane capture step. DIET would be carried out through a nanowire-like structure and the quinone reductase complex (Qrc) would reduce menaquinone (MK). The enzymes solved in this study are highlighted in surface with the same colour code as previous figures and with (metallo)-cofactors shown as spheres. TmcABCD and the membrane-bound Hdr-like complexes could also perform the reduction of DsrC once loaded with sulphur and have therefore been added with dashed arrows.

## References

- 1 Knittel, K. & Boetius, A. Anaerobic oxidation of methane: progress with an unknown process. *Annual review of microbiology* **63**, 311-334, doi:10.1146/annurev.micro.61.080706.093130 (2009).
- 2 Evans, P. N. *et al.* An evolving view of methane metabolism in the Archaea. *Nature Reviews Microbiology* **17**, 219-232, doi:10.1038/s41579-018-0136-7 (2019).
- 3 Hahn, C. J. *et al.* "*Candidatus* Ethanoperedens", a thermophilic genus of *Archaea* mediating the anaerobic oxidation of ethane. *mBio* **11**, e00600-00620, doi:10.1128/mBio.00600-20 (2020).
- 4 Knittel, K., Lösekann, T., Boetius, A., Kort, R. & Amann, R. Diversity and distribution of methanotrophic archaea at cold seeps. *Appl Environ Microbiol.* **71**, 467-479, doi:10.1128/AEM.71.1.467-479.2005 (2005).
- 5 Wegener, G., Laso-Pérez, R., Orphan, V. J. & Boetius, A. Anaerobic degradation of alkanes by marine archaea. *Annual review of microbiology* **76**, 553-577, doi:10.1146/annurev-micro-111021-045911 (2022).
- 6 Yu, H. *et al.* Sulfate differentially stimulates but is not respired by diverse anaerobic methanotrophic archaea. *The ISME Journal* **16**, 168-177, doi:10.1038/s41396-021-01047-0 (2022).
- 7 Reeburgh, W. S. Oceanic methane biogeochemistry. *Chemical reviews* **107**, 486-513, doi:10.1021/cr050362v (2007).
- 8 Krukenberg, V. *et al.* *Candidatus* Desulfofervidus auxilii, a hydrogenotrophic sulfate-reducing bacterium involved in the thermophilic anaerobic oxidation of methane. *Environmental microbiology* **18**, 3073-3091, doi:10.1111/1462-2920.13283 (2016).
- 9 Laso-Pérez, R. *et al.* Thermophilic archaea activate butane via alkyl-coenzyme M formation. *Nature* **539**, 396-401, doi:10.1038/nature20152 (2016).
- 10 Laso-Pérez, R. *et al.* Anaerobic degradation of non-methane alkanes by "*Candidatus* Methanoliparia" in hydrocarbon seeps of the Gulf of Mexico. *mBio* **10**, 10.1128/mbio.01814-01819, doi:10.1128/mbio.01814-19 (2019).
- 11 Krukenberg, V. *et al.* Gene expression and ultrastructure of meso- and thermophilic methanotrophic consortia. *Environ Microbiol* **20**, 1651-1666, doi:10.1111/1462-2920.14077 (2018).
- 12 Hocking, W. P., Stokke, R., Roalkvam, I. & Stee, I. H. Identification of key components in the energy metabolism of the hyperthermophilic sulfate-reducing archaeon *Archaeoglobus fulgidus* by transcriptome analyses. *Front Microbiol* **5**, 95, doi:10.3389/fmicb.2014.00095 (2014).



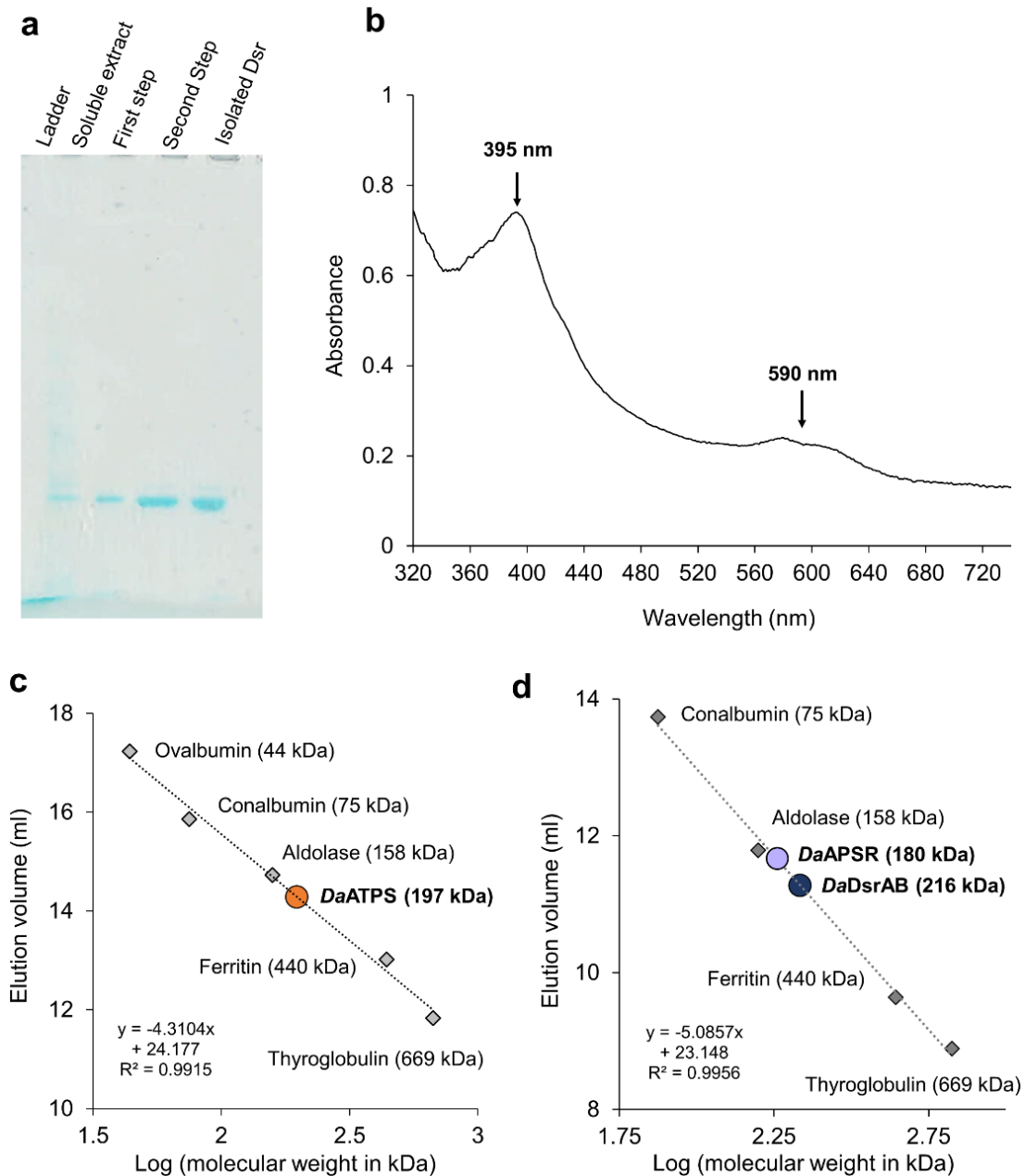
- 13 Marietou, A., Roy, H., Jorgensen, B. B. & Kjeldsen, K. U. Sulfate transporters in dissimilatory sulfate reducing microorganisms: A comparative genomics analysis. *Front Microbiol* **9**, 309, doi:10.3389/fmicb.2018.00309 (2018).
- 14 Simon, J. & Kroneck, P. M. Microbial sulfite respiration. *Adv Microb Physiol* **62**, 45-117, doi:10.1016/b978-0-12-410515-7.00002-0 (2013).
- 15 Jespersen, M., Pierik, A. J. & Wagner, T. Structures of the sulfite detoxifying F<sub>420</sub>-dependent enzyme from *Methanococcales*. *Nature Chemical Biology*, doi:10.1038/s41589-022-01232-y (2023).
- 16 Peck, H. D., Van Beeumen, J. & LeGall, J. Biochemistry of dissimilatory sulphate reduction [and discussion]. *Philosophical transactions of the Royal Society of London. Series B, Biological sciences* **298**, 443-466 (1982).
- 17 Venceslau, S. S., Stockdreher, Y., Dahl, C. & Pereira, I. A. C. The “bacterial heterodisulfide” DsrC is a key protein in dissimilatory sulfur metabolism. *Biochimica et Biophysica Acta (BBA) - Bioenergetics* **1837**, 1148-1164, doi:10.1016/j.bbabi.2014.03.007 (2014).
- 18 Santos, A. A. *et al.* A protein trisulfide couples dissimilatory sulfate reduction to energy conservation. *Science (New York, N.Y.)* **350**, 1541-1545, doi:10.1126/science.aad3558 (2015).
- 19 Pires, R. H. *et al.* Characterization of the *Desulfovibrio desulfuricans* ATCC 27774 DsrMKJOP complex - A membrane-bound redox complex involved in the sulfate respiratory pathway. *Biochemistry* **45**, 249-262, doi:10.1021/bi0515265 (2006).
- 20 Hahn, C. J. *et al.* Crystal structure of a key enzyme for anaerobic ethane activation. *Science* **373**, 118-121, doi:10.1126/science.abg1765 (2021).
- 21 Jumper, J. *et al.* Highly accurate protein structure prediction with AlphaFold. *Nature* **596**, 583-589, doi:10.1038/s41586-021-03819-2 (2021).
- 22 Lampreia, J., Pereira, A. S. & Moura, J. G. in *Methods in Enzymology* Vol. 243 241-260 (Academic Press, 1994).
- 23 Barton, L. L. & Fauque, G. D. Biochemistry, physiology and biotechnology of sulfate-reducing bacteria. *Advances in applied microbiology* **68**, 41-98, doi:10.1016/s0065-2164(09)01202-7 (2009).
- 24 Ellis, R. J. Sulphate activation in higher plants. *Planta* **88**, 34-42, doi:10.1007/BF00396112 (1969).
- 25 Reuveny, Z. Derepression of ATP sulfurylase by the sulfate analogs molybdate and selenate in cultured tobacco cells. *Proceedings of the National Academy of Sciences of the United States of America* **74**, 619-622, doi:10.1073/pnas.74.2.619 (1977).

- 26 Biswas, K. C., Woodards, N. A., Xu, H. & Barton, L. L. Reduction of molybdate by sulfate-reducing bacteria. *Biometals* **22**, 131-139, doi:10.1007/s10534-008-9198-8 (2009).
- 27 Krissinel, E. & Henrick, K. Inference of macromolecular assemblies from crystalline state. *J Mol Biol* **372**, 774-797, doi:10.1016/j.jmb.2007.05.022 (2007).
- 28 Jespersen, M. & Wagner, T. How a methanogen assimilates sulfate: Structural and functional elucidation of the complete sulfate-reduction pathway. 2022.2010.2018.512691, doi:10.1101/2022.10.18.512691 %J bioRxiv (2022).
- 29 Beynon, J. D. *et al.* Crystal structure of ATP sulfurylase from the bacterial symbiont of the hydrothermal vent tubeworm *Riftia pachyptila*. *Biochemistry* **40**, 14509-14517, doi:10.1021/bi015643l (2001).
- 30 Taguchi, Y., Sugishima, M. & Fukuyama, K. Crystal structure of a novel zinc-binding ATP sulfurylase from *Thermus thermophilus* HB8. *Biochemistry* **43**, 4111-4118, doi:10.1021/bi036052t (2004).
- 31 Jespersen, M. & Wagner, T. Assimilatory sulfate reduction in the marine methanogen *Methanothermococcus thermolithotrophicus*. *Nature Microbiology* **8**, doi:10.1038/s41564-023-01398-8 (2023).
- 32 Kushkevych, I. *et al.* Adenosine-5'-phosphosulfate- and sulfite reductases activities of sulfate-reducing bacteria from various environments. *Biomolecules* **10**, 921 (2020).
- 33 Chiang, Y. L. *et al.* Crystal structure of Adenylylsulfate reductase from *Desulfovibrio gigas* suggests a potential self-regulation mechanism involving the C terminus of the beta-subunit. *Journal of bacteriology* **191**, 7597-7608, doi:10.1128/jb.00583-09 (2009).
- 34 Fritz, G. *et al.* Structure of adenylylsulfate reductase from the hyperthermophilic *Archaeoglobus fulgidus* at 1.6-Å resolution. *Proceedings of the National Academy of Sciences of the United States of America* **99**, 1836-1841, doi:10.1073/pnas.042664399 % (2002).
- 35 Ferreira, D. *et al.* The DsrD functional marker protein is an allosteric activator of the DsrAB dissimilatory sulfite reductase. *Proceedings of the National Academy of Sciences of the United States of America* **119**, e2118880119, doi:10.1073/pnas.2118880119 (2022).
- 36 Parey, K., Warkentin, E., Kroneck, P. M. H. & Ermler, U. Reaction cycle of the dissimilatory sulfite reductase from *Archaeoglobus fulgidus*. *Biochemistry* **49**, 8912-8921, doi:10.1021/bi100781f (2010).
- 37 Dahl, C., Kredich, N. M., Deutzmann, R. & Trüper, H. G. Dissimilatory sulphite reductase from *Archaeoglobus fulgidus*: physico-chemical properties of the enzyme and cloning, sequencing and analysis of the reductase genes. *Journal of general microbiology* **139**, 1817-1828, doi:10.1099/00221287-139-8-1817 (1993).

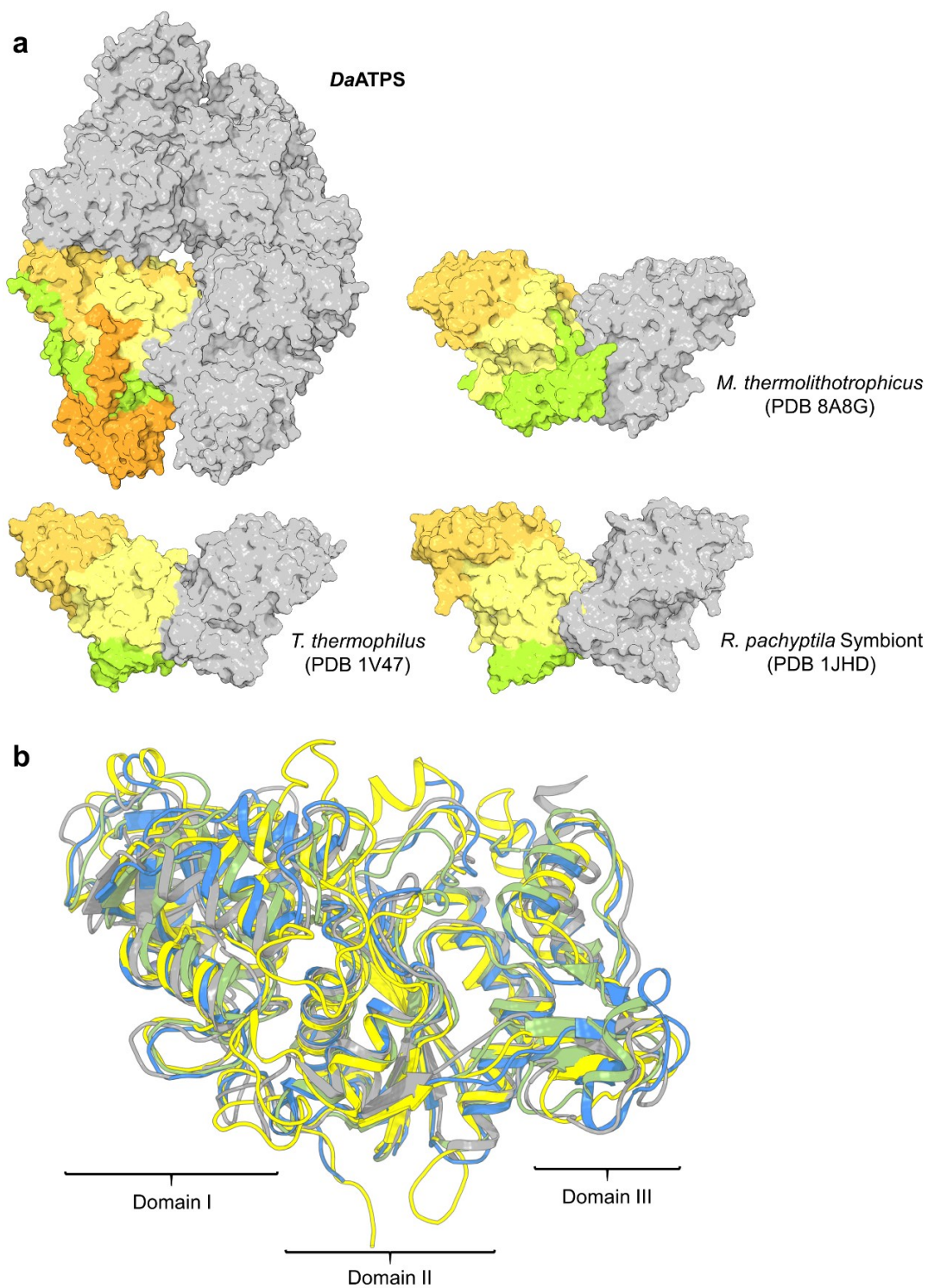
- 38 Oliveira, T. F. *et al.* The crystal structure of *Desulfovibrio vulgaris* dissimilatory sulfite reductase bound to DsrC provides novel insights into the mechanism of sulfate respiration. *J Biol Chem* **283**, 34141-34149, doi:10.1074/jbc.M805643200 (2008).
- 39 Murphy, M. J., Siegel, L. M., Tove, S. R. & Kamin, H. Siroheme: a new prosthetic group participating in six-electron reduction reactions catalyzed by both sulfite and nitrite reductases. *Proceedings of the National Academy of Sciences of the United States of America* **71**, 612-616, doi:10.1073/pnas.71.3.612 (1974).
- 40 Ostrowski, J. *et al.* Characterization of the cysJIH regions of *Salmonella typhimurium* and *Escherichia coli* B. DNA sequences of cysI and cysH and a model for the siroheme-Fe<sub>4</sub>S<sub>4</sub> active center of sulfite reductase hemoprotein based on amino acid homology with spinach nitrite reductase. *J Biol Chem* **264**, 15726-15737 (1989).
- 41 Schiffer, A. *et al.* Structure of the dissimilatory sulfite reductase from the hyperthermophilic archaeon *Archaeoglobus fulgidus*. *J Mol Biol* **379**, 1063-1074, doi:10.1016/j.jmb.2008.04.027 (2008).
- 42 Muyzer, G. & Stams, A. J. The ecology and biotechnology of sulphate-reducing bacteria. *Nat Rev Microbiol* **6**, 441-454, doi:10.1038/nrmicro1892 (2008).
- 43 Bowles, M. W., Mogollón, J. M., Kasten, S., Zabel, M. & Hinrichs, K.-U. Global rates of marine sulfate reduction and implications for sub-sea-floor metabolic activities. *Science (New York, N.Y.)* **344**, 889-891, doi:10.1126/science.1249213 (2014).
- 44 Jørgensen, B. B. Mineralization of organic matter in the sea bed-the role of sulphate reduction. *Nature* **296**, 643-645, doi:10.1038/296643a0 (1982).
- 45 Ramos, A. R., Keller, K. L., Wall, J. D. & Pereira, I. A. The membrane QmoABC complex interacts directly with the dissimilatory adenosine 5'-phosphosulfate reductase in sulfate reducing bacteria. *Front Microbiol* **3**, 137, doi:10.3389/fmicb.2012.00137 (2012).
- 46 Wenk, C. B., Wing, B. A. & Halevy, I. Electron carriers in microbial sulfate reduction inferred from experimental and environmental sulfur isotope fractionations. *The ISME Journal* **12**, 495-507, doi:10.1038/ismej.2017.185 (2018).
- 47 Fritz, G., Büchert, T. & Kroneck, P. M. The function of the [4Fe-4S] clusters and FAD in bacterial and archaeal adenylylsulfate reductases. Evidence for flavin-catalyzed reduction of adenosine 5'-phosphosulfate. *J Biol Chem* **277**, 26066-26073, doi:10.1074/jbc.M203397200 (2002).
- 48 Duarte, A. G., Santos, A. A. & Pereira, I. A. C. Electron transfer between the QmoABC membrane complex and adenosine 5'-phosphosulfate reductase. *Biochimica et Biophysica Acta (BBA) - Bioenergetics* **1857**, 380-386, doi:10.1016/j.bbabi.2016.01.001 (2016).
- 49 Wagner, T., Koch, J., Ermler, U. & Shima, S. Methanogenic heterodisulfide reductase (HdrABC-MvhAGD) uses two noncubane [4Fe-4S] clusters for reduction. *Science* **357**, 699-703, doi:10.1126/science.aan0425 (2017).

- 50 Cline, J. D. Spectrophotometric determination of hydrogen sulfide in natural waters *Limnology and Oceanography* **14**, 454-458, doi:org/10.4319/lo.1969.14.3.0454 (1969).
- 51 Vonrhein, C. *et al.* Data processing and analysis with the *autoPROC* toolbox. *Acta Crystallographica Section D* **67**, 293-302, doi:doi:10.1107/S0907444911007773 (2011).
- 52 Liebschner, D. *et al.* Macromolecular structure determination using X-rays, neutrons and electrons: recent developments in Phenix. *Acta Crystallogr D Struct Biol* **75**, 861-877, doi:10.1107/S2059798319011471 (2019).
- 53 Terwilliger, T. C. *et al.* Decision-making in structure solution using Bayesian estimates of map quality: the PHENIX AutoSol wizard. *Acta Crystallogr D Biol Crystallogr* **65**, 582-601, doi:10.1107/s0907444909012098 (2009).
- 54 Emsley, P., Lohkamp, B., Scott, W. G. & Cowtan, K. Features and development of Coot. *Acta Crystallogr D Biol Crystallogr* **66**, 486-501, doi:10.1107/S0907444910007493 (2010).
- 55 Bricogne, G. *et al.* BUSTER version 2.10. 0. *Global Phasing Ltd, Cambridge, UK* (2017).
- 56 Lemaire, O. N. *et al.* Small membranous proteins of the TorE/NapE family, crutches for cognate respiratory systems in *Proteobacteria*. *Sci Rep* **8**, doi:10.1038/s41598-018-31851-2 (2018).
- 57 Thomas, P. E., Ryan, D. & Levin, W. An improved staining procedure for the detection of the peroxidase activity of cytochrome *P*-450 on sodium dodecyl sulfate polyacrylamide gels. *Analytical biochemistry* **75**, 168-176, doi:10.1016/0003-2697(76)90067-1 (1976).
- 58 Saitou, N. & Nei, M. The neighbor-joining method: a new method for reconstructing phylogenetic trees. *Molecular Biology and Evolution* **4**, 406-425, doi:10.1093/oxfordjournals.molbev.a040454 %J Molecular Biology and Evolution (1987).
- 59 Felsenstein, J. Confidence limits on phylogenies: an approach using the bootstrap. *Evolution* **39**, 783-791, doi:10.2307/2408678 (1985).
- 60 Jones, D. T., Taylor, W. R. & Thornton, J. M. The rapid generation of mutation data matrices from protein sequences. *Computer applications in the biosciences : CABIOS* **8**, 275-282, doi:10.1093/bioinformatics/8.3.275 (1992).
- 61 Tamura, K., Stecher, G. & Kumar, S. MEGA11: Molecular evolutionary genetics analysis version 11. *Molecular Biology and Evolution* **38**, 3022-3027, doi:10.1093/molbev/msab120 % (2021).
- 62 Edgar, R. C. MUSCLE: a multiple sequence alignment method with reduced time and space complexity. *BMC Bioinformatics* **5**, 113, doi:10.1186/1471-2105-5-113 (2004).

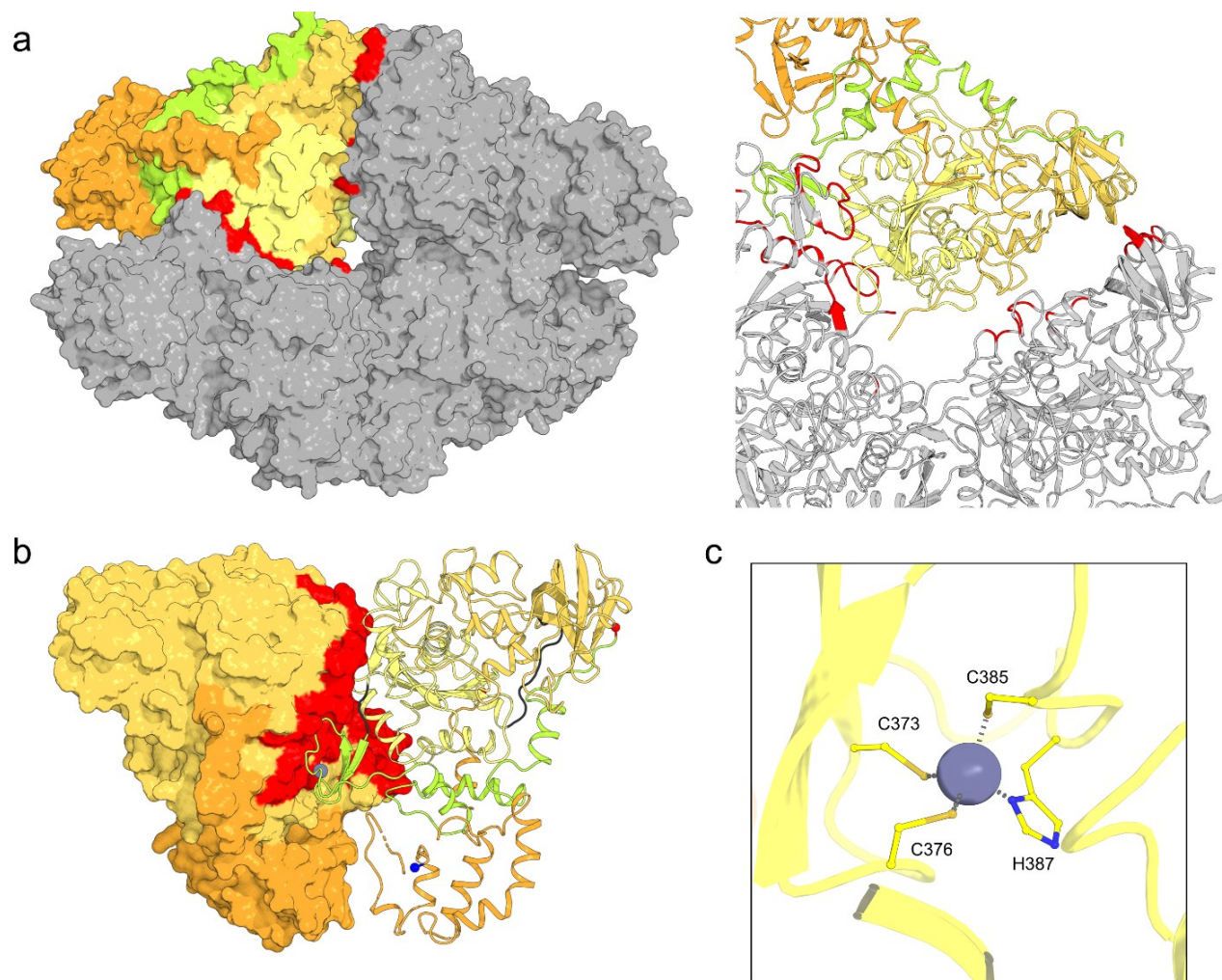
## Extended Data



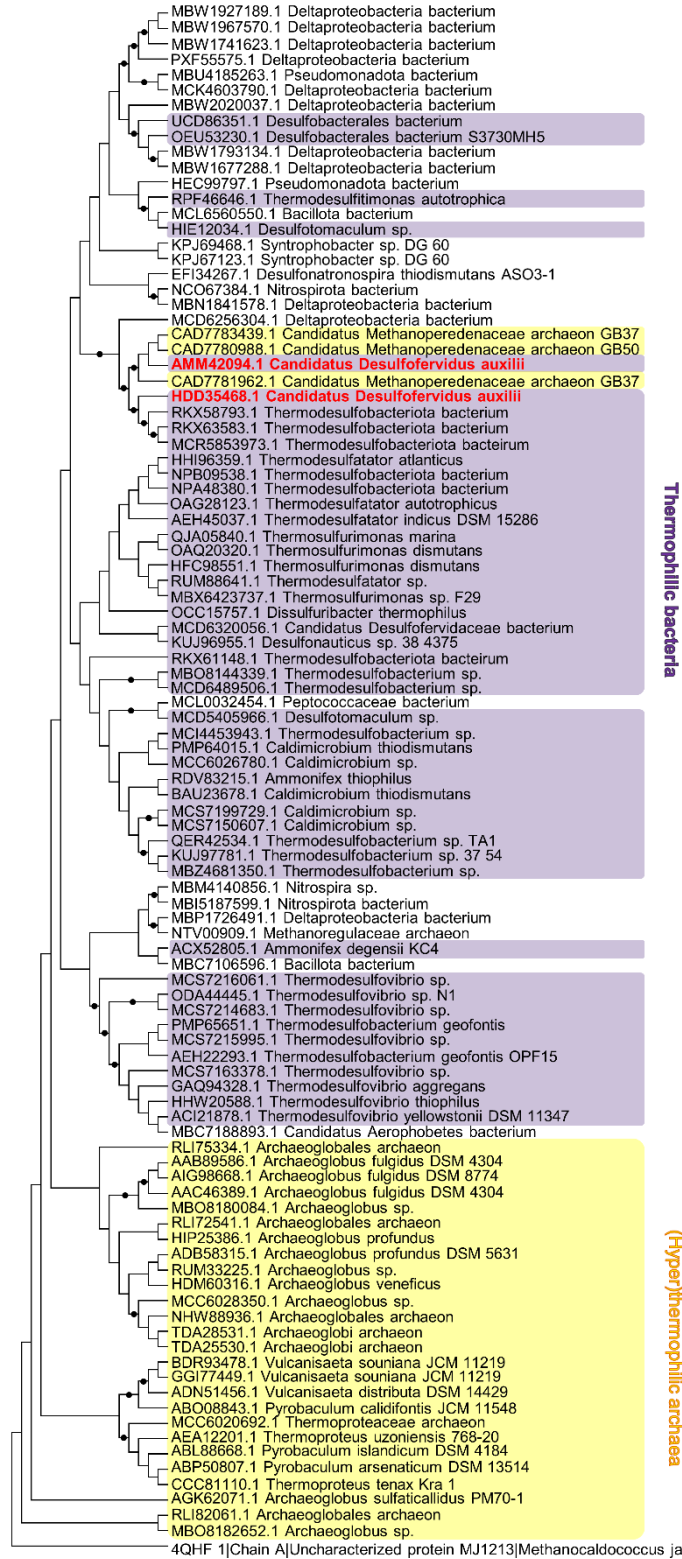
**Extended Data Figure 1. Activity and estimation of oligomerization of *DaATPS*.** **a**, Native PAGE of the soluble extract from the enrichment culture (10  $\mu$ g loaded), the first purification step (5  $\mu$ g loaded) and for the second purification step and the pure dSir 2  $\mu$ g were loaded on the gel coloured by heme staining. **b**, UV-visible spectrum of 0.05 mg *DaDsrAB* measured anaerobically (100%  $N_2$ ) in 50 mM Tris/HCl pH 7.5. *DaDsrAB* displays the typical spectra of [Fe-S]-cluster and siroheme-containing enzymes<sup>3</sup>. **c**, Size exclusion chromatography profile of *DaATPS* and a high molecular weight calibration kit (GE Healthcare). **d**, Gel filtration profile of *DaAPSR* and *DaDsrAB* with a high molecular weight calibration kit (GE Healthcare).



**Extended Data Figure 2. Comparison of ATP sulfurylases.** **a**, Comparison of ATPS in surface representation, coloured by domain I (light orange), II (yellow), III (light green) with the  $\beta$ -subunit from *DaATPS* in orange. The grey surface corresponds to the opposing protomer(s). **b**, Superposition of the monomers of *DaATPS* (yellow, only the  $\alpha$ -subunit), *MtATPS* (blue), *TtATPS* (light green) and *RrsATPS* (grey) are shown in cartoon. Abbreviations and rmsd can be found in Extended Data Table 2.

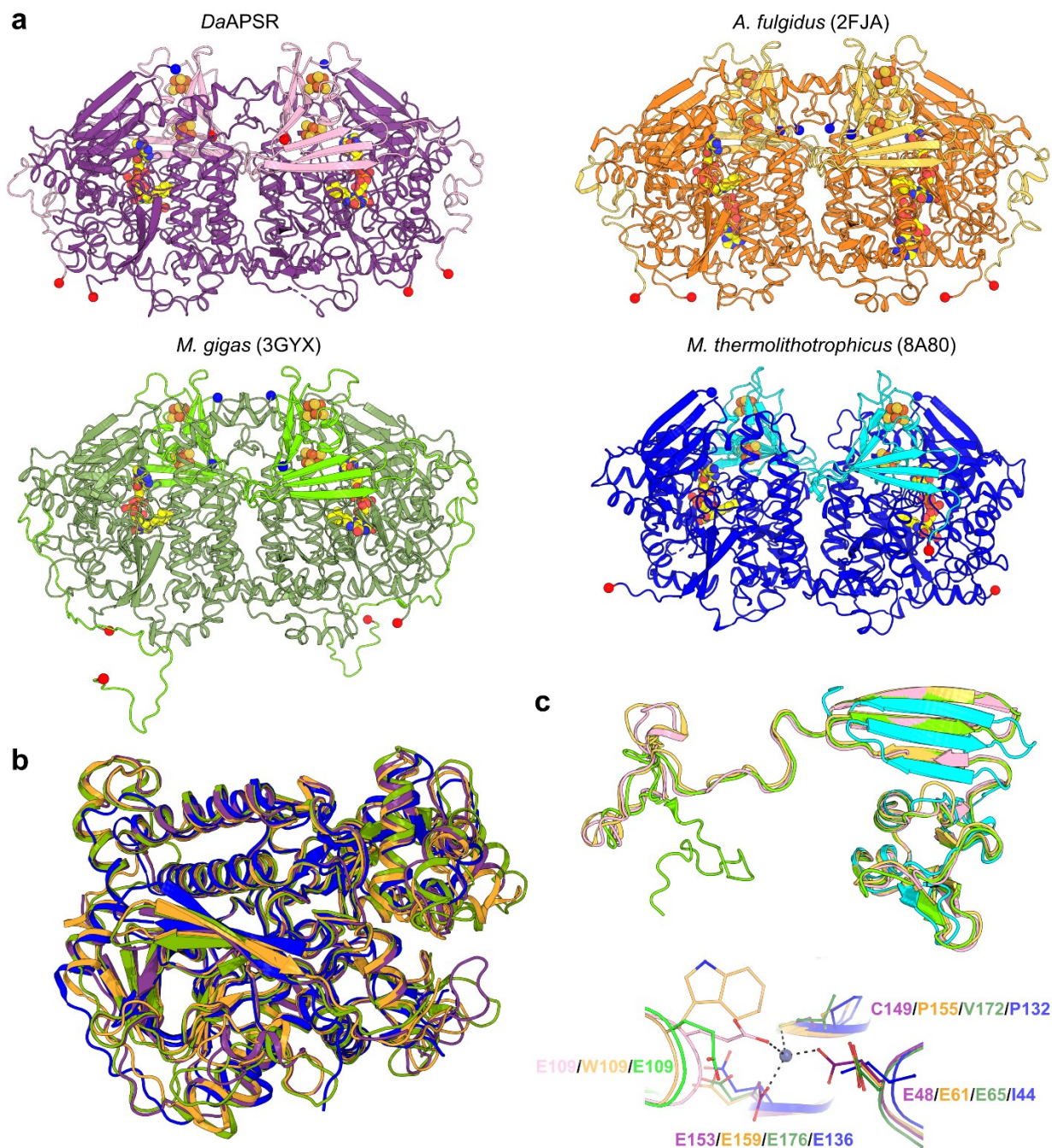


**Extended Data Figure 3. Detailed quaternary structure of *DaATPS*.** **a**, Oligomerisation of *DaATPS*, in surface representation (left) and a close-up in cartoon (right). For **a** and **b**, one heterodimer has the  $\alpha$ -subunit coloured according to its domain affiliation (domain I in light orange, domain II in light yellow, domain III in limon) and the  $\beta$ -subunit in dark orange. The adjacent protomers are shown in grey. The surface area involved in the oligomerisation of *DaATPS* is shown in red. Domain I (residues 1 - 184) establishes the interface to the opposing heterotetramer, totalling a buried area of  $915 \text{ \AA}^2$ , mainly by salt bridges; Domain II (residues 194 - 366) creates the basic dimer-dimer interface with  $1687 \text{ \AA}^2$ , and domain III (residues 370 - 455) also interacts with the adjacent dimer and establishes the main contact to the  $\beta$ -subunit within the dimer. **b**, One heterotetramer, with one half shown in surface ( $\alpha$ -subunit in yellow and  $\beta$ -subunit in bright orange) and the other half in cartoon representation. The dimer-dimer contacts, established by domains II and III, are shown as a red surface. The N- and C-termini are shown by a blue and a red sphere, respectively. **c**, Coordination of the zinc ion, illustrated as a grey sphere. The residues coordinating it are shown as sticks and are labelled. Carbon, nitrogen and sulfur are coloured in yellow, blue and dark yellow, respectively.

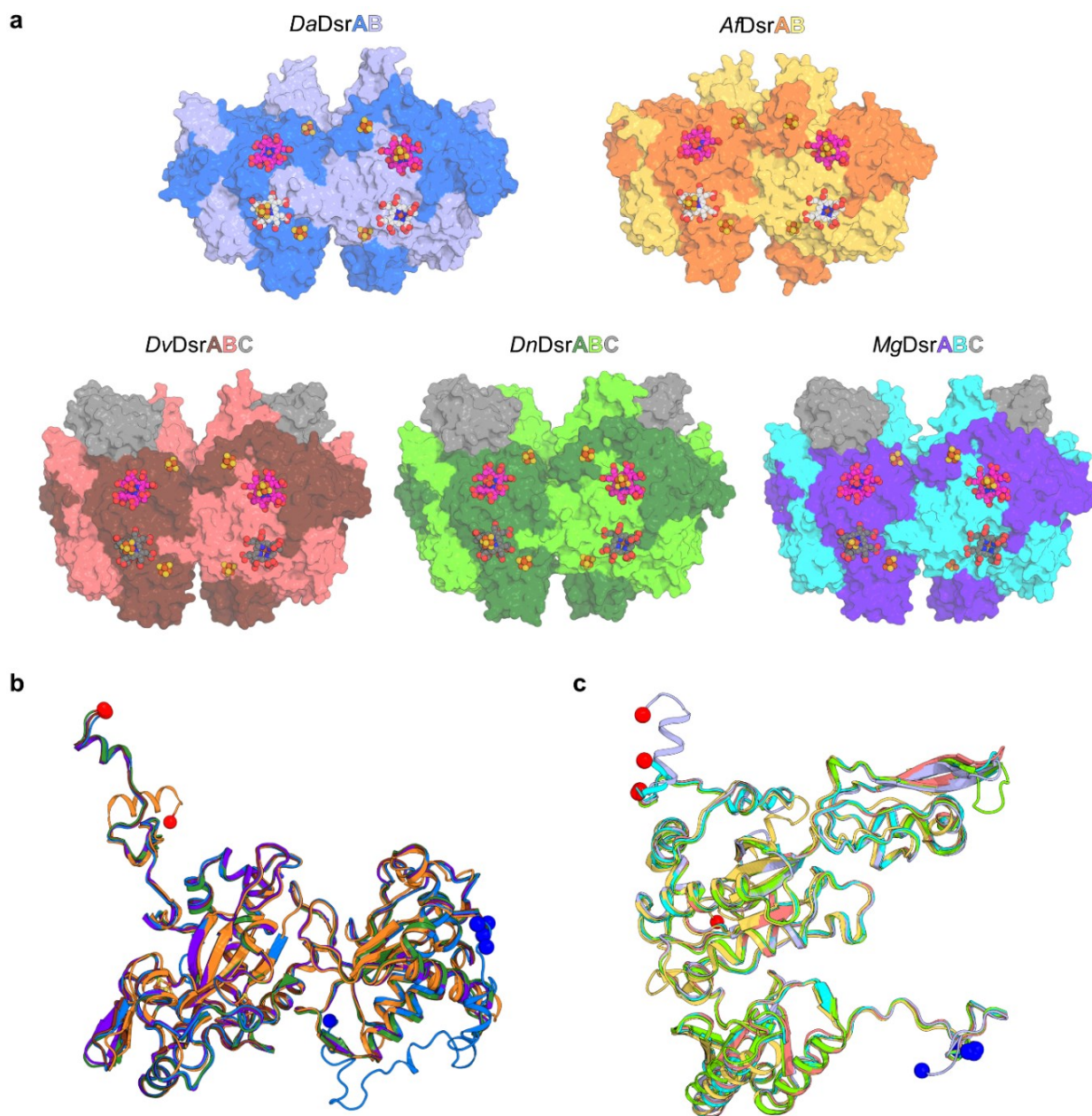


**Extended Data Figure 4. Phylogenetic tree of the ATPS  $\beta$ -subunit.** Phylogenetic analysis of the  $\beta$ -subunit from *DaATPS* (highlighted in bold red) across the NCBI database. (Hyper)thermophilic bacteria and archaea are highlighted by a purple and yellow background, respectively. Bootstrap support values  $\geq 90$  % are shown as dots on interior nodes.

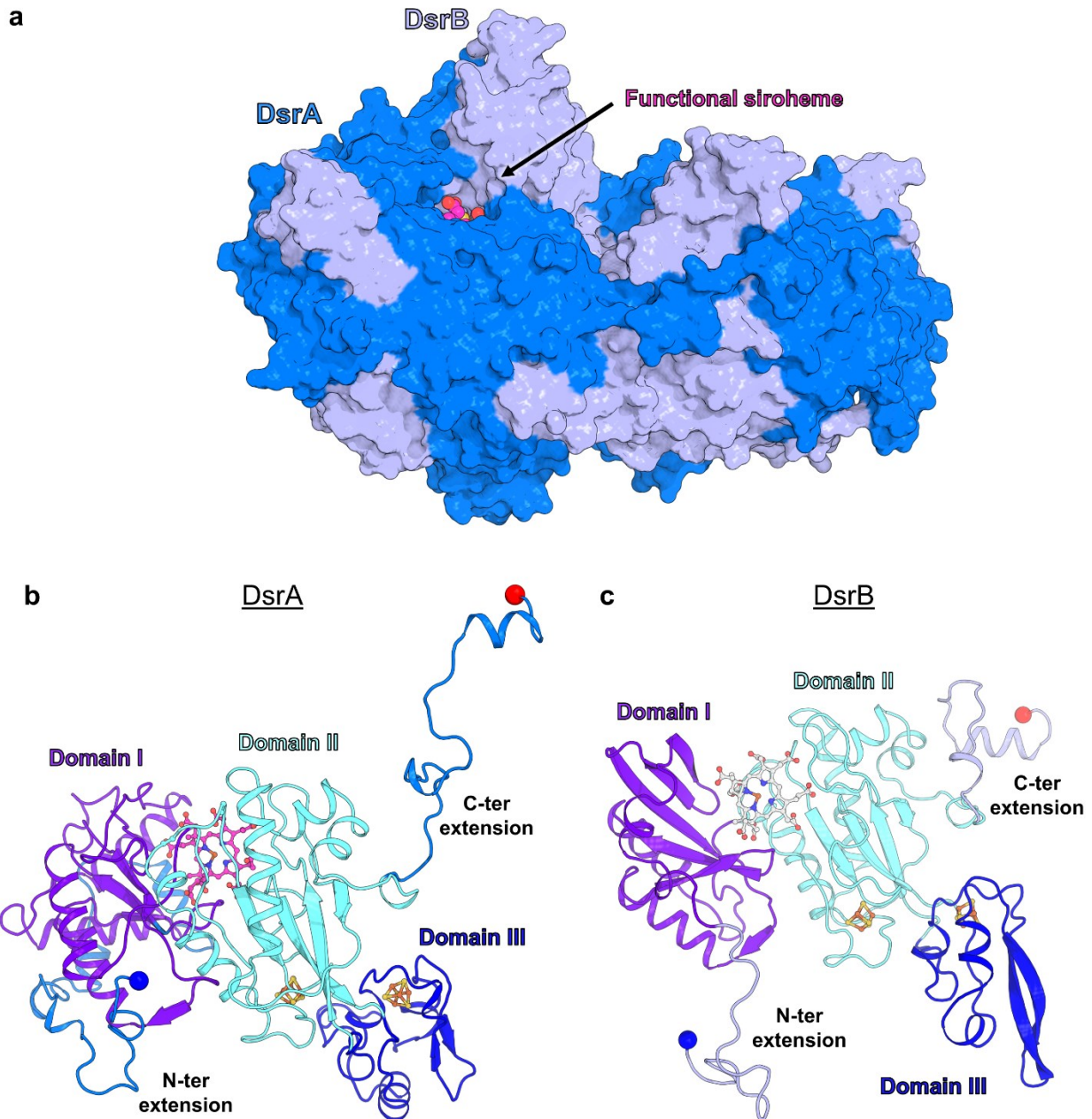




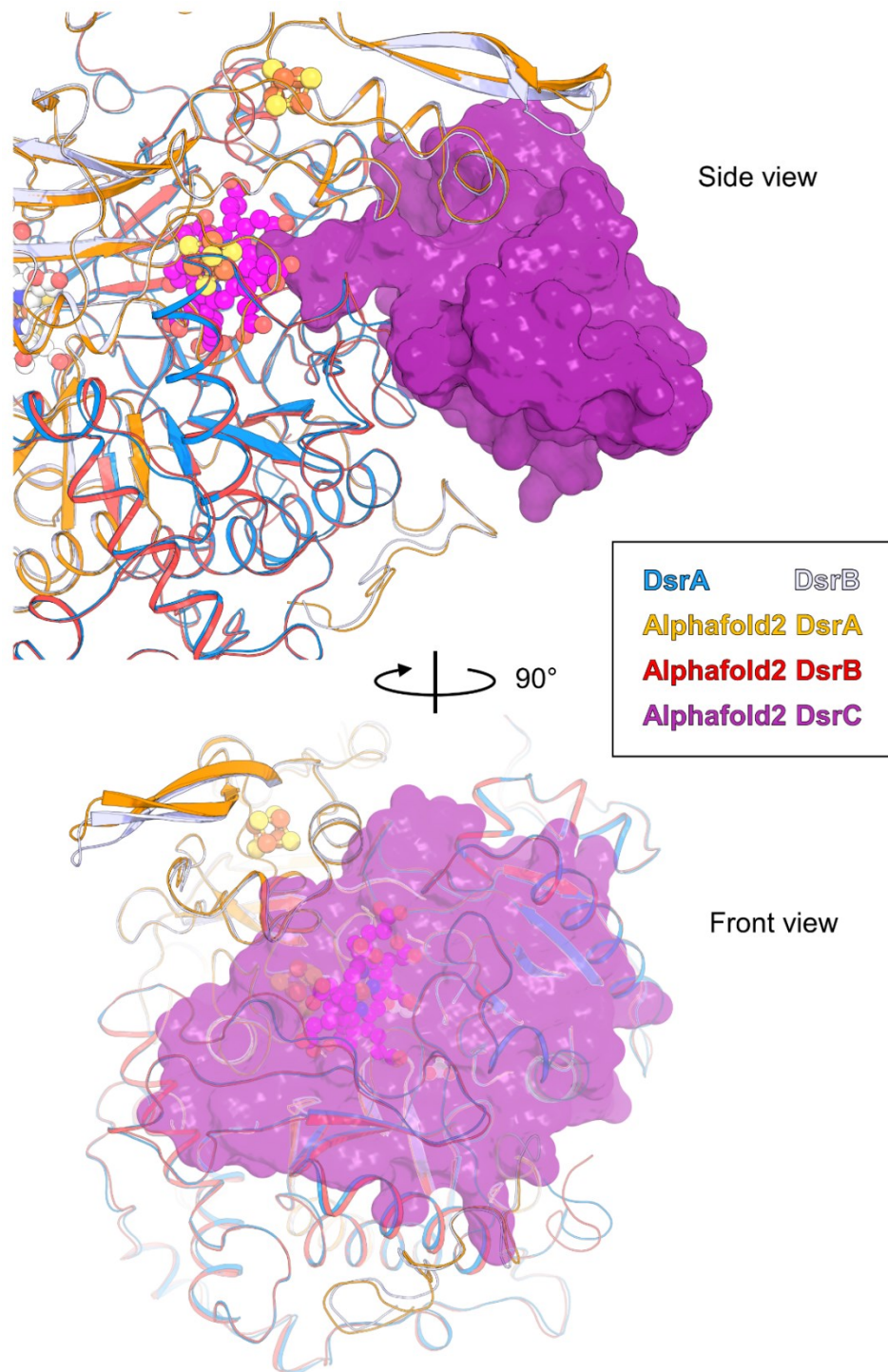
**Extended Data Figure 5. Comparison of *DaAPSR* and its structural homologues.** **a**, Overall comparison of APSRs and one APSR-like PAPSR (blue) in cartoon representation. The  $\alpha$ -subunits of the heterotetramers are shown in a darker colour, and the  $\beta$  subunits in a lighter one. The ligands are displayed in spheres and colour coded as follows, yellow (C), red (O), blue (N), orange (P), dark orange (Fe), and dark yellow (S). The N- and C-termini of the two subunits are shown by a blue and red sphere, respectively. **b**, Superposition of the  $\alpha$ -subunit of *DaAPSR* (purple), *MtPAPSR* (blue), *MgAPSR* (green) and *AfAPSR* (orange-yellow), shown in cartoons. Abbreviations and rmsd can be found in Extended Data Table 2. **c**, Superposition of the  $\beta$ -subunit of *DaAPSR* (light-pink), *MtPAPSR* (cyan), *MgAPSR* (light-green) and *AfAPSR* (light-yellow), shown in cartoons. The bottom panel represents the close-up of the divalent cation binding site at the  $\alpha/\beta$ -subunit interface with the same colour code as in **b** and **c**.



**Extended Data Figure 6. Comparison of dissimilatory sulfite reductases.** **a**, Comparison of DsrAB(C) in surface representation. The DsrA subunits are shown in a darker colour, and the DsrB subunits are lighter. DsrC is coloured in grey. The ligands are displayed in balls and stick with the atoms oxygen, nitrogen, phosphorus, iron and sulfur coloured respectively in red, blue, orange, dark orange and yellow. Sirohydrochlorins have carbon atoms coloured in grey, sirohemes concealed in the enzyme are coloured in white and fully exposed functional sirohemes have carbon atoms coloured in pink. **b**, Superposition of *DaDsrA* (dark blue), *MgDsrA* (purple-blue), *DvDsrA* (brown), *DnDsrA* (dark green) and *AfDsrA* (orange), shown in cartoons. Abbreviations and rmsd can be found in Extended Data Table 2. **c**, Superposition of DsrB of *DaDsrB* (light blue), *MgDsrB* (cyan), *DvDsrB* (salmon), *DnDsrB* (light-green) and *AfDsrB* (yellow-orange), shown in cartoons. The N- and C-termini of DsrA and DsrB of each structure are shown by a blue and red sphere, respectively.



**Extended Data Figure 7. Solvent accessible siroheme and domain organization of DsrA and DsrB.** **a**, Only the functional DsrB-siroheme is accessible to solvent, here indicated by an arrow from one heterodimer. DsrAB complex is represented as a surface, with DsrA being coloured in marine blue and DsrB coloured in light blue. Spheres highlight the functional siroheme. **b**, **c**, Domain organization of (b) DsrA and (c) DsrB. Domain I is shown in purple (DsrA: residues 61-209; DsrB: residues 25-134), domain II in aquamarine (DsrA: residues 210-282, 364-444; DsrB: residues 135-209, 279-367) and domain III in blue (DsrA: 283-363; DsrB: 210-278). The N- and C-terminal extensions are coloured in marine blue for DsrA and light blue for DsrB. The N- and C-termini are shown by a blue and red sphere, respectively. For all panels, atoms are coloured as follows, with the carbon, oxygen, nitrogen, iron and sulfur atoms coloured in pink/white, red, blue, dark orange and yellow, respectively.



**Extended Data Figure 8. Comparison of the experimental structure with the AlphaFold2 DsrABC model.** DsrAB experimentally and modelled by AlphaFold2 are shown as cartoons. DsrC modelled by AlphaFold2 is represented as a plain (top) and transparent (bottom) surface. Metallocofactors are highlighted by balls, with atoms coloured as follows: pink (C), red (O), blue (N), orange (Fe) and yellow (S), respectively.

**Extended Data Table 1.** X-ray analysis statistics.

	<b>ATPS</b>	<b>SAD-APSR</b>	<b>APSR</b>	<b>Dsr</b>
<b>Data collection</b>				
Synchrotron source	SLS PXIII	SOLEIL PXI	SOLEIL PXI	SOLEIL PXI
Wavelength (Å)	2.07505	1.74013	0.97856	1.74013
Space group	<i>P2<sub>1</sub>2<sub>1</sub>2</i>	<i>P2<sub>1</sub></i>	<i>P2<sub>1</sub></i>	<i>P2<sub>1</sub></i>
Resolution (Å)	86.60 – 2.34 (2.65 – 2.34)	78.40 – 1.90 (1.99 – 1.90)	74.09 – 1.65 (1.74 – 1.65)	127.23 – 2.48 (2.66 – 2.48)
Cell dimensions				
a, b, c (Å)	123.44, 92.10, 121.51	66.33, 132.74, 98.31	66.44, 115.26, 97.91	127.24, 75.76, 205.50
$\alpha, \beta, \gamma$ (°)	90, 90, 90	90, 98.80, 90	90, 98.93, 90	90, 90.30, 90
R <sub>merge</sub> (%) <sup>a</sup>	26.3 (143.2)	27.3 (208.9)	37.1 (238.4)	19.2 (104.4)
R <sub>pim</sub> (%) <sup>a</sup>	7.5 (40.7)	11.2 (97.0)	7.2 (49.7)	7.9 (45.6)
CC <sub>1/2</sub> <sup>a</sup>	0.994 (0.661)	0.994 (0.369)	0.995 (0.607)	0.991 (0.580)
I/ $\sigma_I$ <sup>a</sup>	10.7 (1.8)	9.5 (1.6)	8.9 (1.8)	8.3 (1.6)
Spherical completeness <sup>a</sup>	55.6 (9.3)	77.9 (29.1)	81.4 (29.9)	72.2 (18.7)
Ellipsoidal completeness <sup>a</sup>	92.2 (70.9)	91.0 (66.1)	96.2 (74.6)	92.7 (61.4)
Redundancy <sup>a</sup>	12.9 (13.1)	13.5 (10.4)	27.3 (23.1)	6.8 (5.9)
Nr. unique reflections <sup>a</sup>	32,753 (1,639)	102,958 (5,148)	141,648 (7,084)	100,887 (5,046)
<b>Refinement</b>				
Resolution (Å)	47.24 – 2.34	48.57 – 1.90	49.51 – 1.65	48.72 – 2.48
Number of reflections	32,733	102,757	141,620	100,863
R <sub>work</sub> /R <sub>free</sub> <sup>b</sup> (%)	20.35/22.31	15.78/17.64	16.15/19.39	19.83/22.17
Number of atoms				
Protein	9,234	12,183	12,232	27,868
Ligands/ions	39	191	321	713
Solvent	161	1,258	1,325	363
Mean B-value (Å <sup>2</sup> )	38.82	20.15	19.77	44.57
Molprobit clash score, all atoms	2.27	4.08	1.95	4.47
Ramachandran plot				
Favoured regions (%)	97.97	97.31	97.69	96.43
Outlier regions (%)	0.27	0.07	0	0.20
rmsd <sup>c</sup> bond lengths (Å)	0.009	0.011	0.009	0.009
rmsd <sup>c</sup> bond angles (°)	1.247	0.980	1.137	1.479

<sup>a</sup> Values relative to the highest resolution shell are within parentheses. <sup>b</sup> R<sub>free</sub> was calculated as the R<sub>work</sub> for 5 % of the reflections that were not included in the refinement. <sup>c</sup> rmsd, root mean square deviation.

**Extended Data Table 2. Sequence and structural alignment of *Da*ATPS.** Sequence alignment was 85 performed using PyMOL version 2.2.0 (Schrödinger, LLC).

<b>ATPS (alignment on the <math>\alpha</math>-subunit)</b>			
Name of the organisms	Abbreviation	PDB code	Rmsd in Å (aligned C $\alpha$ )
<i>Candidatus Desulfofervidus auxilii</i>	<i>Da</i> ATPS		
<i>Methanothermococcus thermolithotrophicus</i>	<i>Mt</i> ATPS	8A8G	1.855 (310)
<i>Thermus thermophilus</i>	<i>Tt</i> ATPS	1V47	1.964 (290)
Endosymbiont of <i>Riftia pachyptila</i>	<i>Rrs</i> ATPS	1JHD	1.956 (266)
<b>APSR (alignment on the <math>\alpha</math> and <math>\beta</math> subunits)</b>			
<i>Candidatus Desulfofervidus auxilii</i>	<i>Da</i> APSR		
<i>Archaeoglobus fulgidus</i>	<i>Af</i> APSR	2FJA	0.698 (566)
<i>Megalodesulfovibrio gigas</i>	<i>Mg</i> APSR	3GYX	0.584 (594)
<i>Methanothermococcus thermolithotrophicus</i>	<i>Mt</i> PAPSR	8A8O	1.075 (475)
<b>Dsr (alignment on the <math>\alpha</math>-subunit)</b>			
<i>Candidatus Desulfofervidus auxilii</i>	<i>Da</i> DsrAB		
<i>Archaeoglobus fulgidus</i>	<i>Af</i> DsrAB	3MM5	0.818 (372)
<i>Desulfovibrio vulgaris</i>	<i>Dv</i> DsrABC	2V4J	0.433 (378)
<i>Desulfomicrobium norvegicum</i>	<i>Dn</i> DsrABC	2XSJ	0.575 (403)
<i>Megalodesulfovibrio gigas</i>	<i>Mg</i> DsrABC	3OR2	0.467 (387)
<b>Dsr (alignment on the <math>\beta</math>-subunit)</b>			
<i>Archaeoglobus fulgidus</i>	<i>Af</i> DsrAB	3MM5	0.601 (297)
<i>Desulfovibrio vulgaris</i>	<i>Dv</i> DsrABC	2V4J	0.411 (328)
<i>Desulfomicrobium norvegicum</i>	<i>Dn</i> DsrABC	2XSJ	0.484 (321)
<i>Megalodesulfovibrio gigas</i>	<i>Mg</i> DsrABC	3OR2	0.544 (349)

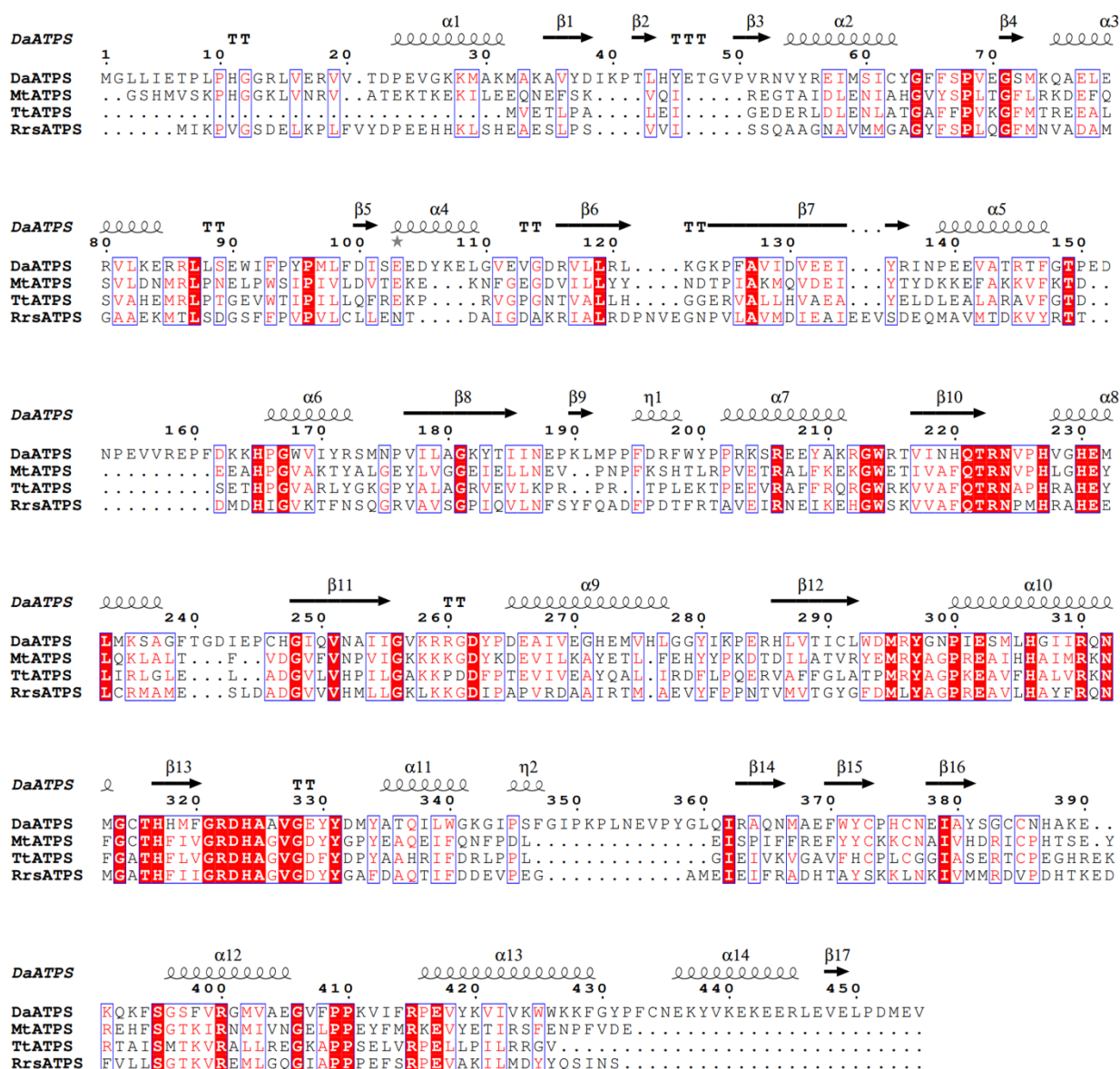
## References for Extended Data

- 1 Edgar, R. C. MUSCLE: a multiple sequence alignment method with reduced time and space complexity. *BMC Bioinformatics* **5**, 113, doi:10.1186/1471-2105-5-113 (2004).
- 2 Robert, X. & Gouet, P. Deciphering key features in protein structures with the new ENDscript server. *Nucleic Acids Res* **42**, W320-W324, doi:10.1093/nar/gku316 (2014).
- 3 Murphy, M. J., Siegel, L. M., Tove, S. R. & Kamin, H. Siroheme: a new prosthetic group participating in six-electron reduction reactions catalyzed by both sulfite and nitrite reductases. *Proceedings of the National Academy of Sciences of the United States of America* **71**, 612-616, doi:10.1073/pnas.71.3.612 (1974).

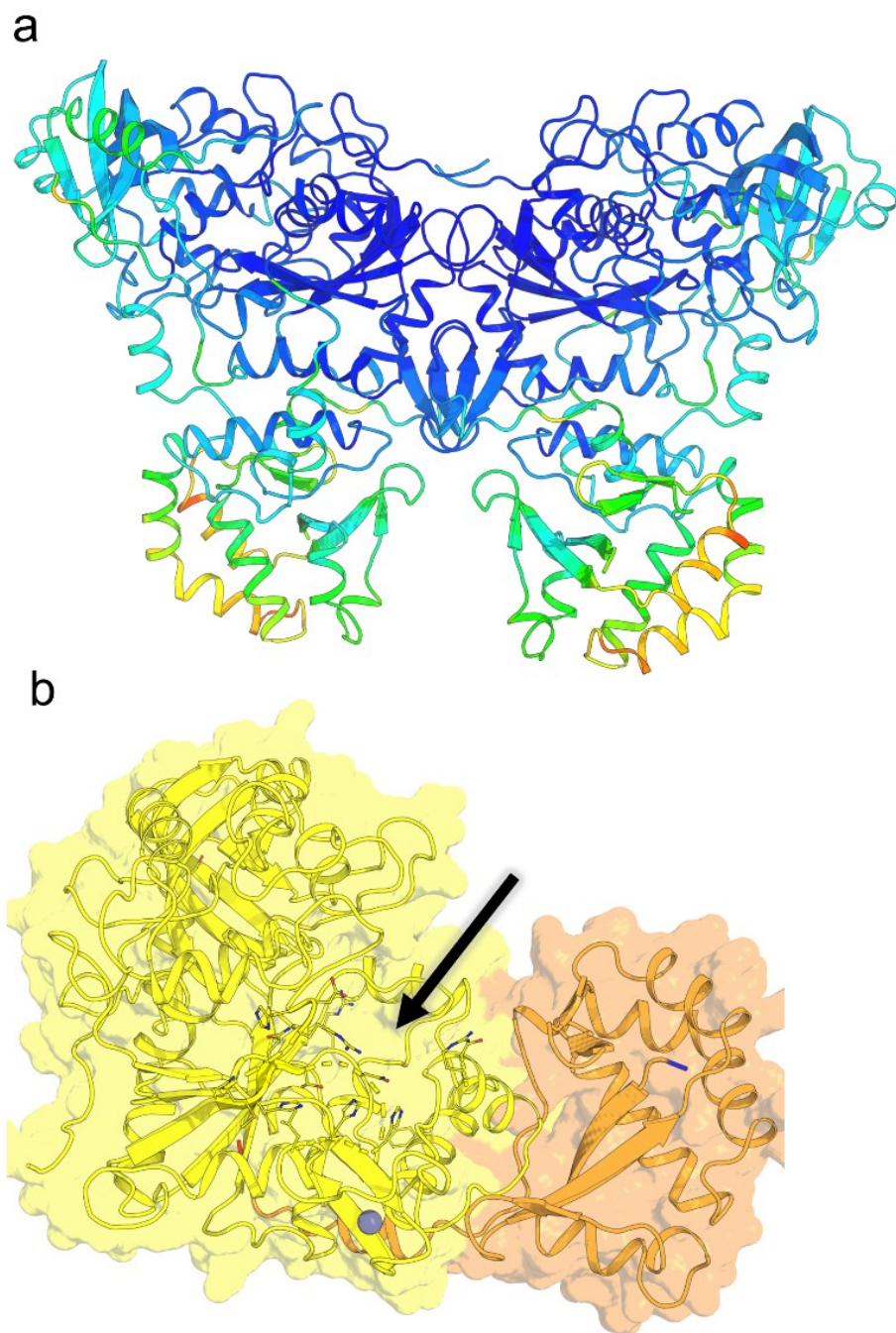




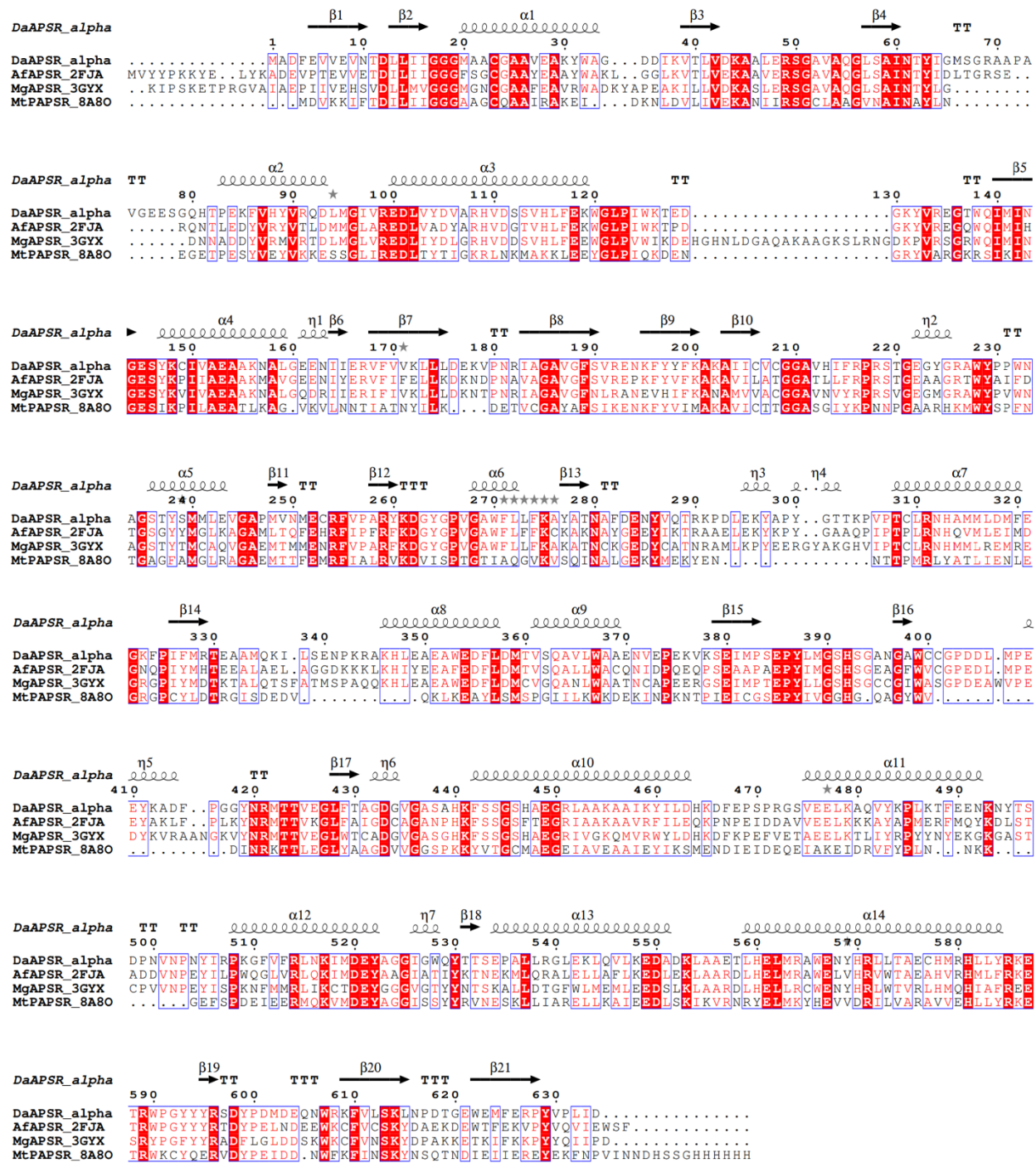
## Supplementary Information



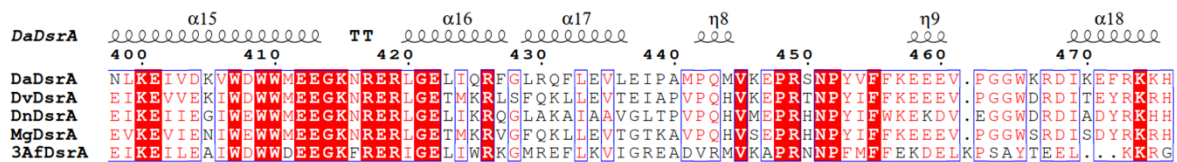
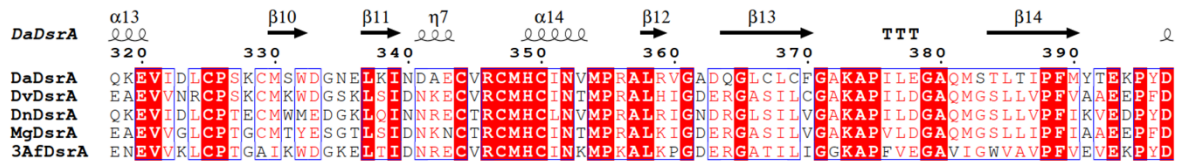
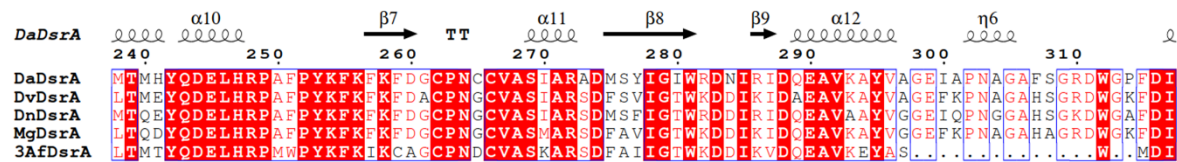
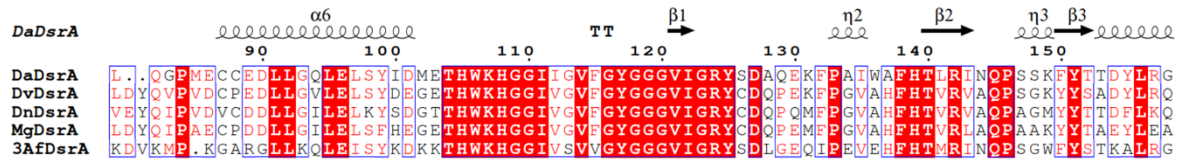
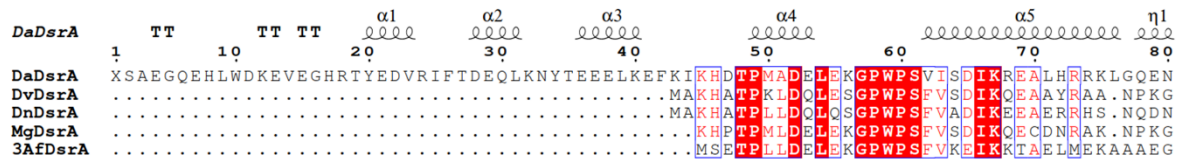
**Supplementary Figure 1. Sequence conservation across ATP sulfurylases.** DaATPS: *Candidatus Desulfofervidus auxilii* (WP\_066065687); MtATPS: *Methanothermococcus thermolithotrophicus* (PDB: 8A8G); TtATPS: *Thermus thermophilus* (PDB: 1V47), RrsATPS: Endosymbiont from *Riftia pachyptila* (PDB: 1JHD). Perfectly conserved residues are highlighted with a red background. Sequence alignment was done using MUSCLE<sup>1</sup>, secondary structure prediction was performed with ESPrnt 3.0<sup>2</sup>.



**Supplementary Figure 2.** **a**, B-factor profile of *DaATPS*, blue to red indicate low to high B-factors, respectively and **b**, accessibility of the active site, highlighted by a black arrow. *DaATPS* shown in cartoon with the  $\alpha$ -subunit in yellow and the  $\beta$ -subunit in bright-orange, with a transparent surface. The residues coordinating the substrate are shown as sticks with the atoms carbon, nitrogen, oxygen and sulfur are shown in light yellow, blue, red and yellow, respectively. The zinc ion is illustrated by a grey sphere.

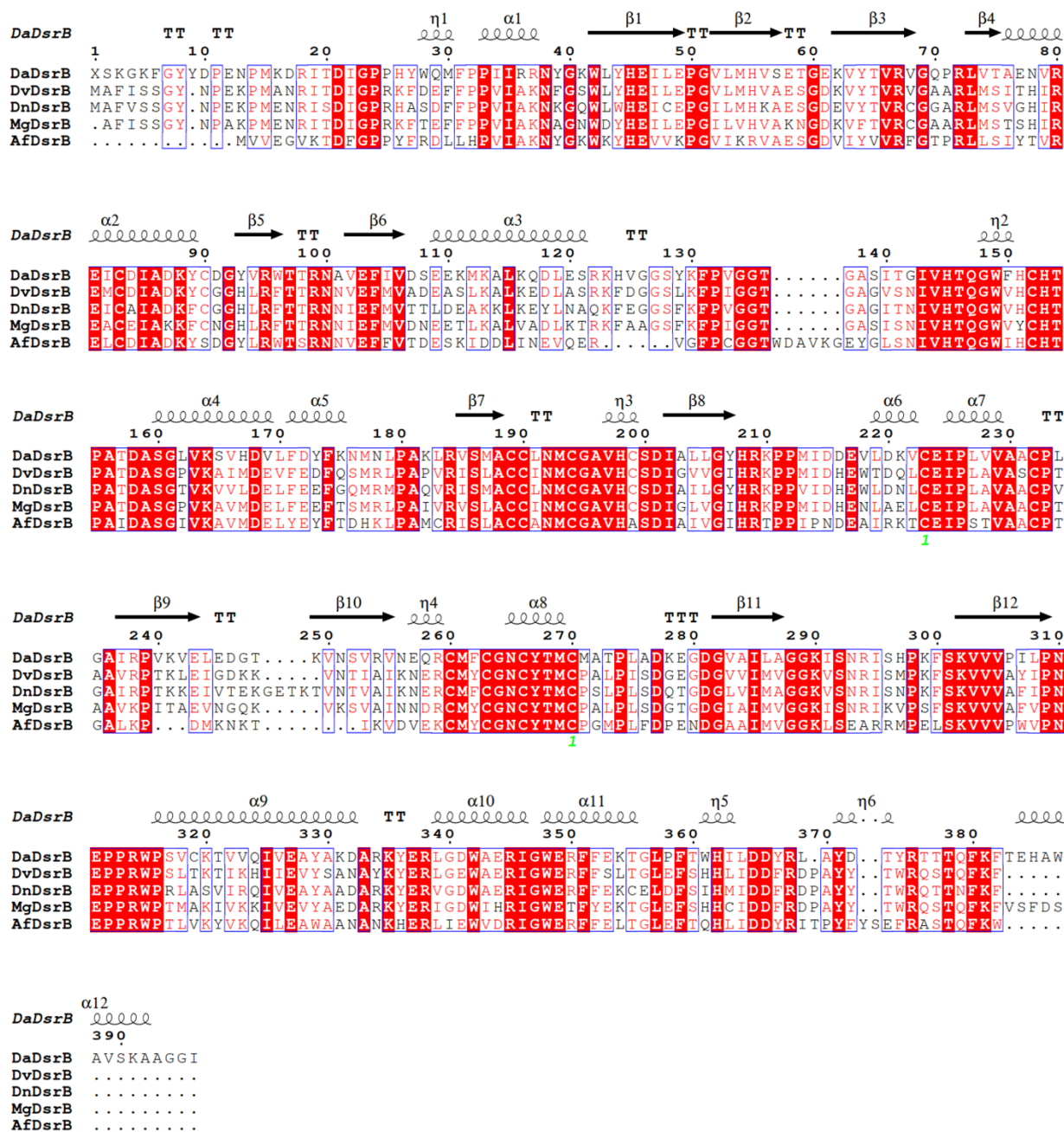


**Supplementary Figure 3. Sequence conservation across the alpha subunit of (P)APS reductases.** *DaAPSR*: *Candidatus Desulfobacterium auxilii* (WP\_066060364); *AfAPSR*: *Archaeoglobus fulgidus* (PDB: 2FJA) *Megalodesulfobacterium gigas* (*MgAPSR*, PDB: 3GYX) and the PAPS reductase from *Methanothermococcus thermolithotrophicus* (*MtPAPSR*, PDB: 8A80). Perfectly conserved residues are highlighted with a red background. Sequence alignment was done using MUSCLE<sup>1</sup>, secondary structure prediction was performed with ESPrnt 3.0<sup>2</sup>.



DaDsrA  
DvDsrA  
DnDsrA  
MgDsrA  
3AfDsrA

**Supplementary Figure 4. Sequence conservation across DsrA.** DaDsrA: *Ca. D. auxilii*; DvDsrA: *Desulfovibrio vulgaris*; DnDsrA: *Desulfomicrobium norvegicum*; MgDsrA: *Megalodesulfovibrio gigas*; AfDsrA: *Archaeoglobus fulgidus*. PDB codes can be found in Extended Data Table 4. Perfectly conserved residues are highlighted with a red background. Sequence alignment was done using MUSCLE<sup>1</sup>, secondary structure prediction was performed with ESPrnt 3.0<sup>2</sup>.



**Supplementary Figure 5. Sequence conservation across DsrB.** DaDsrB: *Ca. D. auxilii*; DvDsrB: *Desulfovibrio vulgaris*; DnDsrB: *Desulfomicrobium norvegicum*; MgDsrB: *Megalodesulfovibrio gigas*; AfDsrB: *Archaeoglobus fulgidus*. PDB codes can be found in Extended Data Table 4. Perfectly conserved residues are highlighted with a red background. Sequence alignment was done using MUSCLE<sup>1</sup>, secondary structure prediction was performed with ESPrift 3.0<sup>2</sup>

## References for Supplementary

- 1 Edgar, R. C. MUSCLE: a multiple sequence alignment method with reduced time and space complexity. *BMC Bioinformatics* **5**, 113, doi:10.1186/1471-2105-5-113 (2004).
- 2 Robert, X. & Gouet, P. Deciphering key features in protein structures with the new ENDscript server. *Nucleic Acids Res* **42**, W320-W324, doi:10.1093/nar/gku316 (2014).
- 3 Murphy, M. J., Siegel, L. M., Tove, S. R. & Kamin, H. Siroheme: a new prosthetic group participating in six-electron reduction reactions catalyzed by both sulfite and nitrite reductases. *Proceedings of the National Academy of Sciences of the United States of America* **71**, 612-616, doi:10.1073/pnas.71.3.612 (1974).

## Chapter VI

### Structure of a methane-generating enzyme isolated from wastewater treatment plant sludge

**Marion Jespersen<sup>1</sup>, Grace d'Angelo<sup>2</sup>, Almud Lonsing<sup>3</sup>, Sonja Dunemann<sup>4</sup>, Marie-Caroline Müller<sup>1</sup>, Nevena Maslač<sup>1</sup>, Bruno Hüttel<sup>4</sup>, Manuel Liebeke<sup>2</sup>, Jens Harder<sup>3</sup>, and Tristan Wagner<sup>1\*</sup>**

<sup>1</sup> Microbial Metabolism research group, Max Planck Institute for Marine Microbiology, Bremen, Germany.

<sup>2</sup> Department of Symbiosis, Max Planck Institute for Marine Microbiology, Bremen, Germany.

<sup>3</sup> Department of Molecular Ecology, Max Planck Institute for Marine Microbiology, Bremen, Germany.

<sup>4</sup> Max Planck Genome Centre, Cologne, Germany.

\*Correspondence: [twagner@mpi-bremen.de](mailto:twagner@mpi-bremen.de)

*Manuscript in preparation*

## Abstract

Microbial life continuously influences our planet and modern society by driving the global element cycle. As only a fraction of microbes can be cultivated, access to the molecular processes behind their bioconversion capabilities is limited. While omics technologies, recombinant protein production, and molecular modelling have unravelled the function and mechanisms of many enzymes from these uncultivable microbes, there is an unpredictable gap between these models and the environmental reality. Here, we bridge this gap by studying a natural enzyme from a complex heterogeneous microbial population. The mesocosm of a wastewater treatment plant was studied as it contains *Methanothrix* species, a methanogen considered to be the prime methane producer on planet Earth. Moreover, *Methanothrix* are extremely important in the anaerobic degradation of organic matter through the disproportionation of acetate. The methane-generating enzyme (methyl-coenzyme M reductase, MCR) was targeted because of its high natural cellular abundance, intrinsic colour, and typical three-subunit pattern on gel electrophoresis that simplified to follow the enzyme during purification. The raw sludge was processed, and the proteins were fractionated by chromatography, leading to an enriched population of MCR. The last step of isolation was performed by crystallization and led to the isolation of a single MCR. The structure of the  $(\alpha\beta\gamma)_2$  complex was refined to a resolution of 2.5 Å and harbours a classical F<sub>430</sub>-factor and five post-translational modifications, as corroborated by mass spectrometry. Together with the structure of the MCR isolated from Black Sea mats, this work opens the door to environmental enzymology, where proteins from natural microbial sources could be investigated by ultimately sorting them through crystallization.



## Introduction

In a world where greenhouse gases are under constant survey for their role in global warming, methane is of particular importance. This hydrocarbon has 80 times more greenhouse gas potency than CO<sub>2</sub> and has been accumulating in our atmosphere since the industrial era. Half of the yearly methane is biologically produced by methanogenic archaea<sup>1</sup>. While methanogens can be found in anaerobic ecological niches worldwide, their contribution to the methane budget varies depending on substrate availability and their metabolism<sup>2</sup>. Among methanogens, acetoclastic methanogens that metabolize acetate are of particular importance. Acetate is a product of anaerobic fermentation that must be removed to stimulate anaerobic organic matter degradation<sup>3</sup>. Methanogens belonging to the *Methanotrix* genus are highly performant in converting acetate into CH<sub>4</sub> and CO<sub>2</sub>, even at low acetate concentrations where they outcompete *Methanosarcina* species<sup>4-6</sup>. This process is critical for biodegradation, as inhibition of methanogenesis would lead to the accumulation of acetate, inhibiting the fermentation of heterotrophic anaerobes and syntrophs, and might provoke disruption of the trophic chain<sup>7</sup>. Due to this particularity, they are commonly found in wastewater treatment plants but also have a significant impact on environmental niches such as wetlands<sup>2</sup>.

Due to their global carbon-transformations, these anaerobic archaea are considered to be the main CH<sub>4</sub> producers on our planet<sup>6</sup>. *Methanotrix* species can also form consortia with fermenting bacteria, receiving electrons directly by conductive pili<sup>8, 9</sup>. When physically electronically connected, *Methanotrix* can even reduce CO<sub>2</sub> to CH<sub>4</sub> via a mechanism that should involve the central C1 processing pathway<sup>10</sup>. Alternatively, some *Methanotrix* species can harvest artificial electron donors such as a cathode instead of bacterial partners, performing the bioelectrochemical conversion of CO<sub>2</sub> to CH<sub>4</sub> with biotechnological potential<sup>11</sup>.

Because of the reasons mentioned above, a detailed molecular dissection of the catabolism from *Methanotrix*, notable via structural means, is of great motivation to understand how these enzymes work, especially when considering the CO<sub>2</sub> fixation pathway occurring in environmental conditions. Although they thrive in nature, *Methanotrix* are difficult to grow under laboratory conditions. The extended period of growth and the low biomass yield still allowed the biochemical characterization of the main enzymes of the acetoclastic pathway but limited structural studies<sup>6</sup>. Their syntrophic cultivation with another bacterium or growth on an electrode, which allows the CO<sub>2</sub> fixation pathway to be studied, is also limited in terms of biomass quantities. An alternative

would be the recombinant production of the target enzyme in another organism, such as *Escherichia coli*. However, due to the complex nature of the O<sub>2</sub>-sensitive and highly elaborated metallo-cofactors, post-translational modifications or the requirement of chaperones, the enzymes produced may be found in inclusion bodies or be inactive.

A possibility would be to isolate enzymes from a natural source, for instance, a microbial consortium containing an abundant population of *Methanothrix*. Obtaining a single enzyme from a microbial consortium is highly challenging due to the heterogeneity of the microbial composition. In addition, an environmental sample would contain multiple organisms from the same species harbouring proteins of almost identical amino acid sequence (i.e. > 95% identity) that might be impossible to separate through chromatography. To our knowledge, such a tour de force of obtaining a single protein population from an environmental microbial consortium has only been reported once, for the methane (CH<sub>4</sub>) capturing enzyme of anaerobic methane oxidizers sampled from Black Sea mats<sup>12</sup>. In this case, crystallization was performed to ultimately separate one enzyme from a mixture, a process that took about three years.

In this work, we targeted Methyl-Coenzyme M reductase (MCR) from a *Methanothrix* population derived directly from activated sludge sampled from a wastewater treatment plant. MCR is the rate-limiting step of methanogenesis due to its complicated thiy radical reaction generating biological CH<sub>4</sub><sup>13-16</sup>. It is a perfect target for this proof of concept as the complex of three subunits is expected to be highly abundant. The F<sub>430</sub> cofactor of the enzyme provides a yellow colour with a typical absorbance that could be followed during purification. As previously done by Shima and colleagues 12 years ago<sup>12</sup>, we relied on crystallization to “select” only one MCR out of the heterogeneous mixture for structural characterisation of the complex.

## Materials & Methods

### Metagenome sequencing and fluorescence in situ hybridization

Metagenome sequencing was performed on a Sequel IIE PacBio at the Max Planck-Genome-centre of Cologne.

The samples for fluorescence in situ hybridization (FISH)<sup>17</sup> were fixed with 2% (v/v) formaldehyde for 1 h at 21°C. 1 µL of sample was pipetted into a reaction well on a glass slide (Paul Marienfeld GmbH & Co. KG, Lauda-Königshofen, Germany). After air drying, the samples were washed carefully with MilliQ water and air dried again. The cells were embedded in 0.1% (w/v) low electroendosmosis (LE) agarose (Biozyme Biotech Trading GmbH, Vienna, Austria) by adding 20 µl to a well and air drying overnight. The samples were hybridized with the tetralabelled FISH probe MX825<sup>18</sup> Atto 594 (5' TCG CAC CGT GGC CGA CAC CTA GC 3') and newly designed helper oligonucleotides (5' GGC TTC CCT ACG GCA CCG ACA ACG G 3', 5' GAG TAT CGT TTA CGG CTA GGA CTA CCC GGG 3', 5' GGA TGC TTC ACA GTA CGA ACT GAC GAC GGC 3', 5' GGA TGC TTC ACA GTA CGAACT GAC GAC GGC 3') in a hybridization buffer containing 50% (v/v) formamide, 900 mM NaCl, 20 mM Tris/HCl (pH 8.0) and 0.01% SDS (w/v) for 2.5 h at 46°C. Afterwards, the samples were washed at 48°C with washing buffer (28 mM NaCl, 20 mM Tris/HCl pH 8.0, 5 mM EDTA and 0.01% (w/v) sodium dodecyl sulfate (SDS)) for 15 min and in autoclaved deionized water for 1 min. The dried samples were covered with embedding medium citifluor-vectashield (4:1 (vol/vol)) with 1 µg/ml 4',6'-diamidino-2-phenylindole (DAPI). Coverslips were added and the samples were sealed with clear nail polish. The cells were visualized using an epifluorescence microscope (Zeiss Axioimager.D2).

### MCR purification directly from activated sludge.

5 L of activated sludge collected from the wastewater treatment plant in Osterholz-Scharmbeck were immediately taken to purify MCR directly from the activated sludge without an enrichment. The 5 L, stored in a Duran bottle and sealed with a butyl rubber stopper to maintain an anaerobic atmosphere, were kept for 5 h at room temperature. The sludge was harvested by centrifugation at 500 × g for 60 min at 4 °C. The 5 L of activated sludge yielded a 1.68 kg pellet, which was

aliquoted in ~ 300 g cell pellets. Cell pellets were frozen in liquid N<sub>2</sub> and stored at -80 °C until further use.

285 g of activated sludge pellet was thawed under warm water and diluted with 230 ml of 50 mM Tris/HCl pH 8.0 and 2 mM dithionite (DTT).

285 g (corresponds to ~ 0,85 L from the original sample) of activated sludge pellet resulted in a protein content of 96 mg after sonication.

From here on all steps were performed on ice, if possible. The cell lysate was placed in a sonication glassware and homogenized by sonication: 10 cycles with one min at 75 % intensity followed by 1.5 min break (probe KE76, SONOPULS Bandelin). Cell debris as well as other contaminations from the sludge were removed via centrifugation (15,000 x g, 45 min at 4 °C) followed by ultracentrifugation of the supernatant (100,000 x g, 90 min, 4 °C). The filtered sample was applied to a 5 ml HisTrap high performance column (GE healthcare, Germany), which was previously equilibrated with lysis buffer. The supernatant was passed twice through a 0.2 µm filter and loaded on a 5 ml Q Sepharose high performance column (GE healthcare). A gradient of 0 to 0.5 M NaCl was applied for 60 min with a flow rate of 2 ml min<sup>-1</sup>. Fractions of 1.5 ml were collected. MCR eluted between 0.11 and 0.15 M NaCl. The MCR fractions were pooled (~ 25 ml) and diluted with 100 ml HIC buffer (50 mM Tris/HCl pH 8.0, 2 M (NH<sub>4</sub>)<sub>2</sub>SO<sub>4</sub> and 2 mM DTT). The sample was passed through a 0.2 µm filter and half of it was loaded on a 1 ml Phenyl-Sepharose high-performance column, previously equilibrated with HIC buffer. Once the sample was loaded it was washed with 1 M (NH<sub>4</sub>)<sub>2</sub>SO<sub>4</sub> followed by elution of MCR using a gradient of 1 to 0 M (NH<sub>4</sub>)<sub>2</sub>SO<sub>4</sub> in 40 min with a flow rate of 0.6 ml min<sup>-1</sup>. Fractions of 0.7 ml were collected. MCR eluted between 0.62 and 0.37 M (NH<sub>4</sub>)<sub>2</sub>SO<sub>4</sub> and the respective fractions were pooled. The second half of the Q Sepharose pool was loaded and treated the same way as the first half. The pooled MCR fractions of both runs were merged and concentrated in a 100-kDa-cutoff filter (Merck Millipore, Darmstadt, Germany) at 3,900 x g. The buffer was exchanged to storage buffer (50 mM Tris/HCl pH 8.0, containing 10 % v/v glycerol and 2 mM DTT) and concentrated to a volume of 300 µl. The concentrated sample was passed onto a Superose 6 30/100 GL (GE Healthcare), equilibrated in storage buffer. MCR eluted at a flow rate 0.4 ml min<sup>-1</sup> in a sharp Gaussian peak at an elution volume of 20 ml. The fractions containing MCR were concentrated in a 100-kDa-cutoff filter and the final quantity of protein, 0.6 mg, was estimated by the Bradford method (Bio-Rad, Munich,

Germany). The High resolution Clear Native PAGE (hrCN PAGE) was adapted from Lemaire et al.<sup>19</sup>

### **Crystallization of MCR directly purified from activated sludge.**

The sample was immediately crystallized at a concentration of 30 mg.ml<sup>-1</sup>. MCR crystal was obtained by the sitting drop method at 20 °C in a polystyrene (SWISSCI) clover plate containing 100 µl of crystallization solution in the reservoir. MCR (1.4 µl) at a concentration of 30 mg ml<sup>-1</sup> was mixed with 0.7 µl reservoir solution. Yellow plate-shaped crystals appeared after a few weeks in the following crystallization condition: 0.1 M Bis-Tris pH 8.5, 25 % w/v polyethylene glycol 3,350. Prior to freezing to liquid nitrogen, the crystals were soaked in the crystallization solution supplemented with 15 % v/v ethylene glycol for a few seconds.

### **X-ray crystallography and structural analysis.**

Data were collected at 100 K at the synchrotron SOLEIL (Saint Aubin, France) on the beamline Proxima-I and were processed with *autoPROC*<sup>20</sup>. The structure was first solved by using *PHENIX* with the crystal structure from *Methermicoccus shengliensis* (PDB 7NKG)<sup>21</sup> as a template. After inspection of the electron density, manual sequencing was performed and the sequence was match against the different  $\alpha$ ,  $\beta$  and  $\gamma$  subunit obtained from the metagenome. The attributed sequence was employed to generate an Alphafold2<sup>22</sup> model of the three different subunits and replace each subunit of the preliminary model from the initial molecular replacement. The model was further manually built with *COOT* and refined with *PHENIX*.<sup>23, 24</sup> Translational-liberation screw was applied over the refinement and hydrogens were added in riding position in the last refinement cycles. The model was validated through the MolProbity server.<sup>25</sup> Figures were generated with PyMOL (Schrödinger, LLC).

**Table 1.** Data collection and refinement statistics.

<b>MCR from a <i>Methanothrix</i> species isolated from wastewater plant</b>	
<b>Data collection</b>	
Wavelength (Å)	0.97856
Space group	$P2_1$
Resolution (Å)	19.89 – 2.50 (2.72 – 2.50)
Cell dimensions	
a, b, c (Å)	118.18, 231.50, 145.98
$\alpha$ , $\beta$ , $\gamma$ (°)	90, 112.60, 90
$R_{\text{merge}}$ (%) <sup>a</sup>	14.7 (115.4)
$R_{\text{pim}}$ (%) <sup>a</sup>	5.4 (42.9)
$CC_{1/2}$ <sup>a</sup>	0.997 (0.662)
$I/\sigma_I$ <sup>a</sup>	10.0 (1.9)
Spherical completeness <sup>a</sup>	69.5 (15.3)
Ellipsoidal completeness <sup>a</sup>	94.3 (70.1)
Redundancy <sup>a</sup>	8.1 (7.9)
Nr. unique reflections <sup>a</sup>	173,000 (8,651)
<b>Refinement</b>	
Resolution (Å)	19.89 – 2.50
Number of reflections	172,970
$R_{\text{work}}/R_{\text{free}}$ <sup>b</sup> (%)	18.54/19.88
Number of atoms	
Protein	56,409
Ligands/ions	612
Solvent	294
Mean B-value (Å <sup>2</sup> )	66.02
Molprobit clash score, all atoms	5.98
Ramachandran plot	
Favoured regions (%)	96.83
Outlier regions (%)	0.34
rmsd <sup>c</sup> bond lengths (Å)	0.013
rmsd <sup>c</sup> bond angles (°)	1.554

<sup>a</sup> Values relative to the highest resolution shell are within parentheses. <sup>b</sup>  $R_{\text{free}}$  was calculated as the  $R_{\text{work}}$  for 5 % of the reflections that were not included in the refinement. <sup>c</sup> rmsd, root mean square deviation.

### **Mass spectrometry identification.**

MCR crystals were dissolved and passed on a SDS PAGE (**Figure 2**). The band corresponding to the MCR alpha subunit was processed for in gel digestion and preparation based on the protocol from Kurth et al. 2021<sup>21</sup>.

The results from the MS/MS were analysed with Proteome Discoverer and the peptide spectral annotator (<http://www.interactivepeptidespectralannotator.com/PeptideAnnotator.html>)

## **Results**

### **Native purification of the MCR population from the active sludge.**

The sampled active sludge was first subjected to metagenome sequencing to evaluate the composition of the microbial population. By using the sequences of the MCR from *Methanotherix thermoacetophila* PT ( $\alpha$ -subunit ABK14360,  $\beta$ -subunit ABK14363, and  $\gamma$ -subunit ABK14361), we listed homologues from the metagenome. As a result, we found 121, 109, and 90 sequence matches for the  $\alpha$ -,  $\beta$ -, and  $\gamma$ -subunit, respectively. While a detailed phylogenetic analysis of all these sequences would assign the sequence to different sub-species, or even close *Methanosarcinales* homologues, this result already witnesses the high microbial diversity from the biomass.

FISH was performed to evaluate the proportion of *Methanotherix* compared to the total microbial population in the original sample to assess the proportion of the *Methanotherix* population in the biological sample (**Figure 1A**). The microscopic image showed a fluorescent signal of the specific probe for long-shaped filament microbes, the typical known morphology of *Methanotherix*<sup>26</sup>. This image, overlaid with the untargeted DAPI signal, highlights once more the microbial diversity of the sample.

The pelleted biomass was frozen at -80 °C to weaken the cell membrane integrity. The cell suspension was subjected to sonication with the expectation of breaking down only part of the microbial population. As shown in **Figure 1**, the cells with filamentous shape were absent after sonication, but some coccoids were still present, and we suspect that the lysis protocol already enriched the protein fraction with cellular content from *Methanotherix*. The supernatant from simple

centrifugation still contained light blackish particles that would damage the chromatographic columns. Therefore, an ultracentrifugation step was added. The purification followed a three-step protocol in which MCR was followed on SDS PAGE (**Figure 1**) and by its absorbance at 415 nm. The final MCR enrichment reached 0.6 mg of protein, corresponding to about 1% of the total protein content of the cell extract after sonication. The crystallized sample yielded large yellow crystals after only two weeks, which were immediately harvested for the synchrotron experiment.

### **MCR identification through electron density and mass spectrometry sequencing.**

The two irradiated crystals were recovered and dissolved in SDS PAGE loading buffer to confirm the presence of the MCR complex (**Figure 2**). The three bands visible on the SDS gel were cut and used for mass spectrometry identification. Meanwhile, data diffraction analyses from the best crystal presented moderately anisotropy and the diffraction limits resulted in 2.50-Å along a, 2.83-Å along b and 3.13-Å along c. The structure, obtained in a monoclinic form (**Table 1**), was solved with a molecular replacement by using the structure from *Methermicoccus shengliensis* as a template (PDB 7NKG) due to its high conservation with the sequence from *Methanotheroxiphila thermoacetophila* PT. Three MCR were fitting in the asymmetric unit, allowing the exploitation of the non-crystallography symmetry to improve maps. The early electron density obtained after refinement was precise enough to visualize substitutions (**Figure 2**). By combining the metagenomic sequences, the mass spectrometry identification and the electron density map of the three different subunits across the six-fold non-crystallography symmetry, we were able to identify the correct sequence. An alphafold model was generated with the attributed sequence and utilised for the refinement. The excellent final statistics of the model as well as the fit of the residues in the electron density confirmed the sequence assignment.

### **The overall arrangement of MCR of *Methanotheroxiphila***

The arrangement in the asymmetric unit (**Figure 3A**) suggests a higher oligomeric arrangement than a trimer of  $(\alpha\beta\gamma)_2$  (with a molecular weight expected to be at 808-kDa). The trimeric interface involves only the  $\alpha$ -subunit, in particular the N-terminal (residue 6 to 20), the helix-loop 40-63, Glu86, Tyr87, Glu142, loop 183-191, and the C-terminal (543-559). In this arrangement, the



cavities that provide access to the active site, are located on the sides and are exposed to the solvent. In other words, the high degree of oligomerisation will not hinder the access of the substrate to the catalytic centre (**Figure 3B**).

The PISA server (accessed on the 1<sup>st</sup> of July 2023) calculated an overall surface of 168,188 Å<sup>2</sup> with a  $\Delta G^{\text{diss}}$  of -35.3 kcal.mol<sup>-1</sup> (in comparison, each ( $\alpha\beta\gamma$ )<sub>2</sub> assembly have an average  $\Delta G^{\text{diss}}$  of -202.4 kcal.mol<sup>-1</sup>). Rather, the calculation based on the structure suggests that the trimeric assembly will not be stable in solution. Since the size exclusion chromatography led to an aberrant elution volume during the purification (an elution volume of 20 ml on the Superose 6 column would represent an estimated molecular weight below 100-kDa), a high-resolution clear native PAGE (hrCN-PAGE) was employed. The fraction with enriched MCR presented a molecular weight different to the previous MCR profiles, in which purified MCR from *Methanothermococcus thermolithotrophicus*<sup>27</sup> and *M. shengliensis*<sup>21</sup> migrate below the 242-kDa marker. Here, the major band is located between 242-kDa and 480-kDa and other bands of higher molecular weight are present. While this might be a migration artefact, this result does not contradict the trimeric state in solution.

The MCR dimer has an extremely conserved architecture with its structural homologues, the closest being MCR from *M. shengliensis* as predicted from the sequence (root mean square deviation of the  $\alpha$ ,  $\beta$ , and  $\gamma$  subunits being 0.38 Å (out of 464 C $\alpha$ ), 0.37 Å (out of 355 C $\alpha$ ), 0.40 Å (out of 205 C $\alpha$ ), respectively), but is also similar to the one from *M. barkeri* (rmsd of the  $\alpha$ ,  $\beta$ , and  $\gamma$  subunits being 0.44 Å (out of 472 C $\alpha$ ), 0.60 Å (out of 411 C $\alpha$ ), 0.46 Å (out of 218 C $\alpha$ ), respectively). The studied MCR exhibits two structural specificities: the loop 19-26 of the  $\alpha$ -subunit is smaller compared to all other reported structures, and an extension close to the C-terminal of the  $\gamma$ -subunit (residues 225-234) exists, wrapping around the  $\alpha$ -subunit. These two specificities, however, are located far from the active site and its entrance.

### **A perfectly conserved active site with five post-translational modifications**

Electrostatic surface analysis revealed the same characteristics as previously shown, with the entry of the catalytic cavity being mainly positively charged, while the outer region is instead negatively charged (**Figure 4B**)<sup>21</sup>. The active site contains a classic F<sub>430</sub>, coenzyme M and coenzyme B bound

(**Figure 5**) in the same fashion as previously described<sup>16</sup>, illustrating the evolutionary pressure on the complicated thiyl radical reaction. MCRs are known to harbour a gallery of post-translational modifications ranging from a core of three conserved post-translational modifications to various additions, which is not corroborating the phylogeny<sup>16</sup>. Based on its homology to the compared MCR structures, we expected the three modification gallery in *M. shengliensis*. However, based on the electron density profile complemented by mass spectrometry, a gallery of five known modifications is expected, as reported in **Figure 5B**. As previously demonstrated, the functions of these modifications are still elusive, and the structural information gathered in this work does not provide additional clues regarding their function but supports their presence under natural conditions.

## Discussion

85-99% of the microbial population cannot be isolated, which is a significant limitation in unravelling the fundamental processes involved in natural biological transformations. Often referred to as "microbial dark matter", the metabolic pathways predicted by the complementary analysis of genomes, transcripts, proteins, and metabolites with the different omics need to be further corroborated by biochemical means to validate the functions of gene products and characterise the reactions performed. The new revolution in terms of deep learning algorithms (e.g., AlphaFold2<sup>22</sup> and RosettaFOLD<sup>28</sup>) will guide this function prediction to some extent, but without knowing the activity determinants (e.g. metallo-cofactors) and due to the limited conformational space, these methods provide only restricted information on catalytic processes<sup>29</sup>. On the other hand, recombinant expression is a powerful method to produce fully engineered proteins and facilitate their purification. However, incorrect folding and lack of activity because of the necessity of chaperones or the absence of cofactors can be expected in several cases.

Here, we used the example of a multi-subunit enzyme with post-translational modification and a cofactor, which could be challenging to express in a recombinant host such as *E. coli*. However, compared to the classical approach of axenic culture or even a microbial enrichment, we took the challenge to isolate the enzyme from a mesocosm in which the organism of interest is naturally evolving with its community (e.g. receiving electrons through DIET and fixing CO<sub>2</sub>). This has only been done once before<sup>12</sup> and has been repeated in this study by obtaining the structure of a

single MCR. The isolation was made possible by the selective crystallisation process. Crystals appeared within two weeks in the MCR enriched fraction, in contrast to the 2011 study where crystals took three years to appear. Many factors may have contributed to MCR crystallization; for instance, one *Methanotherix* population was already dominant during this period in the wastewater treatment plant. The sonication process could have facilitated the selective lysis of the archaea compared to the bacterial population, which possibly decreased the contamination with bacterial proteome. Finally, the crystallisation might have been enhanced by the robustness and high stability of MCR, as its globular nature facilitates the contacts to establish a crystalline lattice.

The trimeric form observed in the asymmetric unit might be an artefact from crystallisation, and additional biophysical experiments should be undergone. Interestingly, the polyethylene glycol contained in the crystallisation solution might have mimicked the cellular molecular crowding, and since MCR is expected to be present at extremely high intracellular concentrations, the trimer might still transiently exist. This oligomerisation might be handy to stabilise the complex even further or to protect the reactive F<sub>430</sub> cofactor. The isolated MCR from *Methanotherix* exhibits the typical catalytic site reported in other cultivated methanogens and contains five post-translational modifications.

In conclusion, the methodology presented here, with a three-step protein enrichment by chromatography followed by isolation through crystallisation, could pave the way for a more detailed study of *Methanotherix* under quasi-environmental conditions. Future work could improve the process by exploiting the morphology of *Methanotherix* by implementing a microbial enrichment step using differential centrifugation. By following the principles described in our work, it will be possible to study the CO<sub>2</sub>-conversion pathway operating under DIET if the archaeon establishes a natural syntrophic interaction with the microbial consortium. Together with the molecular basis of the acetoclastic metabolism, we will understand the various reactions that orchestrate the final degradation of organic matter, producing the majority of biological CH<sub>4</sub>.

**Funding.** This research was funded by the Max-Planck Gesellschaft. MJ was supported by the Deutsche Forschungsgemeinschaft Schwerpunktprogramm 1927 „Iron-sulfur for Life“ (WA 4053/1-1).

**Acknowledgements.** We thank the Max Planck Institute for Marine Microbiology and the Max Planck Society for continuous support. We acknowledge the SOLEIL synchrotron for beam time

allocation and the beamline staff of Proxima-1 for assistance with data collection. We are thankful to Christina Probian and Ramona Appel for their continuous support in the Microbial Metabolism laboratory.

**Conflicts of Interest.** The authors declare no conflict of interest.

**Author contributions:** TW, JH, MJ, MCM, and NM designed the research. JH collected the wastewater treatment samples. MJ purified and crystallized the MCR directly from the sludge, MJ and TWA solved the structures, refined and validated the models. GA and ML performed mass spectrometry, AL performed FISH, SD and BH sequenced and analysed the metagenome. TW wrote the initial version of the article and all co-authors are contributing to the manuscript writing.

## List of Figures

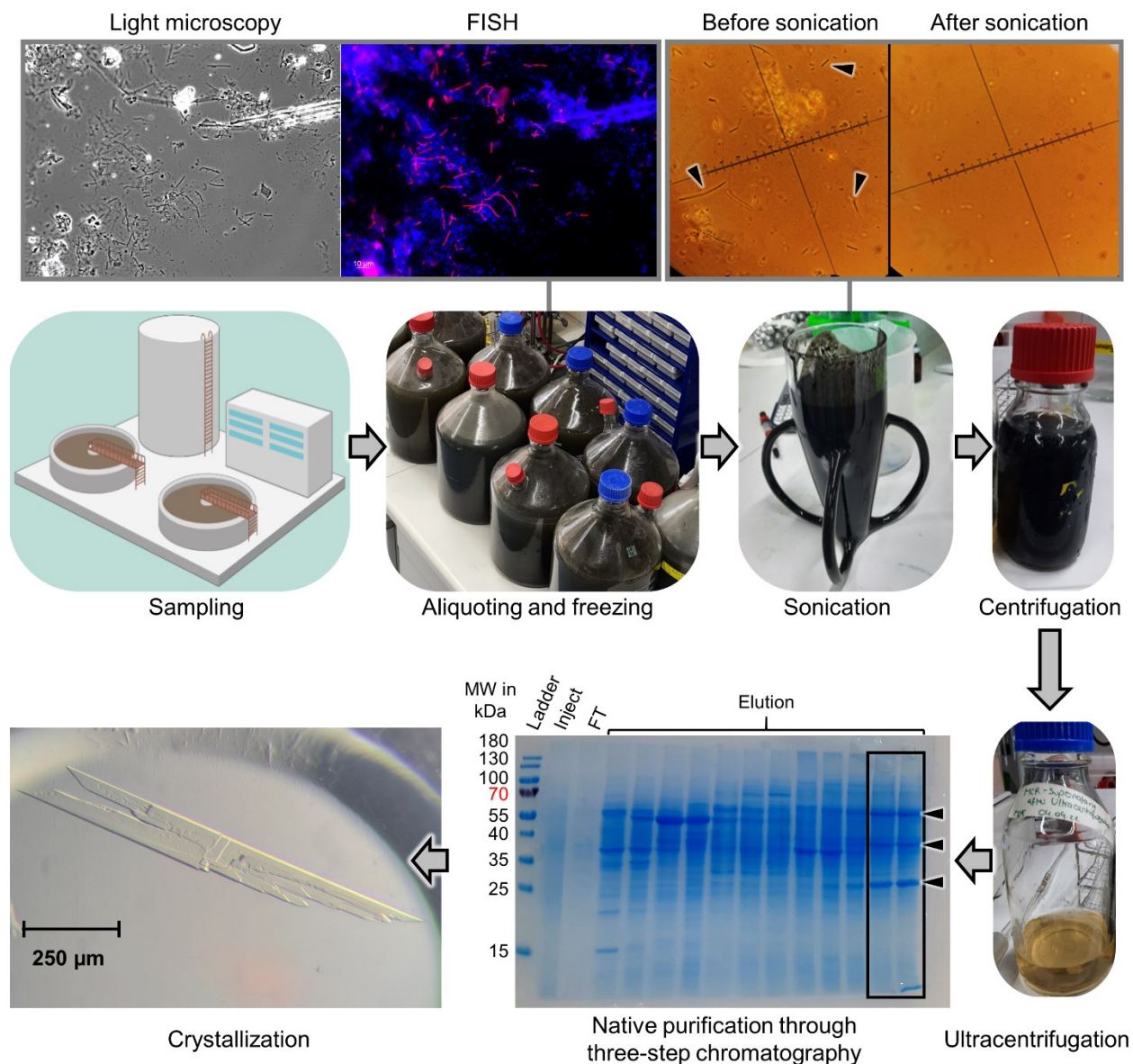


**Figure 1. Purification scheme of the MCR population from the active sludge.** On the top left is the microbial population in the wastewater treatment plant sample under light and fluorescent microscopy. The FISH treated sample contains the DAPI staining (blue) and a specific probe for *Methanothrix* (pink). The top right presents light microscopy pictures before and after sonication. Arrows point to cells exhibiting the typical morphology of *Methanothrix* species. The central scheme shows the pipeline used in the study. The SDS PAGE at the bottom shows the first purification step containing the ladder (MW for Molecular Weight), the soluble fraction after ultracentrifugation (inject), the flow through (FT) and the different fractions from the elution. The three arrows highlight the expected  $\alpha$ ,  $\beta$ , and  $\gamma$  subunits of the MCR population. The fractions containing the three bands were observed at 425 nm.

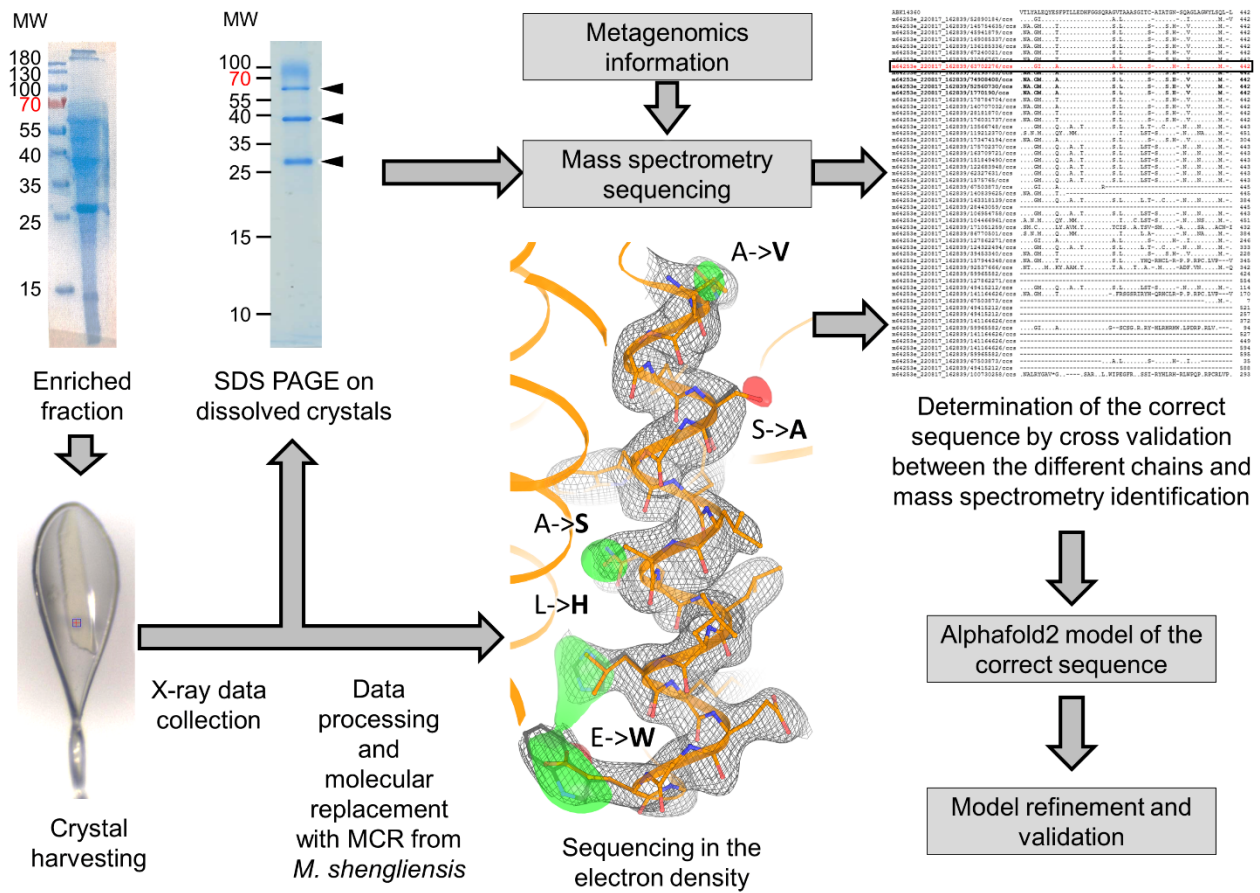


**Figure 2. The methodology employed to identify and refine the structure of MCR from *Methanotherix*.** On the top left is the SDS PAGE corresponding to the enriched fraction used for crystallisation. The SDS PAGE on the right side presents the dissolved crystals after X-ray irradiation. The three arrows indicate the expected  $\alpha$ ,  $\beta$ , and  $\gamma$  subunits of the isolated MCR. Molecular weights (MW) are in kDa. The bottom left displayed the crystal exposed to X-ray radiation. The central picture represents a segment of the  $\alpha$ -subunit with the sequence of MCR from *M. shengliensis* derived after molecular replacement. The  $2F_o-F_c$  electron density map is contoured at  $1 \sigma$  and shown as a black mesh. The  $F_o-F_c$  difference map is displayed as a transparent surface and contoured at  $4 \sigma$  and  $-4 \sigma$  for the positive and negative difference, respectively. The structure from the molecular replacement (*M. shengliensis* sequence) is coloured orange and shown in a cartoon, with residues of importance in balls and sticks. Transparent sticks and balls highlight the refined structure of MCR from *Methanotherix* with the correct sequence. Atoms are coloured orange/black (C), red (O), and blue (N).

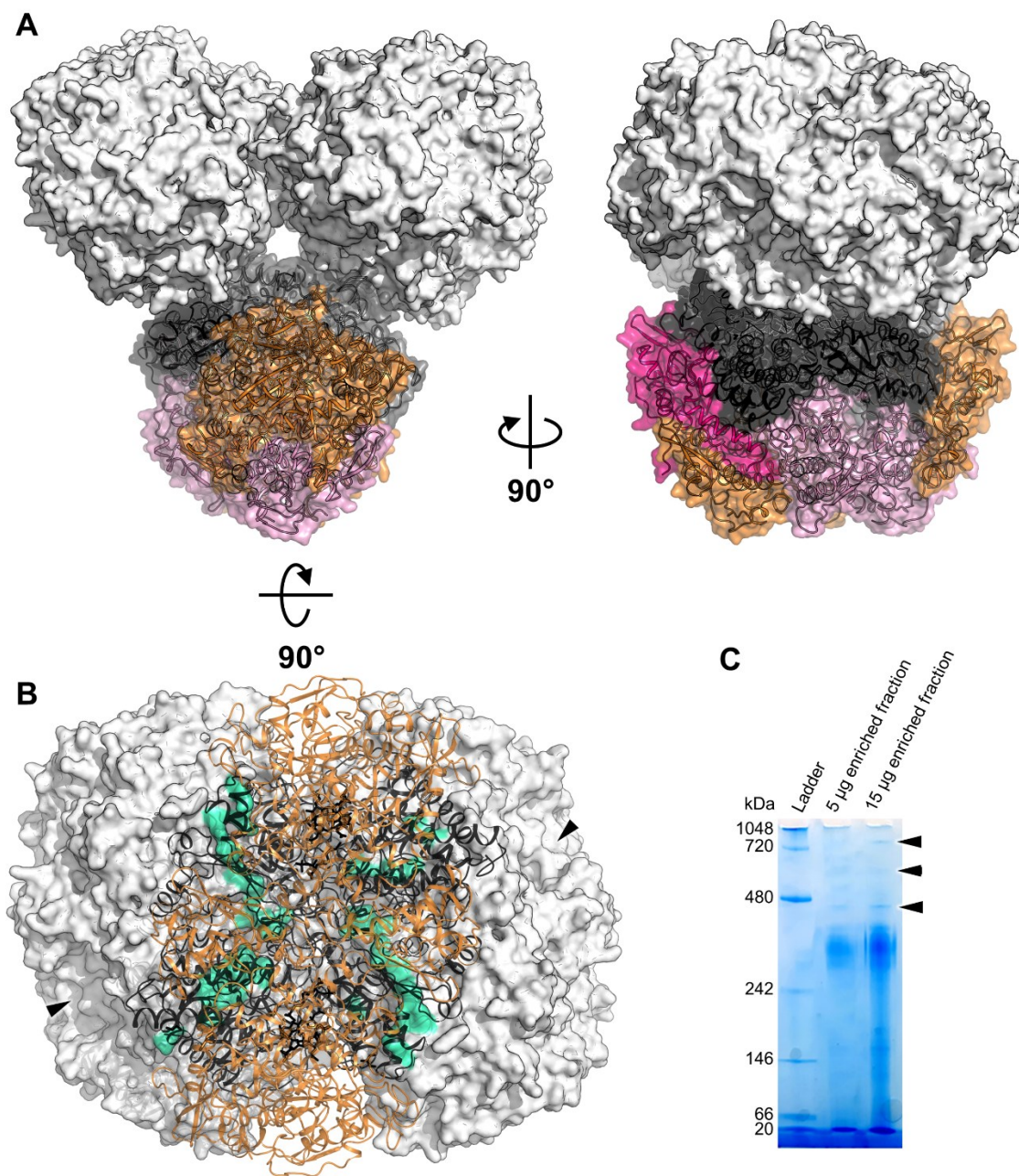


**Figure 3. A trimeric arrangement of MCR from *Methanotherix* in the asymmetric unit. A.** Side and top views of the trimeric arrangement of MCR from *Methanotherix* in the asymmetric unit. The three MCRs are shown as a white surface, except for one of them coloured by chain:  $\alpha$ , black;  $\beta$ , magenta;  $\gamma$ , red;  $\alpha'$ , grey;  $\beta'$ , pink;  $\gamma'$ , orange (prime chains correspond to the opposing dimer). **B.** Side view of the trimeric arrangement with the facing MCR displayed as transparent cartoons with the subunits  $\alpha$   $\alpha'$  in black and all others in orange. The cyan colour on the surface of the opposing two other MCR highlights the binding area from the facing MCR. The arrows mark the substrate entry sites that are not obstructed by the trimeric assembly. **C.** hrCN PAGE of the enriched MCR fraction. Arrows point to forms of MCR with higher molecular weight.

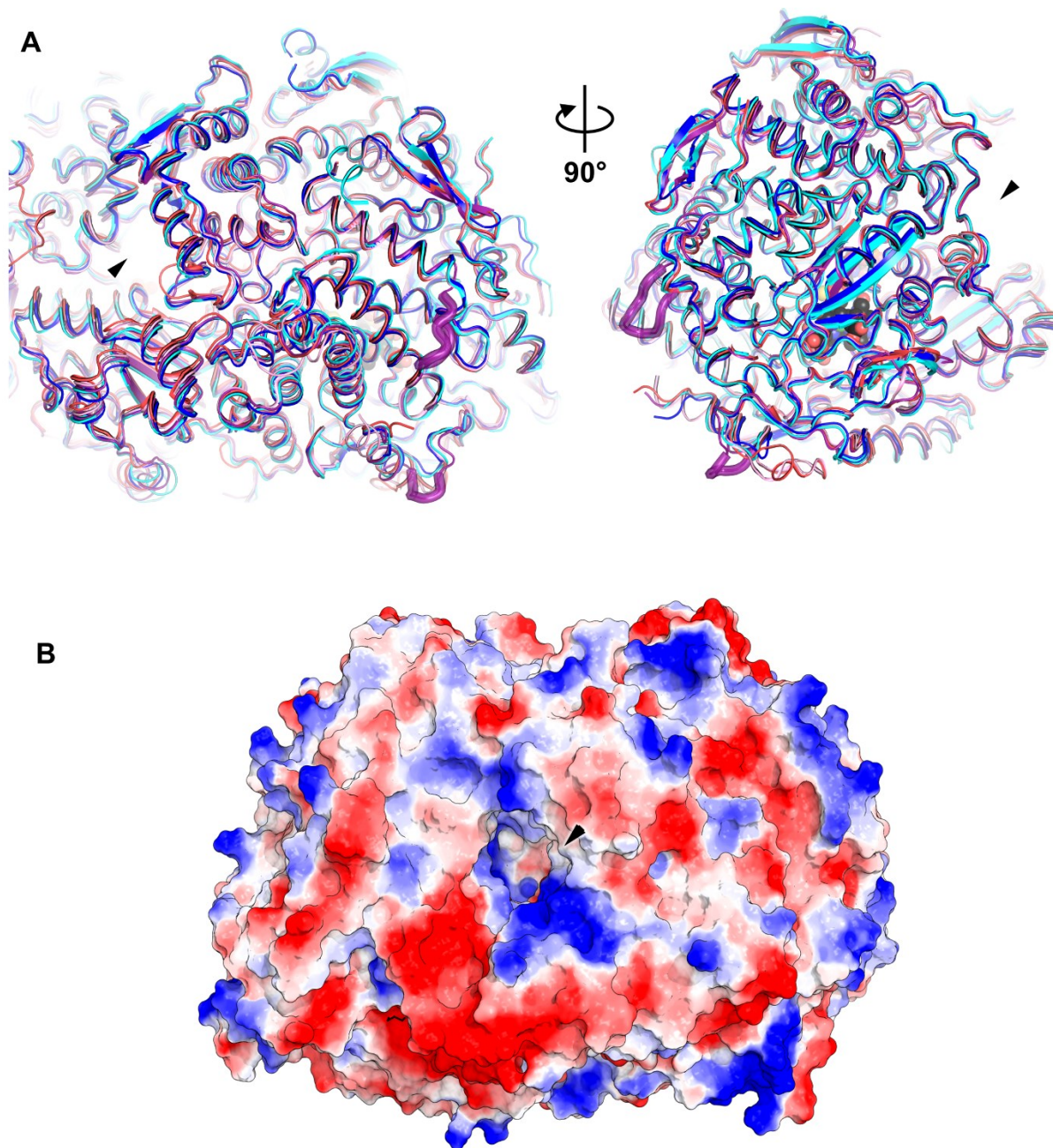


**Figure 4. Comparison of MCR from *Methanotherix* with structural homologues and electrostatic surface. A.** Superposition of the MCR from *Methanotherix* (purple), *M. shengliensis* (red, 7NKG), *Methanosarcina barkeri* (pink, 1E6Y), *Methanothermococcus thermolithotrophicus* (cyan, 5N1Q) and MCR type I from *Methanothermobacter marburgensis* (blue, 5A0Y). All structures are superposed on the  $\alpha$ -subunit of MCR type I from *M. marburgensis*. **B.** Electrostatic profile of MCR from *Methanotherix* in which negative and positive charges are coloured from red to blue. An arrow marks the entrance to the active site.



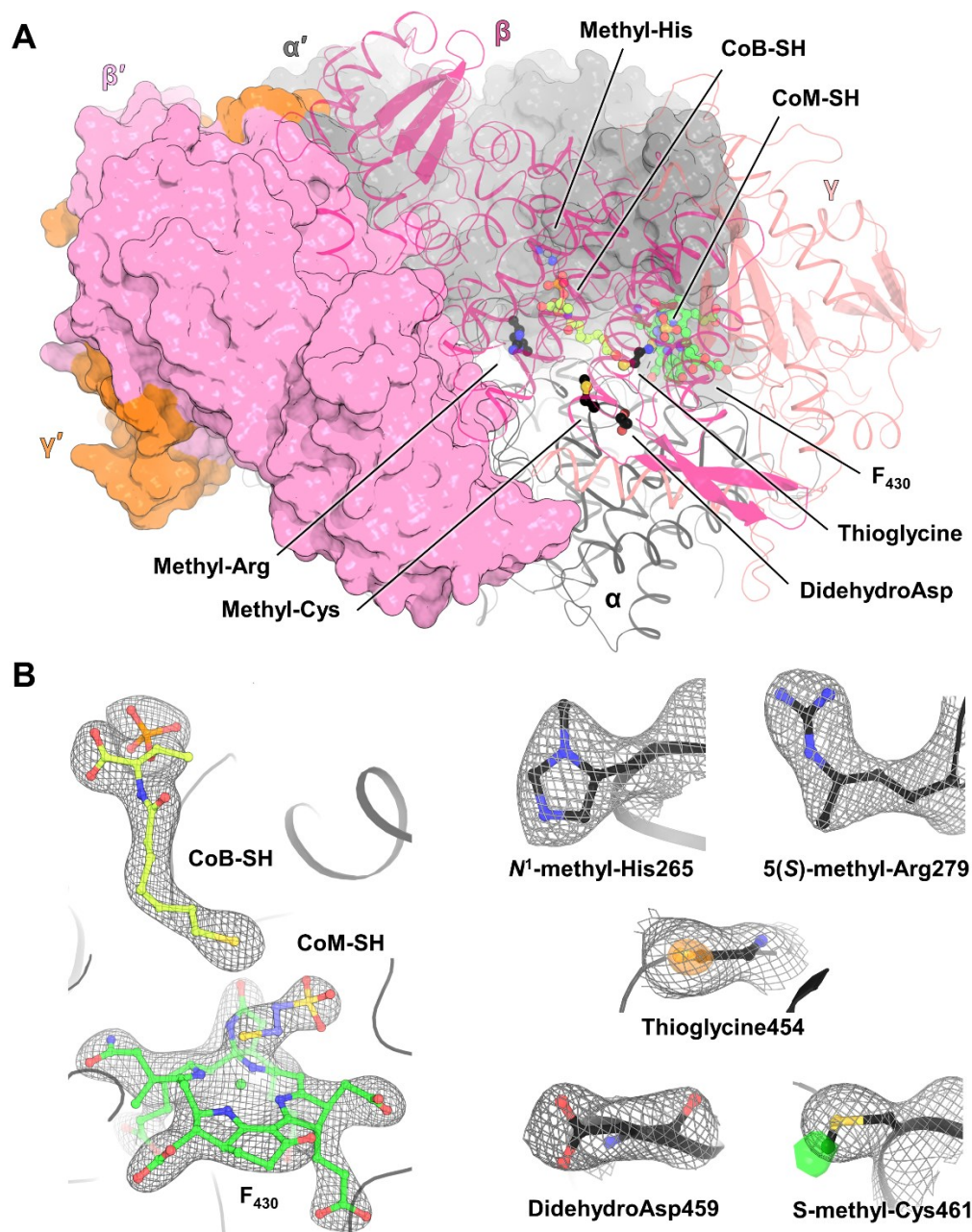


**Figure 5. Active site and modifications of MCR from *Methanotherix*.** **A.** Overall view of the dimer with one heterotrimer shown in surface and the other one in transparent cartoon. The  $\alpha'$  chain carries the methyl-Histidine. **B.** Close-up of the bound coenzymes and  $F_{430}$  (left) and post-translational modifications (right). The  $2F_o - F_c$  electron density map calculated based on the non-crystallography symmetry is contoured at  $1.6 \sigma$  and shown as a black mesh. The thioglycine exhibits an orange surface corresponding to the same  $2F_o - F_c$  electron density map contoured at  $4 \sigma$  to visualize the sulphur atom. For the methyl-cysteine, since the methyl group is absent in the electron density, the  $F_o - F_c$  difference of an omit map for the methyl is shown as a transparent green surface. For all, molecules and residues of interest are in balls and sticks and colour coded as follows black/green/limon/slate (C), red (O), blue (N), yellow (S), and orange (P).

## References

1. Thauer, R. K.; Kaster, A. K.; Seedorf, H.; Buckel, W.; Hedderich, R., Methanogenic archaea: ecologically relevant differences in energy conservation. *Nat Rev Microbiol* **2008**, *6* (8), 579-91.
2. Lyu, Z.; Shao, N.; Akinyemi, T.; Whitman, W. B., Methanogenesis. *Curr Biol* **2018**, *28* (13), R727-R732.
3. Kurth, J. M.; Op den Camp, H. J. M.; Welte, C. U., Several ways one goal-methanogenesis from unconventional substrates. *Appl Microbiol Biotechnol* **2020**, *104* (16), 6839-6854.
4. Jetten, M. S. M.; Stams, A. J. M.; Zehnder, A. J. B., Methanogenesis from Acetate: a Comparison of the Acetate Metabolism in *Methanothrix-Soehngeni* and *Methanosarcina* spp. *Fems Microbiol Lett* **1992**, *88* (3-4), 181-197.
5. Berger, S.; Welte, C.; Deppenmeier, U., Acetate activation in *Methanosaeta thermophila*: characterization of the key enzymes pyrophosphatase and acetyl-CoA synthetase. *Archaea* **2012**, *2012*, 315153.
6. Smith, K. S.; Ingram-Smith, C., Methanosaeta, the forgotten methanogen? *Trends Microbiol* **2007**, *15* (4), 150-5.
7. Welte, C.; Deppenmeier, U., Bioenergetics and anaerobic respiratory chains of aceticlastic methanogens. *Biochim Biophys Acta* **2014**, *1837* (7), 1130-47.
8. Martins, G.; Salvador, A. F.; Pereira, L.; Alves, M. M., Methane Production and Conductive Materials: A Critical Review. *Environ Sci Technol* **2018**, *52* (18), 10241-10253.
9. Lovley, D. R., Syntrophy Goes Electric: Direct Interspecies Electron Transfer. *Annual Review of Microbiology*, Vol 71 **2017**, *71*, 643-664.
10. Rotaru, A. E.; Shrestha, P. M.; Liu, F. H.; Shrestha, M.; Shrestha, D.; Embree, M.; Zengler, K.; Wardman, C.; Nevin, K. P.; Lovley, D. R., A new model for electron flow during anaerobic digestion: direct interspecies electron transfer to *Methanosaeta* for the reduction of carbon dioxide to methane. *Energ Environ Sci* **2014**, *7* (1), 408-415.
11. Liu, C. Q.; Sun, D. Z.; Zhao, Z. Q.; Dang, Y.; Holmes, D. E., Methanothrix enhances biogas upgrading in microbial electrolysis cell via direct electron transfer. *Bioresour Technol* **2019**, *291*.
12. Shima, S.; Krueger, M.; Weinert, T.; Demmer, U.; Kahnt, J.; Thauer, R. K.; Ermler, U., Structure of a methyl-coenzyme M reductase from Black Sea mats that oxidize methane anaerobically. *Nature* **2012**, *481* (7379), 98-101.

13. Ragsdale, S. W., Biochemistry of Methyl-Coenzyme M Reductase: The Nickel Metalloenzyme that Catalyzes the Final Step in Synthesis and the First Step in Anaerobic Oxidation of the Greenhouse Gas Methane. *Metal Ions Life Sci* **2014**, *14*, 125-145.
14. Wongnate, T.; Sliwa, D.; Ginovska, B.; Smith, D.; Wolf, M. W.; Lehnert, N.; Raugei, S.; Ragsdale, S. W., The radical mechanism of biological methane synthesis by methyl-coenzyme M reductase. *Science* **2016**, *352* (6288), 953-8.
15. Thauer, R. K., Methyl (Alkyl)-Coenzyme M Reductases: Nickel F<sub>430</sub>-Containing Enzymes Involved in Anaerobic Methane Formation and in Anaerobic Oxidation of Methane or of Short Chain Alkanes. *Biochemistry* **2019**, *58* (52), 5198-5220.
16. Lemaire, O. N.; Wagner, T., A Structural View of Alkyl-Coenzyme M Reductases, the First Step of Alkane Anaerobic Oxidation Catalyzed by Archaea. *Biochemistry* **2022**, *61* (10), 805-821.
17. Amann, R.; Fuchs, B. M., Single-cell identification in microbial communities by improved fluorescence in situ hybridization techniques. *Nat Rev Microbiol* **2008**, *6* (5), 339-48.
18. Raskin, L.; Stromley, J. M.; Rittmann, B. E.; Stahl, D. A., Group-specific 16S rRNA hybridization probes to describe natural communities of methanogens. *Appl Environ Microbiol* **1994**, *60* (4), 1232-40.
19. Lemaire, O. N.; Wagner, T., Gas channel rerouting in a primordial enzyme: Structural insights of the carbon-monoxide dehydrogenase/acetyl-CoA synthase complex from the acetogen *Clostridium autoethanogenum*. *Biochimica et Biophysica Acta (BBA) - Bioenergetics* **2021**, *1862* (1), 148330.
20. Vonrhein, C.; Flensburg, C.; Keller, P.; Sharff, A.; Smart, O.; Paciorek, W.; Womack, T.; Bricogne, G., Data processing and analysis with the autoPROC toolbox. *Acta Crystallographica Section D* **2011**, *67* (4), 293-302.
21. Kurth, J. M.; Muller, M. C.; Welte, C. U.; Wagner, T., Structural Insights into the Methane-Generating Enzyme from a Methoxydotrophic Methanogen Reveal a Restrained Gallery of Post-Translational Modifications. *Microorganisms* **2021**, *9* (4).
22. Jumper, J.; Evans, R.; Pritzel, A.; Green, T.; Figurnov, M.; Ronneberger, O.; Tunyasuvunakool, K.; Bates, R.; Zidek, A.; Potapenko, A.; Bridgland, A.; Meyer, C.; Kohl, S. A. A.; Ballard, A. J.; Cowie, A.; Romera-Paredes, B.; Nikolov, S.; Jain, R.; Adler, J.; Back, T.; Petersen, S.; Reiman, D.; Clancy, E.; Zielinski, M.; Steinegger, M.; Pacholska, M.; Berghammer, T.; Bodenstein, S.; Silver, D.; Vinyals, O.; Senior, A. W.; Kavukcuoglu, K.; Kohli, P.; Hassabis, D., Highly accurate protein structure prediction with AlphaFold. *Nature* **2021**, *596* (7873), 583-589.
23. Emsley, P.; Lohkamp, B.; Scott, W. G.; Cowtan, K., Features and development of *Coot*. *Acta Crystallographica Section D-Biological Crystallography* **2010**, *66*, 486-501.

24. Liebschner, D.; Afonine, P. V.; Baker, M. L.; Bunkoczi, G.; Chen, V. B.; Croll, T. I.; Hintze, B.; Hung, L. W.; Jain, S.; McCoy, A. J.; Moriarty, N. W.; Oeffner, R. D.; Poon, B. K.; Prisant, M. G.; Read, R. J.; Richardson, J. S.; Richardson, D. C.; Sammito, M. D.; Sobolev, O. V.; Stockwell, D. H.; Terwilliger, T. C.; Urzhumtsev, A. G.; Videau, L. L.; Williams, C. J.; Adams, P. D., Macromolecular structure determination using X-rays, neutrons and electrons: recent developments in *Phenix*. *Acta Crystallogr D* **2019**, *75*, 861-877.
25. Chen, V. B.; Arendall, W. B.; Headd, J. J.; Keedy, D. A.; Immormino, R. M.; Kapral, G. J.; Murray, L. W.; Richardson, J. S.; Richardson, D. C., *MolProbity*: all-atom structure validation for macromolecular crystallography. *Acta Crystallogr D* **2010**, *66*, 12-21.
26. Touzel, J. P.; Prensier, G.; Roustan, J. L.; Thomas, I.; Dubourguier, H. C.; Albagnac, G., Description of a New Strain of *Methanothrix-Soehngenii* and Rejection of *Methanothrix-Concillii* as a Synonym of *Methanothrix-Soehngenii*. *Int J Syst Bacteriol* **1988**, *38* (1), 30-36.
27. Hahn, C. J.; Lemaire, O. N.; Kahnt, J.; Engilberge, S.; Wegener, G.; Wagner, T., Crystal structure of a key enzyme for anaerobic ethane activation. *Science* **2021**, *373* (6550), 118-121.
28. Baek, M., Efficient and accurate prediction of protein structures and interactions using RoseTTAFold. *Acta Crystallogr A* **2022**, *78*, A235-A235.
29. David, A.; Islam, S.; Tankhilevich, E.; Sternberg, M. J. E., The AlphaFold Database of Protein Structures: A Biologist's Guide. *J Mol Biol* **2022**, *434* (2), 167336.

# Chapter VII

## CO<sub>2</sub>-Fixation Strategies in Energy Extremophiles: What Can We Learn From Acetogens?

**Olivier N. Lemaire<sup>1</sup>, Marion Jespersen<sup>1</sup> and Tristan Wagner<sup>1\*</sup>**

<sup>1</sup> Microbial Metabolism Group, Max Planck Institute for Marine Microbiology, Bremen, Germany.

\*Correspondence: [twagner@mpi-bremen.de](mailto:twagner@mpi-bremen.de)

Keywords: acetogenic bacteria, hydrogenotrophic methanogens, CO<sub>2</sub>-fixation, formate dehydrogenase, evolution, biotechnology, coupled reaction

MINI REVIEW article

Frontiers in Microbiology

Received 15 December 2019

Accepted: 05 March 2020

Published online: 03 April 2020

Sec. Microbial Physiology and Metabolism

DOI: [10.3389/fmicb.2020.00486](https://doi.org/10.3389/fmicb.2020.00486)

## Abstract

Domestication of CO<sub>2</sub>-fixation became a worldwide priority enhanced by the will to convert this greenhouse gas into fuels and valuable chemicals. Because of its high stability, CO<sub>2</sub>-activation/fixation represents a true challenge for chemists. Autotrophic microbial communities, however, perform these reactions under standard temperature and pressure. Recent discoveries shine light on autotrophic acetogenic bacteria and hydrogenotrophic methanogens, as these anaerobes use a particularly efficient CO<sub>2</sub>-capture system to fulfill their carbon and energy needs. While other autotrophs assimilate CO<sub>2</sub> via carboxylation followed by a reduction, acetogens and methanogens do the opposite. They first generate formate and CO by CO<sub>2</sub>-reduction, which are subsequently fixed to funnel the carbon toward their central metabolism. Yet their CO<sub>2</sub>-reduction pathways, with acetate or methane as end-products, constrain them to thrive at the “thermodynamic limits of Life”. Despite this energy restriction acetogens and methanogens are growing at unexpected fast rates. To overcome the thermodynamic barrier of CO<sub>2</sub>-reduction they apply different ingenious chemical tricks such as the use of flavin-based electron-bifurcation or coupled reactions. This mini-review summarizes the current knowledge gathered on the CO<sub>2</sub>-fixation strategies among acetogens. While extensive biochemical characterization of the acetogenic formate-generating machineries has been done, there is no structural data available. Based on their shared mechanistic similarities, we apply the structural information obtained from hydrogenotrophic methanogens to highlight common features, as well as the specific differences of their CO<sub>2</sub>-fixation systems. We discuss the consequences of their CO<sub>2</sub>-reduction strategies on the evolution of Life, their wide distribution and their impact in biotechnological applications.

## Introduction

CO<sub>2</sub>, the most oxidized state of carbon, has become a major concern to society due to its greenhouse gas properties and its increasing accumulation in our atmosphere since the 20th-century. Efficient CO<sub>2</sub>-sequestration techniques, as well as concomitant applications in biochemical synthesis and alternative energy source storage, being developed to reduce its impact on global warming (Schuchmann and Müller, 2013). Yet CO<sub>2</sub> is a stable, inert molecule. The few applicable chemical processes allowing its unfavorable fixation (like the Monsanto and Cativa processes) require high temperatures and pressures as well as expensive and polluting catalysts while only exhibiting moderate catalytic rates (Appel et al., 2013; Fujita et al., 2013; Schuchmann and Müller, 2013). New alternative chemistry based on metal-organic framework (Hou et al., 2019) or transition metal-free catalysis (Cherubini-Celli et al., 2018) are upcoming and might be applied in the near future. Nevertheless, none of these artificial processes matches the efficiency of their biological counterpart.

At least six different autotrophic carbon fixation pathways exist among the domains of Life (Berg et al., 2010; Fuchs, 2011; Appel et al., 2013). The most common scenario is a two-step process where CO<sub>2</sub> is branched on a reactive group (carboxylation) and then reduced (e.g., Calvin–Benson–Bassham or the 3-hydroxypropionate 4-hydroxybutyrate cycle). To date, there is only one exception that uses the reverse way, CO<sub>2</sub>-reduction before carboxylation: the reductive acetyl-CoA pathway. This pathway constitutes the “cheapest” option to fix CO<sub>2</sub> in term of energy-consumption and is thought to be the most ancient one (Berg et al., 2010; Martin and Thauer, 2017).

The reductive acetyl-CoA pathway has two CO<sub>2</sub> entry points: the methyl-branch, where a reductive cascade turns CO<sub>2</sub> in a methyl-group (Figure 1A, reaction from the CO<sub>2</sub>-activation to the methyl-H<sub>4</sub>F for acetogens or methyl-H<sub>4</sub>MPT for methanogens) and the carbonyl-branch. In the latter, CO<sub>2</sub> is converted into carbon monoxide (CO; Figure 1A), further combined with the methyl group and Coenzyme A (CoA) to ultimately produce acetyl-CoA, the “turntable” of the central carbon metabolism (Ragsdale and Pierce, 2008; Thauer et al., 2008; Berg et al., 2010; Sousa et al., 2013; Fuchs and Berg, 2014).

Hydrogenotrophic methanogens (Euryarchaea, simplified as methanogens below) and autotrophic acetogens (Bacteria, simplified as acetogens below) use the reductive acetyl-CoA pathway to

derive their cellular carbon and energy by growing on H<sub>2</sub> plus CO<sub>2</sub>. The final product for methanogens and acetogens are methane and acetate, respectively. Under physiological conditions, such metabolism provides less than half a molecule of ATP per acetate/methane, constraining these organisms to live at the “thermodynamic limits of Life” (Buckel and Thauer, 2013; Schuchmann and Müller, 2014). Nevertheless, methanogens and acetogens are found in various ecological niches, ranging from rumen to deep-sea volcanoes and they are crucial actors in organic matter conversion and element cycling (e.g., carbon assimilation and nitrogen fixation). Despite drastically low energy yields, their doubling time is surprisingly short: ranging from only one to a few hours under laboratory conditions (Thauer et al., 2008; Basen et al., 2018).

The energy metabolism of acetogens and methanogens was puzzling for a long time until the discovery of energy conserving enzymes (i.e., Rnf and Ech membrane complexes), which use low-potential electrons from ferredoxins, reduced by H<sub>2</sub> oxidation via flavin-based electron bifurcation (**Figure 1D**). The use of low-potential electrons provided a rational explanation as to how these organisms derive enough energy to survive and grow under such stringent metabolic conditions (Buckel and Thauer, 2013, 2018; Schuchmann and Müller, 2014; Peters et al., 2018). Considered to be among the first metabolic processes, methanogenesis and acetogenesis might have been crucial for shaping ecosystems since the first Lifeforms arose.

This review summarizes our current understanding of the CO<sub>2</sub>-activation steps orchestrated by these fantastic machineries, which evolved to fulfill the physiological needs for carbon-assimilation and energy-conservation. The structural knowledge gathered from hydrogenotrophic methanogens provides insights in the shared and distinct features between the acetogenic and methanogenic CO<sub>2</sub>-conversion systems, due to both metabolic adaptation and ecological specialization.

### **The CO<sub>2</sub>-reduction/fixation complex in methanogens**

The entire energy metabolism of methanogens relies on highly efficient CO<sub>2</sub>-capture. This challenging task is overcome by the formyl-methanofuran dehydrogenase (Fwd) complex catalyzing both the reduction of CO<sub>2</sub> and the conversion of formate (HCOO<sup>-</sup>) into a formyl group (Figures 1A, 2). So far, two isoforms of this enzyme are described, containing either a molybdenum- or tungsten-dependent formate dehydrogenase (Fdh) subunit (Bertram et al., 1994;



Thauer et al., 2008; Leimkühler and Iobbi-Nivol, 2016; Wagner et al., 2018). Depending on the organism, the molybdo/tungstopterin cofactor can be coordinated by a cysteine or seleno-cysteine. Unlike nearly all described Fdh that perform formate oxidation releasing CO<sub>2</sub>, methanogenic and acetogenic Fdh physiologically run toward CO<sub>2</sub>-fixation. Until now, only a few enzymes found in the *Synthrophobacter* genus share this feature (de Bok et al., 2003).

The reaction remained a mystery for a long time: how can the enzyme couple formate to the C1-carrier methanofuran (MFR) without any ATP investment (Bertram et al., 1994)? The secret was eventually unraveled by its crystal structure (Wagner et al., 2016). The overall complex is constituted of an unprecedented electron transfer apparatus containing a total of 46-[Fe<sub>4</sub>S<sub>4</sub>] clusters flanked by two catalytic modules, a tungstopterin-dependent Fdh and a binuclear metallo-hydrolase. Based on the molecular details, a scenario of the reaction has been proposed where; (1) CO<sub>2</sub> is funneled to the active site of Fdh by a selective, hydrophobic channel; (2) CO<sub>2</sub> is reduced to formate (Figures 1A,B, 2A,B; Wagner et al., 2016); (3) a second hydrophilic tunnel channels and accumulates formate at the active site of the metallo-hydrolase; and (4) formate is condensed on the amino-group of MFR as a formyl-group. The accumulation of formate is predicted to thrive the conversion of formate to a formyl group on MFR without the investment of ATP, an endergonic reaction under standard conditions. However, since Fdh are reversible, the driver of the overall reaction is the electron donor.

From MFR the formyl group is transferred to the second C1-carrier tetrahydromethanopterin (H<sub>4</sub>MPT), successively dehydrated and fully reduced (i.e., by the F<sub>420</sub> cofactor or alternatively with H<sub>2</sub> by the [Fe]-hydrogenase) to a methyl group (dashed line, Figure 1A). The methyl-H<sub>4</sub>MPT represents the crossroad between carbon-assimilation and energy conservation (Thauer, 2012). The latter is formed during the methyl group transfer from nitrogen-bound methyl-H<sub>4</sub>MPT to the thiol group of the coenzyme-M acceptor. The methyl-transfer is coupled to a sodium translocation across the membrane, used to feed the ATP-synthase, which is generating only half an ATP per processed C1-unit (Schäfer et al., 1999). Finally, methylated coenzyme-M becomes oxidized to heterodisulfide with coenzyme-B (CoB-S-S-CoM), releasing methane by using the F<sub>430</sub>-cofactor (Thauer et al., 2008; Thauer, 2012; Sousa et al., 2013).

### **Electron-bifurcation fuels methanogenic CO<sub>2</sub> fixation**

The electron donor for the Fwd complex is predicted to be reduced ferredoxin or a direct electron transfer by the heterodisulfide reductase (Costa et al., 2010; Kaster et al., 2011; Milton et al., 2018). Two versions of this enzyme have been described in hydrogenotrophic methanogens depending on the coupled electron donor: a [NiFe]-hydrogenase or a Fdh (the structurally characterized hydrogenase-dependent one called the Hdr/Mvh complex is shown in Figures 1, 2B).

The overall process starts with the transfer of two electrons from the donor (H<sub>2</sub> or formate) to a flavin. Flavin-based electron bifurcation then splits the two electrons at different potentials (Figures 1D, 2B). The high-potential electron is used for the exergonic reduction of the heterodisulfide. The low-potential electron reduces ferredoxin or might even be directly delivered to the 46-[Fe<sub>4</sub>S<sub>4</sub>] relay of the formyl-methanofuran dehydrogenase to allow CO<sub>2</sub>-capture. The whole reaction is performed in two rounds (Wagner et al., 2017).

### **Diversity of CO<sub>2</sub>-activation systems in acetogens**

Like methanogens, acetogenic bacteria perform initial CO<sub>2</sub>-reduction via molybdo/tungstopterin-dependent Fdh. However, in contrast to methanogens, all described acetogenic CO<sub>2</sub>-reducing systems produce detectable formate, indicating that CO<sub>2</sub>-reduction and formate condensation are uncoupled (Yamamoto et al., 1983; Schuchmann and Müller, 2013, 2014; Wang et al., 2013). Formate conversion into a formyl group on a C1-carrier (i.e., tetrahydrofolate, H<sub>4</sub>F) is thermodynamically unfavorable and acetogens must therefore invest one ATP. Then, the successive dehydration and reduction into methenyl, methylene and finally methyl group can occur, similar to the methanogenic process but involving different systems, reductants and cofactors (Mock et al., 2014; Schuchmann and Müller, 2014). The methyl group is further fused to CO and CoA by the CO dehydrogenase/acetyl-CoA synthase complex (CODH/ACS) to form acetyl-CoA (see below, Figures 1, 2C; Ragsdale, 2008; Can et al., 2014).

Despite a common Fdh module, acetogens evolved their CO<sub>2</sub>-fixation system in many variations, a real example of “mix and match” from the redox module toolbox, as already shown for sulfate-reducing organisms (Grein et al., 2013). Some of them have been reported to be molybdopterin dependent (e.g., *Acetobacterium woodii*) while others require tungstopterin (e.g., *Moorella*

*thermoacetica*, *Clostridium autoethanogenum*, etc.). There are selenium-dependent or selenium-free formate dehydrogenases and some organisms encode both (Yamamoto et al., 1983; Schuchmann and Müller, 2013; Wang et al., 2013). This diversity allows the use of different electron donors (Schuchmann and Müller, 2014).

*Acetobacterium woodii* uses a hydrogen-dependent CO<sub>2</sub>-reductase (HDCR) which couples the oxidation of H<sub>2</sub> to the reduction of CO<sub>2</sub> (Schuchmann and Müller, 2013). The enzyme is composed of a selenocysteine–molybdopterin dependent Fdh linked to a [FeFe]-hydrogenase via an electron bridge (Figure 2B, 2). The genome also encodes a cysteine-dependent Fdh isoform, supposedly expressed under selenium deprivation. The reduction of CO<sub>2</sub> to formate with H<sub>2</sub> is slightly endergonic at standard conditions (Figure 2A). However, at the relatively important threshold concentration of H<sub>2</sub>, necessary for acetogenesis in *A. woodii* (measured at 0.0025 Bar, around thirty times superior to the threshold of hydrogenotrophic methanogens; Thauer et al., 2008), the equilibrium concentration of generated formate becomes sufficient to fuel the methyl branch of the pathway (Schuchmann and Müller, 2014). The enzyme can also perform carbon fixation by ferredoxin oxidation, albeit exhibiting a 1000-times lower reaction rate (Figure 2B, 2). This ability is thought to be crucial in presence of CO, a strong inhibitor of hydrogenases. The coupling of HDCR with CODH is an efficient way to regenerate reduced ferredoxin.

*Moorella thermoacetica* contains a two subunit NADPH-dependent Fdh containing selenocysteine and tungstopterin cofactor, which catalyzes the reversible formate generation through NADPH oxidation (Figure 2B, 3; Thauer, 1972; Yamamoto et al., 1983). Despite being thermodynamically highly unfavorable under standard conditions, it appears that the NADPH-dependent Fdh is the only formate generating enzyme in *M. thermoacetica*. High NADPH/NADP<sup>+</sup> and CO<sub>2</sub>/formate ratios are necessary to push the reaction toward carbon reduction.

*Clostridium autoethanogenum* exploits a seven subunit complex (Hyt/Fdh), the so far most complicated formate-generating system in acetogens (Figure 2B, 4; Wang et al., 2013; Schuchmann and Müller, 2014). The selenium-dependent tungstopterin-containing Fdh module performs CO<sub>2</sub>-reduction by receiving electrons from H<sub>2</sub>-oxidation via a [FeFe]-hydrogenase subunit (similar to HDCR) or by concomitant oxidation of NADPH and ferredoxin through an internal confurcation event (Figures 1D, 2B, 4). Like in HDCR, the reduced ferredoxin could directly come from CO-oxidation by the CODH. Where and how the electron confurcation is

carried out is still unresolved, as the only known flavin cofactor present in the complex (in HytB) is thought to be not involved (Wang et al., 2013). A novel type of electron bifurcation is thus suspected, one that is similar to the related electron-bifurcating hydrogenase. The structural features of this bifurcation mechanism have to be deciphered and as said by Buckel and Thauer (2018): “A crystal structure is urgently needed to solve this problem.”

### **A common CO<sub>2</sub>-fixation system: The CO-dehydrogenase/acetyl-CoA synthase**

While methanogens and acetogens employ different strategies to reduce CO<sub>2</sub> for the methyl-branch, the activation step of the carbonyl-branch, catalyzed by Ni,Fe-containing CODH, is remarkably conserved (Lindahl, 2002; Jeoung et al., 2019).

The initial CO<sub>2</sub>-reduction to CO, powered by low-potential electrons from ferredoxins or flavodoxins (Ragsdale et al., 1983; Can et al., 2014; Schuchmann and Müller, 2014), occurs at the C-cluster composed of a Fe-[NiFe<sub>3</sub>S<sub>4</sub>] (Figure 1C). CO is transferred to the ACS by a long internal hydrophobic channel (Figure 2C; Doukov et al., 2002; Can et al., 2014). Here, it is fixed on the A-cluster, which is composed of a Ni-[Fe<sub>4</sub>S<sub>4</sub>] cluster bridged to another Ni atom (Ragsdale and Pierce, 2008). Ultimately, the ACS forms acetyl-CoA by associating the CO-ligand, CoA and the methyl-ligand from the methyl-branch. A cobalamin-containing FeS protein (CoFeSP) serves as a shuttle for the methyl group between the Methyl-H<sub>4</sub>F and the ACS. The transfer mechanism from the CoFeSP to the ACS is so far unknown. The enzyme thus performs the biological equivalent of the Monsanto and Cativa processes, where CO and methanol are converted to acetate by metal-based catalysts (Appel et al., 2013).

Even if the overall reaction is the same between methanogens and acetogens some subtleties concerning the CODH/ACS composition exist. According to the classification of Lindahl (2002), archaea and predominantly methanogens use preferentially Ni,Fe-CODH of Class I and II (also called acetyl-CoA decarbonylases/synthases), which consist of five different subunits that form oligomeric complexes of approximately 2-MDa. This super-complex contains the CODH/ACS (Doukov et al., 2002; Can et al., 2014), the CoFeSP and the enzyme responsible for methyl-transfer from methyl-H<sub>4</sub>F to cobalamin. These three sub-complexes are separated in acetogenic systems. The CODH subunit in methanogens contains two extra [Fe<sub>4</sub>S<sub>4</sub>]-clusters, putatively implicated in the rerouting of electrons. Acetogenic complexes have been extensively studied (Ragsdale and Kumar, 1996; Ragsdale and Pierce, 2008) thanks to a few available crystal structures of the whole

CODH/ACS complex from *M. thermoacetica* (Doukov et al., 2002; Darnault et al., 2003; Kung et al., 2009) and the knowledge gathered on this enzyme has already been reviewed (Can et al., 2014).

Beside these slight differences, all classes of the CODH/ACS complex are thought to be homologous and thus may have been acquired from a common ancestor (Sousa et al., 2013).

## Conclusion and perspectives

As previously depicted, the Fdh subunit and CODH/ACS complex are conserved in methanogens and acetogens. These elementary modules are therefore thought to have evolved before the divergence of acetogens and methanogens, thus in the Last Universal Common Ancestor (LUCA) (Sousa et al., 2013; Martin and Thauer, 2017). Because they harbor “ancestral” cofactors like Fe-S clusters or tungstopterin and since the substrates H<sub>2</sub> and CO<sub>2</sub> should have been abundant in Early Earth, these pathways are considered to be among the first, if not the first, biological energetic processes (Fuchs, 2011; Sousa et al., 2013; Martin and Thauer, 2017). Understanding the mechanisms and limitations of methanogenesis and acetogenesis will help to unravel the fundamental questions of how Life arose from the pre-existing inorganic world and could provide information about its first evolutionary steps in the new organic one.

While the carbonyl-branch of the reductive acetyl-CoA pathway might be an early and highly conserved invention in LUCA, the methyl-branch is not. Here, methanogens and acetogens use non-homologous enzymes to perform similar reactions. This parallel evolution gave birth to a variety of formate-generating, CO<sub>2</sub>-reducing enzymes, albeit using similar modules (Sousa et al., 2013) and invented different strategies for C1-reduction and formate condensation by the use of different C1-carriers. The evolutionary plasticity of the methyl-branch compared to the strict conservation of the carbonyl-branch might derive from its requirement for low-potential electrons. Because of the low-potential of the CO<sub>2</sub>/CO couple, the CODH could not adapt to a partner other than ferredoxin for CO generation, while the CO<sub>2</sub>-reduction to formate can accommodate different electron donors, allowing variability of enzymes according to the metabolic needs for physiological requirements.

Furthermore, the functional modules coupled to Fdh systems might be the foundation for other “modern” enzymes, from the formate-hydrogen lyase complex to the respiratory complex I (Marreiros et al., 2016). Elucidating methanogenic and acetogenic enzymes has therefore the potential to provide hints to how the ancestral energetic pathways diversified, thereby creating new processes and gradually giving birth to the plethora of bio-energetically important complexes.

A striking difference between formate generating enzymes from acetogens and methanogens is the energy investment. While methanogens bypass the latter (Figure 1A), acetogens need to sacrifice one ATP to allow formate fixation. They counterbalance this energy loss via substrate level phosphorylation of acetyl-phosphate in the last step of acetogenesis. In comparison, no ATP is generated through methanogenesis (Figure 1A). Nevertheless, ATP sparing is critical for energy-limited extremophiles and one could ask why acetogens did not develop an equivalent of the Hdr/Mvh/Fwd coupling system. The explanation could come from the use of low-potential ferredoxins. The last step of methanogenesis releases CoB-S-S-CoM, which is recycled by the heterodisulfide reductase (downhill reaction) with the concomitant generation of low-potential electrons (uphill reaction). Most of these low-potential electrons generated in the cell are assumed to be dedicated for the CO<sub>2</sub>-fixation (Figure 2B, 1; Thauer, 2012). Acetogenic bacteria are restricted to ecological niches with higher H<sub>2</sub> pressure than methanogens. The main reason is that electron bifurcating [FeFe]-hydrogenases are necessary for ferredoxin reduction (Schuchmann and Müller, 2012, 2014), the electron acceptor for the downhill reaction being NAD(P)<sup>+</sup>. According to the current knowledge, the uphill electron generated during the flavin-based electron bifurcation could have a lower potential if the electron downhill is the heterodisulfide ( $E_0' \approx -140$  mV) compared to NAD(P)<sup>+</sup> ( $E_0' = -320$  mV). Therefore, the ferredoxins reduced via electron bifurcation in methanogens are expected to have higher reducing power compared to acetogens. Thus, in the latter the potential could not be low enough to allow both, formate generation and conversion to formyl group, unlike in methanogens. Thus, despite sparing one ATP, coupling formate generation and fixation may be not favorable for acetogenic bacteria and will not sustain a metabolic high-flow toward acetyl-CoA synthesis.

A way to bypass H<sub>2</sub> is CO-oxidation. To handle CO, acetogens use different strategies. *A. woodii* thrives episodically on weak CO concentrations, possible due to the reversibility of the CO inhibition of the HDCR system and the ability to oxidize ferredoxin, albeit with a weak turnover

(Figure 2B, 2; Schuchmann and Müller, 2013; Bertsch and Müller, 2015; Ceccaldi et al., 2017). Acetogenic bacteria, which use CO as substrate, like *M. thermoacetica* and *C. autoethanogenum*, exhibit metabolic adaptations. For instance, albeit it has not been tested so far, the NADPH-dependent Fdh system from *M. thermoacetica* should be insensitive to CO as it is not directly using the CO-sensitive hydrogenase, like the HDCR. However, the enzyme depends on a high NADPH/NADP<sup>+</sup> ratio or high pressure of CO<sub>2</sub>. The Hyt/Fdh system from *C. autoethanogenum*, a chimera between HDCR and the electron bifurcating/confurcating hydrogenase (Figure 2B, 4), shows a reactional plasticity by switching from the CO-sensitive hydrogenase to NADPH plus ferredoxin oxidation to drive CO<sub>2</sub>-reduction despite inhibition (Wang et al., 2013). Interestingly, to date, a formyl group generation directly driven by CO-oxidation has never been found in any CO fermenting acetogen. Still, the low redox potential of the CO<sub>2</sub>/CO couple could allow an Fwd-like coupled mechanism, sparing a molecule of ATP, crucial for such energetic extremophiles.

The diversity of the electron-donating Fdh systems reflects and allowed the widespread distribution of these microbes, from H<sub>2</sub> rich to CO saturated niches. However, their dependence on oxygen-sensitive cofactors constrains them to strictly anaerobic but also metal-rich environments, since such carbon fixation pathways require more metallic cofactors than the others. Studying the diversity of these systems provides modern snapshots of the evolution of such “ancestral” organisms to accommodate various ecological niches.

Because syngas (H<sub>2</sub>/CO<sub>2</sub>/CO) is the main source of carbon and energy for hydrogenotrophic methanogens and acetogens, they are excellent “bio-converters.” For instance, acetogens turn industrial waste gases, rich in H<sub>2</sub>, CO and CO<sub>2</sub>, to butanediol, ethanol or acetate, potential biofuels or starting points for new chemical synthesis (Wang et al., 2013; Mock et al., 2015; Liew et al., 2016). With the discovery of genetically tractable acetogens (Liew et al., 2016; Basen et al., 2018) the possibilities for bio-compound synthesis, and bioremediation are expanding.

Moreover, acetogenic CO<sub>2</sub>-activation systems as HDCR and Hyt/Fdh are a treasure trove to realize the Holy Grail reaction of our century: the reversible hydrogenation of CO<sub>2</sub> to formate, offering a stable way to store energy with the concomitant advantage of trapping the greenhouse gas (Schuchmann and Müller, 2013; Müller, 2019).

Studies of acetogenic physiology and carbon fixation pathways are still an ongoing growing field. More work has to be conducted to truly understand their enzymes, metabolic fluxes, the molecular

juggling of their reactions and their limitations. It is crucial to ensure the success of biotechnological applications, including synthetic biology, that will – let’s hope – bring a brighter future.

**Author contributions.** All authors participated to the manuscript writing.

**Funding.** This work was funded by the Max-Planck-Gesellschaft and the Deutsche Forschungsgemeinschaft priority program 1927, “Iron-Sulfur for Life” WA 4053/1-1.

**Acknowledgements.** We would like to acknowledge the Max Planck Institute for Marine Microbiology for continuous support.



# List of Figures

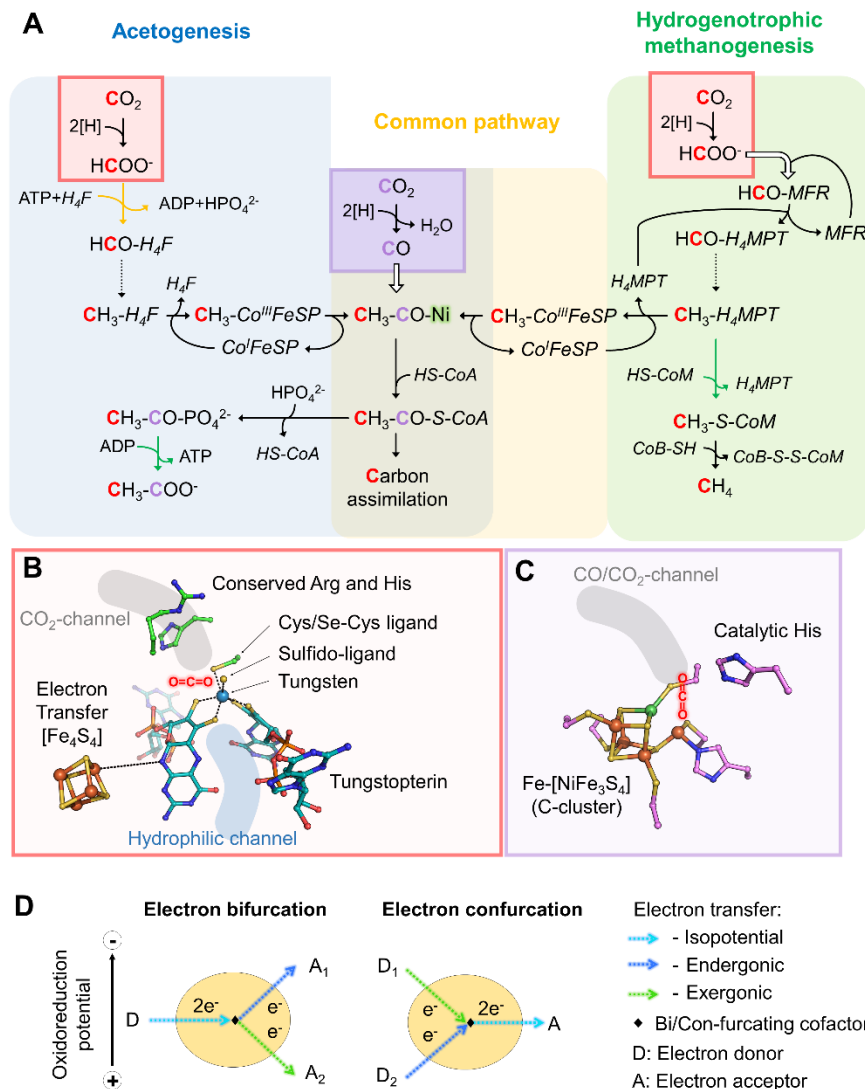


**Figure 1. Variations in the reductive acetyl-CoA pathway between acetogenic bacteria and hydrogenotrophic methanogens, implicated active sites and mechanisms.** (A) Differences in the reductive acetyl-CoA pathway between acetogenic bacteria (left and middle) and methanogenic archaea (right and middle). Acetogens and methanogens share a conserved “carbonyl” branch (common pathway) used to build biomass for both and to conserve energy for acetogens. The green arrows correspond to reactions coupled to energy-conservation (ATP or electrochemical ion gradient generation across the membrane) and the orange one to ATP hydrolysis-coupled reaction. Dashed arrows correspond to three successive reactions: dehydration and two reduction steps. White arrows indicate the usage of an internal channeling system between two active sites. Red and purple squares highlight CO<sub>2</sub>-reduction events, in red Fdh reaction and in purple the CODH reaction. The ACS contains the A-cluster harboring the binuclear Nickel center highlighted by a green glow. The cofactors involved in these processes are: tetrahydrofolate (H<sub>4</sub>F), tetrahydromethanopterin (H<sub>4</sub>MPT),

coenzyme A (CoA-SH), methanofuran (MFR), reduced/oxidized corrinoid FeS containing protein (Co<sup>I</sup>/CH<sub>3</sub>-Co<sup>III</sup>-FeSP), coenzyme B (CoB-SH), coenzyme M (CoM-SH). (B) Close up of a Fdh catalytic site (PDB code 5T5I) containing the tungstopterin, which could be replaced by molybdopterin for other Fdh. Carbons are colored in green for the residues involved in the catalysis and dark cyan for the tungstopterin. Dashed line between the [Fe<sub>4</sub>S<sub>4</sub>]-cluster and the pterin represents the hypothetical electron transfer from the cluster to the tungstopterin. (C) Close up of the catalytic site of CODH from *Moorella thermoacetica* (PDB code 1MJG) containing the C-cluster. Carbons from protein residues are colored in light pink. For both panels, B and C, nitrogen, oxygen, phosphorous, sulfur, iron, tungsten, and nickel are colored as dark blue, red, light orange, yellow, orange, metallic blue, and green, respectively. A molecule highlights the putative CO<sub>2</sub> position in both panels. (D) Scheme of electron bifurcation/confurcation mechanism. During electron bifurcation, a two-electron transfer from an electron donor (D) is bifurcated by a specific cofactor to both endergonic and exergonic one-electron transfers to two different acceptors (A<sub>1</sub> and A<sub>2</sub>). The overall reaction is slightly exergonic. The opposite reaction occurs during electron confurcation.

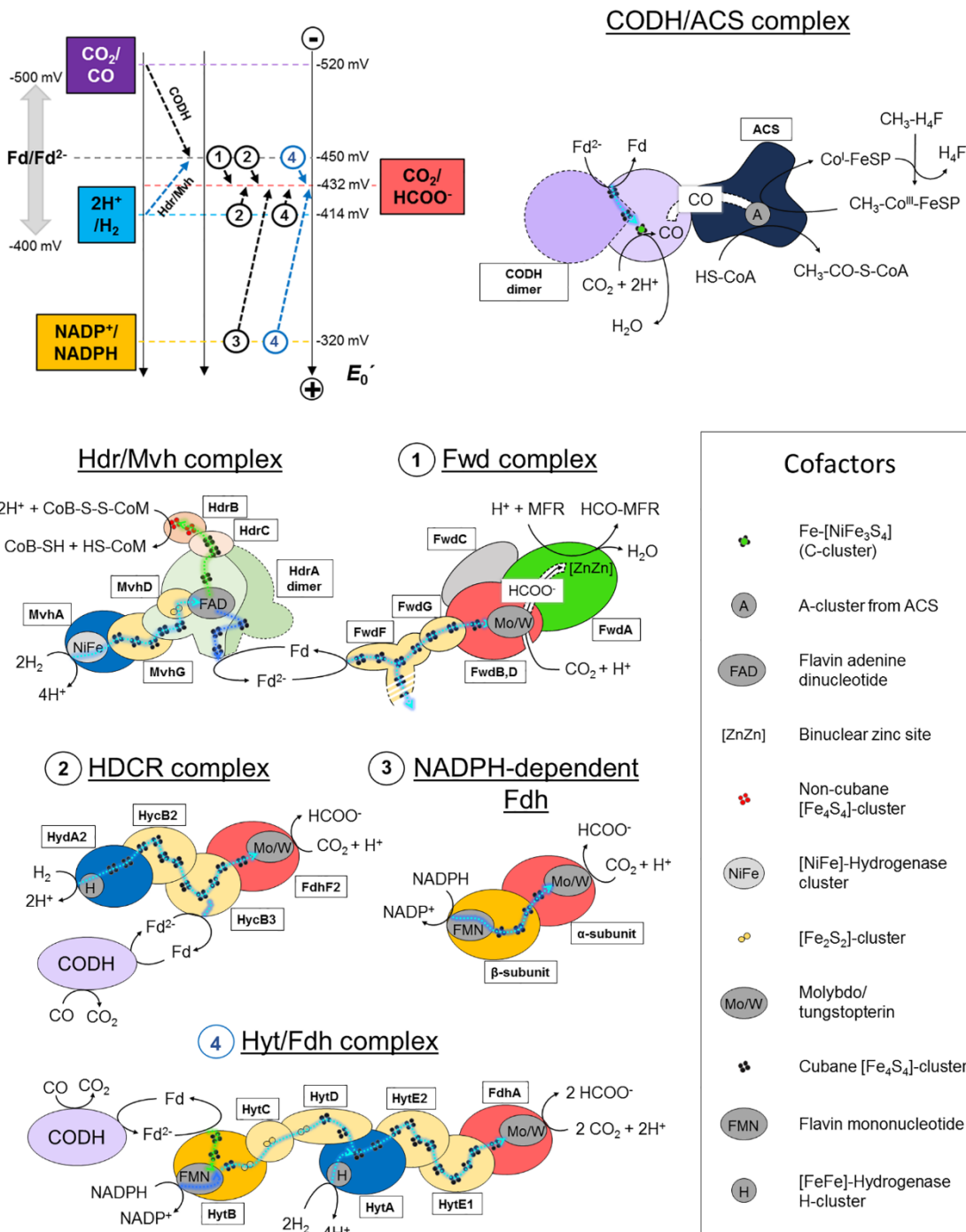


**Figure 2.  $\text{CO}_2$ -activation strategies in hydrogenotrophic methanogens and acetogens.** (A) Standard redox potential ( $E_0'$ ) of redox couples implicated in  $\text{CO}_2$ -activation in methanogenic and acetogenic processes. Dashed arrows schematize the reactions performed by the enzymes listed in panel B. A name or circled number indicates which complex is implicated. The blue arrows correspond to a coupled electron confurcating reaction. To simplify the scheme, the endergonic reaction of the Hdr/Mvh complex ( $\text{CoB-S-S-CoM}/\text{CoB-SH} + \text{CoM-SH} = -140 \text{ mV}$ ) has been omitted. Standard redox potentials were taken from Schuchmann and Müller (2014). Ferredoxin can exhibit potentials ranging from -400 to -500 mV, depending on the organism. An averaged potential

of -450 mV is thus used in the figure. (B,C) Schemes of the characterized and putative organizations of the enzymes involved in CO<sub>2</sub>-reduction in hydrogenotrophic methanogens and acetogens. Catalytic subunits are colored according to their substrate as in panel A. All electron transfers except for con/bifurcation events are shown as cyan dashed lines. For con/bifurcation events, the endergonic reactions are colored in dark blue and exergonic in light green, as illustrated in Figure 1D. Due to the absence of acetogenic structural data, hypothetical architectures are represented based on their original publications, biochemical data and homologies (Yamamoto et al., 1983; Schuchmann and Müller, 2013; Wang et al., 2013). Monomeric forms are schematized. The localization of the electron conurbation event in the Hyt complex is purely hypothetical. The [NiFe]-hydrogenase module from the Hdr/Mvh complex can be replaced by a Fdh. All known cofactors involved in the different reactions of panels B and C are listed. Fd stands for oxidized ferredoxin and Fd<sup>2-</sup> for reduced ferredoxin.

## References

Appel, A. M., Bercaw, J. E., Bocarsly, A. B., Dobbek, H., DuBois, D. L., Dupuis, M., et al. (2013). Frontiers, opportunities, and challenges in biochemical and chemical catalysis of CO<sub>2</sub> fixation. *Chem. Rev.* 113, 6621–6658. doi: 10.1021/ cr300463y

Basen, M., Geiger, I., Henke, L., and Müller, V. (2018). A genetic system for the thermophilic acetogenic bacterium *Thermoanaerobacter kivui*. *Appl. Environ. Microbiol.* 84, e2210–e2217. doi: 10.1128/AEM.02210-17

Berg, I. A., Kockelkorn, D., Ramos-Vera, W. H., Say, R. F., Zarzycki, J., Hügler, M., et al. (2010). Autotrophic carbon fixation in archaea. *Nat. Rev. Microbiol.* 8, 447–460. doi: 10.1038/nrmicro2365

Bertram, P. A., Karrasch, M., Schmitz, R. A., Böcher, R., Albracht, S. P., and Thauer, R. K. (1994). Formylmethanofuran dehydrogenases from methanogenic archaea. Substrate specificity, EPR properties and reversible inactivation by cyanide of the molybdenum or tungsten iron-sulfur proteins. *Eur. J. Biochem.* 220, 477–484. doi: 10.1111/j.1432-1033.1994.tb18646.x

Bertsch, J., and Müller, V. (2015). CO metabolism in the acetogen *Acetobacterium woodii*. *Appl. Environ. Microbiol.* 81, 5949–5956. doi: 10.1128/AEM.01772-15

Buckel, W., and Thauer, R. K. (2013). Energy conservation via electron bifurcating ferredoxin reduction and proton/Na<sup>+</sup> translocating ferredoxin oxidation. *Biochim. Biophys. Acta* 1827, 94–113. doi: 10.1016/j.bbabi.2012.07.002

Buckel, W., and Thauer, R. K. (2018). Flavin-based electron bifurcation, a new mechanism of biological energy coupling. *Chem. Rev.* 118, 3862–3886. doi: 10.1021/acs.chemrev.7b00707

Can, M., Armstrong, F. A., and Ragsdale, S. W. (2014). Structure, function, and mechanism of the nickel metalloenzymes, CO dehydrogenase, and acetyl-CoA synthase. *Chem. Rev.* 114, 4149–4174. doi: 10.1021/cr400461p

Ceccaldi, P., Schuchmann, K., Müller, V., and Elliott, S. J. (2017). The hydrogen dependent CO<sub>2</sub> reductase: the first completely CO tolerant FeFe-hydrogenase. *Energy Environ. Sci.* 10, 503–508. doi: 10.1039/C6EE02494G

Cherubini-Celli, A., Mateos, J., Bonchio, M., Dell'Amico, L., and Companyó, X. (2018). Transition metal-free CO<sub>2</sub> fixation into new carbon-carbon bonds. *ChemSusChem* 11, 3056–3070. doi: 10.1002/cssc.201801063

Costa, K. C., Wong, P. M., Wang, T., Lie, T. J., Dodsworth, J. A., Swanson, I., et al. (2010). Protein complexing in a methanogen suggests electron bifurcation and electron delivery from formate to heterodisulfide reductase. *Proc. Natl. Acad. Sci. U.S.A.* 107, 11050–11055. doi: 10.1073/pnas.1003653107

Darnault, C., Volbeda, A., Kim, E. J., Legrand, P., Vernède, X., Lindahl, P. A., et al. (2003). Ni-Zn-[Fe<sub>4</sub>-S<sub>4</sub>] and Ni-Ni-[Fe<sub>4</sub>-S<sub>4</sub>] clusters in closed and open  $\alpha$  subunits of acetyl-CoA synthase/carbon monoxide dehydrogenase. *Nat. Struct. Biol.* 10, 271–279. doi: 10.1038/nsb912

de Bok, F. A., Hagedoorn, P. L., Silva, P. J., Hagen, W. R., Schiltz, E., Fritsche, K., et al. (2003). Two W-containing formate dehydrogenases (CO<sub>2</sub>-reductases) involved in syntrophic propionate oxidation by *Syntrophobacter fumaroxidans*. *Eur. J. Biochem.* 270, 2476–2485. doi: 10.1046/j.1432-1033.2003.03619.x

Doukov, T. I., Iverson, T. M., Seravalli, J., Ragsdale, S. W., and Drennan, C. L. (2002). A Ni-Fe-Cu center in a bifunctional carbon monoxide dehydrogenase/acetyl-CoA synthase. *Science* 298, 567–572. doi: 10.1126/science.1075843

Fuchs, G. (2011). Alternative pathways of carbon dioxide fixation: insights into the early evolution of life? *Annu. Rev. Microbiol.* 65, 631–658. doi: 10.1146/annurev-micro-090110-102801

Fuchs, G., and Berg, I. A. (2014). Unfamiliar metabolic links in the central carbon metabolism. *J. Biotechnol.* 192(Pt B), 314–322. doi: 10.1016/j.jbiotec.2014.02.015

Fujita, E., Muckerman, J. T., and Himeda, Y. (2013). Interconversion of CO<sub>2</sub> and formic acid by bio-inspired Ir complexes with pendent bases. *Biochim. Biophys. Acta* 1827, 1031–1038. doi: 10.1016/j.bbabi.2012.11.004

Grein, F., Ramos, A. R., Venceslau, S. S., and Pereira, I. A. (2013). Unifying concepts in anaerobic respiration: insights from dissimilatory sulfur metabolism. *Biochim. Biophys. Acta* 1827, 145–160. doi: 10.1016/j.bbabi.2012.09.001

Hou, S. L., Dong, J., and Zhao, B. (2019). Formation of C-X bonds in CO<sub>2</sub> chemical fixation catalyzed by metal-organic frameworks. *Adv. Mater.* 32:e1806163. doi: 10.1002/adma.201806163

Jeoung, J. H., Martins, B. M., and Dobbek, H. (2019). Carbon monoxide dehydrogenases. *Methods Mol. Biol.* 1876, 37–54. doi: 10.1007/978-1-4939-8864-8\_3

Kaster, A. K., Moll, J., Parey, K., and Thauer, R. K. (2011). Coupling of ferredoxin and heterodisulfide reduction via electron bifurcation in hydrogenotrophic methanogenic archaea. *Proc. Natl. Acad. Sci. U.S.A.* 108, 2981–2986. doi: 10.1073/pnas.1016761108

Kung, Y., Doukov, T. I., Seravalli, J., Ragsdale, S. W., and Drennan, C. L. (2009). Crystallographic snapshots of cyanide- and water-bound C-clusters from bifunctional carbon monoxide dehydrogenase/acetyl-CoA synthase. *Biochemistry* 48, 7432–7440. doi: 10.1021/bi900574h

Leimkühler, S., and Iobbi-Nivol, C. (2016). Bacterial molybdoenzymes: old enzymes for new purposes. *FEMS Microbiol. Rev.* 40, 1–18. doi: 10.1093/femsre/fuv043

Liew, F., Henstra, A. M., Winzer, K., Köpke, M., Simpson, S. D., and Minton, N. P. (2016). Insights into CO<sub>2</sub> fixation pathway of *Clostridium autoethanogenum* by targeted mutagenesis. *mBio* 7:e00427-16. doi: 10.1128/mBio.00427-16

Lindahl, P. A. (2002). The Ni-containing carbon monoxide dehydrogenase family: light at the end of the tunnel? *Biochemistry* 41, 2097–2105. doi: 10.1021/bi015932%2B

Marreiros, B. C., Calisto, F., Castro, P. J., Duarte, A. M., Sena, F. V., Silva, A. F., et al. (2016). Exploring membrane respiratory chains. *Biochim. Biophys. Acta* 1857, 1039–1067. doi: 10.1016/j.bbabi.2016.03.028

Martin, W. F., and Thauer, R. K. (2017). Energy in ancient metabolism. *Cell* 168, 953–955. doi: 10.1016/j.cell.2017.02.032

Milton, R. D., Ruth, J. C., Deutzmann, J. S., and Spormann, A. M. (2018). *Methanococcus maripaludis* employs three functional heterodisulfide reductase complexes for flavin-based electron bifurcation using hydrogen and formate. *Biochemistry* 57, 4848–4857. doi: 10.1021/acs.biochem.8b00662

Mock, J., Wang, S., Huang, H., Kahnt, J., and Thauer, R. K. (2014). Evidence for a hexaheteromeric methylenetetrahydrofolate reductase in *Moorella thermoacetica*. *J. Bacteriol.* 196, 3303–3314. doi: 10.1128/JB.01839-14

Mock, J., Zheng, Y., Mueller, A. P., Ly, S., Tran, L., Segovia, S., et al. (2015). Energy conservation associated with ethanol formation from H<sub>2</sub> and CO<sub>2</sub> in *Clostridium autoethanogenum* involving electron bifurcation. *J. Bacteriol.* 197, 2965–2980. doi: 10.1128/JB.00399-15

Müller, V. (2019). New horizons in acetogenic conversion of one-carbon substrates and biological hydrogen storage. *Trends Biotechnol.* 37, 1344–1354. doi: 10.1016/j.tibtech.2019.05.008

Peters, J. W., Beratan, D. N., Bothner, B., Dyer, R. B., Harwood, C. S., Heiden, Z. M., et al. (2018). A new era for electron bifurcation. *Curr. Opin. Chem. Biol.* 47, 32–38. doi: 10.1016/j.cbpa.2018.07.026

Ragsdale, S. W. (2008). Enzymology of the Wood-Ljungdahl pathway of acetogenesis. *Ann. N. Y. Acad. Sci.* 1125, 129–136. doi: 10.1196/annals.14 19.015

Ragsdale, S. W., and Kumar, M. (1996). Nickel-containing carbon monoxide dehydrogenase/acetyl-CoA synthase. *Chem. Rev.* 96, 2515–2540. doi: 10.1021/cr950058%2B

Ragsdale, S. W., Ljungdahl, L. G., and DerVartanian, D. V. (1983). Isolation of carbon monoxide dehydrogenase from *Acetobacterium woodii* and comparison of its properties with those of the *Clostridium thermoaceticum* enzyme. *J. Bacteriol.* 155, 1224–1237. doi: 10.1128/jb.155.3.1224-1237.1983

Ragsdale, S. W., and Pierce, E. (2008). Acetogenesis and the Wood-Ljungdahl pathway of CO<sub>2</sub> fixation. *Biochim. Biophys. Acta* 1784, 1873–1898. doi: 10.1016/j.bbapap.2008.08.012

Schäfer, G., Engelhard, M., and Müller, V. (1999). Bioenergetics of the archaea. *Microbiol. Mol. Biol. Rev.* 63, 570–620.

Schuchmann, K., and Müller, V. (2012). A bacterial electron-bifurcating hydrogenase. *J. Biol. Chem.* 287, 31165–31171. doi: 10.1074/jbc.M112.395038

Schuchmann, K., and Müller, V. (2013). Direct and reversible hydrogenation of CO<sub>2</sub> to formate by a bacterial carbon dioxide reductase. *Science* 342, 1382–1385. doi: 10.1126/science.1244758



Schuchmann, K., and Müller, V. (2014). Autotrophy at the thermodynamic limit of life: a model for energy conservation in acetogenic bacteria. *Nat. Rev. Microbiol.* 12, 809–821. doi: 10.1038/nrmicro3365

Sousa, F. L., Thiergart, T., Landan, G., Nelson-Sathi, S., Pereira, I. A., Allen, J. F., et al. (2013). Early bioenergetic evolution. *Phil. Trans. R. Soc. B* 368:20130088. doi: 10.1098/rstb.2013.0088

Thauer, R. K. (1972). CO<sub>2</sub>-reduction to formate by NADPH. The initial step in the total synthesis of acetate from CO<sub>2</sub> in *Clostridium thermoaceticum*. *FEBS Lett.* 27, 111–115. doi: 10.1016/0014-5793(72)80421-6

Thauer, R. K. (2012). The Wolfe cycle comes full circle. *Proc. Natl. Acad. Sci. U.S.A.* 109, 15084–15085. doi: 10.1073/pnas.1213193109

Thauer, R. K., Kaster, A. K., Seedorf, H., Buckel, W., and Hedderich, R. (2008). Methanogenic archaea: ecologically relevant differences in energy conservation. *Nat. Rev. Microbiol.* 6, 579–591. doi: 10.1038/nrmicro1931

Wagner, T., Ermler, U., and Shima, S. (2016). The methanogenic CO<sub>2</sub> reducing-and-fixing enzyme is bifunctional and contains 46 [4Fe-4S] clusters. *Science* 354, 114–117. doi: 10.1126/science.aaf9284

Wagner, T., Ermler, U., and Shima, S. (2018). “Tungsten-containing formylmethanofuran dehydrogenase,” in *Encyclopedia of Inorganic and Bioinorganic Chemistry* (online), ed. A. Messerschmidt (Hoboken: John Wiley and Sons, Inc).

Wagner, T., Koch, J., Ermler, U., and Shima, S. (2017). Methanogenic heterodisulfide reductase (HdrABC-MvhAGD) uses two noncubane [4Fe-4S] clusters for reduction. *Science* 357, 699–703. doi: 10.1126/science.aan 0425

Wang, S., Huang, H., Kahnt, J., Mueller, A. P., Köpke, M., and Thauer, R. K. (2013). NADP-specific electron-bifurcating [FeFe]-hydrogenase in a functional complex with formate dehydrogenase in *Clostridium autoethanogenum* grown on CO. *J. Bacteriol.* 195, 4373–4386. doi: 10.1128/JB.00678-13

Yamamoto, I., Saiki, T., Liu, S. M., and Ljungdahl, L. G. (1983). Purification and properties of NADP-dependent formate dehydrogenase from *Clostridium thermoaceticum*, a tungsten-selenium-iron protein. *J. Biol. Chem.* 258, 1826–1832.

**Conflict of Interest:** The authors declare that the research was conducted in the absence of any commercial or financial relationships that could be construed as a potential conflict of interest.

# Chapter XIII

## Discussion and perspectives

Microbial activity is constantly shaping the Earth's biogeochemistry, for example by anaerobic sulfate-reducing bacteria, methanogenic archaea, and autotrophic acetogens, all of which dominate the carbon cycle, feed ecosystems, and orchestrate the degradation of biological matter. In this chapter, I will discuss the results of my research projects on the assimilatory and energetic metabolism of these anaerobic energy extremophiles. Under the strict exclusion of oxygen, I have obtained new structural insights and metabolic information by studying pure cultures, an enriched culture and a microbial sample from a mesocosm.

Overall, this thesis reports the biochemical and structural elucidation of the complete set of cytosolic enzymes involved in the archaeal assimilatory and bacterial dissimilatory  $\text{SO}_4^{2-}$  reduction pathways. Furthermore, I have investigated enzyme complexes involved in the energy metabolism of methanogenic archaea and acetogenic bacteria.

### **8.1 A unique pathway to assimilate sulfate in *Methanothermococcus thermolithotrophicus***

At the start of my PhD, the molecular mechanisms of sulfur acquisition by methanogens from sulfur sources with oxidation states higher than  $\text{S}^{2-}$  were essentially unexplored. Several studies described how methanogens acquire sulfur from environmental sulfides, metal sulfides, and, for some, from elemental sulfur and  $\text{SO}_3^{2-}$  (refs. 41,44-46,150), but assimilatory  $\text{SO}_4^{2-}$  reduction in hydrogenotrophic methanogens was quite controversial<sup>151</sup>. Although there has been increasing evidence suggesting that certain methanogens have the genomic capacity to carry out  $\text{SO}_4^{2-}$  reduction, and even two assimilatory proteins, have been recombinantly produced and biochemically characterized (APS/PAPS reductase)<sup>30,53-55</sup>, only one methanogen has been successfully grown on  $\text{SO}_4^{2-}$  as a sole source of sulfur<sup>45</sup>. It is important to note that *Methanobrevibacter ruminantium* has also been reported to grow on  $\text{SO}_4^{2-}$ , but its cultivation

medium contained yeast extract and trypticase that provide alternative sources of sulfur (such as the amino acids cysteine and methionine)<sup>152</sup>. Additionally, a previous study reported that  $\text{SO}_4^{2-}$  does not serve as a sulfur substrate for *M. ruminantium*, and the organism does not encode the  $\text{SO}_4^{2-}$ -activating enzymes like a conventional ATPS<sup>53,153</sup>.

In **Chapter II**, I demonstrated the existence of a  $\text{SO}_4^{2-}$  assimilation pathway in *Methanothermococcus thermolithotrophicus*, of which each enzyme was structurally and biochemically characterized. This led to the discovery of a new type of PAPS reductase and a new class of PAP phosphatase, which seems to be exclusive to the domain of archaea. The enzymes were originally annotated as a dissimilatory APS reductase (aprAB) and a DHH phosphoesterase, highlighting the need to complement *in silico* analysis with physiological, biochemical, and structural studies to gain a proper understanding of microbial metabolic pathways.

### **Thioredoxin-dependent APS/PAPS reductases as a control point for the sulfur metabolism in methanogens**

Although this thesis describes the  $\text{SO}_4^{2-}$  reduction pathway of *M. thermolithotrophicus*, many questions about the enzymes that make up the pathway remain. For example, it is intriguing that *M. thermolithotrophicus* has adapted a dissimilatory APS reductase to an assimilatory PAPS reductase when it already encodes for an assimilatory thioredoxin-dependent PAPSR (WP\_018154242). Furthermore, one might ask why an energy-limited organism, such as a hydrogenotrophic methanogen, would invest in the generation of PAPS to then convert it via a PAPS reductase to  $\text{SO}_3^{2-}$  and PAP, rather than reducing APS directly, as it has been described for other  $\text{SO}_4^{2-}$  assimilating organisms<sup>85,154</sup>. The answer to both questions may lie in the regulation of the overall sulfur metabolism. PAPS acts as a metabolic intermediate that integrates the control of  $\text{SO}_4^{2-}$  assimilation with other cellular processes, such as sulfation reactions. Therefore, regulation of PAPS reductase activity would provide a control point for the overall flux of sulfur in the cell.

The thioredoxin-dependent PAPSR catalyzes the reversible reduction of PAPS to  $\text{SO}_3^{2-}$  and PAP. This reversible reaction would allow to efficiently balance the presence of  $\text{SO}_3^{2-}$  in the  $\text{SO}_4^{2-}$  reduction pathway with the biosynthesis of sulfonated compounds. Interestingly, we could not detect the backward reaction of the PAPS reductase from *M. thermolithotrophicus* with

ferricyanide but measured its activity towards  $\text{SO}_3^{2-}$  and AMP production. I speculate that this enzyme has a higher affinity for PAPS than its thioredoxin-dependent counterpart and efficiently operates towards  $\text{SO}_3^{2-}$  production to fuel Fsr to generate  $\text{HS}^-/\text{S}^{2-}$  for sulfur assimilation. In excess of  $\text{SO}_3^{2-}$ , the thioredoxin-dependent PAPS R would generate PAPS and feed the sulfotransferase(s). This hypothesis would explain why only *M. thermolithotrophicus* has been shown to grow on  $\text{SO}_4^{2-}$  while other methanogens, such as *M. infernus*, which have the genomic potential to do so via thioredoxin-dependent APS/PAPS reductases, cannot. To test this idea, the genes encoding the dissimilatory-like PAPS R of *M. thermolithotrophicus* would have to be transferred into the genome of a methanogen containing all the other enzymes required for  $\text{SO}_4^{2-}$  reduction, such as *M. infernus*, and then observe if growth on  $\text{SO}_4^{2-}$  as the sole sulfur source is indeed possible. Since *M. infernus* is not genetically tractable, *Methanocaldococcus jannaschii* could be the alternative, but the latter lacks the ATPS, APSK, and PAPP<sup>155,156</sup>. The whole  $\text{SO}_4^{2-}$  reduction machinery described in **Chapter II** (except Fsr) would have to be transferred into *M. jannaschii* to investigate if the PAPS R from *M. thermolithotrophicus* allows growth on  $\text{SO}_4^{2-}$  as a sole source of sulfur. In addition, the physiological roles of the described assimilatory APS/PAPS R in *M. jannaschii* in relation to the sulfur metabolism could be further investigated<sup>156</sup>.

*M. jannaschii* was isolated from a white smoker chimney where  $\text{SO}_3^{2-}$  can be formed by the partial oxidation of sulfides with  $\text{O}_2$  (ref. 71). Upon  $\text{SO}_3^{2-}$  exposure, Fsr was shown to be highly expressed and certainly serves as a first line of defense, as we also observed it in *M. thermolithotrophicus*. However, part of the intracellular  $\text{SO}_3^{2-}$  could also be used to produce PAPS via the thioredoxin-dependent PAPS R (or converted to APS via the APS R) to balance the intracellular  $\text{SO}_3^{2-}$  levels and to synthesize sulfonated metabolites. This would explain the presence of an assimilatory PAPS R<sup>54</sup>. However, the assimilatory APS R and PAPS R in *M. jannaschii* have only been investigated for their activity towards  $\text{SO}_3^{2-}$  production<sup>54,55</sup> and *M. jannaschii* lacks the gene encoding for a PAPP. It would require an alternative enzyme/strategy to generate PAP to form PAPS by the PAPS R. Therefore, this hypothesis is purely speculative, and future studies are required to fully understand the physiological roles of those thioredoxin-dependent enzymes.

The presence of the new class of PAPP in a variety of archaea might support the idea of a thioredoxin-dependent PAPS R providing PAPS for sulfotransferases. While the gene encoding for the PAPP is predominantly found in *Euryarchaeota*, many of the methanogens encoding for a

putative PAPP are not known to assimilate  $\text{SO}_4^{2-}$  (e.g. *Methanotorrus formicicus*, *Methanocaldococcus bathoardescens*, *Methanocaldococcus vulcanius*, etc.). The counterargument, however, is the presence of genes encoding for an ATPS and APSK in e.g. *M. formicicus*, *M. bathoardescens*, *M. vulcanius*, or *M. infernus* (see **Chapter II**, Supplementary Fig. 8). It is more likely that in these cases  $\text{SO}_4^{2-}$  is assimilated to produce sulfonated secondary metabolites, but this is probably not efficient enough to fuel the whole sulfur metabolism, and therefore growth cannot be sustained on  $\text{SO}_4^{2-}$  as the sole sulfur source but requires the presence of  $\text{SO}_3^{2-}$  or sulfides. Overall, the enzymes associated with  $\text{SO}_4^{2-}$  assimilation that are encoded in the genomes of certain methanogens and ANME<sup>53</sup> need further investigation, as each species may have adapted specific strategies for intracellular sulfur-trafficking.

### **What is the ecological benefit of *M. thermolithotrophicus* to assimilate $\text{SO}_4^{2-}$ ?**

As discussed in **Chapter II**, *M. thermolithotrophicus* may have acquired an  $\text{SO}_4^{2-}$  reduction pathway to adapt to a fluctuating sulfur source availability and for niche expansion. However, since the data obtained was exclusively from laboratory conditions, it would be valuable to investigate the need for *M. thermolithotrophicus* to assimilate  $\text{SO}_4^{2-}$  *in situ*. To do so, we would need to go to the site from which the methanogen was originally isolated. As *M. thermolithotrophicus* was taken from the sandy geothermally heated sea floor of the beach at Stufe di Nerone close to Naples (Italy), about 3 m away from the shore in about 0.5 m depth<sup>157</sup>, it should be easy to access and study *M. thermolithotrophicus* environment. First, it would be interesting to determine the physicochemical parameters of the habitat. Determining the  $\text{CO}_2$  and  $\text{H}_2$  partial pressures will estimate to which degree the hydrogenotrophic methanogen would have access to energy supply and to fuel the hydrogenases (**Chapter III**). Quantifying the different sulfur species either directly on site with microsensors or after core sampling via colorimetric assays, like the methylene blue method for  $\text{S}^{2-}$  or ion chromatography, e.g. for  $\text{SO}_4^{2-}$ , will provide insights into the bioavailable sulfur substrates for *M. thermolithotrophicus*. GeneFISH, a method to detect specific genes and ribosomal RNA (rRNA) at the single cell level, links a potential metabolic function to microbial taxonomy and would allow to target and visualize Fsr or the dissimilatory-like PAPS from *M. thermolithotrophicus* in the environmental sample. This way, we would obtain information about the abundance of the organism in the environment and the expected expressed

genes. Furthermore, it would be very interesting to analyze the microbial community of *M. thermolithotrophicus* and if the organism can co-occur or even compete with other SRB for the common substrate H<sub>2</sub> and, in this case, SO<sub>4</sub><sup>2-</sup>. The metabolic versatility of *M. thermolithotrophicus* highlights the need to reconsider the notion that methanogenesis is inhibited upon SO<sub>4</sub><sup>2-</sup> exposure, mainly due to out-competition by SRB. Metagenomics, the untargeted approach to sequence the entire genetic material of all organisms within a sample, will provide not only insights into the microbial community in the environment but also their functional capacity. Complementing this technique with metatranscriptomics will reveal the presence of active and dynamic populations. Furthermore, transcriptomic analysis will reveal whether SO<sub>4</sub><sup>2-</sup> is being metabolized by *M. thermolithotrophicus in situ*.

#### **Assimilatory SO<sub>4</sub><sup>2-</sup> reduction in methanogens - an early origin or a more recent trait?**

Structural and spectroscopic investigations of the F<sub>420</sub>-dependent sulfite reductase of *M. thermolithotrophicus* and *M. jannaschii* showed that this enzyme performs a unidirectional reduction of SO<sub>3</sub><sup>2-</sup> to HS<sup>-</sup>/S<sup>2-</sup>, like assimilatory sulfite reductases, but shares an overall architecture with dissimilatory ones (**Chapter IV**). The enzyme does not contain certain extensions, as reported for aSirs and dSirs, making it the most compact and “primitive” sulfite reductase structurally characterized so far. This interesting mix of features of both assimilatory and dissimilatory sulfite reductases and their primitive organization affirms the previous suggestion that Fsr would provide a plausible picture of a sulfite reductase prototype<sup>76</sup>. Group I Fsr has been identified mainly in non-cytochrome methanogens, the majority of which are thermophilic *Methanococcales*, and this order has been proposed to have a more ancient origin than the cytochrome-containing methanogens<sup>53,76</sup>. Although the origin of Fsr remains uncertain, it is likely that methanogens had Fsr early in their evolution. In contrast, phylogenetic analysis suggests that most of the enzymes that constitute the SO<sub>4</sub><sup>2-</sup> assimilation pathway in *M. thermolithotrophicus* are more recent acquisitions. The ATPS, APSK, and PAPSR were probably acquired through horizontal gene transfer (HGT) and are thought to be of bacterial origin. However, genes obtained via HGT at different times and individually incorporated into the pathway are typically not organized into operons, but are rather located at different genomic sites. It is therefore intriguing that these enzymes, including the PAPP, which is proposed to be of archaeal origin, are clustered in the same

genomic region. In fact, all the  $\text{SO}_4^{2-}$  assimilation enzymes, except Fsr, are located on a single operon. This may have a regulatory function to uncouple  $\text{SO}_4^{2-}$  assimilation from  $\text{SO}_3^{2-}$  detoxification, as discussed in **Chapter II**, but the different position in the genome could also be due to an early origin of Fsr.

Before the Great Oxygenation Event (about 2.4 billion years ago), oceanic  $\text{SO}_4^{2-}$  concentrations were less than  $200 \mu\text{M}$ <sup>158</sup>. Methanogenesis dominated the carbon cycle as low  $\text{SO}_4^{2-}$  concentrations suppressed  $\text{SO}_4^{2-}$  reduction rates. However, there is evidence for minor microbial  $\text{SO}_4^{2-}$  reduction that dating back to about 3.47 billion years ago<sup>159</sup>, and it has been suggested that this ancient biogenic sulfide originated from minor  $\text{SO}_4^{2-}$  reduction activities of methanogens<sup>76</sup>. It is interesting to note that *M. thermolithotrophicus* requires only  $100 \mu\text{M}$   $\text{SO}_4^{2-}$  to show robust growth. Since SRMs were most likely not abundant competitors for methanogens at that time (about 3.47 billion years ago), *M. thermolithotrophicus* may have adapted to increasing  $\text{SO}_4^{2-}$  concentrations as a strategy to outcompete other methanogens or microorganisms by thriving in these changing, more oxidized conditions. Although it is highly unlikely that the pathway described in *M. thermolithotrophicus* existed in earlier times, there is further genomic evidence that methanogenesis and dissimilatory  $\text{SO}_4^{2-}$  reduction were, and potentially still are, intertwined in certain archaea. Some members of the *Archaeoglobi* and the deeply-rooted *Korarchaeota* show the genomic potential to carry out both, an anaerobic  $\text{CH}_4$  metabolism and a dissimilatory sulfur metabolism<sup>30,160</sup>. In both cases, methane metabolism preceded the sulfur metabolism, which has been proposed to have been horizontally transferred from the *Firmicutes* to the *Korarchaeota*<sup>30</sup>. Overall, the  $\text{CH}_4$  and  $\text{SO}_4^{2-}$  metabolisms are not as strictly separated as long assumed, but the origin of co-occurring methanogenesis and  $\text{SO}_4^{2-}$  reduction pathways within one organism remains elusive. A complementary approach of metagenomics, metaproteomics, metatranscriptomics, evolutionary phylogeny and biochemical studies may help to gain more insight into the present and past role of  $\text{SO}_4^{2-}$  reduction in methanogens.

### **Differential transcriptomics to analyze the sulfur metabolism of *M. thermolithotrophicus***

While I was able to show that cells grown on  $\text{SO}_4^{2-}$  do deplete the substrate from the medium, most of the enzymes of the assimilatory  $\text{SO}_4^{2-}$  reduction pathway from *M. thermolithotrophicus* were recombinantly expressed in *E. coli*. To prove that the enzymes described in this study are indeed



expressed *in vivo*, we performed differential transcriptomics. I collected samples in triplicate from cultures grown in serum flasks and on the substrates  $S^{2-}$ ,  $SO_3^{2-}$  or  $SO_4^{2-}$  in early, mid and late exponential phase and stationary phase. In collaboration with Stian Torset from the MPI Bremen, Germany, we obtained some initial insights into the transcription of  $SO_4^{2-}$  assimilating genes from the different cultures. We found that the *fsr* gene was up-regulated in the  $SO_3^{2-}$  samples, while genes for the  $SO_4^{2-}$  assimilation pathway, especially *sat*, were up-regulated in the  $SO_4^{2-}$  grown cells. However, in the stationary phase samples the expression of *sat* drops dramatically. The dissimilatory-like PAPS<sub>R</sub> was significantly and substantially associated with  $SO_4^{2-}$  addition, whereas the thioredoxin-dependent PAPS<sub>R</sub> was not. The expression of *fsr* did not vary much across time points, except in the  $S^{2-}$  grown samples, where its expression started high and then decreased drastically. In the  $SO_4^{2-}$  grown cells *fsr* remained expressed at all times, while the remaining  $SO_4^{2-}$  reducing machinery decreased over time. In addition, the Fsr isoform that was proposed to be a nitrite reductase (see below) is not co-expressed with our characterized Fsr, however, with low significance. Although the transcriptomic studies need further refinement, they confirm that the genes we have recombinantly expressed in *E. coli* are indeed transcribed in *M. thermolithotrophicus* under  $SO_4^{2-}$  dependent growth.

### **The second Fsr isoform in *M. thermolithotrophicus*: an F<sub>420</sub>-dependent nitrite reductase?**

We discovered two Fsr isoforms in *M. thermolithotrophicus*, both belonging to Group I Fsr (**Chapter IV**), and characterized biochemically, structurally, and spectroscopically the one that is overexpressed during  $SO_3^{2-}/SO_4^{2-}$  growth. As recently reported by our group, the other isoform is highly expressed under diazotrophic conditions during the early exponential phase<sup>161</sup>. In the genome of *M. thermolithotrophicus*, the second isoform of *fsr* clusters next to *narK*, encoding for a putative nitrate transporter, and *narB*, encoding for a molybdopterin-dependent nitrate reductase<sup>161,162</sup>. The up-regulation of these genes is explained by the stress induced upon nitrogen limitation and the need for the cell to take up nitrogen in any form, such as via  $NO_3^-$  reduction<sup>161</sup>. It has been reported that *M. thermolithotrophicus* can grow on  $NO_3^-$  as its sole nitrogen source<sup>163</sup>, which may involve these genes. Most sulfite reductases reduce  $NO_2^-$  (refs. 46,164), and a Group II Fsr from ANME lacking sulfite reductase activity<sup>72</sup> was shown to have an F<sub>420</sub>-dependent nitrite reductase (Fnir) activity, albeit at very low rates. Moreover, the Fnir activity of Group I Fsr from

*M. jannaschii* has recently been characterized<sup>73</sup>. Considering that bottom seawater and vent effluent gases can contain  $\text{NO}_2^-$ , it is plausible that methanogens have evolved a detoxification system to transform the toxic compound<sup>73,74</sup>. Perhaps *M. thermolithotrophicus* has adapted the second isoform exclusively for  $\text{NO}_2^-$  conversion, to supply the cell with ammonia and detoxify the oxidant. To our surprise, the cultivation of *M. thermolithotrophicus* on  $\text{NO}_3^-$  remained unsuccessful for our group and for the team of Prof. Dr. Biswarup Mukhopadhyay (personal communication)<sup>163</sup>. Close examination of the gene encoding the nitrate reductase revealed an internal stop codon that would cause loss of activity. It is possible that the original strain, which was able to grow on  $\text{NO}_3^-$ , lost this metabolic ability over the years. In other words, without the constraint of using  $\text{NO}_3^-$ , a mutant containing the stop codon propagated and was the one kept in the strain collection. First analysis of the differential transcriptomic data collected from *M. thermolithotrophicus* cultures grown on  $\text{S}^{2-}$ ,  $\text{SO}_3^{2-}$  or  $\text{SO}_4^{2-}$  support this hypothesis, as the second isoform transcript was not up-regulated in any sample of the different sulfur substrates.

In both cases,  $\text{SO}_3^{2-}$  and  $\text{NO}_2^-$  reduction, the methanogen once again demonstrates its ability to facilitate assimilatory or anabolic pathways by using the low redox potential of  $\text{H}_2$ , made accessible for some reactions by the  $\text{F}_{420}$ -reducing hydrogenase (or in some cases via the  $\text{F}_{420}$ -reducing formate dehydrogenase).

### **The potential of the $\text{F}_{420}$ -reducing hydrogenases of *M. thermolithotrophicus* for efficient and more robust bioinspired $\text{H}_2$ conversion catalysts**

One of the main energy carrier molecules that fuel the  $\text{SO}_4^{2-}$  assimilation and methanogenesis pathways in *M. thermolithotrophicus* is reduced  $\text{F}_{420}$ . In **Chapter III**, the enzyme responsible for the reversible reduction of  $\text{F}_{420}$  was structurally and spectroscopically characterized: the  $\text{F}_{420}$ -reducing hydrogenase (Frh). Two Frh isoforms were crystallized, one containing Se in the active site, whereas the other one is Se-free. Both Frh isoforms in *M. thermolithotrophicus* oligomerize in the dodecameric ball shape, as observed in homologs. In addition, the [NiFe] hydrogenase showed a dynamic behavior between the dodecameric and a dimeric form. To validate whether this is an artifact of purification and crystallization, it would be worthwhile to follow the dynamic behavior of *MtFrh*, e.g. using analytical ultracentrifugation, dynamic light scattering or mass

photometry, and to observe if effectors (e.g. addition of F<sub>420</sub>, H<sub>2</sub>) would influence the dynamics.

The [NiFe] isoform was further studied by resonance Raman (RR) and infrared (IR) spectroscopy and proved the complete redox state cycle of an O<sub>2</sub>-sensitive [NiFe] hydrogenase, which makes Frh from *M. thermolithotrophicus* an attractive enzyme to study the [NiFe]-redox states. Despite its robust activity and suitable behavior for spectroscopy, the isolated [NiFe] hydrogenase from *M. thermolithotrophicus* is O<sub>2</sub>-sensitive and favors H<sub>2</sub> oxidation, as [NiFe] hydrogenases in general tend to be inhibited by the product H<sub>2</sub>. [NiFeSe] hydrogenases, on the other hand, are attractive alternatives as blueprints for H<sub>2</sub>-producing catalysts because they exhibit lower product inhibition for the H<sub>2</sub> production and show an increased overall activity and fast reactivation after O<sub>2</sub> exposure, especially when low potentials are applied<sup>66,165,166</sup>. Selenium's larger size and greater ability to polarize compared to sulfur, together with the ease of oxidation and reduction of selenocysteine compared to cysteine, are possible reasons for the higher activity of [NiFeSe] hydrogenases<sup>67</sup>. In addition, the rapid oxidation of selenocysteine helps to protect the transition metal core, and the enzyme can quickly reactivate itself after inactivation by O<sub>2</sub> (ref. 67). A selenocysteine-to-cysteine variant confirmed the role of selenium in the maturation process, protection against oxidative damage, and the high activity of [NiFeSe] hydrogenases<sup>167</sup>. Based on these characteristics, the [NiFeSe] hydrogenase has been proposed as the most efficient molecular H<sub>2</sub> evolution catalyst for use in water splitting<sup>67</sup>. The reason why *M. thermolithotrophicus* encodes both isoforms, and not just the more efficient and robust Se-containing one, is linked to the element availability in their environment. It was demonstrated in *Desulfovibrio vulgaris* Hildenborough that the addition of Se to the growth medium leads to a strong repression of the [FeFe] and [NiFe] hydrogenases and an increase of [NiFeSe] hydrogenases<sup>168</sup>. Under Se-limited conditions, *M. thermolithotrophicus* can upregulate the expression of the [NiFe] hydrogenase, a clever strategy given that sulfur is a much more abundant element than selenium. Furthermore, the coexistence of different hydrogenases certainly contributes to the overall efficiency and robustness of the organism's hydrogen and energy metabolism, enabling it to efficiently produce reduced F<sub>420</sub> as needed.

While biomimetic studies have validated the higher activity and O<sub>2</sub> tolerance of [NiFeSe] hydrogenases compared to the [NiFe] isoforms, the exact role of selenium and whether the secondary coordination sphere improves the performance of this enzyme remains unknown<sup>67</sup>.

Therefore, the next approach should be to obtain a higher resolution structure of the F<sub>420</sub>-reducing [NiFeSe] hydrogenase from *M. thermolithotrophicus*. The structural data we present in **Chapter III** provides a general overview of the architecture. However, high-resolution data are required to obtain accurate insights into the position of the active site residues. It is worth mentioning that the purification of the [NiFeSe] hydrogenase was not targeted but that the enzyme was accidentally co-purified with the [NiFe] hydrogenase. By testing different Se sources and increasing their concentrations in the cultivation medium, it could be possible to purify and crystallize more of the [NiFeSe] isoform to obtain a higher resolution X-ray crystal structure. Crystallographic studies on a high-resolution crystal of [NiFeSe] Frh from *M. thermolithotrophicus* and spectroscopic analysis of the crystal and high-purity enzyme in solution may provide new insights into a bioinspired, highly efficient H<sub>2</sub>-producing catalyst.

#### **SO<sub>4</sub><sup>2-</sup> dependent growth of *M. thermolithotrophicus* in fermenter: potential and limitations**

In 1986, Daniels and his team grew *M. thermolithotrophicus* to a maximum OD<sub>600</sub> of 0.84 on S<sup>2-</sup> as a sulfur substrate and to an OD<sub>600</sub> of 0.75 on 4.4 mM SO<sub>4</sub><sup>2-</sup> after 15 - 20 hours<sup>45</sup>. At the beginning of my PhD, I optimized the cultivation conditions for *M. thermolithotrophicus* and adapted the protocol for its growth medium based on the high cell density medium for *M. jannaschii* of Mukhopadhyay et al. 1999 (ref. 169). The addition of higher salt concentrations and more trace elements increased the growth of *M. thermolithotrophicus* from a maximum OD<sub>600</sub> of 1.1 with 2 mM Na<sub>2</sub>S to a maximum OD<sub>600</sub> of 4.6 with 1 mM Na<sub>2</sub>S. The apparent need for higher salt and metal concentrations might reflect the environmental parameters of *M. thermolithotrophicus*, which may resemble those of an active geothermal area. After gradual adaptation to SO<sub>4</sub><sup>2-</sup> as the sole source of sulfur, *M. thermolithotrophicus* exceeded the sulfide-dependent growth and reached a maximum OD<sub>600</sub> of 7. Overall, growing *M. thermolithotrophicus* on SO<sub>4</sub><sup>2-</sup> was reproducible, yielding high cell densities, and the laboratory commonly uses this method to harvest large quantities of biomass (e.g. for cofactor purification). While SO<sub>3</sub><sup>2-</sup> is a mild reductant<sup>170</sup>, SO<sub>4</sub><sup>2-</sup> is not, and there was a concern that the complete elimination of S<sup>2-</sup> from the medium would not allow *M. thermolithotrophicus* to grow without an additional reducing agent. To my surprise, the archaeon was able to reduce the medium on its own after a few hours, standing at 65 °C, given that SO<sub>4</sub><sup>2-</sup> was added as a sulfur source. The importance of letting the culture stand until the media was

fully reduced (indicated by the color shift of resazurin from pink to transparent) was already observed by Daniels et al. 1986 (ref. 45). We thought that the source of reducing power is unlikely  $S^{2-}$ , as the  $SO_4^{2-}$  grown cells did not smell sulfidic nor produced measurable  $S^{2-}$  (measured with an  $H_2S$  microsensor and the methylene blue method<sup>171</sup>). Since the  $SO_4^{2-}$  assimilation process would require ATP, it seems logical that the methanogen has a tight regulation of the pathway and will not produce an excess of  $S^{2-}$ . However, this finding is in disagreement with previous results, where the addition of 4.4 mM  $SO_4^{2-}$  led to the formation of 0.1-0.2 mM  $S^{2-}$  at the early stationary phase<sup>45</sup> and would explain why the resazurin turns transparent. In this study, the headspace and liquid of media were analyzed via gas chromatography, which makes it a more accurate approach<sup>45</sup>. Compared to flask culture, the situation is different in a fermenter as  $H_2S$  will escape in the headspace. Considering a growth at pH 6.2 and the pK for the  $H_2S \rightleftharpoons HS^-$  equilibrium being 7.04, the sulfide generated by *M. thermolithotrophicus* will not accumulate in such an open system. Future experiments aiming to understand the nature of reducing equivalents released by the archaeon would be of special interest for fundamental and applied research.

The potential to assimilate  $SO_4^{2-}$  and grow exclusively on this sulfur source could be transferred to other methanogens used in the biotechnological sector. The advantages of using  $SO_4^{2-}$  over  $S^{2-}$  as a sulfur substrate, in addition to being cheaper and non-toxic to humans, are that there is no precipitation of cations such as iron and no loss of sulfur substrate, as  $SO_4^{2-}$  is not volatile at pH 7 or lower pH values<sup>170</sup>. Potential limitations are the energy demands of the pathway, which do not appear to be dramatic when considering our experiments, and the temperature requirements of the involved enzymes. The enzymes were purified from a thermophilic organism with an optimal temperature of 65 °C<sup>172</sup>, and their transfer to a mesophilic methanogen might result in no or reduced activity. However, genetically tractable *Methanothermobacter* species grow in the same temperature range and are therefore, interesting targets<sup>155</sup>.

Overall, **Chapters II and IV** shed light on the  $SO_4^{2-}$  reduction machinery in *M. thermolithotrophicus*, which intertwined with the dissimilatory pathway by the organization of the enzymes. This work also proposes avenues for further research into the archaeon behavior in its natural environment, where the microbial community might influence the metabolic pathways in an unexpected way.

## 8.2 A snapshot of the $\text{SO}_4^{2-}$ reduction pathway from an ethanotrophic consortium

In **Chapter V** we worked with an enrichment culture sampled from a deep-sea hydrocarbon seep. The sample was enriched for the ethane-oxidizing archaeon *Candidatus* *Ethanoperedens thermophilum* and its  $\text{SO}_4^{2-}$  reducing partner bacterium *Candidatus* *Desulfofervidus auxilii*<sup>113</sup>. Despite a rather inhomogeneous sample and a low biomass to work with (60 mg of proteins in the soluble fraction), it was possible to purify, crystallize, and structurally identify the main cytosolic  $\text{SO}_4^{2-}$  reducing enzymes from the central energy metabolism of *Ca. D. auxilii*. Using this native approach, it was possible to obtain the first structure of an ATPS from an SRB bound to its physiological partner. While the ATPS and APSR were active, I could not detect any reliable activity for DsrAB. This may be because this enzyme requires membrane partner proteins, which were not present in the sample of the purified enzyme, nor would they be present in the soluble fraction after ultracentrifugation of the cell extract. However, to the best of my knowledge, this would be the first time that DsrAB is unable to reduce  $\text{SO}_3^{2-}$  or thiosulfate, at least partially, with  $\text{MV}_{\text{red}}$  as the electron donor. Since other metalloenzymes (e.g. APSR) were active,  $\text{O}_2$  contamination, which could have inhibited DsrAB, can be ruled out. Despite the inactive DsrAB, this study provides new information on the dissimilatory sulfate reduction pathway of *Ca. D. auxilii*.

Following on from the previous discussion of possible crossroads in the central sulfur metabolism of methanogens, *Ca. D. auxilii* also has the genomic potential for a parallel  $\text{SO}_4^{2-}$  assimilation pathway. It contains genes encoding for putative assimilatory  $\text{SO}_4^{2-}$  reduction enzymes such as two APS kinases (locus tag: BLFGPEAP\_00131 and BLFGPEAP\_00807). The sulfur group of the produced PAPS could be transferred to an acceptor by a non-canonical sulfotransferase to build up sulfonated metabolites. However, the genome of *Ca. D. auxilii* also encodes a putative PAPS reductase (BLFGPEAP\_00432), which could reduce PAPS to  $\text{SO}_3^{2-}$  and PAP. The three genes are transcribed at a low levels under the growth conditions used<sup>113</sup>. What would be the advantage of generating  $\text{HS}^-/\text{S}^{2-}$  in this way rather than directly from the dissimilatory pathway? While the importance of PAPS as a key metabolite suggests possible answers, a thorough investigation is needed to unravel the physiological role of these genes.

Within the sulfur metabolism of *Ca. D. auxilii*, several questions remain, in particular concerning the possible electron donors for APSR and DsrAB. Does the transfer of electrons occur directly from the membrane to the enzyme or via an intermediate carrier? Furthermore, how are electrons transferred from the archaeal community to the bacteria? Cryo-electron tomography promises to provide further insights into the electron transfer between *Ca. Ethanoperedens thermophilum* and *Ca. D. auxilii*. Nevertheless, as discussed in **Chapter V**, the successful isolation and study of proteins in the microbial consortium opens up future avenues for the comprehensive characterization of other complexes.

### **8.3 Crystallization as a selective process to ultimately separate individual proteins from microbial dark matter**

While the enzymes previously characterized in this thesis were obtained by recombinant expression in *Escherichia coli* or from pure cultures, **Chapter V** demonstrated that native purification of catabolic enzymes from enrichments is possible. In **Chapter III**, I explained the importance of the crystallization process for the separation of the Frh isoforms. **Chapter VI** develops this concept further. Here, MCR from the acetoclastic methanogen *Methanothrix*, proposed to be the main biological methane producer on Earth, was purified directly from wastewater treatment sludge, and a crystal structure was obtained.

The experiment was originally established in collaboration with Prof. Dr. Jens Harder and a master class from the MPI Bremen, Germany, taught by our group on the purification of the methanogenic enzyme. The master class worked on microbial enrichment obtained by physical separation. The enrichment consisted of about 40 % of the *Methanothrix* population based on FISH. Metagenomics and proteomics confirmed multiple subspecies in the enrichment, making the purification of a single enzyme challenging. The master class purified and crystallized the MCR from the enrichment, which resulted in diffracting protein crystals a few weeks later.

Therefore, I wanted to see if it was possible to purify this abundant enzyme directly from the wastewater sludge sample, collected four months later from the same wastewater treatment plant. Here, the isolation was performed on the crude sludge without prior sedimentation of the sample or separation of the middle liquid layer. Although this process was more laborious than the

enrichment approach and required additional ultracentrifugation steps, MCR was successfully crystallized and its structure solved.

Overall, **Chapters V and VI** have shown that targeted enzymes can be purified and crystallized from highly heterogeneous samples. As the enzymes are purified directly from their mesocosm, they are equipped with their natural (metallo)cofactors, post-translational modifications, and bound to physiological partners. This direct approach avoids the “bottle effect” that can occur with isolated strains and allows the targeting of 85-99% of the microorganisms that cannot be isolated<sup>173</sup>, potentially providing blueprints for new carbon sequestration enzymes.

#### **8.4 CO<sub>2</sub> fixation machinery of autotrophic acetogens as a promising avenue for carbon sequestration - Hyt/FdhA, a case study**

At the time of writing the review on the CO<sub>2</sub> fixation strategies of acetogens (**Chapter VII**), no structures of the CO<sub>2</sub> fixation complexes of acetogens were available. I therefore decided to study the Hyt/Fdh complex of *C. autoethanogenum* in the hope of obtaining structural data. With the help of Dr. Olivier N. Lemaire and Christina Probian from the MPI Bremen, *C. autoethanogenum* was grown in a fermenter at 37 °C with H<sub>2</sub>, CO<sub>2</sub>, and fructose as the main substrates. After adapting the protocol, the purification under anaerobic conditions and yellow light led to the isolation of the seven-subunit complex obtained in the correct stoichiometry. However, despite several crystallization attempts, no diffracting crystals were obtained (10-15 mg ml<sup>-1</sup> of pure Hyt/Fdh were plated on seven different crystallization kits with the addition of FAD, and FMN, with or without formate). The recent elucidation of the cryo-EM structure of HDCR from *T. kivui*<sup>129</sup> may explain why the crystallization of Hyt/Fdh was unsuccessful. HDCR forms flexible filaments arranged in ring-shaped superstructures, identified by cryo-electron tomography<sup>129</sup>. If Hyt/Fdh assembles in a similar way, it would be the wrong approach to try to solve the structure by protein crystallization followed by X-ray crystallography. To obtain a diffracting protein crystal, the complex must arrange itself symmetrically and repetitively so that the crystal lattice extends in three dimensions. Achieving the repetitive arrangement required for crystal growth is hampered by the structural constraints imposed by the formation of filaments, their large size, and their dynamic nature. Therefore, we took alternative approaches, using biochemical and spectroscopic techniques to gain



more insight into Hyt/Fdh. One of the first objectives was to confirm the enzyme activity and understand the electron flow in the complex. Since the formate production via ferredoxin and NADPH is dependent on the [FeFe] hydrogenase, it was suggested that electron bifurcation is mediated by the H-cluster of the [FeFe] hydrogenase. To verify this hypothesis, we first confirmed the [FeFe] hydrogenase (HytA subunit) activity on a native gel, where the reduction upon H<sub>2</sub> oxidation was monitored by the appearance of blue color from MV<sub>ox</sub> to MV<sub>red</sub>. To investigate the active site of HytA, we collaborated with Dr. Sven Stripp from the Technical University Berlin, Germany, who performed Fourier Transform Infrared (FTIR) spectroscopy on Hyt/Fdh. FTIR is a technique that analyses the interaction between matter and infrared light by measuring the frequency and intensity of infrared radiation absorbed or emitted by a sample. The infrared absorbance in the range of 2,150 to 1,750 cm<sup>-1</sup>, generated by the ligands of the H-cluster, serves as a distinctive marker to probe the redox state of [FeFe] hydrogenases<sup>144</sup>. For conventional [FeFe] hydrogenases, the “H<sub>2</sub>-N<sub>2</sub>” difference spectrum shows the transition from the oxidized H<sub>ox</sub> state (negative bands) to the one-electron reduced H<sub>red</sub> species (positive bands) when the gas atmosphere is switched from N<sub>2</sub> to 10% H<sub>2</sub> (**Figure 11**). Upon H<sub>2</sub> addition, the active site of HytA forms the reduced H<sub>hyd</sub>\* state, which is reversible when the H<sub>2</sub> is replaced by N<sub>2</sub> (ref. 174). The observation of a single reduced state of the H-cluster is in good agreement with canonical [FeFe] hydrogenases, and HytA is unlikely to be the site where the electron confurcation occurs. It is more likely that Hyt/Fdh performs a mechanism similar to that described for the electron bifurcating [FeFe] hydrogenase HydABC (see Introduction, **Figure 9**)<sup>144</sup>.

Many [FeFe] hydrogenases are extremely sensitive to CO, which is a competitive inhibitor of H<sub>2</sub>-oxidation. However, the [FeFe] hydrogenase from HDCR *A. woodii* is CO tolerant, as the inhibition is completely reversible<sup>149</sup>. Since *C. autoethanogenum* can grow on CO, it is expected that HytA would also be tolerant to CO<sup>131</sup>. Whether CO inhibits HytA or the binding can be reversed by the addition of H<sub>2</sub> can be investigated using FTIR spectroscopy. This technique will also allow us to determine whether the H-cluster is reduced during formate oxidation or to monitor the reduction of CO<sub>2</sub> during H<sub>2</sub> oxidation, providing valuable insights into the electron flow.

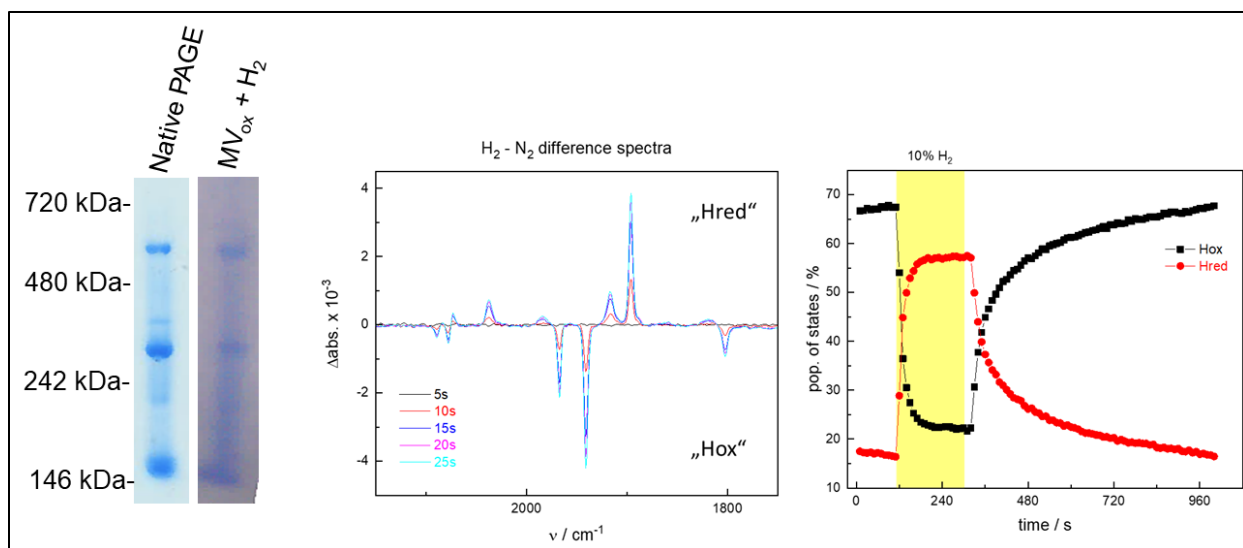


**Figure 11. Characterization of HytA from *C. autoethanogenum*.** Left panel: Native gel of the purified Hyt/Fdh complex, which forms three different oligomeric states. The complex in a 1:1 stoichiometry of all subunits has an expected molecular weight of 282-kDa, which likely corresponds to the middle band. The right gel shows the activity of HytA indicated by the blue dye from reduced MV. Middle and right panel: FTIR “H<sub>2</sub>-N<sub>2</sub>” difference spectra of the H-cluster of HytA.

The formate dehydrogenase, FdhA, shows original structural features as its amino acid sequence is closer to that of the molybdopterin-containing formate dehydrogenase, FdhH, from *E. coli* (about 60% identity) than to the tungsten-containing formate dehydrogenase from *Desulfovibrio gigas* (about 25% identity), both of which have been structurally characterized<sup>175,176</sup>. Therefore, FdhA may represent a new type of selenocysteine-containing tungsten enzyme. After the purification of the Hyt/Fdh complex, the activity of FdhA was monitored on a native gel and by the addition of formate and MV<sub>ox</sub>, which turned blue upon oxidation of formate to CO<sub>2</sub> (**Figure 12**). In addition, the activity of FdhA towards CO<sub>2</sub> production was verified by FTIR spectroscopy.

Although the experimental data are only preliminary, the addition of formate with ferricyanide as an artificial electron acceptor generated the typical signals for CO<sub>2</sub> (**Figure 12**). It is important to note that under these assay conditions, according to the findings from Dr. Sven Stripp, FdhA dissociated from HytA and can produce CO<sub>2</sub> in the absence of the hydrogenase. It appears that FdhA forms a rather loose association with the rest of the complex, as I have also observed this behavior when the complex becomes too dilute or under certain purification conditions. For example, at higher concentrations of ammonium sulfate ((NH<sub>4</sub>)<sub>2</sub>SO<sub>4</sub>), FdhA is lost, and only the

Hyt complex can be obtained. Trying stabilizing the complex through crosslinkers under mild conditions would be worthwhile.

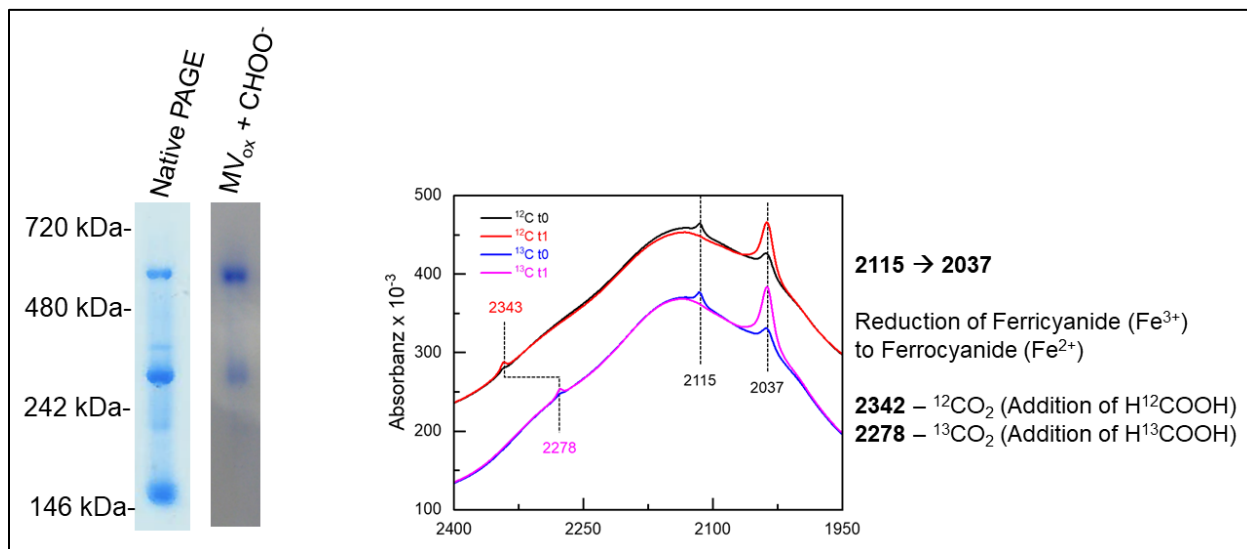


**Figure 12. Characterization of FdhA from *C. autoethanogenum*.** Left panel: Native gel of the purified Hyt/Fdh complex, which forms three different oligomeric states. The right gel shows the activity of FdhA indicated by the blue dye from reduced MV. Right panel: FTIR spectra of the W-dependent FdhA active site.

FTIR spectroscopy provided valuable information about the nature of the [FeFe] hydrogenase and the activity of FdhA, but to obtain a global picture of the overall architecture and the reaction mechanism of the complex, a structure is required. In collaboration with Dr. Jan Schuller, who elucidated the structure of HDCR from *T. kivui*<sup>129</sup>, and his PhD student Tristan Reiftrau, I obtained the first preliminary cryo-electron microscopy structure of the partial Hyt/Fdh complex (**Figure 13**). With the advent of AlphaFold, a deep learning-based protein structure prediction system, it is now possible to accurately predict the 3D structure of proteins from their amino acid sequences<sup>177</sup>. The predicted Hyt/FdhA complex superposes well with the preliminary cryo-EM structure of HytA-E<sub>1,2</sub> but without FdhA. It appears that despite testing different cross-linking agents (such as bis(sulfosuccinimidyl)suberat (BS3) and glutaraldehyde) and multiple enzyme concentrations (final concentrations on the grid: 0.5 mg ml<sup>-1</sup>, 1.25 mg ml<sup>-1</sup>, 1.5 mg ml<sup>-1</sup>, and 2.5 mg ml<sup>-1</sup>) of fresh and unfrozen, as well as frozen Hyt/Fdh, it was not possible to obtain sufficient images of the whole complex. The best result was obtained with the unfrozen Hyt/Fdh sample with a final concentration of 1.5 mg ml<sup>-1</sup>, which had been cross-linked with 5 mM BS3.

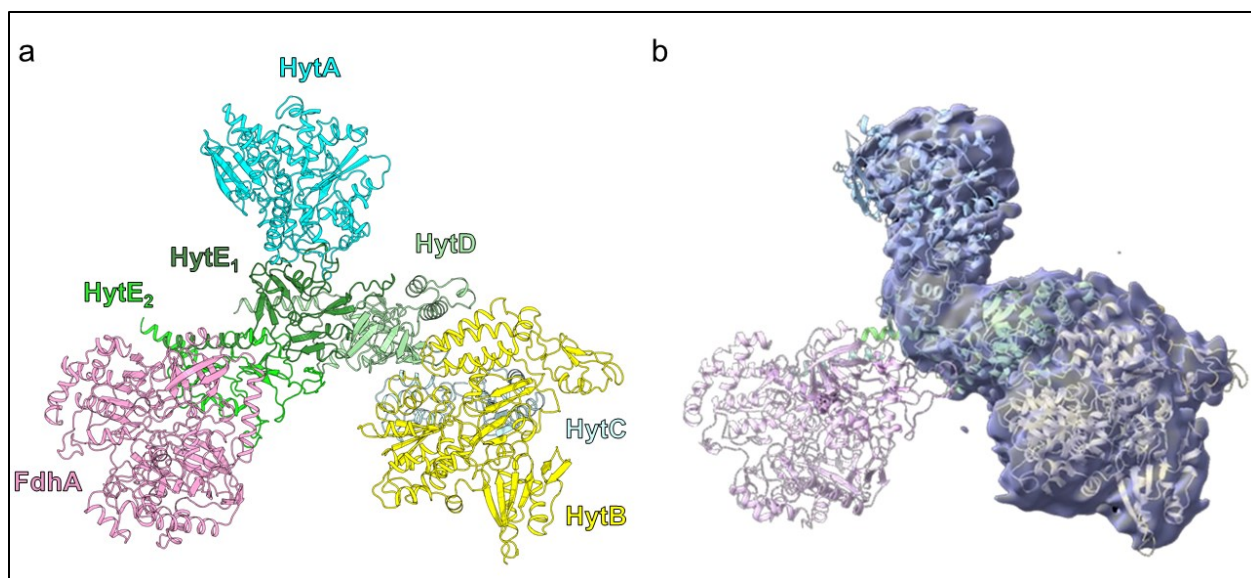


**Figure 13. Structural organization of Hyt/Fdh.** **a**, The AlphaFold predicted model of Hyt/Fdh in cartoon representation. Each subunit is indicated by a different color and labeled with the same color code. **b**, The partial cryo-EM structure of HytA-E<sub>1,2</sub> in transparent surface representation, superposed to the AlphaFold predicted model.

For the next purification of Hyt/Fdh, it would be worthwhile to cross-link the complex immediately after the last purification step, or even before if size exclusion chromatography is performed, to avoid that dilution of the complex leads to its dissociation. One of the biggest challenges for further characterization of Hyt/Fdh is to stabilize the complex without creating artifacts and to find better storage conditions, as the complex has been shown to disassemble over time. Based on the organization of the predicted model and the preliminary cryo-EM structure of Hyt/Fdh, it can be predicted that the complex is likely to form filaments, as observed in HDCR<sup>129,178</sup>. However, to obtain detailed information on the electron flow of the complex and whether Hyt/Fdh forms filaments that also arrange in ring-shaped superstructures, a high-resolution cryo-EM structure of Hyt/Fdh as well as tomography on *C. autoethanogenum* cells is required.

During the purification of Hyt/Fdh, I purified a highly expressed 2x[4Fe4S]-cluster containing ferredoxin (OVY50687) from *C. autoethanogenum*. For this ferredoxin, a midpoint potential of -320 mV was determined via electron paramagnetic resonance (EPR) spectroscopy in collaboration with Prof. Dr. Antonio J. Pierik (Kaiserslautern University, Germany). EPR spectroscopy is a technique that detects and analyses the behavior of unpaired electrons in a magnetic field,

providing insight into the electronic structure and properties of paramagnetic species. Based on the expression levels, this is likely to be the ferredoxin used by the Hyt/Fdh complex and may be useful for further biochemical studies. For example, it would be valuable to test whether CO-fuelled CO<sub>2</sub> fixation can be performed *in vitro*. As we can purify the CODH, Hyt/Fdh, ferredoxin, and the formate-tetrahydrofolate synthetase (Fts) natively in our laboratory, it would be theoretically possible to set up an assay in which the addition of CO, oxidized ferredoxin, NADPH, ATP, and tetrahydrofolate (H<sub>4</sub>F) should result in the production of formyl-tetrahydrofolate (HCO-H<sub>4</sub>F, avoid formate inhibition). Three reaction products could be followed over the reaction: HCO-H<sub>4</sub>F by high-performance liquid chromatography (HPLC), the production of inorganic phosphate (P<sub>i</sub>) using the malachite green kit, and NADPH oxidation by spectrophotometry (**Figure 14**). This assay would demonstrate the powerful bioconversion capabilities of *C. autoethanogenum* enzymes and a proof of concept of an *in vitro* CO<sub>2</sub>-fixation module from CO.

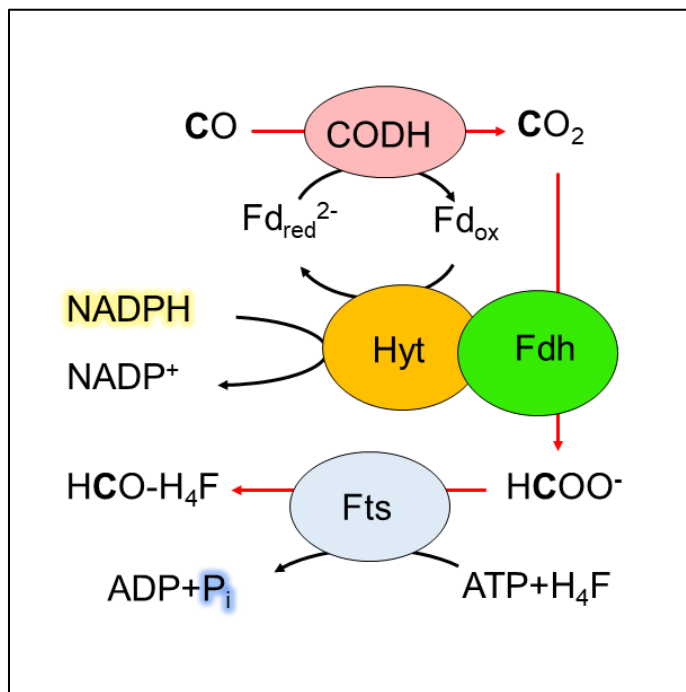


**Figure 14. Scheme of CO-fueled CO<sub>2</sub> fixation assay.** The products that can be measured besides HCO-H<sub>4</sub>F are highlighted by a glow.

Although more work is needed to fully understand the oligomeric state and the molecular mechanism of Hyt/Fdh, the astounding CO<sub>2</sub> fixation abilities of acetogens are already being transferred to other model organisms to generate more whole-cell biocatalysts for CO<sub>2</sub> capture and H<sub>2</sub> storage. Recently, the successful production of HDCR from *A. woodii* in *E. coli* was demonstrated<sup>179</sup>. Recombinant expression of this enzyme complex transforms *E. coli* into a biocatalyst capable of hydrogen-driven CO<sub>2</sub> reduction without the need for external cofactors or endogenous enzymes<sup>179</sup>.

## 8.5 Concluding remarks

In summary, my thesis has explored various aspects of the metabolisms employed by anaerobic energy-limited microbes, including sulfate and sulfite reduction, H<sub>2</sub> production, and CO<sub>2</sub> fixation strategies, providing valuable insights into fundamental biological processes and potential applications. I was the first to show how a methanogen assimilates SO<sub>4</sub><sup>2-</sup>, and by deciphering the individual enzymes in the pathway, I discovered a new type of PAPS reductase and an archaeal PAP phosphatase. Structural and biochemical insights of the last enzyme of the pathway, the F<sub>420</sub>-dependent sulfite reductase, detailed its reaction centers and electronic pathway while providing new details on the evolution of sulfite reductases. From the same organism, we obtained the first F<sub>420</sub>-reducing [NiFeSe] hydrogenase structure as well as the first structure of an F<sub>420</sub>-reducing [NiFe] hydrogenase from a *Methanococcales*, fueling Fsr with electrons via the F<sub>420</sub>. The structural and spectroscopic analyses confirm previous findings but also describe new features of the [NiFe] hydrogenase, such as a new oligomeric state and subtle differences in the active site while characterizing the different [NiFe] redox states. In addition to the assimilatory sulfate reduction pathway of a methanogen, this work also describes the structures of the main cytosolic dissimilatory enzymes of a bacterium isolated from an enrichment culture. The first structure of an ATP sulfurylase from an SRB was obtained, which forms a complex with a small protein of unknown function and oligomerizes in a previously unseen manner. The purification of MCR from *Methanotherix* directly from activated wastewater treatment sludge was further proof of the concept that it is possible to obtain X-ray structures from environmental samples by targeting highly expressed candidates. By reviewing the structurally characterized CO<sub>2</sub>-fixation machinery of

methanogens, we were able to highlight common features and differences between hydrogenotrophic methanogens and autotrophic acetogens. This knowledge allowed me to study the Hyt/Fdh complex and gain the first preliminary insights into the organization of this seven-subunit complex.

With this thesis, I hope to have shown that energy-limited anaerobic microorganisms are indeed a treasure trove for the discovery of new enzymes that have the potential to help us move closer to a carbon-neutral and sustainable society.





## References for Introduction and Discussion

- 1 Müller, V. New horizons in acetogenic conversion of one-carbon substrates and biological hydrogen storage. *Trends in Biotechnology* **37**, 1344-1354, doi:10.1016/j.tibtech.2019.05.008 (2019).
- 2 Rand, D. A. J. & Dell, R. M. *Hydrogen energy: challenges and prospects*. (The Royal Society of Chemistry, 2007).
- 3 Fukuzumi, S. Bioinspired energy conversion systems for hydrogen production and storage. *Eur. J. Inorg. Chem.* **2008**, 1351-1362, doi:10.1002/ejic.200701369 (2008).
- 4 Sordakis, K. *et al.* Homogeneous catalysis for sustainable hydrogen storage in formic acid and alcohols. *Chemical reviews* **118**, 372-433, doi:10.1021/acs.chemrev.7b00182 (2018).
- 5 Joó, F. Breakthroughs in hydrogen storage—formic acid as a sustainable storage material for hydrogen. *ChemSusChem* **1**, 805-808, doi:10.1002/cssc.200800133 (2008).
- 6 Schaaf, T., Grünig, J., Schuster, M. R., Rothenfluh, T. & Orth, A. Methanation of CO<sub>2</sub> - storage of renewable energy in a gas distribution system. *Energy, Sustainability and Society* **4**, 2, doi:10.1186/s13705-014-0029-1 (2014).
- 7 Martin, M. R., Fornero, J. J., Stark, R., Mets, L. & Angenent, L. T. A single-culture bioprocess of *Methanothermobacter thermautotrophicus* to upgrade digester biogas by CO<sub>2</sub>-to-CH<sub>4</sub> conversion with H<sub>2</sub>. *Archaea* **2013**, 157529, doi:10.1155/2013/157529 (2013).
- 8 Heffernan, J. K. *et al.* Enhancing CO<sub>2</sub>-valorization using *Clostridium autoethanogenum* for sustainable fuel and chemicals production. *Frontiers in bioengineering and biotechnology* **8**, 204, doi:10.3389/fbioe.2020.00204 (2020).
- 9 Carr, S. & Buan, N. R. Insights into the biotechnology potential of *Methanosarcina*. *Front Microbiol* **13**, 1034674, doi:10.3389/fmicb.2022.1034674 (2022).
- 10 Wolfe, J. M. & Fournier, G. P. Horizontal gene transfer constrains the timing of methanogen evolution. *Nature Ecology & Evolution* **2**, 897-903, doi:10.1038/s41559-018-0513-7 (2018).
- 11 Weiss, M. C. *et al.* The physiology and habitat of the last universal common ancestor. *Nat Microbiol* **1**, 16116, doi:10.1038/nmicrobiol.2016.116 (2016).
- 12 Fuchs, G. Alternative pathways of carbon dioxide fixation: insights into the early evolution of life? *Annual review of microbiology* **65**, 631-658, doi:10.1146/annurev-micro-090110-102801 (2011).

- 13 Schuchmann, K. & Müller, V. Autotrophy at the thermodynamic limit of life: a model for energy conservation in acetogenic bacteria. *Nature Reviews Microbiology* **12**, 809-821, doi:10.1038/nrmicro3365 (2014).
- 14 Hoehler, T. M. & Jørgensen, B. B. Microbial life under extreme energy limitation. *Nature Reviews Microbiology* **11**, 83-94, doi:10.1038/nrmicro2939 (2013).
- 15 Thauer, R. K., Kaster, A.-K., Seedorf, H., Buckel, W. & Hedderich, R. Methanogenic archaea: ecologically relevant differences in energy conservation. *Nature Reviews Microbiology* **6**, 579-591, doi:10.1038/nrmicro1931 (2008).
- 16 Müller, V. & Frerichs, J. in *Encyclopedia of Life Sciences* (John Wiley & Sons Ltd, Chichester, UK, 2013).
- 17 Barton, L. L. & Fauque, G. D. Biochemistry, physiology and biotechnology of sulfate-reducing bacteria. *Advances in applied microbiology* **68**, 41-98, doi:10.1016/s0065-2164(09)01202-7 (2009).
- 18 Thauer, R. K., Jungermann, K. & Decker, K. Energy conservation in chemotrophic anaerobic bacteria. *Bacteriological reviews* **41**, 100-180, doi:10.1128/br.41.1.100-180.1977 (1977).
- 19 Karlson, B., Bellavitis, C. & France, N. Commercializing LanzaTech, from waste to fuel: An effectuation case. *Journal of Management & Organization* **27**, 175-196, doi:10.1017/jmo.2017.83 (2021).
- 20 Bailera, M., Lisbona, P., Romeo, L. M. & Espatolero, S. Power to Gas projects review: Lab, pilot and demo plants for storing renewable energy and CO<sub>2</sub>. *Renewable and Sustainable Energy Reviews* **69**, 292-312, doi:10.1016/j.rser.2016.11.130 (2017).
- 21 Kondaveeti, S., Mohanakrishna, G., Lee, J. K. & Kalia, V. C. Methane as a substrate for energy generation using microbial fuel cells. *Indian journal of microbiology* **59**, 121-124, doi:10.1007/s12088-018-0765-6 (2019).
- 22 Quader, A. K. M. A. Natural gas and the fertilizer industry. *Energy for Sustainable Development* **7**, 40-48, doi:10.1016/S0973-0826(08)60353-1 (2003).
- 23 van Schyndel, J., Goos, E., Naumann, C., Hardi, J. S. & Oswald, M. Effects of compounds in liquefied methane on rocket engine operation. *Aerospace* **9**, 698, doi:10.3390/aerospace9110698 (2022).
- 24 Boucher, O., Friedlingstein, P., Collins, B. & Shine, K. P. The indirect global warming potential and global temperature change potential due to methane oxidation. *Environmental Research Letters* **4**, 044007, doi:10.1088/1748-9326/4/4/044007 (2009).
- 25 Vallero, D. in *Air Pollution Calculations* Ch. 8, (ed Vallero, D.) 175-206 (Elsevier, 2019).

- 26 Ramanathan, V., Cicerone, R. J., Singh, H. B. & Kiehl, J. T. Trace gas trends and their potential role in climate change. **90**, 5547-5566, doi:10.1029/JD090iD03p05547 (1985).
- 27 Berghuis, B. A. *et al.* Hydrogenotrophic methanogenesis in archaeal phylum *Verstraetearchaeota* reveals the shared ancestry of all methanogens. *Proceedings of the National Academy of Sciences of the United States of America* **116**, 5037-5044, doi:10.1073/pnas.1815631116 (2019).
- 28 Vanwonterghem, I. *et al.* Methylotrophic methanogenesis discovered in the archaeal phylum *Verstraetearchaeota*. *Nature Microbiology* **1**, 16170, doi:10.1038/nmicrobiol.2016.170 (2016).
- 29 Evans, P. N. *et al.* Methane metabolism in the archaeal phylum *Bathyarchaeota* revealed by genome-centric metagenomics. *Science (New York, N.Y.)* **350**, 434-438, doi:10.1126/science.aac7745 (2015).
- 30 McKay, L. J. *et al.* Co-occurring genomic capacity for anaerobic methane and dissimilatory sulfur metabolisms discovered in the *Korarchaeota*. *Nature Microbiology* **4**, 614-622, doi:10.1038/s41564-019-0362-4 (2019).
- 31 Borrel, G. *et al.* Comparative genomics highlights the unique biology of *Methanomassiliicoccales*, a *Thermoplasmatales*-related seventh order of methanogenic archaea that encodes pyrrolysine. *BMC Genomics* **15**, 679, doi:10.1186/1471-2164-15-679 (2014).
- 32 Lyu, Z., Shao, N., Akinyemi, T. & Whitman, W. B. Methanogenesis. *Current Biology* **28**, R727-R732, doi:10.1016/j.cub.2018.05.021 (2018).
- 33 Kurth, J. M., Op den Camp, H. J. M. & Welte, C. U. Several ways one goal—methanogenesis from unconventional substrates. *Applied Microbiology and Biotechnology* **104**, 6839-6854, doi:10.1007/s00253-020-10724-7 (2020).
- 34 Lang, K. *et al.* New mode of energy metabolism in the seventh order of methanogens as revealed by comparative genome analysis of “*Candidatus* methanoplasma termitum”. *Appl Environ Microbiol* **81**, 1338-1352, doi:10.1128/aem.03389-14 (2015).
- 35 Kristjansson, J. K., Schönheit, P. & Thauer, R. K. Different K<sub>s</sub> values for hydrogen of methanogenic bacteria and sulfate reducing bacteria: An explanation for the apparent inhibition of methanogenesis by sulfate. *Archives of Microbiology* **131**, 278-282, doi:10.1007/BF00405893 (1982).
- 36 Shima, S., Huang, G., Wagner, T. & Ermler, U. Structural basis of hydrogenotrophic methanogenesis. *Annual review of microbiology* **74**, 713-733, doi:10.1146/annurev-micro-011720-122807 (2020).
- 37 Katayama, T. & Kamagata, Y. in *Hydrocarbon and lipid microbiology protocols: isolation and cultivation* (eds Terry J. McGenity, Kenneth N. Timmis, & Balbina Nogales) 177-195 (Springer Berlin Heidelberg, 2017).

- 38 Canfield, D. E., Habicht, K. S. & Thamdrup, B. The Archean sulfur cycle and the early history of atmospheric oxygen. *Science (New York, N.Y.)* **288**, 658-661, doi:10.1126/science.288.5466.658 (2000).
- 39 Eser, B. E., Zhang, X., Chanani, P. K., Begley, T. P. & Ealick, S. E. From suicide enzyme to catalyst: The iron-dependent sulfide transfer in *Methanococcus jannaschii* thiamin thiazole biosynthesis. *J Am Chem Soc* **138**, 3639-3642, doi:10.1021/jacs.6b00445 (2016).
- 40 Rauch, B. J. & Perona, J. J. Efficient sulfide assimilation in *Methanosarcina acetivorans* is mediated by the MA1715 protein. *Journal of bacteriology* **198**, 1974-1983, doi:10.1128/JB.00141-16 (2016).
- 41 Perona, J. J., Rauch, B. J. & Driggers, C. M. in *Molecular Mechanisms of Microbial Evolution* (ed Rampelotto, P. H.) 371–408 (Springer, 2018).
- 42 Caffrey, S. M. & Voordouw, G. Effect of sulfide on growth physiology and gene expression of *Desulfovibrio vulgaris* Hildenborough. *Antonie van Leeuwenhoek* **97**, 11-20, doi:10.1007/s10482-009-9383-y (2010).
- 43 Jiang, J. *et al.* Hydrogen sulfide—Mechanisms of toxicity and development of an antidote. *Scientific Reports* **6**, 20831, doi:10.1038/srep20831 (2016).
- 44 Payne, D., Spietz, R. L. & Boyd, E. S. Reductive dissolution of pyrite by methanogenic archaea. *ISME J* **15**, 3498-3507, doi:10.1038/s41396-021-01028-3 (2021).
- 45 Daniels, L., Belay, N. & Rajagopal, B. S. Assimilatory reduction of sulfate and sulfite by methanogenic bacteria. *Appl Environ Microbiol* **51**, 703-709, doi:10.1128/AEM.51.4.703-709.1986 (1986).
- 46 Johnson, E. F. & Mukhopadhyay, B. A new type of sulfite reductase, a novel coenzyme F<sub>420</sub>-dependent enzyme, from the methanarchaeon *Methanocaldococcus jannaschii*. *J Biol Chem* **280**, 38776-38786, doi:10.1074/jbc.M503492200 (2005).
- 47 Kuivila, K. M., Murray, J. W., Devol, A. H. & Novelli, P. C. Methane production, sulfate reduction and competition for substrates in the sediments of Lake Washington. *Geochimica et Cosmochimica Acta* **53**, 409-416, doi:10.1016/0016-7037(89)90392-X (1989).
- 48 Sela-Adler, M. *et al.* Co-existence of methanogenesis and sulfate reduction with common substrates in sulfate-rich estuarine sediments. *Frontiers in Microbiology* **8**, doi:10.3389/fmicb.2017.00766 (2017).
- 49 Kristjansson JK, S. P. Why do sulfate-reducing bacteria outcompete methanogenic bacteria for substrates? *Oecologia* **60(2):264-266**, doi:10.1007/BF00379530 (1983).
- 50 Balderston, W. L. & Payne, W. J. Inhibition of methanogenesis in salt marsh sediments and whole-cell suspensions of methanogenic bacteria by nitrogen oxides. *Appl Environ Microbiol* **32**, 264-269, doi:10.1128/aem.32.2.264-269.1976 (1976).

- 51 Fink, C. *et al.* A shuttle-vector system allows heterologous gene expression in the thermophilic methanogen *Methanothermobacter thermautotrophicus*  $\Delta$ H. *mBio* **12**, e02766-02721, doi:10.1128/mBio.02766-21 (2021).
- 52 Pereira, I. A. *et al.* A comparative genomic analysis of energy metabolism in sulfate reducing bacteria and archaea. *Front Microbiol* **2**, 69, doi:10.3389/fmicb.2011.00069 (2011).
- 53 Yu, H. *et al.* Comparative genomics and proteomic analysis of assimilatory sulfate reduction pathways in anaerobic methanotrophic archaea. *Front Microbiol* **9**, 2917, doi:10.3389/fmicb.2018.02917 (2018).
- 54 Cho, M. K. Discovery of novel 3'-phosphoadenosine-5'-phosphosulfate (PAPS) reductase from methanarcheon *Methanocaldococcus jannaschii*. (Baylor University, 2013).
- 55 Lee, J. S. *et al.* Discovery of a novel adenosine 5'-phosphosulfate (APS) reductase from the methanarcheon *Methanocaldococcus jannaschii*. *Process Biochemistry* **46**, 154-161, doi:10.1016/j.procbio.2010.08.004 (2011).
- 56 Buckel, W. & Thauer, R. K. Energy conservation via electron bifurcating ferredoxin reduction and proton/Na<sup>+</sup> translocating ferredoxin oxidation. *Biochimica et Biophysica Acta (BBA) - Bioenergetics* **1827**, 94-113, doi:10.1016/j.bbabi.2012.07.002 (2013).
- 57 Grinter, R. & Greening, C. Cofactor F<sub>420</sub>: an expanded view of its distribution, biosynthesis and roles in bacteria and archaea. *FEMS Microbiology Reviews* **45**, doi:10.1093/femsre/fuab021 (2021).
- 58 Greening, C. *et al.* Physiology, biochemistry, and applications of F<sub>420</sub>- and F<sub>o</sub>-dependent redox reactions. *Microbiol Mol Biol Rev* **80**, 451-493, doi:10.1128/MMBR.00070-15 (2016).
- 59 Borrel, G. *et al.* Phylogenomic data support a seventh order of methylotrophic methanogens and provide insights into the evolution of methanogenesis. *Genome biology and evolution* **5**, 1769-1780, doi:10.1093/gbe/evt128 (2013).
- 60 Thauer, R. *et al.* Hydrogenases from methanogenic archaea, nickel, a novel cofactor, and H<sub>2</sub> storage. *Annual review of biochemistry* **79**, 507-536, doi:10.1146/annurev.biochem.030508.152103 (2010).
- 61 Cheng, N. *et al.* Platinum single-atom and cluster catalysis of the hydrogen evolution reaction. *Nature Communications* **7**, 13638, doi:10.1038/ncomms13638 (2016).
- 62 Ilina, Y. *et al.* X-ray crystallography and vibrational spectroscopy reveal the key determinants of biocatalytic dihydrogen cycling by [NiFe] hydrogenases. *Angew. Chem. Int. Ed.* **58**, 18710-18714, doi:10.1002/anie.201908258 (2019).
- 63 Lubitz, W., Ogata, H., Rüdiger, O. & Reijerse, E. Hydrogenases. *Chemical reviews* **114**, 4081-4148, doi:10.1021/cr4005814 (2014).

- 64 Ogo S., *et al.* [NiFe], [FeFe], and [Fe] hydrogenase models from isomers. *Sci. Adv.* **6**, eaaz8181, doi:10.1126/sciadv.aaz8181 (2020)
- 65 Watanabe, T. *et al.* The bacterial [Fe]-hydrogenase paralog HmdII uses tetrahydrofolate derivatives as substrates. *Angew. Chem. Int. Ed.* **58**, 3506-3510, doi:doi.org/10.1002/anie.201813465 (2019).
- 66 Vignais, P. M. & Billoud, B. Occurrence, classification, and biological function of hydrogenases: an overview. *Chemical reviews* **107**, 4206-4272, doi:10.1021/cr050196r (2007).
- 67 Wombwell, C., Caputo, C. A. & Reisner, E. [NiFeSe]-hydrogenase chemistry. *Accounts of Chemical Research* **48**, 2858-2865, doi:10.1021/acs.accounts.5b00326 (2015).
- 68 Huang, G., Wagner, T., Ermler, U. & Shima, S. Methanogenesis involves direct hydride transfer from H<sub>2</sub> to an organic substrate. *Nature Reviews Chemistry* **4**, 213-221, doi:10.1038/s41570-020-0167-2 (2020).
- 69 Vitt, S. *et al.* The F<sub>420</sub>-reducing [NiFe]-hydrogenase complex from *Methanothermobacter marburgensis*, the first X-ray structure of a group 3 family member. *J Mol Biol* **426**, 2813-2826, doi:10.1016/j.jmb.2014.05.024 (2014).
- 70 Hidalgo, R., Ash, P. A., Healy, A. J. & Vincent, K. A. Infrared spectroscopy during electrocatalytic turnover reveals the Ni-L active site state during H<sub>2</sub> oxidation by a NiFe hydrogenase. *Angew. Chem. Int. Ed.* **54**, 7110-7113, doi:10.1002/anie.201502338 (2015).
- 71 Jones, W. J., Leigh, J. A., Mayer, F., Woese, C. R. & Wolfe, R. S. *Methanococcus jannaschii* sp. nov., an extremely thermophilic methanogen from a submarine hydrothermal vent. *Archives of Microbiology* **136**, 254-261, doi:10.1007/BF00425213 (1983).
- 72 Heryakusuma, C. *et al.* A reduced F<sub>420</sub>-dependent nitrite reductase in an anaerobic methanotrophic archaeon. *Journal of bacteriology* **204**, e0007822, doi:10.1128/jb.00078-22 (2022).
- 73 Heryakusuma, C., Johnson, E. F., Purwantini, E. & Mukhopadhyay, B. Nitrite reductase activity in F<sub>420</sub>-dependent sulfite reductase (Fsr) from *Methanocaldococcus jannaschii*. *Access Microbiol* **5**(4)doi:10.1099/acmi.0.000482.v2 (2023).
- 74 Bourbonnais, A., Lehmann, M. F., Butterfield, D. A. & Juniper, S. K. Subseafloor nitrogen transformations in diffuse hydrothermal vent fluids of the Juan de Fuca Ridge evidenced by the isotopic composition of nitrate and ammonium. *Geochem. Geophys. Geosyst.* **13**, doi:10.1029/2011GC003863 (2012).
- 75 Cao, H. *et al.* Microbial sulfur cycle in two hydrothermal chimneys on the Southwest Indian Ridge. *mBio* **5**, 10.1128/mbio.00980-00913, doi:10.1128/mbio.00980-13 (2014).

- 76 Susanti, D. & Mukhopadhyay, B. An intertwined evolutionary history of methanogenic archaea and sulfate reduction. *PLoS One* **7**, doi:10.1371/journal.pone.0045313 (2012).
- 77 Staley, J. & Reysenbach, a.-l. Biodiversity of microbial life: foundation of Earth's biosphere. *Molecules* **8**, doi:10.3390/80200223 (2003).
- 78 Muyzer, G. & Stams, A. J. The ecology and biotechnology of sulphate-reducing bacteria. *Nat Rev Microbiol* **6**, 441-454, doi:10.1038/nrmicro1892 (2008).
- 79 Jørgensen, B. B., Findlay, A. J. & Pellerin, A. The biogeochemical sulfur cycle of marine sediments. *Front. Microbiol.* **10**, doi:10.3389/fmicb.2019.00849 (2019).
- 80 Weber, A. & Jørgensen, B. B. Bacterial sulfate reduction in hydrothermal sediments of the Guaymas Basin, Gulf of California, Mexico. *Deep Sea Research Part I: Oceanographic Research Papers* **49**, 827-841, doi:10.1016/S0967-0637(01)00079-6 (2002).
- 81 Jørgensen, B. B. Mineralization of organic matter in the sea bed—the role of sulphate reduction. *Nature* **296**, 643-645, doi:10.1038/296643a0 (1982).
- 82 Wenk, C. B., Wing, B. A. & Halevy, I. Electron carriers in microbial sulfate reduction inferred from experimental and environmental sulfur isotope fractionations. *The ISME Journal* **12**, 495-507, doi:10.1038/ismej.2017.185 (2018).
- 83 Marietou, A., Roy, H., Jorgensen, B. B. & Kjeldsen, K. U. Sulfate transporters in dissimilatory sulfate reducing microorganisms: A comparative genomics analysis. *Front Microbiol* **9**, 309, doi:10.3389/fmicb.2018.00309 (2018).
- 84 Hocking, W. P., Stokke, R., Roalkvam, I. & Steen, I. H. Identification of key components in the energy metabolism of the hyperthermophilic sulfate-reducing archaeon *Archaeoglobus fulgidus* by transcriptome analyses. *Front Microbiol* **5**, 95, doi:10.3389/fmicb.2014.00095 (2014).
- 85 Neumann, S., Wynen, A., Trüper, H. G. & Dahl, C. Characterization of the *cys* gene locus from *Allochromatium vinosum* indicates an unusual sulfate assimilation pathway. *Molecular Biology Reports* **27**, 27-33, doi:10.1023/A:1007058421714 (2000).
- 86 Rabus, R. *et al.* in *Advances in Microbial Physiology* Vol. 66 (ed Robert K. Poole) 55-321 (Academic Press, 2015).
- 87 Chartron, J. *et al.* Substrate recognition, protein dynamics, and iron-sulfur cluster in *Pseudomonas aeruginosa* adenosine 5'-phosphosulfate reductase. *Journal of Molecular Biology* **364**, 152-169, doi:10.1016/j.jmb.2006.08.080 (2006).
- 88 Crane, B. R. & Getzoff, E. D. The relationship between structure and function for the sulfite reductases. *Current opinion in structural biology* **6**, 744-756, doi:10.1016/s0959-440x(96)80003-0 (1996).

- 89 Knittel, K., Lösekann, T., Boetius, A., Kort, R. & Amann, R. Diversity and distribution of methanotrophic archaea at cold seeps. *Appl Environ Microbiol.* **71**, 467-479, doi:10.1128/AEM.71.1.467-479.2005 (2005).
- 90 Knittel, K. & Boetius, A. Anaerobic oxidation of methane: progress with an unknown process. *Annual review of microbiology* **63**, 311-334, doi:10.1146/annurev.micro.61.080706.093130 (2009).
- 91 Hallam, S. J. *et al.* Reverse methanogenesis: Testing the hypothesis with environmental genomics. *Science* **305**, 1457-1462, doi:10.1126/science.1100025 (2004).
- 92 Scheller, S., Yu, H., Chadwick, G. L., McGlynn, S. E. & Orphan, V. J. Artificial electron acceptors decouple archaeal methane oxidation from sulfate reduction. *Science* **351**, 703-707, doi:10.1126/science.aad7154 (2016).
- 93 Haroon, M. F. *et al.* Erratum: Anaerobic oxidation of methane coupled to nitrate reduction in a novel archaeal lineage. *Nature* **501**, 578-578, doi:10.1038/nature12619 (2013).
- 94 Ettwig, K. F. *et al.* Archaea catalyze iron-dependent anaerobic oxidation of methane. *Proceedings of the National Academy of Sciences of the United States of America* **113**, 12792-12796, doi:10.1073/pnas.1609534113 (2016).
- 95 Cai, C. *et al.* A methanotrophic archaeon couples anaerobic oxidation of methane to Fe(III) reduction. *The ISME Journal* **12**, 1929-1939, doi:10.1038/s41396-018-0109-x (2018).
- 96 Chang, Y.-H. *et al.* Microbial methane cycling in a terrestrial mud volcano in eastern Taiwan. *Environ Microbiol.* **14**, 895-908, doi:10.1111/j.1462-2920.2011.02658.x (2012).
- 97 Grossman, E. L., Cifuentes, L. A. & Cozzarelli, I. M. Anaerobic methane oxidation in a landfill-leachate plume. *Environmental Science & Technology* **36**, 2436-2442, doi:10.1021/es015695y (2002).
- 98 Crowe, S. A. *et al.* The methane cycle in ferruginous Lake Matano. *Geobiology.* **9**, 61-78, doi:10.1111/j.1472-4669.2010.00257.x (2011).
- 99 Sivan, O. *et al.* Geochemical evidence for iron-mediated anaerobic oxidation of methane. *Limnol. Oceanogr.* **56**, 1536-1544, doi:10.4319/lo.2011.56.4.1536 (2011).
- 100 Martens, C. S. & Berner, R. A. Methane production in the interstitial waters of sulfate-depleted marine sediments. *Science* **185**, 1167-1169, doi:10.1126/science.185.4157.1167 (1974).
- 101 Reeburgh, W. S. Methane consumption in Cariaco Trench waters and sediments. *Earth and Planetary Science Letters* **28**, 337-344, doi:10.1016/0012-821X(76)90195-3 (1976).
- 102 Hahn, C. J. *et al.* Crystal structure of a key enzyme for anaerobic ethane activation. *Science* **373**, 118-121, doi:10.1126/science.abg1765 (2021).



- 103 Laso-Pérez, R. *et al.* Thermophilic archaea activate butane via alkyl-coenzyme M formation. *Nature* **539**, 396-401, doi:10.1038/nature20152 (2016).
- 104 Zehnle, H. *et al.* *Candidatus* Alkanophaga archaea from Guaymas Basin hydrothermal vent sediment oxidize petroleum alkanes. *Nature Microbiology* **8**, doi:10.1038/s41564-023-01400-3 (2023).
- 105 Lemaire, O. N. & Wagner, T. A structural view of alkyl-coenzyme M reductases, the first step of alkane anaerobic oxidation catalyzed by archaea. *Biochemistry* **61**, 805-821, doi:10.1021/acs.biochem.2c00135 (2022).
- 106 Sørensen, K. B., Finster, K. & Ramsing, N. B. Thermodynamic and kinetic requirements in anaerobic methane oxidizing consortia exclude hydrogen, acetate, and methanol as possible electron shuttles. *Microbial ecology* **42**, 1-10, doi:10.1007/s002480000083 (2001).
- 107 Nauhaus, K., Boetius, A., Krüger, M. & Widdel, F. *In vitro* demonstration of anaerobic oxidation of methane coupled to sulphate reduction in sediment from a marine gas hydrate area. *Environmental microbiology* **4**, 296-305, doi:10.1046/j.1462-2920.2002.00299.x (2002).
- 108 Wegener, G., Krukenberg, V., Riedel, D., Tegetmeyer, H. E. & Boetius, A. Intercellular wiring enables electron transfer between methanotrophic archaea and bacteria. *Nature* **526**, 587-590, doi:10.1038/nature15733 (2015).
- 109 Milucka, J. *et al.* Zero-valent sulphur is a key intermediate in marine methane oxidation. *Nature* **491**, 541-546, doi:10.1038/nature11656 (2012).
- 110 Krukenberg, V. *et al.* *Candidatus* Desulfofervidus auxilii, a hydrogenotrophic sulfate-reducing bacterium involved in the thermophilic anaerobic oxidation of methane. *Environmental microbiology* **18**, 3073-3091, doi:10.1111/1462-2920.13283 (2016).
- 111 Krukenberg, V. *et al.* Gene expression and ultrastructure of meso- and thermophilic methanotrophic consortia. *Environmental microbiology* **20**, 1651-1666, doi:10.1111/1462-2920.14077 (2018).
- 112 Nauhaus, K., Albrecht, M., Elvert, M., Boetius, A. & Widdel, F. *In vitro* cell growth of marine archaeal-bacterial consortia during anaerobic oxidation of methane with sulfate. *Environmental microbiology* **9**, 187-196, doi:10.1111/j.1462-2920.2006.01127.x (2007).
- 113 Hahn, C. J. *et al.* "*Candidatus* Ethanoperedens", a thermophilic genus of *Archaea* mediating the anaerobic oxidation of ethane. *mBio* **11**, e00600-00620, doi:10.1128/mBio.00600-20 (2020).
- 114 Chen, L. *et al.* Improvement of direct interspecies electron transfer via adding conductive materials in anaerobic digestion: mechanisms, performances, and challenges. *Frontiers in Microbiology* **13**, doi:10.3389/fmicb.2022.860749 (2022).

- 115 Smith, K. S. & Ingram-Smith, C. *Methanosaeta*, the forgotten methanogen? *Trends Microbiol* **15**, 150-155, doi:10.1016/j.tim.2007.02.002 (2007).
- 116 Zhu, J. *et al.* The genome characteristics and predicted function of methyl-group oxidation pathway in the obligate acetoclastic methanogens, *Methanosaeta* spp. *PLOS ONE* **7**, e36756, doi:10.1371/journal.pone.0036756 (2012).
- 117 Vítězová, M., Kohoutová, A., Vítěz, T., Hanišáková, N. & Kushkevych, I. Methanogenic microorganisms in industrial wastewater anaerobic treatment. *Processes* **8**, 1546, doi:10.3390/pr8121546 (2020).
- 118 Holmes, D. E. *et al.* Metatranscriptomic evidence for direct interspecies electron transfer between *Geobacter* and *Methanothrix* species in methanogenic rice paddy soils. *Applied and Environmental Microbiology* **83**, e00223-00217, doi:10.1128/AEM.00223-17 (2017).
- 119 Rotaru, A.-E. *et al.* A new model for electron flow during anaerobic digestion: direct interspecies electron transfer to *Methanosaeta* for the reduction of carbon dioxide to methane. *Energy & Environmental Science* **7**, 408-415, doi:10.1039/C3EE42189A (2014).
- 120 Shima, S. *et al.* Structure of a methyl-coenzyme M reductase from Black Sea mats that oxidize methane anaerobically. *Nature* **481**, 98-101, doi:10.1038/nature10663 (2012).
- 121 Goubeaud, M., Schreiner, G. & Thauer, R. K. Purified methyl-coenzyme-M reductase is activated when the enzyme-bound coenzyme F<sub>430</sub> is reduced to the nickel(I) oxidation state by titanium(III) citrate. *Eur J Biochem.* **243**, 110-114, doi:10.1111/j.1432-1033.1997.00110.x (1997).
- 122 Rowe, A. *et al.* Sediment disturbance negatively impacts methanogen abundance but has variable effects on total methane emissions. *Frontiers in Microbiology* **13**, doi:10.3389/fmicb.2022.796018 (2022).
- 123 Fung Min, L., Michael, K. p. & Séan Dennis, S. in *Liquid, Gaseous and Solid Biofuels* (ed Fang Zhen) Ch. 5 (IntechOpen, 2013).
- 124 Ragsdale, S. W. & Pierce, E. Acetogenesis and the Wood-Ljungdahl pathway of CO<sub>2</sub> fixation. *Biochimica et biophysica acta* **1784**, 1873-1898, doi:10.1016/j.bbapap.2008.08.012 (2008).
- 125 Berg, I. A. *et al.* Autotrophic carbon fixation in archaea. *Nature Reviews Microbiology* **8**, 447-460, doi:10.1038/nrmicro2365 (2010).
- 126 Sousa, F. L. *et al.* Early bioenergetic evolution. *Philosophical transactions of the Royal Society of London. Series B, Biological sciences* **368**, 20130088, doi:10.1098/rstb.2013.0088 (2013).
- 127 Wimmer, J. L. E. *et al.* Energy at origins: favorable thermodynamics of biosynthetic reactions in the Last Universal Common Ancestor (LUCA). *Frontiers in Microbiology* **12**, doi:10.3389/fmicb.2021.793664 (2021).

- 128 Basen, M., Geiger, I., Henke, L. & Müller, V. A genetic system for the thermophilic acetogenic bacterium *Thermoanaerobacter kivui*. *Appl Environ Microbiol* **84**, doi:10.1128/aem.02210-17 (2018).
- 129 Dietrich, H. M. *et al.* Membrane-anchored HDCR nanowires drive hydrogen-powered CO<sub>2</sub> fixation. *Nature* **607**, 823-830, doi:10.1038/s41586-022-04971-z (2022).
- 130 Mock, J. *et al.* Energy conservation associated with ethanol formation from H<sub>2</sub> and CO<sub>2</sub> in *Clostridium autoethanogenum* involving electron bifurcation. *Journal of bacteriology* **197**, 2965-2980, doi:10.1128/jb.00399-15 (2015).
- 131 Wang, S. *et al.* NADP-specific electron-bifurcating [FeFe]-hydrogenase in a functional complex with formate dehydrogenase in *Clostridium autoethanogenum* grown on CO. *Journal of bacteriology* **195**, 4373-4386, doi:10.1128/jb.00678-13 (2013).
- 132 Abrini, J., Naveau, H. & Nyns, E.-J. *Clostridium autoethanogenum*, sp. nov., an anaerobic bacterium that produces ethanol from carbon monoxide. *Archives of Microbiology* **161**, 345-351, doi:10.1007/BF00303591 (1994).
- 133 Lemaire, O. N. & Wagner, T. Gas channel rerouting in a primordial enzyme: Structural insights of the carbon-monoxide dehydrogenase/acetyl-CoA synthase complex from the acetogen *Clostridium autoethanogenum*. *Biochimica et Biophysica Acta (BBA) - Bioenergetics* **1862**, 148330, doi:10.1016/j.bbabi.2020.148330 (2021).
- 134 de Lima, L. A. *et al.* Faster growth enhances low carbon fuel and chemical production through gas fermentation. *Frontiers in bioengineering and biotechnology* **10**, doi:10.3389/fbioe.2022.879578 (2022).
- 135 Valgepea, K. *et al.* H<sub>2</sub> drives metabolic rearrangements in gas-fermenting *Clostridium autoethanogenum*. *Biotechnology for Biofuels* **11**, 55, doi:10.1186/s13068-018-1052-9 (2018).
- 136 Nwaokorie, U. J. *et al.* Deletion of genes linked to the C1-fixing gene cluster affects growth, by-products, and proteome of *Clostridium autoethanogenum*. *Frontiers in bioengineering and biotechnology* **11**, doi:10.3389/fbioe.2023.1167892 (2023).
- 137 Mitchell, P. The protonmotive Q cycle: a general formulation. *FEBS Lett.* **59**, 137-139, doi:10.1016/0014-5793(75)80359-0 (1975).
- 138 Buckel, W. & Thauer, R. K. Flavin-based electron bifurcation, ferredoxin, flavodoxin, and anaerobic respiration with protons (Ech) or NAD<sup>+</sup> (Rnf) as electron acceptors: a historical review. *Frontiers in Microbiology* **9**, doi:10.3389/fmicb.2018.00401 (2018).
- 139 Peters, J. W., Beratan, D. N., Schut, G. J. & Adams, M. W. W. On the nature of organic and inorganic centers that bifurcate electrons, coupling exergonic and endergonic oxidation–reduction reactions. *Chemical Communications* **54**, 4091-4099, doi:10.1039/C8CC01530A (2018).

- 140 Peters, J. W., Miller, A. F., Jones, A. K., King, P. W. & Adams, M. W. Electron bifurcation. *Curr Opin Chem Biol* **31**, 146-152, doi:10.1016/j.cbpa.2016.03.007 (2016).
- 141 Baymann, F. *et al.* On the natural history of flavin-based electron bifurcation. *Frontiers in Microbiology* **9**, doi:10.3389/fmicb.2018.01357 (2018).
- 142 Demmer, J. K. *et al.* Insights into flavin-based electron bifurcation via the NADH-dependent reduced ferredoxin:NADP oxidoreductase structure. *J Biol Chem* **290**, 21985-21995, doi:10.1074/jbc.M115.656520 (2015).
- 143 Buckel, W. & Thauer, R. K. Flavin-based electron bifurcation, a new mechanism of biological energy coupling. *Chemical reviews* **118**, 3862-3886, doi:10.1021/acs.chemrev.7b00707 (2018).
- 144 Katsyv, A. *et al.* Molecular basis of the electron bifurcation mechanism in the [FeFe]-hydrogenase complex HydABC. *Journal of the American Chemical Society* **145**, 5696-5709, doi:10.1021/jacs.2c11683 (2023).
- 145 Schuchmann, K., Chowdhury, N. P. & Müller, V. Complex multimeric [FeFe] hydrogenases: biochemistry, physiology and new opportunities for the hydrogen economy. *Frontiers in Microbiology* **9**, doi:10.3389/fmicb.2018.02911 (2018).
- 146 Schuchmann, K. & Müller, V. Direct and reversible hydrogenation of CO<sub>2</sub> to formate by a bacterial carbon dioxide reductase. *Science* **342**, 1382-1385, doi:10.1126/science.1244758 (2013).
- 147 del Barrio, M. *et al.* Interaction of the H-cluster of FeFe hydrogenase with halides. *Journal of the American Chemical Society* **140**, 5485-5492, doi:10.1021/jacs.8b01414 (2018).
- 148 Schuchmann, K. & Müller, V. A bacterial electron-bifurcating hydrogenase. *J Biol Chem* **287**, 31165-31171, doi:10.1074/jbc.M112.395038 (2012).
- 149 Ceccaldi, P., Schuchmann, K., Müller, V. & Elliott, S. J. The hydrogen dependent CO<sub>2</sub> reductase: the first completely CO tolerant FeFe-hydrogenase. *Energy & Environmental Science* **10**, 503-508, doi:10.1039/C6EE02494G (2017).
- 150 Stetter, K. O. & Gaag, G. Reduction of molecular sulphur by methanogenic bacteria. *Nature* **305**, 309-311, doi:10.1038/305309a0 (1983).
- 151 Liu, Y., Beer, L. L. & Whitman, W. B. Methanogens: a window into ancient sulfur metabolism. *Trends Microbiol* **20**, 251-258, doi:10.1016/j.tim.2012.02.002 (2012).
- 152 Rajagopal, B. S. & Daniels, L. Investigation of mercaptans, organic sulfides, and inorganic sulfur compounds as sulfur sources for the growth of methanogenic bacteria. *Current Microbiology* **14**, 137-144, doi:10.1007/BF01568365 (1986).

- 153 Bryant, M. P., Tzeng, S. F., Robinson, I. M. & Joyner, A. E., Jr. in *Anaerobic Biological Treatment Processes* Vol. 105 *Advances in Chemistry* Ch. 3, 23-40 (AMERICAN CHEMICAL SOCIETY, 1971).
- 154 Setya, A., Murillo, M. & Leustek, T. Sulfate reduction in higher plants: Molecular evidence for a novel 5'-adenylylsulfate reductase. *Proceedings of the National Academy of Sciences of the United States of America* **93**, 13383-13388, doi:10.1073/pnas.93.23.13383 (1996).
- 155 Lyu, Z. & Whitman, W. B. Transplanting the pathway engineering toolbox to methanogens. *Current Opinion in Biotechnology* **59**, 46-54, doi:10.1016/j.copbio.2019.02.009 (2019).
- 156 Susanti, D., Frazier, M. C. & Mukhopadhyay, B. A genetic system for *Methanocaldococcus jannaschii*: An evolutionary deeply rooted hyperthermophilic methanarchaeon. *Front Microbiol* **10**, doi:10.3389/fmicb.2019.01256 (2019).
- 157 Huber, H., Thomm, M., König, H., Thies, G. & Stetter, K. O. *Methanococcus thermolithotrophicus*, a novel thermophilic lithotrophic methanogen. *Archives of Microbiology* **132**, 47-50, doi:10.1007/BF00690816 (1982).
- 158 Habicht, K. S., Gade, M., Thamdrup, B., Berg, P. & Canfield, D. E. Calibration of sulfate levels in the Archean ocean. *Science* **298**, 2372-2374, doi:10.1126/science.1078265 (2002).
- 159 Shen, Y., Buick, R. & Canfield, D. E. Isotopic evidence for microbial sulphate reduction in the early Archean era. *Nature* **410**, 77-81, doi:10.1038/35065071 (2001).
- 160 Liu, Y.-F. *et al.* Genomic and transcriptomic evidence supports methane metabolism in *Archaeoglobi*. *mSystems* **5**, 10.1128/msystems.00651-00619, doi:10.1128/msystems.00651-19 (2020).
- 161 Maslač, N., Sidhu, C., Teeling, H. & Wagner, T. Comparative transcriptomics sheds light on remodeling of gene expression during diazotrophy in the thermophilic methanogen *Methanothermococcus thermolithotrophicus*. *mBio* **13**, e02443-02422, doi:10.1128/mbio.02443-22 (2022).
- 162 Moreno-Vivián, C., Cabello, P., Martínez-Luque, M., Blasco, R. & Castillo, F. Prokaryotic nitrate reduction: molecular properties and functional distinction among bacterial nitrate reductases. *J Bacteriol.* **181**, 6573-6584, doi:10.1128/jb.181.21.6573-6584.1999 (1999).
- 163 Belay, N., Jung, K.-Y., Rajagopal, B. S., Kremer, J. D. & Daniels, L. Nitrate as a sole nitrogen source for *Methanococcus thermolithotrophicus* and its effect on growth of several methanogenic bacteria. *Current Microbiology* **21**, 193-198, doi:10.1007/BF02092121 (1990).
- 164 Stroupe, M. E. & Getzoff, E. D. in *Tetrapyrroles: Birth, Life and Death* (eds Martin J. Warren & Alison G. Smith) 375-389 (Springer New York, 2009).

- 165 Marques, M. C., Coelho, R., Pereira, I. A. C. & Matias, P. M. Redox state-dependent changes in the crystal structure of [NiFeSe] hydrogenase from *Desulfovibrio vulgaris* Hildenborough. *International Journal of Hydrogen Energy* **38**, 8664-8682, doi:10.1016/j.ijhydene.2013.04.132 (2013).
- 166 Barbosa, T. M., Baltazar, C. S. A., Cruz, D. R., Lousa, D. & Soares, C. M. Studying O<sub>2</sub> pathways in [NiFe]- and [NiFeSe]-hydrogenases. *Scientific Reports* **10**, 10540, doi:10.1038/s41598-020-67494-5 (2020).
- 167 Marques, M. C. *et al.* The direct role of selenocysteine in [NiFeSe] hydrogenase maturation and catalysis. *Nature Chemical Biology* **13**, 544-550, doi:10.1038/nchembio.2335 (2017).
- 168 Valente, F. M. *et al.* Selenium is involved in regulation of periplasmic hydrogenase gene expression in *Desulfovibrio vulgaris* Hildenborough. *Journal of bacteriology* **188**, 3228-3235, doi:10.1128/jb.188.9.3228-3235.2006 (2006).
- 169 Mukhopadhyay, B., Johnson, E. F. & Wolfe, R. S. Reactor-scale cultivation of the hyperthermophilic methanarchaeon *Methanococcus jannaschii* to high cell densities. *Appl Environ Microbiol* **65**, 5059-5065, doi:10.1128/AEM.65.11.5059-5065.1999 (1999).
- 170 Rothe, O. & Thomm, M. A simplified method for the cultivation of extreme anaerobic Archaea based on the use of sodium sulfite as reducing agent. *Extremophiles* **4**, 247-252, doi:10.1007/PL00010716 (2000).
- 171 Cline, J. D. Spectrophotometric determination of hydrogen sulfide in natural waters *Limnology and Oceanography* **14**, 454-458, doi:org/10.4319/lo.1969.14.3.0454 (1969).
- 172 Whitman, W. B. in *Bergey's manual of systematics of archaea and bacteria*. (eds M.E. Trujillo, S. Dedysh, P. DeVos, B. Hedlund, P. Kämpfer, F.A. Rainey and W.B. Whitman) 1-9 (2015).
- 173 Escudeiro, P., Henry, C. S. & Dias, R. P. M. Functional characterization of prokaryotic dark matter: the road so far and what lies ahead. *Current Research in Microbial Sciences* **3**, 100159, doi:10.1016/j.crmicr.2022.100159 (2022).
- 174 Wittkamp, F., Senger, M., Stripp, S. T. & Apfel, U. P. [FeFe]-Hydrogenases: recent developments and future perspectives. *Chemical Communications* **54**, 5934-5942, doi:10.1039/C8CC01275J (2018).
- 175 Raaijmakers, H. C. A. & Romão, M. J. Formate-reduced *E. coli* formate dehydrogenase H: the reinterpretation of the crystal structure suggests a new reaction mechanism. *JBIC Journal of Biological Inorganic Chemistry* **11**, 849-854, doi:10.1007/s00775-006-0129-2 (2006).
- 176 Raaijmakers, H. *et al.* Gene sequence and the 1.8 Å crystal structure of the tungsten-containing formate dehydrogenase from *Desulfovibrio gigas*. *Structure* **10**, 1261-1272, doi:10.1016/s0969-2126(02)00826-2 (2002).

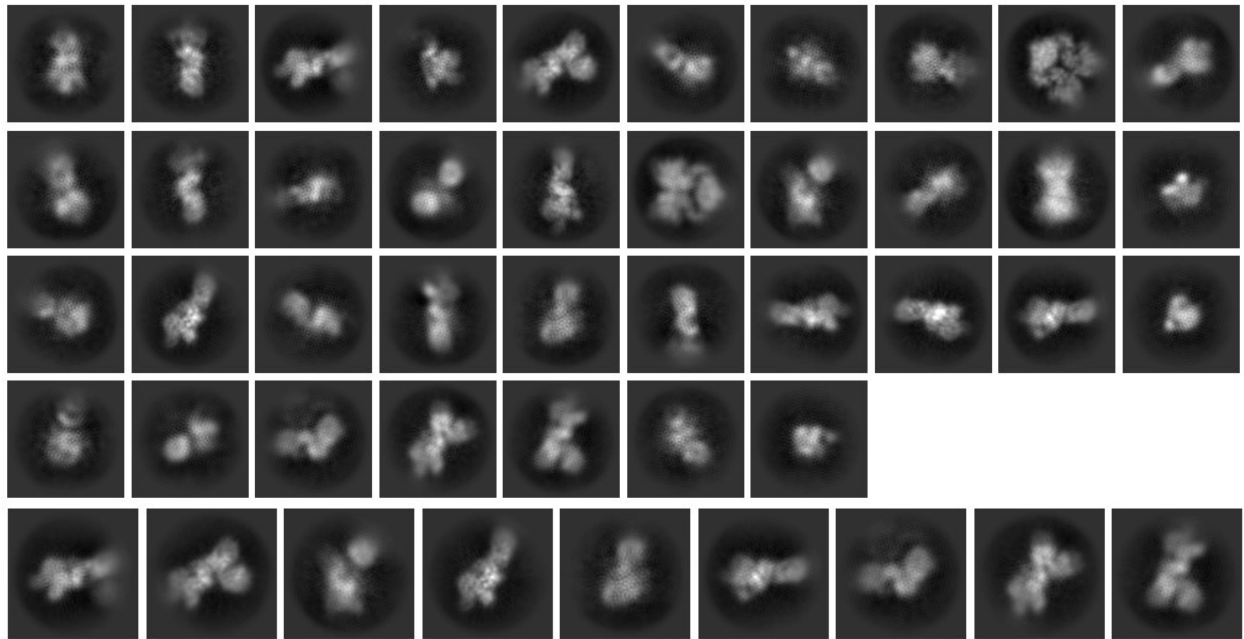
- 177 Jumper, J. *et al.* Highly accurate protein structure prediction with AlphaFold. *Nature* **596**, 583-589, doi:10.1038/s41586-021-03819-2 (2021).
- 178 Schuchmann, K., Vonck, J. & Müller, V. A bacterial hydrogen-dependent CO<sub>2</sub> reductase forms filamentous structures. *The FEBS Journal* **283**, 1311-1322, doi:10.1111/febs.13670 (2016).
- 179 Leo, F., Schwarz, F. M., Schuchmann, K. & Müller, V. Capture of carbon dioxide and hydrogen by engineered *Escherichia coli*: hydrogen-dependent CO<sub>2</sub> reduction to formate. *Applied Microbiology and Biotechnology* **105**, 5861-5872, doi:10.1007/s00253-021-11463-z (2021).



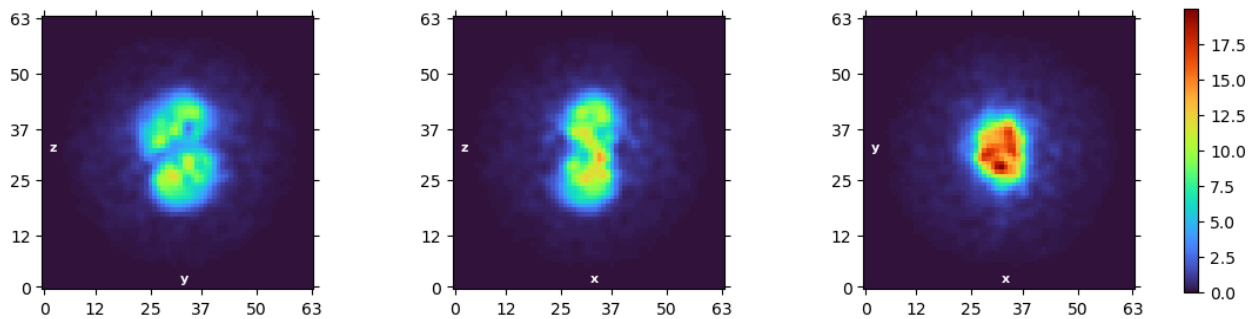
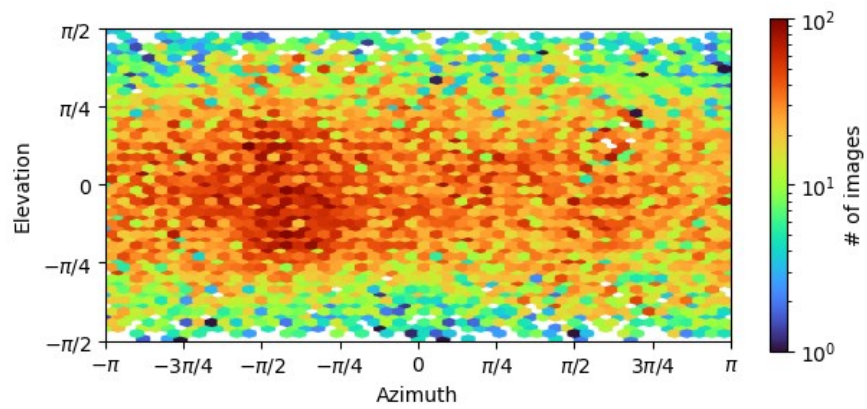


# Appendix

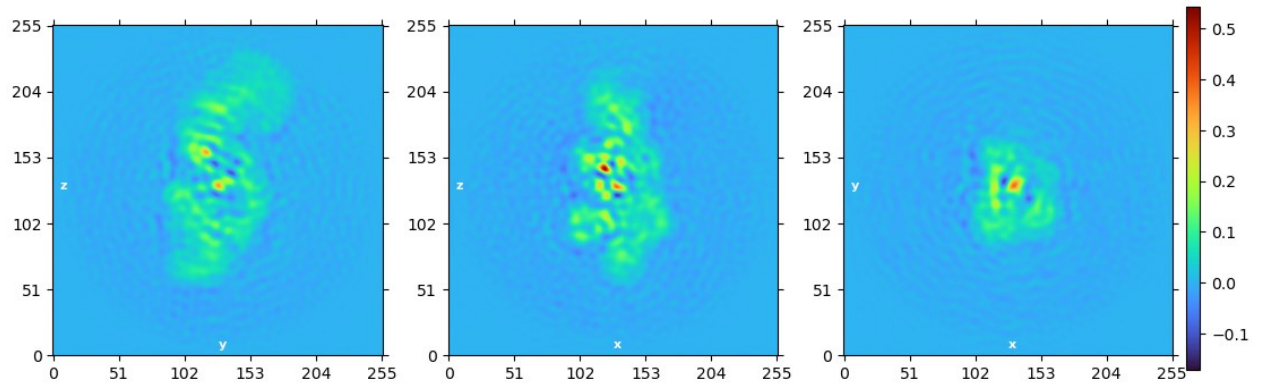
## Selected 2D classes of Hyt/Fdh from *C. autoethanogenum*



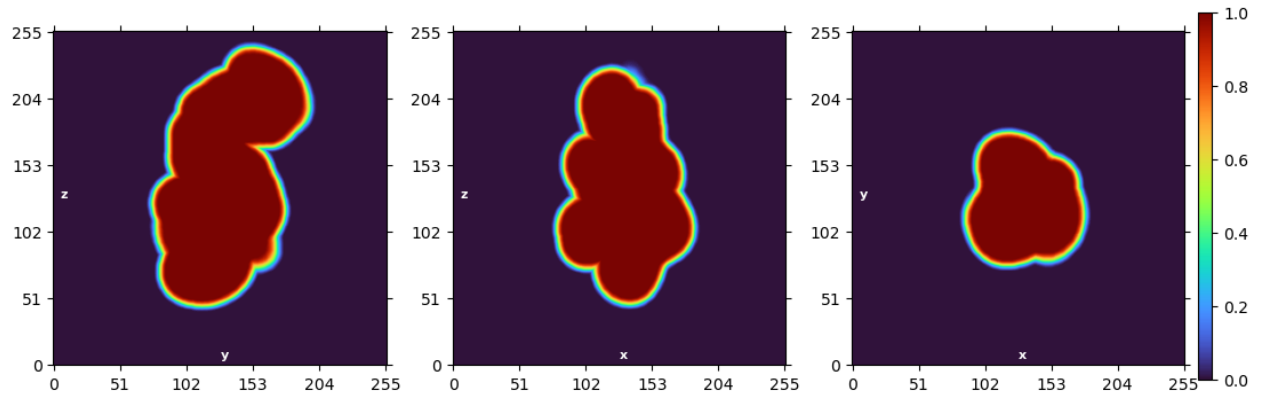
## 3D *ab initio*



### Real space slices iteration



### Real space mask iteration



# Acknowledgements

Firstly, I would like to thank PD. Dr. Christiane Dahl, Prof. Dr. Inês Cardoso Pereira and Dr. Tristan Wagner for agreeing to review this thesis and to be a part of my examination committee. I would also like to thank Prof. Dr. Rudolf Amann, Dr. Olivier Lemaire and Mustafa Rasim Törer for agreeing to be members of my examination board.

My greatest thanks to Dr. Tristan Wagner for welcoming me to the Microbial Metabolism Group and for his dedicated supervision throughout my PhD. Not only has he supported, advised and guided me throughout this thesis, but given me the opportunity and means to study what I became truly passionate about. Your passion for science is truly contagious and I have learnt a lot from you in these past years.

A big thank you to the Microbial Metabolism group, a great team where everyone was always willing to help each other. In particular, I would like to thank Dr. Olivier Lemaire, to whom I could always turn to for valuable feedback and help. Additionally, I extend my heartfelt thanks to Ramona Appel and Christina Probian for their tremendous help in the laboratory - this work would have been impossible without your aid and support.

I am also incredibly grateful to all of the collaborators and colleagues who have contributed to and supported me in the research presented in this thesis. In particular, I would like to thank Prof. Dr. Antonio Pierik and Dr. Jan Schuller for welcoming me into their laboratory and introducing me to new techniques, as well as their welcoming and supportive students.

A big thanks to PD. Dr. Christiane Dahl, Prof. Dr. Inês Cardoso Pereira, Prof. Dr. Jens Harder, Prof. Dr. Rudolf Amann, Prof. Ulrich Ermler, Prof. Silke Leimkühler, Dr. Dirk de Beer and Dr. Sven Stripp for helpful suggestions and discussions during my thesis advisory committee meetings.

Many thanks to Paloma Garrido Amador, Nevena Maslač, Marie-Caroline Müller and Darjan Gande for proofreading this thesis.

I would like to thank the MPG and DFG for founding my research. I am privileged because I had the opportunity to be a member of the SPP 1927 program “Iron-Sulfur for Life”, founded by the DFG, where I met inspiring researchers followed by many stimulating scientific discussions.

In addition, I want to thank everyone behind the MarMic program and especially my MarMic class. It has been a life changing experience and I am grateful to have been a part of it.

My PhD would not have been possible without the incredible support of great friends during those years. I want to thank the Bremen crew for the many fun parties, travels, spiritual support and overall great company! A special thanks to Coraline for being a loving and supportive friend and for many great bouldering and climbing afternoons.

I don't have enough words to thank Nevena, Paloma and Darjan - you made my time in Bremen special and unforgettable. Nevena, thank you for being twins to the end and for the endless coffee breaks. Darjan, thanks for fun trips with bed bug hunting and margarita nights. Paloma, thank you for epic boxing sessions and to more summits to hike. I will be forever grateful for the amazing and empowering friendship that we have and to all the memories, we share.

Oliver, vielen Dank für alles - besonders dafür, dass ich immer auf dich zählen kann.

Of course one of my biggest thanks goes to my family. Mama, Papa, Claudia, Sam, Katrin, Dan, Annelie, Simon, Björn, Ylenia, Jaron und Mina - ohne eure ständige Unterstützung wäre ich nicht hier. Ich danke euch, dass ihr immer an mich glaubt und mir immer wieder klarmacht, was wichtig ist und für mich da seid!

**Declaration on the contribution of the candidate to a multi-author article/manuscript  
which is included as a chapter in the submitted doctoral thesis**

**Chapter: 2**

**Contribution of the candidate in % of the total work load (up to 100% for each of the following categories):**

Experimental concept and design:	ca. <u>70%</u>
Experimental work and/or acquisition of (experimental) data:	ca. <u>90%</u>
Data analysis and interpretation:	ca. <u>70%</u>
Preparation of Figures and Tables:	ca. <u>70%</u>
Drafting of the manuscript:	ca. <u>70%</u>

**Chapter: 3**

**Contribution of the candidate in % of the total work load (up to 100% for each of the following categories):**

Experimental concept and design:	ca. <u>30%</u>
Experimental work and/or acquisition of (experimental) data:	ca. <u>50%</u>
Data analysis and interpretation:	ca. <u>50%</u>
Preparation of Figures and Tables:	ca. <u>60%</u>
Drafting of the manuscript:	ca. <u>70%</u>

**Chapter: 4**

**Contribution of the candidate in % of the total work load (up to 100% for each of the following categories):**

Experimental concept and design:	ca. <u>70%</u>
Experimental work and/or acquisition of (experimental) data:	ca. <u>80%</u>
Data analysis and interpretation:	ca. <u>70%</u>
Preparation of Figures and Tables:	ca. <u>70%</u>

### **Chapter: 5**

**Contribution of the candidate in % of the total work load (up to 100% for each of the following categories):**

Experimental concept and design:	ca. <u>50%</u>
Experimental work and/or acquisition of (experimental) data:	ca. <u>50%</u>
Data analysis and interpretation:	ca. <u>70%</u>
Preparation of Figures and Tables:	ca. <u>80%</u>
Drafting of the manuscript:	ca. <u>70%</u>

### **Chapter: 6**

**Contribution of the candidate in % of the total work load (up to 100% for each of the following categories):**

Experimental concept and design:	ca. <u>50%</u>
Experimental work and/or acquisition of (experimental) data:	ca. <u>60%</u>
Data analysis and interpretation:	ca. <u>60%</u>
Preparation of Figures and Tables:	ca. <u>20%</u>
Drafting of the manuscript:	ca. <u>10%</u>

### **Chapter: 7**

**Contribution of the candidate in % of the total work load (up to 100% for each of the following categories):**

Experimental concept and design:	ca. <u>NA</u>
Experimental work and/or acquisition of (experimental) data:	ca. <u>NA</u>
Data analysis and interpretation:	ca. <u>30%</u>
Preparation of Figures and Tables:	ca. <u>20%</u>
Drafting of the manuscript:	ca. <u>30%</u>

**We declare that all authors of these manuscripts have been informed on and did not object to the listed contributions of the candidate as author.**

## Versicherung an Eides Statt

Ich, Marion Jespersen

versichere an Eides Statt durch meine Unterschrift, dass ich die vorstehende Arbeit selbständig und ohne fremde Hilfe angefertigt und alle Stellen, die ich wörtlich dem Sinne nach aus Veröffentlichungen entnommen habe, als solche kenntlich gemacht habe, mich auch keiner anderen als der angegebenen Literatur oder sonstiger Hilfsmittel bedient habe.

Ich versichere an Eides Statt, dass ich die vorgenannten Angaben nach bestem Wissen und Gewissen gemacht habe und dass die Angaben der Wahrheit entsprechen und ich nichts verschwiegen habe.

Die Strafbarkeit einer falschen eidesstattlichen Versicherung ist mir bekannt, namentlich die Strafandrohung gemäß § 156 StGB bis zu drei Jahren Freiheitsstrafe oder Geldstrafe bei vorsätzlicher Begehung der Tat bzw. gemäß § 161 Abs. 1 StGB bis zu einem Jahr Freiheitsstrafe oder Geldstrafe bei fahrlässiger Begehung.

---

Ort, Datum / Unterschrift